STRONG MICROWAVES IN PLASMAS

Volume 2

Institute of Applied Physics
Nizhny Novgorod 1991

Academy of Science of the USSR
Institute of Applied Physics

STRONG MICROWAVES IN PLASMAS

PROCEEDINGS OF THE
INTERNATIONAL WORKSHOP
Suzdal, 18 - 23 September 1990

Edited by
A.G. Litvak

In two volumes
Volume 2

Nizhny Novgorod 1991

Nonlinear processes in plasmas /Theory and microwave experiment/

CONTENTS OF VOLUME 2

Nonlinear processes in plasmas /Theory and microwave experiment/

V.I.Arkhipenko, E.Z.Gusakov, A.N.Savel'ev 501
Coherent parametric phenomena in an inhomogeneous plasma

N.A.Bogatov, M.S.Gitlin, A.G.Litvak, A.G.Luchinin, G.S.Nusinovich 520
Phase conjugation of millimeter-wave radiation by degenerate four-wave mixing in saturable -absorbing media

H.Schlüter 525
Spectroscopic determination of RF field strengths

D.M.Karfidov, K.F.Sergeichev, I.A.Sychov 541
Effective electron collision frequency in plasma with driven strong Langmuir turbulence

G.M.Fraiman, I.Yu.Kostyukov 547
Langmuir soliton damping and pumping by the electron beam

G.M.Batanov, V.A.Ivanov, M.E.Konyzhev, A.A.Ravaev, V.D.Seleznev, A.I.Khomenko 553
Generation of high potentials in the plasma by the interaction with intense microwave radiation

L.M.Gorbunov, A.N.Moskalev 559
Numerical investigation of beat-wave electron acceleration in inhomogeneous plasmas

A.M.Sergeev, E.V.Vanin. 575
Nonlinear dynamics of ultrashort electromagnetic pulses in plasmas

S.V.Bulanov, V.I.Kirsanov, A.S.Sakharov 595
The theory of ultrarelativistic plasma wake excitation by short laser pulses

S.V.Bulanov, V.I.Kirsanov, A.S.Sakharov 615
On the maximum field of the relativistically strong Langmuir wake-wave

V.A.Buts, I.I.Lapidus, S.S.Moiseev, O.G.Chkhetiani 621
Fluctuations, chaos and auto-oscillations in plasma wave systems

T.A.Gryaznova, E.G.Filonenko, I.P.Shashurin 634
The influence of electron density profile on the antenna self-mathing effect with microwave discharge

M.Lontano, N.Lunin. 639
Propagation of electromagnetic waves
in a modulated density plasma

V.P.Silin, S.A.Uryupin 645
Elecromagnetic field cyclotron absorption
in a turbulent plasma

V.Yu.Bychenkov, V.N.Novikov, V.P.Silin, 651
V.T.Tikhonchuk
On the transformation of the energy anisotropy
of electrons into the electromagnetic energy
of pulsations

S.I.Popel, V.N.Tsytovich 656
On increase of efficiency of plasma heating
by an electron beam generating RF waves

S.I.Popel, V.N.Tsytovich 660
New theory of the "spectral gap" filling in
the generation process of currents driven by
strong RF lower-hybrid waves

Zh.Kiss' ovski, A.Shivarova 665
Effect of the high-frequency field in the
drift wave instability

V.V.Gulenko, V.V.Gushchin 669
On nonlinear interaction of high-frequency
and low-frequency waves in confined plasma

Development of high - power microwave sources

A.V.Gaponov, M.I.Petelin 677
High-power high-frequency classical electronics: status, trends and problems

H.Jory, K.Felch, C.Hess, H.Huey, E.Jongewaard, J.Neilson, R.Pendleton, M.Tsirulnikov 693
Millimeter-wave, megawatt gyrotron development for ECR heating applications

K.Kreischer, T.Grimm, W.Guss, R.Temkin, K.Y.Xu 713
Research at MIT on high frequency gyrotrons for ECRH

V.E.Zapevalov, A.N.Kuftin 726
Powerful 80 - 150 GHz gyrotrons

T.Nagashima, K.Sakamoto, S.Maebara, M.Tsuneoka, Y.Okazaki, K.Hayashi, S.Miyake, T.Kariya, Y.Mitsunaka, Y.Itoh, T.Sugawara, T.Okamoto 739
Test results of 0.5 MW gyrotron at 120 GHz and 1.5 MW at 2 GHz klystron for fusion applications

G.Mourier 751
Current gyrotron development at Thomson Tubes Electroniques

V.I.Kurbatov, S.A.Malygin, E.G.Vasilyev 765
Commercial gyrotrons for thermonuclear investigations

I.I.Antakov, L.A.Aksenova, E.V.Zasypkin, M.A.Moiseev, L.G.Popov, E.V.Sokolov, V.K.Yulpatov 773
Multi-cavity phase-locked gyrotrons for low-hybrid heating in toroidal plasmas

I.I.Antakov, E.V.Zasypkin, A.P.Keyer, V.S.Musatov, V.E.Mjasnikov, E.V.Sokolov 779
Microwave device for low-hybrid heating of toroidal plasmas

L.A.Aksenova, V.V.Alikaev, V.E.Zapevalov, V.I.Il'in, V.N.Il'in, A.P.Keyer, A.N.Kuftin V.E.Myasnikov, V.A.Flyagin, V.A.Khmara 783
The development of 140 GHz, 1MW CW gyrotrons for ITER

M.Thumm 791
Electrodynamic systems for mode conversion, transmission and diagnostics of high-power millimeter- wave radiation

The CRPP/ABB Quasi Optical Gyrotron Development Group presented by M.Q.Tran 812
Quasi-optical gyrotron development at the CRPP

E.Borie, G.Dammertz, O.Dumbrajs, G.Gantenbein, T.Geist, G.Hochschild, M.Kuntze, I.Mobius, H.-U.Nickel, B.Piosczyk, M Thumm 832
High power 140 Ghz Gyrortrons at KfK

O.Dumbrajs, O.A.Elnor 847
Mode selection for a frequency step-tunable gyrotron

Sh.E.Tsimring 853
Axisymmetrical resonators, waveguide tapers and mode transformers for gyrotrons

Y.Aso, J.J.Barroso, P.J.Castro, R.A.Correa, G.O.Ludwig, A.Montes, M.C.A.Nono, J.O.Rossi 859
35 GHz gyrotron construction at INPE

V.M.Bykov, V.P.Gubanov, A.V.Rostov, S.D.Korovin, G.A.Mesyats, S.D.Polevin, V.V.Rostov, A.M.Roitman 866
Relativistic pulse-periodic microwave oscillators

I.A.Selivanov, A.V.Fedotov, A.G.Shkvarunets 872
The excitation of fundamental mode of coaxial plasma slow-down structure of a PCM-amplifier

N.I.Karbushev, A.S.Shlapakovskii 878
A theory of the dielectric Cherenkov maser with a high-current hollow relativistic electron beam

V.L.Bratman 884
Cyclotron autoresonance masers

I.Alexeff, M.Rader, F. Dyer 903
A Review of the Development of the Orbitron MASER

A.N.Didenko, V.I.Rashchikov 909
High power microwave generation mechanism in virtual cathode system with anode plasma

K.G.Kostov, N.A.Nikolov, I.P.Spassovsky, J.N.Velichkov, V.A.Spassov 914
An excitation of transverse electric (TE) modes in magnetized vircator system

T.J.Orzechowski 921
Intense microwave generation using free-electron lasers

G.P.Gallerano 938
High power high efficiency mm-wave FEL for ECRH in plasma

N.S.Ginzburg 954
Optical guiding and superradiance effects in spatial localized ensembles of electron - oscillators

N.I.Karbushev, A.D.Shatkus 974
Canalization of radiation by transversely bounded beam-plasma slab

V.I.Miroshnichenko, Ya.B.Fainberg 980
Stimulated scattering of an extraordinary electromagnetic wave by an electron beam in a magnetized plasma

COHERENT PARAMETRIC PHENOMENA IN AN INHOMOGENEOUS PLASMA

Arhipenko V.I., Gusakov E.Z., Savel'ev A.N.
A.F.Ioffe Physical-Technical Institute
Leningrad, USSR
Institute of Physics
Minsk, USSR

INTRODUCTION

In the presence of a strong microwave a plasma is parametrically unstable. According to a conventional viewpoint, the instability leads to excitation of a large number of degrees of freedom and converts plasma into a turbulent state, which is characterized by wide spectra of excited waves (Ref.1,2). The random phase hypothesis, acceptable under these assumptions, enables to average out dynamic wave equations and get kinetic wave equations describing spectrum energy evolution. Phase correlations and, more generally, coherent phenomena which are so important, for instance, in nonlinear optics, are supposed negligible in this approach. The weak turbulence theory based on this approximation was developed at first for homogeneous plasma and then generalized for inhomogeneous and nonstationary plasma (Ref.3). At first sight, the theory of decay parametric instability in an inhomogeneous plasma gives good reasons for such a generalization. Actually, according to Ref.4-6. the effect of convective losses of parametrically excited waves from the narrow three-wave resonance region leads to both increase of parametric phenomena threshold and modification of their nature. Exponential growth of plasma wave amplitudes in an inhomogeneous plasma saturates in a linear approximation (Ref.7,8). Thus, in the vicinity of the resonant point $\mathbf{x} = \mathbf{x}_d$, where the decay condition $\mathbf{k}_0(\mathbf{x}_d) = \mathbf{k}_1(\mathbf{x}_d)+\mathbf{k}_2(\mathbf{x}_d)$ is fulfilled, only the convective, spatial amplification of thermal noises takes place and no "real" instability is excited. The physical reason for such a stabilization is the absence of waves returning back into the decay region even a small part of convectively lost energy. The spatial amplification is described

by a matrix S_{jk} , where the element S_{jk} is equal to the ratio of outgoing (a_k) and incident (a_j) wave amplitudes. Usually, the dependence of the amplification coefficients on frequency and wave vectors is rather smooth, so that in the presence of a pump wave the amplification of wide spectra of noncorrelated plasma noises is predicted. It is quite natural to describe such a turbulent plasma state using the weak turbulence theory.

At the same time, it should be emphasized that excitation of real absolute parametric instability is also possible in an inhomogeneous plasma (Ref.6,9-12). This instability saturates due to nonlinear processes at higher level and gives rise to the spectra of plasma waves, which qualitatively differ from the above mentioned. As a rule, the instability arises if a part of convectively lost energy can return back to the region of three-wave resonance, i.a. if a "feedback loop" appeared. Theoretical analysis shows a number of possibilities for the feedback loop to occur. The simplest among them is realized when decay conditions are fulfilled for a pare of spaced points, and group velocities of daughter waves are opposite Ref.6,9. In this case, the absolute instability mechanism can be clarified using the WKB analysis (Fig.1).

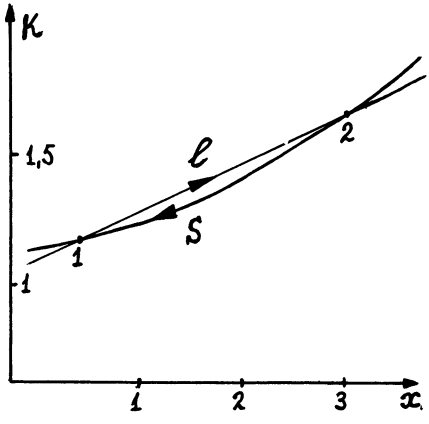

Fig.1 Dispersion curves $k_1(x)$- "1", and k_0-k_s -"s". Arrows show the group velocity directions (dimensionless values)

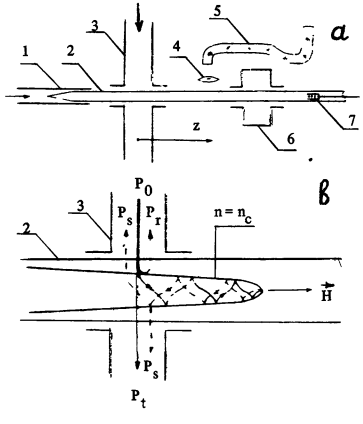

Fig.2 The experimental setup(a) and wave propagation scheme (b) 1-3cm waveguide; 2-glasstube; 3-10cm waveguide; 4,5-optical diagnostics;6-cavity diagnost.; 7-multigrid analyzer

Parametric interaction of **l** and **s** daughter waves is localized in the vicinities of the decay points $\mathbf{x}_{d1}$ and $\mathbf{x}_{d2}$, where spatial wave amplification occurs. Incident "l" wave is amplified by factors $S_{ll}(1)$ and $S_{ll}(2)$ respectively. At the same time, excitation of the other "s" wave is described by the transform coefficients $S_{sl}(1)$ and $S_{sl}(2)$. Due to opposite direction of the daughter wave group velocities the energy of the waves can circulate between the decay points increasing with time, if the transform coefficients are large enough for the following inequality $|S_{ls}(2)\ S_{sl}(1)|>1$ to be satisfied. This temporal energy increase indicates absolute instability excitation. It can be shown that the total amplification of **l** wave incident on the feedback loop is given by

$$S_{ll} = \frac{S_{ll}(1)\ S_{ll}(2)}{1 - S_{ls}(2)\ S_{sl}(1)\ \exp(i\Phi)}, \qquad (1)$$

where $\Phi = \int_{z_{d1}}^{z_{d2}} (\mathbf{k}_{lx} - \mathbf{k}_{sx} - \mathbf{k}_{px})dx + \pi$,

and wave vectors are calculated taking into account absorption of the waves. The threshold and growth rate of the absolute instability can be found from the following equation:

$$1 - S_{ls}(2)\ S_{sl}(1)\ \exp(i\Phi) = 0 \qquad (2)$$

In case of weak absorption of the daughter waves $||\exp(i\Phi)|-1|\ll 1$, the instability threshold is determined by plasma inhomogeneity:

$$|S_{ls}(2)\ S_{sl}(1)| = 1$$

In the opposite case the threshold is determined by balance between pumping and absorption of energy. It should be noted that Eq.(2) which determines the dependence of instability growth rate on pump power, also provides a firm limitation on the wave frequencies. Actually, Eq.2 cannot be fulfilled for all frequencies satisfying the decay condition $\omega_p=\omega_l+\omega_s$, but only for discrete frequency spectrum ω_{sn}. This can be easily shown taking into account the dependence $\Phi(\omega_s)$. Excitation of discrete spectra is the basic feature of absolute instabilities in an inhomogeneous plasma. The feature permits to suggest that, in contrast to convective instability, the absolute instability, involving a small number of excited eigenmodes, can be a coherent process. The coherence is especially possible near the threshold of the

instability, where the single eigenmode exists. Obviously, the weak turbulence theory, neglecting phase correlation, fails to describe such a coherent phenomena, therefore it is necessary to develop nonlinear theory of the absolute instabilities in an inhomogeneous plasma. Until recently, there were no distinct experimental evidences of the absolute parametric instability accompanied by coherent phenomena. This can be explained by difficulties of detailed, local, unperturbing plasma wave measurements, on one hand, and by plasma nonstationarity connected with low frequency turbulence, which impedes interpretation of experimental data, on the other.

At present paper a review of such microwave experiments is given. Different mechanisms of instability excitation, associated with coherent spatial structure of pump wave and existence of several resonant points are investigated. It is shown that at nonlinear stage the absolute instabilities manifest themselves as coherent anomalous reflection and absorption of microwave power. Coherent phenomena are observed both near instability threshold and far from it. Nonlinear theory of the experimentally observed instabilities is developed.

2. COHERENT PARAMETRIC REFLECTION OF RF WAVES IN PLASMA

The experiment was performed in a linear device containing magnetized and partly ionized argon plasma inhomogeneous both radially and axially $n_e=n_e(r,z)$ (Ref.13). The plasma was produced by a cyclotron breakdown in a chamber 1m long and 2cm in diameter (Fig.2). Axial magnetic field and plasma parameters were as follows: H=3kG, p=1-2 10^{-2}torr, T_e=1-2 eV, $n_e \leqslant 10^{12} cm^{-3}$. An oblique electrostatic wave (OEW) at a frequency $f_0=\omega_0/2\pi$=2350 MHz, was excited by a waveguide basically in the form of the fundamental Trivelpiece-Gould (TG) mode. The dispersion relation for the wave is $k_\perp^2 = \left[\omega_{pe}^2(r,z)/\omega^2 - 1 \right] k_\parallel^2$, where $k_\parallel$ and $k_\perp$ are the components of the wave vector parallel and transverse to the magnetic field. The wave can propagate in a plasma with density higher than the critical value: $n(r,z)>n_c$. For this mode the plasma near the axis acts as a waveguide with a weak longitudinal gradient. As the wave propagates in this waveguide in the direction of decreasing density, it slows down and its electric field increases. Near the point at which the critical density surface intersects the chamber axis (focal point), the OEW is converted into a "warm plasma wave"

and the electric field attains its maximum value:

$$E_0 = \frac{\left(2P_0'/\omega_0\right)^{1/2} k_0^{3/2}}{\left(1 + 3r_d^2 b k_0^3\right)^{1/2}} \exp\left\{i\int_{-\infty}^{z}(k_0 + ik_0'')dz' - \frac{k_0 r^2}{2b} - i\omega_0 t\right\} + \text{c.c.},$$

where $P_0' = \varkappa P_0$ is the portion of the power P_0, that goes into supplying the excitation of the fundamental mode, with $\varkappa \simeq 0.2$; k_0 is the longitudinal wave number found by solving the equation

$$3r_d^2 k_n^2 - z/a - 2(2n+1)/bk_n - i\varepsilon'' = 0 \quad ,$$

with n=0 ; a and b are the density length scales for the plasma near the axis:

$$\varepsilon_\parallel = 1 - \omega_{pe}^2(r,z)/\omega^2 + i\varepsilon_\parallel'' = z/a + r^2/b^2 + i\varepsilon_\parallel'' \quad ,$$

and k_0'' is the damping rate of the mode due to electron-plasma collisions and Landau damping.

It is just in the neighborhood of the focal point, that one should expect nonlinear plasma effects, e.g., the parametric instability $l_0 \rightarrow l_0' + s$ to appear at quite low pump power ($P_0 \leqslant 10$ mW). In this decay the reflected fundamental TG mode and the ion acoustic (IA) wave, propagating in the direction of decreasing plasma density, are generated. The instability threshold is defined not by the radial, but the axial plasma gradient. Since the decay condition

$$2k_0(z_0) = \omega_s/c_s \equiv k_s \qquad (4)$$

(where ω_s and c_s are the frequency and velocity of the ion acoustic wave) is satisfied for the process at only a single point, one should expect that the instability will give rise to spatial amplification of acoustic noise incident on the decay region. Thus the spectral density of the scattered wave is given by the expression (Ref.15) $p_s = AS$, where the constant A is determined by the plasma noise level and the amplification factor is

$$S = \exp\left[2\pi\varkappa\right] = \exp\left[ak_0 E_0^2(r=0)/8n_c T_e\right] \qquad (5)$$

The first experiments (Ref.16) showed that when the pump power P_0 exceeds 10 mW, a red-shifted by $f_s = \omega_s/2\pi$ = 2-3 MHz satellite line appears in the spectrum of the signal reflected by

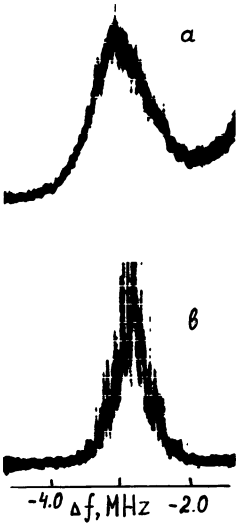

Fig.3 The backscattered spectra. (a)- the convective instability; (b)- the absolute instability.

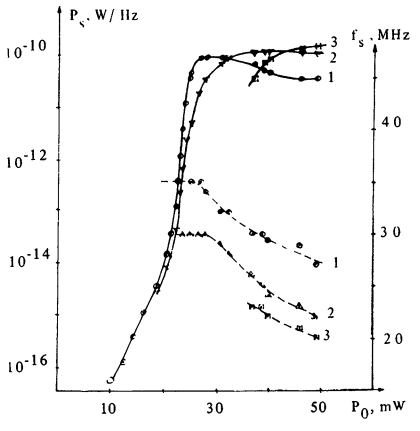

Fig.4 The scattered power vs. pump power. Curves 1,2,3 corresp. to consecutively appeared lines in scattered spectrum. Dashed lines are their eigenfrequencies

the plasma (Fig.3 a,b). At small power $P_0<20$ mW the scattered spectrum is rather wide ($\delta f\simeq 1$MHz) and smooth. The line profile corresponds to the predictions of the convective instability theory (Ref.17). The dependence of scattered power on the pump power at $P_0<20$ mW is also close to the theoretically predicted exponential one (5) Fig.4. However, at higher power when $S>10^3$, the dependence $p_s(P_0)$ rises sharply that evidences excitation of a stronger process, i.e. an absolute instability. To clarify mechanism of the absolute instability the special experiment was carried out. This was done using the TG mode at a shifted frequency $f_s' = f_0 + \Delta f$ as a pump wave. The shifted wave scatters on parametrically excited IA wave at the point z_ζ defined by $2k_0(z_\zeta, f_s)=k_s$, displaced from the point z_0 by a distance $\Delta z=z_\zeta-z_0=-2\Delta f a/f_0$. The peak spectral density A_s of the satellite of the probing wave was measured as a function of the frequency shift Δf and converted into a function of spatial shift. Peaks of the $A(\Delta f)$ dependence (Fig.5) correspond to the IA generation points, whereas the exponentially decaying part of this function at $\Delta f<-70$ MHz and $\Delta f<140$ MHz shows damping of the wave. We conjecture that th-

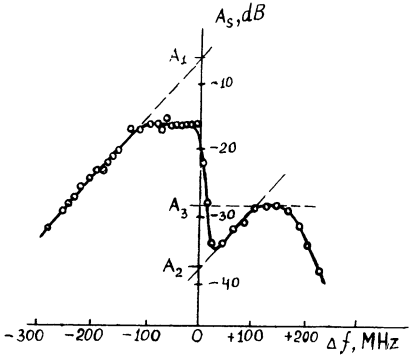

Fig.5 The probing of spatial structure of excited IA waves

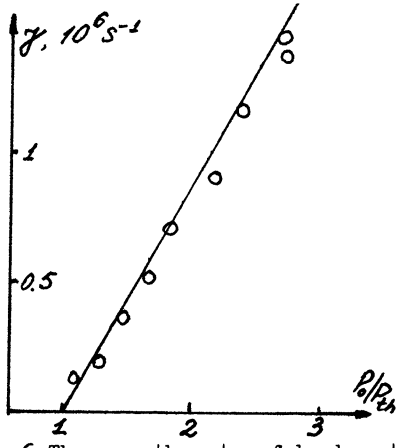

Fig.6 The growth rate of backscattering absolute instability vs. pump power. Experimental (dots) and theoretical (solid line) data.

largest peak is associated with the resonant point where spatial amplification occurs due to the following decay: $l_0 \longrightarrow l_0' + s$. This amplification can be obtained from the Fig.5 as a ratio of outgoing and incident wave amplitudes: $S=10^{0.1(A_1-A_2)} \approx 3\cdot10^3$.

The IA wave amplitude in the region of the smaller peak exceeds the thermal noise by a factor of 10^6. Such a high incident IA wave amplitude may result from the interaction between the strong parametrically reflected satellite l_0' and a small admixture of the first radial TG mode l_1 in the pump wave. The resonant point for this process $l_1 \longrightarrow l_0' + s$ is determined by the condition $k_0(z_1)+k_1(z_1)= \omega_s/c_s$, where $k_1(z)$ can be found from Eq. (3) at n=1. Using this relation and the equation $2k_\zeta(f_\zeta,z)=k_s$, it can be shown that for f_s=2.1 MHz the probing wave will scatter at point $z=z_1$ for Δf=160 MHz, which is close to the abscissa of the smaller peak on Fig.5. The power of the fist radial mode P_1 can be estimated from the peak ratio on Fig.5 as $P_1 \approx 10^{-1} P_0$ (Ref.18). Inspite of its relatively small amplitude, the first TG mode gives rise to an important effect. Through the $l_1 \longrightarrow l_0' + s$ decay it excites an IA wave that returns a part of the convectively lost energy back to the $l_0 \longrightarrow l_0' + s$ decay region, that is, the first mode provides a feedback loop, giving rise to the absolute parametric instability in the inhomogeneous plasma.

According to the theory of the instability (Ref.18), the threshold power is mainly determined by a balance between the amplification in the decay regions and wave absorption in the feedback loop. Theoretical threshold value of the spatial amplification turned out to be $S_{th} \approx 10^3$, close to the experimental value. Growth rate of the absolute instability is determined by the time of IA wave propagation in the feedback loop (Ref.18):

$$\gamma = \frac{\pi \alpha_{th} c_s}{z_0 - z_1} \left(\frac{P}{P_{th}} - 1 \right) \qquad (6)$$

The growth rate (6) is much smaller than the value predicted by the homogeneous plasma theory for the same instability. As it is seen from Fig.6, the experimental results are in a good agreement with the dependencies given by Eq. (6).

The theoretical analyses predicts the excitation of a discreet IA frequency spectrum as well. According to Ref.18 the lines in the spectrum are to be separated by the value $\delta f = c_s/(z_0 - z_1)$ which is also equal to the inverse time of propagation of the IA wave in the feedback loop. However, the first experimental results did not support this prediction. Though the scattered spectrum became more rough at $P_0 > 20$ mW, it did not possess stable line structure Fig.3b. At first sight, this points out to excitation of a noncoherent wave process as a consequence of absolute instability. But the former investigations have proved that the wide spectrum is rather due to the microscopic plasma density fluctuations than to the intrinsic stochastic behavior of the wave system. Short time interval measurements ($\tau \approx 10$ μs) of the scattered spectrum at the absolute instability stage showed drastic difference from the results of continuous measurements (Fig.3b). This spectrum consisted of a small number (from one to three) of narrow lines with $\delta f \leqslant 0.1$ MHz, separated by 0.3-0.5 MHz. Width and shape of the satellite and pump wave agree and are determined by how long the sampling window of the analyzer remains open. The frequency and amplitude of the lines changed from one measurement to the next. These variations are evidently related to fluctuations of macroscopic plasma parameters resulting from discharge instability. The cavity diagnostics showed in this regime the density variation $\delta n/n \approx 10\%$. The very moment the density fluctuations became smaller ($\delta n/n \approx 1\%$), the stable line structure was observed in the scattered continuously measured

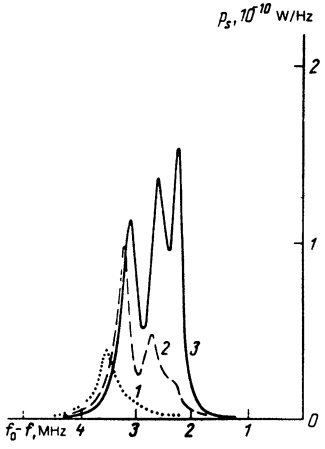

Fig.7 The spectra of scattering in low fluctuating discharge.

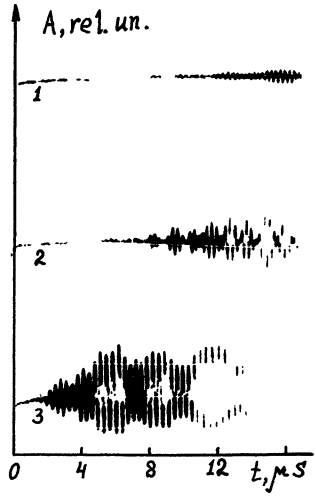

Fig.8 The onset of backscattered signal. Curves 1,2,3 correspond to P_0 = 25 mW, 30 mW, 40 mW.

spectrum. The sequence of different lines appearing in the spectrum is shown on Fig.7. When threshold of the absolute instability is exceeded, a narrow line at a frequency $f \approx f_0-3.5$ MHz appears (curve 1 on Fig.7). Its width depends on density fluctuation level 100 kHz $<\delta f<$ 200 kHz. At $P_0>30$ mW the increase of the satellite amplitude reaches saturation at a level $p_s = 2\cdot10^{-10}$ W/Hz (Fig.4(1)). An estimate shows that the level corresponds to almost total reflection of pump power near the focal point. At this power the second narrow line shifted by $f_0-f=2.8$ MHz appears in the spectrum of scattered signal (Fig.7(2)). Curve 2 on Fig.4 shows the amplitude dependence of this second line on the pump power. At $P_0>$ 30 mW the first line amplitude decreases with pump power in contrast to the behavior of the second line. The strong parametric reflection is also coherent but it takes place at higher plasma density in scattering by IA wave at frequency f_s= 2.8 MHz. When pump power is raised further, the next step of this peculiar series of events occurs. Yet another narrow line appears in the spectrum at a frequency $f = f_0-2.4$ MHz and gradually becomes higher than the other (Fig.7(3)).

At a pump power P_0=30 mW the frequencies of the lines begin

to decrease smoothly (Fig.7.4). This behavior is apparently due to an increase of longitudinal plasma scale length and a proportional increase of the feedback loop size z_0-z_1 , connected with an additional plasma ionization at the focus.

We studied the time behavior of the scattered signal by measuring time evolution of the amplitude of the signal detected by RF diode in the waveguide system, A(t). It can be seen from oscilloscope trace 1 on Fig.8 that slightly above the threshold (P_{th}=25 mW) the rise time of the sinusoidal component of the signal is long (τ=12 μs), apparently due to small growth rate of the absolute instability near the threshold. The amplitude of the oscillations increases with pump power and their rise time becomes shorter: τ=7 μs at P_0=30 mW (trace 2 on Fig.8.). In this case the A(t) dependence becomes more complicated and looks like beats of sinusoidal signals of approximately the same frequency. The scattered signal remains coherent even at higher pump power P_0=40 mW, but the rise time of the signal decreases to 2-3 μs. When the threshold is exceeded by this amount , the coherent parametric reflection plays a significant role in the plasma energy balance, that is confirmed by the correlation between the electron flux (W~ 20 eV) and reflected RF signal (trace 2 and 1 on Fig.9).

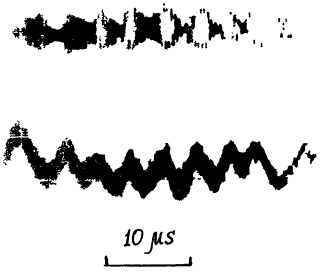

Fig.9 The time correlation between backscattered signal and flux of fast electrons.

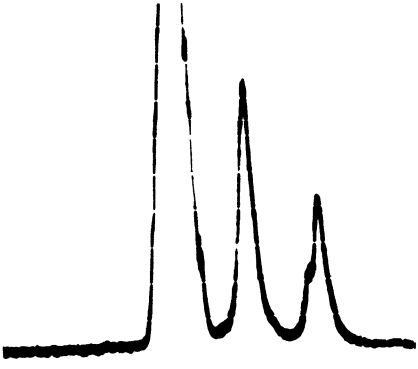

Fig.10 The anti-Stocks component of scattered spectrum.

Thus, the coherent backscattering exists not only near the threshold of the absolute instability, but at powers two and even three times higher. However, the strong parametric reflection at high RF power is due to the feedback loop eigenmode which is close to the threshold of excitation as well. The eigenmode is generated in denser plasma and in this way a kind of skin effect takes place. The RF power incident on the plasma is anomalously reflected due to this eigenmode and does not reach the focal point where the instability threshold would be strongly exceeded. So, in this experiment the inhomogeneous plasma maintains the backscattering instability near the threshold of excitation.

3. COHERENT PARAMETRIC ABSORPTION OF RF POWER IN PLASMA

Further RF pump power increase ($P_0 > 80$ mW) was accompanied by a decrease of the red-shifted parametrically reflected satellite and gave rise to an anti-Stocks component of the scattered spectrum, that is, a blue -shifted satellite $f-f_0 \simeq 1$ MHz. Impulse measurements showed that these red-shifted and blue shifted satellites did not exist simultaneously. At low plasma density fluctuations the pump power excess of a certain value $P_0 \simeq 80 \div 100$ mW caused jump transition from the Stocks to the anti-Stocks generation mode, so that the final scattered spectrum (Fig.10) had not the red-shifted satellite at all and the blue-shifted part of the spectrum consisted of a few narrow equidistant lines. In some discharges such a spectrum was achieved smoothly, without jump transition and at essentially lower pump power $P_0 \simeq 15 \div 20$ mW (Fig.11(1)). In these cases strong parametric reflection did not

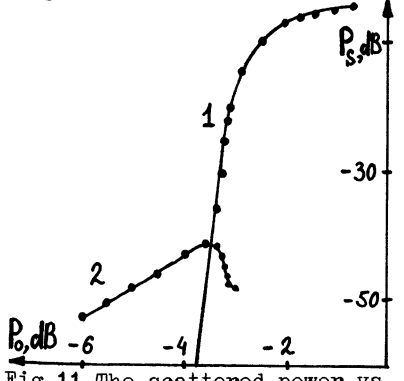

Fig.11 The scattered power vs. pump power. Anti-Stocks (1) and Stocks (2) spectrum components

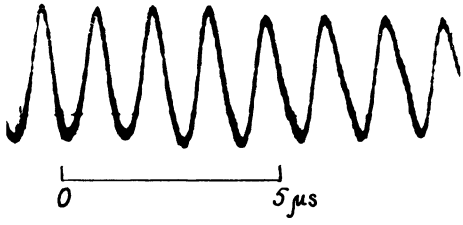

Fig.12 The oscillogram of RF scattered signal, detected by RF diode.

occur at all and the backscattering process $1_0 \longrightarrow 1_0' + s$ was suppressed at the initial. convective stage of the parametric instability (Fig.11(2)).

At first sight it seems that excitation of a scattered spectrum consisted of only anti-Stocks component (Fig.10) cannot be associated with a parametric instability. Therefore we first of all suggested another mechanism - scattering of the pump wave on an ion acoustic wave exciting in plasma due to ion acoustic instability. Such a wave, propagating oppositely to the pump wave and giving rise to the anti-Stocks spectrum component, could be excited by an electron current which compensates losses of fast electrons accelerated by the RF wave. However, this mechanism fails to explain very narrow spectrum line and coherence of the observed scattering process, manifesting itself in an ideal monochromatic signal from HF detector (Fig.12). More efficient explanation of the experimental data is based on the assumption that the anti-Stocks spectrum component is generated in the process of secondary scattering on a parametrically excited acoustic wave. The IA wave generation seems to be due to forward scattering $1_0 \longrightarrow 1_1' + s$, producing the first radial TG mode $1_1'$ at a frequency $f_1 = f_0 - \Delta f$. From dispersion curves for this parametric process, shown on Fig,1, one can see that decay condition $k_{1_0}(z) = k_{1_1'}(z) + k_s$, $k_s < 0$ is fulfilled for a pair of spaced points, if IA wave frequency varies within certain limits (tangent point of these curves corresponds to $f_s \simeq 1$ MHz). Moreover, group velocities of the excited waves have opposite directions. According to results of Ref.6, excitation of absolute parametric instability is possible under these conditions. The linear theory of the instability is given in the Introduction and the theory of nonlinear stage is described in the last part of the paper. Summarizing theory results, we can conclude that threshold of the absolute instability is determined by absorption of the excited waves.

$$\exp\left\{\pi(\varkappa_1 + \varkappa_2) - \int_{z_{d1}}^{z_{d2}} (k_s'' + k_1'')\,dz\right\} = 1 \qquad (7)$$

The value of power threshold for the fundamental eigenmode of the feedback loop is equal to $P_{th} \simeq 20$ mW which is close to the experimentally observed threshold (Fig.11). Corresponding eigenvalue of IA wave frequency is $f_{s0} \simeq 0.85$ MHz that also does

not differ too much from the experimental one $f_{s0} = 0.9 \div 1.0$ MHz (Fig.10). Following the theory, growth rate of the instability depends on time interval which is necessary for the IA wave to pass the feedback loop

$$\gamma = \frac{c_s \pi (\varkappa_1 + \varkappa_2)}{2(z_{d1} - z_{d2})} \Bigg|_{P_{th}}^{P_0} \qquad (8)$$

A comparison of the theoretical and experimental results for the absolute instability increment is given on Fig.13.

So far the only source of information on the absolute instability was the anti-Stocks spectral component l_0' generated in the secondary parametric process $l_0 + s \longrightarrow l_0'$, because the red-shifted forward scattered primary wave l_1 propagated to the low density plasma, where was effectively absorbed and could not be registered using the experimental scheme shown on Fig.2. To register this wave, the fast particles analyzer , shown on Fig.2, was moved into plasma close to the region of wave interaction that lead to reflection of the wave and arising of anti-stoks component in the scattered spectrum, namely red-shifted lines $f_0 - f \simeq 1$ MHz and 2 MHz (Fig.14). We note that the described coherent parametric

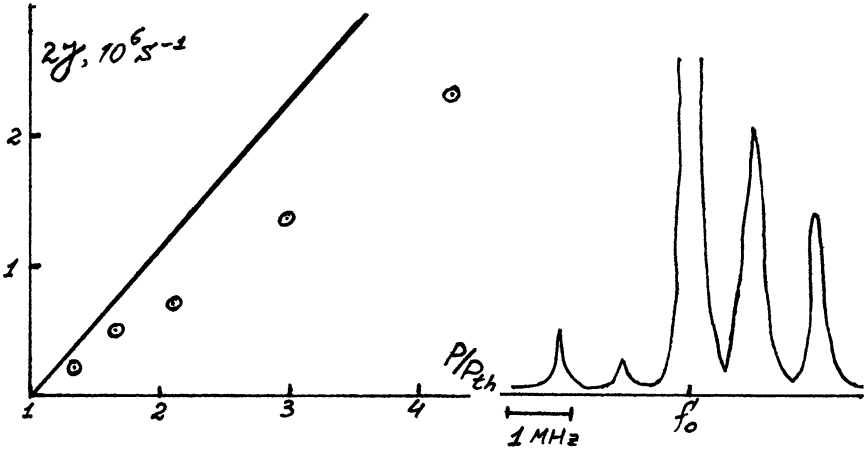

Fig.13 The forward scattering instability growth rate vs.pump power.Points-experimental data, solid line-theory.

Fig.14 Scattering spectrum, containing the Stocks component reflected by the multygrid analyzer.

process was accompanied by anomalous RF power absorption by the plasma, resulted, particularly, in sufficient increase of fast electron production.

In these experiments coherent wave interaction displays so brightly due to small number of excited radial eigenmodes, which is a specific feature of our axial-symmetrical experimental system. Moreover, the used local scattering method is easy-feasible and does not disturb plasma. It can be suggested that coherent phenomena are also essential in other cases of interaction with plasma of intensive waves, but their role may be masked by both large number of excited degrees of freedom and impossibility, as a rule, to use local measurement methods in experiments.

As an example, last lower-hybrid heating experiments carried out on FT-2 tokamak using the enhancement scattering method for plasma diagnostics (Ref.19), also indicate excitation of coherent parametric processes. For instance, in the central part of the tokamak plasma LH pump wave at a frequency 900 MHz gave rise to oscillations at a lower frequency 620÷670 MHz with very narrow spectral line $\Delta f \simeq 2$ MHz. These oscillations were localized inside narrow spatial region near the lower-hybrid resonance point for waves at a frequency of 600 MHz. It is possible that such a localized and quasi-monochromatic oscillations result from excitation of an absolute parametric instability.

4. NONLINEAR THEORY OF ABSOLUTE PARAMETRIC INSTABILITY IN AN INHOMOGENEOUS PLASMA

The methods used in the weak turbulence theory cannot be applied for theoretical description of the above mentioned coherent processes of forward and backward induced scattering, therefore development of nonlinear dynamic theory is necessary. We note that both instabilities result in noticeable powers of scattered waves and in considerable variations of plasma radiation, so it is quite naturally to regard the pump wave depletion effect as the main reason for saturation of the absolute instabilities. Development of analytical theory based on the pump depletion mechanism was strongly delayed for a lack of accurate solution of the problem concerning nonlinear stage of a convective instability in an inhomogeneous plasma. At present time the solution of the nonlinear three-wave problem is known (Ref.20) and below we shall use the accurate formulae from that paper. For this

purpose, using Ref.20, we introduce all the necessary definitions and formulate mathematically the three-wave problem in an inhomogeneous plasma:

$$v_1\frac{dy_1}{dz} = iy_2y_3\exp\{-i\Psi(z)\}$$

$$v_2\frac{dy_2}{dz} = iy_1y_3^*\exp\{ i\Psi(z)\} \qquad (9)$$

$$v_3\frac{dy_3}{dz} = iy_1y_2^*\exp\{ i\Psi(z)\}$$

Here $\Psi(z) = \int_0^z \Delta k(z')dz' = \int_0^z (k_1-k_2-k_3)dz' \simeq z^2/2h^2$ is resonance phase mismatch near the decay point $z_d=0$, h is the plasma density length scale, $y_m(z)$ $(m=1,2,3)$ are proportional to the amplitudes of the interacting waves, v_m and k_m are the projections of group velocities and wave vectors onto plasma inhomogeneity direction. We note that v_1, k_1 correspond to the wave at the highest frequency (pump) and the following relation is valid: $v_1>v_3>0>v_2$. In Ref.20 it was shown that far from resonance, where $|z/h| \gg 1$, squares of absolute values of wave amplitudes become asymptotically constant $|y_m|^2 \propto |A_m|^2$, where $|A_m|^2$ are proportional to the powers of incident and outgoing waves. In this case the asymptotic behavior of Eq.9 solutions turns out simple, for instance for $y_3(z)$, it looks as follows:

$$y_3^{(\nu)} \propto A_3^{(\nu)}\exp\left\{-i\left[\varkappa_1^{(\nu)} + \varkappa_2^{(\nu)}\right]\mathrm{Ln}|z/h|\right\} + O(h/z) , \qquad (10)$$

where $O(h/z)$ is a rapidly oscillating function that decay as h/z for $z \longrightarrow \pm\infty$, upper index $\nu=\mathrm{sigh}(v_m\cdot z)$ labels quantities referring to incident $(\nu)=(-)$ and outgoing $(\nu)=(+)$ waves, $A_3^{(\nu)}=|A_3^{(\nu)}|\cdot\exp(i\phi_3^{(\nu)})$ are complex constants, and the dimensionless parameters $\varkappa_m^{(\nu)}$ $(m=1,2,3)$ are given by

$$\varkappa_m^{(\nu)} = h\cdot|A_m^{(\nu)}|^2/|v_pv_j| , \quad m\neq p\neq j \qquad (11)$$

Asymptotic behavior of the other amplitudes is similar to (10).Relations between complex asymptotic wave amplitudes have the simplest form in the case of absence of one of the incident daughter waves, which just corresponds to the boundary conditions

for the absolute instability to occur. If we put, for instance, $æ_2^{(-)} \propto |A_2^{(-)}|^2 = 0$ for $z/h \to +\infty$, then obtain from Ref.20:

$$2\pi æ_3^{(+)} = \mathrm{Ln}\left\{1 + \left[\exp(2\pi æ_3^{(-)}) - 1\right]\exp(2\pi æ_1^{(-)})\right\} ;$$

$$æ_2^{(+)} = æ_3^{(+)} - æ_3^{(-)} ; \qquad æ_1^{(+)} = æ_1^{(-)} + æ_3^{(-)} - æ_3^{(+)} ;$$

$$\phi_1^{(+)} = \phi_1^{(-)} + \arg\left\{\Gamma(1-iæ_1^{(+)})\Gamma(1+iæ_1^{(-)})\right\} ; \qquad (12)$$

$$\phi_2^{(+)} = \phi_2^{(-)} + \arg\left\{\Gamma(1-iæ_3^{(+)})\Gamma(1+iæ_3^{(-)})\right\} ;$$

$$\phi_3^{(+)} = \phi_1^{(-)} - \phi_3^{(-)} + 3\pi/4 + \arg\left\{\Gamma(1+iæ_1^{(-)})\Gamma(1+iæ_2^{(+)})\Gamma(1-iæ_3^{(-)})\right\} ;$$

These formulae permit to develop an analytical theory of the absolute parametric instability in the case when decay points are distant enough for their mutual influence be negligible. It is possible to apply these formulae to the mentioned above absolute instability $l_0 \longrightarrow l_1' + s$. For this process the corresponding decay conditions $\Delta k(z) \equiv k_{l_0}(z) - k_{l_1'}(z) + k_s$, $\omega_{l_0} = \omega_{l_1'} + \omega_s$; can be fulfilled for a pair of spaced points, if IA frequency $\omega_s = k_s/c_s$ (Fig.1) ranges within certain limits. We shall assume here, for simplicity, that wave absorption is absent and $\Delta k(z)$ is a parabolic function. Under these conditions, the system of equations, describing parametric wave interactions in the feedback loop, can always be reduced to Eqs.9 choosing appropriate dimensionless coordinate z and correspondingly redefining wave amplitudes. The phase mismatch $\Psi(z)$ then becomes

$$\Psi(z) = q \cdot z - z^3/3 , \qquad (13)$$

where the only dimensionless parameter q governs the distance between resonant points and physically means deflection of IA frequency from the value that corresponds to the case of exact tangent position of the decay dispersion curves $k_m(\omega_n, z)$ Fig.1. The solution of Eq.9, describing the absolute instability excitation, must not contain waves incident on the decay region except the pump wave which at $z \to -\infty$ satisfies the following

condition: $|y_1(z)|^2 \longrightarrow |A_1|^2$. Obviously, such a nontrivial solutions cannot exist for arbitrary value of parameter q, so this mathematical problem is a spectral one. It is easy to verify that for $q^{3/4} \gg 1$ resonant wave interaction near each of the decay points $z_{1,2} = \pm q^{1/2}$ can be well regarded as independent, that is, we can use formulae (12) consecutively to each three-wave interaction point. In this case wave amplitudes between the resonances are well described by such a simple approximate formulae, as

$$y_1(z) \propto \text{const} \cdot \exp\left\{ i\left(\text{æ}_2 - \text{æ}_3\right) \text{Ln} \left| \frac{q^{1/2} - z}{q^{1/2} - z} \right| \right\}$$

This permits to calculate all the necessary dependencies which have the simplest form when expressed in dimensionless quantities q and $\text{æ}_m^{(\nu)}$, m=1,2,3. to connect the following dimensionless results with the physical quantities, one should use formula (11), where $h^2=(4q_n)^{-1/2}$ (n=0,1,2,3...N are the numbers of the feedback loop eigenmodes).

$$|y_m^{(\nu)}|^2 \underset{z \longrightarrow \pm\infty}{\propto} |A_m^{(\nu)}|^2 = 2\text{æ}_m^{(\nu)} \cdot |v_p v_j| \cdot q_n(\text{æ}_1^{(-)}), \quad m \neq p \neq j \qquad (14)$$

The feedback loop "eigenfrequencies" $q_n = q_n(\text{æ}_1^{(\nu)})$ can be found by solving Eq.15 for $\text{æ}_1^{(-)} \geqslant \text{æ}_{th} = \text{Ln}(2)/2\pi$, where æ_{th} is the "pump power" threshold value.

$$\frac{2}{3} q_n^{3/2} = \pi\left(n + \frac{1}{4}\right) + \left(\hat{\text{æ}}_2 - \text{æ}_{th} - \hat{\text{æ}}_3\right) \cdot \text{Ln}\left(8q_n^{3/2}\right) + \\ + \arg\left\{\Gamma(1+i\text{æ}_{th})\Gamma(1+i\hat{\text{æ}}_3)\Gamma(1-i\hat{\text{æ}}_2)\right\}; \qquad (15)$$

Here $\hat{\text{æ}}_2 = \text{æ}_1^{(-)} - \text{æ}_{th}$; $\hat{\text{æ}}_3 = \text{æ}_{th} + \frac{1}{2\pi} \text{Ln}\left[1 - \exp(-2\pi\text{æ}_1^{(-)})\right]$.

"Powers" $\text{æ}_{2,3}^{(+)}$ of the excited daughter waves l_1' for $z \longrightarrow +\infty$ and s for $z \longrightarrow -\infty$ are given by the simple formula

$$\varkappa_2^{(+)} = \varkappa_3^{(+)} = \begin{cases} 0 & , \quad \varkappa_1^{(-)} < \varkappa_{th} \\ \mathrm{Ln}\left[\exp(2\pi\varkappa_1^{(-)}) - 1\right] & , \quad \varkappa_1^{(-)} \geqslant \varkappa_{th} \end{cases} \qquad (16)$$

Using formula (15), the dependencies $q_n = q_n(\varkappa_1^{(-)})$ were computed for the principal and first eigenmodes of the feedback loop. The results are shown on Fig.15(1,2) (dashed lines) together with corresponding "accurate" dependencies (solid lines), computed directly from the initial system of equations (9),(13). A good agreement of these curves should be noted not only for the first eigenmode, but for the fundamental one. Formula (16) for powers of the parametrically excited waves also shows a good agreement with computational results (Fig.15(3)).

The theory permits generalization for a more realistic plasma model, taking into account both weak wave absorption and spatial variation of matrix elements of the parametric interaction. The corresponding formulae are mush more complicated than (15),(16), therefore they are not given here. We note that the approach developed above, gives also an opportunity to calculate excitation of another absolute instability concerning the parametric backscattering $l_0 \longrightarrow l_0 + s$, discussed in part 2 of this paper.

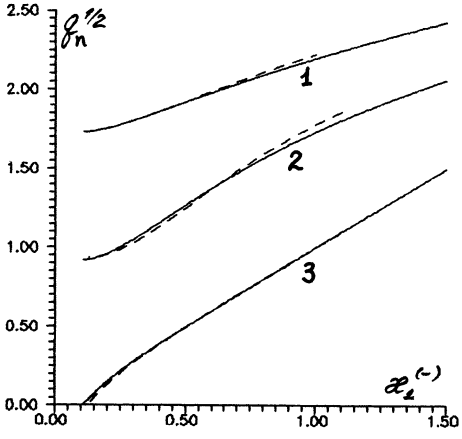

Fig.15 "Eigenfrequencies" (1,2) and forwardscattered "power" (3) for the fundamental(2) and first(1) eigenmodes of the feedback loop

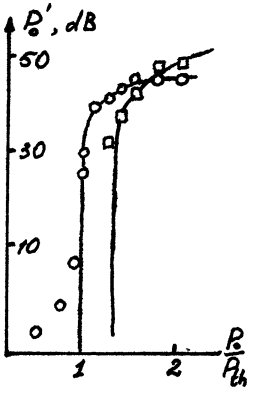

Fig.16 Powers of backscattered eigenmodes vs pump power.Theory(solid lines),experiment(dots)

Leaving aside, for lack of space, all details, we give only a comparison of the experimental and theoretical dependencies of red-shifted satellite powers on pump power (Fig.16). The figure shows a good agreement between theory (solid lines) and experiment (dots), which confirms our theoretical interpretation of the coherent phenomena occurred in the experiments, discussed in this paper.

REFERENCES

1. B.B.Kadomtsev Kollektivnye yavleniya w plazme (Collective Phenomena in Plasmas), Nauka,Moscaw,1976
2. V.N.Tsytovich Theory of Turbulent Plasma, Plenum,New York,1974
3. V.P.Silin,V.T.Tihonchuk Zh.Eksp.Teor.Fiz. 81,2039 (1981)
4 Piliya A.D. In Proc.of 10th Conf.on Phenomena. in Ionised Gases,Oxford,1971,320
5. Perkins F.W.,Flick J. Phys.Fluids 14,2012 (1971)
6. Rosenbluth M.N. Phys.Rev.Lett. 29,565 (1972)
7. Piliya A.D. Zh.Eksp.Teor.Fiz. 64,1237 (1973)
8. Rosenbluth M.N.,White R.B.,Liu C.S. Phys.Rev.Lett.31,1190,1973
9. Piliya A.D. Pis'ma Zh.Eksp.Teor.Fiz. 17,374 (1973)
10. Pesme D.,Laval G.,Pellat R. Phys.Rev.Lett. 31,203 (1973)
11. Gusakov E.Z.,Piliya A.D.,Fedorov V.I. Fiz.Plazmy 3,1328 (1977)
12. Gusakov E.Z.,Piliya A.D. Fiz.Plazmy 6,509 (1980)
13. Arhipenko V.I.,Budnikov B.N.,Romanchuk I.A.,Simonchik L.V. Fiz. Plasmy 7,396 (1981)
14. Budnikov V.N. et.al. Fiz.Plasmy 6,1050 (1980)
15. Arhipenko V.I. et.al. Zh.Tehn.Fiz. 55,293 (1985)
16. Arhipenko V.I. et.al. Pis'ma Zh.Eksp.Teor.Fiz. 39,453 (1984)
17. Arhipenko V.I. et.al. Fiz.Plazmy 13,693 (1987)
18. Arhipenko V.I. et.al. Zh.Eksp.Teor.Fiz. 93,1221 (1987)
19. Budnikov V.N. et.al. Pis'ma Zh.Eksp.Teor.Fiz. 48,480 (1988)
20. Gusakov E.Z.,Savel'ev A.N. Zh.Eksp.Teor.Fiz. 94,89 (1988)

PHASE CONJUGATION OF MILLIMETER-WAVE RADIATION BY DEGENERATE FOUR-WAVE MIXING IN SATURABLE-ABSORBING MEDIA

Bogatov N.A.,Gitlin M.S.,Litvak A.G.,Luchinin A.G.,Nusinovich G.S.
Institute of Applied Physics of the USSR Academy of Sciences
46,Uljanov Str., Gorky, U S S R

Electromagnetic millimeter-wave radiation finds nowadays wide application in radars, communication, remote sensing, molecular spactroscopy, etc. In spite of numerous advantages of this frequency range, the effect of atmospheric refraction and scattering of millimeter waves may lead to large amplitude and phase fluctuations of the signal. These fluctuations can be avoided if we use phase-conjugation (PC) devices which realize PC in the real time scale. When a signal wave

$$\vec{\mathcal{E}}_s(\vec{r},t)=\frac{1}{2}\left[\vec{E}(\vec{r})e^{i\omega t}+\vec{E}^*(\vec{r})e^{-i\omega t}\right]$$

is incident onto a PC-device, it generates a PC wave

$$\vec{\mathcal{E}}_c(\vec{r},t)=\frac{1}{2}\left[\vec{E}^*(\vec{r})e^{i\omega t}+\vec{E}(\vec{r})e^{-i\omega t}\right]$$

Propagating again through optically inhomogeneous medium, a PC wave automatically regenerates its initial wave front.

In decemeter and centimeter wavelength regions, PC antennas made in the form of an array of discrete parametric mixers [1] are used for wave front correction in the real time scale. However, the application of parametric antenna arrays for PC in the mm wavelength range is rather complicated because of the decrease of characteristic scale of wave front inhomogeneities. Thus, a possibility of PC in the mm wavelength range by four-wave mixing (FWM) in the nonlinear medium for which cubic nonlinearity is inherent, seems to be rather attractive. Such a technique is widely used for PC in optical and IR regions [2,3].

PC by FWM is realized as follows. Two quasiplane counter-propagating pump wave beams are directed to the nonlinear medium.

The third (signal) wave beam to be conjugated is also directed there at the angle θ to the pump beam. The signal wave interferes with the forward pump wave that results in periodical modulation of the succeptability of the nonlinear medium with the period $\Lambda_{fs} = \lambda/(2\sin\theta/2)$. The scattering of the backward pump wave beam at this grating results in a wave which is conjugate to the signal one. In its turn, the interference of the backward pump wave beam also leads to periodic modulation of succeptability of the nonlinear medium with the period $\Lambda_{bs} = \lambda/(2\cos\theta/2)$. The scattering of the forward pump wave at this grating also results in the generation of the wave conjugate with respect to the signal wave. In FWM process Brag's condition is automatically fulfilled, so the scattering of pump waves at these refractive index variations is phase matched.

Recently, a possibility to use fully or partially ionized low-temperature plasma for PC of mm waves has been studied intensively. Plasma seems to be a rather promising nonlinear medium suitable for realization of FWM at long millimeters ($\lambda \gtrsim$ 3 mm). However, effective FWM at shorter waves ($\lambda \lesssim 2$ mm) requires generation of homogeneous plasma in large volumes ($\sim 10^3$ cm^3) with high density ($n_e \sim 10^{14}$ cm^{-3}) and low electron temperature ($T_e \simeq 1$ eV)[4]. Such plasma parameters are rather difficult to obtain.

For PC of the short millimeter wavelength radiation we suggest using the mechanism of nonlinearity caused by saturation of resonant transitions between rotational levels of dipole molecules. The efficiency of nonlinear wave interation in such gas media increases with a decrease of the wavelength due to resonant absorption growth. Advantages of these nonlinear media are attributed to simplicity of production, convenience of use and short response time. From all gases with strong absorption lines in the mm region, OCS is the most suitable for experimental investigation of FWM. A linear OCS molecule (dipole momentum is 0.71 Debye) is characterized by a relatively low chemical activity and a simple well-studied rotational spectrum [5] . Spectral lines of transitions between rotational levels in the ground vibrational state of OCS are equidistant in frequency with the separation $\approx$ 12 GHz. In the range 150...200 GHz, the absorption coefficient in the centre of the rotation lines α_0 at T = 200 K is from 0.02 to

0.05 cm^{-1} that allowed for experimental realization of such a situation when optical thickness of the media in the centre of rotation lines is large enough $\alpha_0 L \gtrsim 1$. Theoretical investigations of degenerate FWM efficiency in the saturable-absorbing media (given in [6]) showed that at $\alpha_0 L = 2$ the maximum reflectivity into the conjugate wave is about 1%, this reflectance being obtained by radial frequency tuning to the spectral line centre when pump wave intensity is equal to the saturation intensity J_{sat} of the resonant transition.

A scheme of an experimental setup on which the investigation on mm wave PC by degenerate FWM in gaseous OCS has been started is given in the figure. Powerful microwave radiation ($\lambda = 1.64$ mm, $P_{max} \simeq 100$ kW) was produced by a gyrotron with a pulsed magnetic field ($\tau_{rad} = 40$ μ s) 1. The gyrotron radiation was transformed into a quasigaussian wave beam with the radius of about 40 mm by a parabolic mirror 2. The beam was sent through a quartz window 3 into a vacuum metallic chamber 4 (diameter 180 mm, length 350 mm) filled with gaseous OCS. The vacuum chamber was placed into a thermostat 5 and cooled by dry ice up to $T \approx 200$ K to increase the absorption coefficient. The back wall of the chamber 6 serves at the same time as a mirror which forms a backward propagating pump wave beam and, thus, it was placed normally to the incident pump wave beam ($\vec{k}_f$). A signal beam ($\vec{k}_s$) was formed by a beam splitter 7 (made of a lavsan film) with the reflectivity 5% and by the iris 8. The signal wave beam was sent to the chamber (at the angle 7° to the forward pump wave) with the lavsan film mirror 9 whose reflectivity was 50%. Microwave diodes 10 and 11, placed into collimators, serve for measuring the intensity of the signal wave and the conjugate wave, respectively.

By varying the magnetic field and changing the gyrotron resonator diameter, the frequency of microwave radiation was tuned to the rotation line centre with the accuracy $\simeq$ 10 MHz. When OCS pressure in the chamber was $\simeq$ 5 Torr, the width of the spectral line $\Delta\nu_L$ ($\Delta\nu_L \approx 35$ MHz) exceeded significantly the frequency detuning from the line centre and thus the optimal frequency condition for FWM was fulfilled. At this gas pressure the saturation intensity of rotation transition was $J_{sat} \approx 75$ W/cm^2. The intensity of the pump wave beams required for rotation transition saturation can be easily reached when

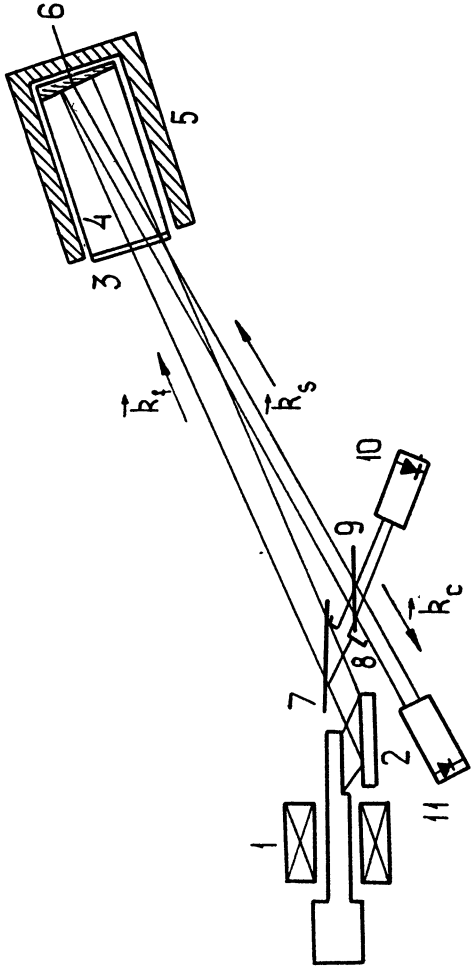
6
5
4
3
R_t
R_s
10
9
R_c
8
7
2
11
1

the gyrotron radiation power was several tens of kilowatt. The optical thickness in the centre of the spectral line 15 ← 14 ($\tilde{\nu}$ = 182.4 GHz, λ = 1.64 mm) which was measured in our experiments was $\alpha_0 L \simeq 1.4$. Thus, we have a possibility to reach 0.7% reflectivity to the conjugated wave.

REFERENCES

1. Special Issue on Active and Adaptive Antennas. // IEEE Trans Antennas and Propagation, AP-12, 1964, N2.
2. Optical Phase Conjugation. // Ed. by R.Fisher. - N.Y., Acad. Press, 1983.
3. Zel'dovich B.Ya., Pilipetsky N.F., Shkunov V.V.// Principles of Phase Conjugation, N.Y.,Springer, 1985.
4. Nebenzahl I., Ron A., Rostoker N. Reflected phase-conjugate wave in plasma. // Phys.Rev.Lett., 1988, 60, N11, p.1030-1032.
5. Burenin A.V., Val'dov A.N., Demkin V.M. et al.// Tables of spectral lines, OCS rotation spectrum. // Scientific Council on Spectroscopy of the USSR Acad.Sci., Moscow, 1979.
6. Betin A.A., Dyatlov A.I., Kulagina S.N. et al. // Degenerate four-wave interaction in the resonant medium with pump wave variations taken into account. // Quant.Electron., 1986, 13, N10, p.1975-1980.

SPECTROSCOPIC DETERMINATION OF RF FIELD STRENGTHS

H. Schlüter
Institute of Experimental Physics II
University Bochum

INTRODUCTION

For modelling of microwave plasmas it is important to have detailed knowledge about local rf electric field strengths. Comparisons of different energy dissipation channels with each other, for instance, have to start from a given rf power density distribution. Sometimes ist is rather questionable to conclude on the spatial distribution inside the plasma from "vacuum" conditions outside because simple models of field penetration may fail due to complications which arise e.g. from resonances and cut-offs and particularly from non-linear wave-plasma interactions involved, but also from the influence on the skin resistance exerted by a mixture of neutral plasma components. The spatial distribution of some species may depend on the rf amplitudes themselves. At high electron densities and/or in presence of a static magnetic field the plasma boundaries may be strongly influenced by the formation of oscillating space charge sheaths. Moreover the coupling of the different oscillation modes is another potential source of non-linearity which obstructs a simple estimate of the rf electric field strengths inside the plasma.

This situation presents a great challenge to apply diagnostic methods allowing to perform local measurements of rf electric field strengths. In case different modes are present, the polarization of the field and in case of internally excited modes even the frequency may be of additional interest. Sometimes the power locally absorbed is the interesting property ($\sim \gamma \cdot E^2$, with γ as absorption frequency) rather than the field strength itself.

Obviously antennae or probes may be used to obtain information. Limitations are given by thermal loads,

perturbations introduced into the plasma and possibly by calibration problems. These difficulties can be reduced by the application of spectroscopic methods which are solely addressed in this paper.

In the presence of suitable molecular species the appearance of (parity) forbidden lines due to electric fields yields a sensitive method, provided laser induced fluorecence is used [1]. This method so far has addressed dc and rf field strengths up to the range of MHz [2].

The dynamic Stark effect (of atomic lines) is particularly applicable at high microwave frequencies, in the case of strong field strengths even without laser induced fluorescence. In contrast to this rather direct method, information may be inferred from additional line intensity caused by rf fields in the case of pulsed or modulated operation; this indirect method relies on the applicability of a corona excitation model. Studies using these two spectroscopic methods in hydrogen and helium plasmas are presented below.

PULSED MICROWAVE PLASMA (9.4 GHz)

In a microwave generated hydrogen plasma as shown in fig.1 the electric field strength of a strong 9.4 GHz pulse is expected to lead to a broadening of the H_β-line due to the rf Stark effect. In addition to a central component satellites appear, their displacements being given by the microwave frequency and their relative intensity being a measure of the electric field strength. Except for very high frequencies the structures overlap resulting in an effective line broadening, as depicted by the example of fig.2. By comparing calculated profiles with the observed ones the rf electric field strength E can be determined. In the case of helium also a line shift can be expected. More details on the rf Stark effect are considered below.

The time sequence of fig.3 reveals that at the time of the strong microwave pulse H_β is broadened indeed. In addition the line intensity is increased noticeably above the previous level and relaxation sets in after the disappearance of the microwave pulse. The intensity increase is a measure of E^2 on the basis of a corona intensity model mentioned in the introduction. In fig.3 the intensity increase is depicted as a function of E^2 the values of which are determined from the rf Stark effect.

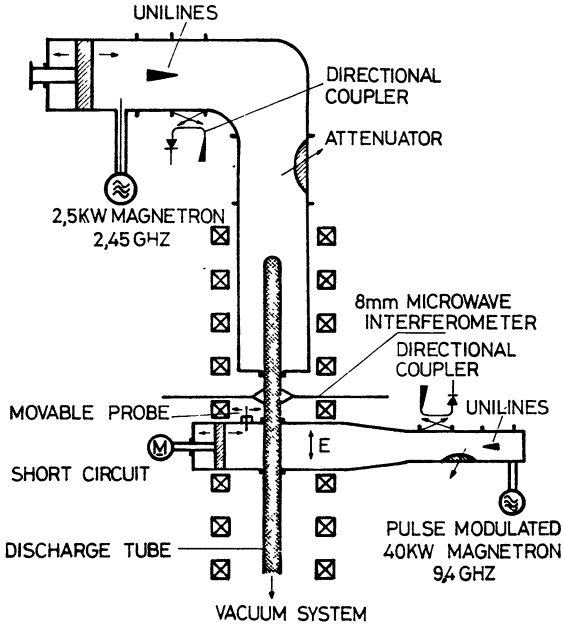

Fig. 1: To a target plasma generated at 2.45 GHz a strong 9.4 GHz pulse (0.5 - 0.7 μs) is applied by a Fabry-Perot-type microwave resonator [3].

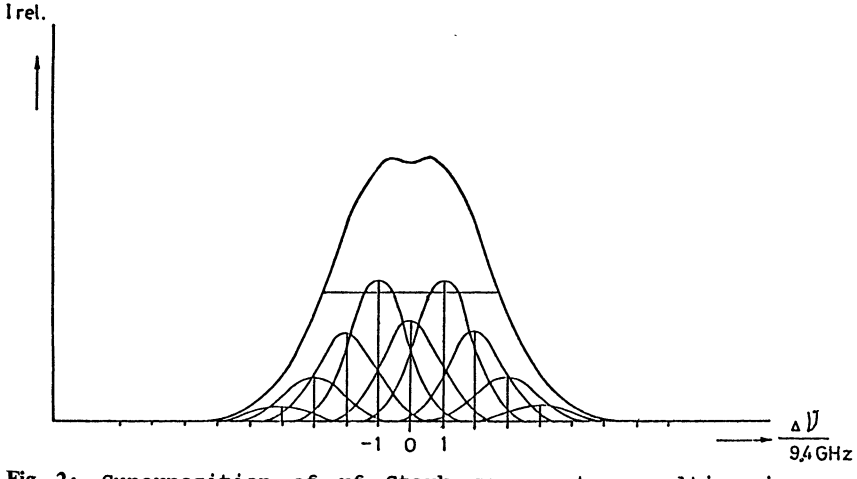

Fig. 2: Superposition of rf Stark components resulting in an effective broadening of the line H_β. The rf amplitude is 2 kV/cm.

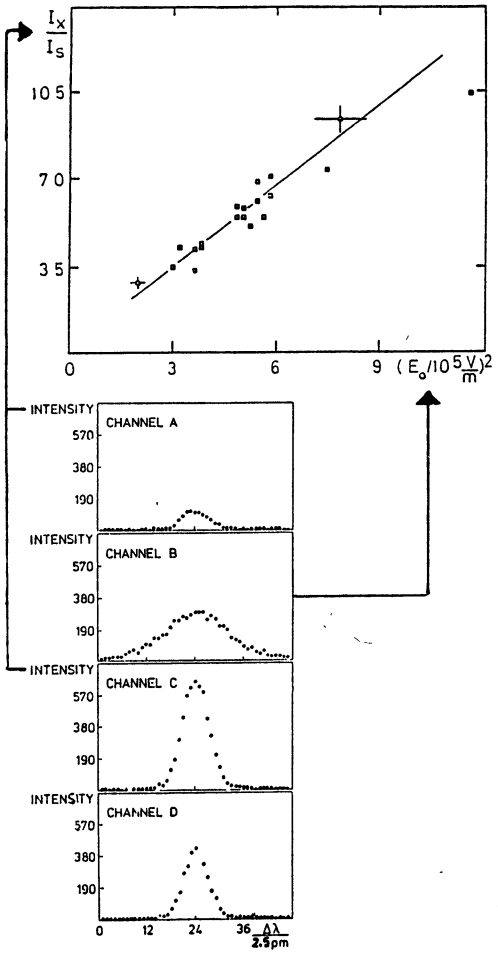

Fig.3: The time development of the H_β line is shown in the vertically arranged sequence CH.A to CH.D. Only CH.B refers to the 9.4 GHz pulse switched on. In the upper diagram the intensity increase in CH.B in proportion to CH.A is plotted against E^2 (E is the rf amplitude obtained from the rf Stark effect).

The resulting linear dependence in E^2 can be understood from the following energy equation plus corona excitation relation.

$$\nu_e \frac{e^2 E^2}{m_e \omega^2} = \nu_i e V_i + \sum_j \nu_j e V_j + 2\nu_e \frac{m_e}{M} \langle \varepsilon \rangle + \frac{\langle \varepsilon \rangle}{\tau_{Diff}}$$

rf power transferred | ionization | excitation | elastic losses | diffusion losses

excitation → $\sim I_j$ line intensity in pure corona model

test wave:

$$\nu_e \frac{e^2}{m_e \omega^2} d(E^2) \simeq e V_i d\nu_i + \sum_j e V_j d\nu_j$$

because

$$e V_i \left| \frac{d\nu_i}{d(E^2)} \right| , \; e V_j \left| \frac{d\nu_j}{d(E^2)} \right| \gg \frac{\langle \varepsilon \rangle}{n_e} \left| \frac{dn_e}{d(E^2)} \right| , \; \left| \frac{d\langle \varepsilon \rangle}{d(E^2)} \right|$$

wing of the EED | "bulk" of the EED

test wave: a) microwave pulse b) hf-modulation

With changing E^2 the change of the elastic loss rate is small and of the diffusion loss rate slow. For a fast pulse - or modulated operation as considered below - there is a 1:1 relation between wave absorption and inelastic losses (ionization, excitation with rates ν_i, ν_j and potentials Vi, V_j). Since the various inelastic channels show rather similar behaviour, with high accuracy the change of wave absorption is reflected in the change of a particular excitation rate ν_j from the ground state. For cases of strict corona conditions at low electron densities, i.e. in case of predominant population of an excited level from the ground state, the deexcitation (solely) by spontaneous emission provides a rather instantaneous response to changes of E^2. The situation is helped by the fact that the tail of the distribution function - responsible for excitation - responds rather fast, whereas the bulk of the distribution is responding relatively slowly; see

e.g. calculations of Dilonardo et al.[4]. Thus it is not surprising that modulation of E^2 (see below) is not associated with appreciable modulation of electron density n_e or mean electron energy $\langle\epsilon\rangle$, though there are strong variations of the excitation rates.

The line intensity method yields relative values of E^2. An absolute calibration, however, is possible [5].

MODULATED STATIONARY RF DISCHARGE (27 MHz)

The line intensity corona method can be applied to a steady state helium rf discharge (27 MHz, with static magnetic field) by using modulation of the rf source at 330 kHz. The choice of this frequency eliminates the time scale of diffusion losses and avoids complications of the assumed simple corona model due to metastables [6]. Fig 4 shows the experimental set-up.

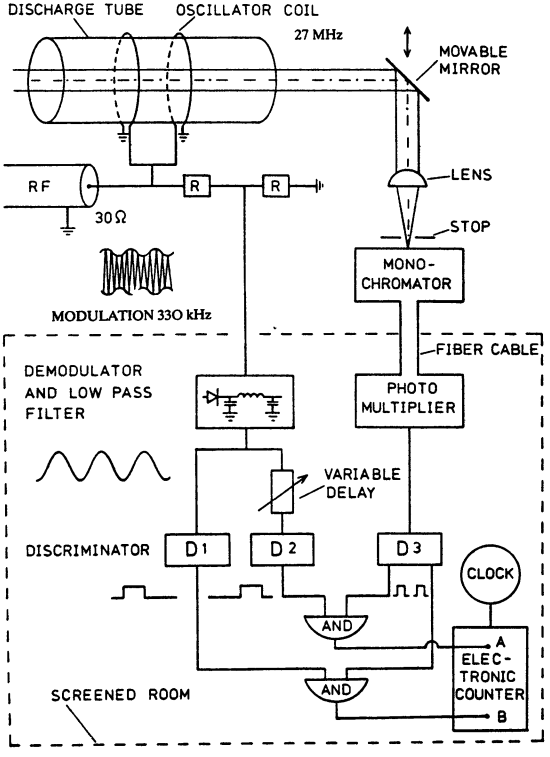

Fig.4: Experimental set-up of the modulated stationary rf discharge at 27 MHz.

The axial inhomogeneity of the discharge being rather small or well-known, radial resolution of the light emission was possible in this case by end-on observation without resorting the Abel-inversion techniques of side-on measurements. Fig.5 depicts the modulated light intensity as a function of radius. For comparison also the radial dependence of the unmodulated light emission (on the 501.5 nm line from the excited state 3^1P to 2^1S) is shown, demonstrating the influence of diffusion in the steady state energy balance equation. In this case a good model of the local rf energy deposition was available, provided the effective absorption frequency was known; in this case the latter property could be determined by comparison of the expected deposition profile (sensitive to the effective γ) with the observed one. The curve fitted to the measurements in fig.6 leads to a value of γ far above the electron-neutral collision frequency, appropriate for the non-linear, turbulent situation considered [7].

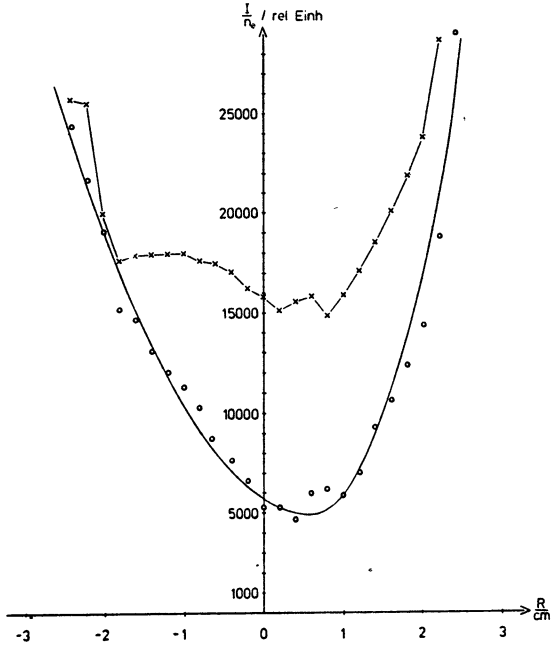

Fig. 5: Radial intensity profiles of the HeI 501.5 nm line normalized against the electron density profile. Open circles denote measurements with modulation, crosses without.

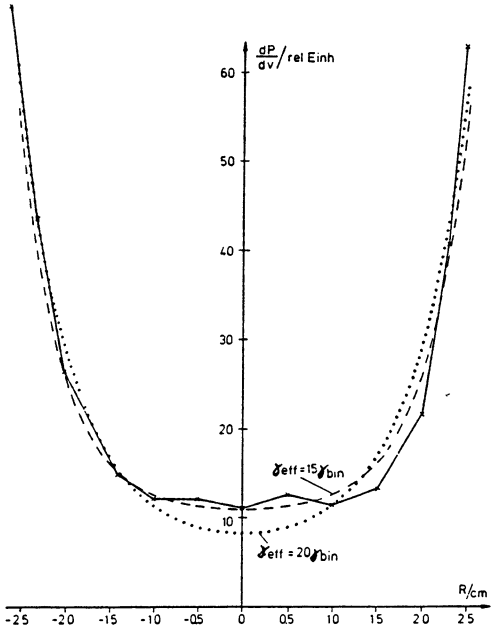

Fig. 6: Power density profiles measured (solid curve) and calculated for multiples γ_{eff} of the binary collision frequency γ_{bin}. For $1 \cdot \gamma_{bin}$ the profile looks quite different.

BEAM PLASMA EXPERIMENT

The dynamic Stark effect in helium leads to satellites of forbidden line components in addition to the effects on the allowed transition mentioned above. They may be used to determine frequency and field strength of plasma instabilities. In the beam plasma experiment - supported by additional microwave and probe diagnostics [8] - the development of the intensity is expected to reach a stage described by the "single wave model" [9], the beam electrons being trapped in a saturated wave field with $E^2/\omega^2 \sim n_e^{-1/3}$ (n_e the electron density of the target plasma).

Fig.7 gives the spectroscopic observations. Though detection of the satellites is difficult in pure emission, the differentiation against impurity radiation is obtained by observation at different densities n_e, since the satellites display a frequency separation given by the plasma frequency ω_p which is determined independently. Table 1 shows good

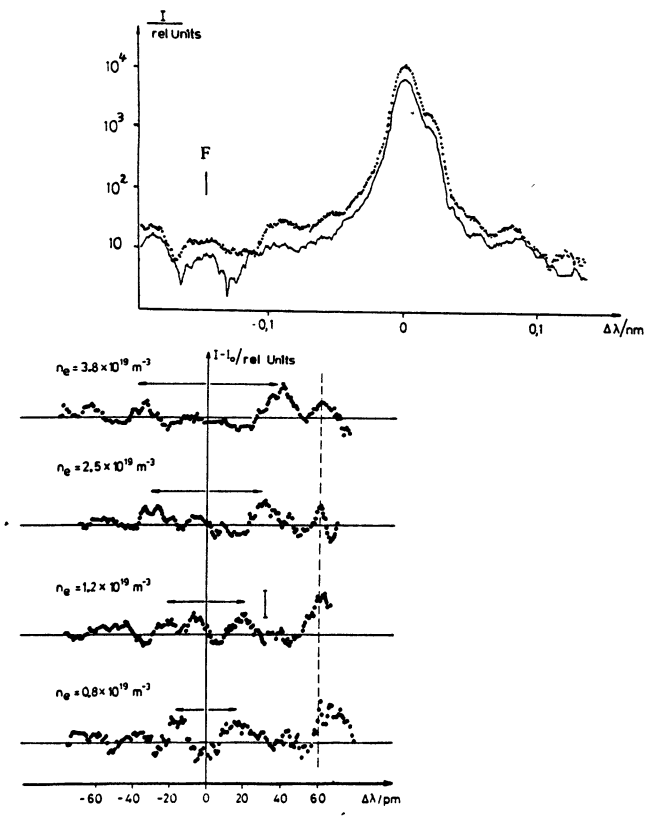

Fig. 7: Typical profiles of the HeI 447.1 nm line with and without beam injection. The lower part (enlarged around F) shows the results of subtraction of unperturbed profiles from perturbed ones (after normalization) for different electron densities n_e. F marks the position of the forbidden line.

agreement of the trapping field strengths calculated with those obtained from the satellite intensities.

TABLE 1 -E in 10^5 V/m from

Far satellite intensity	Near satellite intensity	Trapping model
1.4	1.0	1.2
1.2	0.9	1.1
1.0	1.0	1.1
1.1	0.85	1.0

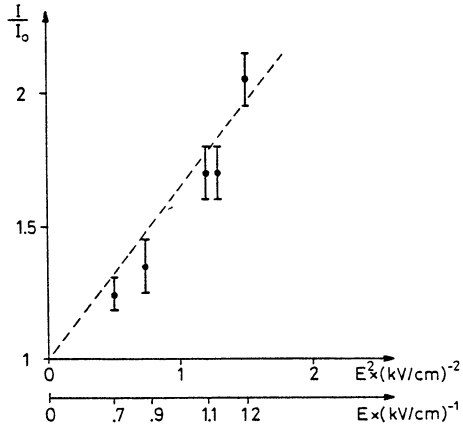

Fig. 8: The ratio of the intensity of the HeI 447.1 nm line with beam injection in relation to the one without is plotted against the rf amplitude E and E^2.

Even in the situation of the beam plasma experiment, the corona intensity model appears to work. The increased line intensity in the presence of the (pulsed) trapping field stength is correctly related to E^2, therefore also to $n_e^{-1/3}/\omega_p \sim n_e^{-4/3}$. This is shown in fig.8 and fig.9.

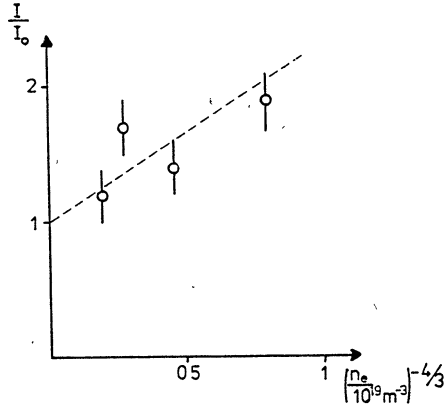

Fig. 9: I/I_0 (as in fig. 8) is plotted against the electron density $n_e^{-4/3}$.

PULSED MODEL MICROWAVE PLASMA (34.8 GHz)

In order to study the details of the dynamic Stark effect of deuterium lines, the arrangement of fig. 10 is used. Plasmas operated by a 2.45 GHz (2.5 kW) microwave resonator are subjected to the electric field of a pulsed 34.8 GHz magnetron (110 kW), the electric field focused to the discharge center by means of lenses.

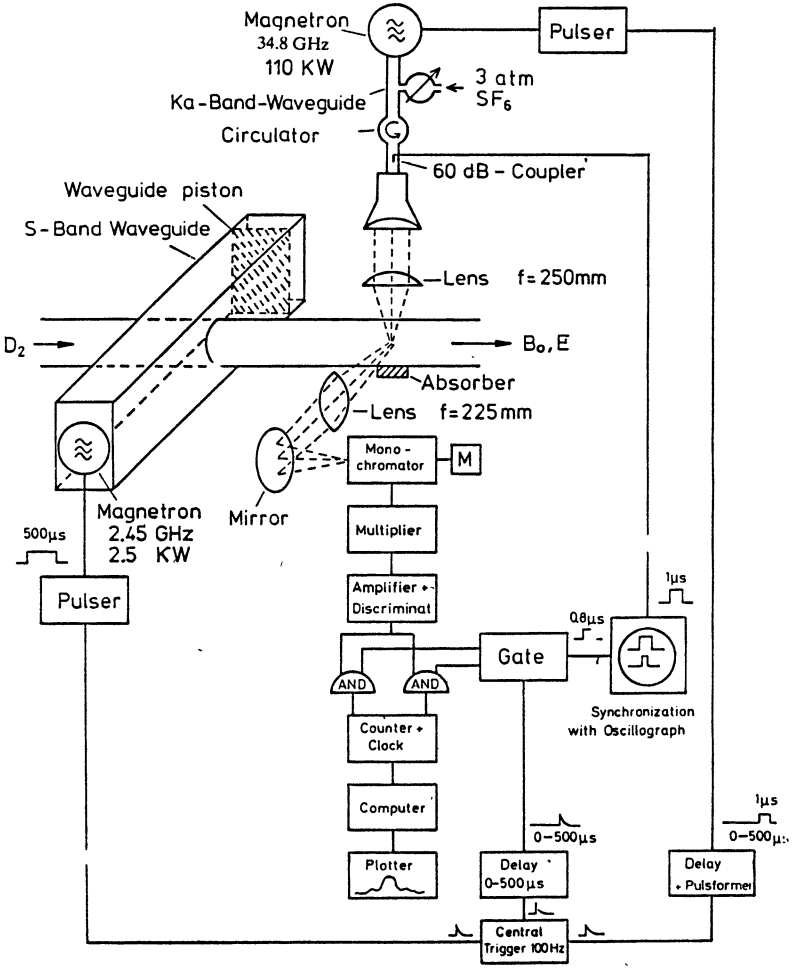

Fig. 10: Schematic diagram of the experiment

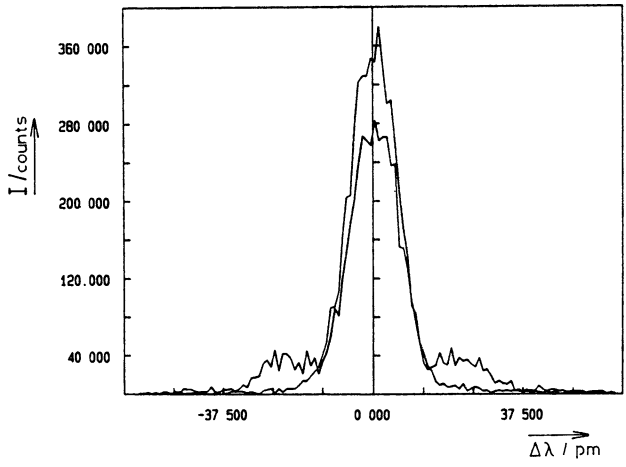

Fig. 11: Line profile of D_γ with the microwave turned on and off.

Fig. 11 demonstrates the satellites observed for the example of D_γ. In table 2 the results obtained from various lines and from the first and second order satellites are composed.

By observing at different directions of polarization, the direction of the electric field can be determined, since there is a large difference in satellite intensity for π- and σ-direction (fig. 12).

For H_α a detailed study includes fine structure and Zeeman effect. Fig. 13 gives a typical calculated line pattern. Satisfying agreement between theory and experiment can be obtained for the whole profile as confirmed by fig. 14 (E = 2.3 kV/cm in this case).

TABLE 2 -rf amplitudes E evaluated from ratios of intensity of the first and second order satellite respectively to the intensity of the central component; $\Delta\lambda$ is the observed wavelength distance of the first order satellite from the centroid of the considered line.

Line	$\Delta\lambda$/pm	First order satellite		Second order satellite	
		I_1/I_0	E/kV/cm	I_2/I_0	E/kV/cm
D_β	27.5	0.0876	1.34	0.00726	1.00
D_τ	22.0	0.24	1.24	0.0318	1.36
D_δ	19.5	0.639	1.35	0.179	1.35

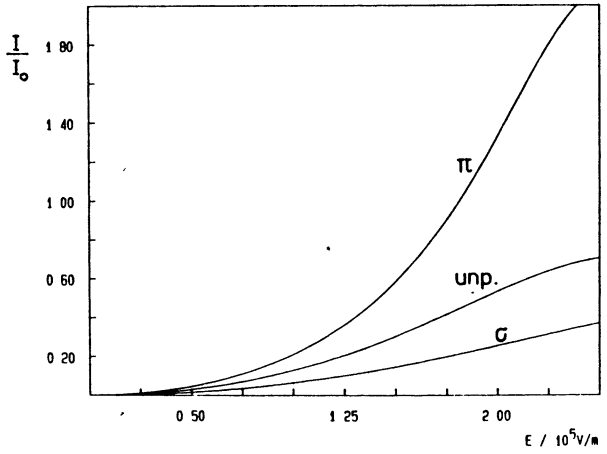

Fig. 12: Intensity ratio of the first order satellite to the central component of D_α calculated for different polarization directions as a function of the rf amplitude E; observation perpendicular to E.

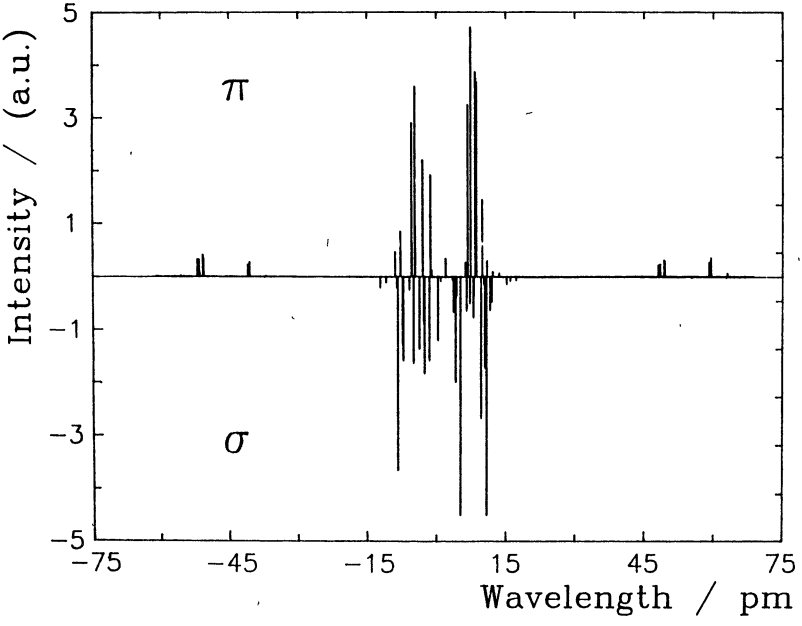

Fig. 13: Dynamic Stark pattern of D_α calculated for π- and σ-polarization with Zeeman effect (B = 140 mT) and fine structure included; observation perpendicular to B; E = 3 kV/cm.

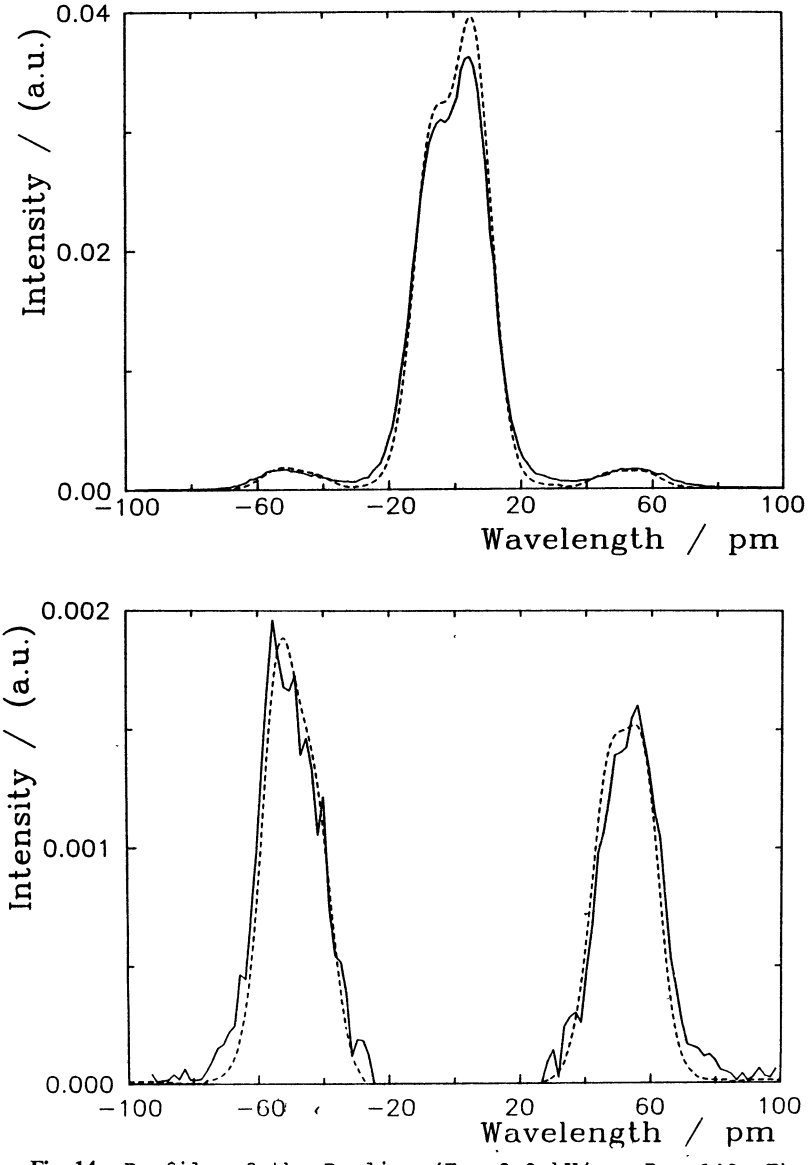

Fig. 14: Profile of the D_α line (E = 2.3 kV/cm, B = 140 mT); the areas of the calculated profile (dashed curve) and of the measured one are equal to one another. The lower diagram shows the result of subtraction of the unperturbed line profile from the profile modified by dynamic Stark splitting.

Presently the extension of the dynamic Stark effect method to higher gas pressures - and consequently to higher electron densities - is studied. For instance at atmospheric pressures the absence of van der Waals broadening is not trivial and has to be experimentally excluded. At 9.4 GHz and about 160 kW electron densities of $\geq 5 \cdot 10^{20}/m^3$ have to be expected so that the Stark effect due to the intrinsic plasma microfield is superimposed to effects of the dynamic Stark effect. This superposition is complicated, theoretically studied [10,11], but not yet sufficiently experimentally verified.

SUMMARY AND OUTLOOK

The dynamic Stark effect is quantitatively applicable to strong rf fields even when fine structure and Zeeman effect complicate the situation [12]. However, when the influence of simultaneous strong Stark broadening of the plasma is present the situation is more complicated and deserves further study.

To alleviate the problems of weak intensities in pure emission, of course, intra-cavity laser absorption [13] or laser induced fluorescence can be resorted to, though it is difficult to record an intense central line and relatively weak satellites simultaneously by this method.

The corona intensity model gives good results for E^2 (or the local power deposition) in pulsed and modulated operation. Whereas the experimental difficulties are modest, the main requirement for its use is to make sure of the validity of the corona population model. Also calibration is not trivial, in case absolute values of E are needed. If neccesary spatial resolution is possible by means of Abel inversion or again by laser induced fluorescence.

ACKNOWLEDGEMENTS

These investigations are part of the joint efforts within the Sonderforschungsbereich 191 "Niedertemperaturplasmen" and the Verbundobjekt "Plasma-Strahlungsquellen", the latter supported by the Bundesministerium für Forschung und Technologie.

REFERENCES

1. G.A. Moore, G.F. Davis, R.A. Gottscho, Phys. Rev. Lett. 52 538 (1984).
2. J.Derouard, N. Sadeghi, Opt. Comm. 57, 239 (1986).
3. G. Böhm, Z. Nat.Forsch. 35a, 293 (1979).
4. M. Dilonardo, M. Capitelli, C. Gorse, J. Wilhelm, R.Winkler, Contrib. Plasma Phys. 28, 543 (1988).
5. G. Himmel, M. Osterhold, Z. Nat.Forsch. 40a, 1220 (1985).
6. G. Himmel, A. Kamp, Plasma Phys. Cont. Fusion 27, 457 (1985).
7. H.D. Leppert, H. Schlüter, Phys. Lett. 55a, 146 (1975)
8. P. Andrzejewski, J. vom Scheidt, Plasma Phys. Contr. Fusion, 28, 371 (1986).
9. W.E. Drummond, J.H. Malmberg, T.M. O'Neil, J.R. Thomson, Phys. Fluids 13, 2422 (1970).
10. V. P. Gavrilenko, E.A. Oks, Sov. Phys. JETP 53, 1122 (1981).
11. D.G. Yakovlev, V.Yu. Yasewich, Sov. Phys. JETP 65, 40 (1987).
12. S. Hirsch, G. Himmel, Z. Phys.D 16, 35 (1990).
13. R.A. Akhmedzhanov, I.N. Polushkin, Yu.V. Rostovstev, M.Yu.Ryabikin,Yu.M.Shagiev, V.V. Yazenko, Sov. Phys. JETP 63, 30 (1986).

EFFECTIVE ELECTRON COLLISION FREQUENCY IN PLASMA WITH DRIVEN STRONG LANGMUIR TURBULENCE

D.M.Karfidov, K.F.Sergeichev, I.A.Sychov

General Physics Institute, Academy of Science of the USSR
Vavilov str.,38, Moscow, 117942, USSR

The strong Langmuir turbulence (SLT) of the plasma has been shown [1] to manifest itself as a gas of collapsing Langmuir cavities. It follows from the complex observations of such consequences of SLT as multiple bursts of weak electromagnetic radiation, the short-wave ion-sound generation and the growth of fast electron tails from the plasma electron bulk distribution. All of these phenomena testify in favor of the energy absorption from sources driving the SLT.

In this paper we report on the effective electron collision rate, ν_{ef}, at the SLT-regime in plasmas drawn by an intense electron beam. We have taken an interest in the dependence of ν_{ef} on the turbulent pumping level, including its transition to a saturation.

The studies of ν_{ef} were carried out in a microwave cavity resonator with a turbulent plasma inside by means of Q-factor measurements.

Experimental device

The experimental device shown in Fig.1, consists of a metal cylindrical vacuum tube (diameter 7 cm and length 120 cm) used as a cavity resonator owing to the transverse conducting walls, one shaped at a diaphragm with a small coupling aperture (diameter 0.8 cm) in its center and the other one in the form of a wire grid (its cell length being 0.1 cm) in order to separate the positive plasma column from the region of a cathode voltage drop, where there are strong plasma disturbances.

The plasma was produced by plasma-beam discharge in argon at

the pressure of $3 \cdot 10^{-4}$Torr, the wire grid used as a grounded anode. A weak static magnetic field ≤100 Oe was used to confine the plasma. After the discharge pulse the afterglow plasma column decayed and its noises calmed down. The radial density profile of the afterglow plasma is quite

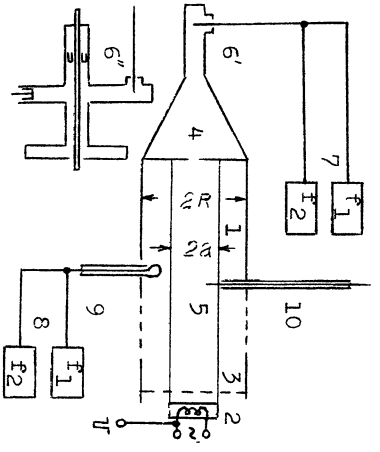

Fig.1. Experimental device 1 - cavity resonator; 2 - hot cathode; 3 - grid anode; 4-coupling aperture; 5-plasma turbulence zone; 6-H_{11}-mode launcher; 6-E_{01} mode launcher; 7 - microwe test generators; 8-microwave receivers; 9-loop antenna; 10--Langmuir probe.

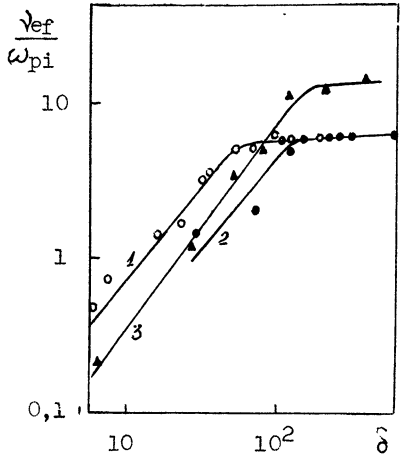

Fig.2. The effective collision rate, ν , depending on the turbulent pumping parameter δ. Curves 1,2 were measured for H-mode at plasma densities $n_0=1.2 \cdot 10^{11}$ cm^{-3} and $1.8 \cdot 10^{11}$ cm^{-3}, respectively. Curve 3 was measured for the E_{01q}-mode at $n_0=1.8 \cdot 10^{11}$ cm^{-3}. (Axial numbers of the modes are pointed out in the text).

close to the Bessel function, $n = n_0 J_0(r/R)$, and at the same time the axial density profile is rather uniform. The SLT was driven in a fairly quiet afterglow plasma by an electron beam emitted by the same cathode used before for plasma production. The electron beam channel had a diameter close to the cathode one, 3 cm. The electron beam energy, U_b was varied over the limits $200 \leq U_b \leq 2000$ ev.

The SLT has been shown in an earlier work [1] to arise when the threshold condition of the modulational instability was realized.

One of two cylindrical modes could be excited by microwave

test generators, either the H_{11q}-mode or the E_{01q}-mode, being distinqished by their electric field structures and their axial mode numbers, which are calculated from the formula:

$$q = 2L/\lambda\ (1 - \lambda^2/\lambda_c^2 - n/n_c)^{1/2}$$

where λ_c=3.41 R and λ_c=2.61 R are the cut-off wave lengths for the H_{11q} and E_{01q}- modes, respectively; n is a mean value of the plasma density. The mode excitation was carried out by one of the varieties of the coupling shown in Fig.1. The type of the cavity mode was identified by an unperturbing loop antenna placed near the resonator wall. The cavity was tuned in resonance at two values of the plasma density: $n_0=1.2\cdot10^{11}cm^{-3}$ and $n_0=1.8\cdot10^{11}cm^{-3}$. The power of the test generators was chosen much lower than the thresholds for all the parametric processes.

Measurement technique

The variations of both the resonance frequency, Δf , and the Q-factor in the form, $\Delta(1/Q)$ due to insertion of the plasma into the resonator are given by the well known expressions [2]:

$$\Delta f/f = 2^{-1}C_F' n_0/n_c \qquad (1)$$

$$\Delta(Q^{-1}) = C_F' n_0/n_c\cdot(\nu_{ef}/2\pi f)\cdot(a/R)^2(1-a^2/2R^2)\ ,$$

which were deduced from the perturbation theory as the first degree of an approximation with the following assumptions: the effective collision rate, ν_{ef}, is much less than $\omega = 2\pi f$; the turbulent region is limited by the electron beam radius, a, where ν_{ef} is taken to be constant. Here, $n_c=m\omega^2/4\pi e^2$ is the critical plasma density for the test frequency, f ; C_F' is the transversal form-factor of an homogeneous plasma filling the cavity. In the case of the H_{11q} -mode, C_F' does not depend on the axial mode number q and very weakly depends on the ratio a/R. However, in the case of the E_{01q}-mode, there is a complicated dependence of C_F' on q and a/R. Here we adduce the following evaluations of C_F':for the Bessel form of the plasma density distribution with n/n_0 = 0.7 at $n_0 = 1.8\cdot10^{11}cm^{-3}$, C_F' = 1.5 for the H_{11q}-mode, q - 35 and C_F' = 1.5 for the E_{01q}-mode, q = 30.

Since the axial component of the electric field of the E_{01q} mode is approximately 5 times greater than its transversal component in the limits of the beam radius this mode can be considered to be a longitudinal electric mode while the H_{11q}-mode is a purely transversal one. The latter circumstance was used for comparing the turbulent collision rate, ν_{ef}, measured

for these two qualitatively different cases of mutual orientation of the electron beam direction and the microwave electric field one: $\vec{I}_b \| \vec{E}_\sim$ and $\vec{I}_b \perp \vec{E}_\sim$, respectively.

The measurement technique of the Q-factor in the conditions of an afterglow plasma, whose density continuously decreases, has some peculiarities because the plasma frequency ω_{pe} instead of the test frequency ω was used as a variable quantity. A similar situation, but with the increase of ω_{pe}, takes place in the presence of an additional ionization of background gas by the electron beam drawing the plasma turbulence. Thus, to derive the Q-factor we were obliged to find a way to convert the recorded resonance curve taken in the time scale into the test frequency scale. This problem was solved by using a pair of test generators with fixed difference of frequencies Δf=10 MHz at $f_1 \simeq f_2 \simeq$6GHz.As a result we obtained separately a pair similar resonance oscillograms with their maxima shifted in time. The time shift related to the difference Δf=10 MHz was used for scaling the resonance curves.

The values of ν_{ef} were found to be calculated from the simple expression:

$$\nu_{ef} = (C_F' n_0/n_c)^{-1} \cdot (R/a)^2 \cdot 2/(1-1/2\cdot(a/R)^2) \cdot (\Delta f_t - \Delta f_0) \quad (2)$$

where Δf_t and Δf_0 are, respectively, the resonance width in presence of the turbulence and the initial resonance width without it. In this experiment we had Δf_0=5MHz.

Results

Results of measurements of ν_{ef} are shown in Fig.2 in terms of the ratio of ν_{ef} to the plasma ion frequency ω_{pi} depending on the dimensionless parameter

$$\delta = 6\cdot 10^{-3} (n_b/n_0) \cdot (T_e/mv_b^2)^{-2},$$

which characterizes the beam pumping of the turbulence. The condition δ = 1 was proved in [1] to be the threshold one for the SLT excitation. The mean Langmuir field energy appears to be approximately directly proportional to δ excluding the saturation of the SLT at high values of δ. Curves 1 and 2 were me assured in the resonance of the H_{11q}-mode for two values of plasma density $n_0 = 1.2\cdot 10^{11} cm^{-3}$ (q = 40) and $n_0 = 1.8\cdot 10^{11} cm^{-3}$ (q = 35), respectively. Curve 3 was measured in the resonance of the E_{01q}-mode at a density $n_0 = 1.8\cdot 10^{11} cm^{-3}$ (q = 30).

One can see that ν_{ef} increases almost linearly with δ until the saturation regime approaches $\delta \leq 10^4$, when ν_{ef}/ω_{pi} achieves its top value. One can see also from a comparison of curves 2 and 3 that the saturation value of δ remains constant while the respective saturation value of ν_{ef}/ω_{pi} becomes 3 times larger in case of the E_{01q}-mode. As the plasma density increases, the saturation value of δ grows, for example, 2 times in case of curve 2 as compared to curve 1.

The obtained results can be explained by the following reasons. The microwave field absorption by the rare formerly collisionless plasma is probably due to the turbulent plasma density perturbations, whose role becomes more important as their scales get shorter and their amplitudes larger, which promotes the intensification of the plasma polarization effects and the microwave field absorption.

In the SLT state the multiple density cavities undergo longitudinal compression (along the beam direction) in their final stage, the transversal one being essentially less than the former. The density perturbation unisotropy may be characterized by an excentricity, $\theta = k_{\parallel}/k_{\perp}$, which is the ratio of axial and radial wave numbers. It should be noted that the minimum longitudinal length of the compressed cavities is of order 10 r_{De}(r_{De} is the Debye length). If we consider the SLT saturation state as that of a dense packing of the collapsing cavities, the longitudinal packing should be θ times (i.e. 3 times) more dense than the transverse one, that means more effective dissipation of the E_{01q}-mode related to the H_{11q}-mode. This very result to be observed. A small divergence between curves 2 and 3 in the region of $\delta \sim 10^4$ in the case of curve 3 corresponds to the one evaluated from our earlier work [1] by an extrapolation of the dependence of the relative SLT-energy density, $W_1/n_0T_0=\varphi(\delta)$ up to 1, when the relative parameter finds its natural limit.

It should be noted that the measured values of ν_{ef} essentially surpass those predicted by the theory of the Langmuir plasmon dissipation: $\nu_{ef\ theor} \leq \omega_{pi}$ [5]. On the other hand there is a theoretical evaluation of the electromagnetic energy absorption rate by the plasma turbulence [6]:

$$\nu_{ef}=\omega_{pe}(k_m r_{De})^2 \qquad (4)$$

where k_m is the optimum wave number of the modulational in stability. If our assumption related to a mean Langmuir energy density at the turbulence saturation state, $\langle W_L/n_0T_e \rangle \sim 1$, is true, then the main part of the Langmuir wave phase volume is of the order of $kr_{De} \sim 0.3$, that the substitution into (4) gives $\nu_{ef} \sim 0.1\omega_{pe}$. This evaluation of ν_{ef} is seen to approach the measured result.

References

1. Karfidov D.M. at al., JETP Lett., Vol.48, 348, 1988.
2. Golant V.E. "Microwave-methods of plasma investigation", 1968, Nauka, or Heald M.A., Wharton C.B. Plasma diagnostics with microwaves, J.Wiley & Sons Inc., New York·London·Sydney
3. Wong A.Y., Cheung P.Y.Phys.Rev.Lett., 1984, Vol.52, 1744
4. Cheung P.V., Wong A.Y. Phys. Fluids, 1985, Vol.28, 1538.
5. Shapiro V.D., Shevchenko V.I. "Basic Plasma Physics" , 1984,Vol.2, Energoatomizdat, Moscow.
6. Litvak A.G., Fraiman G.M. in "Interactions of Strong Electromagnetic Waves with Collisionless Plasmas" , 1980, Gor'kiy.

LANGMUIR SOLITON DAMPING AND PUMPING BY THE ELECTRON BEAM

G.M.Fraiman, I.Yu.Kostyukov
Institute of Applied Physics, Academy of Sciences of the USSR
Uljanov Street 46, 603600 Nizhny Novgorod; USSR

It is known that in the frames of a traditional model of Landau damping of plasma waves, arbitrary clusters of oscillations with a monotonically decaying spatial Fourier spectrum damp due to the interaction with beams having an arbitrary distribution function. Indeed, when a monoenergetic electron beam with the initial velocity V_b passes through a HF field cluster $E(x,t)$, a time averaged work at the beam is described by the relation:

$$q(V_b) = n_o V_b \langle \Delta I \rangle , \quad \langle \Delta I \rangle = \frac{1}{2} \frac{\partial}{\partial I_o} \langle I_\sim^2 \rangle ,$$
$$I_\sim = \int_{-\infty}^{+\infty} eE(x,t)dx , \quad t = \frac{x}{V_b}, \quad t(x=0) = t_o , \qquad (1)$$
$$I_o = \frac{mV_b^2}{2}$$

where n_o is the electron beam density, $\langle \Delta I \rangle$ is the time-averaged energy gain. Then, for an arbitrary velocity distribution function $f(V)$, the dissipating power is expressed through:

$$Q = \int_{-\infty}^{+\infty} q(V)\, f(V)\, dV \qquad (2)$$

It is seen from (1, 2) that the sign of Q depends on the sign of $\langle \Delta I \rangle$. In particular, for the monochromatic field cluster we have:

$$E(x,t) = E_\sim(x)\sin(\omega t)$$
$$\langle \Delta I \rangle \propto - \frac{\partial}{\partial k} |E_k|^2 , \text{ при } \quad k = \frac{\omega}{V} \qquad (3)$$

and this value is positive for the fields with a monotonically decreasing Fourier spectrum.

According to (1-3) a stationary Langmuir soliton can not be pumped by a monoenergetic beam with arbitrary energy [1]. At the same time, experiments have shown that the similar fields (with monotonic profiles) can be easily excited by electron beams both in the layers adjacent to an electrode and in the region of the plasma resonance [2-4]. Our paper is concerned with the development of models permitting to understand these effects.

The presence of the static electric field in a cavern which slows down or accelerates electrons is the most prominent feature by which the interaction of electron beams in caverns differs from the Landau model. Qualitatively, this permits one to expect that even when the structure of a HF field is constant, electrons may give up their energy , since due to the presence of the static field, the time of their existence in the retarding phase can increase. Qualitatively, it is easier to describe the interaction process when the space coordinate rather than time is taken as the independent variable in the equation of motion:

$$\begin{cases} \dfrac{dI}{dx} = eE_{\sim}(x)\sin(\omega t) \ , \\ \dfrac{dt}{dx} = \dfrac{1}{V(I,x)} \ , \\ I(x=0) = I_o \ , \ t(x=0) = t_o \end{cases} \tag{4}$$

$I(V,x)$ is the energy of an electron in the static field. In the nonrelativistic approximation we have:

$$I(V,x) = \frac{mV^2}{2} + U(x) \tag{5}$$

In such a formulation if we are interested in the variation of the energy of the beam electrons along the route of length L, we should average over the input phase $\varphi_o = \omega t_o$. To the accuracy

same as in the Landau model, one can obtain the following system:

$$\begin{cases} \langle \Delta I \rangle = \langle I(L, f_o, I_o) - I_o \rangle = \frac{1}{4} \frac{\partial}{\partial I_o} |I_\sim|^2 \\ I_\sim = \int_0^L eE_\sim(x) \exp(i\theta_o(I_o, x)) dx \\ \theta_o(I_o, x) = \omega \int_0^x \frac{dx}{V(I_o, x)} \end{cases} \tag{6}$$

Note that we have written down (6) in the form analogous to formula (1) used in the description of Landau damping.

To conclude the survey of general results, we will give two more remarks. Firstly, the relation (1) can also be generalized to the nonlinear field regime. The corresponding calculations, based on the fact that (4) are Hamiltonian equations, show that in the calculation of θ_o in (5) it suffices to take into account the averaged ponderomotive force. I.e. in the nonrelativistic approximation, $V(I_o, x)$ may be determined from:

$$I_o = \frac{mV^2}{2} + U(x) + \frac{e^2 E_\sim^2}{4m\omega^2} \tag{7}$$

Our second remark concerns the accuracy of description within (6-7). It appears that $|\theta_\sim| = |\omega t_\sim| \ll 1$ is a small parameter of the problem:

$$\omega t_\sim \propto \left| E_\sim / \frac{\partial V}{\partial x} \right| \tag{8}$$

It means that the electron time lag per period should be small in comparison with this period.

Using (6) we will analyze the problem of the interaction of the beam having the velocity V and the stationary Langmuir soliton. Note that if in (6) we have:

$$E_\sim(x) = \frac{E_o}{\mathrm{ch}(k_o x)} \quad , \qquad U(x) = \frac{U_o}{\mathrm{ch}^2(k_o x)} \tag{9}$$

then we can obtain an analytical result:

$$<\Delta I>= \left(\frac{\pi}{2}\right)^2 A\frac{\partial}{\partial V}\frac{1}{ch^2\left(\frac{\pi}{2k_o}\frac{\omega}{V}\right)}\begin{cases}\cos^2\left(\frac{1}{2k_o}\frac{\omega}{V}\operatorname{arcch}\frac{V^2-V_\sim^2}{V^2+V_\sim^2}\right) & \frac{V}{V_\sim}\geq 1.\ ,\\ \sin^2\left(\frac{1}{2k_o}\frac{\omega}{V}\operatorname{arcch}\frac{V_\sim^2-V^2}{V_\sim^2+V^2}\right) & \frac{V}{V_\sim}< 1.\end{cases}$$

$$A = \frac{(eE_o/k_o)^2}{mV} \quad , \quad \frac{mV_\sim^2}{2} = U_o \ . \tag{10}$$

For the running soliton we have :

$$E_\sim(x) = \frac{E_o\exp(ikx)}{ch(k_o\xi)} \ , \quad U(x) = \frac{U_o}{ch^2(k_o\xi)} \ , \quad \xi = x - V_{rp}t$$

when : $k_o \gg k$, $V \gg V_\sim$ one should substitute ω for $\omega - kV_{rp}$, V for $V - V_{rp}$ and $\frac{\omega}{V}$ for $\frac{\omega}{V} - k$ in (10).

The first relation in the set (10) corresponds to the transit beams of electrons, the second one corresponds to the reflected ones. It is readily seen from here that if $U_o = 0$, i.e. the potential energy of the static field specified by the conditions of quasineutrality is compensated by the potential of the averaged motion, then we have an ordinary Landau damping of a stationary soliton [1]. In the general case ($U_o \neq 0$) the asymptotic formula of Landau damping can be applied for beams with the energies:

$$\frac{mV^2}{2} \gg \sqrt{U_o m\omega^2/k_o^2} \tag{11}$$

For the beams with the energy satisfying the inverse inequality, there exist generation zones alternating with absorption zones (Fig. 1). In this case, the width of the zones diminishes, while the increment maximum (in our approximation) increases without restriction as the beam energy approaches U_o (the minimal energy corresponding to the transit regimes).

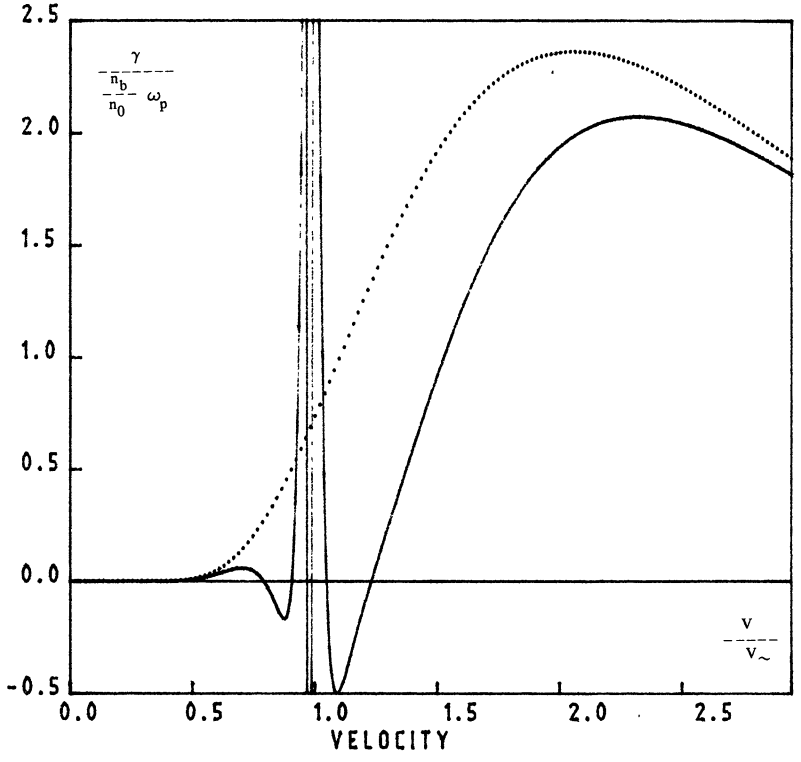

Fig.1

a) The normalized increment of the stationary langmuir soliton pumping: $\gamma\left(\omega_p \frac{n_b}{n_0}\right)^{-1} = \left(\omega_p \frac{n_b}{n_0}\right)^{-1} \frac{d}{dt} \ln\left(\frac{1}{8\pi}\int_{-\infty}^{+\infty} E_{\sim}^2 dx\right)$ a function of the normalized beam velocity: $\frac{V}{V_{\sim}}$, $\frac{mV_{\sim}^2}{2} = \frac{e^2E_o^2}{4m\omega^2}$ (a solid line).

$k_o r_{de} = \frac{1}{3}$, $E_o^2 = 96\pi n_o T (k_o r_{de})^2$, $U_o = \frac{e^2E_o^2}{4m\omega^2}$.

b) The same dependence for the stationary soliton in the absence of the static field $U_o = 0$ (a dashed line).

We will now present our estimates for the first generation zone. In a nonisothermal plasma $T_e \gg T_i$, $U_o = \frac{e^2 E_\sim^2}{4m\omega^2}$. The increment maximum $\gamma_{max} \simeq \frac{\pi^3}{2} \omega_p \frac{n_b}{n_o} \exp\left\{ 2\left(1 - \frac{1}{k_o r_{de}} \right)\right\}$ is achieved for the beams with the energy $\frac{mV^2}{2} \simeq kT_e$, the width of the first zone: $\Delta\left(\frac{mV^2}{2} \right) \simeq \sqrt{kT_e mV_\sim^2}$.

Finally we would like to emphasize that unlike the Cerenkov pumping mechanism of the moving soliton [1], which is realized for sufficiently epithermal electrons, qualitatively new effects (the possibility to pump solitons) are achieved at low beam energies.

REFERENCES

1. Rudakov L.I. Slowdown of the electron beams in plasma with the high level of Langmuir turbulence. Dokl. Akad. Nauk SSSR, 1972, v.207, vyp.4, p.821-823.
2. Brodsky Yu.Ya., Nechuev S.I., Slutsker Ya.Z., Feigin A.M., Fraiman G.M. A new mechanism of2 generation of intensive Langmuir oscillations in plasma. Fizika plazmy, 1989, v.15, vyp.10, p.1187-1196.
3. Stenzel R.L. Instability of the sheat-plasma resonance. Phys. Rev. Lett., 1988, v.60, N8, p.704-707.
4. Cheng P.Y., Wong A.Y. Nonlinear evolution of electron-beam plasma interactions. Phys. Fluids, 1985, v.28, N5, p.1538-1548.

GENERATION OF HIGH POTENTIALS IN THE PLASMA BY THE INTERACTION WITH INTENSE MICROWAVE RADIATION

* G.M. Batanov, V.A. Ivanov, M.E. Konyzhev
** A.A. Ravaev, V.D. Seleznev, A.I. Khomenko
(*) General Physics Institute, USSR Academy of Sciences, Moscow
(**) Moscow Radiotechnical Institute, USSR Academy of Sciences

A study of strong electromagnetic field interaction with the plasma is vital both from the viewpoint of fundamental and applied plasma physics. In particular, generation of strong Langmuir waves in the plasma with microwave radiation (MWR) and charged particle acceleration by this wave [1], MWR power conversion into the quasi-stationary electric current power in the plasma [2] as a key process in the promising method of the long-distance wireless energy transmission with MWR [3] are of great interest.

Here we consider experiments on the plasma interaction with 5×10^5 and 10^7 W/cm^2 MWR intensities. A carcinotron using a relativistic electron beam generated MWR pulse 50 ns long, with the

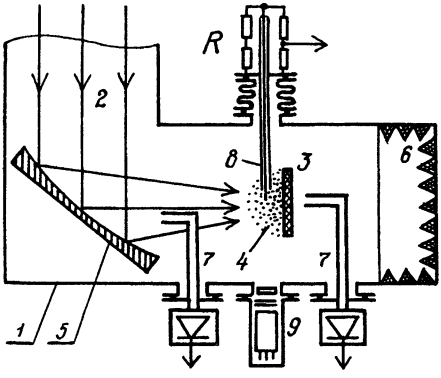

Fig.1. The first experiment diagram: 1-vacuum chamber; 2-MWR beam; 3 - dielectric plate; 4 - plasma; 5-focusing mirror; 6-MWR absorbing panels; 7 - waveguide antennas; 8-plasma probe; 9- X-ray detector.

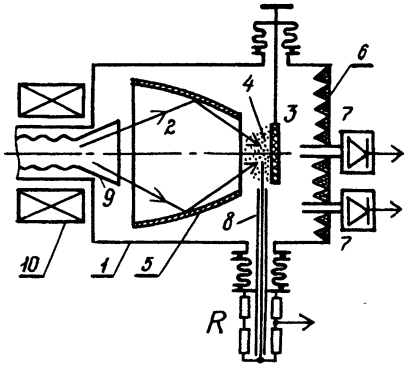

Fig.2. The second experiment diagram: notations 1-8 are as for Fig.1; 9 - carsinotron; 10 - magnetic field solenoid.

wavelength of λ=3 cm and the power of P=100 MW [4]. The main oscillation mode at the carcinotron output was TM_{02}. Two MWR focusing system modifications were used (Figs.1 and 2). At the first one, the converter transformed TM_{02} mode into the transverse wave which was focused into the vacuum chamber (residual air pressure was 10^{-3} Pa) by a quasi-optic system of mirrors. The focused MWR had almost Gaussian intensity profile with a maximum value of intensity $I=5\times10^5$ W/cm^2 (Fig.3a). At the second modification the maximum intensity reached 10^7 W/cm^2 due to the TM_{02} mode MWR was directly focused into the vacuum chamber by an elliptic mirror (Figs.2 and 3b). To measure MWR pulse intensity and duration, the scanning waveguide antennas with the calibrated attenuation were used. The antennas were matched with the semiconductor or Pockels effect transducers. The plasma flare was studied in visible and soft X-ray radiation ranges. Dynamics of plasma density was measured with a Langmuir probe and microwave (MW) interferometer at a wavelength of 8 mm. The onset of the critical plasma density was detected with the cut-off of MWR transmitted through the plasma. The space profile measurements of the plasma potential were provided by a scanning electric probe with an ohmic load of 10^4 Ohms with the 10 ns time-resolved.

In the experiments, the plasma was produced by a MWR discharge

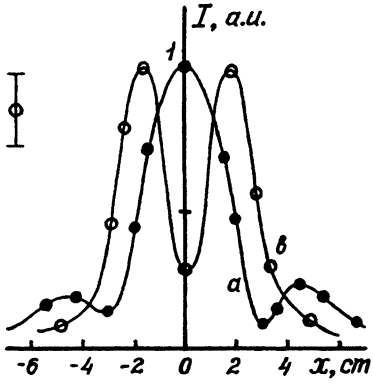

Fig.3. Space profile of the MWR intensity in relative units: a - the first modification of the experiments; b - the second one.

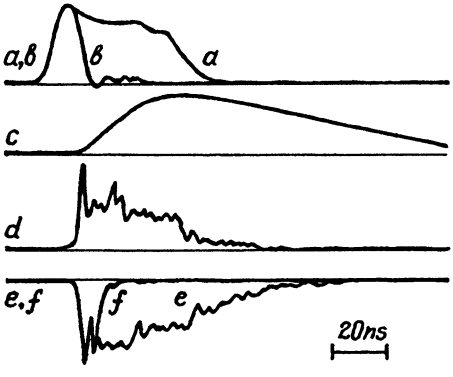

Fig.4. Oscillograms: a,b-pulse envelops of incident and transmitted MWR; c-plasma density; d-potential; e,f-soft X-ray with quantum energy of 1.5 and 15 keV, respectively.

on the surface of the dielectric plate placed into the focus of a high-power MWR beam. For the first experiment modification the typical oscillograms of signals are shown in Fig.4. The plasma generation is accompanied by the cut-off of MWR transmitted through the plasma, the occurrence of the high potential jump (up to 15 kV) and the soft X-ray radiation (1-25 keV).

The high potential existed in a limited central plasma area (Fig.5), whose dimension increased during MWR pulse. Outside this area the potential did not exceed few hundred volts. Near the high potential jump region the plasma density is close to the critical one (10^{12} cm^{-3}) for the incident MWR and decreases with a distance from the dielectric plate. In the high potential area the plasma density exceeded the critical one fitting the data on a cut-off of transmitted MWR.

When the probe external load R was varied in the range of 10^4 to 0.1 Ohm, the unipolar positive circuit current flowing via the system probe-plasma-chamberwall increased from 1 to 500 A (Fig.6) just as evaluated ion saturation current from the plasma to the probe was less than 10^{-2} A. Under these conditions cathode spots and local arc craters on the probe surface were observed. Therefore, the probe submerged in the high potential plasma area was a strongly electron emitting. The electron emission (a thermo- or auto-emission) from the probe makes its potential to approach the

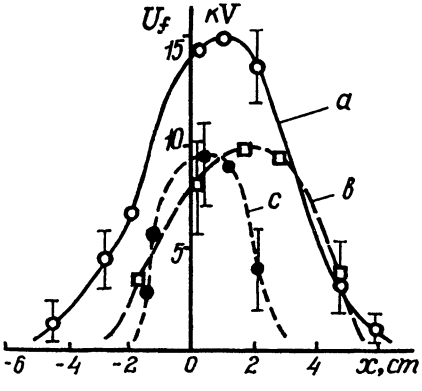

Fig.5. Plasma potential profile: a-at a distance of 1 cm from the plate surface; b,c - 3 and 4 cm, respectively.

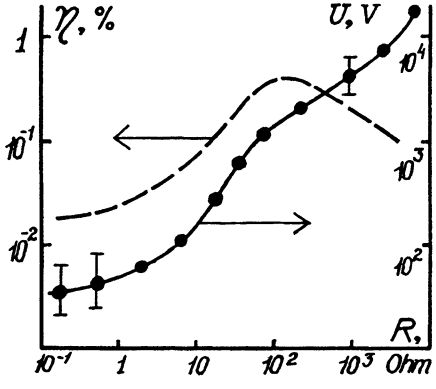

Fig.6. Loading characteristic and the efficiency η of the MWR energy conversion at the external load R.

plasma one and decreases it at high currents.

A study of the space-profile soft X-ray radiation has proved that we dealt with the bremsstrahlung one. Fast electrons generated under the plasma-MWR interaction produced X-ray radiation at hitting the dielectric plate (Fig.7). When the plasma potential deminished the X-ray intensity reduced by several times and the circuit current increased. This is an evidence that majority fast electrons moved against the potential jump and participated in a generation of the electric current between the plasma and the chamber wall. As well as at medium intensities of the MWR [5], we observed the phenomenon of the MWR power conversion into the quasi-stationary direct electric current. The efficiency of this process difined by formula $\eta = U^2/RP$ as a function of the load value is illustrated in Fig.6, showing that the maximum value of η is 0.4 % at the load of about 200 Ohm and the potential of several kV. Since only a fraction of plasma electron energy is dissipated on the external load, it is of interest to determine the total power of the fast electron plasma flow participating in the current transfer. Using the volt-ampere characteristic of the experimental system as a converter, we calculated fast electron flow power: $P_e = \int U(J)dJ$ which is shown in Fig.8. This data yields the minimum estimate of the MWR power convertion efficiency into fast electron power about 1 %. Similar measurements with a MWR intensity of 10^7 W/cm^2 gave close value 2 % with a maximum of the

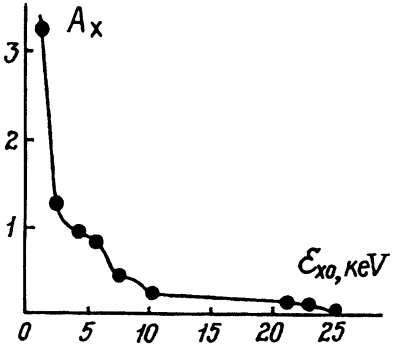

Fig.7. Intensity of the soft X-ray radiation vs. the foil-filter cutoff energy of the detector.

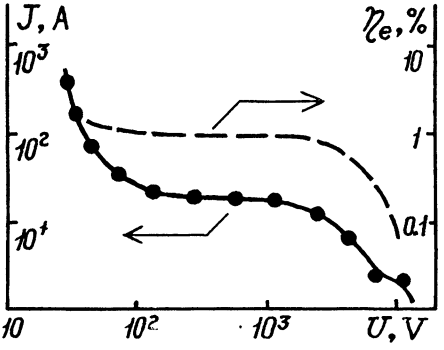

Fig.8. V(J) characteristic and the efficiency of the MWR energy conversion into the energy flux of plasma fast electrons η_e.

potential amplitude 100 kV. Under these conditions the high potential jump in the plasma appeared during and due to the processes of heating or acceleration of electrons when the plasma interaction with the high intensity MWR took place. The presence of the potential jump near the critical plasma density indicated that the electrons were heated or accelerated in this local area, and, as a consequence, that sufficiently local charge-separating electric field in the plasma occurred.

Heating of electrons in the plasma due to the Coulomb collisions up to the high temperature causing the potential jump is unlikely. Indeed, a simple equation needed to estimate the electron energy $\mathcal{E}_e$ in the MWR field E is:

$$\frac{d\mathcal{E}_e}{dt} = \frac{e^2E^2\nu}{m(\omega^2+\nu^2)} - \mathcal{E}_e\tilde{\nu} ,$$

where the maximum estimate $\mathcal{E}_e$ is given by the formula:

$$\mathcal{E}_{e\,max} \simeq \left[Z^2e^4\left(\frac{M}{m}\right)^{1/2}\cdot\frac{e^2E^2}{m\omega^2}n\delta\right]^{1/3} .$$

Here ω is a MWR cyclic frequency, m and e are the mass and charge of the electron, M is an average mass of ions and atoms in the plasma, Z is its nuclear charge, n and δ are the density of gas layer near the dielectric plate and its thickness, ν is the effective frequency of the electron collisions, $\tilde{\nu}$ is the effective frequency of energy loss by electrons, related to their drift:

$$\nu \simeq \frac{Z^2e^4n}{\mathcal{E}_{eo}^{3/2}m^{1/2}} ; \quad \mathcal{E}_{eo} \simeq \frac{e^2E^2}{m\omega^2} = \frac{2e^2\lambda^2 I}{\pi mc^2} ; \quad \tilde{\nu} \simeq \frac{v_s}{\delta} \simeq \frac{1}{\delta}\left(\frac{2\mathcal{E}_{eo}}{M}\right)^{1/2} .$$

At $I=10^7$ W/cm^2, we obtain $\mathcal{E}_{emax} \leq 1$ keV, which is much less than the value of the recorded potential. So we deal with the electron acceleration in the plasma.

We believe that the most probable mechanism for the electron acceleration is the mechanism associated with driving a strong Langmuir wave in the area of the plasma resonance. The value of Langmuir wave electric field E_ℓ and its locality scale ℓ at a plasma resonance region are given by the expressions [6]:

$$E_{\ell max} \simeq \frac{E}{s}(2\pi kL)^{-1/2} ; \quad \ell \simeq sL ,$$

where k is the MWR vector, L is the characteristic scale of the

plasma inhomogeneity, s is the parameter which equal:

$$s = max\left\{\frac{\nu}{\omega}, \left(\frac{r_D}{L}\right)^{2/3}, \left(\frac{eE}{m\omega^2 L}\right)^{1/2}, \left(\frac{2\pi eE}{m\omega^2 \lambda}\right)^{2/3}\right\},$$

where expressions in parantheses reflect effects of various Langmuir wave dissipation mechanisms. The former two are the linear Coulomb collisions and Landau damping (r_D is the Debye radius). The latter two mechanisms are non-linear for the field E_ℓ : wave breaking of strong Langmuir oscillations and relativistic detuning of the electron oscillation synchronism. Even at $I=10^7$ W/cm^2, the latter effect is negligible as compared with the effect of the wave breaking, which overrises also the linear mechanisms. Here, accelerated electrons, according to [6] may have large maximum $\mathcal{E}_{emax}$ and medium $\overline{\mathcal{E}}_e$ energies:

$$\mathcal{E}_{emax} \simeq 2\pi e E_{\ell max} \cdot \ell = eE(\lambda L)^{1/2}; \quad \overline{\mathcal{E}}_e \simeq \frac{eE}{2\pi}(\lambda L)^{1/2}.$$

Estimates at $I=10^7$ W/cm^2 yield $\mathcal{E}_{emax}$=100-200 keV, $\overline{\mathcal{E}}_e$=15-35 keV which agrees with experimental data by an order of magnitudes.

Thus, the existence of high positive potential in the plasma under the interaction with intense MWR is proved to be caused by driving and the non-linear mechanism of tipping over of the Langmuir wave in the plasma resonance accompanied by the acceleration of minority plasma electrons. Fast electrons exit from the resonant area produced the quasi-stationary electric field of the charge separation and the unipolar current circulating in the system. Here, up to 1 % of the incident MWR power is converted into the current and the fraction of the power dissipated by the external load is about 0.4 %. Although these values are much lower than those obtained for medium MWR intensities and the mcs-pulse durations [5], we hope for the conversion efficiency growth with the increased duration of the high intensity MWR pulse.

References

[1] T. Tajima, J.Dawson, Phys. Rev. Lett. 1979, 43, p.267.
[2] G.A. Askaryan et al., JETP Lett. 1979, 29, p.648.
[3] G.A. Askaryan et al., Sov. Tech. Phys. Lett. 1989, 15.
[4] E.B. Abubakirov et al., Abstr. VIII Int. Conf. on High Power Particles Beams, Novosibirsk. 1990, Pt.2, p.265.
[5] G.M.Batanov, V.A.Ivanov, Proc. General Phys. Inst. 1988, 16.
[6] S.V. Bulanov et al., Physics Reports. 1990, 186, N 1, p.1.

NUMERICAL INVESTIGATION OF BEAT-WAVE ELECTRON ACCELERATION IN INHOMOGENEOUS PLASMAS

L.M.Gorbunov, A.N.Moskalev
P.N.Lebedev Physics Institute, Academy of Sciences of the USSR
Moscow

The plasma beat-wave accelerator (PBWA) is one of the most promising collective acceleration ideas proposed in recent years /1-3/. This accelerator uses two-frequency laser pulse to excite the charge-density waves (plasma waves). The wave is then used to accelerate electrons. The effective excitation is reached by carrying out the resonant condition $\omega_1 - \omega_2 = \omega \simeq \omega_p$, which connects the difference of laser wave frequencies $\omega_{1,2}$ with plasma frequency $\omega_p = \sqrt{4\pi e^2 N/m}$, determined by plasma concentration N. Hence the strict limitation on plasma density follows and even small variations in plasma density influence essentialy on the process of acceleration. The results of numerical investigations of beat-wave electron acceleration in inhomogeneous plasmas are presented in this report.

1. Basic equations

1. The plasma wave field. The equation for complex slowly varying amplitude of plasma wave excited by two-frequency electromagnetic pulse has been discussed in many papers (e.g. Refs.4-10). It is

$$-2i\frac{\partial q}{\partial \xi} - q\cdot\delta + \frac{3}{2}q|q|^2 = a_1 a_2^* \qquad (1)$$

where $q = eE_l(\xi, X)/2mc\omega$ is dimensionless amplitude of plasma wave; the variable $\xi = \frac{\omega}{v_g}(x - v_g t)$ determines a distance from leading edge of laser pulse in moving with pulse frame; dependence upon variable X is connected with a density variation $\delta = \left(\omega_p^2(X) - \omega^2\right)/\omega^2 = \delta N(X)/N_0$; v_g is the group velocity of pulse, $N_0 = m\omega^2/4\pi e^2$ is the resonant plasma concentration in linear approximation, $a_{1,2} = eE_{1,2}^{tr}/2mc\omega_{1,2}$ are dimensionless amplitudes of electromagnetic waves. The

derivation of Eq. (1) used the assimptions $|q| < 1$, $|a_{1,2}| < 1$, and $|\delta| < 1$. Besides dissipation, thermal motion of electrons, ion dynamics, electromagnetic cascading, generation of plasma wave harmonics, transverse effects are omitted. All thise problems has been discussed in literature and conditions of validity Eq.(1) were formulated in Ref. 11.

Transforming to real quantities in Eq.(1) ($q = -iQ\exp(i\varphi)$, $a_{1,2} = A_{1,2}\exp(i\varphi_{1,2})$) we obtain:

$$2\frac{dQ}{d\xi} = -A_1 A_2 \cos\theta \qquad (2)$$

$$2Q\frac{d\theta}{d\xi} - Q\delta(x) + \frac{3}{2}Q^3 = A_1 A_2 \sin\theta, \qquad (3)$$

where $\theta = \varphi - \varphi_1 - \varphi_2$. The real electric field of plasma wave is expressed through values Q and θ by means of relation

$$E(\xi, x) = \frac{eE^{\ell}}{2mc\omega} = 2Q(x,\xi)\cos\left[\xi + \theta(\xi, x)\right] \qquad (4)$$

2. Equation of electron motion. The trajectory of accelerated electron is described in the form $X = V_g(t - t_o) + X_o + X_1(t)$, where X_o and V_g are position and velocity of particle in initial time t_o respectively. From equation of motion of relativistic particle for the value $y_1 = x_1\omega/c$ we obtain

$$\frac{d^2 y_1}{d\tau^2} = 2\left[\gamma_o^{-2} - 2\frac{dy_1}{d\tau}\sqrt{1-\gamma_o^{-2}} - \left(\frac{dy_1}{d\tau}\right)^2\right]^{3/2} Q(y,\eta)\cos\left[\eta + \theta(y,\eta)\right] \qquad (5)$$

where $\tau = \omega t$ is dimensionless time, $y = \frac{\omega}{c}x_o + \tau - \tau_o + y_1$; $\eta = \frac{\omega}{c}x_o + y_1 - \tau_o$, $\gamma_o = \left(1 - v_g^2/c^2\right)^{-\frac{1}{2}}$. The electron energy in initial time to is equal $\varepsilon_o = mc^2\gamma_o$. In the next time the energy is calculated by means of formula

$$\gamma(\tau) = \frac{\varepsilon}{mc^2} = \left[\gamma_o^{-2} - 2\frac{dy_1}{d\tau}\sqrt{1-\gamma_o^{-2}} - \left(\frac{dy_1}{d\tau}\right)^2\right]^{-\frac{1}{2}} \qquad (6)$$

3. Scheme of calculations. We prepouse that the pulse form, its initial position and density profile of plasma are given. Also we believe to be known initial position of a accelerated electron (place of injection). The electric field accelerating of the particle is calculated from Eq. (4). Then Eq. (5) is used to obtain the values y_1, $dy_1/d\tau$ and energy (6) over small time inteval $\Delta\tau$. After that by means of Eq. (4) we determine the field acting on the particle by new position of pulse, coordinate and velocity of the particle. From Eq. (5) we obtain the values y_1, $dy_1/d\tau$ and energy in time

$2\Delta\tau$ and so on. Thus we investigate the plasma wave excitation and electron acceleration in inhomogeneous plasmas. In our consideration the electric field of plasma wave is calculated not only in place of particle but in all space between the electron and leading edge of laser pulse.

II. Excitation of plasma waves in homogeneous plasmas

For more clear understanding the plasma wave excitation in inhomogeneous plasmas let us consider shortly the main results for homogeneous plasmas.

a). Linear approximation; nonresonant concentration.

We neglect the nonlinearity of plasma wave in Eq. (1) (third term in the left side) and suppose, that value of a detuning δ is not equal zero. The solution of Eq. (1) in this case has the next form /12, 13/

$$q = \frac{i}{2} e^{i\delta\xi/2} \int_0^{\xi} d\xi' a_1(\xi') a_2^*(\xi') e^{i\delta\xi'/2}, \qquad (7)$$

where dependence of amplitudes $a_{1,2}$ on variable ξ is connected with pulse form. For a square pulse from Eq. (7) we find

$$q = -\frac{a_1 a_2^*}{\delta}\left(1 - e^{-i\xi\delta/2}\right) \qquad (8)$$

Using expressions (8) and (4) we obtain the field of plasma wave

$$E = 2\frac{A_1 A_2}{\delta}\left\{\sin\xi - \sin\left[\xi\left(1+\frac{\delta}{2}\right)\right]\right\} \qquad (9)$$

In first term of Eq. (9) the field changes with the frequency ω and it determines the forced wave. The second therm corresponds to free oscillations of electrons with frequency ω_p The both kinds of oscillations have the equale amplitudes and the resultant field (9) is the an amplitude-modulated plasma wave with period of envelope $\xi_0 = \pi/|\delta|$ and the maximum value of amplitude $E_{0,max} = 2A_1A_2/|\delta|$. The slow changed phase of the wave has the jumps on π . (Fig.1).

As one example else we consider the pulse with linearly increasing intensity

$$a_1(\xi)\, a_2^*(\xi) = A_{10} A_{20} (\xi/L)\, e^{i(\varphi_{10} - \varphi_{20})}$$

From Eqs. (7) and (4) we find the solution also in the form of sum two waves with frequencies ω and ω_p

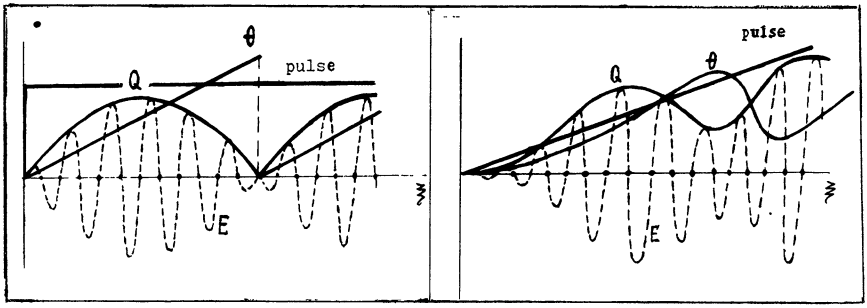

Fig.1 Fig.2

Electric field E, amplitude Q and phase θ of a plasma wave excited by the laser pulse of square form (Fig.1) and the laser pulse with increased intensity (Fig.2) in homogeneous plasma with nonresonant density ($\delta \neq 0$) (linear approximation).

$$E = 2\frac{A_{10}A_{20}}{L\delta}\left\{\sqrt{\xi^2+\frac{4}{\delta^2}}\,\sin\left(\xi - \operatorname{arctg}\frac{2}{\xi\delta}\right) + \frac{2}{\delta}\sin\left[\frac{\xi}{2}\left(1+\frac{\delta}{2}\right)\right]\right\}$$

In this case the amplitude of forced wave (first term) grows with increasing of ξ but the amplitude of free oscillations (second term) is the constant. The modulation amplitude is not full and the variations of phase are less than π (Fig.2).

Thus the plasma wave excited of two-frequency laser pulse has in general case modulated amplitude and not stationary phase. The values of variation amplitude and phase are connected with the laser pulse form. Only in the limit very slow increasing intensity it is possible ignore the excitation of free plasma wave and consider one forced wave with frequency ω.

By including a dissipation in consideration the free plasma wave have been neglected on the distance $\xi > \omega/\nu$ from the leading edge of square laser pulse. Only forced wave with constant amplitude exsists for more longer distances.

b) Nonlinear wave; $\delta = 0$. In accordance with linear theory the amplitude of plasma wave envelope grows by reduction of detuning. It is necessary in this case take in consideration nonlinearity of plasma wave. For zeroth detuning this problem was considered in Ref.4. For square laser pulse it is possible to

obtain analitical solution of Eq. (2) and (3) and corresponding curves are shown in Fig.3. As in the case of linear theory for $\delta \neq 0$ the nonlinear theory gives by $\delta = 0$ the amplitude modulated plasma wave. More considerable difference between those two theories arises in phase variation. In linear theory the phase changes in direct proportion to variable ξ and because the space periodicity of electric field takes place. In nonlinear theory the phase varies more complicated manner (Fig.3) and the electric field losses the special periodicity.

The period of amplitude oscillation and maximum value of amplitude can be evaluated from qualitative consideration (Ref. /14/). The amplitude of excited plasma wave is sufficiently small on the short distance from the leading edge of the laser pulse and according to Eq. (1) it grows linearly by increase of variable ξ ($q = \frac{i}{2} a_1 a_2^* \xi$). The nonlinear shift of frequency enlarges by growth of amplitude and it may be evaluated from soulution of Eq. (1) with zero right side ($\ln q = -\frac{3i}{4} \int_0^{\xi} d\xi' |q(\xi')|^2$). The period ξ_0 of amplitude oscillation is evaluated by putting linearly approximated value q in expression for nonlinear shift of frequency and taking it to be equal π. The resul is $\xi_0 \simeq (16\pi / A_1^2 A_2^2)^{1/3}$. Maximum of amplitude

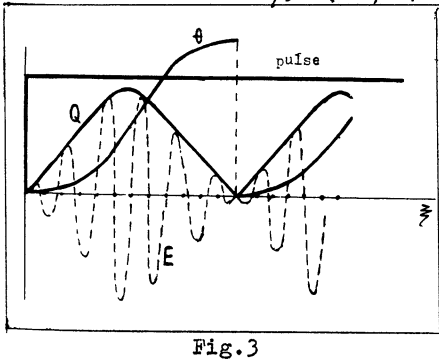

Fig.3

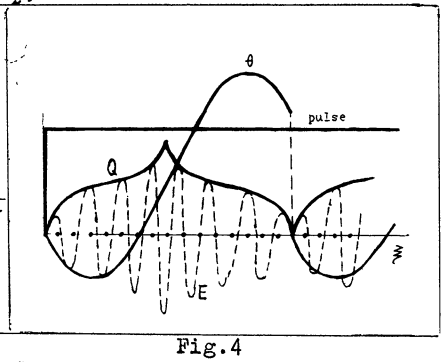

Fig.4

Electric field E , amplitude Q and phase θ of plasma wave excited by the laser pulse of square form in homogeneous plasma by $\delta = 0$ (Fig. 3) and by $\delta = \delta_c$ (Fig.4) (nonlinear approximation).

takes place by $\xi = \xi_0/2$ and can be evaluated by means of linear expression for q. The result is given by $E_{max} \simeq (A_1 A_2)^{1/3}/4\,(2\pi)^{1/3}$.

c). Nonlinear resonance. It has been shown /5/ that excitation of nonlinear plasma wave with nonvanishing value δ is accompanied by nonlinear resonance. In thise conditions in wide range of variable ξ the nonlinear shift of frequency practicaly compensates that dephasing between free oscillations and driven force which is determined of detuning δ. In process of amplitude growth the frequency of free nonlinear oscillation is approuched to the frequency of driven force. Because of negative sign of nonlinear frequency shift this tuning is possible for positive detuning δ_c when a plasma density is higher than value N_0. For the laser pulse with square form Eqs. (2) and (3) have the first integral and solution can be obtained in implisit form /15/. The corresponding critical detuning is $\delta_c \simeq (3^{4/3} 2^{1/3}/4)\,(A_1 A_2)^{2/3}$. The electric field of plasma wave, the slow varying amplitude and phase are shown in Fig.4 /16,17/. The amplitude of electric field has the maximum value $E_{max} \simeq (A_1 A_2)^{1/3}/2(2\pi)^{1/3}$ by $\xi \simeq 8{,}5/(A_1 A_2)^{2/3}$.

III. Plasma wave excitation and electron acceleration in plasma with linear density profile

For square form laser pulse the analytic implicit solution of Eqs. (2) and (3) can be obtained in inhomogeneous plasmas by consideration the detuning δ as parameter depending from coordinate x. The analysis of this solution is presented in Ref.18. However the results of numerical investigations have more obvious feature. The evolution of amplitude Q (envelope) and phase θ is shown in Fig.5 for pulse propogating in direction of increasing concentration. It is clear seen in regions with different values of density the discussed above regimes. The dotted lines in Fig.5 show the region of nonlinear phase stabilization of plasma wave to be discussed in Ref. 18. Also in Fig.5 the corresponding density variations are shown.

The influence of plasma inhomogeneity on the electron acceleration depends essentialy on the ralation between two scales. The first one is connected with inhomogeneity and determines the length of resonant exitation region of plasma waves ℓ_N. The second scale characterizes the distance of dephasing

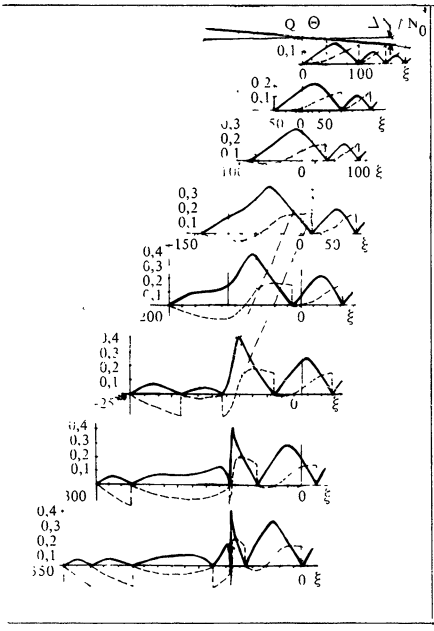

Fig. 5

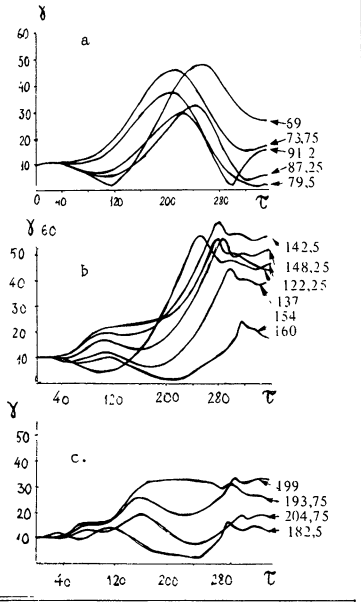

Fig. 6

Fig.5. Variation of amplitude Q (solid line) and phase θ (dashed line) of plasma wave excited by propogation of square laser pulse in inhomogeneous plasma in direction of increasing density ($A_1 \cdot A_2 = 7{,}3 \cdot 10^{-3}$, $\delta_c \simeq 0{,}1$) .

Fig.6. Variation with time $\tau = \omega t$ the energy of electrons to be injected in plasma wave by $\delta = -0{,}2$ in different points with respect to leading edge of laser pulse.

on π the wave and particle in homogeneous plasma by electron acceleration (so-colled length of acceleration which is nearly equal to $l_a \sim \gamma_0^2 (c/\omega)$). We shall speak that inhomogeneity has small scale if the inequality $l_N \ll l_a$ is fulfilld. In the case of opposite inequality ($l_N \gtrsim l_a$) it is usefull to speak about the long scale inhomogeneity.

The time variation of electron energy $\gamma(\tau)$ is shown in Fig.6. The parcticles were injected in space where plasma density was 20 % lower the linear resonant density N_0 . The

leading edge of pulse is placed in moment of injection in different points. In Fig.6(a,b,c)itis shown three groups of the curves with various distances from the leading edge of the laser pulse up to particle injection point. The exact value of distance is lebeled near every curve. Small difference in distances corresponds to injection of particle in various periods of plasma wave. The electric field was nearly equal in all initial positions of particles.

According to Fig.6 in initial stage the electron is accelerated and then it begins to brake. This result is immediate consequence of plasma inhomogeniety which introduces the variation of plasma wave phase and leads to change the sign of electric field acting on particle. Then the electric field changes the sign once more and electron begins to be accelerated again. The number of such stages of acceleration and deacceleration due to distance between the particle and leading edge of laser pulse in moment of injection. This number is more larger than that distance is longer.

The electron obtains main energy by crossing the region of nonlinear resonance. If electron is injected on short distance from leading edge of laser pulse then the accelerating field is sufficiently low and gain in energy relatively small (Fig. 6a). For electron to be injected on long distance from leading edge of laser pulse the amplitude of plasma wave is great but in narrow region. Out of this region the phase has jumps and acting on the particle field changes the sign (Fig.6c) There is a certain interval of initial distances between particle and leading edge for which the phase of plasma wave is practicaly constant in the vicinity of resonant density (nonlinear phase stabilization /18/) and amplitude of plasma wave is sufficiently high (Fig. 6b). From presented in Ref.18 equations we obtain for considered conditions that interval of phase stabilization begins from ξ =125 and cames to end by $\xi \sim 170$. Inside of this interval for every initial particle position there is corresponding range of density variation. But realy the permissible density variations are not wide and equal nearly 4 %. This interval of nonlinear phase stabilization is shown in Fig.5 by means of sloping dotted lines.

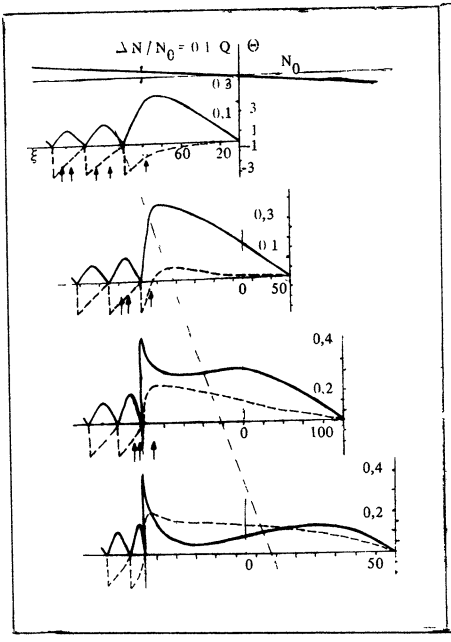

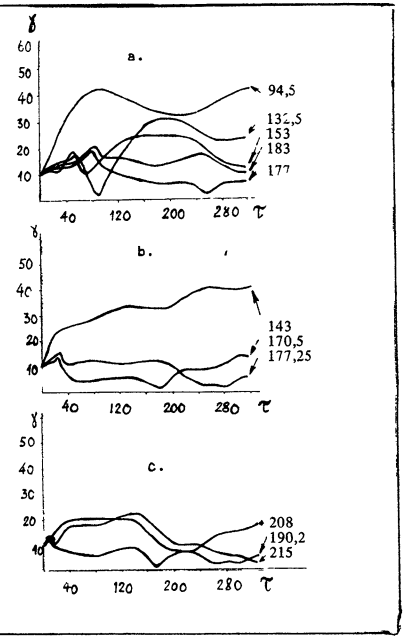

Fig.7 Fig.8.

Fig.7. Variation of amplitude Q (solid lines) and phase θ (dashed lines) of plasma wave excited by propagation of square laser pulse in inhomogeneous plasma in direction of decreasing density ($A_1 \cdot A_2 = 7,3.10^{-3}$, $\delta_c \simeq 0,1$).

Fig.8. Variation with time $\tau = \omega t$ the energy of electrons to be injected in plasma wave by different distances from leading edge of laser pulse. The points of injection are shown in Fig.7 by means of arrows.

Fig.7 shows the evolution of amplitude Q and phase θ of plasma wave excited by the laser pulse of square form propagating in direction of decreasing density. This picture differs essentially from Fig.5. The phase variation of plasma wave proves to be more slow in region $\delta < \delta_c$. The interval of nonlinear phase stabilization is wider but amplitude of wave is lower. This result due to differenc in excitation of nonlinear plasma oscillations with frequencies more higher ($\delta > \delta_c$) and more lower ($\delta < \delta_c$) than resonant frequency ($\delta = \delta_c$). More smooth

phase variation leads to increasing of acceleration time (Fig.8). But efficienty of acceleration is not so high because of smoller wave amplitude and efficienty decreases in process of time by going the particle out the resonant region.

These examples show that in inhomogeneous plasmas the electron acceleration depends on the sign of density gradient and efficienty of acceleration is higher by motion of particle in direction of more dense plasma.

We investigate also excitation of plasma wave of laser pulse with linearly increasing intensity on leading edge. In accordance with results of linear theory for homogeneous plasmas the jumps of phase vanish expect the region of nonlinear resonance ($\delta \simeq \delta_c$). Therefore the transitions from a acceleration stage to deacceleration one are more smooth. The regime of nonlinear phase stabilization is safed for considered form of laser pulse.

The most considered runs correspond to inequality $\ell_N < \ell_a$. In the limit $\ell_N \ll \ell_a$ the distance between accelerated particle and leading edge of laser pulse is practicaly constant. For given retardet time which is proportional to this distance the electric field of plasma wave in inhomogeneous plasma (various values detuning) was investigated in Ref. 15 . However there are some runs for which the condition $\ell_N \sim \ell_a$ is satisfied. As example we show the curve with figure 94,5 in Fig. 8a. In correspondence with this curve the electron is accelerated sufficiently long time. This result arises because of the phase variation which connected with plasma inhomogeneity is partly compensated by phase slippage in process of acceleration. Analogious possibility increas of acceleration lenth was discussed for laser wake-field accelerator /19/ and this problem is now in progress for PBWA.

IY. Electron acceleration in plasma with hump-shaped form of concentration

Considered above the linear form of density variation is very convenient for investigation the influence of plasma inhomogeneity on electron acceleration as more simple example of density variation. However nonmonotonic density variation is more naturaly. In this part we present some results of numerical investigation the influence on process of electron acceleration a region of more high density (hump-shaped form of density).

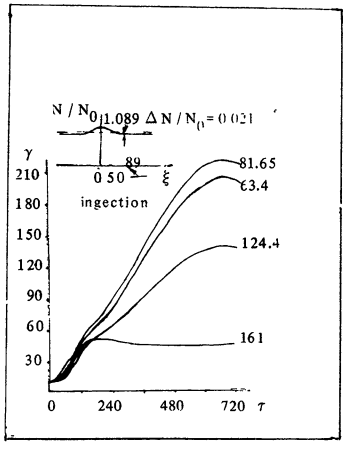

Fig.9a

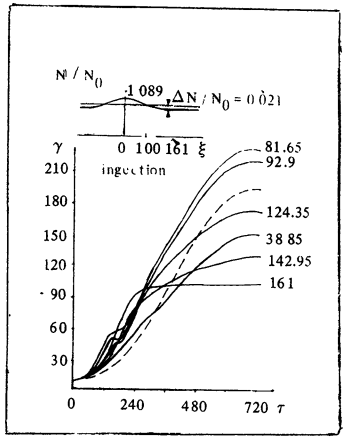

Fig.9b

Fig.9.Electron energy γ as a function of time $\tau = \omega t$ for hump-shaped form of density
a) scale length of hump $\frac{z}{\ell_0}$ =100
b) scale length of hump $\frac{z}{\ell_0}$ =200
c) scale length of hump $\frac{z}{\ell_0}$ =432.
The dashed line in Fig.9b shows the electron energy in homogeneous plasma.

We shall consider in this section only laser pulses of square form. Besides we suppose that ground density is nearly 2 % smaller and maximum density is nearly 9 % higher than linear resonant density N_0 .

In Fig.9a the results are shown for relatively narrow hump the length of which is more smaller than length of acceleration ℓ_a . In all calculations the injection place was in the same point indicated in Fig.9a, but the leading edge of laser pulse has different positions. Corresponding distances are shown by means of figures by curves. It is clear that narrow hump has a week influence on process of acceleration.

For hump with more length scale the acceleration increases visible in the region of higher density, however sufficiently narrow region arises with reduced the rate of acceleration and in

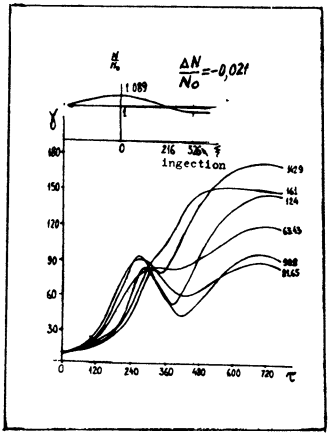

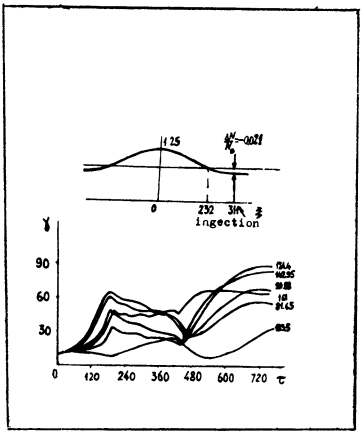

Fig. 9c

Fig. 10

Fig.10. Energy of electrons γ as a function of time τ crossing the region of dense plasma with large scale length (N_{max}/N_0) = 1,25).

this region the electron is even deaccelerated (Fig. 9b). The dotted line in Fig. 9b shows the energy of electron in homogeneous plasma with density ~ 2 % lower the linear resonant density N_0 . Thus the density splash increases the rate of acceleration for some positions of electrons relatively the leading edge of laser pulse.

Figure 9c shows the results of calculation for more wide hump. In this case the scale length of hump approaches to the acceleration scale length. The change of wave phase because of plasma inhomogeneity leads in fact to absence of acceleration in the region with more higher density. As result this region is losted for acceleration and energy of accelerated particles is reduced. This conclusion is confirmed of calculations with more higher hump of concentration (Fig. 10).

In summary the density splash with very small scale length has week influence on process of acceleration. For more dimension of hump it is possible to increas of electron energy if density in splash is approached to nonlinear resonant value.

The long splash reduces essentialy the acceleration efficiency. The growth of electron energy is irregular and it is practicaly absence by particle to cross of density hump.

Y. Conclusion

In initial experiments /20,21/ on excitation of plasma waves by means of two-frequency laser pulse the electric fields were obtained with value 10^9 V/m, what nearly two order higher than in ordinary linear accelerator. However these fields were exited only in narrow regions of space with scale length less than 2 mm. The attents to increase the length of plasma wave excitation /22/ and experiments with neodim-glass laser /23/ show

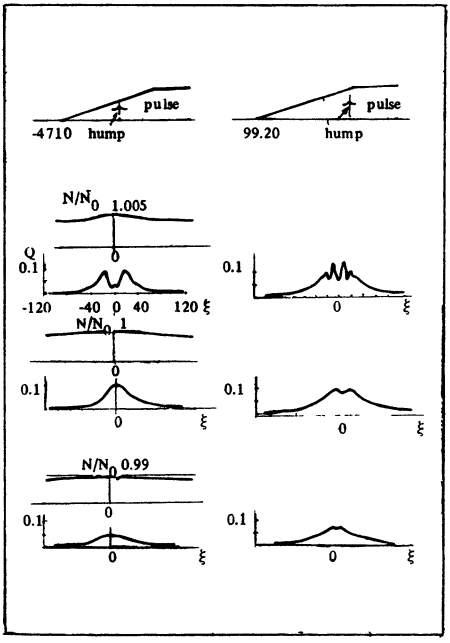

Fig.11

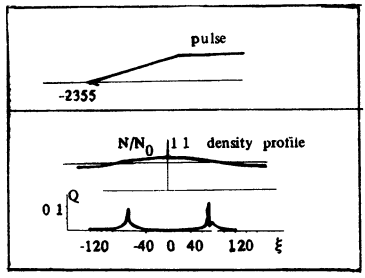

Fig.12

Fig.11. Plasma wave amplitude Q as a function of distance at two moments of time and for three maximum values of density
a) (N_{max}/N_0)=1,005 ; b) (N_{max}/N_0)=1 ;
c) (N_{max}/N_0)=0,99.

Fig.12. Plasma wave amplitude Q excited by laser pulse with slow increasing leading edge in a inhomogeneous plasma ($\frac{3}{3}$ =9420).

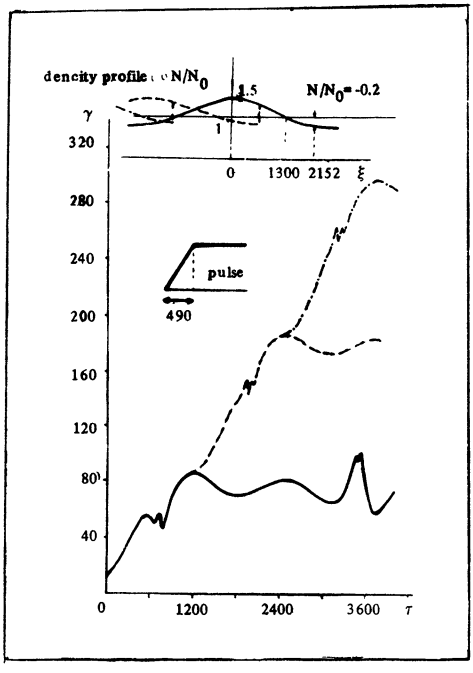

Fig.13
Electron energy γ as a function of time τ by acceleration in plasma with jumps of density. The density and pulse form are shown in top part of picture.

that conditions on homogeneity and reproduction of plasma are most dificalt for realisation.

We consider for exampl the experiment /24/ where it is measured the dependence of plasma wave excitation and electron acceleration from plasma density. The plasma wave begins detected when the maximum value of density exceeds the linear resonant value N_0 . The accelerated electrons were detected in more narrow interval near N_0 of maximum values of density.

In corresponding to experiment of Ref.24 conditions (long laser pulse, small plasma dimension) the amplitude of plasma wave Q is shown in Figs.11 (a,b,c) in two times (two laser pulse positions) and for three values maxima of density. It is clear that by exceeding density maximum the form of function Q becomes complicated however always there is the resonant region where amplitude of plasma wave is sufficiently high. By increasing of density maximum still more the regions of plasma wave excitation move apart and become more narrow (Fig. 12). As shown above the efficiency of electron acceleration in this case reduces (Fig. 10).

It is possible to increase the efficiency of electron acceleration by variation of plasma density on the scale length comparable with scale length of acceleration. We considered multy - step profile of density (Fig. 13). By means of that profile it is possible obtain the electron acceleration in more long time

than that in homogeneous plasma. The jump of density correspond the time of electron transition from phase of acceleration to the pase of retardarion. After going through the jump a electron turn out to beginning of acceleration phase.

The presented here results of numerical investigation of electron acceleration in PBWA are based on most simple model. We believe the inclusion in this model the new effects will give the possibility to investigate experimental realisations with more precision.

References

1. Tajima T., Dawson J.M. Phys.Rev.Lett. 1979, 43, 267.
2. Chen F.F. Laser Accelerators: Preprint PPG-1107-Los-Angeles, UCLA, 1987.
3. Fainberg Ja.B. Jorn.Pl.Phys. (USSR), 1987, 13, 607.
4. Rosenbluth M.N., Liu C.S. Phys.Rev.Lett., 1972, 29, 701.
5. Tang C.M., Sprangle P., Sudan R.N. Phys.Fluids, 1985, 28,1974.
6. Mc Kinstrie C.J., Forslund D.W., Phys.Fluids, 1987, 30, 904.
7. Mori W.B. IEEE Trans.Plasma Sci. 1987, 15, 88.
8. Karttunen S.J., Salomaa R.R.E. Phys.Rev.Lett. 1986, 56, 604.
9. Noble R.J. Phys.Rev.A. 1985, 32, 460.
10. Mendonca J.T., J.Plasma Physics, 1985, 34, 115.
11. Gibbon P., Bell A.R. Phys.Rev.Lett. 1988, 61, 1599.
12. Karttunen S.J., Salomaa R.R.E. IEEE Trans. Plasma Sci., 1987, 15, 134.
13. Gorbunov L.M . Kirsanov V.I. Preprint FIAN N167, 1988 (in Russian).
14. Chen F.F. Physica Scripta, 1990, 30, 14.
15. Karttunen S.J., Salomaa R.R.E. Physica Scripta, 1989, 39, 741.
16. Karttunen S.J., Salomaa R.R.E. Physica Scripta, 1986, 33,370.
17. Miano G. Phys.Fluids, 1988, 31, 848.
18. Gorbunov L.M., Kirsanov V.I. Sov. Phys. JETP, 1989, 69, 329.
19. Gorbunov L.M., Kirsanov V.I.,Mtingwa S., Ramazashvili R.R. Short reports FIAN N10, 27, 1989.
20. Clayton C.E., Joshi C., Darrow C., Umstadter. Phys.Rev.Lett. 1985, 54, 2343.
21. Ebrahim N.A. et al. Proc. 1986 Laser Acceler. Conf. Stanford, CA, June 2-6 (1986).

22.Clayton C., Joshi C., Leemans W., Marsh K., Williams R. Workshop on Advanced Acceler. Concepts, January 1989, Arrowhead, 1989.
23.Dangor A.E., Dymoke-Bradshaw A.K.L., Dyson A.E., Phys.Scripta, 1990, 30, 107.
24.Kitagawa Y. et al. Preprint Institute of Laser Engineering, Osaka, Japan, N90018, 1989.

NONLINEAR DYNAMICS OF ULTRASHORT ELECTROMAGNETIC PULSES IN PLASMAS

A. M. Sergeev and E. V. Vanin
Institute of Applied Physics
Academy of Sciences of the USSR
Nizhny Novgorod, USSR

Recent progress in relativistic microwave electronics and powerful subpicosecond laser generation technology has stimulated interest in interaction of ultrashort electromagnetic pulses with nonlinear media. Being a classical example of a nonlinear medium and a traditional object of laboratory investigations, the plasma demonstrates an extreme variety in behavior under the action of the electromagnetic fields. Characteristic rise and relaxation times of nonlinear response can be varied by a few orders of magnitude depending on particle concentration, wavelength, external magnetic field, etc. Thus, the ultrashort pulse duration should be defined as a particular notion with respect to the phenomenon in question. In this paper we take interest in electromagnetic wave - plasma interaction processes faster than the relaxation of the nonlinear plasma response. In this context, we will treat the interaction as essentially dynamical and the plasma, as a medium with long-term memory propeties. The nonsteady state of the nonlinear coupling and the plasma wake generation are two main features essential to the basic physical effects and applications.

As an illustration, we propose a typical formulation of the problem on the nonlinear dynamics of an ultrashort pulse [1]. Let a one-dimensional packet of electromagnetic waves with an envelope $A(z,t)$ of the electric field $\mathcal{E}=\frac{1}{2}\left[A(z,t)\exp\{i\omega_0 t-ik_0 z\}+c.c.\right]$ be described by a parabolic equation

$$-\frac{2i}{k_0}\left(\frac{\partial A}{\partial z}+\frac{1}{v_{gr}}\frac{\partial A}{\partial t}\right)-\frac{1}{k_0}\frac{\partial^2 k_0}{\partial\omega_0^2}\frac{\partial^2 A}{\partial t^2}+\frac{1}{k_0^2}\left(\frac{\partial^2 A}{\partial z^2}-\frac{1}{v_{gr}^2}\frac{\partial^2 A}{\partial t^2}\right)+nA=0\ , \quad (1)$$

where v_{gr} is the group velocity and n is the perturbation of the squared refractive index of the medium (for isotropic plasma, (-n) should denote the normalized perturbation of electron density). We shall count time since the pulse arrival at a given point in space, i.e., we shall introduce a new variable $\tau=t-z/v_{gr}$. In variables τ,z the medium response to electromagnetic field (with

the transport processes neglected) is given by

$$n(z,\tau)=-\int_{-\infty}^{\tau} G(\tau-\tau')F\left[|A(z,\tau')|^2\right]d\tau' \quad . \qquad (2)$$

Assume that the kernel G has a characteristic time scale τ_n, that corresponds, for example, to the relaxation of n perturbation or to the oscillating response with a frequency $\Omega \sim \tau_n^{-1}$. With the pulse duration $\tau_p \gg \tau_n$ the relationship (2) becomes local in time so that after the wave packet passing the wake is negligibly small in the medium. On the contrary, in processes with long-term response (media with long-term memory) the wake can be pronounced (see Fig. 1). Exactly this situation will be discussed as related to the

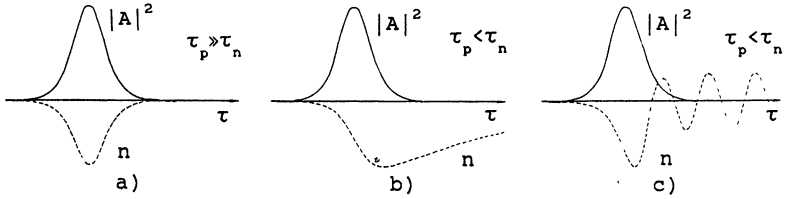

Fig.1 Examples of nonlinear medium response: a) local-in-time (steady-state) response, b) relaxation response, c) oscillating response.

plasma processes. We shall enumerate the most interesting processes in the increasing τ_n order (and, therefore, τ_p that satisfy the ultrashort pulse requirement).

For subpicosecond laser pulses of intensities 10^{16}-10^{20} W/cm^2 there are two groups of problems related to the laser pulse dynamics in ionized medium and the pulse interaction with completely ionized plasma. In the first case, of greatest interest are the upward spectrum transformation effects (ionization self-conversion) and the generation of a dense nonequilibrium plasma with assigned properties. Development of new tunable sources of coherent UV radiation [2] and creation of an active plasma medium for an X-ray laser [3] can be the main applications. The second case concerns the generation of the Langmuir wake in a collisionless plasma by an ultrashort optical pulse and the possible use of this wake for the electron and photon acceleration in a strong plasma wake [4,5].

For nanosecond pulses, the effects of interest are manifested, in particular, in the interaction of microwave (millimetre and centimetre) radiation of free-electron lasers with

laboratory plasma. Of primary importance are the problems on the nonlinear modification of the spatial pulse structure in plasma. Thus, the ionization self-compression of radiation is useful in obtaining extremely short (with pulse duration of the order of a few field periods) microwave pulses, while the spatio-temporal self-focusing in collisionless plasma is important as a restriction in the toroidal plasma heating by the FEL radiation [6].

In the ionospheric modification by powerful millisecond pulse radiation the interaction can also be described in terms of the ultrashort processes since the characteristic relaxation times of thermal nonlinearity (due to the diffusion redistribution of heated plasma) are $1 - 10^2$sec [7].

This rough classification can be continued and supplemented but we only make the remark that even steady-state processes can sometimes be easily understood from the viewpoint of the dynamic interaction of a short pulse with matter using developed spatio-temporal analogies in the nonlinear wave physics (modulation instability - plane wave instability, collapse - self-focusing). It appears that the spatial structure of the electromagnetic beam, subject to the self-action with wind in the atmosphere [8], is fully analogous to the form of a two-dimensional wave packet propagating in a medium with long-term relaxation of nonlinearity.

1. Consider first the frequency self-conversion and the wave packet compression in terms of the model (1),(2) in the case of long-term relaxation of nonlinear perturbations [9]. Advertizing the nonlinear compression with the initial duration $\tau_p < \tau_n$ might seem strange since it is generally adopted that exactly τ_n is the minimum scale restricting the wave packet compression in the nonlinear medium. That is why, for example, quartz glass in optical fibers with marginally small response time $\tau_n < 10^{-14}$sec is used for obtaining ultrashort pulses in femtosecond optics. Meanwhile, a process leading to the wave energy concentration is possible in the opposite case of media with long-term memory. This process, a combination of the features of collapse [10] and self-steepening [11], is independent of the nonlinearity sign and accompanied by significant self-conversion of radiation frequency.

We now rewrite Eq. (1) in a dimensionless form

$$-i\frac{\partial A}{\partial z} + \alpha_d \frac{\partial^2 A}{\partial \tau^2} + nA = 0 \ , \qquad (1')$$

where $\alpha_d = \pm 1$ corresponds to a medium with positive (+) or negative group velocity dispersion. Using Eqs. (1') and (2) it can be shown that for the field distributions with a monotonically decreasing auto-correlation function $K(z,\tau)=\int_{-\infty}^{+\infty}|A(z,\tau')A(z,\tau+\tau')|^2 d\tau'$ (of a single pulse type) there is a theorem on sign definiteness of the frequency shift $\overline{\Delta\omega}(z)=(2\pi W)^{-1}\int_{-\infty}^{+\infty}\Omega|A_\Omega(z)|^2 d\Omega$ and acceleration of the "mass centre" $\bar{\tau}(z)=W^{-1}\int_{-\infty}^{+\infty}\tau'|A(z,\tau')|^2 d\tau'$ of the wave packet:

$$W\frac{d\overline{\Delta\omega}}{dz} = \frac{1}{2} W \alpha_d \frac{d^2\bar{\tau}}{dz^2} = \alpha_n \int_{-\infty}^{+\infty}\left|G(\tau')\frac{\partial K(z,\tau')}{\partial \tau'}\right| d\tau' \qquad (3)$$

Here $W=\int_{-\infty}^{+\infty}|A(z,\tau)|^2 d\tau$ is the wave energy retained along the wave propagation path, $A_\Omega(z)$ is the Fourier image of the envelope $A(z,\tau)$. A direct consequence of this theorem is the possibility of continuous conversion (increase or decrease depending on the sign of the nonlinearity α_n) of the carrier frequency of the wave packet in nonlinear media with memory.

Variation of the global pulse characteristics $\overline{\Delta\omega}$ and $\bar{\tau}$ is due to the inhomogeneous frequency variation inside the wave packet and the wave energy redistribution. To reveal the dynamics of local characteristics we shall consider the most interesting case $\tau_p \ll \tau_n$ where the medium response G is constant during the pulse $G=\alpha_n$. Rewriting Eq. (1') as a set of equations for the real amplitude $\sqrt{2N}$ and frequency $\frac{1}{2}\alpha_n v$ of the field $A(z,\tau)=\sqrt{2N(z,\tau)}\exp\left\{\frac{i}{2}\alpha_n\int_{-\infty}^{\tau} v(z,\tau')d\tau'\right\}$ and taking a quasiclassical approximation $\left(\left|\frac{\partial}{\partial\tau}\left(\frac{1}{\sqrt{N}}\frac{\partial^2\sqrt{N}}{\partial\tau^2}\right)\right|^2 \ll 4N\right)$ we find

$$\frac{\partial v}{\partial z} + v\frac{\partial v}{\partial \tau} = 4\alpha N \ , \qquad (4)$$

$$\frac{\partial N}{\partial z} + \frac{\partial}{\partial \tau}(Nv) = 0 \ , \qquad (5)$$

where $\alpha=\mathrm{sign}(\alpha_d\alpha_n)$.

The equations (4)-(5) coincide (accurate to commutation of the spatial and temporal coordinates) with the gas-dynamic

equations including a nonlocal equation of state $p=-4\alpha\int N^2 d\tau$, which combines "pressure" and "particle density". Unlike the traditional gas dynamics, these equations do not have solutions of the Riemann wave type (shock waves of the envelopes). Since the particle acceleration in the medium is proportional to the particle density and is therefore different on the initially inhomogeneous gas profile, the breaking process is accompanied by accumulation of the matter towards the profile sharpening. If the gas velocity is a linear function of the coordinate τ, $\omega\sim(\tau-\tau_0)$ (i.e., the wave packet frequency undergoes linear self-modulation), then the distribution contracts wholly at the point $\tau=\tau_0$ with increasing z and the arising singularity captures the finite mass of the matter (i.e., the wave energy density in the wave packet goes locally to infinity). Obviously, the formation of a singularity is independent of the sign of α; at $\alpha<0$ it develops on the leading front and at $\alpha>0$ at the rear front of the pulse. Self-similar collapsing solutions with increasing frequency self-modulation have the form of a breaking triangular pulse:

$$N(z,\tau)=(\tau-\tau_0)\omega(z), \qquad \omega(z,\tau)=\alpha_n(\tau-\tau_0)u(z), \tag{6}$$

where the functions $\omega(z)$ and $u(z)$ are defined by ($\alpha=-1$ is taken):

$$z-z_0=\left(\frac{\pi}{8\omega_0}\right)^{\frac{1}{2}}\operatorname{erf}\left\{\ln^{\frac{1}{2}}\left(\frac{\omega}{\omega_0}\right)^{\frac{1}{2}}\right\}, \quad u=\left(4\omega\,\ln\frac{\omega}{\omega_0}\right)^{\frac{1}{2}}, \quad \omega(z_0)=\omega_0, \quad u(z_0)=0. \tag{7}$$

Near the breaking coordinate $z=z_*=z_0+\left(\frac{\pi}{8\omega_0}\right)^{\frac{1}{2}}$ the pulse duration and the frequency shift are given by

$$\tau_p(z\to z_*)=\tau_p(z_0)(z-z_*)\left(8\omega_0\ln\frac{1}{z_*-z}\right)^{\frac{1}{2}}, \tag{8}$$

$$\overline{\Delta\omega}(z\to z_*)=\frac{1}{3}\alpha_n\tau_p(z_0)\left(8\omega_0\ln\frac{1}{z_*-z}\right)^{\frac{1}{2}}. \tag{9}$$

When approaching the singularity the quasiclassical approximation does not hold not only on the periphery but also in the energy-carrying part of the pulse thus restricting the minimum scale of the field localization to $\tau_p\simeq\sqrt{2W}$. We emphasize that the frequency shift in (9) has only a logarithmic factor of growth, which justifies the use of a parabolic approximation.

Figure 2 shows fragments of the numerical calculation for the dynamics of a pulse with an initially Gaussian form within the framework of Eqs. (1')-(2) with G=1.* The front half of the packet

* Possibly, the tendency towards manifestation of this effect

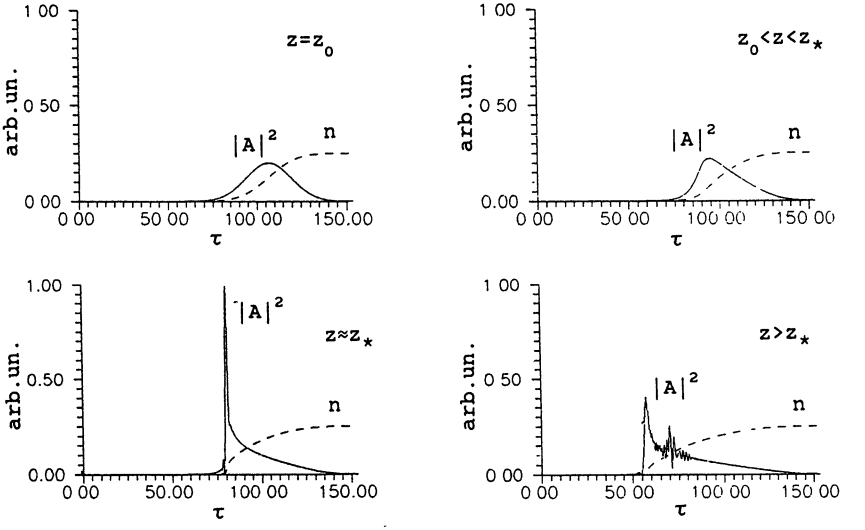

Fig.2 Dynamics of self-compression process in a nonlinear medium with long term memory.

clearly demonstrates the behavior described analytically in terms of the triangular intensity distribution breaking with trapping near one third of the initial wave energy into the minimum scale. The dispersion term (the second derivative of the real amplitude disregarded in (4)) terminates the compression process at $\tau_{p0}/\tau_p^{min}\simeq 15$ and causes some modulation instability. Qualitatively, the evolution of the wave packet, as it propagates beyond the breaking coordinate, resembles the dynamics of a spreading triangular pulse formed by the rear half of the Gaussian distribution (solutions (8) and (9) with a substitution $(z_*-z)\to z$).

We now demonstrate the possibilities of using this discovered effect to form ultrashort laser and microwave pulses. As media with long-term nonlinear response, it is possible to take, in particular, a dense plasma with additional ionization (e.g., impactionization) in the presence of an electromagnetic pulse (the defocusing ionization nonlinearity - the frequency up-conversion, compression on the leading front) or a fluid with Kerr nonlinearity mechanism, which is localized (to avoid the

---

was noticed back in [12] where the authors tried to treat it as formation of a shock wave of the envelope [11].

self-focusing instability) in a jet or a capillary light guide (frequency down-conversion, compression on the leading front). Thus, the microwave pulse at a wavelength λ=3cm with initial duration τ_p=3nsec and energy flux density S=100kW/cm^2 can be compressed to the limiting duration $\tau_p^{min}\simeq 0.3$nsec ($l_p=c\tau_p^{min}\simeq 3\lambda$) on a path of about 6m in helium plasma (the gas pressure $p=3\cdot 10^{-2}$Torr) with an electron density half the critical value $N=5\cdot 10^{11}$cm^{-3}. The pulse of a CO_2 laser with τ_p=3psec, $S=4\cdot 10^{12}$W/cm^2 (p=30Torr) in a plasma with $N=10^{18}$cm^{-3} on a path 5cm undergoes compression up to 200fsec.† Finally, a light pulse at λ=600nm with the initial values τ_p=0.5psec and $S=2\cdot 10^{12}$W/cm^2 on a path of about 4cm in benzine will form into an ultrashort electromagnetic bunch of duration 30fsec.

2. The pulse compression effect discussed above is caused by the group velocity variation due to frequency self-conversion. Thus, in the ionization self-effect problem the group velocity increases from the leading front towards the central part of the pulse thus leading to pulse breaking. On the other hand, the group velocity is affected inevitably by the plasma electron density perturbations since

$$\delta v_{gr} = - c \frac{\omega_{p0}^2}{\omega_0^2} \left(1 - \frac{\omega_{p0}^2}{\omega_0^2}\right)^{-\frac{1}{2}} \left(\frac{\delta N}{2N_0} - \frac{\delta\omega}{\omega_0}\right). \qquad (10)$$

Obviously, for a rather short pulse in an initially prepared plasma ($\omega_{p0}^2\neq 0$) the second term in (10) dominates on a long path because of the accumulating frequency increase effect. However, if the pulse travels through a not preionized gas ($\omega_{p0}^2=0$) the group velocity can only decrease when plasma is produced and, therefore, the effects discussed in Sect. 1 are not manifested. In this new situation the possibilities of frequency self-conversion cannot be analyzed within the framework of the parabolic equation (1') and a different approach, based on the spatio-temporal nonlinear geometrical optics of wave fields, is required [2].

Initial in the problem are the transfer equations for energy and frequency of a quasiharmonic field $\vec{\mathcal{E}}=\vec{e}A(z,t)\cos[\varphi(z,t)]$ with the real amplitude A and the real phase φ:

† Pulse compression in a CO_2 laser was observed experimentally in [13] and explained by the frequency modulation in a nonlinear medium and the pulse compression in the outlet glasses of the laser setup.

$$\frac{\partial}{\partial t}\left(\frac{A^2}{8\pi}\right) - \frac{\partial}{\partial z}\left(v_{gr}\frac{A^2}{8\pi}\right) = -\frac{e^2A^2}{2m\omega^2} < \Gamma(A,\varphi)\ \mathrm{Sin}^2\varphi >, \qquad (11)$$

$$\frac{\partial\omega^2}{\partial t} - v_{gr}\frac{\partial\omega^2}{\partial z} = \frac{\partial}{\partial t}(\omega_p^2), \qquad (12)$$

$$\frac{\partial N}{\partial t} = < \Gamma(A,\varphi) >. \qquad (13)$$

Here $\omega=\frac{\partial\varphi}{\partial t}$ and $k=-\frac{\partial\varphi}{\partial z}$ are assumed as related by a local dispersion equation $k^2c^2=\omega^2-\omega_p^2$; Γ is the growth rate of electron density, which, in a linearly polarized field, can depend also on the phase (i.e., the local value) of the electric field; the angular brackets denote averaging over the oscillation period. In Eq. (11) we take into account the energy spent for imparting kinetic energy to produced electrons and neglect the influence of transport electron collisions on wave dissipation as well as the electromagnetic energy loss by extracting electrons from atoms. This should be reasonable if the oscillation energy exceeds appreciably the ionization potential $U_{\sim}=\frac{e^2A^2}{2m\omega^2} \gg I$. In Eq. (13) we assume that Γ is independent of electron density, i.e., we restrict ourselves to the field ionization processes. It is convenient to represent $\Gamma=\Gamma_0 N_m F\left(\frac{A}{A_0},\varphi\right)$, where N_m is the ionized molecule density (which is assumed to be constant), Γ_0 and A_0 are the ionization frequency and the field amplitude, characteristic of this ionization process, F is a dimensionless function that describes the form of "switching" ionization with the field growth and the possible dependence on oscillation phase. An introduction of Γ_0, A_0 and the initial frequency ω_0 makes it possible to rewrite Eqs. (11)-(13) in universal dimensionless variables:

$$\frac{A^2}{A_0^2} = u\ ,\quad \frac{\omega^2}{\omega_0^2} = w\ ,\quad \frac{4\pi Ne^2}{m\omega_0^2} = n\ ,\quad \frac{4\pi N_m e^2\Gamma_0 t}{m\omega_0^2} \Rightarrow t\ ,\quad \frac{4\pi N_m e^2\Gamma_0 z}{m\omega_0^2 c} \Rightarrow z\ .$$

It is convenient to follow the ionizing pulse properties by counting the spatial coordinate from the leading front of the pulse (in new variables $z'=-t$), i.e., turning over to independent variables $\xi=z'+t$, $t=t$. If the pulse is rather short and the perturbations it introduces to the permittivity are small ($n\ll 1$), then all changes in form of the envelope, frequency and, therefore, structure $n(\xi,t)$ are noticeable only at distances well over the pulse length $\left(\frac{\partial n}{\partial t} \ll \frac{\partial n}{\partial\xi}\right)$. To investigate these accumulating effects we transform Eqs. (11)-(13) to

$$\frac{\partial u}{\partial t} + \frac{\partial}{\partial\xi}\left(\frac{nu}{2w}\right) = -\frac{< F\ \mathrm{Sin}^2\varphi >}{w}\ , \qquad (11')$$

$$\frac{\partial \omega}{\partial t} + \frac{n}{2\omega}\frac{\partial \omega}{\partial \xi} = < F > , \qquad (12')$$

$$\frac{\partial n}{\partial \xi} = < F > . \qquad (13')$$

The main properties of nonlinear dynamics within Eqs. (11')-(13') can be demonstrated using, as an example, the simplest solution describing the evolution of a rectangular pulse of electromagnetic field

$$u = \begin{cases} u(t) , & 0 \le \xi \le l(t) , \\ 0 , & \xi < 0 , \ \xi > l(t) , \end{cases}$$

with variable length $l(t)$ and carrier frequency ($\omega=\omega(t)$). The frequency-averaged density of produced plasma increases linearly along the coordinate inside the pulse and reaches a level $n=n_{wake}=\alpha(t_r)l(t_r)$ (n_{wake} is the plasma density in the wake), where the time t_r corresponds to passing of the rear front of the pulse through a given point in space. The length of the wave packet satisfies a relation

$$l = l_0 \frac{\omega}{\omega_0} , \qquad (14)$$

that describes the dispersion spreading of the pulse in plasma. We should emphasize that in this situation the dispersion effect reflects the nonlinear character of the interaction since the electron concentration (responsible for dispersion) is defined by the field itself.

The equations for $u(t)$, $\omega(t)$ and $\alpha(t)$ can easily be investigated for particular dependences of the ionization probability on the electric field. We turn first to the model dependence $F=\left(\frac{A}{A_0}\sin\varphi\right)^{2p}$ ($p>0$), when the r.h.s. parts of (11) and (13) yield:

$$\frac{< F \sin^2\varphi >}{\omega} = - \frac{C\, u^{p+1}}{2\omega(p+1)} , \quad < F > = C\, u^p ,$$

where $C = \frac{\Gamma(p+\frac{1}{2})}{\sqrt{\pi}\,\Gamma(p+1)}$ and Γ denotes the gamma-functions of the corresponding arguments. Let us represent Eq. (11) in an illustrative form

$$\frac{\partial u}{\partial t} + \frac{C}{2\omega} u^{p+1} = - \frac{C}{2\omega}\frac{u^{p+1}}{p+1} ; \qquad (15)$$

it follows that the dispersive and the dissipative factors of the amplitude decrease differ solely in coefficient, and for rather sharp functions of the ionization frequency switching ($p\gg1$) the influence of dissipation (heating of produced plasma) on the field

decrease can be neglected. Solving Eqs. (15), (12') and (13') yields a relation between frequency and amplitude

$$u = u_0 \, \omega^{-\frac{p+2}{p+1}}, \tag{16}$$

and particular relations for time variation:

$$\omega = \left[1 + \frac{p^2+4p+2}{2(p+1)} C u_0^p t \right]^{\frac{p+1}{p^2+4p+2}}, \tag{17}$$

$$u = u_0 \left[1 + \frac{p^2+4p+2}{2(p+1)} C u_0^p t \right]^{-\frac{p+2}{p^2+4p+2}}. \tag{18}$$

In order to specify the conditions for the fastest transformation of the radiation spectrum we shall find the time the carrier frequency increases η times from (17). For arbitrary p and $\eta \geq 2$ it is possible to use the expression:

$$t_\eta = 2 \left(\frac{\eta}{u_0}\right)^p \frac{(p+1)}{C(p^2+4p+2)} \eta^{\frac{3p+2}{p+1}}. \tag{19}$$

Clearly, the dependence of t_η on the curve F(A) (actually on p) is defined appreciably by the initial pulse intensity. At $u_0 < \eta$ it seems advantageous, from the view point of frequency conversion rate, to use the equally probable ionization over the field phase, i.e., p = 0. On the contrary, for high fields ($u_0 > \eta$) the "threshold" ionization is preferable. In this case, for a short time $t \approx 2u_0^2 \sqrt{\frac{\pi}{p}}$ the electric field amplitude decreases down to 1, which is accompanied by a u_0-fold increase in frequency; then the medium ionization is terminated so that the conversion process is over.

The "threshold" ionization of the medium makes it possible to decrease the energy spent to create plasma due to electron production mainly in the field maximum phase. This property is clearly illustrated by the energy variation law $W = ul$ of a short pulse with frequency conversion

$$W = W_0 \, \eta^{-\frac{1}{p+1}}. \tag{20}$$

Obviously, at $p \to \infty$ the carrier frequency can be increased a finite number of times with an infinitely small decrease of the total pulse energy.

Using the power-law dependence F(A), which is convenient for analysis, it is easy to find the form of the wake after a short ionizing pulse:

$$n = n_0 \left[1 + \frac{p^2+4p+2}{2(p+1)} C u_0^p |z| \right]^{-\frac{p^2+p-1}{p^2+4p+2}} . \qquad (21)$$

We now turn to a physically more interesting case of tunneling ionization where $F=\exp\left(-\frac{A_0}{|A \sin\varphi|}\right)$. First of all, it should be noted that at $A \ll A_0$ (the only domain where "tunneling" can be spoken about), the pulse parameter transformation is similar to that considered above at $p \gg 1$ because of the exponentially sharp growth of the ionization rate with increasing field. Thus, to find the relation between the carrier frequency and the amplitude one can neglect the losses due to electron heating assuming that the field amplitude decreases only because of the dispersion spreading. Consequently, the sought relation reads

$$A^2\omega = \text{const} , \qquad (22)$$

as follows consistently from the limiting transition in (16). Using (22) it is easy to define the time the frequency increases by a factor of η:

$$t_\eta = \sqrt{8\pi}\, u_0^{\frac{1}{4}}\, \eta^{\frac{7}{4}} \exp\left\{ \sqrt{\frac{\eta}{u_0}} \right\} \left[1 - \eta^{-\frac{7}{4}} \exp\left\{ \frac{1-\sqrt{\eta}}{\sqrt{u_0}} \right\} \right] . \qquad (23)$$

Thus, it is apparent that for strong frequency conversion the pulse propagation path in homogenous gas should be increased exponentially.

The relation (22) can be substituted into (11) to determine the law by which the wave packet energy decreases due to the heating of produced electrons. In view of (14) we find:

$$\frac{W - W_0}{W_0} = - 4 \sqrt{u_0} \left(1 - \frac{1}{\sqrt{\eta}} \right) . \qquad (24)$$

It follows that for arbitrary large pulse frequency shifts the relative losses of pulse energy do not exceed the finite (small) value $4\sqrt{u_0}$. To make a reasonable interpretation we should remind that we neglect the energy losses for the free electron birth in the atom ionization process. Calculating the electron density in the wake

$$n_{wake} \simeq 4\, u_0^3\, l_0\, |z|^{-1} \ln^5 \frac{|z|}{\sqrt{8\pi}\, u_0^2} \qquad (25)$$

and the total losses by electron production

$$W \sim \int n_{wake}\, I\, dx \sim \ln^6 |z|$$

we find the diverging integral. This means that the admissible

propagation path as well as the frequency increase factor, have natural restrictions in an idealized model. Estimates show that the maximum attainable increase in frequency with the ionization losses neglected is of order

$$\eta_{max} \simeq \left(\frac{u}{\bar{I}} \right)^{\frac{1}{3}} .$$

The main features of the frequency conversion of a short ionizing pulse in gas, which were found in the analysis of the geometrooptical approximation, are fully confirmed by the numerical investigation of the Maxwell equations with plasma description by particle codes or by the model relation (13). Figure 3 demonstrates the pulse shape and electric field spectrum variation as well as the plasma wake when the pulse propagates in a gas with the normalized frequency of ionization $F=50\exp\left(-\frac{4}{|\sqrt{u}\ \mathrm{Sin}\varphi|}\right)$. Estimates of the experimental situation

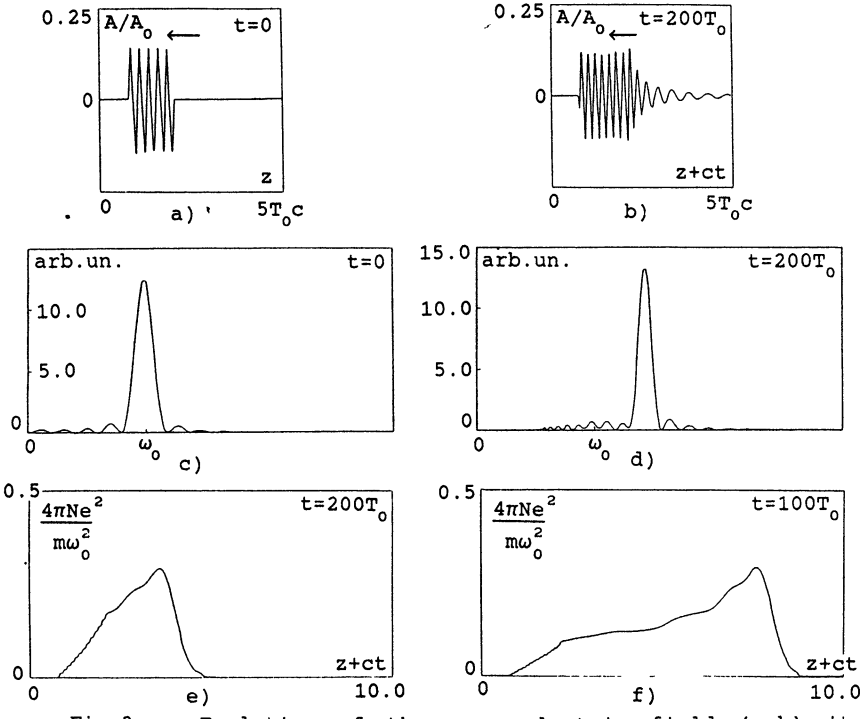

Fig.3 Evolution of the wave electric field (a,b) its spectrum (c,d) and the plasma wake (e,f) at ionizing pulse propagation in gas.

indicate that the pulse of a CO_2 laser with the duration < 1psec and the intensity $4\cdot10^{14}W/cm^2$ will double its frequency when propagating in a gas with the ionization potential 15eV and the pressure $3\cdot10^2$Torr at a distance of 1cm. A similar path length is needed for the subpicosecond pulse of an eximer (KrF) laser with the intensity $3\cdot10^{15}W/cm^2$ in a gas with the ionization potential 25eV and the pressure $2\cdot10^4$Torr.

3. Consider now the electromagnetic pulse dynamics in a plasma with an oscillating nonlinear response G (see Eq. (2)). Assume that the wave packet, moving in plasma, excites long-lived Langmuir oscillations. Since the pulse duration $\tau_p<\tau_n\simeq\omega_p^{-1}$ it is possible to neglect the ion perturbation in the medium and consider a pure electronic plasma response. As nonlinear effects, we shall consider the relativizm and the electrostriction and neglect the higher field harmonic generation assuming for simplicity that the electromagnetic field in the pulse is circularly polarized [14].

To describe the interaction of the electromagnetic and the plasma fields by the equation for the vector $\vec{A}_\perp$ and the scalar φ potentials, we can formulate, using the dimensionless variables

$$A=\frac{eA_\perp\omega_0}{\sqrt{2}mc^2\omega_p}\ ,\quad \Phi=-\frac{\omega_0^2e\varphi}{\omega_p^2mc^2}\ ,\quad \tau\omega_p\Rightarrow\tau\ ,\quad \frac{z\omega_p^2}{2k_0c^2\omega_0^2}\Rightarrow z\ ,$$

($A_\perp$ is the complex amplitude of the rotating field $\vec{A}_\perp$), equations similar to (1)-(2) (see Ref. [15]):

$$-i\frac{\partial A}{\partial z}+\frac{\partial^2A}{\partial\tau^2}-\Phi A=0\ , \tag{26}$$

$$\frac{\partial^2\Phi}{\partial\tau^2}+\Phi=-|A|^2\ , \tag{27}$$

where G(t')=-Sin(t'). This parabolic approximation holds at $\left|\frac{e\varphi}{mc^2}\right|$, $\left|\frac{e\vec{A}_\perp}{mc^2}\right|\ll 1$ provided that noticeable variations of the envelope and the wave packet frequency are manifested only on large paths $L\gg\frac{\omega^2}{\omega_p^2}c\tau_p$, $(\omega_p\ll\omega)$.

By analogy with the frequency shift sign definiteness theorem (3) for a medium with a monotonically decreasing response, we find:

$$\frac{d\overline{\Delta\omega}}{dz}=-\frac{1}{2}\frac{d^2\overline{\tau}}{dz^2}=\frac{1}{2\overline{W}}\left(\Phi_1^2-\Phi_2^2\right)\ , \tag{28}$$

where $\Phi_{1,2}$ are the plasma oscillation amplitudes before and after

the pulse passing through the point with a coordinate z. Thus, if the plasma is not excited before the pulse arrival, the pulse will inevitably slow down losing energy (decreasing in frequency) due to the excitation of Langmuir oscillations [16] (except for the solitons of a discrete spectrum where $\Phi_2=0$; see below). This effect has stimulated the use of short laser pulses as near-light wake field generators that can be used for the electron acceleration [4].

The central frequency of the wave packet can be increased ("acceleration of photons") if a near-light Langmuir wave is excited in the plasma beforehand [5] while the pulse is put into the phase required $\left(\frac{\partial\Phi}{\partial\bar{\tau}}>0\right)$ and does not produce strong perturbation of the oscillation field. Actually, at a fixed amplitude Φ_1 the value Φ_2 depends on the nonlinear interaction between the vortical and the potential fields so that the right-hand side of Eq. (28) is defined by the electromagnetic pulse intensity. In general, the sign of $\Phi_1^2-\Phi_2^2$ along the z coordinate can be varied, i.e., the system will alternately be in the photon accelerator or the wake field generator phase.

The maximum attainable increase in frequency can be easily found if the pulse duration remains much less than the Langmuir oscillation period ($\tau_p \ll 2\pi$) during the whole time of evolution. Approximating the electromagnetic field distribution by the δ-function we find for the field "mass centre"

$$\frac{d^2\bar{\tau}}{dz^2} = W - 2\Phi_1 \mathrm{Cos}\bar{\tau} , \qquad (29)$$

an equation describing the nonlinear oscillations of the wave packet between the accelerating and the decelerating phases of the Langmuir potential. It is easy to find that

$$\Delta\omega_{max} = \sqrt{2\Phi_1}\left[\left(1-\frac{W^2}{4\Phi_1^2}\right) - \frac{W}{2\Phi_1}\arccos\left(\frac{W}{2\Phi_1}\right)\right]^{\frac{1}{2}} . \qquad (30)$$

Thus, taking account of the pulse effect on plasma oscillations decreases the frequency increase efficiency so that the wave packet cannot be accelerated at all if the number of quanta is large enough there

$$W > W_{cr}=2\Phi_1 . \qquad (31)$$

The oscillation dynamics of a short pulse in the deformed grating of plasma waves is closely related to the existence of electromagnetic polarons, a peculiar type of localized nonlinear wave structures [15]. A numerical experiment shows that when

oscillating between the accelerating and the decelerating phases the initially narrow wave packet will inevitably broaden losing part of quanta through their emission to the allowed Brillouin zones of the periodic electron density profile. Such an evolution can result in formation of a stationary wave $A(z,\tau)=a(\tau)\exp\{i\gamma z\}$ for which the oscillation amplitudes (but not the phases) before and after the pulse passing through a given point z coincide (Fig. 5 a)). The defect of the periodic grating $\Phi(\tau)$, which is the local deepening and shifting in the oscillation phase, captures the electromagnetic pulse, which resembles the formation of self-localized holes in ionic crystals [17]. A detailed investigation shows that polarons have a continuous spectrum of states with respect to γ and Φ_1 in the plane of these parameters below the bottom of the lowest Brillouin zone.

At $\Phi_1 \to 0$ the polaron zone vanishes. Meanwhile, the solitary distributions $A(z,\tau)$ exist in this case in the form of the solitons of a discrete (in γ) spectrum [14, 18]. Indeed, from Eq.(2) with a periodic kernel G it should be apparent that without the harmonic $\Omega=1$ in the temporal spectrum $|A|^2$ the nonlinear plasma response after the pulse passing is absent; this exactly corresponds to a completely localized (both in A and Φ) structure. An example of such a structure is the so-called Nishikawa soliton

$$A = \frac{3\,\mathrm{sh}\left(\tau/\sqrt{2}\right)}{\mathrm{ch}^2\left(\tau/\sqrt{2}\right)}\exp\left\{-i\frac{z}{2}\right\}, \quad \Phi = -\frac{3}{\mathrm{ch}^2\left(\tau/\sqrt{2}\right)},$$

with the eigenvalue $\gamma=-\frac{1}{2}$. A detailed analysis indicates that the solitons of a discrete spectrum are unstable. This instability is due to the asymmetry in the distribution $\Phi(\tau)$ in the presence of a perturbation in the soliton structure $A(z,\tau)$. Actually, when a small harmonic $\Omega=1$ appears in the spectrum $|A|^2$, plasma oscillations are excited ($\Phi_2 \neq 0$) leading, in the absence of oscillations before the pulse ($\Phi_1=0$), to the sign-definite frequency drift and the wave packet slowdown. Consequently, the soliton breaks away from the discrete level and ceases to exist.

4. It seems interesting to generalize these premises concerning the photon acceleration and wake field generation to the case of ultrarelativistic amplitudes of the potentials and large shifts of the electromagnetic pulse frequency. For this purpose, by analogy with Sect. 2, it is possible to use a

geometrooptical description for the quasiharmonic vector potential, which reduces to

$$\frac{\partial}{\partial\tilde{\tau}}\left(\omega\tilde{A}^2\right) + c^2\,\frac{\partial}{\partial z}\left(k\tilde{A}^2\right) = 0\ , \tag{32}$$

$$\frac{d\omega^2}{dz} = \frac{1}{v_{gr}}\,\frac{\partial}{\partial t}\left(\frac{\omega_{p0}^2}{1+\tilde{\Phi}}\right)\ , \tag{33}$$

$$\frac{\partial^2\tilde{\Phi}}{\partial t^2} = \omega_{p0}^2\,\frac{1-2\tilde{A}^2-(1+\tilde{\Phi})^2}{2(1+\tilde{\Phi})^2}\ . \tag{34}$$

We have introduced a normalization of the scalar potential and the amplitude of a rotating vector potential to the relativistic values: $\tilde{\Phi}=\frac{e\varphi}{mc^2}$, $\tilde{A}=\frac{e|\vec{A}_\perp|}{\sqrt{2}mc^2}$.

We now consider in detail the case of a short (to the relativistic plasma oscillations scale) pulse where the field distribution can be approximated by the δ-function. Equation (32) can then be written in the form of reduced quantum number conservation law:

$$N = kc\int_{-\infty}^{+\infty}\tilde{A}^2dt = \text{const}\ . \tag{35}$$

If there are no plasma oscillations before the pulse, then solving Eqs. (33) and (34) under the condition (35) yields the frequency decrease law by the plasma wake field generation:

$$\omega = \omega_0\left[1 - \frac{3N}{2c}\,\omega_{p0}\left(\frac{\omega_{p0}}{\omega_0}\right)^3 z\right]^{\frac{1}{3}}\ . \tag{36}$$

Substituting this equation into the integral (35) it is easy to find the electromagnetic energy decrease law when plasma waves are excited (for more details see the paper by S.V.Bulanov et al. in this book).

If a relativistically strong plasma wave is excited by an external source in plasma, it is easy to find the maximum attainable frequency of the wave packet in the photon accelerator scheme. Without back influence of the pulse on the wave, i.e., at N→0, we have:

$$\omega_{max} = \omega_0\left(\frac{1}{\sqrt{1+\Phi_{min}}} + \sqrt{\frac{1}{1+\Phi_{min}} - \frac{1}{1+\Phi_{max}}}\right)\ , \tag{37}$$

where ω_0 is the wave packet frequency corresponding to the phase-group synchronizm condition $v_{ph}=v_{gr}(\omega_0)$, v_{ph} is the plasma wave velocity, $\Phi_{min}=\frac{1}{2}\left(P_0^2 - \sqrt{P_0^4+4P_0^2}\right)$ and $\Phi_{max}=\frac{1}{2}\left(P_0^2 + \sqrt{P_0^4+4P_0^2}\right)$

are the minimum and the maximum values of the plasma oscillation potential, $P_0 = \frac{1}{\omega_{p0}}\left(\frac{\partial\tilde{\Phi}}{\partial t}\right)_{max}$ is the maximum value of the derivative, which is defined by the power of the source exciting plasma oscillations (if these are generated by a preceding laser pulse, for example, $P_0 = \frac{2\pi e^2\omega_{p0}}{m^2\omega_0^2c^2}\int_{-\infty}^{+\infty} W_{EM}dt$, where W_{EM} is the electromagnetic energy density). In the limiting case of ultrarelativistic plasma oscillations ($P_0 \gg 1$) it is possible to achieve $\omega_{max} = 2\omega_0 P_0 \gg \omega_0$.

If the back influence of the accelerated wave packet on the Langmuir wave is taken into account, then the frequency increase efficiency falls like the case of weakly relativistic nonlinearity. The critical number of quanta at which the pulse acceleration becomes impossible is given by

$$N_{cr} = 2P_0. \qquad (38)$$

It is seen that at small amplitudes of the potential $\tilde{\Phi}$ this

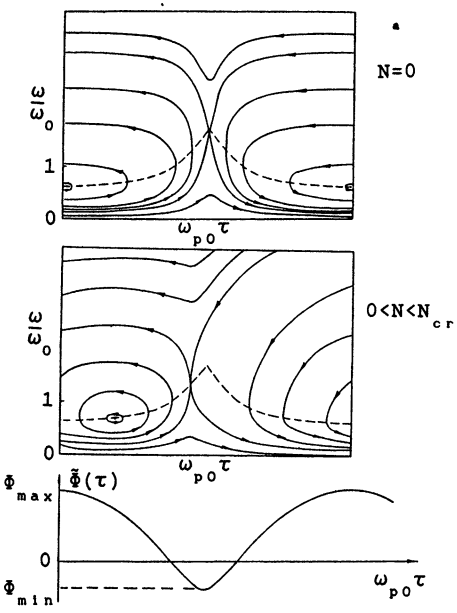

Fig.4 Phase trajectories for short electromagnetic pulse with small ($N \to 0$) and finite ($0 < N < N_{cr}$) amplitudes in the relativistically strong plasma wake.

critical value transforms to (31). Figure 4 in the plane of the variables $(\frac{\omega}{\omega_0}, \omega_{p0}\tau)$ presents the phase trajectories of a dynamic system (33)-(35), which describe the wave packet evolution along the z coordinate. Obviously, the maximum variation in frequency is achieved when moving along the phase trajectory close to the separatrix curve. As N increases, the "acceleration" domain in the plane narrows and disappears once the bifurcation value N_{cr} is exceeded.

A generalization of Eqs. (26)-(27) to the case of relativistically strong amplitudes of the potentials is the equations

$$-i\frac{\partial\tilde{A}}{\partial z} + \frac{\partial^2\tilde{A}}{\partial\tau^2} - \frac{\omega_0^2}{\omega_{p0}^2}\,\frac{\tilde{\Phi}}{1+\tilde{\Phi}}\,\tilde{A} = 0\ , \qquad (39)$$

$$\frac{\partial^2\tilde{\Phi}}{\partial\tau^2} = \frac{1-2|\tilde{A}|^2-(1+\tilde{\Phi})^2}{2(1+\tilde{\Phi})^2}\ . \qquad (40)$$

One of the steady-state solutions of this set, which is obtained by numerical integration, is shown in Fig. 5 b).

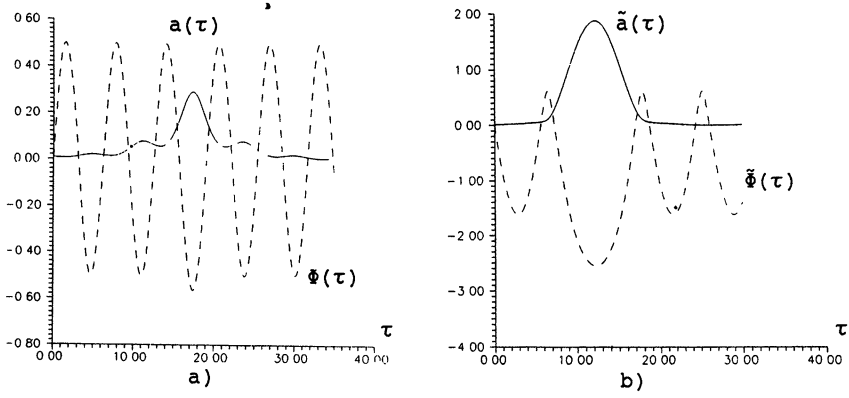

Fig.5 Structures of electromagnetic "polarons" in the case of weak (a) and strong (b) relativistic nonlinearity.

5. While the dynamics of one-dimensional ultrashort pulses in plasma is investigated widely and efficiently enough at present, the theoretical analysis of similar non-one-dimensional processes (except for trivial situations, reduced, for example, to a local temporal response) is at the initial stage. One of the most interesting models to generalize the problem formulation to three-dimensional geometry can be obtained by adding the term $\alpha_\perp\Delta_\perp A$ ($\alpha = \pm 1$), describing the transverse pulse dynamics, to the

right-hand side of Eq. (1). Evidently, depending on the relation between the longitudinal and the transverse pulse scales, as well as between the signs of α_d and $\alpha_\perp$, the evolution processes will be changed radically. If, for example, the wake field is excited by a not so wide electromagnetic wave packet with $L_\perp < c\tau_p \frac{\omega}{\omega_p}$, then a substitution $\frac{\partial^2}{\partial\tau^2} \to \Delta_\perp$ is needed in Eq.(26). Consequently, instead of the quantum redistribution inside the wave packet along the "local" time coordinate, the main process is the transverse pulse compression started on the rear front and "creeping" towards the leading front with the pulse propagation in plasma (accumulating effect). An insight into the temporal structure of the vector and scalar potentials at some point is given by the self-similar form of the solutions‡ which is valid for the initial rectangular pulse of the field:

$$A = e^{\alpha\tau}\, a(\vec{r}_\perp e^{\alpha\tau}) \exp\{-icz\, e^{2\alpha\tau} - i\chi(\tau)\} , \qquad (41)$$

$$\Phi = e^{2\alpha\tau}\, \varphi(\vec{r}_\perp e^{\alpha\tau}) , \qquad (42)$$

where c=const>0, which yields a negative frequency shift, $\alpha = \text{const} \sim \left[\int |A|^2 d\vec{r}_\perp\right]^{\frac{1}{2}}$. A detailed analysis of the self-similar solutions (41) and (42) suggests that owing to the electromagnetic field amplification with transverse evolution of the pulse the Langmuir wake in plasma contracts to a narrow string with the maximum amplitude of the scalar potential $\Phi_{max} \sim \frac{e^{2\alpha\tau_p}}{4\alpha^2+1}$. In particular, this dynamic channeling phenomenon can, unlike the quasi-stationary relativistic self-focusing [20, 21], play an important role in increasing the electron acceleration domain when the wake is excited by a subpicosecond laser pulse.

Note in conclusion that under some conditions the dynamics of small-duration electromagnetic wave packets in plasma can be described by the same equations as for the dynamic self-focusing [22, 23, 24]. In spite of the different formulation of the initial and boundary conditions, this analogy is of course useful in finding general rules and going deeper into the general pattern of the interaction between ultrashort laser pulses and plasma.

‡ Similar "exponential" self-similarities have been known for media with relaxation nonlinearity in nonlinear optics since long ago [19].

1. S.A.Akhmanov, V.A,Visloukh, A.S.Chirkin. Optics of femtosecond laser pulses. Nauka, Moscow, 1988.
2. V.B.Gil'denburg, A.V.Kim, A.M.Sergeev. Pis"ma v ZhETF, v.51, 91 (1990).
3. Special Issue Appl. Phys.B, No.3-4 (1990).
4. T.Tajima, J.M.Dawson. Phys.Rev.Lett., v.43, 267 (1979).
5. S.C.Wilks, J.M.Dawson, W.B.Mori, T.Katsouleas, M.E.Jones. Phys.Rev.Lett., v.62, 2600 (1989).
6. M.Lontano, A.M.Sergeev, A.Cardinali. Phys.Fluids B, v.1, 901 (1989).
7. Thermal Nonlinear Phenomena in Plasmas. Collected Papers. Inst.Appl.Phys., USSR Acad.Sci., Nizhny Novgorod, 1979.
8. V.V.Vorobjov, V.V.Shemetov. Izv.VUZov - Radiofizika, v.22, 441 (1978).
9. A.V.Kim, S.F.Lirin, A.M.Sergeev, E.V.Vanin, L.Stenflo. Phys.Rev.A, v.42, 2493 (1990).
10. V.E.Zakharov, ZhETF, v.62, 1745 (1972).
11. L.A.Ostrovsky, ZhETF, v.54, 1235 (1968).
12. R.A.Fisher, W.K.Bishel. J.Appl.Phys., v.46, 4921 (1975).
13. P.B.Corcum. Opt.Lett., v.8, 514 (1983).
14. V.A.Kozlov, A.G.Litvak, E.V.Suvorov. ZhETF, v.76, 148 (1979).
15. V.A.Mironov, A.M.Sergeev, E.V.Vanin, G.Brodin. Phys.Rev.A., v.42, 4862 (1990).
16. S.V.Bulanov, V.I.Kirsanov, A.S.Sakharov. Pis'ma v ZhETF, v.40, 176 (1989).
17. A.N.Stoneham. Theory of Defects in Solids. V.2, Mir, Moscow, 1978.
18. Ya.L.Bogomolov, I.A.Kol'chugina, A.G.Litvak, A.M.Sergeev. Phys.Lett., v.91A, 447 (1982).
19. F.Shimizu. IBM J.Res.Develop., v.17, 286 (1973).
20. P.Sprangle, E.Esarey, A.Ting. Phys.Rev.Lett., v.64, 2011 (1990).
21. A.B.Borisov, A.V.Borovsky, V.V.Korobkin, A.M.Prokhorov, C.K.Rhodes, O.B.Shiryaev. Phys.Rev.Lett., v.65, 1753 (1990).
22. V.A.Petrishchev, V.I.Talanov. Kvantovaya Elektronika, v.3, 35 (1971).
23. A.G.Litvak, V.A.Mironov, A.M.Sergeev. In: Nonlinear Waves 3. Springer-Verlag, p.240 (1990).
24. L.M.Gorbunov, A.S.Shirokov. Kvantovaya Elektronika, v.12, 146 (1985).

THE THEORY OF ULTRARELATIVISTIC PLASMA WAKE EXCITATION BY SHORT LASER PULSES

Bulanov S.V., Kirsanov V.I., Sakharov A.S.
General Physics Institute, USSR Academy of Sciences
Moscow, USSR

I. Introduction

The idea of the effective charged particle acceleration by the field of longitudinal wave, excited by an intense laser pulse in a plasma [1], was stimulating both theoretical [2-9] and experimental [10-13] activities to develop new accelerating techniques. This concept of accelerator attracts attention of investigators as a possible approach to provide extremely high acceleration gradients of charged particles more then two orders greater than that in conventional accelerators. A successive development in this direction could lead to the construction of rather compact accelerators with the energy of accelerated particles over 1 TeV.

Up to now the most attention was paid to the plasma beat-wave accelerator (PBWA) scheme [1], that utilizes the resonant excitation of plasma wave by two-frequency laser pulse. The theoretical predictions of the possibility to create high acceleration gradients over 1 GeV/m are now proved by experiments on beat-wave excitation [10,11]. As alternative approaches to the plasma wave excitation there were considered the laser wakefield accelerator (LWFA) [7], in which the Langmuir wave is generated by a short laser pulse of high intensity, and the plasma wakefield accelerator (PWFA) concept [1,8,9] that is based on the plasma wave excitation by high current relativistic electron bunch.

There are some reviews containing detailed comparison of all the mentioned above concepts [2-6]. We turn to look at them from the point of view of their ability to challenge with the traditional accelerating technique that is believed to provide in the nearest future the accelerating fields about 0.1 GV/m [14].

In conventional accelerators the increase in the final

energy of accelerated particles can be provided by enlarging the length of the system. The situation with the plasma wave based accelerators is quite different. Although it is possible to utilize extremely high acceleration gradients, the final energy gain of the accelerated particles is principally limited by the spatial dephasing between them and the plasma wave in the course of acceleration [1].

First let us discuss whether the weakly nonlinear plasma wave is sufficient to provide at the same time high gradients and high final energy of accelerated particles. In this case the maximum particle energy gain will be given by the formula [1]:

$$W_{max} \simeq 2\varepsilon mc^2 \gamma_{ph}^2 , \qquad (1)$$

where $\gamma_{ph} = (1 - v_{ph}^2/c^2)^{-1/2}$, v_{ph} is the phase velocity of the plasma wave, ε is the relativistic nonlinearity parameter of the plasma wave which can be expressed via the amplitude of the plasma wave electric field $\varepsilon = eE_p/m\omega_p c$. For PWFA γ_{ph} is equal to the relativistic factor of the driver-bunch; for laser-driven plasma wave $\gamma_{ph} = \omega_0/\omega_p$, where ω_0 is the carrying frequency of the laser pulse, $\omega_p = (4\pi e^2 n_0/m)^{1/2}$ is the plasma electron frequency ($\omega_p \ll \omega_0$).

Considering a weakly nonlinear plasma wave ($\varepsilon \ll 1$), one should apply the restriction on the plasma electron frequency (under the given electric field) $\omega_p \gg eE_p/mc$. Then for the given value of γ_{ph} one can obtain from (1) the limitation on the maximum energy of the particles accelerated in a weakly nonlinear plasma wave excited by the laser pulse with a given frequency ω_0 (or given corresponding wavelength λ_0) :

$$W_{max}[eV] \ll 10^{13} \left(E_p[GV/m] \lambda_0[\mu m] \right)^{-2} . \qquad (2)$$

As it can be seen from (2), for a weakly nonlinear plasma wave with electric field E_p = 10 GV/m (much over that of the conventional accelerators) it is not possible to obtain the final energies over TeVs in PBWA or LWFA for the available intensive laser radiation ($0.26\mu m < \lambda_0 < 10.6\mu m$).

In the case of PWFA the maximum particle energy is limited by the energy losses and deceleration of the driving bunch as well as by the particle acceleration [15], so that both detune the resonance between plasma wave and accelerated particle. The deceleration of the driver can be considerable reduced by the proper profiling of the bunch [16] which allows to obtain a

sufficiently high ratio of the accelerating field value $E_+ = E_p$ to decelerating one E_- (acting on the driver) $R = E_+/E_- \gg 1$ [16]. If one needs to provide the particle to gain energy (1) one should have $R > 2\gamma_{ph}\varepsilon$ (as $t_{acc} \simeq 2\omega_p^{-1}\gamma_{ph}^2$ [1], $t_{dec} \simeq \omega_p^{-1}\gamma_{ph}R/\varepsilon$ and $t_{acc} < t_{dec}$).

To obtain the energy of an accelerated particle over 1 TeV in a weakly nonlinear plasma wave ($\varepsilon \ll 1$) with the acceleration rate about 10 GeV/m it is necessary to have the extreme parameters of the driving bunch: the density $n_b > 10^{16} cm^{-3}$ and energy much over 1 GeV. In addition, the profiling of the bunch should be provided to get high enough transform ratio. Thus, it became doubtfull that it is possible to obtain technically the parameters that provide superiority of PWFA on weakly nonlinear wave over the traditional accelerator schemes.

There are suggestion to avoid difficulties concerning with the limitation of the final electron energy for the plasma based accelerators by using a multi-stage system [3], but on this way the problems with precise synchronization immediately arise. Other approach suggests that the proper plasma density profiling [15,17] could keep the accelerated electron in the phase with the plasma wave. However, it could not improve the situation radically.

The more was the understanding of the discussed above problem the more was the interest to the strong nonlinear plasma wave excitation ($\varepsilon > 1$) [6,18-23]. The PBWA cannot be used for exciting such a strong nonlinear wave as the increase in the electron relativistic mass destroys the resonant excitation of the plasma wave. Nevertheless both PWFA and LWFA concepts can provide strongly nonlinear plasma wakefield generation with $\varepsilon > 1$.

In the present review we concentrate in general on LWFA. The interest to this accelerating concept is also backed by the rapid development of the laser technology that makes available for investigators the subpicosecond laser pulses in whose field the electron oscillation velocity is about the speed of light [24,25].

II. Basic equations

The interaction of a short intense laser pulse with a plasma can be described by the set of Maxwell equations and the fully relativistic cold electron fluid equations. In the one dimensional case ($L_{tr} \gg k_p^{-1} = c/\omega_p$) all variables can be

considered as functions of the longitudinal coordinate x and time t. Since the laser field is purely transverse we take the transverse component of the vector $\mathbf{q}=\mathbf{p}/mc$ as a variable characterizing these fields and write it in the form

$$\mathbf{q}_{tr} = \frac{1}{2}\left[\mathbf{a}\exp(-i\omega_0 t+ik_0 x) + \mathbf{a}^*\exp(i\omega_0 t-ik_0 x)\right], \qquad (3)$$

where k_0 is the wave vector of the radiation, which is related to ω_0 by the linear dispersion relation ($\omega_0^2 = k_0^2c^2+\omega_p^2$), and $\mathbf{a}$ is a complex amplitude which is convenient to choose as a function of the variables t and $\xi = x-v_g t$ ($v_g = c^2k_0/\omega_0$ is the group velocity of a laser radition in the linear approximation). As usual, the envelope approximation approach (3) assumes:

$$\partial/\partial\xi \ll k_0, \qquad \partial/\partial t \ll c\partial/\partial\xi \ll \omega_0. \qquad (4)$$

The ponderomotive force of HF field produces the longitudinal redistribution of the plasma electrons at the background of heavy immobile ions. The field of charge separation we describe by the dimensionless electrostatic potential $\phi = e\varphi/mc^2$, considering it in the form $\phi = \phi_0+\phi_{hf}$, where ϕ_0 and ϕ_{hf} are slowly varying and high frequency parts of the potential, respectively.

Assuming that the plasma density is fairly low [19,20]

$$\omega_0^2/\omega_p^2 \gg (1+q^2)/(1+\phi)^2 \qquad (5)$$

we can neglect ϕ_{hf} and obtain the set of equation for ϕ_0 and $\mathbf{a}$ [19-23]

$$\frac{d^2\phi_0}{d\xi^2} - k_p^2\frac{1+|\mathbf{a}|^2/2-(1+\phi_0)^2}{2(1+\phi_0)^2} = 0, \qquad (6)$$

$$2i\omega_0\frac{\partial\mathbf{a}}{\partial t} + \frac{\omega_p^2}{\omega_0^2}c^2\frac{\partial^2\mathbf{a}}{\partial\xi^2} + 2v_g\frac{\partial^2\mathbf{a}}{\partial\xi\partial t} = -\omega_p^2\frac{\phi_0}{1+\phi_0}\mathbf{a}. \qquad (7)$$

It is worth to mention, that by changing the sign of inequality in (5) to the equality one, the condition relating the limiting values of q^2, ϕ and $\beta_0 = v_g/c = (1-\omega_p^2/2\omega_0^2)$ can be obtained. These limiting values correspond to the case when the longitudinal electron velocity becomes equal to v_g and wave-breaking (that can be accompanied by the electron trapping in the longitudinal wave) takes place. Thus, it is easily to understand that the condition (5) is equivalent to the consideration of the plasma wave which is far from breaking.

The application of the equation (6) for the resonant beat wave excitation by the given two frequency laser pulse in a weakly

nonlinear case ($|\mathbf{a}|^2 < 1$) was considered in Ref.[26]. For arbitrary nonlinearity the similar equation was obtained in Ref.[27] where the relativistic envelope solitons were studied. In the absence of transverse fields Eq.(6) describes free nonlinear plasma wave [28]. In contrast with Refs.[26,27] the set of Eqs.(6),(7) [19] takes into consideration the evolution of the laser pulse field. The similar equations in coordinates t, $\xi = x-ct$ were discussed in Ref.[21]. For a weakly relativistic case Eqs.(6),(7) go over into those obtained in Ref.[8]. The laws of conservation for this set of equation we discuss in Sec.IV of the present paper.

III. Quasi-Static Approximation

Let us assume the complex amplitude of the laser pulse $\mathbf{a}(\xi,t)$ to be a given function of coordinate ξ and treat the temporal dependence as a parameter. For the high intensity ($|\mathbf{a}| \gg 1$) ultra short (with the length $L \leqslant \sqrt{2}/|\mathbf{a}|k_p$) inside the pulse location region we have from (6)

$$\phi_0 = k_p^2 \int_{\infty}^{\xi} d\xi' \int_{\infty}^{\xi'} d\xi'' |\mathbf{a}(\xi'')|^2 \leqslant 1 . \qquad (8)$$

Joining the solution (8) and the solution for free plasma wave behind the pulse we can find the wakefield amplitude

$$\Delta\phi = \sqrt{A(A+4)} , \quad A = \left[\int |\mathbf{a}|^2 k_p d\xi/2\right]^2 . \qquad (9)$$

It can be seen from (9) that though the electric potential inside the pulse is relatively small, the amplitude of the wakefield can be fairly great. For example, for $(k_p L)|\mathbf{a}_0| \simeq \sqrt{2}$ it follows from (9) that $\Delta\phi \simeq |\mathbf{a}_0|^2/2 \gg 1$.

The potential of charge separation field generated by the short laser pulse is shown in Fig.1a [22]. The similar results for the electric field and the plasma electron density one can find in [21].

Going now to pulses with a relatively larger length ($L > k_p^{-1}$) we consider as one more example the plasma wave excitation by the electromagnetic pulse of square shape ($|\mathbf{a}|^2 = const$ at $-L < \xi < 0$, $|\mathbf{a}|^2 = 0$ at $\xi < L$, $\xi > 0$) [19,20]. According to Ref.[19], in the region of the ultrarelativistic ($|\mathbf{a}| \gg 1$) electromagnetic pulse location the potential ϕ_0 oscillates between 0 and $\phi_{max} \simeq |\mathbf{a}|^2/2$ with the period $\lambda_p \simeq 2\sqrt{2}|\mathbf{a}|k_p^{-1}$. The corresponding maximum electric field

is about

$$E_p = \frac{mc\omega_p}{e} |\mathbf{a}|/\sqrt{2} . \qquad (10)$$

The pulse of length $L = L_s = \lambda_p s$ ($s=1,2,3,\ldots$) does not leave a plasma wave behind itself. If, on the other hand, the length of the pulse differs from L_s, even by a relatively small amount, $|L - L_s| \geqslant (|\mathbf{a}|k_p)^{-1}$, the amplitude of the ultrarelativistic plasma wakefield behind the pulse and the period of this wave will be approximately the same as the corresponding quantities in the pulse location region. This fact is associated with the relativistic increase in the electron mass at $\phi_0 \gg 1$, which has the consequence that the work performed by the RF pressure force on the plasma electrons at the trailing edge of the pulse (under the condition $\phi_0(\xi=-L) \equiv \phi_{02} \gg 1$) is smaller by a factor of ϕ_{02} than that at the leading edge.

For the same reason, in the case when the trailing edge of the laser pulse is not sharp ($\delta\xi_2 > |\mathbf{a}_2|^{-1}k_p^{-1}$, here and below the low cases 1 or 2 correspond to the quantities on the leading or trailing fronts of the pulse, respectively) the effect of the shape of this edge on the efficiency of the excitation of plasma wakefield will be of miner importance.

If the rise time of the pulse is short enough ($\delta\xi_1 k_p < |\mathbf{a}_1|^{-1}$) we can use the equations derived for a pulse with a sharp front, and the amplitude of the wakefield will be maximum. Under the condition $\delta\xi_1 k_p > |\mathbf{a}_1|^{-1}$, an increase of the rise time of the pulse will result in a decrease in the amplitude of the excited plasma wave down to the value $|\mathbf{a}_2|/\sqrt{2}$ (for the pulse with a sharp trailing edge). Finally, if the amplitude of the pulse rises and decays slowly at the both edges of the pulse $\delta\xi_{1,2}k_p > |\mathbf{a}_{1,2}|^{1/2}$, no wakefield will be excited at all.

Thus, in the ultrarelativistic case the nonlinear wakefield of the maximum amplitude will be excited by short laser pulse (or pulse with short leading front) with a duration about $\omega_p^{-1}/|\mathbf{a}_0|$, that determines its spectrum width $\Delta\omega \geqslant \omega_p|\mathbf{a}_0|$.

IV. Laser Field Evolution and Plasma Wave Excitation

Eq.10 has the first integral

$$\int d\xi \left\{ |\mathbf{a}|^2 - \frac{iv_g}{\omega_0}\left[\mathbf{a}^* \frac{\partial \mathbf{a}}{\partial \xi} - \mathbf{a}\frac{\partial \mathbf{a}^*}{\partial \xi}\right]\right\} = \text{const.} \qquad (11)$$

Taking $\mathbf{a}$ in the form $\mathbf{a} = |\mathbf{a}|e^{i\vartheta(\xi,t)}$ and utilizing the usual

definition of the local frequency of electromagnetic radiation $\omega(\xi,t)$ as the time derivative of the whole phase in the laboratory frame $\omega = \frac{\partial}{\partial t}(\omega_0 t - \vartheta(x-v_g t,t)) \simeq \omega_0 + v_g \partial\vartheta/\partial\xi$, one can rewrite (11) in the form

$$\int d\xi |\mathbf{a}|^2 \omega = \text{const} . \qquad (12)$$

The combination of variables $|\mathbf{a}|^2\omega$ in (12) (since the modulus of amplitude is defined as $|\mathbf{a}| = e|E|/m\omega c$) is proportional to the density of transverse radiation photon number $N = |E|^2/\omega$. Thus, Eq.(12) (or Eq.(11)) may be interpreted as the conservation law of the total photon number.

In addition, from Eq.10 one can get the relationship

$$\frac{\partial}{\partial t}\int d\xi \left(\frac{i v_g}{\omega_0}\frac{\partial \mathbf{a}^*}{\partial \xi} + \mathbf{a}^* \right)\left(\frac{i v_g}{\omega_0}\frac{\partial \mathbf{a}}{\partial \xi} - \mathbf{a} \right) = \frac{1}{2} v_g \frac{\omega_p^2}{\omega_0^2}\int d\xi |\mathbf{a}|^2 \frac{\partial}{\partial \xi}\frac{1}{1+\Phi_0} ,$$

that can be transformed to the expression for the laser field energy losses

$$\frac{\partial}{\partial t}\int d\xi \left(\frac{|E|^2+|B|^2}{16\pi} \right) = -\frac{1}{16}\left(\frac{m\omega_p c}{e} \right)^2 \int d\xi |\mathbf{a}|^2 \frac{\partial}{\partial \xi}\frac{1}{1+\Phi_0} . \qquad (13)$$

Using Eq.(6) it is easy to show, in agreement with the total energy conservation law, that the right hand side of Eq.(13) is equal to the rate of the energy input into the plasma wakefield (taken with the opposite sign).

To study qualitatively the evolution of the fairly short laser pulse ($(k_p L)|\mathbf{a}_0| < 1$) one can use a rough model based on the conservation laws mentioned above. Assuming that the laser pulse is characterized by a certain average value of frequency $\langle\omega(t)\rangle$ and by the integral $Q(t) = \int d\xi |\mathbf{a}|^2$, it is possible to obtain (using also Eq.(8)) the next formulae

$$Q(t) = (1-t/t_{nl})^{-1/3} Q(0), \quad \langle\omega(t)\rangle = (1-t/t_{nl})^{1/3}\langle\omega(0)\rangle . \qquad (14)$$

where the characteristic time of the nonlinear pulse energy depletion is given by

$$t_{nl} = \frac{8}{3}(k_p Q(0))^{-1}\omega_0^2/\omega_p^3 \qquad (15)$$

The approximate solutions (14) predict, that the decrease in the laser pulse frequency $\langle\omega(t)\rangle$ (and in the pulse total energy) is accompanied by the growth of the integral $\int d\xi |\mathbf{a}|^2$ as well as by the increase in the amplitude of the excited wakefield (according to (9)). The considered model is valid as

far as the inequalities $t < t_{nl}$ and $(k_p L)|a_0(t)| < 1$ are satisfied.

The linear spreading being taken into consideration does not affect the process of wake excitation as in this case as for pulses of a low intensity [29].

The results of the numerical solution of the set of Eqs.(6),(7) are shown in Figs.1a,b,c (for the moments of time $t = 0$, $t = 2t_{nl}$ and $t = 4t_{nl}$, where, for the chosen parameters of pulse, $t_{nl} \simeq 4 \cdot 10^3 \omega_p^{-1}$) and in Fig.2. The dependencies presented in Fig.1 as well as the temporal changes in normalized energy of the laser pulse and in the plasma wakefield normalized amplitude (Fig.2) corroborate the general tendencies previously discussed in the frame of the rough model. In addition, as it can be seen in Fig.2, the laser pulse energy losses can be fairly considerable for an ultrarelativistic pulse in contrast with the low intensity case [8]. For the chosen parameters the laser pulse loses about one half of its total energy per time $t \simeq 4t_{nl}$.

As the local frequency measurements are hardly possible to carry for picosecond laser pulses it is reasonable to present here the temporal evolution of the pulse spectrum. In Fig.3 one can see the down shift of the laser pulse frequency and the broadening of its spectrum.

The set of Eqs.(6),(7) is valid for the description of the plasma wakefield excitation and the distortion of the pulse shape and spectrum until the minimum value of the pulse local frequency $\omega_{min}(t)$ would become comparable with the plasma electron frequency ω_p.

Let us now consider the plasma wave excitation by a considerably longer laser pulse: $2\sqrt{2}|a_0| > Lk_p \gg 1$ with a short leading front $\delta\xi_1 k_p \leqslant |a_0|^{-1}$. With exception of a narrow region near the leading front, the pulse propagates at a speed close to that of light $v_g' \simeq c$ ($(c - v_g') \ll (c - v_g)$). This is due to the relativistic decrease in the effective plasma frequency in the region of the pulse where $\phi \gg 1$. The considerable changes, similar to those of the short pulse, appear only just behind the leading edge of the pulse.

Figs.4a,b illustrate the plasma wave excitation and distortion of a long enough pulse with a short leading front in the sequential moments of time. In this case some difference in details compared to the evolution of a short laser pulse can be

connected with an energy income into the region of the leading front from the main body of the pulse. The value of t_{nl} is determined in this case by expression (15), where the integration in $Q(0)$ is carried over the region $\Phi_0 \leqslant 1$ in the vicinity of the leading edge and is approximately given by the expression

$$t_{nl} \simeq |\mathbf{a}|^{-1}\omega_0^2/\omega_p^3 . \qquad (16)$$

The pulse shape and spectrum distortion can change the plasma wake amplitude and wavelength and, thus, detune a synchronism between the plasma wave and the accelerated particle and finally limit the acceleration. A comparison of the acceleration time in a nonlinear plasma wave excited by the given laser pulse ($t_{acc} \simeq 4\omega_p^{-1}\phi_{max}^{1/2}\gamma_{ph}^2$) with the time of nonlinear distortion t_{nl} confirms that the particle acceleration in the wakefield is, in fact, limited by the pulse evolution. As a result, the maximum energy gain is limited by the value of order $mc^2\gamma_{ph}^2$.

Note, that in accordance with formula (13), the losses of the laser field energy due to the plasma wave excitation may be attributed to the regions of the pulse where the derivative $\frac{\partial}{\partial\xi}\frac{1}{1+\Phi_0}$ is positive. The process inverse to the plasma wave excitation which is known as a frequency upshift effect ("photon acceleration" [30]) takes place for a laser pulse propagating together with a plasma wave in a phase corresponding to the negative sign of $\frac{\partial}{\partial\xi}\frac{1}{1+\Phi_0}$. For a given linear plasma wave this process was considered in Ref.[30].

Using our previous analysis we can predict that utilizing of a strong nonlinear plasma wave gives a little advantage for the "photon accelerator". This is due to a fairly small region of a nonlinear plasma wave suitable for the effective "photon acceleration" (since the length of the region where $\frac{\partial}{\partial\xi}\frac{1}{1+\Phi_0} < 0$ and simultaneously $\Phi_0 \leqslant 1$ is about $1/4\Phi_{max}$ part of the nonlinear plasma wave length $\lambda_p \simeq 4k_p^{-1}\phi_{max}^{1/2}$). As a result, the process of the laser pulse frequency upshift will be effective while the pulse propagates together with the plasma wave a distance about $2k_p^{-1}\phi_{max}^{-1/2}\gamma_{ph}^2$ or during the time about t_{nl}. But even small changes in plasma wavelength in the wake at time fairly less than t_{nl} destroys the resonance between "accelerated" pulse and wakefield. Thus, the utilizing of a nonlinear plasma wave could give the advantage only for the particle accelerating scheme.

V. Nonstationary Breaking Wakefield and Particle Acceleration

As it was shown in Ref.[28] the limiting field amplitude of the stationary nonlinear plasma wave in a cold plasma is equal to

$$E_{max} = \alpha_0 \sqrt{2(\gamma_{ph}-1)}, \quad \alpha_0 = mc\omega_p/e. \qquad (17)$$

Further investigations have shown that the thermal effects should be taken into consideration even for nonrelativistic plasma electron temperature $T_e > mc^2\gamma_{ph}^{-2}$ [31,32]. In this case the limiting value E_{max} reduces with compare to that in a cold plasma (17) and is determined by the expression

$$E_{max} \simeq \alpha_0 \beta^{-1/4} \left[\ln(2\gamma_{ph}^{1/2}\,\beta^{1/2})\right]^{1/2}, \quad \beta = 3T_e/(mc^2). \qquad (18)$$

The formulae (17),(18) concern the limitation of an electric field in a free plasma wave. However, the wakefield induced by a driving bunch or laser pulse can not be considered in full sense as a purely free plasma wave and the limiting field value for this case requires a special treatment.

At first glance, the plasma wakefield excitation by a relativistic electron bunch with the density close to $n_0/2$ [18] seems to be ideal to obtain in plasma the value of electric field as great as one needs. That is based on the assumption that in the region occupied by the bunch-driver the plasma electrons, being accelerated backward, formally can gain the energy over the energy in the stationary wave with the amplitude (17). That can result in excitation of a breaking wake-wave with the field amplitude over that of Akhiezer and Polovin. But one can make sure that it is not possible due to the bunch-driver deceleration.

Still we have an alternative possibility to use a laser pulse in order to get E_{max} over that given by the wave breaking limit (17). In contrast with the driver-bunch case, plasma electrons at the leading front of the laser pulse are accelerated forward and even can be trapped when the condition (5) is broken. However, if the wave breaking does not appear inside the region occupied by the laser pulse it can still appear in the wake behind it. For the laser pulse of square shape considered above such a case can be realized under the combination of inequalities

$$\sqrt{2}|\mathbf{a}| < \gamma_{ph}, \qquad \gamma_{ph} < |\mathbf{a}|^2/4, \qquad (19a,b)$$

the first of which provides the coherent motion of plasma

electrons inside the pulse while the second one corresponds to the wave breaking of the plasma wave behind the pulse. From (19a) and expression (10) the limiting value of the electric field in the nonstationary breaking wake immediately follows:

$$E_{max} = a_0 \gamma_{ph}/2. \qquad (20)$$

It is easy to see that for the given pulse in the underdense plasma the field (20) is fairly greater than that predicted by formulae (17),(18).

The distance between the pulse leading front and the wave breaking region is approximately equal to the nonlinear plasma wave length $\lambda_p = 2\sqrt{2}|\mathbf{a}|$. The structure of the wake field in this case will not be stationary and the region of multi-stream electron motion will spread towards the pulse with a relative velocity $d\xi/dt \simeq c - v_{ph}$.

The comparison of the time during which the pulse covers the nonlinear plasma wave length with the characteristic time of the pulse front distortion (16) shows that the laser pulse evolution is negligible during the formation of the breaking wake under the condition (19a). Thus, it is principally possible to generate the field over (17) by the relativistically strong laser pulse.

For a more realistic case of the laser pulse with a smooth intensity profile ($L > (k_p a_0)^{-1}$) the condition of coherent electron motion in the region of pulse location is : $a_0 < \gamma_{ph}^3 k_p^2 L^2$ and is hardly possible to be broken and fields up to $E_{max} = a_0 \gamma_{ph}^2 k_p L$ could be achieved.

The PIC stimulation has been carried to demonstrate the discussed above possibility of generation of a nonstationary breaking plasma wake with E_{max} over that of Akhiezer and Polovin (17) as well as to examine the effectiveness of electron acceleration in such a wake.

For a relativistically strong laser pulse (but not fairly intense to generate the field over (17) in the wake) a similar stimulation had been carried in Ref.[33].

The laser pulse enters into a homogeneous plasma with a sharp boundary from vacuum. The wave breaking appears near the boundary at the moment when the pulse has covered in plasma the distance about the nonlinear plasma wave length (if the laser intensity is high enough to provide it).

In our simulation a smooth enough pulse with duration about five laser wave length and with extremely high amplitude $a_0 = 30$

penetrates into the underdense plasma with a plasma electron frequency eight times lower than ω_0 ($\gamma_{ph} \simeq 8$). The results of simulation corresponding to the sequential stages of pulse propagation are presented in Fig.5a,b. In the top parts of each figure one can see the spatial profiles of electrostatic field E_x (normalized on a_0) and the envelopes of the laser pulse intensity $|E_\perp|^2$ (in arbitrary units). In the bottom parts, the electron phase spaces (p_x/mc versus x) are shown. The coordinate x is measured from the plasma boundary and is normalized to the laser vacuum wavelength $\lambda_0 = 2\pi c/\omega_0$ (which for the chosen parameters is equal to $0.785\ k_p^{-1}$).

Fig.5a ($t = 60\ T_0$, where $T_0 = 2\pi\omega_0^{-1}$ is the laser field period) corresponds to the moment of time just after the breaking of the wake near the plasma boundary. One can see that the electric field in the wake varies approximately linearly from $10a_0$ just behind the pulse down to the value about $-10a_0$ in the region of breaking. The wavelength of the nonlinear plasma wave is about $40k_p^{-1}$. Note, that such an amplitude of the electric field is two and half times higher than the limiting value of the electric field (17) in stationary (non-breaking) plasma wakefield. If the laser pulse would not change during its propagation through the plasma these electrons could be accelerated in such a field up to the energies about $2\gamma_{ph}^2\Phi_{max}mc^2 \simeq 10^4 mc^2$.

Actually, the laser pulse evolution leads to the growth of the efficiency of the energy transform to the plasma wake (see section IV). That, in its turn, results in the plasma wave length growing. Both the acceleration of the trapped particles (their displacement towards the laser pulse) and enlarging of the length of nonlinear wave lead to the decreasing of the longitudinal electric field in the region occupied by the trapped electrons, but the last effect dominates. Still, up to the moment when trapped electrons get in the decelerating electric field they still can gain considerable energy.

In Fig.5b the trapped electrons are about to get into decelerating part of the wake due to the effect of enlarging plasma wave length that accompanied the laser field evolution. Up to this moment their energies are already about $\gamma_{ph}^3 mc^2$.

The dephasing between the trapped plasma electrons and "breaking wake" can be to a certain extent compensated by the

longitudinal plasma density profiling. This possibility is illustrated by Fig.6. The results presented in Fig.6 correspond to uniform plasma and to the plasma with parabolic increase in the plasma density (which is about 20% for the considered interval of time).

VI. The Problem of Nonlinear Self-Focusing

The realistic view on LWFA can not avoid the problems concerned with the final transverse size of the laser pulses [9,21,22,34], especially the problem of transverse laser field evolution.

Considering the nonlinearity as the result of the relativistic electron mass growth has led to the conclusion that relativistic optical guiding of laser pulses is possible in the underdense plasma [21]. More adequate approach to the problem included also the plasma electron density redistribution under the ponderomotive force [34]. If one is to consider the intense plasma wake generation, the account should be also taken of the effect of longitudinal electron motion on the relativistic electron mass variation.

Qualitative analysis taking into account all the mention above nonlinear effects has been carried in Refs.[21,22], utilizing the generalization of the one dimensional model results to the 3D case. The effective plasma electron frequency has been obtained in the form $\omega_p^{eff} = \omega_p/(1+\phi)^{1/2}$ and refractive index has been determined by the expression

$$\eta = 1 - \frac{1}{2}\omega_p^2 / [\omega_0^2 (1+\phi)] \quad . \qquad (21)$$

The negative transverse gradient of the refractive index $\partial\eta/\partial r$ can lead to self focusing of the laser pulse.

Refractive index variations in the region occupied by the short laser pulse (where the corresponding scalar potential is small $\phi < 1$) are fairly small even for $\delta n/n_0 \gg 1$. Thus, for the short laser pulse one can resume that the self-focusing due to the relativistic nonlinearity can be considerably compensated by the increase in the plasma electron density. The same conclusion is valid for a fairly short leading front of a laser pulse. It is worth to mention that additional limitation of the laser pulse self-focusing can be a result of downshift frequency conversion considered in Sec. IV as the frequency downshift on the axis should be maximum.

If the pulse is sufficiently long (as for example in Fig.4) then for the main part of the pulse (where $\phi \gg 1$) both the relativistic effects and the electron density redistribution lead to the self-focusing. The discussion of the possible optical guiding of the laser pulse with the characteristic size of amplitude variation $\delta\xi > k_p^{-1}|a|^{1/2}$[9] is out of the scoop of the present paper as such a pulse does not excite the plasma wave.

The leading edge of a pulse that generates intense nonlinear wake can diffract [21]. The question is whether this "erosion" of the leading front results in the sufficient energy losses from the main body of the ultrarelativistic pulse .

For the case of fairly large transverse size of laser pulse ($L_{tr}k_p \gg 1$) the additional suggestion may be made for the structure of the 3D wake: the radial field of a nonlinear wake-wave can be focusing for electrons more than in a half of the accelerating phase [22] (in contrast with the 1D case where it is only $\lambda_p/2$).

VII. Conclusion

The main advantage of utilizing relativistically strong laser pulses in LWFA, in contrast with the other plasma-based accelerating schemes, is the possibility to obtain at the same time extremely high accelerating gradients (especially for the case of wave-breaking in the wake) and considerably great final energy of the accelerated particles. As it is shown one can avoid the necessity to inject the accelerating particles for the variant of LWFA with the wave-breaking in the wake.

A laser pulse with the wavelength $\lambda_0 \simeq 1\mu m$, an intensity $I \simeq 10^{19} W/cm^2$ and duration about 0.3ps in a plasma with density $n_0 \simeq 10^{15} cm^{-3}$ ($\omega_0/\omega_p \simeq 1000$) will excite the plasma wave with $E \geqslant 2$ GV/m, according the results derived in Sec.III. Plasma electrons trapped in the field of the plasma wave could acquire an energy of 0.3 TeV over the distance $\simeq 4x_{nl} = 4ct_{nl} \simeq$ 150 m.

The other result of the present paper concerns the possibility of high efficiency laser energy conversion into under dense plasma via nonlinear plasma wave excitation. For parameters of simulation in Sec.V (Fig.6), considering $\lambda_0 \simeq 1\mu m$, $I \simeq 10^{21} W/cm^2$, the main fraction of the pulse energy would be lost in a plasma with a density $n_0 \simeq 10^{19} cm^{-3}$ at the distance less then 1mm.

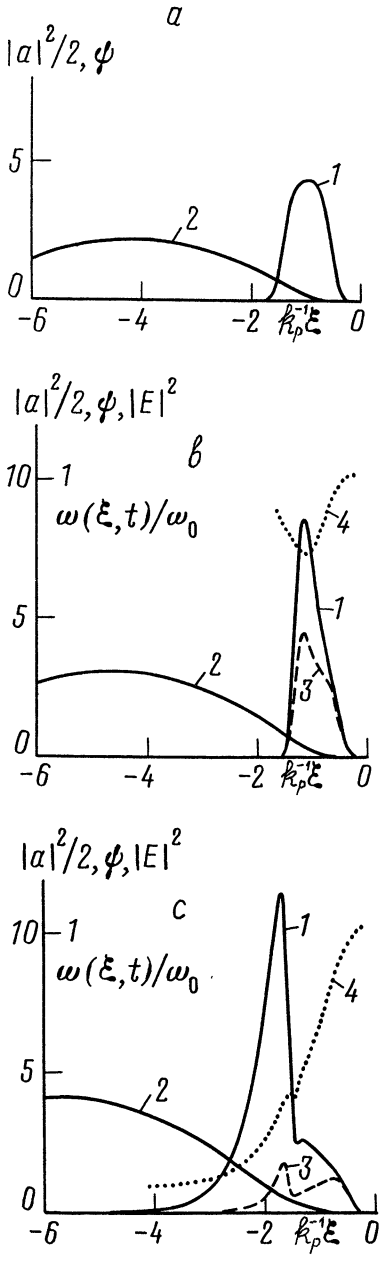

Fig.1

This shows three plots of the nonlinear plasma wave generation by the short laser pulse taken at times 0, $2t_{nl}$ and $4t_{nl}$ (where for chosen parameters $t_{nl}=4\cdot10^3\omega_p^{-1}$). Curve 1 - the quantity $|a|^2/2$; curve 2 - the scalar potential ϕ; curve 3 -the electromagnetic field energy density in units of $8\pi(m\omega_0 c/e)^2$; curve 4 (dotted line) - the ratio of the local frequency of the electromagnetic radiation $\omega(\xi,t)$ to ω_0. The pulse parameters are $a_0=3$, $\omega_0/\omega_p=100$ and $k_pL\simeq$ $\simeq0.7$.

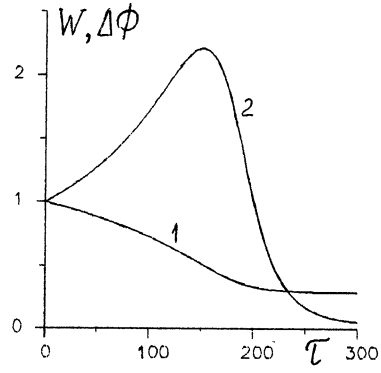

Fig.2

The laser pulse total energy W (curve 1) and the plasma wake-wave amplitude Δφ (curve 2) normalized to their values at t = 0 as functions of time ($\tau=\omega_p^2 t/\omega_0$) for parameters of Fig.1.

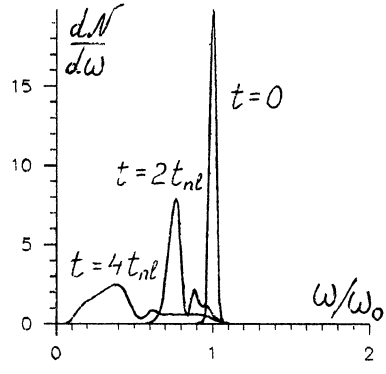

Fig.3

The plots of normalized spectral density of photone number of the laser pulse (presented in Fig.1) for different moments of time. The figure demonstrates the down shift in the laser pulse frequency and broadening of its spectrum.

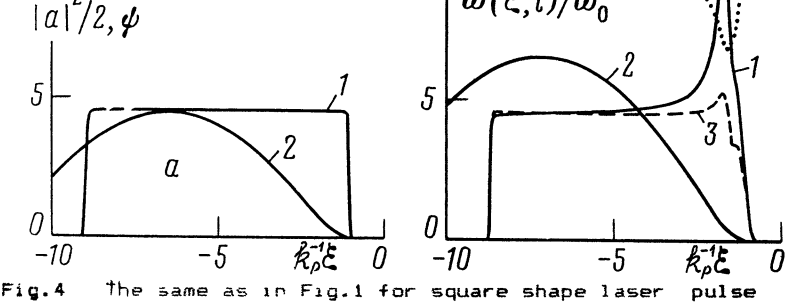

Fig.4 The same as in Fig.1 for square shape laser pulse ($a_0=3$, $\omega_0/\omega_p=100$, $k_pL=8$) for the moments: a - $t=0$; b - $t=8\cdot10^3\omega_p^{-1}$

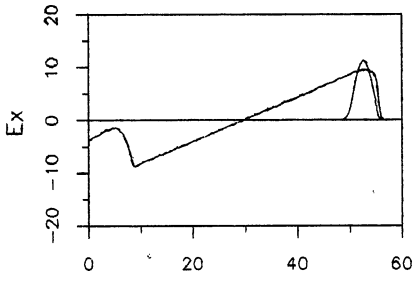

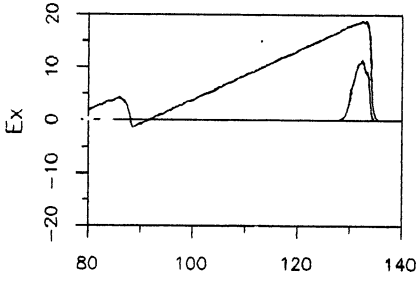

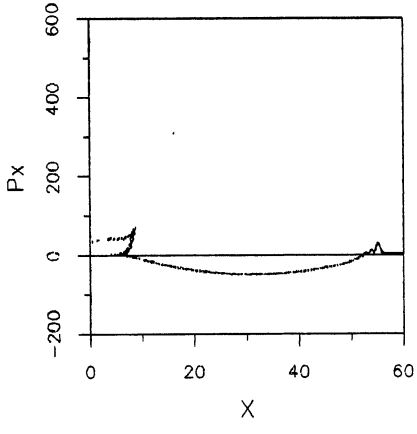

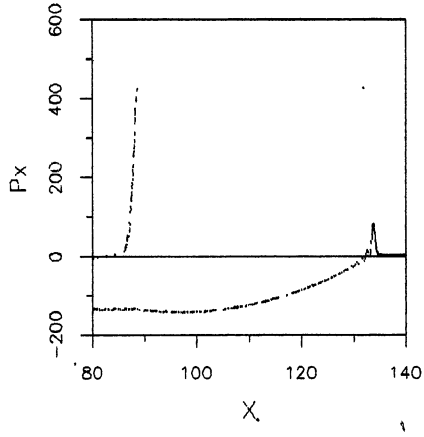

Fig.5a **Fig.5b**

Plasma electrons acceleration in the "breaking wake". Laser pulse parameters are a_0=30, ω_0/ω_p=8, L/λ_0=5. In the top parts one can see the profiles of E_x (normalized to $\frac{mc\omega_p}{e}$) and the envelopes of the pulse intensity $|E_\perp|^2$ (in arbitrary units) for two moments: a- $t = 60T_0$, b- $t = 140T_0$ ($T_0 = 2\pi\omega_0^{-1}$ is the laser field period) In the bottom parts the electron phase spaces (p_x/mc versus x) are shown. The coordinate x normalized to the laser vacuum wavelength $\lambda_0 = 2\pi c/\omega_0$ equals zero at the plasma boundary.

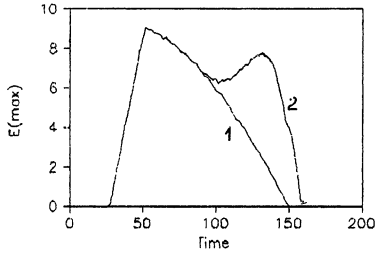

Fig.6a

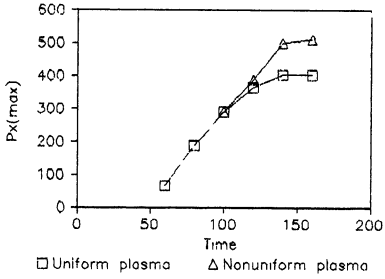

Fig.6b

The demonstration of partial compensation of the dephasing between the trapped plasma electrons and "breaking wake" due to the plasma density profiling. The temporal evolution of the maximum value of E_x (normalized on $\frac{mc\omega_p}{e}$) acting on the trapped electrons is presented in Fig 6a for uniform plasma (curves **1**) and for the plasma with the parabolic increase in density of about 20% for the considered interval of time (curves **2**). In Fig.6b the maximum electron momentum p_x/mc as a function of time is shown.

References

1. Tajima T., Dawson J.M., Phys. Rev. Letters,V.34,No.4,267 (1979)
2. Dawson J.M., *Proc. Laser Accelerat. Part 2, Workshop, Malibu, Calif., Jan. 7-12, 1985*, N.Y, AIP, 55 (1985)
3. Chen F.F., Physica Scripta, V.T30., 24 (1990)
4. Tajima T., Laser and Particles Beams, V.3, 351 (1985)
5. Esarey E., Ting A., Sprangle P., Joyce G., Comments on Plasma Phys., V.12, 291 (1989)
6. Tsytovich V.N., U.De Angelis, Bingham R., Comm. Plasma Phys. and Contr. Fusion, V.12, 249 (1989)
7. Chen P., Dawson J.M., Huff R.W., Katsouleas T., Phys. Rev. Lett., V.54, 693 (1985)
8. Gorbunov L.M., Kirsanov V.I., Zh. Exp. Teor. Fiz., V.93, 509 (1987) (Sov.Phys, JETP, V.66, (1987))
9. Sprangle P., Esarey E., Ting A., Joyce G., Appl. Phys. Lett., V.53, 2146 (1988)
10. Clayton C.E., Joshi C., Darrow C., Umstadter D., Phys. Rev. Lett., V.54, 2343 (1985)
11. Martin F. et al., *Preprint CERN 87-11, ECFA 87/110*, 360 (1987)
12. Itagawa I. et al., *Preprint Inst. of Laser Ingeneering, Osaca Univ. No.9001P, 1989*, SUITA-Osaka 565, Japan (1989)
13. Dangor A.E., Dymoke-Bradshaw A.K.L., Dyson A.E., Physica Scripta, V.T30, 107 (1990)
14.Wilson E.J.N., Physica Scripta, V.T30, 69 (1990)
15. Katsouleas T., Phys. Rev. A, V.33, 2056 (1986)
16. Katsouleas T., Wilks S., Chen P., Dawson J.M., Su J.J., Particle Accelerators, V.22, 81 (1987)
17. Gorbunov L.M., Kirsanov V.I. Mtingva S.K., Kratk. Soobsh. po Fiz., No.10,27 (1989) (Sov. Phys. Lebedev Inst. Reps No.10 (1989))
18. Rozenzweig J., IEEE Trans. on Plasma Sci., V.PS-15, 186 (1987)
19. Bulanov S.V., Kirsanov V.I., Sakharov A.S., Pis'ma Zh. Exsp. Teor. Fiz., V.50, 176 (1989) (Sov. JETP Lett., V.50, 198 (1989))
20. Berezhiani V.I., Murusidze I.J., *"Proc. of the IV Int. Workshop on Nonlinear and Turbulent Processes in Physics, Kiev, USSR, Oct. 9-22, 1989"*, Kiev, 1989, P.235
21. Sprangle P., Eresay E., Ting A., Phys. Rev. A., V.41, 4463 (1990)
22. Bulanov S.V., Kirsanov V.I., Sakharov A.S., Fiz. Plazmy, V.16, 935 (1990) (Sov. J. Plasma Phys. V.16, No.8 (1990))
23. Gorbunov L.M., Kirsanov V.I., in *"Nonlinear Theory of Strong*

Electromagnetic Wave-Plasma Interaction" (Proc. P.N.Lebedev Physical Institute of the USSR Ac. Sci.), to be published in 1991
24. Ebery J.H. et al., Laser Focus., No.10, 84 (1987)
25. Maine P. et al., IEEE J.Quan.Elec., V.24, 398 (1988)
26. Noble R.J. Phys. Rev. A, V.32, 460 (1985)
27. Kozlov V.A., Litvak A.G., Suvorov E.V., Zh. Eksp. Teor. Fiz., V.76, 148 (1979)
28. Akhiezer A.I., Polovin R.V., Zh. Eksp. Teor. Fiz., V.30., 915 (1956) (Sov. JETP, V.3, 696 (1956))
29. Kirsanov V.I., Kratk. Soobsh. po Fiz., No.8, 36 (1987) (Sov. Phys. Lebedev Inst. Reps, No.8, 49 (1987))
30. Wilks S.C., Dawson J.M., Mori W.B., Katsouleas T., Jones M.E., Phys. Rev. Lett., V.62, 2600 (1989)
31. Katsouleas T, Mori W.B., Phys. Rev. Lett., V.61, 90 (1988)
32. Mory W.B., Katsouleas T., Physica Scripta, V.T30, 127 (1990)
33. Bulanov S.V., Naumova N.M., Inovenkov I.N., Sakharov A.S., Fiz. Plazmy., V.16, 767 (1990)
34. Tsinsiadze N.L., Physica Scripta, V.T30, 41 (1990)

ON THE MAXIMUM FIELD OF THE RELATIVISTICALLY STRONG LANGMUIR WAKE-WAVE

S.V.Bulanov, V.I.Kirsanov, A.S.Sakharov
General Physics Institute, USSR Academy of Sciences,
Vavilov str., 38, Moscow, USSR

The problem of exciting the maximum possible longitudinal field of nonlinear plasma oscillations is of fundamental interest in nonlinear plasma physics. The progress in understanding the problem can be very useful for possible applications of strong electrostatic fields for plasma heating and as well for development of new particle accelerating techniques [1,2].

A resonable approach to the problem is to study the maximum possible field in a stationary electron plasma wave. Early results of Akhiezer and Polovin [3] obtained in the cold fluid limit gave the value of the maximum field amplitude

$$E_{max} = \varkappa_0 \sqrt{2(\gamma_{ph}-1)}, \qquad (1)$$

where $\gamma_{ph} = \sqrt{1 - v_{ph}^2/c^2}$, v_{ph} is the plasma wave phase velocity, $\varkappa_0 = mc\omega_p/e$, and $\omega_p = (4\pi e^2 n_0/m_e)^{1/2}$

Further development of the theory has taken account of the thermal effects and led (for 1D "water-bag" model) to the result of Katsouleas and Mori [4]

$$E_{max} \simeq \varkappa_0 \beta^{-1/4} \left[\ln(2\gamma_{ph}^{1/2}\beta^{1/2}) \right]^{1/2}, \qquad (2)$$

where $\beta = 3T_e/(mc^2)$.

The free plasma wave with the field of amplitude (1) or (2) corresponds to the case when the fraction of plasma electrons gains the speed equal to v_{ph} in the direction of wave propagation If the electric field amplitude in the wave exceeds the value (2)(or in the plasma with cold electrons the value (1)), then the validity of the coherent plasma electron motion approach is broken and so-called wave-breaking appears. Wave breaking

phenomenon is accompanied by the trapping of the plasma electrons in the wave as well as the wave shape distortion.

In the present issue we

1. consider the problem of the maximum possible amplitude of the electron stationary wave in a plasma with isotropic and anisotropic electron temperature;
2. discuss the possibility to use a relativistic electron bunch and an ultrarelativistic laser pulse as a possible driver to excite the wakefields much over those predicted by formulas (1),(2) ;
3. demonstrate an effective plasma electron acceleration by the wakefield over the limit (1).

1. Let us consider the stationary one-dimensional plasma wave. Then all the parameters that describe the wave depend only on the combination of the variables $\xi=k_p^{-1}(x-v_{ph}t)$, where $k_p=\omega_p/v_{ph}$. The plasma consists of electron and ion components. Each component is supposed to be characterized by the distribution function, since that it can be described as an ensemble of streams with densities n_α and momenta $\vec{p}_\alpha=\vec{p}_\alpha/m_\alpha c$ for $\alpha = 1,2,3,\ldots$. With the subscript "0" we will indicate the values corresponding to the region where the potential of charge separation field $\phi = e\varphi/mc^2$ is equal to zero. In addition, at $\phi = 0$ we impose the condition of quasi-neutrality and of zero total current.

Using the equations of continuity and motion for each stream one can obtain the value of n_α as a function of potential ϕ. Making the summation over all values of index α the Poison equation can be rewritten in the form

$$d^2\phi/d\xi^2= -\beta_{ph}^2\gamma_{ph}^2\sum_\alpha\frac{Z_\alpha n_{0\alpha}}{n_0}[\beta_{ph}-\beta_{\alpha 0}]\left[(1-G_\alpha^2)^{-1/2}-(1-G_{\alpha 0}^2)^{-1/2}\right], \quad (3)$$

where

$$G_\alpha(\rho_{\alpha 0},\phi)=(1+\rho_{\alpha 0_\perp}^2)^{1/2}/\gamma_{ph}A_\alpha,\ A_\alpha=\sqrt{1+\rho_{\alpha 0_\perp}^2+\rho_{\alpha 0x}^2}-\beta_{ph}\rho_{\alpha x}-Z_\alpha\frac{m}{m_\alpha}\phi, \quad (4)$$

where $\beta_{\alpha 0}=v_{\alpha 0x}/c$ and Z_α is normalized (to the positive elementary charge e) particle charge of α-fraction.

Sagdeev "potential" $U(\phi)$ in the first integral of Eq.3 $((d\phi/d\xi)^2+U(\phi)=const)$ is given by the following expression

$$U(\phi)=\sum_{\alpha} U_{\alpha} = \sum_{\alpha}\frac{m_{\alpha}n_{0\alpha}}{m_e n_0}\beta_{ph}^2\gamma_{ph}^2\left[\beta_{ph}-\beta_{\alpha 0}\right]\times \qquad (5)$$

$$\times\left[A_{\alpha 0}(1-G_{\alpha 0}^2)^{-1/2}-A_{\alpha}(1-G_{\alpha}^2)^{-1/2}-\frac{Z_{\alpha}m_e}{m_{\alpha}}\phi\,(1-G_{\alpha}^2)^{-1/2}\right].$$

The coherent motion approximation is broken for potential $\phi < \phi_{min}$ due to trapping in the wave the electron fraction with the maximum value of the longitudinal momentum $p_{max} = \max(p_{e0x})$. That corresponds to the condition

$$G_{\alpha}(p_{max},\phi_{min}) = 1. \qquad (6)$$

Then the value of E_{max} can be derived from the expression

$$E_{max}=x_0\sqrt{2U(\phi_{min})}\,. \qquad (7)$$

The ion component terms in $U(\phi)$ can be neglected for $(m_e/m_i)\phi \ll 1$. Going in expression (5) from summing to integrating with respect to $\vec{p}_0$ we can obtain the Sagdeev "potential" in the form

$$U(\phi)=\frac{1}{n_0}\int d\vec{p}_0\; f_e(\vec{p}_0)\; U(\vec{p}_0,\phi), \qquad (8)$$

where $f_e(\vec{p}_0)$ is electron distribution function that is assumed to be non zero for $|p_{0x}| \le p_{max}$. Substituting the value of ϕ_{min} into (8) we finally obtain from the wave breaking condition (6) for $|p_0| \ll 1$.

$$U(\phi_{min}) \simeq \frac{1}{2n_0}\int d\vec{p}_0\; f_e(\vec{p}_0)\left[\; p_{0\perp}^2/2 + p_{max}-p_{0x}+1/4\gamma_{ph}\right]^{-1/2}. \qquad (9)$$

Assuming one dimensional distribution function $F_e(p_{ox}) = \int dp_{0\perp} f_e(\vec{p}_0)$ and taking it in the form:

$$F_e(p_{ox}) = \begin{cases} n_0/2p_{max} & \text{for} \quad |p_{0x}| \le p_{max}\,, \\ 0 & \text{for} \quad |p_{0x}| \ge p_{max}\,. \end{cases} \qquad (10)$$

we come to the result (2) [4] and in the limit $|p_{max}| \to 0$ from formula (8) the cold limit result (1) follows.

For 3D symmetrical distribution function

$$F_e(p_{ox}) = \begin{cases} (3/4\pi)n_0/p_{max}^3 & \text{for} \quad |p_{0x}| \le p_{max}\,, \\ 0 & \text{for} \quad |p_{0x}| \ge p_{max}\,, \end{cases} \qquad (11)$$

the maximum field amplitude value obtained from (8) for $p_{max} \gg \gamma_{ph}^{-1}$ will be equal to

$$E_{max} \simeq \varkappa_0 (3/2)^{1/2}/(5T_e)^{1/4}, \qquad (12)$$

where the effective temperature of the electrons is defined as $T_e=2/3\langle\rho^2\rangle$ and is equal to $T_e=\rho^2_{max}/5$.

Note that expression (10) differs from similar one for 1D case (2) by the absence of logarithmic term. Still, as both of them are obtained for the simplest forms of distribution functions and are qualitative results, it is not critical to ignore the difference.

On the contrary, for strong anizotropy of plasma electron temperature $T_{e\perp}/mc^2 \gg (T_{ex}/mc^2)^{1/2}$ the limiting value of the electric field amplitude will reduce approximately by the factor $\left[T_{e\perp}/mc^2 \;/\; (T_{ex}/mc^2)^{1/2}\right]^{1/2}$ compared to value given by the formula (12).

2.The excitation of free nonlinear plasma waves by moving with high velocity drivers [1,5] have been supposed for the purposes of charged particles acceleration. Let us consider the excitation of extremely strong plasma waves by relativistic electrons bunch with the density equal one half of the plasma density (Fig.1). Then, formally, it is possible to obtain the electric field as great as one needs. One can find that at the distance of order $\lambda_p/2$ behind the bunch (where $\lambda_p=4\sqrt{\phi_m}$ and $\phi_m \gg 1$ are the wave-length and amplitude of the nonlinear plasma wave) the electron velocity can equal or exceed the plasma wave phase velocity. That should lead to breaking of the wave. The estimation of the plasma wave electric field in this region gives the value

$$E_{max} = \varkappa_0 \sqrt{L_b k_p},$$

which for sufficiently long bunch could exceed the field value (1). However, taking into account the deceleration of the bunch in this case, one can show that the bunch loses all its energy earlier than it covers in plasma the length $(\lambda_p/2+L_b)$. As well the bunch profiling does not provide the the excitation of the electric fields values greater than (1). Still, it is possible to create in a plasma with nonzero temperature the breaking wakefields with the values over than (2) or (12).

In the case of excitation of wake fields by ultrarelativistic laser pulse the wave-breaking of the plasma wave can appear both

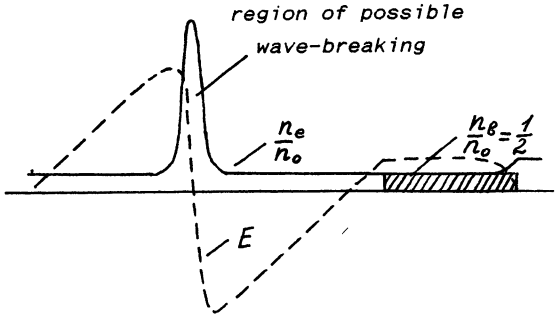

Fig.1 Shematic picture of wakefield excitation by the electron bunch ($n_b=n_0/2$). E is electric field, n_e/n_0 is plasma electron density.

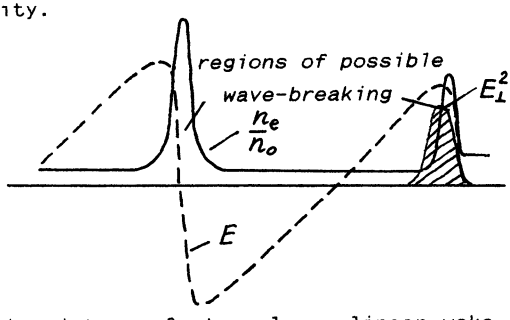

Fig.2 Schematic picture of strongly nonlinear wake excitation by laser pulse.

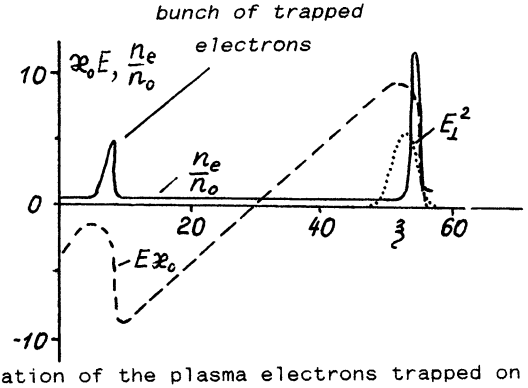

Fig.3 Acceleration of the plasma electrons trapped on the course of wave breaking. Laser pulse intesity is shown in dotted line.

inside the pulse and at the distance λ_p behind the pulse (Fig.2). Occasionally, due to relativistic plasma electron mass growth because of transverse quiver electron oscillations, the wave-breaking in the wake appears while there is no wave-breaking yet in the region of the pulse. Thus, the fields over (1) can be obtained in the breaking wake behind the laser pulse.

3. This conclusion is supported by the numerical simulation results presented in Fig.3 where the longitudinal wakefield E_x and the electron density profiles are shown (for more details see Ref.[7,8]). The maximum value of the wakefild for chosen parameters is about three times greater than for stationary wave. In the left side of Fig.3 one can the spike of plasma electron density. It corresponds to the grope of accelerating electrons trapped on the course of wave-breaking. The total number of these electrons is large enough to reduce at least twice the amplitude of the wake behind the considered region. The numerical simulation has shown that it is possible to accelerate the group of self-injected electrons up to energies over $\gamma_{ph}^3 mc^2$.

References

1. Tajima T., Dawson J.M. Phys. Rev.Letters, V.34, 267 (1979)
2. Dawson J.M., *Proc. Laser Accelerat. Part 2, Workshop, Maliby, Calif. Jan. 7-12,1985*-N.Y,AIP, 55 (1985)
3. Akhiezer A.I., Polovin R.V., Zh. Eksp. Teor. Fiz., V.30, 915 (Sov. JETP V.3, 696 (1956))
4. Katsouleas T, Mori W.B. Phys. Rev. Lett. -1988. -V.61,No.1.-P. 90-93
5. Chen P., Dawson J.M., Huff R.W., and Katsouleas T. Phys. Rev. Lett.-1985.-V.54,No.7.-P.693-696
6. Bulanov S.V., Kirsanov V.I., Sakharov A.S. Pis'ma Zh. Exsp. Teor. Fiz.-1989.- V.50,-P.176-178 (Sov. JETP Letters, V.50,198-201 (1989))
7. Bulanov S.V., Kirsanov V.I., Sakharov A.S. Fiz. Plazmy.-1990.- V.16, No. 8, -P.935-944 (Sov. J. Plasma Phys. V.16, No.8 (1990))
8. Bulanov S.V., Kirsanov V.I., Sakharov A.S., Strong Plasma Wakefield Generation by Short Laser Pulses *Proc. of Int. Workshop "Strong Microwaves in Plasmas", Suzdal, USSR, Sept. 18-23, 1990* (Invited Papers)

FLUCTUATIONS, CHAOS AND AUTO-OSCILLATIONS IN PLASMA WAVE SYSTEMS

V.A.BUTS, I.I.LAPIDUS, S.S.MOISEEV, O.G.CHKHETIANI
Space Research Institute, USSR Academy of Sciences,
Profsoyuznaya 84/32, 117810 Moscow,USSR

I. Introduction

The influence of a weak (but finite) noise on evolution of plasma as well as radiotechnical systems is the subject of the present paper. It is shown for disintegration processes in plasma as a pattern that precence of a noise results in the exponentional growing of "fluctuational" chaos at the amplitude of the pumping wave which are essentially less than ones needed for the dynamic chaos to appear in the system. The study of the multiplicative noise influence on some auto-oscillatinng systems well known in plasma science and radiophysics has shown that at relatively modest noise amplitudes the total disappearance of autooscillations may occur as well as birth of new steady states.

II. The Fluctuational Chaos

In this chapter we will show for the parametric instability as a pattern that precence of a noise may result in the essential transformation of the system behaviour.

Let,s study the disintagrationthe transversal wave into transversal and Langmuir ones (t --> t'+e).

The initial system of equations may be simplified in the case when the frequency of the electromagnetic field essentially exceeds the electron plasma frequecy wP Averaging over the "fast" time results in the following system of equations for slowly varying values.

$$rot\ rot\ \mathcal{E} - k_0^2 \cdot \mathcal{E} \cdot \mathcal{E} - \frac{2ik}{c^2} \cdot \frac{\partial \mathcal{E}}{\partial t} = -\frac{\omega_p^2}{c^2} \cdot \frac{\delta n}{n_0} \cdot \mathcal{E}$$

$$\frac{\partial^2 \delta n}{\partial t^2} + \omega_p^2 \cdot \delta n - V_{tb}^2 \cdot \Delta S_n = \frac{\omega_p^2}{\omega^2} \cdot \frac{\Delta |\mathcal{E}|^2}{16\pi m} \qquad (1)$$

Here $\mathcal{E}$ is the modulation electromagnetic field

$$E = \frac{1}{2} [\mathcal{E} \cdot e^{-i\omega t} + K.C.]$$

S^n - the slow variation of plasma electron density

$$\mathcal{E} = 1 - \frac{\omega_p^2}{\omega^2}, \quad V_{tb} = \frac{T_E}{m}$$

(T^e is the temperature of electrons, m - their mass).

We will look for the solution of eq.(1) in the form:

$$\mathcal{E} = A_i(t)\cdot e^{ik_i r - i\delta t} + A_s(t)\cdot e^{ik_s r}$$

$$S_n = \frac{1}{2}\delta n_p(t)\cdot e^{ik_p r} + \text{K.C.} \qquad (2)$$

Here $k_i = k_s + k_p$, $\delta = \omega_i - \omega_s$ $(\frac{|\delta|}{\omega_{i,s}} \ll 1)$.

Let's $n = n_o + \tilde{n}(t)$, where $\tilde{n}(t)$ is the fluctuating part of n which is supposed to be space uniform. Substituting (2) in (1) and rewriting it in the dimensionless form we get the following system of equations for amplitudes of coupled oscillations:

$$\frac{dC_o}{d\tau} = -i\rho^*\cdot(1+Z)\cdot e^{i\Delta\tau}\cdot C_1$$

$$\frac{dC_1}{d\tau} = -i\rho C_o^*\cdot(1+Z)\cdot e^{-i\Delta\tau} \qquad (3)$$

$$\frac{d^2\rho}{d\tau^2} + \Gamma^2\cdot(1+Z)\cdot\rho = -C_o C_1^*\cdot(1+Z)\cdot e^{-i\Delta\tau}$$

Here: $C_o = \frac{A_i}{A_o}$, $C_i = \frac{A_s}{A_o}$, $\rho = (\frac{\mu^2}{2\alpha A_o^2})^{1/3}\cdot\frac{\delta n}{n_o}$, $A_{i,s} = e_{i,s}A_{i,s}$.

$e_{i,s}$ - unit polarization vector of the electric field of the transversal electromagnetic wave: $(e_{i,s}\cdot k_{i,s} = 0)$, $A_o = A_{i(t=0)}$ -

- initial value of electromanetic wave,

$\mu \equiv \omega_p^2\cdot\cos(\theta/4\omega_i)$, $\alpha \equiv k_p^2\cdot\omega_p^2\cdot\cos(\theta/\omega_i^2)8\pi n_o m$, θ -

- anngle between vectors e_i and e_s; $\tau = (\mu\alpha A_o^2)^{1/3}\cdot t$,

$$\Delta = \frac{\delta}{(\mu\alpha A_o^2)^{1/3}}, \quad Z = \frac{\tilde{n}}{n};$$

$$\Gamma^2 = \frac{\omega_p^2}{(\mu\alpha A_o^2)^{2/3}} \equiv \left(\frac{\omega_p^3 \cdot \cos^2\theta \cdot A_o^2}{32\pi\omega_i^3 n_o m \cdot V_{cp}^2}\right)^{-2/3} \left(V_{cp} = \frac{\omega_p}{k_p}\right).$$

It,s worth to mention that system of equations (3) has a rather universal character. It describes the wide class of disentigration processes including the disintegration of the plasma wave into plasma and ionic sound ones, disintegrative processes in plasma-beam systems.

Let's analyze abruptly some limits. At z=0 and $C_o(\tau) = const = 1$ there is the solution of (3) in the form $\rho=\rho_o e^{i\Omega\tau}$, $C_i=C_{io}e^{i\Omega\tau - i\Delta\tau}$.

The linear stage of the parametric instability is characterized by the increment, which has maximum at $\Delta=\Gamma$ for $\Gamma>>1$, and for the $\Gamma<1$ the increment reaches its maximum at $\Delta=0$.

The modified disintegration takes place in this last case. The essence of such a process is the simultaneous resonanse of both plasma waves (direct and inverse) with corresponding electromagnetic waves.

The analysis of the nonlinear stage of parametric instability ($C_o=const$) was made numerically for different Γ and Δ. For $\Gamma>>1$ the regular periodic exchange between interacting waves has appeared to take place. The characcteristic time scale of this process is determined by the inverse increment of the linear stage. The disintegrationn dynamics changes qualitavitely at $\Gamma<1$. It becomes chaotic. This fact corresponds to the overlapping of resonanses $\omega_i = \omega_s + \omega_p$.

Let's consider now weak fluctuations of density and study the case of small given amplitudes of the pumping wave ($C_o=1$ and $\Gamma>>1$) when only one plasma wave interacts with electromagnetic waves.

The system (3) may be further simplified by the following substitution:

$$\rho(\tau) = \mathcal{P}(\tau)\cdot e^{-i\Gamma\tau} \qquad (4)$$

Here $P(\tau)$ is the new variable. Substituting (4) in (3) and accepting $\Gamma=\Delta$ we get the simple system of equations for amplitudes C_1 and P:

$$\frac{d\mathcal{P}}{d\tau} + \frac{1}{2}\cdot\Gamma\cdot Z\cdot\mathcal{P} = -\frac{i}{2\Gamma}\cdot(1+Z)\cdot C$$

$$\frac{dC}{d\tau} = i\cdot(1+Z)\cdot\mathcal{P} \qquad (5)$$

Here $C = C_1^*$.

Employing the Furutsu-Novikov formula [1] we get the following equations for the first and second order moments:

$$\frac{d\langle\mathcal{P}\rangle}{d\tau} + \frac{1}{2}\cdot\Gamma\cdot D\cdot\{-\frac{1}{2}\cdot\Gamma\cdot\langle\mathcal{P}\rangle - \frac{i}{2\Gamma}\cdot\langle C\rangle\} = -\frac{i}{2\Gamma}\cdot\langle C\rangle + \frac{1}{2\Gamma}\cdot D\cdot\langle\mathcal{P}\rangle$$

$$\frac{d\langle C\rangle}{d\tau} = i\cdot\langle\mathcal{P}\rangle + \frac{D}{2}\cdot\{\Gamma\cdot\langle\mathcal{P}\rangle + \frac{1}{\Gamma}\cdot\langle C\rangle\} \qquad (6)$$

$$\frac{d}{d\tau}\langle\mathcal{P}^2\rangle + D\cdot\Gamma^2\langle\mathcal{P}^2\rangle = -\frac{i}{\Gamma}\cdot\langle C\mathcal{P}\rangle + D\cdot\{\frac{\langle\mathcal{P}^2\rangle}{\Gamma} - \frac{C^2}{2\Gamma^2} - \langle C\mathcal{P}\rangle\}$$

$$\frac{d}{d\tau}\langle C\mathcal{P}\rangle + \frac{D\Gamma}{4}\langle C\mathcal{P}\rangle - \frac{D\Gamma}{2}\langle\mathcal{P}^2\rangle = -\{\frac{i}{2\Gamma} + \frac{D}{4}\}\langle C^2\rangle + i\langle\mathcal{P}^2\rangle + \frac{2}{\Gamma}\langle C\mathcal{P}\rangle \qquad (7)$$

$$\frac{1}{2}\frac{d}{d\tau}\langle C^2\rangle = \langle C\mathcal{P}\rangle\cdot\{i + \frac{D\Gamma}{2}\} + \frac{D}{2\Gamma}\langle C^2\rangle - D\langle\mathcal{P}^2\rangle$$

We have supposed for simplicity that function $z(\tau)$ is the Gaussian δ-correlated random process with the zero average:

$$\langle z(\tau)\rangle = 0, \quad \langle z(\tau)\cdot z(\tau_1)\rangle = 2D\cdot\delta(\tau-\tau_1) \qquad (8)$$

The analysis of (7)-(8) results in the following. At $D\Gamma^{-2}<<1$ the influence of fluctuations is weaqk and dynamics is still regular. At $D\Gamma^{-2}>1$ first order moments are growing with the increment

$$Im\ \omega^{(1)} = \frac{1}{3}\cdot\frac{2}{D\Gamma^{-3}}\cdot\frac{\omega_p}{\Gamma}$$

As far as second moments are concerned we would like to emphasize the following: at $D\Gamma^{-2}>>1$ direct and inverse plasma waves are interacting strongly. This fact results first of all in the behaviour of second order moments. Analysis of equations for these moments results in the increment

$$Im\ \omega^{(2)} \sim D\Gamma^{-2}\frac{\omega_p}{\Gamma} \gg Im\ \omega^{(1)}$$

Dispersionn begins increasing and the system transits quickly to the chaotic regime. Such a developing fluctuational chaos is in same sense a "pure" chaos because it is free of dynamic chaos difficulties such as dechaotization "holes" and "isles" of stability. And the most important point is that the fluctuational chaos developes at essentially lower pumpingwave amplitudes than the dynamical chaos does [2].

III. The Stochastic Suppression of Auto-Oscillations

The Van-der-Pole equation describ auto-oscillations in the various plasma, radiotechnical and biological systems [3]

$$\ddot{X} + \varepsilon\cdot(1 - X^2)\cdot\dot{X} + X = 0,\ \varepsilon > 0 \qquad (9)$$

Equation (9) relates to the system with soft exitation. It means that the point X= X'= 0 is the unstable focus and there is the attracting limit cycle in the phase space> The arbitrary "weak push" transits the system to the auto-oscillating regime.

All types of a noise entering eq.(9) may be classified as natural and technical ones.

Natural noises are always being introduced additively. They are internal attributes of the system. The influence of the additive noice is really the Gaussian Dispersion about the basic state namely the auto-oscillating regime [4].

The multiplicative (technical) noise is the external one and therefore its introduction results in qualitatively different results. Let's assume ε to have the noisy addition:

$$\varepsilon = \varepsilon\cdot(1 + f(t)) \qquad (10)$$

$$\langle f(t)\cdot f(t')\rangle = 2\cdot D\cdot\delta(t-t') \qquad (11)$$

The shortened equation for the energy has the form:

$$E_t = \varepsilon\cdot\left(\frac{(f(E)+F(E))}{T_o(E)}\right) + \varepsilon^{1/2}\left(\frac{\sigma_*(E)}{T_o^{1/2}(E)}\right)\cdot\xi(t) \qquad (12)$$

Here:

$$T_o(E) = 2\pi \qquad (13)$$

$$f(E) = 2\pi\cdot E\cdot(1 - \tfrac{1}{2}E) \qquad (14)$$

$$F(E) = 2\pi\cdot\varepsilon D\cdot E\cdot(1 - E + \tfrac{1}{2}E^2) \qquad (15)$$

$\xi(t)$ is the δ-correlated process with the unit amplitude. The corresponding Fokker-Planck-Kolmogorov (FPK) equation

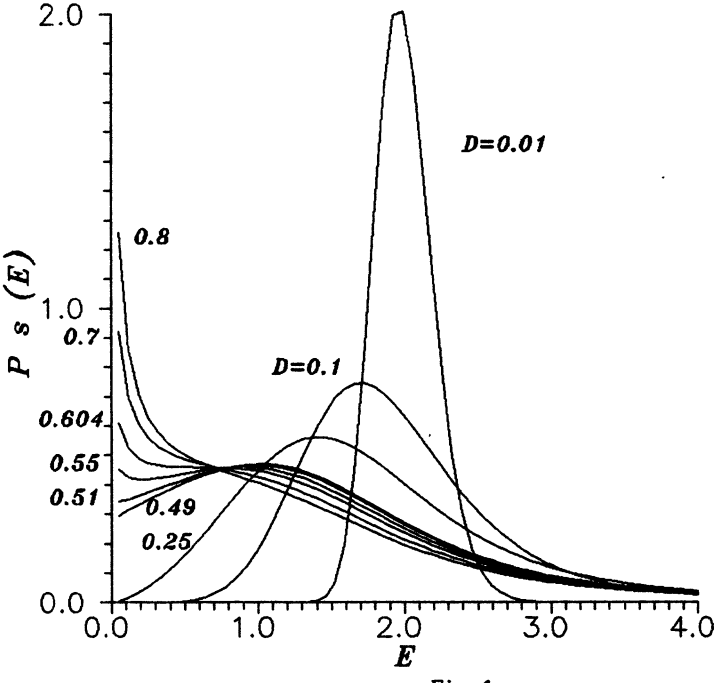

Fig.1

Evolution of a stationary probability density of Van-der-Pole oscillator as a function of the multiplicative noise intensity.

$$\partial_t P = -\varepsilon\cdot\partial_E\left(\frac{f(E)+F(E)}{T_0(E)}\cdot P\right) + \frac{\varepsilon}{2}\cdot\partial_{EE}^2\left(\frac{\sigma_*^2(E)}{T_0(E)}\cdot P\right) \qquad (16)$$

has the stationary solution:

$$P_s(E) = C\cdot E^{\frac{4}{3}\left(\frac{1}{2D\varepsilon}-1\right)}\cdot\left(6-4E+\frac{3}{2}E^2\right)^{-\frac{2}{3}\left(\frac{1}{2D\varepsilon}+1\right)}\cdot \qquad (17)$$

$$\exp\left(-\frac{2}{3\sqrt{5}D\varepsilon}\cdot\operatorname{arctg}\frac{3E-4}{2\sqrt{5}}\right)$$

The distribution of probability $P_s(E)$ varies qualitatively at the noise level $\varepsilon D=1/2$ (fig.1). There is sharp maximum at $E\sim 2$ when $\varepsilon D<<1/2$. It corresponds to the energy of auto-oscillations. At low noise levels the system is involved in weak fluctuating oscillations about the basic state. As the noise level increases the maximum of $P_s(E)$ shifts to smaller values of E. At $\varepsilon D = 1/2$ the integrable pecularity at $E = 0$ arises. The average energy

$$\bar{E} = \int_0^\infty E\cdot P_s(E)dE$$

shifts downstairs as the noise increases. At $\varepsilon D=2$ the pecularity becomes unintegrable corresponding to the total disappearance of auto-oscilations. This fact means that $E = 0$ is now the stable state of equilibrium and excitation of auto-oscillations is impossible.

Consideration of the other widely known type of auto-oscillating systems - systems with hard exitation [6] results in the analogous sequensces:

$$\ddot{X} - \varepsilon\cdot(1 - X^2 + \alpha\cdot X^4)\cdot\dot{X} + X = 0,\ 0 < \varepsilon \ll 1 \qquad (18)$$

At $\alpha < 1/8$ there is the stable focus with $E = 0$, the unstable limit cycle with $E = \frac{1-\sqrt{1-8\alpha}}{2\alpha} \cong 2$ and the stable limit cycle with $E = \frac{1+\sqrt{1-8\alpha}}{2\alpha} \cong 2$. At $\alpha > 1/8$ only the attracting focus $E = 0$ remains in the system ans oscillations don't excite.

Let's assume that ε has the fluctuating component (in addition to the constant one) - the white Gaussian noise, just as in eq.(10),(11). We can also write down the shortened equation for the energy and the corresponding FKP-equation. Within the accuracy of first degree of α the stationary dednsity of probability for the system with hard excitation effected by a multiplicative noise is the following:

$$P_s(E) \cong C\, E^{-\frac{4}{3}\left(\frac{1}{2D\varepsilon}-1\right)} \cdot R_o(E)^{\frac{1+6\alpha}{D\varepsilon}} \cdot R_*(E)^{-\frac{2}{3}} \cdot \tag{19}$$

$$\cdot \exp\left[\frac{2(1-\frac{7}{5}\alpha)}{3\sqrt{5}\,D\varepsilon} \cdot \operatorname{arctg}\frac{3E-4}{2\sqrt{5}} + \frac{\alpha}{D\cdot\varepsilon}\,\frac{66-17E}{15\cdot R_o(E)}\right]$$

The unintegrable singularity at E->0 is evident. Such a singularity is the didrect sequence of the fact that there is always a possibility to break down auto-oscillations in the system with hard excitation influenced by random perturbations. The point $E = 0$ is the absorbing boundary. Any arbitrary traqectory will earlier or late inevitably be "absorbed" by $E = 0$. Nevertheless if $P_s(E)$ has local maxima than the system can stay in corresponding metastable states some definite period of time. Analysis of extrema of $P_s(E)$ is equivalent to the search of tourth-order

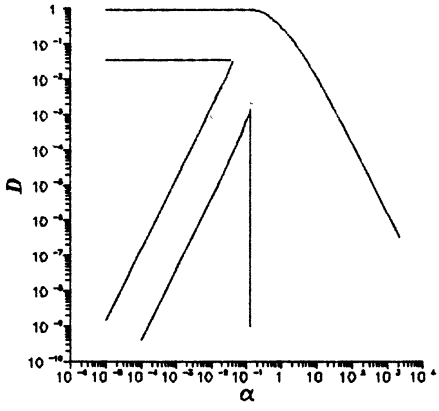

Fig.2

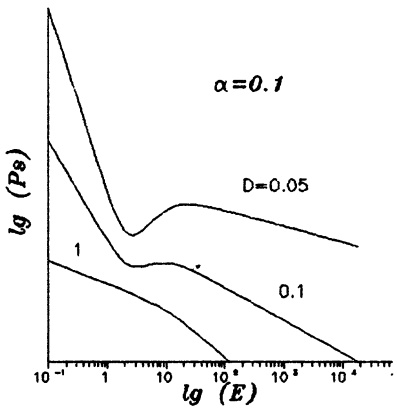

Fig.3

Fig.2 Regions of parameters $(D\varepsilon, \alpha)$ corresponding to different dynamic regimes of the system with hard excitation.
Region III - attracting focus at E = 0 and one metastable state (one local maximum of $P_s(E)$ and one minimum).
Regions I and II - appearance of an additional metastable state in comparison with region III (the maximum at high E).
Region IV - absence of local extrema $P_s(E)$ and singularity at E=0.

Fig.3 Evolution of the stationary probability density of the system with hard excitation as a function of multiplicative noise intensity. The parameter α = 0.1 is conctant for all curves.

polinomial routes:

$$f(E) - 2'F(E) = 0 \qquad (20)$$

The numerical analysis shows that one can divide the plane of parameters ($D\varepsilon$,α) to 4 regions (fig.2). In regions I and II eq.(20) has 4 routes - 2 maxima and 2 minima of $P_s(E)$ corresponds. This fact meaqns that besides the maximum caused by the system own properties there arises an additional maximum of a pure noisy origin. Unfortunately it is situated at very large E values widely dispersed, and the life time of the system in this state is very small. There are 2 routes in region III - 1 maximum and 1 minimum ("noisy" extrema are absent). And there are no real rotex of eq.(20) in region IV. It means that $P_s(E)$ has a singularity at E->0 (fig.3) and decreases monotonously near the point E = 0. Therefore in the system with hard excitation under study the introduction of the white Gaussian noise as an addition to the friction coefficient results in the untrivial reconstruction of the phase portrait of the system. The first feature is that E = 0 becomes a stable focus. Secondly in regand II of the parameters phase space (fig.2) the system acquires an additional metastable state of a pure noisy nature. Transition from regions I and II into region III results in the loss of this state thus in region III the system has besides the attracting focus E = 0 one more metastable state of a pure noisy nature. Transition from regions I and II into region III results in the loss of this state thus in region III the system has besides the attracting focus E = 0 one more metastable-state ($P_s(E)$ has 1 local minimum and 1 maximum). As the noise level grows these extrema draw together merging at the boundary of regions III and IV. Transition into region IV is

characterized by the second reconstruction of the system dynamics. In this region $P_s(E)$ has no local extrema therefore any auto-oscillations will be inevitably supressed. Such a behaviour is analogous to that of Van-der-Pole oscillator.

References

1. Klyatskin, V.I., Statistical description of systems with fluctuating parameters, Moscow, Nauka, 1975 (in Russian).

2. Zaslavskij, G.M., Stochasticity of dynamical systems, Moscow, Nauka, 1984 (in Russian).

3. Landa, P.S., Auto-oscillations in systems with finite number of freedom degrees, Moscow, Nauka, 1980 (in Russian).

4. Lapidus, I.I., Chkhetiani, O.G., On stochastic stabilization of some nonlinear oscillators, Space Research Institute, preprint N°1669, Moscow, 1990 (in Russian).

THE INFLUENCE OF ELECTRON DENSITY PROFILE ON THE ANTENNA SELF-MATCHING EFFECT WITH MICROWAVE DISCHARGE

Gryaznova T.A. , Filonenko E.G., Shashurin I.P.
Kiev State University, Kiev, USSR

One of the most important problems of the electromagnetic field interaction with plasma is the determination of maximum radiation absorption conditions by plasma. Usually, an increase of the microwave power absorption in a weakly inhomogeneous plasma is related to the field strengthening of an incident wave in the regions of plasma resonance [I] and deformation of the density profile. Similar effects can be observed in a number of cases of the microwave antenna operation in the plasma environment, that are of practical importance. Our experiments performed with a monopole antenna [2] showed that when a self-maintained microwave discharge is initiated around it, the antenna matching with a supplying transmission line is improved abruptly (SWR up to ~I.I ÷ I.3) and practically all power applied is absorbed by the microwave discharge plasma. The aim of the present paper is to show that the effect of antenna self-matching with a transmission line is due to the resonance absorption of the microwave power in the inhomogeneous plasma in the region of the local plasma resonance (LPR), $n=n_{cr}$, and to the density profile deformation related to it.

Experimental investigations were made in a circular aperture antenna which was essentially an open end of the coaxial line with a cross-section of 2b/2a=I6 mm/6.95 mm [3] to be dipped into a weakly magnetized ($\omega_H/\omega \sim 0.3$) background plasma created by the dc discharge in argon at 10^{-3} mm Hg.

The measurements were carried out at the 2.46 GHz frequency that ensured the value of the collision parameter $\nu/\omega < 0.01$. The plasma density was $n_e(r,z)$ and the microwave field $E^2 (r,z)$

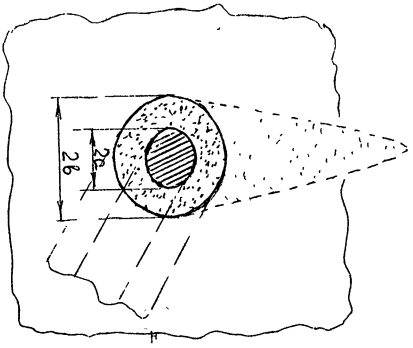

Fig.1.

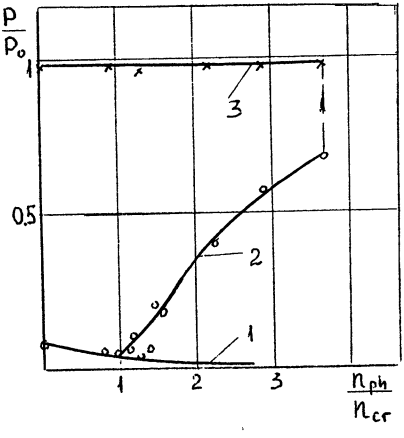

Fig.2.

The power P radiated into a plasma versus the power P_0 supplied to the antenna depending on the background plasma density:

1- calculated value obtained for a homogeneous plasma;
2-experimental value P_0 =1mW;
3- regime of microwave discharge P_0 ~ 20 W.

distribution in the antenna environment was measured by the moving coaxial probe (fig.I). The ratio of the power P emitted into a plasma to the power P_0 supplied to the antenna is shown in fig.2 depending on the background plasma density n_b/n_{cr}

When the plasma density is $n_b/n_{cr} > 1$, the microwave power absorbed by plasma (curve 2) exceeds remarkably the design value obtained for a homogeneous plasma (curve I) [3] . This effect can be explained as follows. When the antenna operates in the plasma environment, the transition layer is formed near its surface which consists of a plasma layer with reduced density as a result of the departure of the charged particles from the homogeneous plasma on the surface of the antenna and the ion layer determined by the antenna's negative potential with respect to the plasma. The presence of the transition layer may essentially increase the electromagnetic energy absorption emitted by the antenna into a plasma. This effect is observed when an electron density in the surrounding homogeneous plasma exceeds a critical one and, therefore, the plasma dielectric permittivity in the transition layer passes zero [4] (LPR region), which leads to the resonance absorption of the microwave power in this region. The experimental dependence (curve 2) is in qualitatively good

agreement with the measured one for the case of the transition layer with linearly increasing electron density [4]. If $P_0 \geq 20W$, at $n_b/n_{cr} > 3$, a self-maintained microwave discharge is ignited in the antenna environment. The discharge ignition (fig.2, dotted line) is accompanied with the antenna-plasma self-matching. The matching is independent of the background plasma and is retained at $n_b = 0$ (curve 3). The improvement of the antenna matching seems to be determined by a change of plasma density when microwave discharges are ignited. The dependences of $n_e(r, z)$ and $E^2(r,z)$ for the case when the antenna is at the floating potential with the power of the microwave signal of the order of a few milliwatts are shown in figs. 3,4. It is obvious that the microwave fields of an aperture antenna are determined basically by the "near" zone and are concentrated in the region of an inhomogeneous plasma layer. A similar dependence for the case of a burning microwave discharge ($n_b = 0$) is depicted in figs. 5,6.

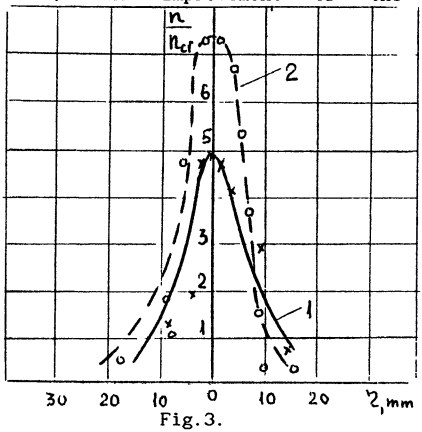

Fig.3.

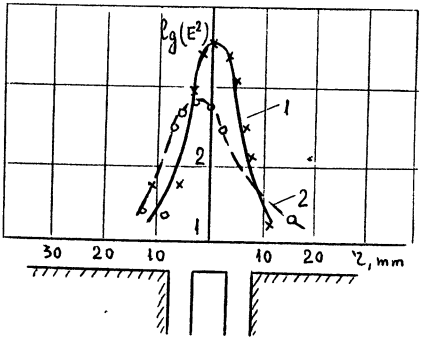

Fig.4.

Plasma density distribution $n/n_{cr}(r, z)$ (fig. 3) and microwave field distribution $E^2(r,z)$ (fig.4) in antenna neighbourhood for $P_0 \sim 1mW$ (z is the distance between antenna surface and coaxial probe).

On the axis of the microwave discharge, the plasma acquires a negative potential of about 100-200 V depending on the applied microwave power. The central antenna electrode acquires approximately the same values. The plasma density in the microwave discharge is always higher than n_{cr}. The maximum plasma

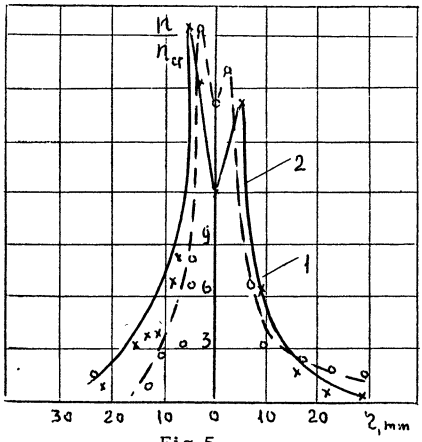

Fig.5.

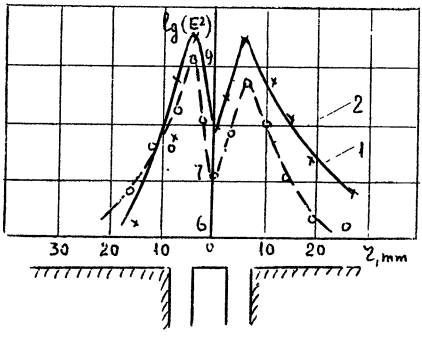

Fig.6.

Plasma density distribution n/n_{cr} (fig.5) and microwave field distribution E^2 (r,z) (fig.6) in antenna neighborhood for the microwave discharge P_0~20W (I - z~3.5mm, 2 - z~7mm).

density decreases by the amount of the power supplied to the antenna and when n_e approaches $(3\div4)n_{cr}$ the matching deteriorates and the discharge decays. The microwave field distribution in the antenna environment (fig.6) has a minimum on the antenna axis, which is evidently related to the inhomogeneous distribution of the electron density.

To explain the antenna-plasma matching effect we calculated a reflection coefficient for a circular aperture antenna dipped into an axially inhomogeneous plasma. Since the condition $E^2/8\pi n_e T_e > 1$ is realized in the experiments with a self-maintained microwave discharge, one can expect the increase in the steepness of the electron density profile in the neighborhood of the point $n = n_{cr}$.

The result of the measurement for the case depicted in fig.5 is shown in Table 1. The values of the reflection coefficient have been calculated for the linear distribution of electron density (I) and for the linear distribution in the presence of the ion layer whose thickness corresponded to the experimental one (2). The rest of the dependences (3)-(6) were plotted as follows: the density was distributed linearly with increased steepness in the LPR region and parabolically in the other regions, the two distributions being sewn smoothly. It is apparent from Table I, that there is some optimum value in the change of density in the LPR region for a given case providing a complete antenna-plasma mat-

Table I

N	$\frac{d(n/n_{cr})}{dz}$	|r|
1.	5.50	0.602
2.	5.55	0.395
3.	8.38	0.348
4.	10.06	0.072
5.	10.90	0.093
6.	11.17	0.126

ching. With the change of the inhomogeneous plasma layer parameters the optimal profile of density varies as well. One may conclude that in the burning regime of the microwave discharge the electron density and the microwave field distribution are set in the antenna environment providing the antenna self-matching with plasma environment. In this sense, a microwave discharge appears to be a self-organized system ensuring the optimal conditions for self-sustainment . From the practical point of view, the effect described is of interest when there is a need to provide a maximum power efficiency into the formed plasma of microwave discharge.

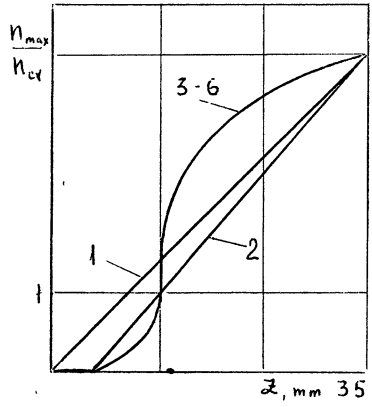

Fig.7.
Calculated model of electron density profile $n_e(z)$:
1 - linear distribution,
2 - linear distribution in the presence of ion layer,
3-6 - parabolic and linear distributions in ZPR region.

References

1. K.Mizuno, Y.S.De Groot. Phys. Fluids, **22**, 2229, 1979.
2. S.M.Levitskii, E.G.Filonenko, I.P.Shashurin. Ukr.Fiz.Zh. (Russ.Ed.), **23**, 318, 1978.
3 T.A.Gryaznova, N.N.Ivanchinov, K.S.Karplyuk, E.G.Filonenko, I.P.Shashurin. Zh.Teor.Fiz., **46**, 1081, 1976.
4. T.A.Gryaznova, E.G.Filonenko, I.P.Shashurin. Zh.Teor.Fiz., **59**, 71, 1989.

PROPAGATION OF ELECTROMAGNETIC WAVES IN A MODULATED DENSITY PLASMA

by

Maurizio LONTANO and Nicolai LUNIN (*)

Istituto di Fisica del Plasma, EURATOM-ENEA-CNR Association, Milano, Italy
(*) Institute of Applied Physics, Soviet Academy of Sciences, Gorky, USSR

I. Introduction

In the field of plasma physics different experimental situations evidence the onset of periodical (or quasi-periodical) density structures which should be consistently taken into account when the dispersive characteristics of the medium are investigated /1/. These conditions can occur in studying, for example, the interaction of high power electromagnetic waves (EMW) or relativistic electron beams with a plasma and the consequent onset and saturation of the excited modulation instability; the excitation of ion acoustic coherent fluctuations induced by the flow of strong currents /2/ or in the process of Brillouin back-scattering of high power radiation /3/. It can also be the case of the creation of plasma slabs through the interference of two high power microwave beams in the laboratory simulation of upper atmosphere plasmas /4,5/. Therefore the analysis of the propagation of EMW's (or longitudinal oscillations) becomes of great interest either for the understanding of the new status of the medium, or for diagnostic purposes.

In Ref.6 a mathematical method has been proposed to compute the reflection coefficient of a non-uniform medium.

Here we shall compare the frequency spectra of the transmitted EM radiation for different density profiles of the modulation, showing that although in principle the stop bands/7,8/ are defined by the relation $\lambda/L_n = 2/\ell$ ($\ell = 1,2,\ldots$), the shape of the single layer strongly determines the effective opacity of the different harmonics (corresponding to different ℓ values). L_n is the typical scale of the density modulation. Furthermore, we shall extend the method discussed in Ref.6 to quasi-periodical density structures and briefly discuss the effect of a density modulation on the propagation of waves close to the density cut-off.

II. Calculation of the transmission coefficient for uniform density modulations

In the following we shall study physical situations in which an EMW of frequency $f = \omega/2\pi$, propagating in the z direction in the non-uniform medium, can be described by the scalar equation

$$\frac{d^2E(z)}{dz^2} + k^2(z)E(z) = 0, \qquad (II.1)$$

with the boundary conditions $E(z_0) = E_0$ and $E'(z_0) = E'_0$, $k^2(z) \equiv \frac{\omega^2}{c^2}\left[1 - \frac{n_e(z)}{n_{cr}}\right]$, and $n_{cr} \equiv \frac{m_e\omega^2}{4\pi e^2} \gg n_e$.

By introducing the new functions

$$\phi_{\pm} \equiv \sqrt{k(z)}\left[E(z) \pm \frac{1}{ik}E'(z)\right], \qquad (II.2)$$

with boundary conditions: $\phi_+(z_0) = \phi_{+,0}$, eq.(II.1) becomes

$$\underline{\Phi}'(z) = \hat{P}(z) \cdot \underline{\Phi}(z). \qquad (II.3)$$

with $\underline{\Phi}(z_0) = \underline{\Phi}_0$, where $\underline{\Phi} \equiv (\phi_+, \phi_-)$, and, in terms of the Pauli matrices,

$$\hat{P}(z) \equiv ik(z)\hat{\sigma}_3 + \frac{k'}{2k}\hat{\sigma}_1. \qquad (II.4)$$

If the propagator $\mathbb{Q}_1(z,z_0)$ is introduced, the solution of eq.(II.3) is given by

$$\underline{\Phi}(z) = \mathbb{Q}_1(z,z_0) \cdot \underline{\Phi}(z_0) \ , \quad \mathbb{Q}_1(z,z_0) = \mathrm{T}\exp\left[\int_{z_0}^{z} \hat{P}(z')\ dz'\right] \qquad (II.5)$$

where the *"time ordering" operator* $\mathrm{T}\exp[\,\cdot\,]$ has been introduced/9-11/.

The explicit evaluation of eq.(II.5) can be performed by means of the *Magnus approximation,* i.e. through an expansion in multiple commutators:

$$\mathbb{Q}_1(z,z_0) = \exp\left[\int_{z_0}^{z} dz_1\ \hat{P}(z_1) + \frac{1}{2}\int_{z_0}^{z} dz_1 \int_{z_0}^{z_1} dz_2 [\hat{P}(z_1), \hat{P}(z_2)] + \cdots\right]. \qquad (II.6)$$

The truncation of this expansion at an arbitrary order does not violate the quasi-unitarity of $\mathbb{Q}_1$, i.e. the conservation of the flux of EMW energy is correctly described. The knowledge of the matrix elements Q_{ij} for a space interval $(0, w)$, with $0 < w$, allows one to compute the transmission and reflection coefficients relevant to that z-range $T_1 = |Q_{22}|^{-2}$, $R_1 = |Q_{21}/Q_{22}|^2$, where $R_1 + T_1 = 1$ due to quasiunitarity ($Q_{11} = Q_{22}^*$, $Q_{12} = Q_{21}^*$).

Moreover, if an EMW propagates across a multilayer plasma made up of N identical slabs, each of width w, the global propagator $\mathbb{Q}_N(Nw,0)$ can be expressed in terms of the propagator $\mathbb{Q}_1(w,0)$ relevant to the single plasma layer:

$$\mathbb{Q}_N(Nw,0) = [\mathbb{Q}_1(w,0)]^N. \qquad (II.7)$$

where use has been made of the periodicity of $k(z)$ in $(0, Nw)$.

To proceed with the relevant computations, it is convenient to consider a single plasma layer as characterized by a uniform background density n_0 and a superimposed small density perturbation δn. By introducing dimensionless variables:

$$2x = k_3 z \ , \quad h = 4\frac{k_0^2 - k_1^2}{k_3^2} \ , \quad \theta = 2\frac{k_2^2}{k_3^2} \ ,$$

being $\lambda_3 = \dfrac{2\pi}{k_3}$ the spatial width of the single plasma layer, $k_0 = \dfrac{\omega}{c}$, $k_0^2 - k_1^2 = \dfrac{\omega^2}{c^2}\left(1 - \dfrac{\omega_{p0}^2}{\omega^2}\right)$ the square of the wavevector relevant to the propagation in the uniform plasma, and $k_2^2 = k_0^2 \dfrac{\delta\omega_p^2}{\omega^2}$, we obtain

$$k^2(x) = h - 2\theta f(x) \qquad -\frac{\pi}{2} < x < +\frac{\pi}{2} \qquad (II.8)$$

where k is dimensionless too, and $f(x)$ contains the explicit dependence of the perturbation on the spatial coordinate z. If the density perturbation is sufficiently small, $\theta \ll 1$, in eq.(II.4) it is possible to single out the smallness parameter $k'(x)/2k(x) = -(\theta/2)(f'(x)/k^2(x))$. By using the properties of $\mathbb{Q}_1$ /6/, and retaining terms up to $O(\theta)$, we obtain:

$$\mathbb{Q}_1\left(\frac{\pi}{2}, -\frac{\pi}{2}\right) \simeq \exp(i\mathscr{I}_0\hat{\sigma}_3) \cdot \exp(\mathscr{I}_1\hat{\sigma}_1 + \mathscr{I}_2\hat{\sigma}_2), \qquad (II.9)$$

where

$$\mathscr{I}_0 = \int_{-\frac{\pi}{2}}^{\frac{\pi}{2}} k(x)\,dx = \mathscr{I}_0^{(0)} + \theta\mathscr{I}_0^{(1)} + \quad , \tag{II.10}$$

$$\mathscr{I}_{\frac{1}{2}} = \int_{-\frac{\pi}{2}}^{\frac{\pi}{2}} \frac{k'(x)}{2k(x)} \begin{bmatrix} \cos 2\Psi(x) \\ \sin 2\Psi(x) \end{bmatrix} dx = \theta\mathscr{I}_{\frac{1}{2}}^{(1)} + \quad , \quad \Psi(x) \equiv \int_{-\frac{\pi}{2}}^{x} dx'\, k(x') .$$

Once the functions $\mathscr{I}_m$ in eq.(II.10) are known to the required degree of accuracy (as we shall see, for actual situations terms of $O(\theta)$ give a satisfactory description of the wave propagation), standard formulas of matrix algebra allow to compute the components of the propagator ($\mathscr{I}^2 = \mathscr{I}_1^2 + \mathscr{I}_2^2$):

$$Q_{11} = \cosh \mathscr{I}\, e^{i\mathscr{I}_0} = Q_{22}^* \ , \quad Q_{12} = \frac{\mathscr{I}_1 - i\mathscr{I}_2}{\mathscr{I}} \sinh \mathscr{I}\, e^{i\mathscr{I}_0} = Q_{21}^* . \tag{II.11}$$

The computation of the matrix elements for the propagator relevant to a modulated density plasma, made up of N identical layers, can be easily performed by introducing the following notation:

$$\mathbb{Q}\left(\frac{\pi}{2}, -\frac{\pi}{2}\right) \equiv \exp(p\,\hat{\underline{\sigma}}) , \tag{II.12}$$

where $p\,\hat{\underline{\sigma}} \equiv p_1\hat{\sigma}_1 + p_2\hat{\sigma}_2 + p_3\hat{\sigma}_3$. The vector p can be determined by equating the explicit form of eq.(II.12), to eqs.(II.11). In particular we obtain

$$\cosh p = \cosh \mathscr{I} \cos \mathscr{I}_0 , \tag{II.13}$$

where $p^2 = p_1^2 + p_2^2 + p_3^2$, which represents the dispersion relation of the EMW propagating in the non-uniform plasma layer, p being a function of the density perturbation amplitude θ . A non-vanishing real part of p corresponds to the evanescent region due to the "resonant interaction" between the wavelength and the typical scale of the density inhomogeneity.

Eq.(II.7) allows one to find immediately the matrix elements of the N-layer medium: $[\mathbb{Q}_1(\pi, 0)]^N = \exp(N\,p\,\hat{\underline{\sigma}})$, i.e.

$$\begin{aligned} [\mathbb{Q}(\pi,0)]_{11}^N &= \cosh(Np) + \frac{p_3}{p}\sinh(Np) = [\mathbb{Q}(\pi,0)]_{22}^{N\,*} \\ [\mathbb{Q}(\pi,0)]_{12}^N &= \frac{p_1 - ip_2}{p}\sinh(Np) = [\mathbb{Q}(\pi,0)]_{21}^{N\,*}, \end{aligned} \tag{II.14}$$

and therefore, the expression of the transmission coefficient

$$T_N = \left[1 + (p_1^2 + p_2^2)\,\sinh^2(Np)/p^2\right]^{-1} . \tag{II.15}$$

III. Transmission spectra

In this Section we shall consider two representative functions $f(x)$: a sinusoidal /6/ and a Gaussian density perturbation.

a) Sinusoidal profile: by putting $f(x) = \cos(2x)$ we find approximately:

$$\mathscr{I}_0^{(0)} = \sqrt{h}\,\pi \ , \quad \mathscr{I}_0^{(1)} = 0 ,$$

$$\mathscr{I}_{\frac{1}{2}}^{(1)} = \frac{\pi}{2h}\begin{bmatrix} -\sin(\sqrt{h}\,\pi) \\ \cos(\sqrt{h}\,\pi) \end{bmatrix} \times \left[\Phi\left[(1-\sqrt{h})\pi\right] - \Phi\left[(1+\sqrt{h})\pi\right]\right],$$

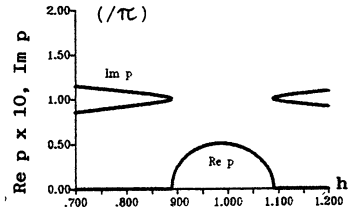

Fig. 1

Fig.1 - Real and imaginary parts of p, (divided by π), as given by eq.(II.14), versus h, for $\theta = 0.1$ in the case of a sinusoidal density perturbation.

Fig.2 - Transmission coefficient T_N as a function of the injected frequency f, for a Gaussian density perturbation profile. The plasma parameters are $n_0 = 10^{12}\ cm^{-3}$, $\lambda_3 = 1.5\ cm$, $\frac{\delta n}{n} = 0.2$, $N = 100$. a) and b) refer respectively to "broad" ($\Delta = 0.4\ cm$) and "narrow" ($\Delta = 0.1\ cm$) perturbation profiles.

Fig. 2

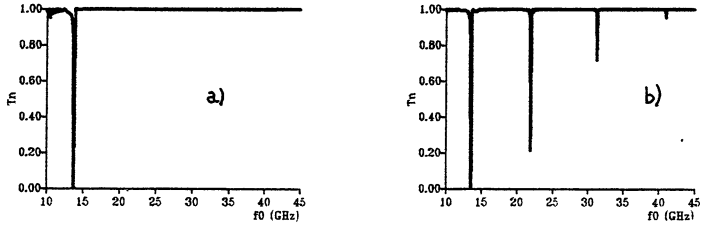

where $\Phi(\alpha) = \frac{\sin\alpha}{\alpha}$. Eq.(II.13) allows one to compute the complex quantity p whose real and imaginary parts are plotted in Fig.1 around the "first resonance", i.e. for $\ell \simeq 1$. It turns out that the "frequency gap" where $Im\ p = 0$ is of negligible extension for harmonics higher than the first so that the frequency spectrum for a sinusoidal modulation is qualitatively very similar to that shown in Fig.2a, relevant to a "broad" Gaussian profile.

b) Gaussian profile: if $f(x) = e^{-\frac{x^2}{\lambda^2}}$, in the limit $\lambda \equiv \frac{\sqrt{2}\,\pi\Delta}{\lambda_3} \ll \frac{\pi}{2}$, we find

$$\mathcal{J}_0^{(0)} \simeq \pi\sqrt{h}\ ,\ \mathcal{J}_0^{(1)} \simeq \lambda\sqrt{\frac{\pi}{h}}\ ,\ \mathcal{J}_2^{(1)} \simeq \lambda\sqrt{\frac{\pi}{h}}\left[\begin{matrix}-\sin(\sqrt{h}\,\pi)\\ +\cos(\sqrt{h}\,\pi)\end{matrix}\right] e^{-h\lambda^2}.$$

The computation of T_N according to eq.(II.15) gives the spectra reported in Figs.2. Here it is shown that if the density profile inside a single layer is "broad" ($\lambda \simeq 1$) an appreciable reflection occurs only at the lowest "resonance", corresponding to $\ell = 1$. On the contrary, when sharp gradients are present, i.e. $\lambda \ll 1$, the harmonic content of the perturbation gives rise to the harmonic structure in the spectrum also at $\ell > 1$, at frequencies

$$f_\ell = \sqrt{f_{pe}^2 + \frac{\ell^2 c^2}{4\lambda_3^2}}\ . \qquad (III.1)$$

IV. Propagation through a slightly non-uniform plasma

If the periodical structure is slightly non-uniform it is still possible to apply the previously described method in an approximated form. Let us assume that $f(x) = e^{-\alpha x}\,\phi(x)$, where

$$\frac{d\ln\phi}{dx} \gg |\alpha|\ , \qquad (IV.1)$$

and $\phi(x)$ determines the basic shape of the density perturbation. When the inequality (IV.1) is satisfied we can neglect the exponential variation inside the single layer and

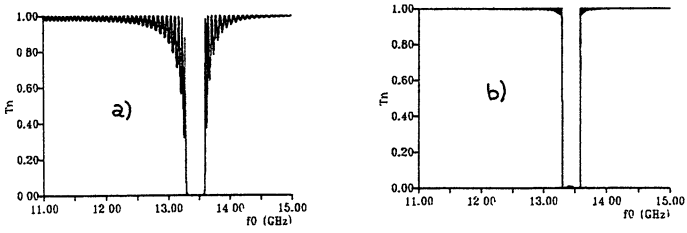

Fig.3 - T_N vs f, for a slightly non uniform sinusoidal modulation. The physical parameters are as in Fig.2; a) and b) refer to $\alpha = 0$ and to $\alpha = 0.05$.

consider only the difference in perturbation amplitude between adjacent layers. Therefore we obtain an ordered product of N propagators

$$\mathbb{Q}(N\pi, 0) = \mathbb{Q}_1[N\pi,(N-1)\pi] \bullet \cdots \bullet \mathbb{Q}(\pi, 0) = = e^{\underline{p}^{(N)}\hat{\underline{\sigma}}} \bullet \cdots \bullet e^{\underline{p}^{(1)}\hat{\underline{\sigma}}}. \qquad (IV.2)$$

By using the Baker-Hausdorff theorem/10/, at the lowest order in the expansion, we obtain:

$$\mathbb{Q}_N(N\pi, 0) \simeq \exp\left[\left(\underline{P}^{(N)}\,\hat{\underline{\sigma}}\right)\right] = \exp\left[P_1^{(N)}\sigma_1 + P_2^{(N)}\sigma_2 + P_3^{(N)}\sigma_3\right], \qquad (IV.3)$$

where $P_i^{(N)} \equiv \sum^{N} p_i^{(j)}$, $i = 1, 2, 3$ and $\underline{P}^{(N)} \equiv (P_1^{(N)}, P_2^{(N)}, P_3^{(N)})$. As it is shown in Figs.3, the main effect of the slow inhomogeneity of the perturbation consists in the suppression of the microstructure otherwise present at the "wings" of the line.

V. Effects of plasma modulation on the linear density cut-off

As it is known, when the refractive index of a wave tends to zero, $\lambda \to \infty$ and the geometrical optics approximation fails. The concept of "linear cut-off" therefore loses its validity for a sufficiently low $\frac{ck}{\omega}$ value. This problem becomes of particular concern when the plasma presents a density modulation, i.e. a small scale structure whose typical spatial length is comparable with the wavelength of the propagating radiation. In Figs.4 the frequency spectra above the linear cut-off are shown for two different situations: *a)* $\lambda_3 = 2\ cm$, $\Delta = 1\ cm$, $N = 10$ and *b)* $\lambda_3 = 1\ cm$, $\Delta = 0.5\ cm$, $N = 20$; in both cases $n_0 = 3 \times 10^{13}\ cm^{-3}$, $\frac{\delta n}{n} = 10\ \%$ and $L = N \times \lambda_3 = 20\ cm$. For the given values, the linear density cut-off corresponding to the peak density occurs at $f_{co} = 51.6\ GHz$. Moreover Figs.4 refer to a rectangular step-like density modulation for which the propagator (II.5) can be computed exactly /6/ in a form valid also close to the linear turning point. We can see from these pictures that non-negligible values of R_N can be found above f_{co} in a spectral range whose width is of several GHz.

VI. Summary

We have studied the problem of the transmission of an EMW across a transparent plasma, characterized by a modulated density profile in the direction of wave propagation. In general, a *resonant interaction* between the wavelength of the EM radiation and the spatial periodicity of the medium gives rise to an enhanced opacity at the frequencies given by eq.(III.1). For a sinusoidal modulation, the "harmonics" higher than the first do not modify the transmitted spectrum, while strong reflection can occur at $\ell = 1$. However, if sharp density gradients are present, appreciable reflection can be found for values of ℓ higher than 1. Within the same mathematical method it is possible to treat approximately the propagation of EMWs through slightly inhomogeneous modulated media; in this case, an increased monochromaticity of the reflected radiation is observed.

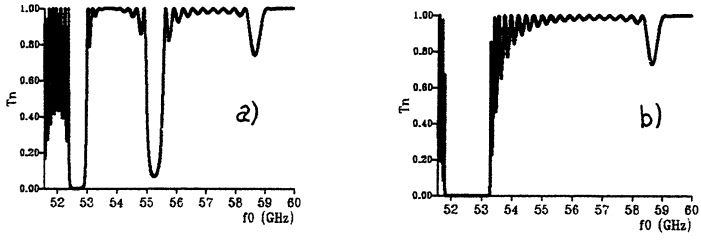

Fig.4 - T_N vs f, above the linear density cutoff, for step-like perturbations. The parameters are as follows: a) $\lambda_3 = 2\ cm$, $\Delta = 1\ cm$, $N = 10$, and b) $\lambda_3 = 1\ cm$, $\Delta = 0.5\ mm$, $N = 20$; $n_0 = 3 \times 10^{13}\ cm^{-3}$, $\frac{\delta n}{n} = 0.1$, and $L = N \times \lambda_3 = 20\ cm$ in both cases. The origin of the x-axis coincides with the position of the linear cut-off relevant to the peak density values.

Finally, the presence of a density modulation makes the frequency corresponding to the linear density cut-off somewhat undetermined by a factor $5 \div 10$ % above the value expected by the linear theory.

Acknowledgements

This work has been performed in the framework of the scientific cooperation agreement between the Soviet Academy of Sciences and the Italian National Research Council (CNR). M.L. acknowledges a useful discussion with U. Gasparino on the experimental uncertainty in the determination of the density cut-off.

References

/1/ - P. Mulser, Proc. I. S. P. P. on *Inertial Confinement Fusion,* ed. by A. Caruso, E. Sindoni, Ed. Compositori, Bologna, 1988, p. 33.

/2/ - P.K. Kaw, A.T. Lin, J.M. Dawson, Phys. Fl., **16**, 1967 (1973).

/3/ - V.P. Denisov, et al., Fizika Plazmy, **16**, 296 (1990).

/4/ - A.L. Vikharev, et al., Sov. Jour. Plasma Phys., **10**, 96 (1984).

/5/ - S.P. Kuo, Y S. Zhang, Phys. Fl. B, **2**, 667 (1990).

/6/ - M. Lontano, N. Lunin, *Propagation of Electromagnetic Waves in a Modulated Density Plasma,* Istituto di Fisica del Plasma, Euratom-ENEA-CNR Association, Internal Report, FP 89/26 (1989); also M. Lontano, N. Lunin, Proc. 17th EPS Conf. on *Contr. Fus. and Plasma Heat.,* (Amsterdam, 1990), ed. by G. Briffod, Adri Nijsen-Vis, F.C. Schueller, vol. 14B, Part IV, p. 1762

/7/ - H. Figueroa, C. Joshi, *Laser Interaction and Related Plasma Phenomena,* vol.7, ed. by H. Hora, G.H. Miley, Plenum Press, New York (1985), p. 241.

/8/ - L. Brillouin and M. Parodi, *Propagation des Ondes dans les Milieux Periodiques,* Masson et Cie Editeurs, Paris, 1956.

/9/ - W Magnus, Comm. in Pure and Appl. Math., **7**, 649 (1954).

/10/ - P. Pechukas, J.C. Light, Journ. Chem. Phys., **44**, 3897 (1966).

/11/ - K F. Milfeld, R.E. Wyatt, Physical Rev. A, **27**, 72 (1983).

ELECTROMAGNETIC FIELD CYCLOTRON ABSORPTION IN A TURBULENT PLASMA

Silin V P., Uryupin S.A.

P N.Lebedev Physical Institute of the Academy of Sciences of the USSR, Leninsky prospect 53, Moscow, 117924, USSR

Cyclotron resonance, at which electromagnetic field frequency ω coincides with the electron Larmor frequency Ω, is used widely for the effective electron heating in the plasma (see, for example, [1]) At such process the absorption power and the line form of the cyclotron resonance depend on the effective electron scattering frequency For example, in an equilibrium fully ionized plasma the cyclotron absorption regularities are determined by the electron–ion collisions Another situation take place in a nonequilibrium nonisothermal plasma of the strong–current discharge along the magnetic field, when the electron scattering is determined by the ion–acoustic turbulence (IAT) Because of the anisotropy of the IAT spectrum the corresponding effective collision frequency is essentially anisotropic and in many times exceeds the electron–ion collision frequency (see, for example, [2,3]). The qualitative change of the electron scattering regularities leads to the new cyclotron absorption regularities in the plasma with IAT The corresponding cyclotron absorption theory is developed in the present report

In order to extract the absorption peculiarities due to alteration of the electron collision frequency we examine the simple situation typical for current–carrying discharge Namely, we suppose constant electric field $\mathbf{E}_o = (0,0,E_o)$, which give rise to the current and IAT, is directed along the plasma confine constant magnetic field $\mathbf{B} = (0,0,B)$ We belive, that homogeneous high–frequency electric field is polarized in the plane orthogonal to the current $\mathbf{E}(t) = E(\cos\omega t,\sin\omega t,0)$ In such fields for the electron

distribution function $f = f(v,\theta,\varphi,t)$ the kinetic equation, which takes into account electron scattering by ion–acoustic waves, has the form

$$\frac{\partial f}{\partial t} + \frac{e}{m_e} E_o (\cos\theta \frac{\partial f}{\partial v} - \frac{\sin\theta}{v} \frac{\partial f}{\partial \theta}) + \Omega \frac{\partial f}{\partial \varphi} +$$

$$+ \frac{e}{m_e} E\{\cos(\omega t-\varphi)[\sin\theta \frac{\partial f}{\partial v} + \frac{\cos\theta}{v} \frac{\partial f}{\partial \theta}] + \frac{\sin(\omega t-\varphi)}{v \sin\theta} \frac{\partial f}{\partial \varphi}\} =$$

$$= \frac{D_{\varphi\varphi}}{v^2 \sin^2\theta} \frac{\partial^2 f}{\partial \varphi^2} + \frac{1}{v^2 \sin\theta} \frac{\partial}{\partial \theta}[\sin\theta(D_{\theta\theta} \frac{\partial f}{\partial \theta} - vD_{v\theta} \frac{\partial f}{\partial v})] +$$

$$+ \frac{1}{v^2} \frac{\partial}{\partial v}[v^2 D_{vv} \frac{\partial f}{\partial v} - vD_{v\theta} \frac{\partial f}{\partial \theta}]. \qquad (1)$$

Here e and m_e are the electron charge and mass, v,θ,φ are the wave–vector coordinates; $\Omega = |e|B/m_eC > 0$; C is the light velocity, $D_{\alpha\beta}$ is the axially symmetrical tensor of quasi–linear diffusion. Following to the works [2,3], we write the tensor $D_{\alpha\beta}$ in the explicit form

$$D_{\varphi\varphi} = \nu \frac{v_t^3}{v} Y(\sin\theta), \quad D_{\theta\theta} = \nu \frac{v_t^3}{v} X_2(\sin\theta),$$

$$D_{v\theta} = \nu \frac{v_t^3 v_s}{v^2} X_1(\sin\theta), \quad D_{vv} = \nu \frac{v_t^3 v_s^2}{v^3} X_o(\sin\theta), \qquad (2)$$

where v_t is the thermal electron velocity, $v_s = \omega_{Li} r_{De}$ is the sound velocity, $\omega_{Le(i)}$ and $r_{De(i)}$ are the electrons(ions) Langmuir frequency and Debye radius. In the formula (2) the frequency ν depends on the ratio of the Knudsen turbulent number $K_N = 6\pi e E_o r_{Di}^2/m_e v_s \omega_{Li} r_{De}^2$ and the parameter $(1+\delta)^2$, where $\delta = \gamma_i/\gamma_e$ is the ratio of the

sound Cherenkov absorption rate on the ions γ_i to the one on the electrons γ_e The frequency ν is equal to

$$\nu = \frac{3}{4}\sqrt{2\pi}\,\frac{eE_o}{m_e v_s}\,\frac{1}{\max\left[\sqrt{K_N}\,,\,(1+\delta)\right]} \qquad (3)$$

The functions $Y(y)$ and $X_n(y)$ $(n = 0,1,2)$, which describe the anisotropy of the tensor $D_{\alpha\beta}$, are determined by the function $\phi(x)$

$$Y(y) = \int_0^y dx\,\phi(x)\,\sqrt{y^2 - x^2}/y^2,$$
$$X_n(y) = \int_0^y \frac{dx\;\phi(x)}{\sqrt{y^2 - x^2}}\,(x/y)^n \qquad (4)$$

In it's turn the function $\phi(x)$ describe the IAT distribution over the wave vector angles. The explicit form of the function $\phi(x)$, which depends on the ratio of the K_N and $(1+\delta)^2$, one can find in the works [2,3].

Let us now determine the rate of dissipation of high–frequency electromagnetic field W. With this aim we shall introduce the average over the azimuthal angle φ small functions

$$\delta f_c(v,\theta,t) = \int_0^{2\pi} d\varphi\,\cos(\omega t - \varphi)\;\delta f(v,\theta,\varphi,t),$$
$$\delta f_s(v,\theta,t) = \int_0^{2\pi} d\varphi\,\sin(\omega t - \varphi)\;\delta f(v,\theta,\varphi,t), \qquad (5)$$

where $\delta f(v,\theta,\varphi,t)$ is linear on the high–frequency field E small addend to the Maxwellian function f_m In the definition the absorbed in a plasma power is expressed through the function δf_c

$$W = eE \int_0^{\infty} dv\, v^3 \int_0^{\pi} d\theta \sin^2\theta\, \delta f_c(v,\theta,t). \qquad (6)$$

Linearizing on the field E and averaging on the angle φ the equation (1) we get the equations for functions δf_c and δf_s At the times exceeding the inverse effective collision frequency ($\nu t >> 1$) we find

$$(\omega - \Omega)\delta f_s - \pi \frac{eEv}{m_e v_t^2} \sin\theta f_m =$$

$$= -\nu \frac{v_t^3}{v^3} \{ \frac{Y(\sin\theta)}{\sin^2\theta} - \frac{1}{\sin\theta} \frac{\partial}{\partial\theta} [X_2(\sin\theta)\sin\theta \frac{\partial}{\partial\theta}] \} \delta f_c, \qquad (7)$$

$$(\omega - \Omega)\delta f_c =$$

$$= \nu \frac{v_t^3}{v^3} \{ \frac{Y(\sin\theta)}{\sin^2\theta} - \frac{1}{\sin\theta} \frac{\partial}{\partial\theta} [X_2(\sin\theta)\sin\theta \frac{\partial}{\partial\theta}] \} \delta f_s \qquad (8)$$

In deriving the eq.'s (7) and (8) we took into account the smallness of the components $D_{v\theta}$ and D_{vv} (2).

Using eq.'s (7) and (8) we find the power W (6). At first let us consider nonresonance frequency region $|\omega - \Omega| >> \nu$. Taking into account smallness of the ratio $\nu/|\omega - \Omega|$, from eq's (7) and (8) we have

$$\delta f_c = \pi(eEv_t/m_e v^2)[\nu/(\omega - \Omega)^2] \times$$

$$\times \frac{f_m}{\sin\theta} \{ Y(\sin\theta) + \frac{\partial}{\partial\theta} [X_2(\sin\theta)\sin\theta\cos\theta] \}. \qquad (9)$$

Expression (9) permits one write down the power W in the form

$$W = \frac{e^2 E^2}{m_e (\omega - \Omega)^2} n_e \nu_{\perp}. \qquad (10)$$

Here $\nu_\perp$ is the collision frequency, which describe anomalous transport across the magnetic field. According to the work [4] the frequency $\nu_\perp$ is equal:

$$\nu_\perp = \{\sqrt{2}\,\nu \ln[(1+\delta)^2/K_N]\}/3\sqrt{\pi}\ln 2 \quad \text{at} \quad K_N << (1+\delta)^2;$$

$$\text{and} \quad \nu_\perp = 0.23\sqrt{2\pi}\,\nu \quad \text{at} \quad K_N >> (1+\delta)^2$$

Note, that in the zero magnetic field limit the expression (10) turn in the one established in the theory of bremsstrahlung absorption of radiation in a plasma with IAT [5,6]

Now we discuss the absorption in the resonance frequency region, when $|\omega - \Omega| << \nu$. In this case from eq.(7) we have

$$\delta f_c = \pi \frac{eE}{m_e v_t \nu} \frac{v^4}{v_t^4} f_m Z(\theta), \tag{11}$$

Here the function $Z(\theta)$ satisfies to the equation investigated earlier in the theory of anomalous transport across the direction of IAT anisotropy (see revue paper [2]) Formula (11) permits one to calculate the power W (6) The absorption rate at cyclotron resonance is described by the expression

$$W = \frac{e^2 E^2}{m_e \nu} n_e \frac{1}{\sqrt{\pi}} 2\sqrt{2}\,\beta_\perp, \tag{12}$$

Here the parameter $\beta_\perp = -\int_0^\pi d\theta \sin^2\theta\, Z(\theta)$ was established in the IAT theory earlier (see [2]): $\beta_\perp = 0.02$ at $K_N << (1+\delta)^2$, $\beta_\perp = 0.67$ at $K_N >> (1+\delta)^2$.

As one can see from the expressions (10) and (12), the increasing of electrons collision frequency in a plasma with IAT leads to the strong spreading of resonance absorption region and to the decreasing of absorption rate at $\omega = \Omega$. So far

as turbulent collision frequency ν (3) depends on the field strength E_o, then changing E_o one can alter the shape of absorption curve and achieve the optimal conditions of electrons heating The expressions (10) and (12) describes the absorption due to electrons scattering on the density fluctuations with the wavelength $1/r_{De}$ Therefore expressions (10) and (12) are applicable at the frequencies ω smaller than electrons Langmuir frequency ω_{Le} In connection with this the expressions (10) and (12) concerns to the case of normal skin–effect

References

1 Bornatici M , Cano R., Barbieri O , Engelmann F. Nuclear Fusion **23** ,No 9, 1153, 1983

2 Bychenkov V Yu , Silin V P., Uryupin S A Phys Reports, **164**, No 3, 119, 1988

3 Bychenkov V Yu , Silin V P , Uryupin S A Comment's on Plasma Phys and Contr Fus , XIII, No 5, 239, 1990

4 Silin V.P., Uryupin S A Physica Scripta, 1990 (in press), Preprint FIAN, No 141, 33p, 1989

5 Silin V P Sov Phys –Lebedev Inst Report, No 5, 59, 1983

6. Silin V P ; Uryupin S.A Zh Eksp and Teor Fiz , **98**, No 1(7), 117, 1990

ON THE TRANSFORMATION OF THE ENERGY ANISOTROPY OF ELECTRONS INTO THE ELECTROMAGNETIC ENERGY OF PULSATIONS

V Yu.Bychenkov, V.N Novikov, V.P.Silin, V.T Tikhonchuk
P N Lebedev Physics Institute, Academy of Sciences of the USSR,
Leninsky av 53, Moscow, 117924, USSR

A plasma with an anisotropic energy distribution of electrons can be unstable under the excitation of quasistatic magnetic fields [1].Up to now a few papers only have been devoted to the investigation of the relaxation of an anisotropic electron plasma There are numerical particles in cell simulations [2,3] and analytical modeling [4,5] Our study of the collisionless relaxation of the anisotropic electron plasma is based on the numerical integration of the Vlasov equation along particles trajectories and the solution of the electromagnetic equations in the framework of the model of the vortex electron anisotropic hydrodynamics(VEAH) which was proposed in Ref.[4,5].

In this paper we present the results of 1 5 dimensional (one spatial dimension and two velocity dimensions) modeling of the Weibel instability based on the following system of equations

$$\frac{\partial f}{\partial t} + v_x\frac{\partial f}{\partial x} = (E_x - v_z B_y)\frac{\partial f}{\partial v_x} + (E_z + v_x B_y)\frac{\partial f}{\partial v_z} = 0, \qquad (1)$$

$$\frac{\partial B_y}{\partial x} = u_z, \quad E_x = \frac{\partial}{\partial x}(P_{xx} + \frac{B_y^2}{2}), \quad \frac{\partial^2 E_z}{\partial x^2} - E_z = -\frac{\partial P_{xz}}{\partial x} \qquad (2)$$

where $f(v_x,v_z,x,t)$ is the electron distribution function, $B_y(x,t)$ and $E_x(x,t)$, $E_z(x,t)$ are the magnetic and electric fields, u_z – the average electron velocity and P_{ij} – the components of the stress tensor are the moments of the distribution function.

The system of equations (1) and (2) has been solved with the periodic boundary conditions. An initial distribution function was taken to be the bi–Maxwellian one with the temperature T_z along z axis and the temperature T_x along x axis We introduced dimensionless variables using the following scaling factors. the time – $(c/v_{tz}\omega_p)$, the coordinate – c/ω_p, the velocity – v_{tz}, the magnetic field – $(m/e)v_{tz}\omega_p$, the electric field – $(mv_{tz}^2/ec)\omega_p$, the stress tensor – mnv_{tz}^2

The main attention has been devoted to the nonlinear evolution of long–wave–length perturbations ($k << 1$), because in this case the analytical results on the large–scale electron vortex motion were obtained recently [4,5] and comparison to numerical solutions has been possible. An initial magnetic field was assumed as a small amplitude

periodic disturbance $B_0 \cos k_0 x$ where $B_0 = 0\,01$, $k_0 = 0\,3$ in dimensionless units and periodicity length $L = 20\,94$ an initial temperature anisotropy was $T_z/T_x = 25$

The initial stage of evolution corresponds to the exponential growth of the magnetic field in accordance with the linear theory of the Weibel instability Later the appearance of the nonlinear effects was manifested in the generation of third and fifth harmonics When the fifth harmonics appeared the amplitude the magnetic field approached the saturation The temporal evolution of the magnetic field energy is depicted in Fig 1 The energy of the electric field was much smaller The saturated energy of the magnetic field was about 3% of the anisotropic part of the thermal energy

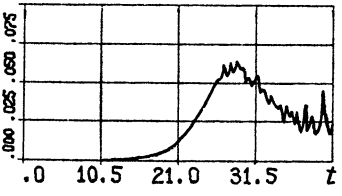

Fig. 1

The spatial spectra of the magnetic field for three time moments $t = 20$, 24, 30 for the same run as in Fig 1 are depicted in Fig 2.The numbers of spatial harmonics are shown on the abscissa axis

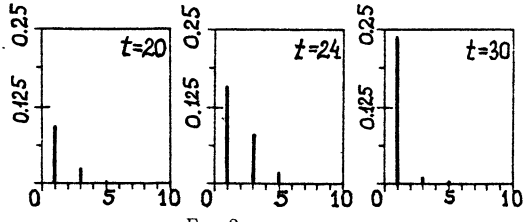

Fig 2

After the magnetic energy saturation the inhibition of the amplitudes of higher harmonics was observed and to the time moment $t = 30$ the first harmonic only was in the spectrum of the magnetic field This effect can be explained as a strong collisionless damping of the short–wave–length spectral components of the electromagnetic pulsations

For the time interval $t < 20$ no considerable changes in the distribution function has been observed The shape of the electron distribution function was approximately the same as an initial one but in every spatial point it was rotated on different angles around the anisotropy axis This local rotation of the distribution functions is due to the rotation of electrons in self–generated magnetic field and corresponds well to the theoretical predictions [4,5] For the $t > 20$ the stage of rotation followed by the stage of the partial

isotropization of the electron distribution function. This is manifested in decreasing of the longitudinal pressure P_{zz} and in increasing of the transversal pressure P_{xx} and the mixed pressure P_{xz} As the example in Fig 3 one can see the snapshots of the electron distribution function for the same run as shown in Fig 1 at point x = L/4 for t = 25 For the comparison the initial distribution (t = 0) is also presented in Fig 3

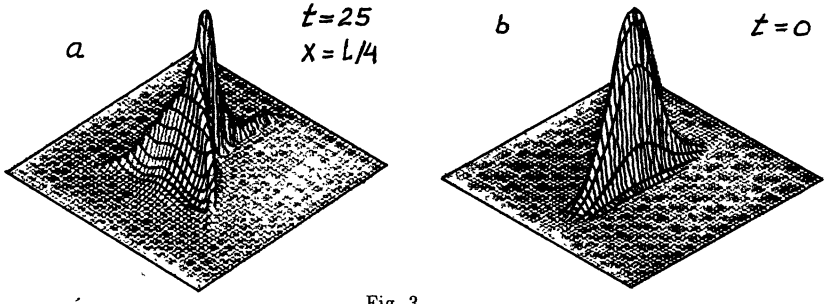

Fig 3

The increasing in the principal wavenumber leads to the increasing of the transformation efficiency of the energy anisotropy into the magnetic energy Fig 4 contains the temporal dependence of the magnetic field energy for k_0 = 1 5 The other parameters are the same as for the previous run This wavenumber corresponds approximately to the maximum of the linear growth rate of the Weibel instability The transformation efficiency grows up to 6–7% which is twice more than that in the long–wave–length case of Fig 1 The further increase in k_0 leads to the decreasing in the growth rate of the instability and in the decreasing in the transformation efficiency This is illustrated in Fig 5 where the temporal evolution of the magnetic energy is shown for k_0 = 3 and L = 10 47 Here the transformation efficiency does not reach more than 1.5% only

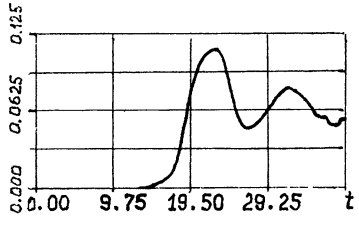

Fig 4

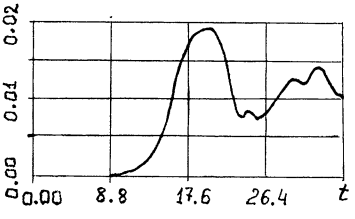

Fig 5

Several runs have been done with a noisy initial magnetic field which is close to the conditions of the numerical modeling in Ref [2,3] The initial magnetic field consisted in ten spatial harmonics with equal amplitudes B_0 = 0 001 and random phases The initial energy of the magnetic pulsations was the same as in previous runs The linear stage of the evolution corresponded to the exponential growth those harmonics which wavenumbers belong to the region of the maximal increment Later the energy transfer to the

long–wave–length side takes place and the instability has been stabilized The quasistationary spectrum of magnetic pulsations is rather broad and slows down to the short–wave–side. This is illustrated in Fig 6 where the spectrum of the magnetic field is given for $T_z/T_x = 25$ and a noisy initial conditions.

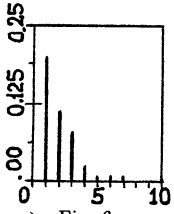

Fig 6

The temporal dependences of the magnetic energy for three different initial values of the temperature anisotropy $T_z/T_x = 2$ (a), 8 (b), 25 (c) are presented in Fig 7 The noisy initial conditions of the magnetic field have been used in these runs. It is obvious that the transformation efficiency does not depend on the initial anisotropy in the case of $T_z/T_x >> 1$.

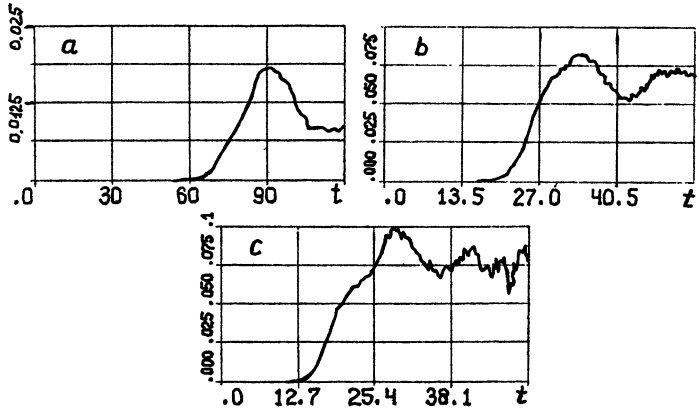

Fig. 7

In conclusion , we studied the efficiency of the transformation of the electron energy anisotropy into the magnetic energy. The transformation coefficient increases with the temperature ratio and saturated for $T_z/T_x >> 1$. The maximum of the transformation achieved when the initial wavenumber belongs to the region of the maximum growth rate. The maximum transformation efficiency never exceeds 10% limit which corresponds well to the results of the particle in cell simulations of Ref [2,3] If the large amount of an energy anisotropy exists in a plasma the Weibel instability can be the mechanism of the production of the high power magnetic pulsations.

References

1. Weibel E.W Phys Rev Lett., **2**, 83, 1959.

2. Morse R.L. and Nielson C.W. Phys. Fluids, **14**, 830, 1971.

3. Davidson R.C., Hammer D A., Haber I. and Wagner C.E Phys Fluids, **15**, 317, 1972.

4. Bychenkov V.Yu., Silin V P. and Tikhonchuk V T Sov. Journ Fizika Plasmy, **15**, 706, 1989: Sov. Journ. Teor Matem Fizik, **82**, 18, 1990.

5. Bychenkov V.Yu., Silin V.P. and Tikhonchuk V.T Proc. Int Workshop on Nonlinear Phenomena in Vlasov Plasmas, Cargese, France, ed. by F Dovel, Editions de Physique, Orsay, p.57, 1989: Phys. Lett. A **138**, 127, 1989.

ON INCREASE OF EFFICIENCY OF PLASMA HEATING BY AN ELECTRON BEAM GENERATING RF WAVES

S.I.Popel & V.N.Tsytovich
Theoretical Department, General Physics Institute,
Vavilova Street 38, Moscow, USSR

The radiative-resonant interactions (RRIs) [1,2] are shown in [2-4] to influence the dynamics of the superthermal electrons of plasma essentially. If a beam instability occurs then in the case of the low density beams the RRIs result in the beam instability development mechanism quite different from the one [5] in which the RRIs were not taken into account (see [6,7]). As it will be shown below this fact allows to increase the efficiency of plasma heating by an electron beam.

Let the electron beam (n_b is the concentration of the beam, v_b is characteristic velocity of the beam electrons and Δv is the spread of electron velocities in the beam, $\Delta v \ll v_b$) be in plasma at the time t=0. It is assumed that $n_b \ll n$, $v_b \gg v_{Te}$ where n is the plasma electron concentration, v_{Te} is the thermal electron velocity of plasma. The condition of kinetic description applicability $\Delta v/v_b \gg (n_b/n)^{1/3}$ is also supposed to be valid. The beam dynamics is described by the system of equations (see [1,2]) in which the quasilinear interactions and the RRIs are taken into account. This system of equations consists of equations defining the dynamics of the electron distribution function and the distribution of the energy of the Langmuir waves excited owing to the beam instability. Under the assumption of the Langmuir waves excitation in the beam propogation direction the system of equations describing the beam dynamics with regard to the terms corresponding to the quasilinear interactions and the RRIs has the following form (see [6,7]; it is also supposed that $v_{Te} \ll v \ll c$ where c is the velocity of light):

$$\frac{\partial F_v}{\partial t} = \frac{4\pi^2 e^2}{m^2} \frac{\partial}{\partial v} \frac{W_v}{v} \left(\frac{\partial F_v}{\partial v} + \frac{\alpha n}{2\pi c^2} \right) + S_v; \qquad (1)$$

$$\frac{\partial W_v}{\partial t} = \frac{4\pi^2 e^2}{m\omega_{pe}} v^2 W_v \left(\frac{\partial F_v}{\partial v}(1 + \frac{8\alpha}{3\pi}(\ln 2 - \frac{11}{24})) + \frac{\alpha n}{2\pi c^2} \right), \qquad (2)$$

where $F_v(t)$ is the one-dimensional electron distribution function which takes into account plasma electrons as well as beam electrons, $n + n_b = \int F_v(t)dv$; $W_v(t)$ is the one-dimensional distribution of the Langmuir waves ($W_v(t) \equiv W_q(t)\big|_{q=\omega_{pe}/v}$, $\int W_q(t)dq = W(t)$ is the wave energy density in plasma at the time t); m, e are the electron mass and charge respectively; $\alpha = e^2/\hbar c \approx 1/137$, $\hbar$ is the Planck's constant; $\omega_{pe} = (4\pi ne^2/m)^{1/2}$; $S_v(t) \sim \alpha * (e/mc)^2 \Delta F_1(t) W_{v_b}(t) v_b^{-1} \mathrm{sign}(v_1(t) - v)$, $v_1(t)$ is the lowest velocity of the beam particles at the time t, $\Delta F_1(t)$ is the jump of the distribution function $F_v(t)$ in the vicinity of $v_1(t)$.

The stationary solution of the system of equations (1)-(2) in the approximation when the term S_v in the Eq.(1) and the term containing $8\alpha(\ln 2 - 11/24)/(3\pi)$ in the Eq.(2) are neglected has the form:

$$F_v = \alpha n(v_o - v)/(2\pi c^2), \qquad (3)$$

where v_o is a constant that may be obtained from the condition of the particle number conservation in the beam velocity region.

Let us consider the case when the condition $n_b/n \gg (\alpha/4\pi) * (v_b/c)^2$ takes place. It is possible to show that in this case the beam instability development process is analogous to the one described in [5] without regard to the RRIs. At the time $t_1 \sim (n/n_b)\ln(1 + W_o/\tilde{W})\omega_{pe}^{-1}$ (where W_o is energy received by waves from the beam particles, $\tilde{W}$ is the wave energy at the time t=0) the lowest velocity of the beam particles $v_1(t)$ diminishes to the magnitude $v_1(t_1) \sim v_{Te}$ and the stationary distribution function (3) with $v_o \approx v_b/2 + 2\pi c^2 n_b/(\alpha n v_b)$ is formed in the velocity region $[v_1(t_1), v_b]$. The beam particles become thermal, i.e. their velocities become of the order of v_{Te}, at the beam electrons free transit time:

$$t_2 \sim (N_D/\omega_{pe})(v_b/v_{Te})^3, \qquad (4)$$

where $N_D \equiv (4\pi/3)n(v_{Te}/\omega_{pe})^3$. Thus in the case considered the value nT_e (where T_e is the electron temperature) increases by the magnitude of the electron beam energy density $E_b \approx mv_b^2 n_b/2$ at

the time $\tau \sim t_2$ (this occurs both if $t_1 \ll t_2$ when the distribution function (3) is formed in the domain $[v_1(t_1), v_b]$ at the time $\sim t_1$ and if $t_1 \gg t_2$ when the state described by (3) does not have enough time to be formed). The plasma heating efficiency in this case has the following form:

$$\eta \equiv E_b/\tau \sim m v_{Te}^3 n_b \omega_{pe}/(N_D v_b)$$

and coincides with that calculated without regard to the RRIs.

Let us consider the case when the following conditions take place: $n_b/n \ll (\alpha/4\pi)(v_b/c)^2$, $v_b \gg v_{Te}\sqrt{2\ln((\sqrt{2\pi}/\alpha)(c/v_{Te}))}$. In this case the number of the beam particles is not sufficient for the stationary distribution function (3) in the velocity domain from $\sim v_{Te}$ to v_b to be formed. So the condition $\Delta F_1(t) > 0$ takes place in this case during all the time of the beam existence (up to the time when the beam particles become thermal). Hence (see the expression for $S_v(t)$ and the Eq.(1)) the particles transfer from the beam (in the case when the condition $n_b/n \gg (\alpha/4\pi)(v_b/c)^2$ takes place the transfer of particles from the beam due to the term $S_v(t)$ in the Eq.(1) occurs only during the time t_1 (after this $\Delta F_1(t)=0$ so $S_v(t)=0$) and the number of particles transferred from the beam due to the term $S_v(t)$ in the Eq.(1) is much smaller than n_b). Most of these particles transfer to the region of velocities of the order of v_{Te}, i.e. the beam particles become thermal. The time of their thermalization is of the order of

$$t_3 \sim (\alpha (v_b/c)^2 (n_b/n)\, \omega_{pe})^{-1}. \qquad (5)$$

The Expression (5) is obtained under the assumption that $t_3 \ll t_2$. Otherwise if $t_3 \gg t_2$ then the beam particles become thermal at the time of the order of t_2. Thus the plasma heating efficiency in this case has the following form:

$$\eta \approx m v_b^2 n_b/(2\min(t_2, t_3)) \sim \\ \sim \max\left\{\alpha\, \omega_{pe} n_b m v_b^2 (v_b/c)^2 (n_b/n),\ m v_{Te}^3 n_b\, \omega_{pe}/(N_D v_b)\right\}. \qquad (6)$$

Consequently (see (6)) if a beam with the concentration $n_b^{(1)} \ll n(\alpha/4\pi)(v_b/c)^2$ and characteristic velocity $v_b \gg v_{Te}(2\ln((\sqrt{2\pi}/\alpha)(c/v_{Te})))^{1/2}$ is injected into plasma then the plasma heating efficiency may be increased as compared with that ob-

tained when a beam with the characteristic velocity v_b and concentration $n_b^{(2)} \gg n(\mathcal{L}/4\pi)(v_b/c)^2$ is injected into plasma. The condition of such an increase is $\mathcal{L}(v_b/c)^2(n_b^{(1)}/n)(n_b^{(1)}/n_b^{(2)})N_D \gg \gg (v_{Te}/v_b)^3$. The ratio of the plasma heating efficiency by the beam with the concentration $n_b^{(1)}$ to the plasma heating efficiency by the beam with the concentration $n_b^{(2)}$ is $\mathcal{L}(v_b/c)^2(v_b/v_{Te})^3 * *(n_b^{(1)}/n)(n_b^{(1)}/n_b^{(2)})N_D$. For example if it is required to increase the value of electron plasma tenperature T_e by the magnitude ΔT using beams with the characteristic velocity v_b, and the conditions $(\mathcal{L}/4\pi)(v_b/c)^2 \ll (2\Delta T/(mv_b^2)) \ll (\mathcal{L}^3/(4\pi)^2)(v_b/c)^6 N_D * *(v_b/v_{Te})^3$ and $v_b \gg v_{Te}(2\ln((\sqrt{2\pi}/\mathcal{L})(c/v_{Te})))^{1/2}$ are supposed to take place, then it is possible to bring about the plasma heating more effectively than by means of one-fold injection of a beam with the concentration $n_b^{(2)} \approx 2\Delta Tn/(mv_b^2)$ into plasma. More effective plasma heating is attained by means of multiple consequent injection of beams of the concentration $n_b^{(1)}$ ($n_b^{(1)} \ll n * *(\mathcal{L}/4\pi)(v_b/c)^2$, $\mathcal{L}(v_b/c)^2(n_b^{(1)}/n)(n_b^{(1)} mv_b^2/(2n\Delta T))N_D \gg (v_{Te}/v_b)^3$) into plasma with the period of the order of t_3.

Thus it is shown that the consideration of the RRIs results in the plasma heating efficiency value which for the beams of the low density ($n_b/n \ll (\mathcal{L}/4\pi)(v_b/c)^2$) differs from that calculated without regard of the RRIs. It is possible to increase the plasma heating efficiency using such beams.

References

1. Tsytovich V.N. Zh. Eksp. Theor. Fiz., 1987, 93, 1680.
2. Tsytovich V.N. Phys. Reports, 1989, 178, 261.
3. Popel S.I., Tsytovich V.N. Fizika plasmy, 1990, 16, 306.
4. Tsytovich V.N., Popel S.I. Comments Plasma Phys. Controlled Fusion, 1989, 12, 171.
5. Ivanov A.A., Rudakov L.I. Zh. Eksp. Theor. Fiz., 1966, 51, 1522.
6. Popel S.I., Tsytovich V.N. Preprint 50, Moscow, FIAN, 1990.
7. Popel S.I., Tsytovich V.N. Kratkie soobshchenija po fizike, 1990, No 4, p.22.

NEW THEORY OF THE "SPECTRAL GAP" FILLING IN THE GENERATION PROCESS OF CURRENTS DRIVEN BY STRONG RF LOWER-HYBRID WAVES

S.I.Popel & V.N.Tsytovich
Theoretical Department, General Physics Institute,
Vavilova Street 38, Moscow, USSR

To describe currents driven by the lower-hybrid (LH-)waves a new approach is proposed, in which the radiative-resonant interactions (RRIs) (see Refs. [1-3]) are taken into account. The main conclusions of the RRIs consideration are: 1) the resonant region (i.e. a region of electron velocities $\vec{v}$ satisfying the condition $\omega_{\vec{q}}=q_{\|} v_{\|}$ where $\omega_{\vec{q}}$ is the frequency of the LH-waves; $v_{\|}$, $q_{\|}$ are the components along the magnetic field of $\vec{v}$ and a wave number $\vec{q}$ respectively) increases and the gap between the lowest phase velocity of waves $\omega_{\vec{q}}/q_{\|}$ and the thermal electron velocity v_{Te} diminishes if one takes into account the RRIs; 2) another radiative interactions namely the radiative-resonant-scattering interactions (RRSIs) on the other hand can provide sufficiently effective generation of the fast particles carrying a driven current; 3) the proposed theoretical scheme permits to obtain the magnitude of a driven current, its growth-time and efficiency of its generation in accordance with observations.

The homogenius plasma in external invariable magnetic field is considered here for simplicity. It is also assumed that $\omega_{He} \gtrsim \gtrsim \omega_{pe} \gg \omega_{\vec{q}} \gtrsim \omega_{pi}$; $\omega_{\vec{q}} \gg \omega_{Hi}$ where ω_{He}, ω_{Hi} are the electron and ion cyclotron frequencies respectively, $\omega_{pe}=(4\pi ne^2/m)^{1/2}$, $\omega_{pi}=\omega_{pe}(Zm/M)^{1/2}$, n is the plasma electron concentration, -e is the electron charge, m is the electron mass, Ze is ion charge, M is ion mass. Let us consider the dynamics of the fast electron distribution function and the movement of the boundaries of the resonant region. If the characteristic time values of the task are much smaller than

$$t_{coll} \sim 1/\nu_e(v_{ph}) = m^2 v_{Te}^3 (v_{ph}/v_{Te})^3 / 4\pi ne^4 L(2+Z) \equiv (1/\tilde{\nu}_e)(v_{ph}/v_{Te})^3, \quad (1)$$

where L is the Coulomb logarithm, v_{ph} is the phase velocity of injected waves ($v_{ph} \gg v_{Te}$) then the terms corresponding to the RRIs and the quasilinear interactions are the most essential in the system of equations describing the dynamics of the superthermal part ($v_{\parallel} \gg v_{Te}$) of the one-dimensional electron distribution function $F_{v_{\parallel}}$ ($n=m\int F_{v_{\parallel}} dv_{\parallel}$) and the distribution of the resonant waves energy $W_{v_{\parallel}}$ ($W_{v_{\parallel}}=\int W_{\vec{q}} \delta(q_{\parallel} - \omega_{\vec{q}}/v_{\parallel}) d\vec{q}$, $\int W_{\vec{q}} d\vec{q}=W$ is the wave energy density in plasma). This self-consistent system of equations (see Ref. [4]) containes the term proportional to $\mathcal{L}=e^2/\hbar c \approx 1/137$ (c is the velocity of light, $\hbar$ is the Planck's constant) which corresponds to the RRIs. The presence of this term leads to new qualitative effects which do not occured if the RRIs are not taken into account. We suppose that the initial electron distribution function $F_{v_{\parallel}}(0)$ has no peaks corresponding to the electron beams in plasma and the following condition takes place:

$$0 > \partial F_{v_{\parallel}}(0)/\partial v_{\parallel} \gg -\mathcal{L} n/2\pi mc^2 \qquad \text{if } v_1(0) \leqslant v_{\parallel} \leqslant v_2(0), \qquad (2)$$

where $v_1(0) \leqslant v_{\parallel} \leqslant v_2(0)$ is the resonant region initially (t=0). Such an initial position of the resonant region corresponds,e.c., to the experimental data [5] if it is assumed that $F_{v_{\parallel}}(0)$ is Maxwellian. We also suppose that the following condition takes place: $\int_{v_1(0)}^{v_2(0)} F_{v_{\parallel}}(0) dv_{\parallel} \geqslant n\mathcal{L}(v_2(0) - v_1(0))^2/4\pi mc^2$. At the time

$$t_0 \sim \frac{1}{\omega_{pe}} (\cos\theta_0)^{-1} \min\left(\frac{2}{\mathcal{L}(v_{ph}/c)^2} ; \frac{1}{4\pi} \frac{nT_e}{W} (\Delta v/v_{Te})^2 (\Delta v/v_{ph})\right), \qquad (3)$$

(where $\cos\theta_0$ is the characteristic value of $q_{\parallel}/|\vec{q}|$, $(\cos\theta_0)^2 \geqslant 2m/M$, $\Delta v=v_2(0)-v_1(0)$) the distribution function $F_{v_{\parallel}}$ becomes almost stationary in the resonant region:

$$F_{v_{\parallel}} \approx \mathcal{L} n(v_0 - v_{\parallel})/2\pi mc^2 \qquad (4)$$

where v_0 is a constant that may be expressed through the values v_1, v_2 from the condition of the particle number conservation in the resonant region. The distribution function does not change outside the resonant region. Thus (see Ref. [4]) two regions of the positive derivative on the distribution function in the vicinities of v_1, v_2 are formed, and the instability which is analogous to the beam instability arises. It is known that if the beam instability occurs the region of the positive derivative on the distribution function propogates by means of a shock wave in

the velocity space (see Ref.[6]). It is shown in [4] that if the condition (2) takes place the resonant region $v_1(t) \leqslant v_\parallel \leqslant v_2(t)$ increases and $v_1(t)$, $v_2(t)$ propogate by means of two shock waves in the velocity space in opposite directions. The time of 2-fold increase of the resonant region is approximately equal to

$$t_1 \simeq 2\ln 2 * \ln(W/W_0) * (\mathcal{A}(v_{ph}/c)^2 \omega_{pe} \cos\theta_0)^{-1}, \qquad (5)$$

where W_0 corresponds to the energy level of the thermal noises. The increase of the resonant region stops if $v_2(t)$ becomes equal to $v_0(t)$. It is shown in [4] that this resonant region increase is small to solve the "spectral gap" problem (see Ref.[7],p.218): $v_{2max} - v_{1min} \ll v_{ph}$. This limitation does not exist if there is a source of particles in the resonant region. Such a source is provided by the RRSIs. The RRSIs are taken into account if it substitutes of $\hat{I}_{\vec{p}} + \hat{J}_{\vec{p}}$ for a quasilinear operator $\hat{I}_{\vec{p}}$ in the term corresponding to the RRIs in the initial equation describing the electron distribution dynamics (see Ref. [4]) (here $\hat{J}_{\vec{p}}$ is a classical operator of induced scattering on the electrons. The RRSIs dominate over the classical induced scattering for the electron velocities obeying the condition (2)). Thus the source Q appears on the right side of the equation describing $\partial F_{v_\parallel}/\partial t$. If the spectrum of the LH-waves consists of the waves with $0 < \cos\theta \ll 1$ ($\cos\theta = (q_\parallel / |\vec{q}|)$), $(\cos\theta)_{max} - (\cos\theta)_{min} \sim \cos\theta_0$ then the estimation of Q under the condition $v_{Te} \ll v_\parallel \ll c$ gives (see Ref.[4]):

$$Q \sim (n\omega_{pe}/mc)\mathcal{A}(v_{Te}/c)(\omega_{pe}/\omega_{He})^2 (W/nT_e)^2 (\cos^2\theta_0 + Zm/M)^{-1/2}, \qquad (6)$$

where $T_e = mv_{Te}^2$. The RRSIs lead to "transfer" (acceleration) of the thermal particles in particular to the particles having the linear resonance with waves. After $v_2(t)$ becomes equal to $v_0(t)$ at the time of the order of t_1 the increase of the resonant region occures only due to the presence of Q. At the time

$$t_2 \sim \mathcal{A}n/2\pi mcQ \qquad (7)$$

$v_2(t)$ becomes of the order of the light velocity c (the condition $F_{v_{ph}}(0) \ll Qt_1 \lesssim Qt_2 v_{ph}/c$ is supposed to take place). The motion of v_1 in the direction to $v_\parallel = v_{Te}$ occures during this time. Thus the gap between the lowest phase velocity of waves and v_{Te} diminishes. Hence the "spectral gap" problem is solved. At the time t_2 the current appears in plasma. Its density is approxi-

mately equal to

$$j_{\parallel} \approx \Delta nec/12\pi \approx 1.94\cdot 10^{-4} nec. \qquad (8)$$

The values of t_0, t_1, t_2 are shown in Ref. [4] to be much smaller than t_{coll} (see (1)) so the approach used above is justified. If the following relation takes place:

$$\tilde{\nu}_e \gg \omega_{pe}(W/nT_e)^2(M/m)^{1/2}(v_{ph}/v_{Te})(\omega_{pe}/\omega_{He})^2 \qquad (9)$$

then the electron distribution function in the domain of the thermal particles is approximately Maxwellian and fast particles are produced with the rate Q. The increase of the fast particles number due to the source Q occures up to formation of the steady-state in the domain of the superthermal electrons with regard to the quasilinear interactions, the RRIs, the RRSIs and the binary collisions between particles. Such a steady-state distribution function was obtained in [8]. The time of steady-state distribution formation in the superthermal particles domain is approximately equal to (see Ref. [8]):

$$t_s \approx (2\tilde{\nu}_e(v_{Te}/c)(v_{Te}/\bar{v}_1)^2)^{-1}, \qquad (10)$$

where $\bar{v}_1$ is the final magnitude of the LH-waves lowest phase velocity attained in the process of the resonant region increase. The value of $\bar{v}_1$ is about $(4\text{-}5)v_{Te}$ for typical parameters of experiments on current drive (see Ref. [8]).

To obtain the efficiency of current drive generation it is necessary to know the wave power dissipated by plasma electrons P_d and the density j_s of steady-state current. According to [8] j_s is of the order of $j_{\parallel}$ given by expression (8) and $P_d \sim \tilde{\nu}_e m^* v_{Te} \Delta n \cdot \ln(c/\bar{v}_1)/(2\pi c)$. Thus the current drive generation efficiency is of the order of

$$\eta \equiv j_s/P_d \sim e(6\tilde{\nu}_e m v_{Te}(v_{Te}/c)^2 \ln(c/\bar{v}_1))^{-1}. \qquad (11)$$

The magnitudes (10), (11) depend on the value $\bar{v}_1$ for obtaining of which the RRIs consideration is essential. It is shown in [4, 8] that the expressions (8), (10), (11) give the values having an order of the experimental magnitudes of a driven current density, growth-time of a driven current and efficiency of current drive generation respectively. Thus the RRIs are of essential

importance for the description of a driven current in plasma.

References

1. Tsytovich V.N. Phys. Reports, 1989, 178, 261.
2. Tsytovich V.N. Zh. Eksp. Theor. Fiz., 1987, 93, 1680.
3. Tsytovich V.N. Radiofizika, 1988, 31, 912.
4. Popel S.I., Tsytovich V.N. Fizika plasmy, 1990, 16, 306.
5. Bernabei S. et al. Phys. Rev. Lett., 1982, 49, 1255.
6. Ivanov A.A., Rudakov L.I. Zh. Eksp. Theor. Fiz., 1966, 51, 1522.
7. Fisch N.J. Rev. Mod. Phys., 1987, 59, 175.
8. Popel S.I., Tsytovich V.N. Kratkie soobshchenija po fizike 1990, No 1, p.18.

EFFECT OF THE HIGH-FREQUENCY FIELD IN THE DRIFT WAVE INSTABILITY

Zh. Kiss'ovski and A. Shivarova
Faculty of Physics, Sofia University, 1126 Sofia, Bulgaria

Abstract. The effect of high-frequency electric field (applied in transverse direction in respect to the static magnetic field) on the behaviour of the dispersion characteristics of the drift waves is studied by using fluid plasma model. The frequency Ω of the oscillating field is in a frequency range determined by $\Omega >> \nu_e$, $\omega_{ci} < \Omega < \omega_{ce}$ where $\omega_{ce,ci}$ are the electron and ion gyrofrequencies and ν_e is the electron - neutral collision frequeency.

Starting with the pionnier work[1] by Fainberg and Shapiro (1967) the nonlinear effect of longitudinal high-frequency field from the range of the lower hybrid waves in the drift wave instability in magnetized plasma has been widely discussed in view of the plasma heating the resonance region. In connection with the possibility for introducing energy into the plasma by means of the field of the Trivelpiece-Gould mode wich is also in the range $\omega_{ci} < \Omega < \omega_{ce}$ the problem for the interaction of this mode with the self-excited drift waves is of interest.

However the transverse field component of the Trivelpiece - Gould mode is larger than the longitudinal one. Although the problem for the interaction of transverse high-frequency field with the dfift wave instability has been discussed by using a kinetic plasma model[2], the obtaining of an simplified results in an explicit form is of interest in connection with comparison with the experiments. Here the nonlinear dispersion relation of the drift waves in the presence of a homogeneous high-amplitude transverse electric field is derived.

We consider inhomogeneous magnetized plasma with a electron density variation $n_o(x)$ in transverse direction in respect to the external magnetic field $\vec{B}_o = B_o \hat{z}$. The high-frequency homogeneous field $\vec{E}_o = E_o \cos \Omega t \hat{x}$ (with frequency $\Omega << \omega_{ce}$) applied to the plasma is parallel to the dencity gradient. The equilibrium state of the plasma is determined by the high-frequency field taken as an high-amplitude one. The components of the electron velocity on

the equilibrium state (zero order approximation) are:

$$V_x^{(o)} = \frac{\Omega}{\omega_{ce}} \frac{c}{B_c} E_o \sin \Omega t$$

$$V_y^{(o)} = - \frac{e}{m\omega_{ce}} E_o \cos \Omega t - \frac{\varkappa T}{\omega_{ce} m} \qquad (1)$$

where m and T are the electron mass and plasma temperature and $\varkappa = (1/n_o)(dn_o/dx)$, respectively. The self-excited drift waves described with quantities of the form $\propto f(t)\exp\{i[\int k_x dx + k_y y + k_z z]\}$ are taken in the perturbed state. In first order approximation, from the equation of motion for the electron:

$$\frac{\partial V_x}{\partial t} + (\vec{V}_o \cdot \nabla) V_x = - \frac{e}{m} E_x - \omega_{ce} V_y - \frac{ik_x T n_e}{m n_o}$$

$$\frac{\partial V_y}{\partial t} + (\vec{V}_o \cdot \nabla) V_y = - \frac{e}{m} E_y + \omega_{ce} V_x - \frac{ik_y T n_e}{m n_o} \qquad (2)$$

after making the substitutions

$$V_x = W_{ex} \exp\{-i(a_{ex}\cos \Omega t + a_{ey}\sin \Omega t)\}$$

$$V_y = W_{ey} \exp\{-i(a_{ex}\cos \Omega t + a_{ey}\sin \Omega t)\} \qquad (3)$$

$$n_e = \eta_e \exp\{-i(a_{ex}\cos \Omega t + a_{ey}\sin \Omega t)\}$$

and averaging over one period of the hihg-frequency oscillations we obtain the slowly varying components of the electron velocity $\vec{V}$:

$$\langle W_{ex} \rangle = \frac{e}{m\omega_{ce}} \langle E_y \exp\{i[a_{ex}\cos\Omega t + a_{ey}\sin\Omega t]\} \rangle - \frac{ik_y T}{m n_o \omega_{ce}} \langle \eta_e \rangle$$

$$\langle W_{ey} \rangle = - \frac{e}{m\omega_{ce}} \langle E_x \exp\{i[a_{ex}\cos\Omega t + a_{ey}\sin\Omega t]\} \rangle - \frac{ik_x T}{mn_o \omega_{ce}} \langle \eta_e \rangle$$

$$\langle W_{ez} \rangle = - \frac{e}{m\nu_e} \langle E_z \exp\{i[a_{ex}\cos\Omega t + a_{ey}\sin\Omega t]\} \rangle - \frac{ik_z T}{mn_o \nu_e} \langle \eta_e \rangle \qquad (4)$$

Here $a_{\alpha x} = (k_x e_\alpha E_o / m_\alpha \omega_{c\alpha}^2)$, $a_{\alpha y} = (k_y e_\alpha E_o / m_\alpha \omega_{c\alpha} \Omega)$, $a_{\alpha x}, a_{ay} << 1$ and $\alpha = e,i$ concerns the electron and ion plasma components, respectively. By introducing into the Poisson equation the electric field , presented also as a sum of the slowly varying field of the drift wave and the fast oscillating field E_1 at frequency Ω ($\vec{E} = \langle \vec{E} \rangle + \vec{E}_1$), we obtain:

$$\vec{E}_1 = - 4\pi \frac{i\vec{k}}{k^2} [-iea_{ix}\langle \eta_e \rangle \cos\Omega t + 2iea_{ey}\langle \eta_e \rangle \sin\Omega t + e(\eta_{1i} - \eta_{1e})] \qquad (5)$$

The fast varying components of the density $\eta_{1\alpha}$ are determined from the two fluid plasma model under the conditions : $k_z^2 T/m\Omega^2 << 1$, $k_\perp^2 T/M\Omega << 1$ (M is the ion mass). After introdusing expressions (4) (with E - field determined from relation (5)) into continuity equation for the electrons, we have:

$$\{-i\omega + \frac{k_z T}{m\nu_e}[1 + \frac{1}{k^2 \lambda_D} a_{ey}^2 \rho(\Omega)] + \frac{ik_y \chi \omega_{pe}^2}{k^2 \omega_{ce}} a_{ey}^2 \rho(\Omega)\} \langle \eta_e \rangle$$

$$- i\frac{k_z e n_o}{m\nu_e} \langle E_z \rangle + n_o \frac{c\chi}{B_o} \langle E_y \rangle = 0 \qquad (6)$$

where λ_D is the Debye length, $\omega_{p\alpha}$ are the plasma frequencies and the expression:

$$\rho(\Omega) = \frac{\Omega^2 (N\Omega^2 - \omega_{pe}^2 \frac{k_z^2}{k^2} - \omega_{pi}^2) - i\frac{1}{2} \frac{\omega_{pe}^2}{\omega_{ce}} \frac{\chi k_x}{k^2} \frac{\Omega^4}{\omega_{ci}}}{[N\Omega^2 - \omega_{pe}^2 \frac{k_z^2}{k^2} - \omega_{pi}^2]^2 - \Omega^2 \frac{\omega_{pe}^4}{\omega_{ce}^2} \frac{k_y^2 \chi^2}{k^4}} \qquad (7)$$

with $N = 1 + (\omega^2_{pe} k_\perp^2 / \omega_{ce} k^2)$ coincides with the corresponding one[1] at $(k_x M/2m) < k_y$.

The corresponding resalt for the ion components is :

$$-i\omega\langle\eta_i\rangle + \frac{e}{n_o}\frac{\varkappa}{B_o}\langle E_y\rangle + \frac{c}{B_o}\frac{n_o}{\omega_{ci}}(k_y\langle E_y\rangle + k_x\langle E_x\rangle) = 0 \qquad (8)$$

Equations (6) and (8) together with the condition for an quasineutrality result in the nonlinear dispersion relation of the drift waves which we have obtained in the presence of high-amplitude high-frequency transverse electric field :

$$\omega^2 + \omega[i\omega_s - \omega_e \frac{B}{1+\beta}(1 + \frac{\beta}{2}\rho_i^2)] + i\omega_e\omega_s - \frac{2\beta}{\rho_i^2}\frac{\omega_e^2}{(1+\beta)^2}(1 + \frac{\beta}{2}\rho_i^2)^2 = 0, \qquad (9)$$

where $\omega_s = (k_z \omega_{ce}\omega_{ci}/k_\perp^2 \nu_e)(1 + \beta\rho_i^2/2)$,
$\omega_e = k_y T \varkappa (1+\beta)/M\omega_{ci}(1 + \beta\rho_i^2/2)$,
$\rho_i^2/2 = -(\omega_{pi}/\omega_{ci})^2 k_\perp^2 \lambda_D^2$, $\beta = a_{ey}^2 \rho(\Omega)/k^2\lambda_D^2$.

The nonlinear effect is due to the action of the pondermotive force appearing at the frequency ω of the drift wave in result of three wave interaction of the type : $\Omega_{1,2} = \Omega \pm \omega$ where $\Omega_{1,2}$ are the side-band frequencies.

Asknowledgements. This work was supported by the Ministry of Sciences and Higher Education of Bulgaria (project N:123).

References

1. Fainberg Ya.B. and Shapiro V.D. 1967 ZhETF,vol.52,293.
2. Sundaram A.K. and Kaw P.K. 1973 Nucl.Fusion,vol.13,901.

ON NONLINEAR INTERACTION OF HIGH-FREQUENCY AND LOW-FREQUENCY WAVES IN CONFINED PLASMA

V.V. Gulenko, V.V. Gushchin
Kharkov State University, 310077, Kharkov, USSR

The development of the physics of nonlinear phenomena and their frequent identity from the oscillatory-wave standpoint stimulated an invention of universal mathematical tool s for the description of wave fields of arbitrary physical origin [1-2]. On introducing of canonical variables and passing over to normal ones, the equations take on a standard form. In particular, the equations describing the interaction of two waves with dispersion laws $\omega_k \equiv \omega(\vec{k})$ and $\Omega_k \equiv \Omega(\vec{k})$ and with complex amplitudes have the following form: $(a_k \equiv a(\vec{k},t);\ b_k \equiv b(\vec{k},t))$

$$\frac{\partial a_k}{\partial t} = -i\frac{\delta H}{\delta a_k^*};\quad \frac{\partial b_k}{\partial t} = -i\frac{\delta H}{\delta b_k^*};\quad H = \int\left(\omega_k|a_k|^2 + \Omega_k|b_k|^2\right)d\vec{k} + H_{int} \equiv H^{(2)} + H_{int}. \quad (1)$$

All "linear" information on the interacting waves is contained in dispersion relation, and the nonlinear one, in the interaction hamiltonian $H_{int} = H^{(3)} + H^{(4)} + \cdots$. The latter is a series expansion with canonical variables, and the coefficients of this expansion are matrix elements, a knowledge of which automatically provides a solution of a broad range of questions in the framework of (1) (see review [1] and the references quoted therein).

An importance of nonlinear wave processes in confined plasmas for a wide range of problems, on the one hand, and considerable difficulties in their analysis, on the other hand, stimulate searches of new ways for their theoretical description. An introduction of hamiltonian formalism for the description of nonlinear effects in semiconfined plasma is a purpose of the paper presented.

Consider the potential surface waves propagating along the

interface $z = 0$ between the dielectric $\varepsilon = \text{const}$ occupying the half-space $z > 0$ and the plasma in the region $z < 0$ We start from the following set of hydrodynamic equations describing the motion of charges:

$$\frac{\partial \rho_\alpha}{\partial t} + \operatorname{div} \rho_\alpha \vec{V}_\alpha = 0 \ , \quad \alpha = e, i \tag{2}$$

$$\frac{\partial \vec{V}_\alpha}{\partial t} + (\vec{V}_\alpha \vec{\nabla}) \vec{V}_\alpha = - \frac{e_\alpha}{m_\alpha} \vec{\nabla} \varphi - V_{T\alpha}^2 \vec{\nabla} \ln \frac{\rho_\alpha + \rho_{0\alpha}}{\rho_{0\alpha}} \tag{3}$$

$$\begin{aligned} \Delta \varphi &= -4\pi \sum_\alpha \frac{e_\alpha}{m_\alpha} \rho_\alpha \ , \quad z < 0 \\ \Delta \varphi &= 0 \ , \quad z > 0 . \end{aligned} \tag{4}$$

If the condition $I_{Bound} = 0$ where

$$I_{Bound} \equiv \int_{z=+0} \frac{\varepsilon \varphi}{4\pi} \frac{\partial^2 \varphi}{\partial z \partial t} d\vec{r}_\perp + \int_{z=-0} d\vec{r}_\perp \left\{ \sum_\alpha \left(\frac{\rho_\alpha V_\alpha^2}{2} + V_{T\alpha}^2 \ln \frac{\rho_\alpha + \rho_{0\alpha}}{\rho_{0\alpha}} - \frac{e_\alpha}{m_\alpha} \varphi \right) - \varphi \frac{\partial^2 \varphi}{\partial z \partial t} \right\} \tag{5}$$

is met, the set of equations (2)-(4) allows for the energy conservation $\partial W / \partial t = 0$

$$W \equiv \int_{z<0} \left\{ \sum_\alpha \left[\frac{\rho_\alpha V_\alpha^2}{2} + (\tilde{\rho}_\alpha + \rho_{0\alpha}) \left(\ln \frac{\tilde{\rho}_\alpha + \rho_{0\alpha}}{\rho_{0\alpha}} - 1 \right) + \frac{(\vec{\nabla}\varphi)^2}{8\pi} \right\} d^3\vec{r} + \frac{\varepsilon}{8\pi} \int_{z>0} (\vec{\nabla}\varphi)^2 d^3\vec{r} . \tag{6}$$

Passing over to Clebsch presentation [1-2], one can present the basic equations (2)-(3) in the canonical form:

$$\frac{\partial \Phi_{\alpha K}(z,t)}{\partial t} = - \frac{\delta H}{\delta \rho_{\alpha K}^*(z,t)} \ ; \ \frac{\partial \rho_{\alpha K}(z,t)}{\partial t} = \frac{\delta H}{\delta \Phi_{\alpha K}^*(z,t)} \ . \tag{7}$$

The equations take on this form after Fourier transform, that is determined as follows:

$$\rho_\alpha(\vec{r}_\perp, z, t) = \frac{1}{2\pi} \int d\vec{K}_\perp \rho_\alpha(\vec{K}_\perp, z, t) e^{i\vec{K}_\perp \vec{r}_\perp} \equiv \frac{1}{2\pi} \int d\vec{K} \rho_{\alpha K}(z,t) e^{i\vec{K}\vec{r}} . \tag{8}$$

The hamiltonian H is the energy W expressed through canonical variables and can be presented in the form of the series

expansion. For example,

$$H^{(3)} = \frac{1}{2\pi} \sum_{\alpha} \int_{z<0} dz\, d\vec{K}_1 d\vec{K}_2 d\vec{K}_3\, \delta(\vec{K}_1+\vec{K}_2+\vec{K}_3) \times$$

$$\times \left\{ \varrho_{\alpha K_1} \left(\frac{\partial \Phi_{\alpha K_2}}{\partial z} \frac{\partial \Phi_{\alpha K_3}}{\partial z} - \vec{K}_2 \cdot \vec{K}_3 \Phi_{\alpha K_2} \Phi_{\alpha K_3} \right) - \frac{1}{6} \frac{V_{T\alpha}^2}{\varrho_{0\alpha}^2} \varrho_{\alpha K_1} \varrho_{\alpha K_2} \varrho_{\alpha K_3} \right\}. \quad (9)$$

The next step is the transition to normal variables, in particular, diagonilizing $H^{(2)}$. The details of this procedure can be found in [3].

The final expressions relating the natural canonical variables $\varrho_{\alpha K}$, $\Phi_{\alpha K}$ to the normal ones have the form

$$\Phi_{e,i}(K,z,t) = \tilde{\Phi}_{e,i}^{HF}(z)(a_K - a_{-K}^*) + \tilde{\Phi}_{e,i}^{LF}(b_K - b_{-K}^*) \quad (11)$$

$$\varrho_{e,i}(K,z,t) = \bar{\varrho}_{e,i}^{HF}(z)(a_K + a_{-K}^*) + \bar{\varrho}_{e,i}^{LF}(b_K + b_{-K}^*). \quad (12)$$

Here $\tilde{\Phi}_{e,i}^{HF,LF}(z)$ and $\bar{\varrho}_{e,i}^{HF,LF}(z)$ are the solutions of the linear boundary value problem and are determined by the following expressions. For high frequencies we have

$$\bar{\varrho}_i(z) = \sqrt{\frac{K\varrho_{0e}}{2\omega}} \left\{ (\varepsilon+1) p e^{pz} + \left[(\varepsilon-1) + (\varepsilon+1)\mu \right] \delta(z) \right\} \quad \bar{\varrho}_e(z) = -\sqrt{\frac{K\varrho_{0e}}{2\omega}}\, p e^{pz} \quad (13)$$

$$\tilde{\Phi}_i(z) = i\mu \sqrt{\frac{\omega K}{2\varrho_{0e}}} \left(\frac{e^{Kz}}{K} - (\varepsilon+1)\frac{e^{pz}}{p} \right) \quad \tilde{\Phi}_e(z) = i \sqrt{\frac{\omega K}{2\varrho_{0e}}} \left(\frac{e^{Kz}}{K} - \frac{e^{pz}}{p} \right) \quad (14)$$

$$\mu \equiv \frac{m}{M} \qquad p \equiv \sqrt{\frac{\varepsilon}{\varepsilon+1}} \frac{1}{r_{De}}$$

For low frequencies we have

$$\bar{\varrho}_i(z) = \sqrt{\frac{\varepsilon\varrho_{0i}}{C_s}} K^2 r_{De} \left(e^{qz} + \frac{\delta(z)}{K} \right) \qquad \bar{\varrho}_e(z) = \mu \sqrt{\frac{\varepsilon\varrho_{0i}}{C_s}} K^2 r_{De} e^{qz} \quad (15)$$

$$\bar{\Phi}_e(z) = -iK r_{De} \sqrt{\frac{\varepsilon C_s}{\varrho_{0i}}} \left(e^{qz} + \varepsilon\alpha e^{Kz} \right) \quad \Phi_i(z) = -iK r_{De} \sqrt{\frac{\varepsilon C_s}{\varrho_{0i}}} \left(e^{qz} - \varepsilon\mu\alpha e^{Kz} \right) \quad (16)$$

$$\alpha \equiv K^2 r_{De}^2 \qquad q \equiv \varepsilon\alpha K .$$

Substituting (11)–(16) into the expansions $H^{(3)}$ and $H^{(4)}$ one can calculate the interaction hamiltonian of any process. These calculations are simplified after writing down $H^{(3)}$ and $H^{(4)}$ symbolically:

$$H^{(3)} = \int d\vec{K}_1 d\vec{u}_2 d\vec{u}_3\, C_e(\vec{K}_1) C_m(\vec{K}_2) C_n(\vec{K}_3) S_{emn}(\vec{K}_1 \vec{K}_2 \vec{K}_3)\, \delta(\vec{K}_1+\vec{K}_2+\vec{K}_3) \quad (17)$$

$$S_{emn}(\vec{K}_1\vec{K}_2\vec{K}_3)\equiv\int dz\,dz_1\,dz_2\,dz_3\,\Lambda_{i\ell}(\vec{K}_1)\Lambda_{jm}(\vec{K}_2)\Lambda_{kn}(\vec{K}_3)T_{ijn}(z-z_1,z-z_2,z-z_3) \quad (18)$$

The indexes have the following meaning: ijk is $(\Phi_i,\Phi_e,\rho_i,\rho_e)$ and emn are (HF. LF, HF*, LF*). For example, in a cold ion case $T_i=0$

$$S_{emn}(K_1K_2K_3)=\int dz\left\{\frac{1}{2}\bar{\rho}^{\ell}_{eK_1}\frac{\partial\bar{\Phi}^{m}_{eK_2}}{\partial z}\frac{\partial\bar{\Phi}^{n}_{eK_3}}{\partial z}-\frac{1}{2}\vec{K}_2\vec{K}_3\bar{\rho}^{\ell}_{eK_1}\bar{\Phi}^{m}_{eK_2}\bar{\Phi}^{n}_{eK_3}\right\}+$$

$$+\left[\frac{1}{2}\bar{\rho}^{\ell}_{iK_1}\frac{\partial\bar{\Phi}^{m}_{iK_2}}{\partial z}\frac{\partial\bar{\Phi}^{n}_{iK_3}}{\partial z}-\frac{1}{2}\vec{K}_2\vec{K}_3\bar{\rho}^{\ell}_{iK_1}\bar{\Phi}^{m}_{iK_2}\bar{\Phi}^{n}_{iK_3}\right]-\frac{1}{6}\frac{V_{Te}^2}{\rho_{oe}^2}\bar{\rho}^{\ell}_{eK_1}\bar{\rho}^{m}_{eK_2}\bar{\rho}^{n}_{eK_3}. \quad (19)$$

On calculating the matrix elements it is possible to write the set of equations (1) for the interaction of HF and LF waves in the form [4,1]

$$\frac{\partial a_K}{\partial t}+i\omega_K a_K=-i\int\left\{V_{K_1K\ K}\,b_{K_1}+V^{*}_{-K_1K_2K}\,b^{*}_{-K_1}\right\}a_{K_2}\,\delta(\vec{K}-\vec{K}_1-\vec{K}_2)- \quad (20)$$

$$-i\int W_{KK_1K_2K_3}a^{*}_{K_1}a_{K_2}a_{K_3}\,\delta(\vec{K}+\vec{K}_1-\vec{K}_2-\vec{K}_3)\,d\vec{K}_1\,d\vec{K}_2\,d\vec{K}_3$$

$$\frac{\partial b_K}{\partial t}+i\Omega_K b_K=-i\int V^{*}_{KK_1K_2}a^{*}_{K_1}a_{K_2}\,\delta(\vec{K}+\vec{K}_1-\vec{K}_2)\,d\vec{K}_1\,d\vec{K}_2. \quad (21)$$

However, unlike [4], where matrix elements are calculated for a narrow packet, a regular procedure for their calculation in a most general form is suggested in this paper.

In particular, the matrix element $V_{K_1K_2K_3}$ is calculated as follows:

$$V_{K_1K_2K_3}=S_{123}(2,3,-1)+S_{132}(2,-1,3)+S_{312}(-1,2,3)+S_{321}(-1,2,3)+$$

$$+S_{213}(3,2,-1)+S_{231}(3,-1,2). \quad (22)$$

After necessary calculations we find:

$$V_{K_1K_2K_3}=\frac{1}{2}\sqrt{\frac{\varepsilon}{\varepsilon+1}}\sqrt{\frac{c_s}{\rho_{oe}}}\left(1+\frac{\vec{K}_1\cdot\vec{K}_2}{K_1\cdot K_2}\right)\frac{\sqrt{K_1K_2}}{K_1+K_2}K_3^2. \quad (23)$$

The expression which determines $W_{KK_1K_3K_4}$, also in a general case, is not given here being too bulky.

Obviously, all results on the HF wave stability in the framework of the set (20), (21) are valid for our case with corresponding changes.

For the transformation of the set (20), (21) to the $\vec{r}_\perp=\{x,y\}$ presentation, one must first introduce new variables which are obtained from (11)-(12) by the integration with respect to z.

This is due to the fact that we used Fourier transform with $\vec{r}_\perp$ when deriving (20), (21). Consequently, the inverse transform should also be two-dimensional and independent of z. So. we use

$$Q_{e,i}(\vec{k},t) = \eta^{HF}_{e,i}(a_k - a^*_{-k}) + \eta^{LF}_{e,i}(b_k - b^*_{-k}) \tag{24}$$

$$R_{e,i}(\vec{k},t) = \xi^{HF}_{e,i}(a_k + a^*_{-k}) + \xi^{LF}_{e,i}(b_k + b^*_{-k}) \tag{25}$$

$$Q_{e,i} \equiv \int dz\, \Phi_{e,i}(\vec{k},z,t) \qquad R_{e,i} = \int dz\, \varphi_{e,i}(\vec{k},z,t)$$
$$\eta^{HF,LF}_{e,i} \equiv \int dz\, \tilde{\Phi}^{HF,LF}_{e,i} \qquad \xi^{HF,LF}_{e,i} \equiv \int dz\, \tilde{\varphi}^{HF,LF}_{e,i}. \tag{26}$$

instead of (11)-(12). Analogously to [4], using (24)-(26) one can reduce the set (20)-(21) to the following form in the presentation

$$\frac{\partial \varphi(\vec{r}_\perp,t)}{\partial t} + \varphi_{0i}\Delta\Phi(r_\perp,t) \simeq 0; \quad \Delta \equiv \frac{\partial^2}{\partial x^2} + \frac{\partial^2}{\partial y^2} \tag{27}$$

$$\frac{\partial \Phi(\vec{r}_\perp,t)}{\partial t} + \frac{c_s^2}{\varphi_{0i}}\varphi(\vec{r}_\perp,t) = -\frac{\omega}{\varphi_{0i}}|\varphi|^2; \qquad T_0 \equiv 4\pi^2 T_{K_0K_0K_0K_0} \tag{28}$$

$$i\left(\frac{\partial}{\partial t} + v_g\frac{\partial}{\partial x}\right)\varphi + \frac{1}{2}\frac{d^2\omega}{dk^2}\frac{\partial^2\varphi}{\partial x^2} + \frac{1}{2k}\frac{\partial^2\varphi}{\partial y^2} = T_0|\varphi|^2\varphi - i\frac{\varepsilon\omega}{\varphi_{0i}}k_0^2 r_{De}^2\varphi(\vec{r}_\perp,t)\int K_1^3\varphi_{3K}e^{i\vec{K}_1\vec{r}_\perp}d\vec{K}_1. \tag{29}$$

In the case of infinitely heave ions, the set (27-29) is reduced to nonlinear Schrödinger equation. Depending on parameters, it has solutions in the soliton and antisoliton form [5].

It is easy to pass over from equations (20), (21) to kinetic equations for substances $\langle a_K a^*_{K_1}\rangle = N_K\delta(\vec{K}-\vec{K}_1)$ and $\langle b_K b^*_{K_1}\rangle = n_K\delta(\vec{K}-\vec{K}_1)$ in the framework of which one can investigate kinetics of HF and LF wave interaction. According to [6], this set has the form

$$\frac{\partial N_K}{\partial t} = \int (T_{K_2KK_1} - T_{K_2K_1K})\,d\vec{K}_1 d\vec{K}_2 \qquad \frac{\partial n_K}{\partial t} = -\int T_{KK_1K_2}\,d\vec{K}_1 d\vec{K}_2 \tag{30}$$

$$T_{K_2KK_1} = 2\pi\left|V_{K_2KK_1}\right|^2(N_{K_1}n_{K_2} - N_K n_{K_1} - N_{K_1}N_{K_2})\delta(\vec{K}-\vec{K}_1-\vec{K}_2)\,\delta(\omega_K - \omega_{K_1} - \Omega_{K_2}). \tag{31}$$

Besides thermodynamically equilibrium solutions, it has nonequilibrium ones: Kolmogorov's power spectra $\sim K^x$, whose exponents are defined by the expressions $x_1 = -S + d + \alpha/2$ and $x_2 = -S - d$ where d is the space dimension, S is the degree of homogeneity of matrix elements, $V_{\varepsilon K_1 \varepsilon K_2 \varepsilon K_3} = \varepsilon^S V_{K_1K_2K_3}$, and the dispersion laws have the form $\omega_K = \omega_0 + c_1 K^\alpha$, $\Omega_K = c_2 K^\beta$. In our case, for the wave interaction we have $\omega_K = \omega_s\left(1 + \frac{1}{2}\sqrt{\varepsilon(\varepsilon+1)}\,K r_{De}\right)$; $\omega_s \equiv \omega_{pe}/\sqrt{1+\varepsilon}$ and $\Omega_K \simeq KC_s$ $\alpha_s = \beta = 1, d = 2$, and according to (23), $S = 2$. This

gives two spectra with a constant flow of the wave number $P_N \sim K^{-7/2}$ and with constant energy flow $P_\varepsilon \sim K^{-4}$. The flow direction is determined by the expressions $\operatorname{sign} P_N = \operatorname{sign}(x_1+\alpha)$ $\operatorname{sign} P_\varepsilon = -\operatorname{sign}(x_2+\alpha)$, which give $P_N < 0$, $P_\varepsilon > 0$, i.e., the first flow can be realized in the longwave region and is directed there, and the second one, in the shortwave region. The investigation of Kolmogorov's spectra locality and stability, with higher nonlinearity taken into account, and a number of other questions are beyond the framework of the paper presented.

Note in conclusion that an alternative variant of hamiltonian formalism, based on the use of Poisson brackets and Lee algebra can be found in review [7].

References

1 Zakharov V.E., Musher S.L., Rubenchik A.M. Phys. Reports 1985, 129, 285.

2 Zakharov V.E., Kuznetsov E.A. Soviet Sci. Rev. C. 1984, 4, 62.

3 Gulenko V.V., Gushchin V.V., Erokhin N.G. In: Nonlinear and Turb. Processes in Physics, Singapore, 1990 (to be published).

4 Zakharov V.E., Rubenchik A.M. J. Appl. Mech. Tech. Phys. 1972, 5, 84.

5 Gulenko V.V., Gushchin V.V., Erokhin N.S., Fadeev A.P. Prepr. IPM Ac. Sci. USSR. 1989, 133, 21 p.

6 Zakharov V.E., Kuznetsov E.A. JETP 1978, 75, 904.

7 Holm D.D., Marsden J.E., Ratiu T., Weinstein A. Phys. Reports, 1985, 123, I.

Development of high - power microwave sources

HIGH POWER MICROWAVE ELECTRONICS:

STATUS, TRENDS AND PROBLEMS

A.V. Gaponov-Grekhov, M.I. Petelin
Institute of Applied Physics, N-Novgorod, USSR

The highest powers of coherent microwaves can be and are produced on the base of the stimulated radiation of electron beams 1) possessing sub-relativistic and relativistic energies and 2) interacting with the RF field in space-developed electrodynamic systems (to convert high-order modes generated by such devices into waves fit for distant transmission, narrow-directed radiation and compact focusing, some effective methods are developed).

The high-power microwaves are applied to plasma heating, plasma diagnostics, material processing, radio location , particle acceleration etc.

VACUUM ELECTRONIC DEVICES AS THE MOST POWERFUL SOURCES OF COHERENT MICROWAVES

In the microwave band , the largest possibilities to produce the coherent electromagnetic radiation are related with methods of classical electronics. As a matter of fact, in this band the smallness of the photon energy $\hbar\omega$ and the breakdown in solids put strict limitations on capacities of principally quantum (masers) and semiconductor (transistors, etc.) sources . On the contrary, in the classical electron devices one electron can radiate a large amount of photons, a broad interaction space can consume a large electron current and is relatively resistant to the RF breakdown , and, not less important, the initial electron energy is unlimited. Exploiting the last factor, the microwave classical electronics step by step entered the region of relativistic electron energies.

RELATIVISTIC ELECTRON BEAMS AND RELATIVISTIC EFFECTS

AS A BASE FOR ENHANCEMENT OF POWERS AND FREQUENCIES

Enlarging the operating voltage of vacuum electron devices, it is possible, according to the Child-Lengmuir law, to enlarge the operation current as well. In addition to the power enhancement, this gives some other favorable consequences [1,2].

A number of these consequences follow immediately from the *kinematics of the wave - particle interaction*, namely, from the synchronism (resonance) condition

$$\omega - k_{\parallel} v_{\parallel} = n \Omega \quad (n = 0, \pm 1, \pm 2 \ldots) ,$$

where ω and $k_{\parallel}$ are the frequency and the longitudinal propagation number of the electromagnetic wave, $v_{\parallel}$ and Ω are the translational velocity and the oscillation frequency of electrons :

a) For microwave devices based on the *stimulated Cherenkov radiation* ($n = 0$), the larger is the electron energy, the more close is the wave phase velocity $\omega/k_{\parallel}$ to the light velocity c and, correspondingly, the *larger is the transverse inhomogeneity scale of the wave field.* This is favorable for mastering higher currents. On the other hand, if the phase and group velocities of the slow wave synchronous to electrons are close to the light velocity, the synchronism is conserved in a relatively broad frequency band. This is favorable for a *broad-band amplification of signal.*

b) For microwave devices based on the *stimulated bremmstrahlung radiation* ($n \neq 0$) in the case of sub-relativistic transverse momentum of electrons $p_{\perp} < m_0 c$ the larger is the electron energy, *the larger is the Doppler excess of the radiated wave frequency* (the dipole radiation : $k_{\parallel} \approx \omega / c$) *over the electron oscillation frequency* [3] :

$$\omega / \Omega \sim \gamma^2.$$

Here $\gamma = (1 - v^2/c^2)^{-1/2} = 1 + e\ U/\ m_0c^2$ is the relativistic mass-factor, U is the operating voltage of the device.

Some important effects in the high-power microwave electronics result from the *relativistic particle dynamics.* Let us point two examples:

a) When *the Cherenkov microwave devices* enter the ultra-relativistic ($\gamma \gg 1$) region , the dependence of the electron velocity on their energy weakens , resulting [4] in 1) a rapid *increase of optimum* (for compact electron bunching) *length* and 2) *reduction of effective* (synchronous longitudinal) *RF field amplitude.* This simplifies , to some extent, difficulties to avoid the RF breakdown.

b) In stationary beams composed of electrons rotating in the homogeneous static magnetic field, the relativistic dependence of the electron cyclotron frequency on the electron energy results in an inertial electron bunching effect being the base for performance of the *cyclotron resonance masers*[5-9]. This effect essential even at sub-relativistic electron energies is used in the *gyrotron* [10-12] .

MODE SELECTION IN RELATIVISTIC-ELECTRON MICROWAVE DEVICES WITH SPACE-DEVELOPED INTERACTION SPACE

How broad can be the interaction space of an electron generator of coherent microwave radiation? Translated to the language of hydrodynamics, the question sounds as follows: for a stream in a channel, how large can be the Reinolds number to provide a well-developed instability, but without turbulence?

The simplest method to obtain the single-mode regime is

to provide conditions, when the *operation mode* is *of the lowest type* and is the *only one synchronous (or resonant) to electrons.* This method quite common for the non-relativistic electronics, being extended to the relativistic region , acquires an attractive quality [13,14]: if the translational velocity of electrons is close to that of light, the selection safe transverse dimension of the interaction space becomes of the order of $\lambda\gamma$, i.e., proportional to the electron energy.

To excite selectively a *mode of a high type* , the simplest method is to organize its *synchronism with electrons* in a regime of *low group velocity.* The method is used in the gyrotron (Fig.1) [10-12], the orotron (Fig. 2) [15,16] (2π - synchronism in the last case) and in Bragg-feedback (π-synchronism in the Cherenkov case) relativistic-electron microwave generators (Fig. 2) [17-21,14]; in all the devices mentioned the electrodynamic system represents an open cavity . In the frame of these methods, an additional improvement of the selectivity can be obtained by using *differences in coupling* of the *electron beam* with modes possessing *different transverse structures* [10-12,1,2].

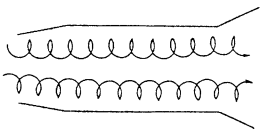

Fig. 1. The gyrotron

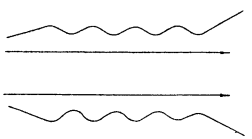

Fig.2. The orotron or the π-mode generator (depending on the synchronism)

There is a large amount of mode selection methods associated with introduction of *irregularities* into the *interaction space.* For example, relatively small irregularities are usually

sufficient to suppress "gyrotron" modes in CARMs or to suppress "orotron" modes in π -mode Cherenkov microwave generators.

A limiting case of the method mentioned is *sectioning of the interaction space* . Let us give two relatively fresh examples:

1) A selective cavity can be composed of a cylindrical waveguide with smooth or impedance cylindrical wall and corrugated waveguide sections at its ends (Fig. 3)[20,21,23,14]. The set of

Fig. 3. Single-electron-beam sectioned microwave generators

parameters in the system is sufficient to regulate independently both the electron-wave coupling and the feedback intensity. The distributed feedback selectivity can be provided by the corrugation profile.

2) In a system with two coaxial electron beams (Fig. 4)[24],

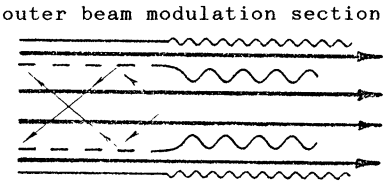

Fig. 4. Double-electron-beam sectioned microwave generator

it is possible to use one beam to drive an auto-oscillator and another to drive an amplifier. If the auto-oscillator is of a low power, it can be easily made single-moded. If it is used to modulate the outer electron beam via a distributed wave coupler, the single mode output of the amplifier can be obtained .

3) In amplifiers (see, for example, Fig. 5) sectioning of

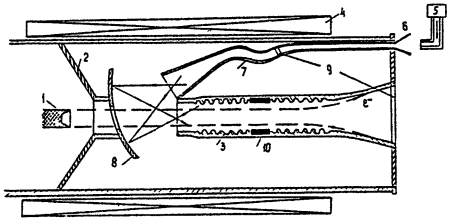

Fig. 5. A 35 GHz 100 MW 44 dB Cherenkov following wave amplifier: 1- cathode, 2-anode,3-slow wave section, 4-solenoid, 5-magnetron, 6-horn, 7- H_{11}- E_{01} mode converter, 8-mirror, 9-windows, 10-absorber.

the interaction space, introducing absorbers, adiabatic tapering of the amplification section ends are used to avoid the self-excitation and to achieve high gains.

THE GYROTRON: THE HIGHEST CW POWERS

AND THE LARGEST PULSE ENERGIES AT SHORTEST MICROWAVES

In principle the gyrotron (Fig.1) can operate at any frequency ω multiple to the electron cyclotron frequency ω_H

$$\omega = n\,\omega_H .$$

However, in practical sub-relativistic ($\beta^2 \ll 1$, U < 100 kV) gyrotrons[12] high efficiencies are obtained only a) at the fundamental cyclotron resonance (n=1), and b) if the wavelength is longer than 5 - 8 mm, at the second harmonic (n = 2).

Today (Table 1) in the sub-relativistic gyrotrons : the largest efficiency is 70 % , the largest pulse power is over 2MW, the largest power in the CW regime is 345 kW, the shortest wave is 0.9 mm in the CW regime and 0.5 mm in the pulse regime . According to the Table, the gyroklystrons-amplifiers (for more details see [30]) have less power than the gyromonotrons -

auto-oscillators, but the difference seems to be temporary.

Table 1. Illustrations to the present state of gyrotrons.

type	λ *mm*	P *kW*	eff *%*	gain *dB*	τ *s*	ref.
gyro-	3	2100	30		$3\cdot10^{-5}$	[25]
monotrons	1	400	20		$3\cdot10^{-6}$	[26]
	0.5	50	5		10^{-4}	[27]
	10	345	30		CW	[28]
	0.9	1.5	6		CW	[29]
gyro-	30	0.7	70 *)	22	CW	[30]
klystrons	30	160	40	30	10^{-4}	[31]

High-power gyrotrons operate at high modes, for their practical use mode converters are necessary (see below) .

Cyclotron radiation devices can be made not only at the sub-relativistic (Table 1), but at higher operation voltages as well. In the latter case higher powers and, using the Doppler effect, higher frequencies become available. Some preliminary results in the field, namely, related to the CARM, are mentioned below.

SUPER-POWER PULSE MICROWAVE GENERATORS AND AMPLIFIERS BASED ON HIGH-CURRENT ELECTRON ACCELERATORS

In the relativistic microwave electronics a number of techniques are used

1) for producing high-voltage high-power pulses:

a) conventional and quasi-conventional pulse transformers,

*) In [32] it was supposed that the 70 % efficiency of the gyroklystron [30] was the orbital one, i.e. representing the relative loss of the electron rotation energy in the interaction space. In reality , this efficiency was measured as the ratio of the output microwave power to the electron beam power (being the product of the gun voltage and the beam current).

b) linear induction pulse formation systems,

c) high-power-storage high-voltage-switch systems,

2) for producing intense electron beams:

a) thermocathodes,

b) field emission (explosion emission) cathodes.

The cheapest to obtain the highest peak microwave powers is a combination of techniques 1-c and 2-b realized in the high-current electron accelerators of direct action [33,34]. The very first microwave auto-oscillators based on these accelerators were created in the early 70-ies [35,36], the powers were some hundreds megawatt, with efficiencies over 10 % . Now (Table 2)

Table 2. Illustrations to the present state of pulse microwave generators and amplifiers driven by high-current accelerators.

type	λ *mm*	P *MW*	eff *%*	gain *dB*	τ ns	ref
generators:						
BWO	30	1500	10		50	[37]
	30	300	30		20	[38]
magnetron	100	1700	35		20	[39]
	30	4000	12		10	[40]
	100	10^4	40		30	[41]
orotron	8	100	10		10	[42]
gyrotron	3	30	2		50	[42]
section.	30	2000	15		50	[43]
	10	10^4	30		700	[44]
	10	600	20		20	[24]
amplifiers:						
Cher. TWT	30	400	40	35	100	[45]
Cher. TWT	8	100	10	44	5	[46]
CARM-TWT	8	10	4	30	20	[47]
CARM-TWT	8	12	6	30	30	[48]

there are 10^9-10^{10}W microwave powers at centimeter and 10^8-10^9 W powers at millimeter wavelengths.

The pulse repetition rate of the microwave devices driven by the high-current-accelerators of direct action is now in some experiments [49] up to 10^2-10^3 Hz .

An effective method to obtain the shortest microwaves is related with the use of the field emission cathodes in linear induction accelerators The most impressive result obtained by this technique is creation of a 35 GHz amplifier with 1 GW peak microwave power, 20 ns pulse duration , 34% efficiency, 43dB gain[50].

Let us note , that for the field (explosion) emission cathodes the pulse duration is limited by 10^{-7}s . Longer pulses need more expensive high-compression electron guns with thermocathodes. There is an intensive activity in the field related to the super-collider problem; for example[51], a 3 cm wavelength 290 MW power 40 % efficiency amplifier is elaborated.

HIGH-POWER MICROWAVE TRANSMISSION AND CONTROL

Mode converters. If a wave produced by an electron device is of a complicated structure , how can it be simplified to be fit for a practical use? This can be done by one of following methods:

1) Relatively low modes of relatively narrow waveguides can be converted one to another a) if non-degenerated, by adiabatic change of the waveguide cross-section (examples: the H_{10} - H_{11} converter , the Marier H_{10} - H_{01} converter[52]), b) if degenerated, by a proper (coupling) extended deformation of the waveguide (examples: the Jouguet H_{10}- H_{01} converter[53]).

2) In waveguides of moderate cross-section one mode can be

Fig.6. Mode converters:

a) adiabatic

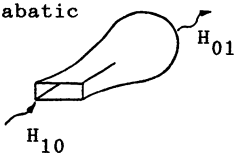

b) degenerated-mode coupling

c) resonant scattering

d) asymmetric-cut curved-mirror

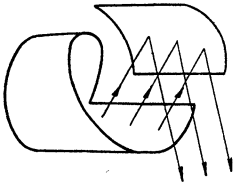

e) adiabatic quasi-optical

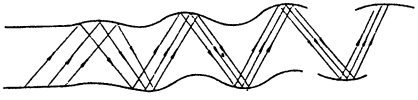

converted to another by the resonant scattering at periodically corrugated walls [54,55] (Fig. 6c, propagation wave numbers related by $k_{\parallel s}-k_{\parallel i}=2\pi/d$). This method, though universal, can be used in practice only to convert moderately high modes .

3) On the other hand, the higher is a mode, the more is the foundation for an asymptotic method , namely , for the method of geometrical optics. In the frame of the method, the initial mode is represented as a system of rays successively reflecting from the waveguide walls (the Brillouin-Keller concept). To change the mode , i.e. to change the configuration of rays , one can use a proper combination of mirrors (the latters, in general case , ought to be curved)[56,57]. This method is universal, but diffraction effects keep its efficiency within 80%.

To enlarge the conversion efficiency, it seems attractive to develop a method combining main merits of all previous ones.

Namely, it should be a method providing an adiabatic quasi-periodic mirror transformation of the initial mode. The converter can be synthesized in the following way. Among rays composing the initial mode, let us appoint one to be "chief" and find points of its reflections from the waveguide wall. Then let us deform the waveguide surface to make it a) focusing near the "chief" ray reflection points and b) defocusing at the remaining area. Then, successively reflecting from the walls, the rays will contract to the "chief" one and, finally, will compose an eigen-mode of an open mirror waveguide with the transverse distribution of the RF field depending on the mirror profile. The idea[58] has been verified by theoretical calculations and by some experiments: for example, the rotating $H_{15.4}$ mode of a circular waveguide was converted into an eigen-mode of a mirror line with efficiency near to 97%.

Waveguides for high power microwave transmission. In the microwave band , the capacity of standard (with cross-sections ~ λ^2) waveguides to transmit high powers rapidly fades with the increase in the frequency). As for broader waveguides, there is a danger to loose the space coherence of the radiation , because relatively small irregularities can couple the main mode to spurious ones . The danger can be avoided by a proper choice of the waveguide parameters , when the difference in the wave decrement indexes of wave modes is sufficiently large . This results not only in the filtration , but , more important, in the reduction of the intermode coupling.

At moderate powers such a performance can be realized in circular cross-section cylindrical waveguides operating at the H_{01} mode. At higher powers a) quasi-cylindrical closed

corrugated-wall waveguides and b) open mirror waveguides are more effective.

Waveguide components for microwave monitoring and control. To be implemented into oversized (open or closed) waveguides and to exclude RF breakdown and overheating at high powers, microwave monitoring and control devices should be composed of smooth metallic surfaces. Recently a number of such components were developed[59], including:

a) waveguide switchers,

b) multiplexers,

c) wave splitters,

d) summators of mutually phase-locked waves,

e) universal polarizers (able to change any initial polarization of a wave to any desirable polarization),

f) bi-directional couplers.

Some of these components contain corrugated (sinus-like) metallic reflectors.

To match oversized waveguides and mirror lines to various loads, a number of quasi-optical elements (focusers, grills etc.) are proposed.

For more detail see [60].

PRESENT AND POSSIBLE APPLICATIONS OF HIGH-POWER MICROWAVES

Any advance of the high-frequency electronics to a new frequency band or a new level of power is usually favorable for development of traditional applications and for birth of new ones.

As for the *traditional applications* , it is quite evident that at higher powers and shorter microwaves

- in the *radio location* better coordinate resolution and

longer operation distances become available;

- more productive *plasma-chemical* processes in more dense gases can be realized;

- some kinds of *material processing* (local hardening of metal surfaces; coating of metals by dielectric films; sintering, joining and annealing of dielectrics and semiconductors) become more efficient.

A specific application of high power millimeter waves is the *electron cyclotron resonance heating*[61] *and current drive* in the magnetically confined *plasma*, the experiments being performed in the frame of the *controlled fusion* program. High power centimeter waves produced by gyrotrons seem perspective for the *current drive in the lower hybrid regime.* A broad field of application of high power millimeter and sub-millimeter waves to the *plasma* research is *diagnostics.*

High power microwaves are used to investigate *non-linear* processes in gases and plasma : *RF discharge, self-focusing* and *stimulated scattering of waves*[62,63]. These effects in their turn can be applied to the *plasma chemistry,* to producing *active medium for UV lasers,* to producing intense *beams of heavy ions* and *neutral particles*, to creation *artificial RF mirrors* in the atmosphere.

An interesting application of powerful millimeter and sub-millimeter waves is *the spectroscopy prohibited lines and small impurities* in gases [64]. An important application of sub-millimeter wave radiation of sufficiently large average power would be the *separation of isotopes* [65].

Another perspective application of high power microwaves is acceleration of particles to ultra-high energies in

super-colliders [66].

Let us hope for further mutually stimulating progress of both the high-power microwave sources and their applications.

REFERENCES

1. Physics of Quantum Electronics, vol. 7-9, Free-Electron Generators of Coherent Radiation, ed. by S.F. Jackson et al. (Reading , Mass : Addison-Wesley), 1980, 1982 .
2. High-Frequency Relativistic Electronics (collect. reviews), ed. by A.V. Gaponov-Grekhov, N-Novgorod, IAP,1979, 1981, 1983, 1984, 1987, 1990.
3. V.L. Ginzburg, Izv. Akad. Nauk SSSR, Ser. Fiz. , Vol.11, pp. 165-182, 1947.
4. M.I. Petelin, Radiofizika, Vol. 13, No. 10, pp. 1586-1588, 1970.
5. R.Q. Twiss, Austral. J. Phys., Vol. 11, No. 4, pp. 567-579, 1958.
6. J. Schneider, Phys. Rev. Lett., Vol.2, No. 12, pp.504-505, 1959.
7. R.H. Pantell, Proc. Symp. on Millimeter waves, N.Y., Polytechnic Press, vol. 9, p. 301, 1959.
8. A.V. Gaponov, Radiofizika, Vol.2, No.5, pp. 836-843, 1959.
9. V.V. Zheleznyakov, Radiofizika, vol.3, No.2, pp. 180-192, 1960.
10. A.V. Gaponov et al., Radiophys. Quantum Electron., Vol. 16, pp. 794-813, 1967.
11. V.A. Flyagin et al., IEEE Trans. Microwave Theory and Techn., Vol. 25, No. 6, pp. 514-521, 1977.
12. The Gyrotron (collect. reviews), ed. by V.A. Flyagin, N-Novgorod, IAP, 1981,1989.
13. R.H. Jackson et al., IEEE Journ. Quant. Electron., Vol. QE-19, No. 3, pp. 346-356, 1983.
14. V.L. Bratman et al., ibid., pp. 282-296.
15. F.S. Rusin, G.D. Bogomolov, in: Electronics of High Powers, ed. by P.L. Kapitza, Vol. 5, Moscow, Mir, pp. 45-51, 1968.
16. A.V. Gaponov et al., Proc. 10th Europ. Conf. on Contr. Fusion and Plasma Phys., Vol. 2, pp. 48-53, Moscow, 1981.
17. G. Bekefi and T.J. Orzechovski, Phys. Rev. Lett., Vol.37, pp.379-382, 1976.
18. N.F. Kovalev et al., Pisma v ZhTF, Vol. 3, pp. 1048-1051, 1977.
19. A.N. Didenko et al., Pisma v ZhTF, Vol. 4, pp. 10-13, 1978.
20. N.F. Kovalev et al., Copyright No. 720591 with priority 14.11.79, Bull. of Invent. No.9, 1980.
21. A.F. Alexandrov et al.,ZhTF, Vol. 51, pp. 1727-1730, 1981.
22. S.P. Bugaev et al., Pisma v ZhTF, Vol. 9, pp. 1385-1389, 1983 .
23. S.P. Bugaev et al., in [2], 1990, pp. 185-205.
24. V.L. Bratman et al.,Pisma v ZhTF , Vol. 14, No.1, pp. 9-13, 1988.
25. A.L. Goldenberg et al., in [12], 1989, pp. 20-39.
26. K. Kreischer et al., in this issue. Vol. 2, pp.713-725.
27. A.G. Luchinin, G.S. Nusinovich, ibid., pp. 55-72.
28. H. Jory et al., IEEE MTT-S, Int. Microwave Symp. Dig., N-Y,

pp. 99-101, 1980.
29. N.I. Zaitsev et al., Radiotekhn. i Elektron., Vol. 19, No. 5, pp. 1056-1060, 1974.
30. A.A. Andronov et al., Infrared Phys., Vol. 18, No.5-6, pp. 385-395, 1978.
31. I.I. Antakov et al., in this issue, Vol. 2, pp. 767-772.
32. V. L. Granatstein, Int. J. Electronics, Vol.57, No. 6, pp.787-799, 1984.
33. S.E. Graibil and S.V. Nablo, Appl. Phys. Lett., Vol.8, No.1, p.18, 1966.
34. S.P. Bugaev et al., ZhTF, Vol. 37, No.12, p.2206, 1967.
35. N.F. Kovalev et al., Pisma v ZhETF, Vol. 18, No.3,pp. 232-235, 1973.
36. Y. Carmel et al., Phys.Rev. Lett., Vol. 33, No.21, pp. 1278-1282, 1974.
37. E.B. Abubakirov et al., Proc. 8th Conf. High-power Particle Beams, Novosibirsk, Vol. 2, pp. 1105-1110 , 1990.
38. A.S. Elchaninov et al., Pisma v ZhTF, Vol. 6, No. 7, pp. 443-447, 1980.
39. G. Bekefi and T.J. Orzechovski, Phys. Rev. Lett., Vol. 37, No.6, pp. 379-382, 1976.
40. L.N. Chekanova et al., Proc. 4th Conf. High-Power Part. Beams, Palaiseau, pp. 839-845, 1981.
41. A.N. Didenko et al., Proc. 3d Conf. High-Power Part. Beams, Novosibirsk, Vol. 2, pp. 683-691, 1979.
42. V.L. Bratman et al., IEEE Trans. on Plasma Sci., Vol.PS-15, No.1, pp2-15, 1987.
43. E.B. Abubakirov et al., Proc. 8th Conf. High-Power Part. Beams, Novosibirsk, pp. 1105-1110, 1990.
44. S.P. Bugaev, ibid., pp. 1135-1140.
45. D. Shiffler et al., SPIE, Vol. 1226, Intense Microwave and Particle Beams, pp. 12-22 , 1990.
46. E.B. Abubakirov et al., ZhTF(Journ.Tech. Phys.), Vol. 60, No.11, pp. 186-190, 1990.
47. V.L. Bratman et al., 7th Symp. High-Current electronics, Tomsk, abstr., part 3, pp. 6-8 1986.
48. G. Bekefi et al., Appl. Phys. Lett., Vol. 54, No. 14, pp.1302-1304, 1989.
49. N.M. Bykov et al., Proc. 8th Conf. High-Power Part. Beams, Novosibirsk, pp. 1141-1146, 1990.
50. T.J. Orzechovski et al., Phys. Rev. Lett., Vol. 57, pp.2172-2175, 1986.
51. M.A. Allen et al., Phys. Rev. Lett., Vol. 63, No. 22, pp. 2472-2475, 1989.
52. P. Marie, L'onde Electrique, Suppl. special, 1957, Vol. 2, p. 471.
53. M. Jouguet, Cabl. et Trans., Vol. 1, No. 2, p. 133, 1947.
54. S.E. Miller, Bell System Technical Journal, Vol. 33, pp. 661-719, 1954.
55. N.F. Kovalev et al., Radiofizika, Vol. 11, No. 6, pp. 783-786, 1968.
56. S.N. Vlasov et al., Radiofizika, Vol. 15, No. 12, pp.1913-1918, 1972.
57. S.N. Vlasov et al., Radiofizika,Vol. 17, No. 1, pp.148-154, 1974.
58. D.V. Vinogradov et al., PCT Gazette, No. 16, pp. 47-49, 1990.
59. V.I. Belousov et al., in [12], 1989, pp.155-160.

60. M.Thumm, in this issue, Vol. 2, pp. 785-805.
61. V.V. Alikaev et al., Pisma v ZhETF, Vol. 15, No. 1, pp. 41-44, 1972.
62. A.G. Litvak, in: Reviews of Plasma Phys., Vol. 10, ed. M. Leontovich, N-Y - London, 1986, p. 2931.
63. A.G. Litvak, in this issue, Vol.1, pp. 267-286.
64. I.I. Antakov et al., Pisma v ZhETF, Vol. 19, No. 10, pp. 634-637, 1974.
65. A. Gover et al., Laser Focus World, Oct.1990, pp. 95-104.
66. J.H. Mulvey (ed.), CERN-87-07 (1987).

MILLIMETER-WAVE, MEGAWATT GYROTRON DEVELOPMENT FOR ECR HEATING APPLICATIONS

H. Jory, K. Felch, C. Hess, H. Huey, E. Jongewaard, J. Neilson, R. Pendleton, and M. Tsirulnikov

Varian Associates, Inc.
811 Hansen Way, Palo Alto, CA 94303 USA

ABSTRACT

To address the electron cyclotron heating requirements of planned fusion experiments such as the International Thermonuclear Experimental Reactor (ITER) and the Compact Ignition Tokamak (CIT), Varian is developing gyrotrons at frequencies ranging from 100-300 GHz with output power capabilities up to 1 MW CW. Experimental gyrotrons have been built at frequencies between 100-140 GHz, and a study program has addressed the critical elements of designing 280-300 GHz gyrotrons capable of generating CW power levels up to 1 MW. Initial test vehicles at 140 GHz have utilized $TE_{15,2,1}$ interaction cavities, and have been designed to generate short-pulse (up to 20 ms) power levels of 1 MW and up to 400 kW CW. Recently, short-pulse power levels of 1040 kW at 38 % efficiency have been obtained and average powers of 200 kW have been achieved. Long-pulse operation has been extended to pulse durations of 0.5 seconds at power levels of 400 kW. Gyrotron oscillators capable of generating output powers of 500 kW CW at a frequency of 110 GHz have recently been designed and a prototype is currently being tested. Design work for a 1 MW CW gyrotron at 110 GHz, is in progress. The 1 MW CW tube will employ an output coupling approach where the microwave output is separated from the spent electron beam.

1. INTRODUCTION

Gyrotron oscillators have been effectively employed in heating magnetically-confined plasmas, at the electron cyclotron resonance (ECR) frequency, in a variety of fusion experiments.[1] In these experiments, gyrotrons with long-pulse or CW output powers of a few hundred kilowatts have been utilized at frequencies up to about 100 GHz. However,

ECR heating in large, reactor-size fusion experiments, will require total input microwave power levels of 10-100 MW at frequencies ranging from 100 GHz to 300 GHz.[2]

To address this need, Varian is developing gyrotrons capable of generating power levels of 1 MW CW at frequencies in the range 100 GHz to 140 GHz. The basic design approach followed in the current gyrotron development program is significantly different than that of earlier efforts at lower frequencies and power levels. While most previous tubes were designed to generate output power in the TE_{0n} or circular-electric class of waveguide mode,[3,4] the current work utilizes TE_{mn} whispering-gallery modes where m>>n. In contrast to circular-electric modes, energy stored in a whispering-gallery-mode cavity is concentrated near the walls of the cavity, thereby requiring a relatively large-diameter electron beam for efficient interaction. The choice of whispering-gallery modes over other classes of interaction circuits is based on an intricate set of design trade-offs that include considerations of mode competition, ohmic losses in the cavity, efficiency, potential depression of the electron beam, and electron gun design.[5] Experimental research with whispering-gallery-mode gyrotrons is also being carried out at MIT,[6] Toshiba,[7] and in the Soviet Union.[8]

In working toward the 1 MW CW output power goal, several experimental vehicles will be constructed and tested to verify the design of the important elements of the gyrotron. The first two tubes in the program have been designed to generate short-pulse power levels of 1 MW and CW or long-pulse (> 1 second) power levels up to 400 kW at a frequency of 140 GHz. The testing of these tubes serves to validate the basic design of the electron gun and interaction circuit. In addition, operation at CW or long-pulse powers up to 400 kW provides useful information concerning whispering-gallery-mode operation at high-average-power levels.

The first experimental tube underwent a series of four tests, the final three following rebuilds of the tube that incorporated various design modifications indicated in the preceding test. During these tests a maximum peak power level of 820 kW and a maximum average power of 80 kW were obtained in the desired whispering-gallery mode at a frequency of 140 GHz. Pulse durations of 60 ms were obtained for output

powers of 400 kW.[9] A photograph of the first experimental tube with the 140 GHz superconducting magnet is shown in Figure 1.

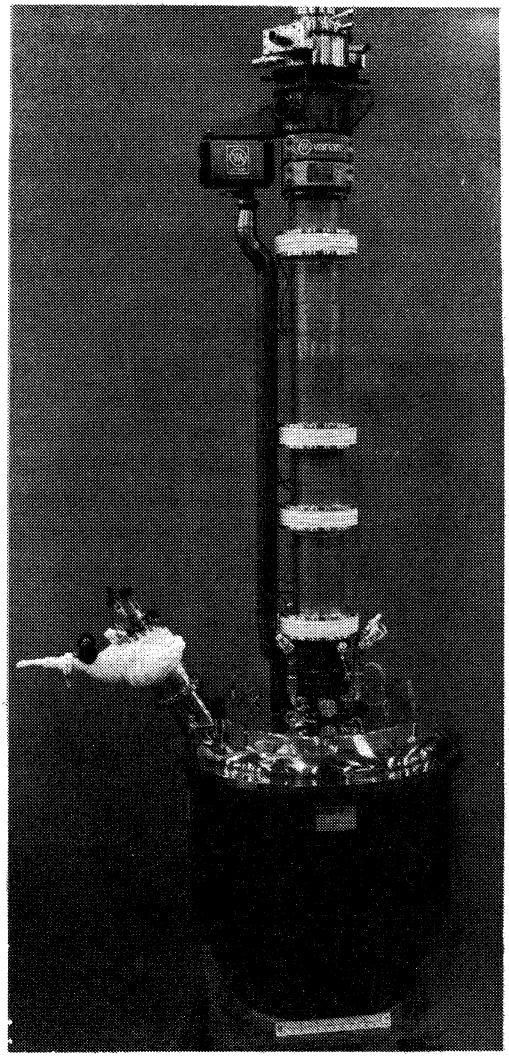

Figure 1. Photograph of first experimental 140 GHz gyrotron and superconducting magnet.

The second experimental tube has been tested and rebuilt twice. The second rebuild of this tube is currently being tested. The second tube was designed to test several new features aimed at overcoming some of the performance limitations of the first experimental tube. Salient features of the second experimental tube and a review of the experimental results to date will be discussed below.

CW gyrotron oscillators capable of generating 500 kW at a frequency of 110 GHz have recently been designed. These tubes will also employ whispering-gallery-mode cavities. The first experimental vehicle has been constructed and is currently being prepared for test.

Future test vehicles are now being designed to achieve full 1 MW CW operation. To be consistent with planned ECR heating experiments in the U.S., the design frequency has been changed from 140 GHz to 110 GHz. The basic philosophy underlying the 1 MW CW work is to extend the design of the 140 GHz, 1 MW pulsed, 400 kW CW test vehicles where possible and add new approaches or capabilities where necessary to achieve reliable 1 MW CW operation.

In the following we summarize the important design features of the second experimental gyrotron, review the results of the first two test iterations on the second tube, and discuss recent test results obtained during the third test sequence on the tube. We will summarize the design of the 110 GHz, 500 kW CW gyrotrons and discuss the major design issues for the first 1 MW CW experimental gyrotron.

2. DESIGN OF SECOND EXPERIMENTAL GYROTRON

The design concept of the second experimental 140 GHz, 1 MW gyrotron is similar to that of the first experimental tube.[9] The design is based on the interaction between a hollow electron beam provided by a magnetron injection electron gun and a simple, tapered cavity designed to generate power in the $TE_{15,2,1}$ mode at 140 GHz. The average radius of the electron beam in the interaction region coincides with the position of the first radial maximum of the electric field in the cavity. Computer simulations of the performance of the electron gun predict perpendicular velocity spreads of less than 5% for operation at a perpendicular to parallel velocity ratio of two. The nominal beam voltage and current for the gun

are 80 kV and 35 A, respectively, though operation at beam voltages of 90-100 kV and beam currents up to 50 A is possible. The magnetic field in the cavity and gun regions is provided by a superconducting magnet. For operation at 140 GHz, a magnetic field of 56 kG is required in the interaction region. The magnetic field in the electron gun is about 2.2 kG.

Output power from the cavity travels through the collector and out of the gyrotron through a double-disc, face-cooled window. The up and down tapers in the collector region are designed to preserve the purity of the generated $TE_{15,2}$ mode. The spent electron beam follows the diverging magnetic field lines out of the cavity and is deposited on the walls of the collector. Several magnetic field coils are employed in distributing the spent electron beam evenly along the collector.

New features in two areas of the tube, aimed at alleviating various problems experienced during the tests of the first experimental tube,[9] have been incorporated into the design of the second tube. Refinements to the beam tunnel have been included in the new tube design to further stabilize this region against spurious oscillations. Several modifications to the collector have been made to detect and prevent the type of damage sustained in the last set of tests on the first tube.[9]

3. TEST RESULTS ON SECOND EXPERIMENTAL GYROTRON

3.1 First test of second experimental gyrotron

During the first series of tests on the second experimental 140 GHz gyrotron, a peak output power of 940 kW was obtained at an efficiency of 35 %. Long-pulse and high-average-power tests were not performed on the tube during this test sequence due to arcing in the cavity region of the tube. The arcing was caused by high local gas pressures generated by various materials used in constructing the beam tunnel adjacent to the cavity.

3.2 Second test of second experimental gyrotron

Following the first test sequence on the second experimental tube, the tube was disassembled and reassembled with a new beam tunnel. The

material that was responsible for the outgassing that led to arcing in the interaction cavity was eliminated from the design.

The second series of tests on the second experimental tube were aimed at achieving high-average-power operation. Following initial short-pulse, parameter variation studies, the tube was aged to an average output power of 160 kW at a peak power of 345 kW. A repetition rate of 120 pps and a pulse duration of 3.9 ms were used in this test.

The second test sequence was cut short by a vacuum leak in the tube that occurred during a time when the tube was not in operation. Subsequent analysis of the tube indicated that the leak was in a cooling line and not related to the operation of the tube in any way.

3.2 Third test of second experimental gyrotron

Following the examination of the tube after the second test sequence, the defective cooling lines were replaced and the tube was reassembled for test. The third series of tests were begun in June 1990 and are still in progress.

During short-pulse operation, output powers up to 1040 kW at 38 % efficiency were obtained. Parameters for operation at 1040 kW are listed in Table I.

Table I
Parameters for 1040 kW operation during Third test of Second Experimental Gyrotron

FREQUENCY	140.155 GHz
OUTPUT POWER	1038 kW
PULSE DURATION	0.5 ms
REPETITION RATE	10 pps
BEAM VOLTAGE	80 kV
BEAM CURRENT	34.3 A
OUTPUT EFFICIENCY	38 %
MEASURED LOSSES	138 kW
TOTAL GENERATED POWER	1176 kW
INTERACTION EFFICIENCY	43 %

A plot of output power and efficiency as a function of beam current is shown in Figure 2. We note that the efficiency was relatively flat over the range of beam currents shown in the figure. Efficiency was optimized for each value of beam current by adjusting the cavity magnetic field and the gun-anode voltage (that controls the perpendicular-to-parallel velocity ratio, α). In general, the gun-anode voltage was increased to the point where current was drawn to the gun-anode electrode.

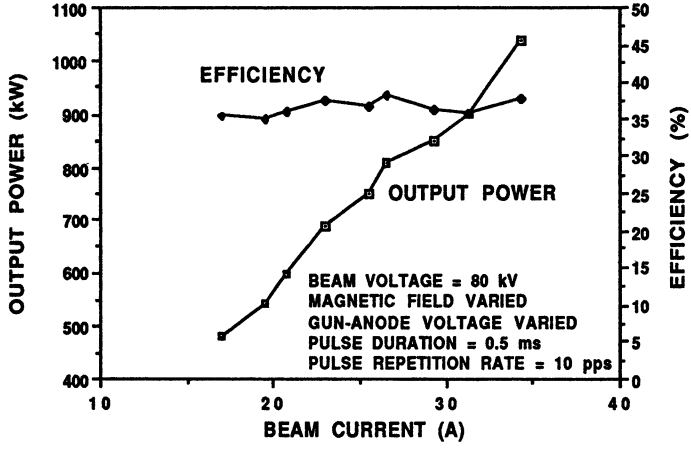

Figure 2. Output power and efficiency as a function of beam current during third test of second experimental gyrotron.

In Figure 3 we plot the value of α estimated from electron gun simulations for each experimental point shown in Figure 2. As noted on Figure 3, the maximum gun-anode voltage without gun-anode current generally decreased with current. This effect is thought to be due to increasing velocity spread with beam current.[10] The increased velocity spread leads to electron beam mirroring at lower values of α or gun-anode voltage. In addition to the lower achievable value of gun-anode voltage, the decrease in α with beam current is also due to the effects of increased space charge in the beam formation region of the electron gun.

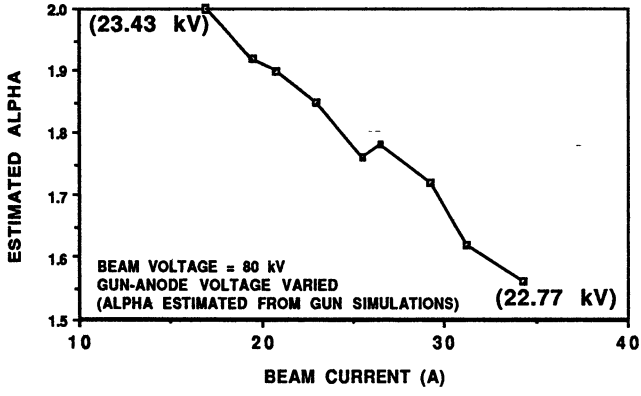

Figure 3. Estimated alpha (α) as function of beam current for experimental points shown in Figure 2.

In Figure 4 we have plotted the same experimental efficiencies as well as those predicted by self-consistent, large-signal calculations for α = 1.5 and 2.0. (The theoretical efficiencies have been adjusted to include the effects of rf losses measured in the tube.) These results show that there is

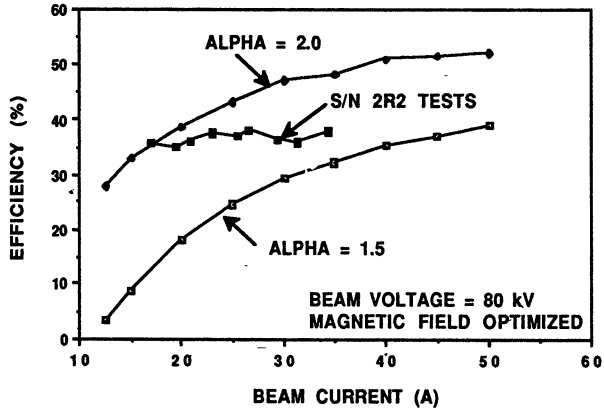

Figure 4. Comparison of theoretical efficiencies as a function of beam current with results obtained during third test of second experimental gyrotron.

good agreement between the observed and predicted efficiencies when the estimated value of α for each experimental point (see Figure 3) is used in the comparison.

At output powers of around 400 kW, short-pulse operation has been extended to duty factors of nearly 50 %, resulting in average output powers of 200 kW. Parameters for 200 kW average power operation are listed in Table II. The output efficiency for 200 kW average power operation was not optimized. Instead, tube parameters were adjusted to enable operation in a regime where tube performance was relatively insensitive to changes in the settings of various parameters (i.e. gun-anode voltage, beam current, cavity magnetic field, beam voltage, etc.).

Table II
Parameters for 200 kW average power operation during Third test of Second Experimental Gyrotron

FREQUENCY	**139.837 GHz**
OUTPUT POWER	**412 kW**
PULSE DURATION	**4.0 ms**
REPETITION RATE	**120 pps**
DUTY FACTOR	**48 %**
AVERAGE POWER	**198 kW**
BEAM VOLTAGE	**80 kV**
BEAM CURRENT	**17.2 A**
OUTPUT EFFICIENCY	**30 %**
MEASURED LOSSES	**61 kW**
TOTAL GENERATED POWER	**473 kW**
INTERACTION EFFICIENCY	**34 %**

Long-pulse operation has been extended to pulse durations of 500 ms at output powers of 350-400 kW. Operating parameters for 380 kW, 500 ms operation are summarized in Table III. Again, these tests were not carried out at optimum efficiency in order to remain at conditions that enabled operation over a wide range of parameter settings. During long-pulse operation, the frequency was monitored as a function of time during the pulse. This was accomplished using a harmonic-mixer based system, similar to one developed at KFK.[11] The intermediate frequency (IF)

produced in the harmonic mixer is directly displayed as a function of time on an HP 5371A Frequency and Time Interval Analyzer. Observed changes in the IF translate directly into changes in the gyrotron output frequency.

Table III
Parameters for 500 ms pulse operation during Third test of Second Experimental Gyrotron

FREQUENCY (end of pulse)	**140.066 GHz**
OUTPUT POWER	**384 kW**
PULSE DURATION	**500 ms**
REPETITION RATE	**0.01 pps**
DUTY FACTOR	**0.5 %**
BEAM VOLTAGE	**80 kV**
BEAM CURRENT	**17.1 A**
OUTPUT EFFICIENCY	**28 %**

An example of the frequency changes present during a 500 ms pulse are shown in Figure 5. As indicated in Figure 5, the frequency typically

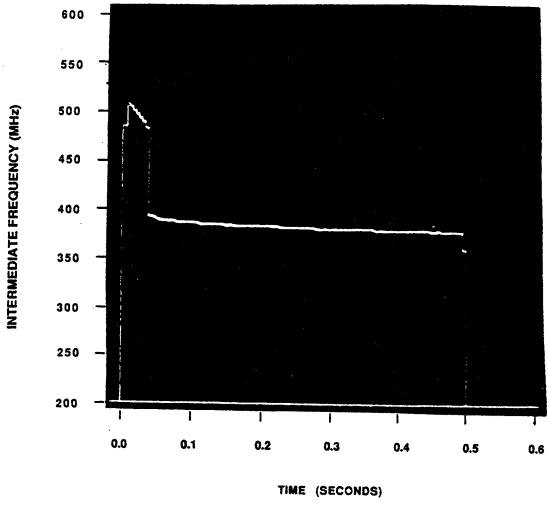

Figure 5. Frequency vs. time within a 500 ms pulse at 380 kW output power during third test of second experimental gyrotron.

takes a 50-100 MHz downward jump after the first 30-60 ms, then decreases quite slowly (about 2 MHz per 100 ms) during the remainder of the pulse. Variations in the frequency are attributed to thermally induced changes in the cavity and output window.

Further long pulse tests on the second experimental tube are still in progress. The current test plan is to extend long-pulse operation at 400 kW to pulse durations in excess of 1 second.

4. 110 GHz, 500 KW CW GYROTRON DESIGN

Gyrotrons capable of generating 500 kW CW at 110 GHz have been designed for ECR heating experiments. The tubes use the same basic approach as the 140 GHz, 1 MW pulsed, 400 kW CW experimental tubes described above, including the use of the $TE_{15,2,1}$ mode in the cavity. Major tube elements such as the electron gun, beam tunnel and cavity are somewhat larger in size as a result of the lower frequency. Power densities in the cavity for operation at 500 kW are somewhat lower than in the 140 GHz tube operating at 400 kW, as a result of the increased cavity size and the reduced ohmic losses at the lower frequency. (For a given mode, output power and loaded Q, power densities in the cavity scale as frequency to the -5/2 power.)

The diameter of the collector remains at five inches, but the collector length has been increased by 18 inches to accommodate the desired 25 % increase in power handling capability. The output window is virtually the same as the 3.5-inch diameter, double-disc design employed on the 140 GHz tubes, but is tuned for 110 GHz operation. Peak temperatures and stresses in the window for 500 kW operation at 110 GHz are similar to those predicted for 400 kW operation at 140 GHz.

The first 110 GHz, 500 kW prototype tube has been constructed and is currently in the initial stages of test.

5. 1 MW CW DESIGN CONSIDERATIONS

In order to extend the capabilities of the present 140 GHz, 1 MW pulsed, 400 kW CW gyrotron design to full 1 MW CW operation at a frequency of 110 GHz, several elements of the tube require additional

design work. The critical areas include the interaction cavity, output coupler, electron beam collector, and output window. Below we review the current design approaches being considered for each of these areas for inclusion into the first 110 GHz, 1 MW CW test vehicles.

5.1 Interaction cavity

In the interaction cavity, the ohmic losses in the cavity walls result in relatively high heat fluxes that must be removed by the cooling design. The present 140 GHz design, based on the $TE_{15,2,1}$ mode, should be capable of withstanding the heat fluxes present at CW power levels of between 400 and 500 kW. To reach 1 MW CW at 110 GHz would require only modest improvements to the 140 GHz, lower power design, due to the larger cavity size and increased ohmic Q present at the lower frequency. However, it has been decided to reduce the cavity power density to a level that is handled routinely in earlier production gyrotrons. This will be accomplished by using a higher-order, whispering-gallery mode in the cavity. A tentative cavity design, employing the $TE_{22,2,1}$ mode, has been chosen.

5.2 Output Coupler and Electron Beam Collector

The problems of output coupling and electron beam collection are interrelated. For full 1 MW CW operation, the electron beam collector must be significantly larger than the present design, that also serves as the output waveguide for the generated microwave power. Since mode conversion considerations preclude use of larger diameter collectors (without lengthening the tube significantly), methods of separating the electron beam from the microwave output are highly desirable. Two possible scenarios are currently being considered in addressing this problem.

5.2.1 Radial beam extraction. One method of separating the electron beam from the rf output provides for the radial extraction of the electron beam through a slot in the output waveguide, while the generated microwave power continues straight through the tube as in the classic design employed in most previous gyrotrons.

Of importance in this approach are the guidance of the electron beam through the gap introduced into the waveguide, mode conversion resulting from the gap, and rf leakage through the gap. A series of tradeoff analyses is currently being carried out to try to minimize these detrimental effects and allow an efficient electron beam/rf separation to take place.

5.2.2 Quasi-optical output coupler. The second approach allows for the radial extraction of the microwave power while the electron beam continues straight through to a large-diameter collector. This approach has been successfully used in Soviet gyrotrons,[8] with the incorporation of a quasi-optical coupler.

Quasi-optical techniques under development at Varian for output coupling include a modified form of the Vlasov coupler technique.[12] The main issues of any output coupling technique are the delivery of microwave power from the cavity to the external world and the delivery of that power in a useable form for highly efficient power transmission. These tenets are actually applicable, whether the coupler is internal or external to the gyrotron. Varian has set a goal to deliver 95% of the available power with typically a TEM_{00} mode purity of 95%. The question of determining mode purity should be addressed by fitting the measured data with a basis set of TEM modes and a final demonstration of low-loss transmission along a quasi-optical or a corrugated transmission line.

The simple analysis of the Vlasov coupler, see Figure 6, involves the propagation of a rotating whispering-gallery mode in circular waveguide characterized by a bounce angle, θ, with respect to the axis. Azimuthally, the waves are propagating between the wall and a caustic determined by $R[\cos(m/x'_{mn})]$ where R is the waveguide radius, m is the azimuthal mode number and x'_{mn} is the n^{th} root of $J'_m(x) = 0$. Assuming the proper helical cut for the rotating whispering-gallery mode, the radiation pattern can be represented by geometrical optics as shown in Figure 6. The azimuthal pattern ranges from an angle α to $-\alpha$ ($\alpha = \arccos(m/x'_{mn})$). The straight edge is the launching edge. The width of the aperture window is the distance from wall to the caustic. Typical experimental results are that about 85% of the power is directed towards the region specified by geometrical optics after one or two mirrors. Mirrors serve to correct much of the radiation pattern and transport it through the magnet bore and out of the gyrotron. However, high-power transmission with high efficiency

and good mode purity for further transmission have not been verified simultaneously.

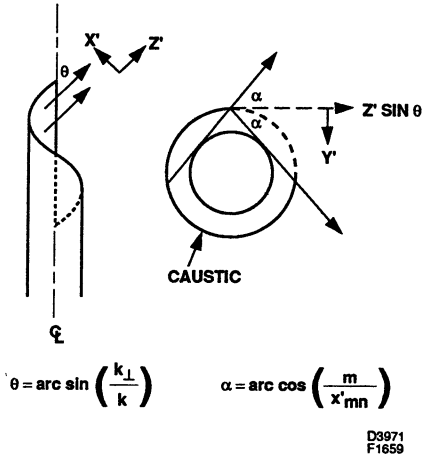

Figure 6. Schematic diagram of standard helical coupler showing geometrical optics representation.

Techniques to improve the Vlasov coupler include the modification of the launching edge by means of a curved lip or visor.[13,14] Another technique is to modify the helical cut to properly account for the path of the propagating plane waves in the waveguide.[14] Still another technique is to propagate a hybrid mode by using a corrugated circular guide as the coupler.[15]

The approach taken at Varian is to gradually transform the effective simple aperture gently by means of a horn or wing structure. The mechanical support for such a structure can be achieved by utilizing an option mentioned by Vlasov, et al.,[12] in which the region of the helical cut not intercepting the simple geometrical optic radiation pattern can still be the original wall of the cylindrical waveguide. The treatment of the helical coupler now as an aperture with a horn or wings (2,3, or 4 sides) leads to a simple effective aperture transition, see Figure 7. By properly shaping the size of the aperture, edge diffraction is also reduced. Control of the azimuthal spread of the horn or wings will also increase the gain of the coupler. This is advantageous for controlling the size of the mirrors. In fact, by controlling the shape of the horn for a plane parallel wave, this

structure can be closed and incorporate a window of rectangular cross section. The resultant highly overmoded rectangular waveguide can propagate a pure or mixed mode. The horn or converter structure can be corrugated for hybrid-mode propagation.

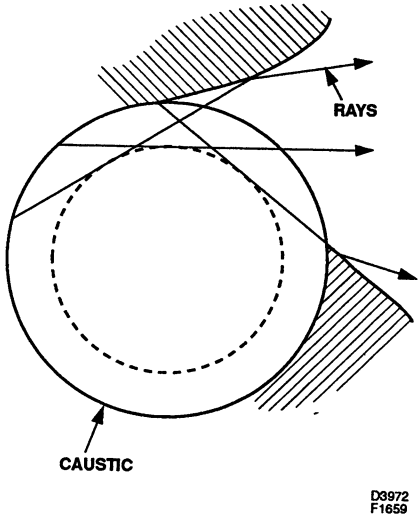

Figure 7. Schematic diagram of aperture/wing coupler geometry.

Another advantage of this aperture-wing technique is in the application of step tuning. In step tuning the gyrotron, the gyrotron is operated in successive azimuthal mode numbers with a fixed radial mode number. Due to the fixed cavity size, the gyrotron is operated at stepped frequencies corresponding approximately to the cutoff frequency of the mode. These modes will then propagate to the coupler with the same bounce angle with respect to the axis. However, in a standard-type Vlasov coupler, slight mode variations will result in different azimuthal angular spreads. In the Varian aperture-wing coupler the azimuthal spread of the set of modes can be controlled. This, of course still requires that the modes from the cavity all have the same rotational direction.

Preliminary low-power, cold-test results, utilizing a $TE_{6,1}$ mode at 66 GHz are shown in Figures 8-10. Mirrors are not used in this set of measurements to illustrate the zeroth order improvement. Figure 8 shows

the azimuthal pattern for a helical coupler. Both the azimuthal (φ) and polar (θ) polarizations are shown. Figure 9 illustrates the improvement of the aperture-wing coupler. A slight dip near the central region in each of the data sets is probably due to input mode impurities, about 5 %, created during the generation of the whispering-gallery mode. A comparison of the helical coupler and an aperture-wing design is shown in Figure 10. Preliminary calculations show that width A, denoted on the pattern of the helical coupler, contains about 77% of the total I_φ power scan (76% including the I_θ polarization). Width B contains 97% of the power (96% with both polarizations). Width C, for the aperture-wing result, contains 98% (96% with both polarizations). Further improvements are expected with the proper helical cut at the base of the aperture. Work is continuing to map the phase front and to determine the mode purity, and power transmission after two mirrors.

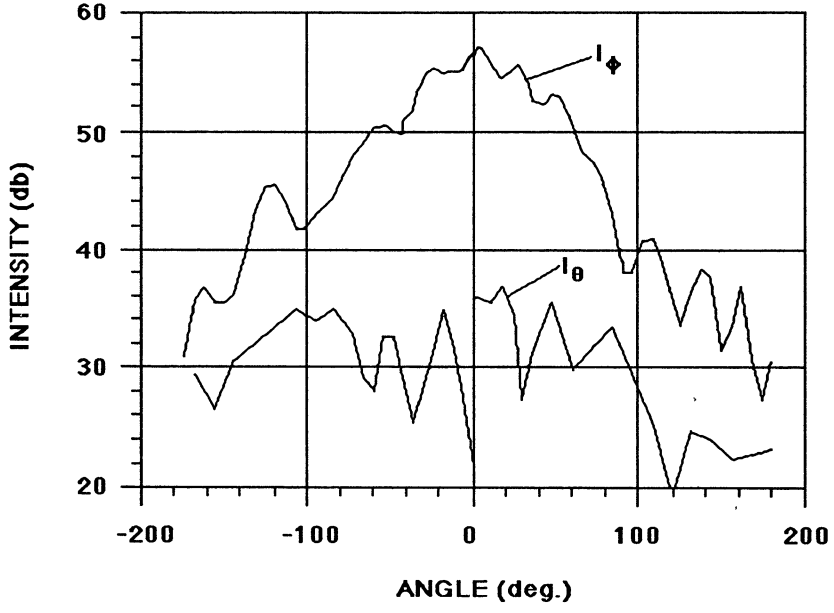

Figure 8. Radiation pattern from a helical coupler showing both polarizations.

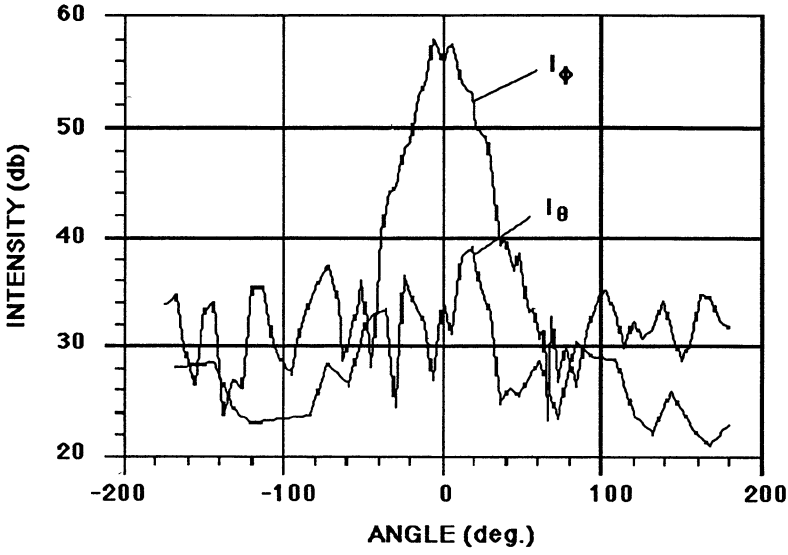

Figure 9. Radiation patterns for coupler with wings.

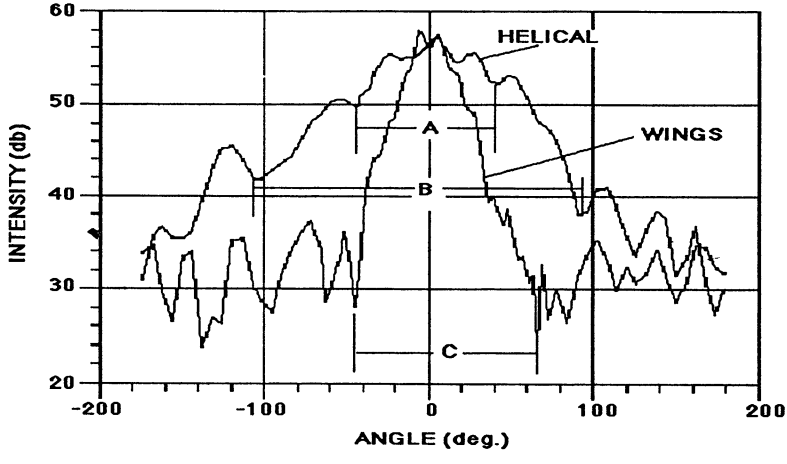

Figure 10. Comparison of radiation patterns from helical coupler and coupler with wings.

5.3 Output window

In any window design that is capable of passing 1 MW CW power levels, the major design limitations stem from the combination of thermal and mechanical stresses induced in the window. This environment calls for strong, low-loss window materials, and mechanical designs that minimize the static stresses due to window coolant and tube vacuum pressures and thermally induced stresses due to rf power absorbed by the window.

The specific geometry of the output window design depends on which output coupling approach is chosen. In the case of the quasi-optical output coupling approach, long, narrow rectangular windows can be made large enough to spread the output power from the tube sufficiently to allow safe operation. For the radial beam extraction configuration, enhanced versions of the existing circular, double-disc design may be employed. The present design is capable of 400 kW CW at 140 GHz, but calculations on new designs predict capabilities up to 1 MW CW at 140 GHz. For operation at 110 GHz, window losses are reduced significantly so that an even greater safety margin should exist.

6. CONCLUSIONS

The results obtained during the most recent tests performed on the second experimental 140 GHz gyrotron have essentially met the 1 MW pulsed and 400 kW CW or long-pulse goals of the initial test vehicles. These results also represent an important step in reaching the 1 MW CW goal of the current development program. Tubes based on the 140 GHz, 1 MW pulsed, 400 kW CW design will be useful in a variety of ECR heating applications in several present-day fusion experiments. Tests on the first 110 GHz, 500 kW CW prototype tube are now in progress. Design work is well underway in preparation for the fabrication of the first experimental 110 GHz, 1 MW CW gyrotron.

ACKNOWLEDGMENT

The 1 MW gyrotron oscillator is being developed under contract with Lawrence Livermore National Laboratory, operated by the University of California for the U. S. Department of Energy, under Prime Contract W-7405-eng-48.

REFERENCES

1. R. Prater, V. S. Chan, and T. C. Simonen, "The Status of Electron Cyclotron Heating and Current Drive and the Role of DIII-D," GA Technologies Report No. GA-A18795, May 1987.

2. K. Kreischer, T. Grimm, A. Mobius, and R. Temkin, "The Design of Megawatt Gyrotrons for the Compact Ignition Tokamak," 13th Int. Conf. Infrared and Millimeter Waves, Conference Digest, 1988, pp. 179-180.

3. H. Jory, "Status of Gyrotron Development at Varian Associates," Proc. 4th Int. Symp. on Heating in Toroidal Plasmas, 1984, Vol. 2, pp. 1424-1430.

4. K. Felch, R. Bier, L. J. Craig, H. Huey, L. Ives, H. Jory, N. Lopez, and S. Spang, "Achievements in the CW Operation of 140 GHz Gyrotrons," 11th Int. Conf. Infrared and Millimeter Waves, Conference Digest, 1986, pp. 43-45.

5. K. E. Kreischer, B. G. Danly, J. B. Schutkeker, and R. J. Temkin, "The Design of Megawatt Gyrotrons," IEEE Trans. Plasma Science, 1985, Vol. PS-13, No. 6, pp. 364-373.

6. T. L. Grimm, K. E. Kreischer, W. C. Guss and R. J. Temkin, "Experimental Study of High Frequency, Megawatt Gyrotrons," 14th Int. Conf. Infrared and Millimeter Waves, Conference Digest, 1989, pp. 81-82.

7. T. Sugawara, et al., "500 kW Whispering Gallery Mode Gyrotron," 14th Int. Conf. Infrared and Millimeter Waves, Conference Digest, 1989, pp. 336-337.

8. Valery A. Flyagin and Gregory S. Nusinovich, "Gyrotron Oscillators," Proc. IEEE, 1988, Vol. 76, No. 6, pp. 644-656.

9. K. Felch, J. Feinstein, C. Hess, H. Huey, E. Jongewaard, H. Jory, J. Neilson, R. Pendleton, D. Pirkle, and L. Zitelli, "Design Considerations in Achieving 1 MW CW Operation with a Whispering-Gallery-Mode Gyrotron," International Electron Devices Meeting, Washington, D.C., Technical Digest, 1989, pp. 755-758.

10. K. Felch, R. Bier, L. J. Craig, H. Huey, L. Ives, H. Jory, N. Lopez, and S. Spang, "CW Operation of a 140 GHz Gyrotron," Int. J. Electronics, 1986, Vol. 61, No. 6, pp. 701-714.

11. G. Gantenbein, T. Geist, and G. Hochschild, "Instantaneous Frequency Measurements on a Gyrotron Output Signal," 14th Int. Conf. Infrared and Millimeter Waves, Conference Digest, 1989, pp. 221-222.

12. S. N. Vlasov, L. I. Zaygryadskaya, and M. I. Petelin,"Transformation of a Whispering-Gallery Mode, Propagating in a Circular Waveguide, into a Beam of Waves," Radio Engineering and Electronic Physics, Oct. 1975, Vol. 20, pp.14-17.

13. S. N. Vlasov, M. Shapiro, and E. Sheinina, "Beam Shaping in the Diffraction of a Whispering Gallery Wave at a Convex Cylindrical Surface," University News-Radiophysics, Vol. 31, No.12, 1988, pp. 1482-1486.

14. M. Iima, et al., "Measurement of Radiation Field from an Improved Efficiency Quasi-optical Converter for Whispering Gallery Mode," 14th International Conf. on Infrared and Millimeter Waves, Conference Digest, 1989, pp. 405-406.

15. A. Mobius and M. Thumm, "Operation of a Helically Cut Quasi-Optical Antenna with Hybrid Modes," 14th International Conf. on Infrared and Millimeter Waves, Conference Digest, 1989, pp. 390-391.

RESEARCH AT MIT ON HIGH FREQUENCY GYROTRONS FOR ECRH

K. Kreischer, T. Grimm, W. Guss, R. Temkin, and K.Y. Xu.

M.I.T. Plasma Fusion Center
Cambridge, MA., USA

Abstract

Research continues at MIT on high frequency (100-300 GHz) megawatt gyrotron oscillators suitable for ECR heating of fusion plasmas. Recent experiments include operation of a two-section cavity in the $TE_{16,2,1}$ mode at 148 GHz. Powers up to 1.2 MW were generated with a 78 kV, 48 A beam, yielding an efficiency of 32%. A peak efficiency of 39% was measured at 26 A. We are continuing our efforts to understand discrepancies between the measured and theoretical efficiencies at high current. Capacitive probes were installed to determine the average beam velocity ratio α. It was found that as the current increased, α corresponding to the highest output power decreased. At 35 A, the measured α was about 1.5, compared with a design value of 1.93. This reduction in α partially explains the discrepancy. We have also operated the gyrotron in a 14 T Bitter magnet into the submillimeter wave regime. Frequencies from 141 GHz ($TE_{15,2,1}$ mode) up to 328 GHz ($TE_{27,6,1}$ mode) were measured. Even though the cavity is highly overmoded at 328 GHz, output powers remain quite high, with a peak output power of 375 kW. Even better results were obtained in the $TE_{22,5,1}$ mode at 267 GHz, where a peak power of 537 kW was produced. The sequence of modes observed was consistent with the predicted coupling between the electron beam and rf field. Initial testing of a 1 MW, 280 GHz gyrotron is planned for early next year.

Introduction

Interest in ECR heating of fusion plasmas has grown in recent years. Advantages of ECRH include efficient, bulk heating of the plasma close to the magnetic axis, and the use of localized heating to modify the temperature profile and suppress plasma disruptions. ECRH can also be used in conjunction with an ion heating system, such as neutral beams, to produce a more balanced heating process and improve stability, or for current drive. From an engineering standpoint, ECRH sources can be located well away from the high radiation that exists near the plasma, and can utilize simple launching structures. Recent

experiments [1] indicate efficient ECR heating with local power deposition is possible, and that it is competitive with alternative heating techniques.

The main obstacle to ECRH has been the lack of suitable sources that can produce high power at the appropriate frequencies (100-300 GHz). However, the rapid development of novel, high power millimeter wave sources has mitigated this problem. In particular, extensive research over the past decade on the gyrotron has shown it to be a viable source for ECRH. The gyrotron is particularly attractive because it is very efficient, compact, and operates at low, cw voltages ($<$ 100 kV). A large, international research effort has been established to study the gyrotron and determine its power and frequency capabilities. Powers up to 2.1 MW [2] and frequencies up to 328 GHz have been produced in ECRH-relevant experiments.

As gyrotrons operate at higher powers and frequencies, it becomes necessary to operate in higher order modes in order to maintain cavity ohmic losses at reasonable levels (below 2 kW/cm^2). Parametric studies [3] indicate that the index ν_{mp} of the lowest order $\mathrm{TE}_{m,p,1}$ mode that can be utilized is given by the equation

$$(\nu_{mp}^2 - m^2) = \frac{2470\mu\beta_{\|}P(MW)\nu^{2.5}(GHz)}{\beta_{\perp}^2\rho_{ohm}(W/m^2)} \tag{1}$$

where $\mu = \pi\beta_{\perp}^2 L/\beta_{\|}\lambda$, $\beta_{\perp}$ and $\beta_{\|}$ are the perpendicular and parallel beam velocities normalized to c, ν and λ are the radiation frequency and wavelength, ρ_{ohm} is the average cavity ohmic losses, and L is the characteristic length of the axial rf field profile. Typically, $\mu \approx 15$, $\beta_{\perp} \approx 0.45$, and $\beta_{\|} \approx 0.25$. The cavity diameter D can be related to λ by the equation $D/\lambda = \nu_{mp}/\pi$. Early experiments were based on the $\mathrm{TE}_{0,1,1}$ mode with $D/\lambda \approx 1$. Present experiments between 100 and 150 GHz have cavities with $D/\lambda \approx 5 - 10$, and the proposed MIT 1 MW, 280 GHz experiment will have a cavity with $D/\lambda \approx 20$. As D/λ increases, mode competition becomes more severe and high efficiency becomes harder to achieve.

The goal of the MIT program is to demonstrate new techniques for achieving efficient, single mode emission and improved output coupling in high frequency, megawatt gyrotrons. This includes the development of new diagnostics of gyrotron performance, thus allowing more rigorous comparison of experimental and theoretical results. We also are developing techniques for efficiently converting the high order modes of the gyrotron into a radiation beam that can be transmitted to a plasma. The long term goal of the M.I.T. program is to determine the highest powers that can be generated by high frequency gyrotrons suitable for ECRH. This research should provide the data needed to make a proper comparison between gyrotrons and alternative heating sources.

The MIT gyrotron operates at a low duty cycle ($\leq$4 Hz with 3μsec pulses). However, the cavity and electron gun are designed to be scalable to continuous (cw) operation. The magnetron injection gun was built by Varian and produces an annular beam with a theoretical $\beta_\perp/\beta_\parallel$ of 1.93 and a spread in $\beta_\perp$ of 4% at 80 kV and 35 A. The design magnetic compression is 30. The beam has a radius of 0.53 cm and thickness of 0.5 mm in the cavity region, and the current density when running at 35 A is 380 A/cm^2. The radiation produced is transmitted to the window by a copper waveguide with a typical diameter of 3 cm. The output window is either a single disk of fused quartz, or a broadband motheye window [4] with minimal reflection over a wide frequency range. The entire system is demountable for simple modification, and a gate valve between the gun and beam tunnel facilitates cavity changes. Two gyrotron test stands are presently available. The first uses a 6.5 T superconducting (SC) magnet with a six inch warm bore. The second has a 14 T Bitter magnet with a four inch bore, and allows us to generate frequencies up to 350 GHz. Both operate from a common, 20 MW pulsed power supply capable of 150 kV and a ripple less than $\pm$1%. Both also have a small gun coil for optimizing the beam quality.

Much of our experimental research has been based on the single, tapered cavity operating in asymmetric modes ($TE_{m,p,1}$ where $m \neq 0$). At the megawatt level, we have concentrated on operation in surface modes ($m \gg p$), which are situated close to the resonator wall. These modes provide good coupling between the rf field and electron beam, and reduced mode competition. Voltage depression due to the space charge field is also reduced. For our $TE_{15,2,1}$ experiments at 140 GHz, a depression of 3.3 kV was calculated for $R_e/R_o = 0.7$, where R_e and R_o are the beam and cavity radii. This corresponds to placement of the beam on the first radial maximum of the rf field. Potential problems with surface modes are the need for good alignment to avoid beam interception, and higher ohmic losses.

Efficiency Studies

A list of the theoretical and experimental characteristics of the cavities that we have investigated can be found in Table I. The best results in all three cases were achieved on the SC magnet test stand when operating in the $TE_{16,2,1}$ mode at 148 GHz. All the cavities were designed to operate near the minimum $Q = 4\pi(L/\lambda)^2$ in order to keep ohmic losses as small as possible. Self-consistent nonlinear theory [5] indicates efficiencies between 45% and 55% should be possible for these designs. The theoretical efficiency η_{TH} was calculated at 80 kV and 35 A, and was reduced by a total of 15% to account for an ohmic loss of 7% in the cavity, uptaper, and output waveguide, a calculated 5% dielectric loss in the output window, and other smaller losses. When operating at the maximum power P_{MAX}, we generally measured efficiencies between 22% and 32%. In all cases the best efficiencies η_{MAX} were obtained at lower currents, typically around 20-25 A.

Table I. Theoretical and measured characteristics of the MIT gyrotron

	Short	Long	Two–Section
L/λ	4.8	6.0	6.3
Q	311	468	508
I_{ST} (A)	4.2	1.8	1.5
P_{TH} (MW)	1.26	1.40	1.46
η_{TH} (%)	45	50	52
P_{MAX} (MW)	0.93	0.77	1.2
η (%)	22	26	32
V (kV)	104	84	78
I (A)	40	36	48
η_{MAX} (%)	30	34	39

This reduction in efficiency at higher currents is highlighted in Fig. 1. This figure shows results from our first experiments, which used the long cavity. The voltage was fixed at 70 kV, and the magnetic fields at the cavity and gun were optimized. We found that the measured efficiency saturated at low current, and remained relatively constant (between 25% and 35%) over a broad range of currents (5A to 30A). Two theory curves are shown, one based on an $\alpha = \beta_\perp/\beta_\parallel$ of 1.93, and the other on beam velocities as measured by our capacitive probe [6]. Both theory curves indicate that the efficiency should peak at 30-35 A, in contrast to our observations of a peak at lower currents. Our capacitive probe indicates that α decreases from 2.0 at 5A to 1.55 at 35A. This reduction is consistent with our experimental observation that, for fixed beam voltages, it is necessary to raise the gun magnetic field at higher beam currents, and therefore reduce the magnetic compression, in order to achieve high power, stable operation and avoid arcing in the electron gun. Figure 1 indicates that a reduction in α partially explains the lower efficiencies at higher currents.

Various attempts were made to increase the output power beyond the 770 kW generated at 84kV and 36A. These included operating in $TE_{m,2,1}$ modes other than the $TE_{16,2,1}$, tuning the cathode power supply to produce a flatter pulse, using windows of different thicknesses, and running at higher beam voltages and currents. In all cases the improvement was minimal. Tapering of the magnetic field in the cavity was also investigated. Tapering becomes more difficult at higher frequencies because of the higher magnetic fields required and the need to taper over a shorter axial distance. In our case, a modest taper of $\pm 1.5\%$ was possible. Both positive and negative tapers were tried with the $TE_{16,2,1}$

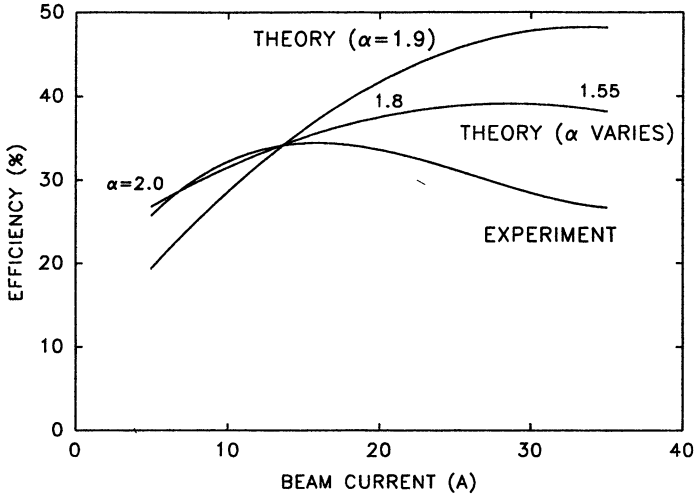

FIG. 1 Comparison of theory and experiment for the long cavity

mode, and in both cases the efficiency dropped about 10% compared to the uniform field results. One possible explanation is deleterious effects on the gun performance when the SC magnetic field is tapered. When the taper is introduced, it is not localized to the cavity region, and the entire axial field profile is modified. Finally, a new cavity with a shorter interaction length was designed and tested. It was hoped that by reducing the cavity Q that the higher efficiencies would shift to higher current. Also, this cavity has a higher starting current I_{ST} of 4.2 A. Multimode theories [7] suggested that mode competition might become a problem if the ratio of the operating current to I_{ST} becomes too large. However, this cavity produced lower efficiencies than the long cavity, probably due to the shorter L (see Table I).

The two-section cavity was selected for our next experiment. This cavity consists of two cylindrical sections of slightly different radii, followed by a linear uptaper. The two cylindrical sections produce an rf axial field profile with a long tail at the cavity input. This tail is known to slightly perturb the beam, causing the electrons to form a tighter bunch that enhances the final efficiency [8]. Simulations confirm these results (see Table I.). This cavity also produces higher efficiencies than our previous cavities for α less than 1.9. For example, when α is 1.5, the two-section cavity can achieve 45% compared to 33-41% for the long and short cavities. The diameters of the two sections are only slightly different, and virtually no mode conversion is produced. Ohmic losses are comparable to

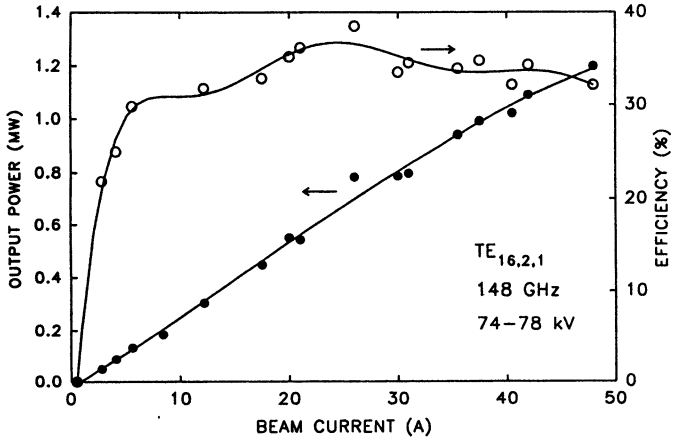

FIG. 2 Experimental results for the two-section cavity.

the other cavity designs.

The input cylindrical section of the two-section cavity was made relatively long to prevent rf leakage back towards the gun. Also, no input taper was included. It was hoped elimination of this taper would prevent higher order axial modes from becoming trapped in the cavity. However, calculation of the cold cavity properties indicated that the second axial mode could exist with a Q of about 600, comparable to the desired mode. Fortunately, simulations with the beam present indicated that this mode should be weak, and that the first axial mode should dominate. It was also hoped that removal of the input taper would reduce competition with transverse modes. This would happen because the frequency of such a mode would increase by about ω/Q due to pulling, and would therefore not be cutoff at the cavity input. This would increase leakage for this mode and lower its Q.

The results of our experiments are shown in Figs. 2-4. In Fig. 2, the maximum emission as a funtion of beam current is shown. For each setting, the magnetic fields at the cavity and gun were optimized. In all cases, single mode emission was observed in the $TE_{16,2,1}$ with a frequency of about 148 GHz. A maximum power of 1.2 MW was obtained at 48 A, for an efficiency of 32%. As in our earlier studies, the efficiency rises quickly as the current is increased, and remains relatively constant between 30% and 40%. A maximum of 39% was measured at 26 A. A comparison between theory and experiment is shown in Fig. 3. The α values shown were obtained with our probe, and again they decrease as the

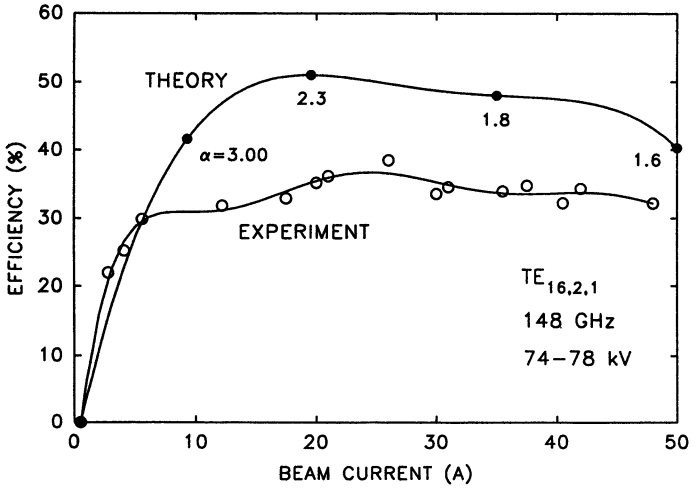

FIG. 3 Comparison of two-section cavity results with theory.

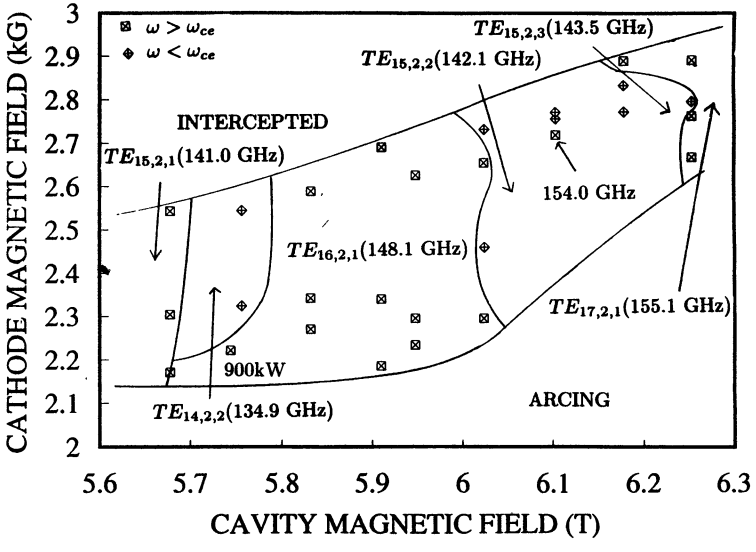

FIG. 4 Mode map for 74 kV, 35 A operation.

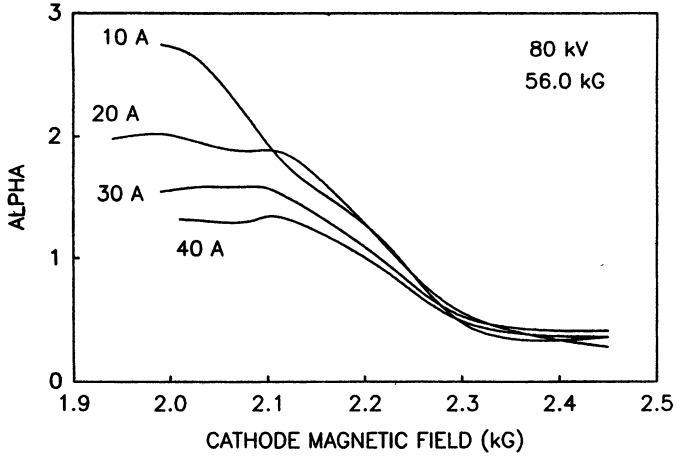

FIG. 5 Measured average α for 1 MW, 140 GHz gun.

beam current increases. Although the discrepancy continues to exist between theory and experiment, it is smaller for this cavity. Also, the variation in α seems to be responsible for the saturation of the efficiency. A detailed mode map is given in Fig. 4 for operation at 74 kV and 35 A. Only the cathode and cavity magnetic fields were varied to generate the data. As the cathode field is increased, the beam expands leading to interception before the cavity. If this field is too small, some of the electrons are mirrored, resulting in an arc. This is consistent with adiabatic theory. The dominant modes are the $TE_{m,2,1}$, which are separated by weaker regions of $TE_{m,2,2}$. The frequencies are in good agreement with theoretical values. No emission was observed in the $TE_{m,3,1}$ modes, which were the main competing modes in the long and short cavity. Based on a comparison of ω and ω_c, it was found that the backward branch of the $TE_{m,2,2}$ modes was being excited. Theory indicates [9] that this branch is more accessible than the forward branch. Access to the forward branch is blocked by the stronger $TE_{m,2,1}$ modes during startup of the gyrotron. The highest power of 900 kW occurs at low cathode magnetic fields where α is the highest. The detuning parameter $\Delta = 2/\beta_\perp^2(1 - \omega_c/\omega\gamma)$ for this operating point is 0.56, consistent with theory.

In addition to the study of novel cavities, we are also developing diagnostics to measure the beam spatial and velocity characteristics. We have impacted the beam on a tantalum foil to produce images. Our concern was that instabilities, such as the diocotron instability, could be causing filamentation of the beam. The images indicated that the beam

density is uniform, and measurements of the diameter and thickness agree with theoretical predictions. To measure the average velocity properties, a capacitive probe was installed in the beam tunnel just before the cavity. This probe consists of two concentric cylinders that measure the static radial electric field of the nonneutral beam. which is then related to the beam density. From this and the current, an average parallel velocity is determined which in turn gives the average α. The capacitive probe works as a passive diagnostic and allows the power and α to be measured simultaneously. No effect on gyrotron performance has been seen.

Probe measurements have shown that α generally agrees with adiabatic theory in its scaling versus cathode magnetic field and anode voltage. An example is shown in Fig 5, which shows how the MW gun operates in the Bitter magnet. At large cathode magnetic fields, α is small as expected. As the field is reduced, α increases and then saturates. The saturation level is dependent on the beam current, and decreases as the current increases. For a 35 A beam, the maximum α measured was between 1.4 and 1.6, well below the design value of 1.93. At present the explanation for this saturation is not known.

We are also developing diagnostics to measure the velocity spread. Theory indicates that perpendicular spreads in excess of 10% are needed before the efficiency is substantially reduced. Two approaches that we have investigated are a retarding potential [10], and measurement of the starting current. In the first approach, a slotted plate selects a small portion of the beam, which is then collected by a plate biased by a repelling voltage. The change in the collected current as this voltage is varied gives the $\beta_{\|}$ electron distribution function. This diagnostic must be carefully designed to minimize the effects of secondary emission and reflected electrons. Measurement of the starting current does not directly measure the distribution function, but can give an indication of the amount of spread present. A short cavity was designed with a starting current of 35 A when α is 2. When a parallel spread of 30% is present (assuming a Gaussian distribution), the current is reduced to 18 A. Tests with this cavity are now in progress.

Submillimeter Operation

We have observed fundamental, submillimeter emission by operating up to 13 T with a Bitter magnet. These experiments were based on the long cavity described in Table I. The diffractive Q ranges from 460 at 140 GHz to 2300 at 328 GHz. A sequence of $TE_{m,p,1}$ modes with p=3 through 6 was excited by varying the cavity magnetic field B_o. This step tunability is shown in Fig. 6. Changing B_o causes a series of discrete modes to be excited in the cavity. For each mode in Fig. 6, the cathode magnetic field B_k was adjusted to

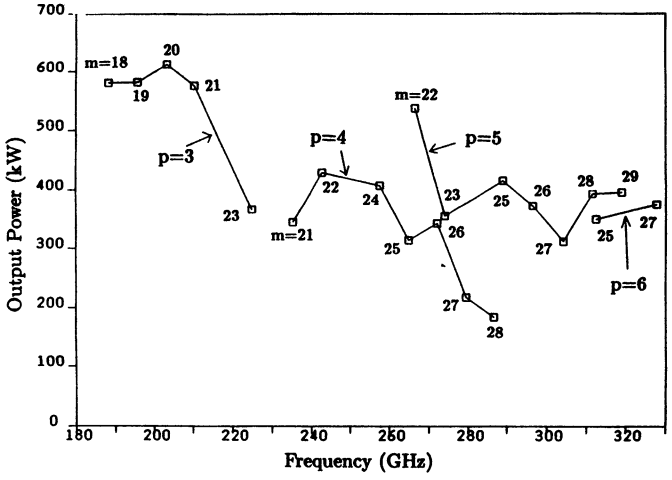

FIG. 6 Step tuning through a sequence of $TE_{m,p,1}$ modes with an 80 kV, 35 A beam

maximize the output power. Output power was measured outside a fused quartz output window. Window losses are about 2% at 180 GHz and increase to greater than 13% at 330 GHz. Although the electron gun design was optimized for operation at 140 GHz, this data indicates that a high quality beam is produced over a wide range of frequencies. The power levels are generally between 300 and 600 kW, and depend on the coupling strength between the beam and rf field, as well as the beam α.

The sequence of modes observed is consistent with the radial position of the beam within the cavity. Nonlinear theory indicates that the coupling between the beam and rf field scales as $J_{m\pm1}(2\pi R_e/\lambda)$, where R_e is the beam radius and the choice of sign depends on the azimuthal rotation of the mode. The strongest coupling occurs when the beam interacts with the first maximum of $J_{m\pm1}$, that is, when $2\pi R_e/\lambda \approx \nu_{m\pm1,1}$. For modes with $m >> 1$, this expression can be written as $2\pi R_e/\lambda \approx m \pm 1$. As B_o is increased, resulting in operation at shorter λ, R_e decreases slightly due to higher magnetic compression B_o/B_k, but the λ scaling dominates. Therefore higher m modes are excited at higher frequencies, as is observed. The radial index p is determined by the relative position of the beam and cavity wall. The cavity radius R_o was chosen such that the beam would couple to the first radial maximum of the $TE_{15,2,1}$ mode at 140 GHz. This also results in strong coupling to neighboring $TE_{m,2,1}$ modes when B_o is varied. As B_o is increased, higher magnetic compression is required to produce a high α beam necessary for strong

emission. This causes the beam to move away from the wall, and eventually the beam decouples from the $p = 2$ modes and couples to the first radial maximum of the $p = 3$ modes. This process continues until the strongest coupling at 328 GHz is to the $p = 6$ modes.

The results at 328 GHz ($TE_{27,6,1}$) represent the highest powers generated by a gyrotron in the submillimeter region. For an 80 kV, 15 A beam the output power and efficiency of the $TE_{27,6,1}$ mode was 214 kW and 18% respectively. At 35 A the power increased to 375 kW for an efficiency of 13%. This corresponds to 430 kW and an efficiency of 15% when window losses are excluded. Although the cavity is highly overmoded at 328 GHz, with a cavity diamter of 16.4λ, the power remains quite high. This suggests that mode competition has not strongly limited the operation of the gyrotron and prevented access to the high efficiency regime. The major problem, especially in pulsed experiments, is exciting the desired mode first so that it can suppress neighboring competing modes.

Even better results were obtained in the $TE_{22,5,1}$ mode at 267 GHz. The output power and efficiency for this mode as measured after the window is shown in Fig. 3. Window losses are about 9%. At each beam current the emission was maximized by varying B_k. The mode was excited by beam currents up to 45 A with a maximum efficiency of 27% and power of 330 kW at 15 A. This power increased to 537 kW at 35 A for an efficiency of 19%. As in our 140-150 GHz measurements, the highest efficiencies occurred at lower currents.We also found that the $TE_{22,5,1}$ mode could be excited over a wide range of parameters, again suggesting that mode competition was not a major limiting factor.

280 GHz Experiments

The next major U.S. tokamak project is C.I.T., an ignition device with a nominal magnetic field of 10 T. This experiment will need 0.5-1 MW gyrotrons operating between 250 and 300 GHz. Although we have already achieved similar parameters, the cavity used was too small to be cw relevant (i.e., ohmic losses were too high). Equation (1) indicates that operation in a very high order $TE_{m,p,1}$ mode, with $(\nu_{mp}^2 - m^2)^{0.5} > 60$ is required. A list of the parameters of the first experiment can be found in Table II, together with the present 140 GHz parameters. The major constraints on the 280 GHz design were the cavity ohmic losses (limited to an average of 2 kW/cm^2), the anode-cathode electric field in the gun (kept below 80 kV/cm to avoid breakdown) and the gun radius smaller than the magnet bore radius. The last constraint allows the gyrotron tube to be assembled and baked outside the magnet, as is presently done with industrial tubes. The cost of the magnet scales strongly with bore size, so there is a strong incentive to keep the bore diameter small. Table II indicates many 280 GHz parameters are similar to parameters of our present experiment, giving us confidence that the experiment will be successful. The

Table II. 1 MW Design Parameters

	140 GHz	280 GHz
Current(A)	35	37
Voltage(kV)	80	90
η_T(%)	36	30
Velocity ratio	1.93	1.6
Beam radius(cm)	0.53	0.75
Cavity radius(cm)	0.75	1.25
Cavity length(L/λ)	6.0	7.0
Diffractive Q	450	620
Magnetic compression	30	44
Cavity current density(A/cm^2)	384	660
Beam thickness(r_L)	3.85	4.2
Voltage depression(%)	4.0	5.6
Emitter radius(cm)	2.89	4.9
Mode	$TE_{15,2,1}$	$TE_{42,7,1}$
Mode separation(GHz)	7.2	4.5

major changes are the radial dimensions of the cavity and beam, and the need to operate in a very high order mode. For our experiments the beam has been postioned on the first radial peak for maximum coupling.

The two major components are a 12 T SC magnet and 1 MW electron gun. The magnet is being built by Wang NMR and contains both NbTi and Nb_3Sn coils. Specifications include a five inch warm bore, field dropoff to 0.3 T at the gun emitter, low helium losses, quench protection, and an optional linear taper of 4%/inch. The main parameters of the gun were calculated using adiabatic theory. Using the highest anode-cathode electric field consistent with cw operation (80 kV/cm), a gun with a magnetic compression of 44 was designed. This gun has an emitter radius of 4.95 cm, and will operate at 90 kV and 50 A. The Herrmannsfeldt gun code was used to optimize the electrode shapes. A design was found with a perpendicular velocity spread of $\pm$5.0%. Initial operation of this experiment is expected in the first half of 1991.

Acknowledgements

This research is supported by the Department of Energy under Contract DE-AC02-78ET51013. The Bitter magnet was provided by the Francis Bitter National Magnet Laboratory. The research described in this paper was conducted by the MIT gyrotron group, which includes M. Blank, M. Basten, J. Casey, T. Grimm, W. Guss, A. Li, R. Temkin, and K.Y. Xu. The author also wishes to thank W. Mulligan and G. Yarworth for their assistance.

References

[1] R. Prater *et al.* in *Plasma Physics and Controlled Fusion*, 1988, Proceedings Twelfth International Conference, Nice (IAEA, Vienna, in press).

[2] A. Sh. Fix *et al.*, Int. J. Electron. **57**, 821 (1984).

[3] K.E. Kreischer, B.G. Danly, J.B. Schutkeker, and R.J. Temkin, IEEE Trans. Plasma Science **PS-13**, 364 (1985).

[4] J.Y.L. Ma and L.C. Robinson, Opt. Acta **30**, 1685 (1983).

[5] A. Fliflet, M. Read, K. Chu, and R. Seeley, Int. J. Electron. **53**, 505 (1982).

[6] W.C. Guss, T.L. Grimm, K.E. Kreischer, J.T. Polevoy, and R.J. Temkin, MIT report PFC/JA-90-13, submitted to J. Appl. Phys. (1990).

[7] O. Dumbrajs, G. Nusinovich, and A. Pavelyev, Int. J. Electron. **64**, 137 (1988).

[8] Yu. V. Bykov, A. L. Goldenberg, Radiophys. Quantum Electronics **18**, 1066 (1975).

[9] K.E. Kreischer and R.J. Temkin, Int. J. Infrared Millimeter Waves, **2**, 175 (1981).

[10] E.G. Avdoshin and A. L. Goldenberg, Radiophys. Quantum Electronics **16**, 461 (1973).

POWERFUL 80-150 GHz GYROTRONS

V.E.Zapevalov, A.N.Kuftin
Institute of Applied Physics, Academy of Sciences of the USSR
46 Uljanov Street, 603600 Gorky, USSR

The electron-cyclotron plasma heating requires millimeter wave sources with an output power about 1 MW or more and pulse duration 1 s or more. At present gyrotrons seem to be the most promising sources in this frequency range [1-4].

In a gyrotron (Fig. 1) the active medium is a flow of electrons moving along helical (in the interaction space) paths, which is produced by an adiabatic magnetron-injector gun. In this system the cathode-emitted electrons move along quasitrochoidal paths in weakly inhomogeneous crossed fields. The electric field component, parallel to the magnetic field, ensures the electron injection into the intermediate region next to the gun. In the intermediate region the electrons move in an increasing magnetic field and, therefore, their oscillatory energy grows. In the interaction region the electrons move in a homogeneous magnetic field B_0, which corresponds to the operating wavelength:

$$\lambda\,(mm) \simeq 10.7/n\,B_0\,(T) \qquad (1)$$

(n is the number of the resonant cyclotron harmonic).

In the collector region the electrons move in a decreasing magnetic field, their oscillatory energy falls while the mean radius of the beam increases ensuring the dissipation of its energy over a large area.

The electrodynamic system of a gyrotron is formed by a section of weakly-inhomogeneous waveguide with cutoff narrowing from the electron gun side and smooth tapering to the output waveguide from the collector side. In other words, this is essentially an open resonator with diffraction output of the radiation.

The problem of separating the electron beam and the output radiation can be solved efficiently by use of a built-in quasi-optical converter shown in Fig. 1 [2]. In this case, the electron beam can be spread over the large area of the collector and the output radiation is converted to a more convenient form for transport to the plasmas.

An increase in operating frequency, output power and pulse duration causes a number of serious problems.

One is due to the formation of an electron beam with sufficiently large oscillatory energy and small spread of oscillatory velocities [1]. Since the spread of total electron energies in a helical electron beam is negligible (in the typical case of small depression of the potential), the spread of longitudinal and transverse electron velocities are related by

$$\delta v_{\parallel} \simeq g^2 \cdot \delta v_{\perp} \qquad (2)$$

where g is the pitch-factor of the electron beam. Since $g \geq 1$, at moderate values of $\delta v_{\perp}$ the quantity $\delta v_{\parallel}$ can be rather significant. An appreciable velocity spread leads to a noticeable decrease in gyrotron efficiency and even to the electron flow instabilities.

For the optimization of electron-optical systems with the aim to minimize the velocity spread we have developed an effective method of numerical simulation. The influence of the factors, which cannot be simulated by a computer, is investigated experimentally. Fig. 2 a shows the dependences of the relative oscillatory energy $t_{\perp} = g^2/(1+g^2)$ and the velocity spread on the beam current for an optimized electron-optical system of a gyrotron at f = 82 GHz. Similar dependences for the preceding commercial gyrotron of the same wavelength range are given for comparison in Fig. 2b. Clearly, the optimization of the electron-optical systems improved substantially the electron beam.

High output power and efficiency require not only high quality of the electron beam but also the mode selection [2]. The point is that in an oversized resonator the mode spectrum is overdense and, therefore, the cyclotron resonance conditions can be satisfied for a few neighboring modes. The mode interaction in a gyrotron is, as rule, the mode competition and can lead to unstable generation, reduced efficiency and complete cutoff of the operating mode generation. Usually, the

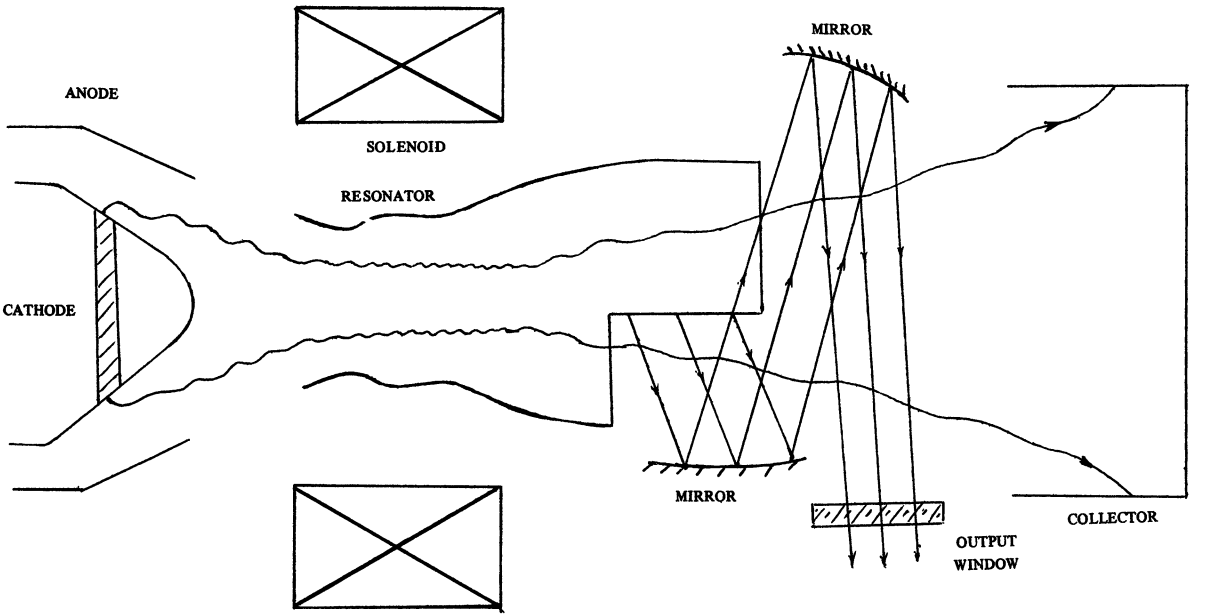

Fig. 1. General scheme of a gyrotron

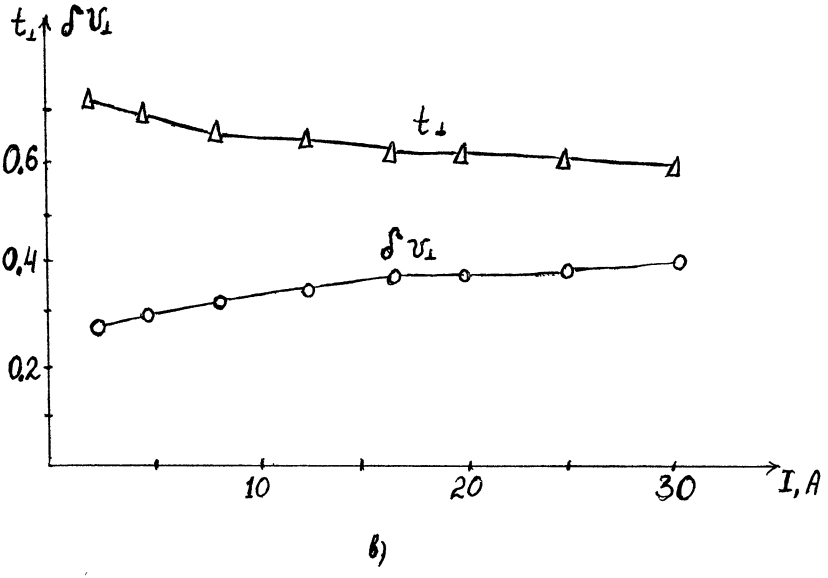

в)

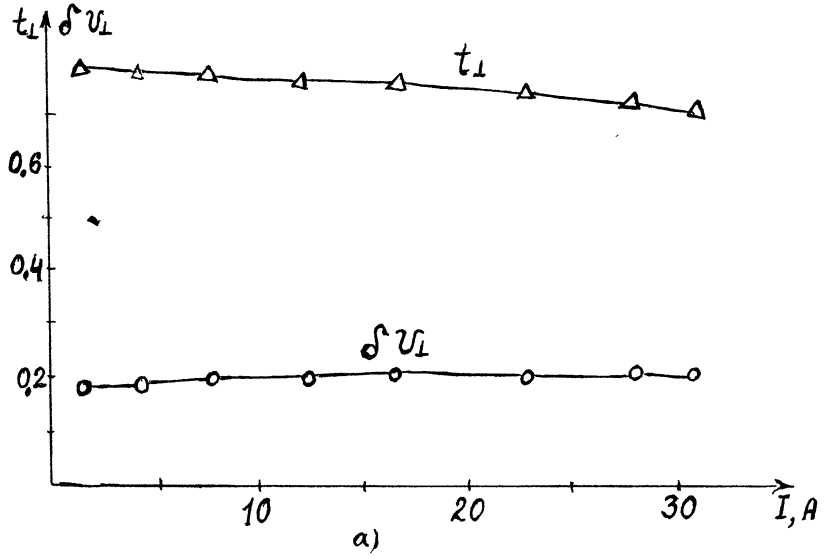

а)

Fig. 2. Relative oscillatory energy and velocity scattering as functions of the beam current

mode selection is performed by decreasing the Q-factor of parasitic modes and their coupling impedance with the electron beam.

Fig. 3 shows calculations for the generation region of a gyrotron intended for plasma heating on T-15 tokamak (λ = 3.6mm). The solid lines indicate the start-up currents of the operating and the parasitic mode in terms of the linear theory. The dashed lines indicate the oscillation boudary in the region of rigid self-excitation. The circle denotes the point of maximum efficiency for the operating $TE_{11,3,1}$ mode. Besides the proper selection the choice of this mode yields admissible ohmic loss density on the resonator walls (about 2 kW/cm^2 at P_{output} = 1MW).

The experimental dependence of output power on magnetic field at fixed voltage and beam current (Fig. 4) confirms the proper selection of the mode. The dependences of output power and efficiency at the operating mode on beam current in the gyrotron for plasma heating on T-15 tokamak are given in Fig. 5. Similar dependences for the gyrotron developed earlier for plasma heating on T-10 are given for comparison (dashed lines in Fig. 5).

The next gyrotron with an operating frequency 100 GHz was developed for future plasma heating experiments on T-15 tokamak; the maximum output power was 0.5 MW (at efficiency $\eta \simeq$ 50 %) and 1 MW (at efficiency $\eta \simeq$ 40 %).

Another gyrotron version operated at 110 GHz and had a built-in quasioptical operating mode converter to the Gaussian beam. The dependences of output power on the magnetic field at a fixed beam current and different accelerating voltages are given in Fig. 6a, and at a fixed voltage and different beam currents, in Fig. 6b. An output power 1 MW was achieved at an efficiency about 40 %.

The ECRH and current drive experiments in a future tokamak ITER require a gyrotron complex with a wavelength about 2 mm and the pulse output power over 2 s. In this case, one encounters the same but still more acute problems and the new ones:

1. The problem of the formation of high-quality intense polyhelical electron beams. It causes technological headaches and makes one to improve the methods for computer analysis of electron beams.

2. The operating mode selection in the oversized electrodynamic system of a gyrotron: For admissible ohmic loss density

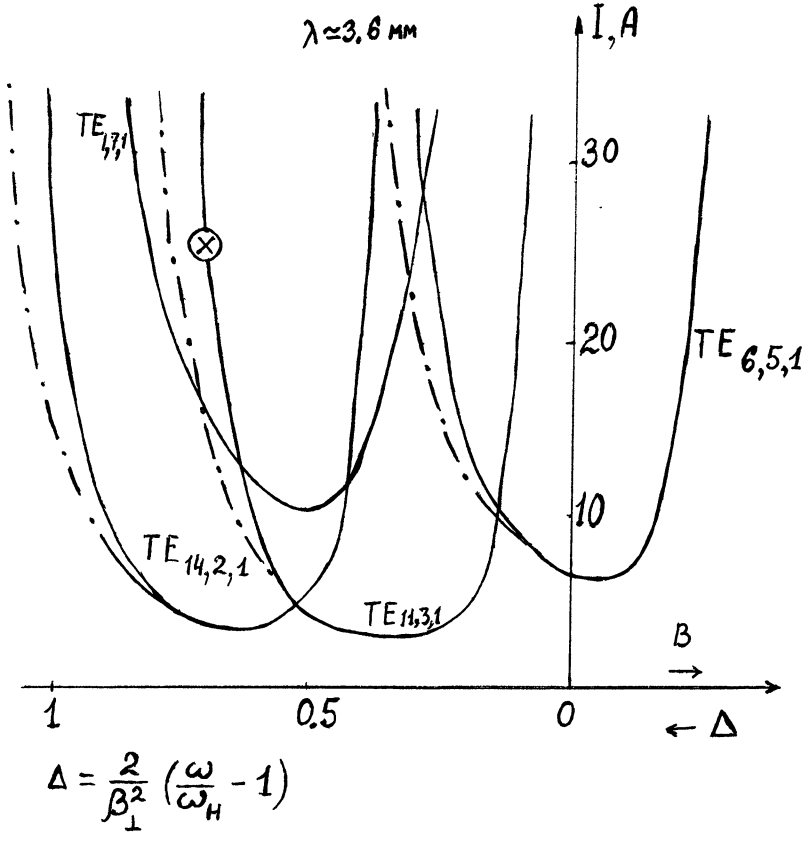

Fig. 3. A calculated region of the gyrotron generation

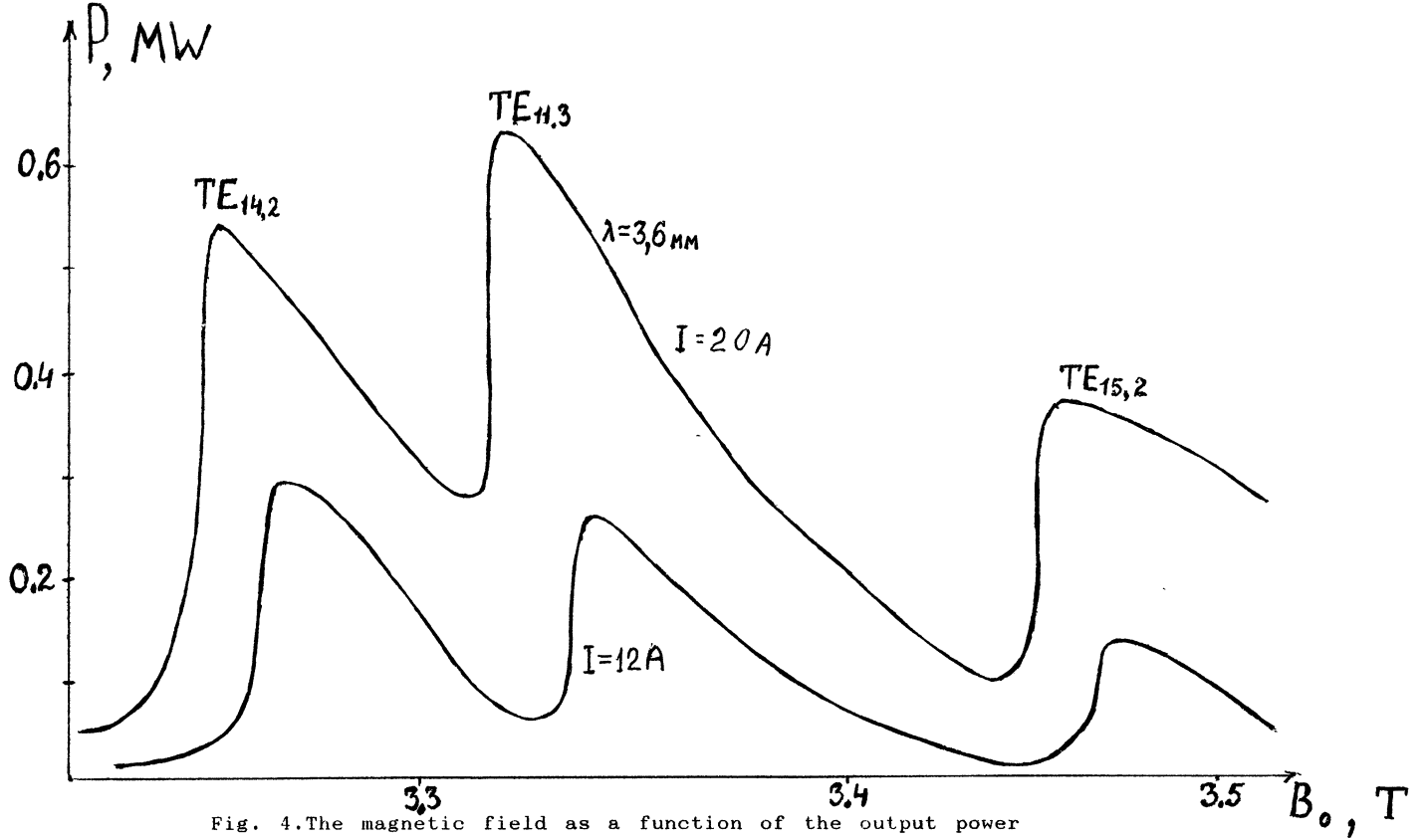

Fig. 4.The magnetic field as a function of the output power

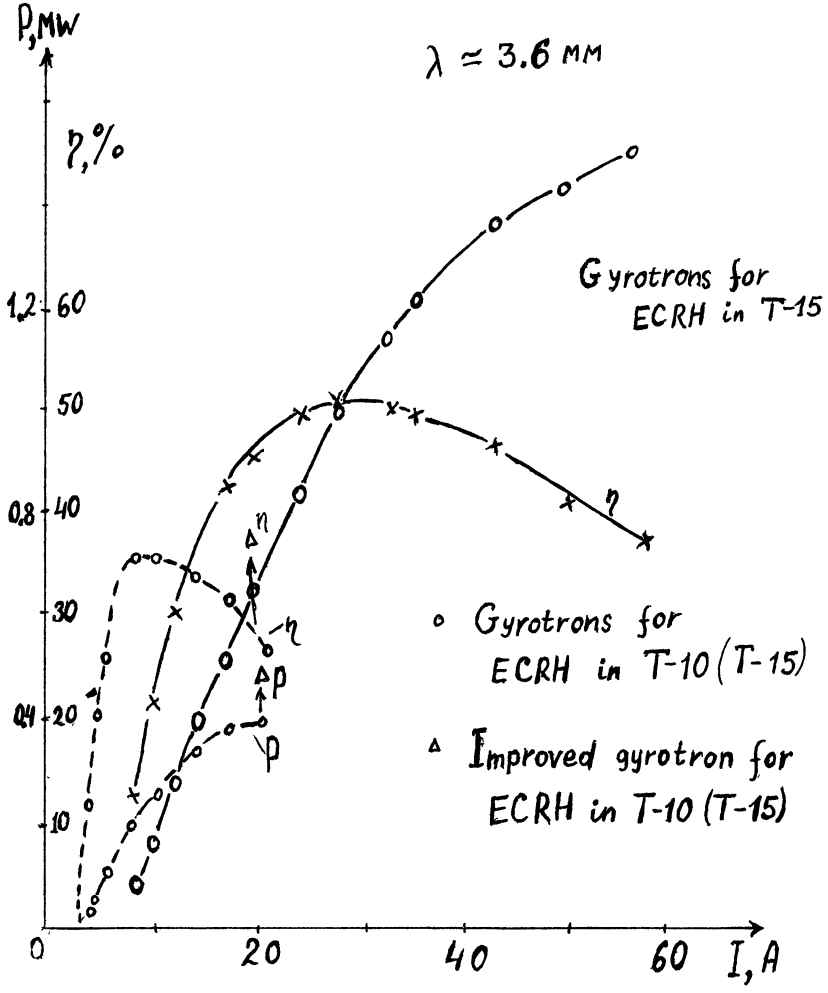

Fig. 5. The output power and efficiency as functions of the beam current

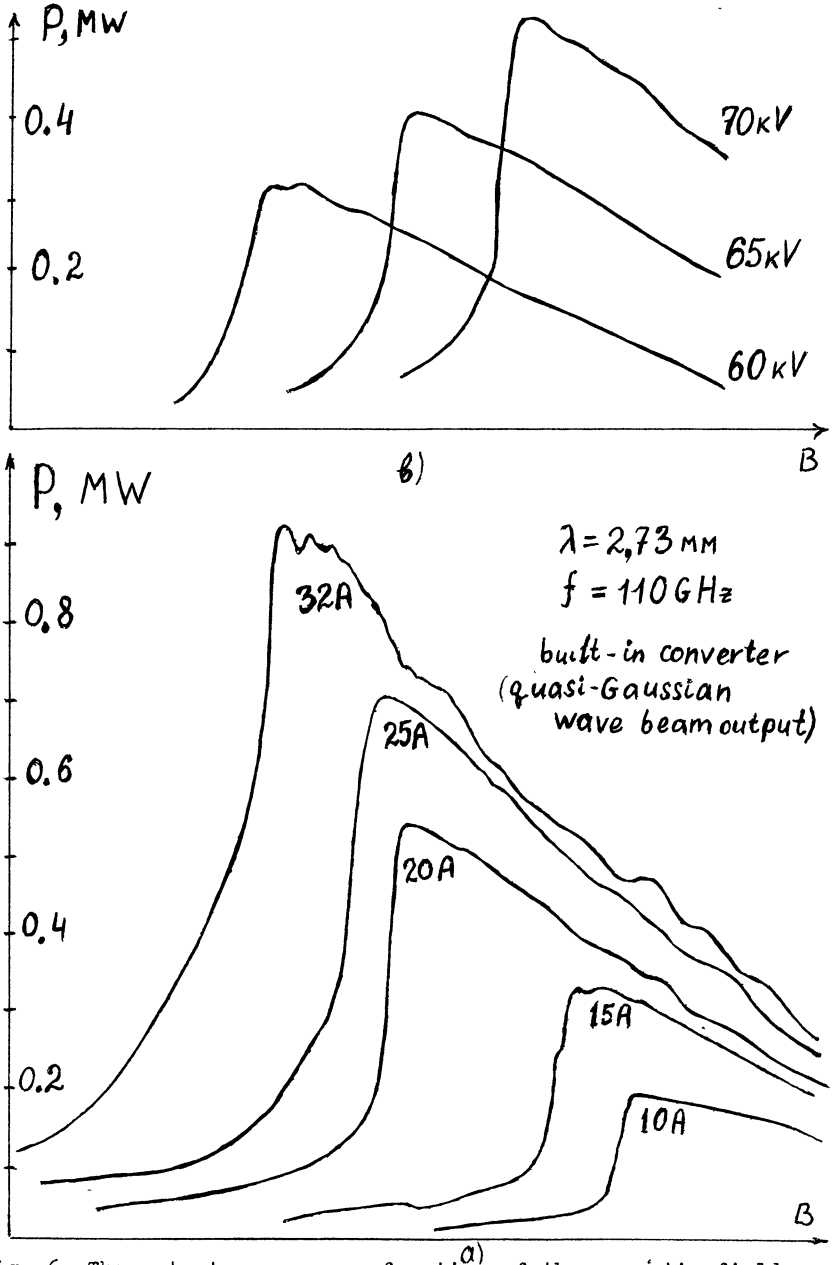

Fig. 6. The output power as a function of the magnetic field

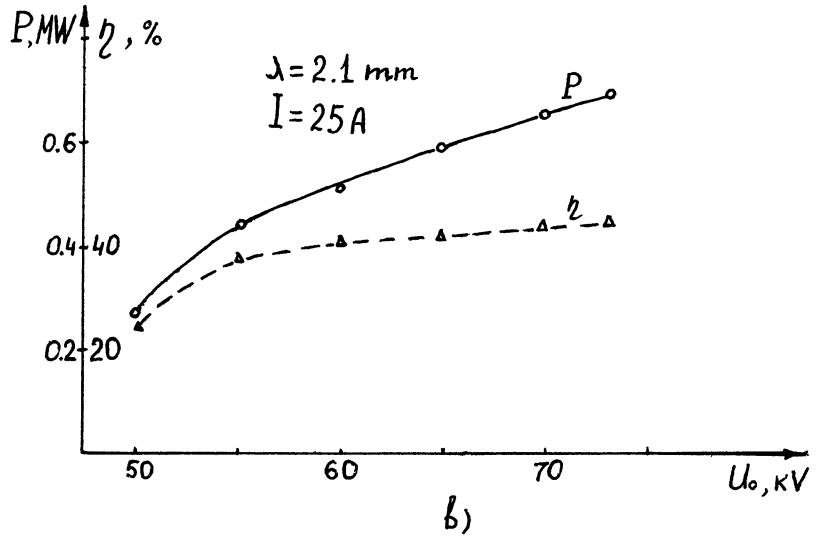

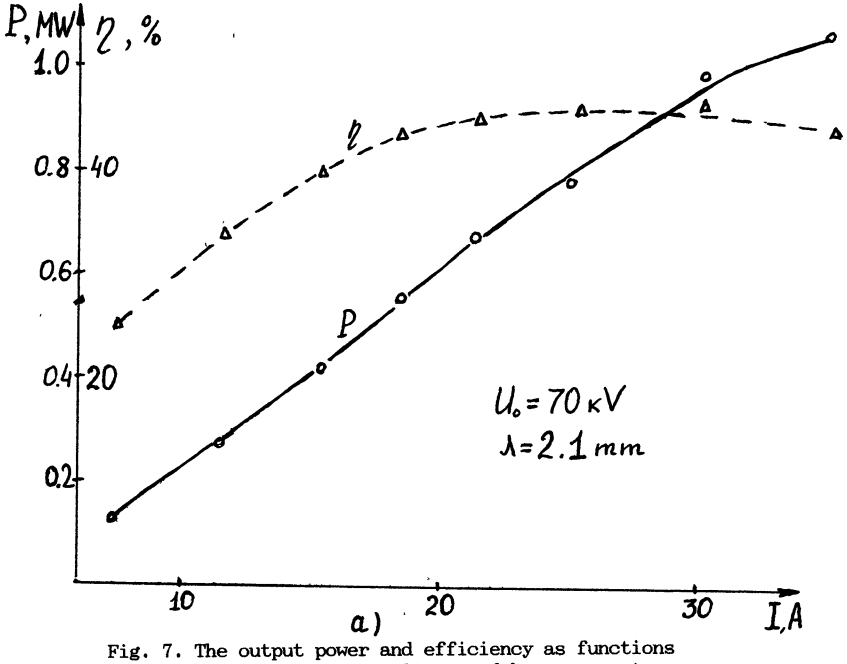

Fig. 7. The output power and efficiency as functions of accelerating voltage and beam current

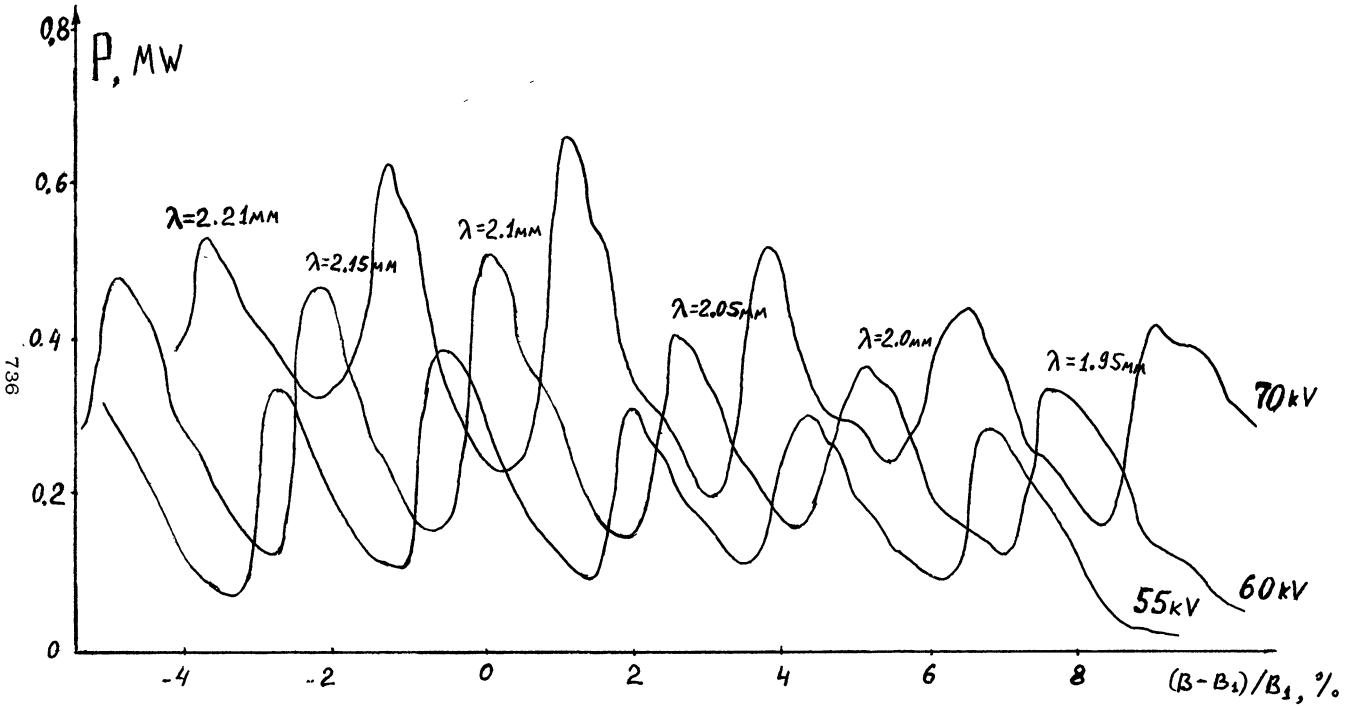

Fig. 8. The gyrotron output power and frequency of the generation as a function of the magnetic field

2 kW/cm^2 the resonator should have the diameter $D/\lambda \geq 15$.

3. The collector heating (separation of the electron beam and the output radiation is desirable).

4. The output window heating.

To overcome the thermal difficulties one needs highly efficient cooling systems. In particluar, the American colleagues proposed a sapphire window with liquid nitrogen cooling to solve the window problem.

A gyrotron with acceptable characteristics in the range 140 GHz was developed and investigated experimentally in the short pulse regime. Dependences of the output power and efficiency on the accelerating voltage (at fixed beam current) and on the beam current at fixed voltage are given in Figs. 7a and 7b, respectively.

There has recently been an increase of interest in the electron frequency tuning in a gyrotron. Fig. 8 shows the dependence of the output power on the magnetic field in the interaction space at fixed beam current and accelerating voltage. Shown near the maxima are the wavelengths of the output radiation. These results show that the magnetic field variation can ensure stepwise tuning of the output radiation frequency with high level of the output power retained. These experimental data are obtained without using a built-in quasioptical converter. Nevertheless, it should be noted that according to the theoretical estimates and preliminary experimental results, the conversion efficiency into the Gaussian beam for the neighboring modes, different solely in azimuthal structure, using a quasioptical converter remains almost unchanged.

In conclusion, Table 1 shows the basic characteristics of the gyrotrons investigated.

Table 1

NN	f, GHz	P, MW	η, %	P_{cav}, kW/cm^2	τ, s	output radiation
1	81	0.5	37	1.2	1.5	Gaussian beam (G.b)
2	82	1.0	50	2.6	10^{-4}	Operating mode (0. m)
		1.5	36	3.9	10^{-4}	
3	100	0.5	50	1.3	10^{-4}	0. m.

4	110	1.0	44	2.9	10^{-4} G. b.
5	114	0.75	44	2.0	10^{-4} O. m.
6	140	0.8	38	2.5	10^{-4} O. m.
7	143	1.0	47	2.8	10^{-4} O. m.

References

1. Gaponov A.V., Flyagin V.A. et al. Int. J. of Electronics, 1981, v.51, N4, p.277-302.
2. Flyagin V.A., Nusinovich G.S. Proc. of IEEE, 1988, v.76, N6, p.644-656.
3. Andronov A.A., Flyagin V.A., Gaponov A.V. et al. Infrared Phys., 1978, v.18, p.385-393.
4. Alikaev V.V., Flyagin V.A. et al. Int. Symp. of Heating in Toroidal Plasmas. July 1978, Grenoble, France, v.2, p.339-349.

TEST RESULTS OF 0.5 MW GYROTRON AT 120 GHZ AND 1.4 MW KLYSTRON AT 2 GHZ FOR FUSION APPLICATIONS

T. Nagashima, K. Sakamoto, S. Maebara, M. Tsuneoka,
Y.Okazaki*, K. Hayashi**, S. Miyake*, T. Kariya*,
Y. Mitsunaka**, Y. Itoh**, T. Sugawara**, and T. Okamoto*
JAPAN ATOMIC ENERGY RESEARCH INSTITUTE
Naka Fusion Research Establishment,
Naka, Ibaraki-ken 311-01, Japan, and
TOSHIBA CORPORATION Electron Tube Division*
Shimoishigami, Ohtawara, Tochigi-ken 329-26, Japan

I. INTRODUCTION

We outline here the development of a high-power 120 GHz gyrotron with a whispering-gallery-mode cavity in progress at JAERI, Naka site, in collaboration with TOSHIBA. The first of these tubes is designed to generate an output power of 500 kW for 30 msec. It has achieved 517 kW for 1 msec limited by the present test power supply. The second tube has a built-in quasi-optical converter in the tube and is designed for 400 kW pulsed operation. The first test result of this tube has achieved 548 kW for 1 msec and 240 kW for 10 msec. Further developments aimed at achieving the first design goal of more than 500-800 kW almost CW at an 110 GHz are currently under way, which will be used for a test facility at JAERI to develop a launching system and related components for the ECH program for JT-60 Upgrade.

We are now operating twenty-four 1 MW-10 sec klystrons in the frequency range of 2 GHz for the JT-60 lower-hybrid range of frequencies (LHRF) heating system. A modification of the electron gun of this klystron has been made recently to improve the withstand voltage near the electron gun. This enables us to evaluate the klystron at a higher beam

voltage to operate up to 1.4 MW during 10 second pulses at a frequency of 2.17 GHz.

II. 120 GHz GYROTRON PROGRAM AND DESIGN

At JAERI, the R&D program of a high-power gyrotron at 120 GHz was started in 1986. In the first stage, the development of a medium power level at 120 GHz were performed in collaboration with MITSUBUSHI ELECTRIC CORP. and TOSHIBA CORP. Both test tubes achieved output power of 150 kW for 10 msec in the TE_{03} cavity mode [1,2].

In the second stage of 1988-1989, the tests aimed at achieving the design goal of 500 kW for the pulse duration of 1 msec limited by the test power supply at TOSHIBA was carried out. This gyrotron named E3960 [3] has a magnetron injection gun with a cathode slope of 25 ° and to produce a laminar electron beam with pitch factor of 1.5 and a beam current of up to 30 A at a beam voltage of 70-80 kV. Here, pitch factor is the ratio of a perpendicular to a parallel velocity of the electron $\alpha = v_{perp}/v_{para}$. The resonant cavity is a simple tapered cavity, which is designed to operate in the whispering-gallery-mode $TE_{12,2}$. The calculated values of resonant frequency and external Q are 120 GHz and 580 for the $TE_{12,2}$ mode, respectively.

The oscillation experiment was carried out on the gyrotron test facility which has the power supply of 80 kV, 40 A for 1 msec and 20 A for 10 msec. Following the relation between the oscillation mode and the frequency (E3960) in Table 1, efforts were made to vary the magnetic field to optimize the output power of the $TE_{12,2}$ mode at 120.1 GHz and the $TE_{9,3}$ mode at 121.8 GHz. For the $TE_{12,2}$ mode, a power of 517 kW was obtained with a beam voltage of 76 kV and a beam current of 29 A at the maximum efficiency of 27.2 % and for the $TE_{9,3}$ mode, 610 kW was observed with the maximum efficiency of 36.1 %. This was probably due to large coupling factor for the $TE_{9,3}$ mode compared with that in the $TE_{12,2}$ mode. The plots of the experimental points for the beam current range

Table 1. The relation between the oscillation mode and the frequency (gyrotron E 3960).

MODE	Oscillation frequency (GHz)		
	experiment		calculated
$TE_{8,3}$	114.09		114.2
$TE_{6,4}$	119.43	119.50	119.7
$TE_{12,2}$	120.04	120.10	120.4
$TE_{9,3}$	121.75	121.80	122.1

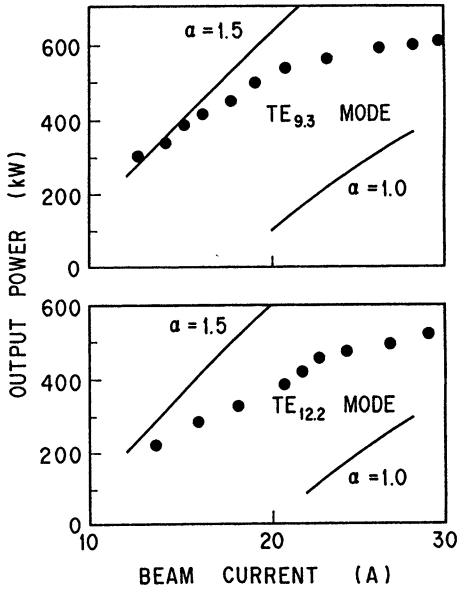

Fig.1. The plots of the experimental powers for beam currents. The solid lines indicate the calculated results assuming the pitch factor α = 1.0 and 1.5 (gyrotron E3960).

between the pitch factor α = 1.0 and 1.5, as shown in Fig. 1 (E3960).

To improve the efficiency of the gyrotron is crucial especially in the case of a huge heating power system in future like FER and/or ITER. To pursue this final goal, another gyrotron named E3970 with a built-in quasi-optical mode converter has been designed. Figure 2 shows the cross section of the gyrotron E3970. For the present design, we have retained almost the same configuration for the gun and cavity as those in E3960 except for a small change of the gun. The cavity has also a simple tapered cavity and is connected to an uptaper and to a Vlasov mode converter[4] (α-cut radiator) [5] with five-stage reflection mirror system. The output window is a single-disc design with edge-cooling (101.6 mm in diameter). This tube is also equipped with a sub-window to monitor the diffraction power on the top of the tube. Gaussian beam output is generated normally to the tube axis. Design parameters of E3970 are summarized in Table 2. Also shown in Fig. 3 is small-signal starting current calculation for 120 GHz with simple tapered cavity design.

Table 2 Design parameters of gyrotron E3970.

Frequency	120 GHz
Beam Voltage	80 kV
Beam Current	17 A
Output Power	400 kW
(Oscillation Power at Cavity	500 kW)
(Efficiency of Vlasov Converter	80 %)
Efficiency	30 %
(Oscillation Efficiency at Cavity	37 %)
Output Mode ($TE_{12,2}$ ~o)	Gaussian-like
Beam Pitch Factor : α	1.55
Beam Velocity Spread : $\Delta V_z/V_z$	1.2 %
Beam Thickness	0.29 mm
External-Q of Cavity	579
Cavity Wall Loading	2.3 kW/cm^2
Magnetic Field at Cavity	4.740 T
Mirror Ratio : Bcav/Bgun	26
Cathode Loading	2.6 A/cm^2
Output RF Profile	~ϕ28 mm (FWHM)
Aperture of Output Window	ϕ101.6 mm (4 ")

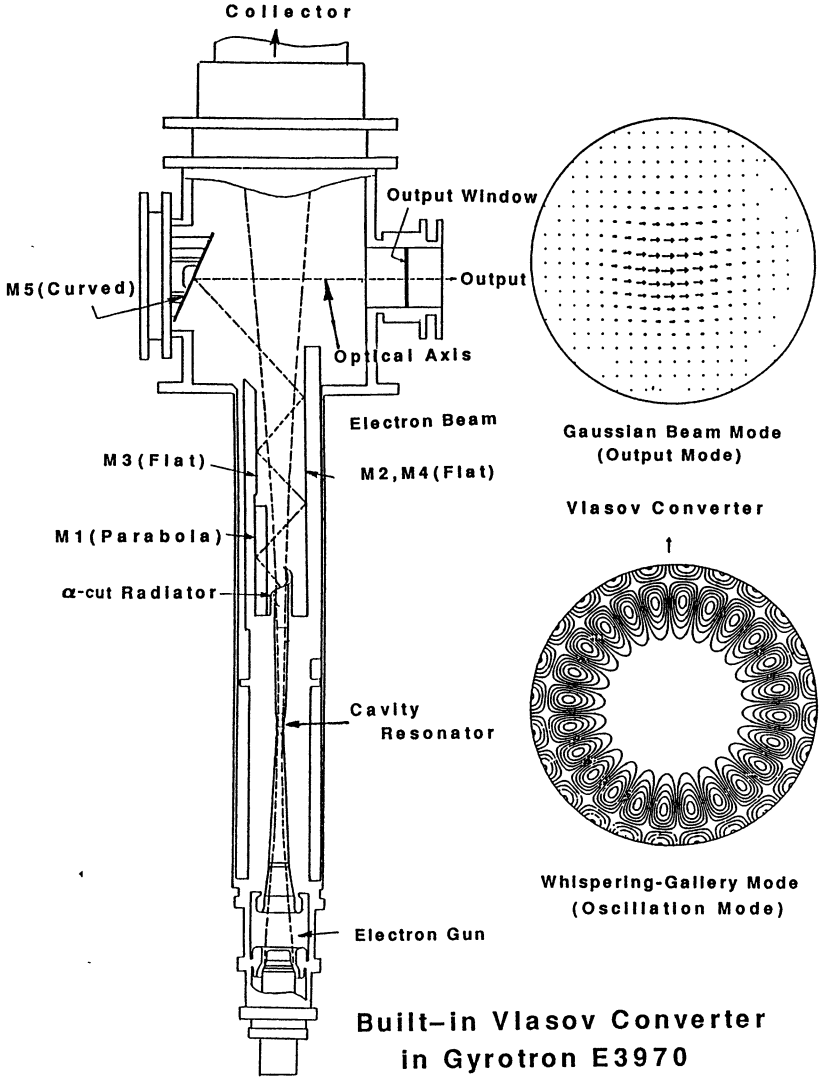

Fig. 2. Outline of gyrotron E3970 with a built-in quasi- optical converter.

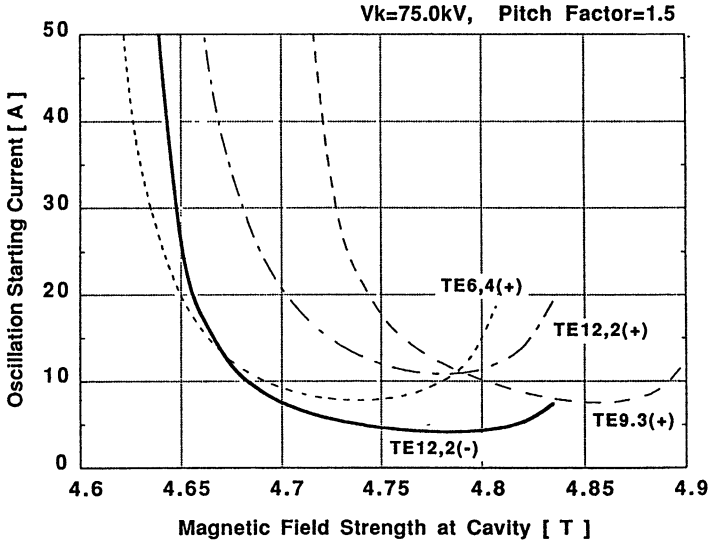

Fig. 3 Calculated oscillation starting current of gyrotron E3970.

III. LATEST 120 GHZ GYROTRON TEST RESULTS

Pulsed data were taken at 0.03 % duty rate and typically at pulse duration of 1 msec. Initial tests employed a beam voltage of 76.7 kV and beam currents of up to 23.5 A

A down taper of 1 m long was connected to the E3970 output flange and the power was transmitted to the dummy load. The output power was estimated from the calorimetric measurement of the dummy load. The oscillation frequency was measured with the cavity type frequency meter. The output mode of the oscillations was confirmed by the frequency.

In Fig. 4, an oscillation map shows the regions of parameter space occupied by the desired 119.7 GHz mode ($TE_{12,2}$). The major competing modes were the $TE_{9,3}$ mode at 121.3 GHz. Figure 5 shows a plot of output power and efficiency vs. beam current for the $TE_{12,2}$ mode oscillation. A maximum power of 548 kW at 30.4 % efficiency is indicated in this plot for a beam voltage 76.7 kV and a beam current of 23.5 A.

Following these initial tests of E3970, in general two effects were observed: 1) the improved mode selectivity against inverse polarity mode; desired mode $TE_{12,2}$ (-) vs. the competing mode $TE_{9,3}$ (+), and 2) higher efficiency; from the cold test of the quasi-optical conversion efficiency is 80 % and so the estimated conversion efficiency in cavity is 37 % which is in good agreement with the cavity-interaction simulation result. The first effect was probably due to the effect of the built-in converter.

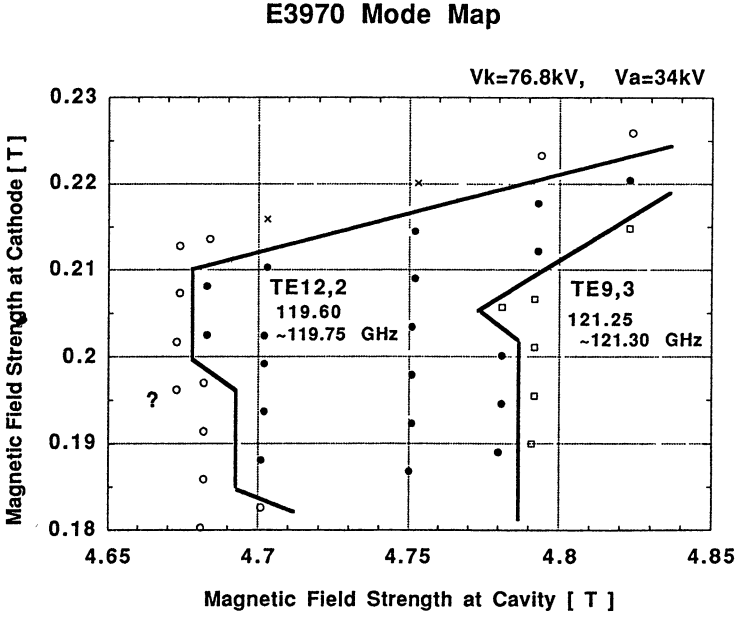

Fig. 4. Power output mode map of gyrotron E3970 at a beam voltage of V_k = 76.8 kV and an anode voltage of V_a = 34.0 kV.

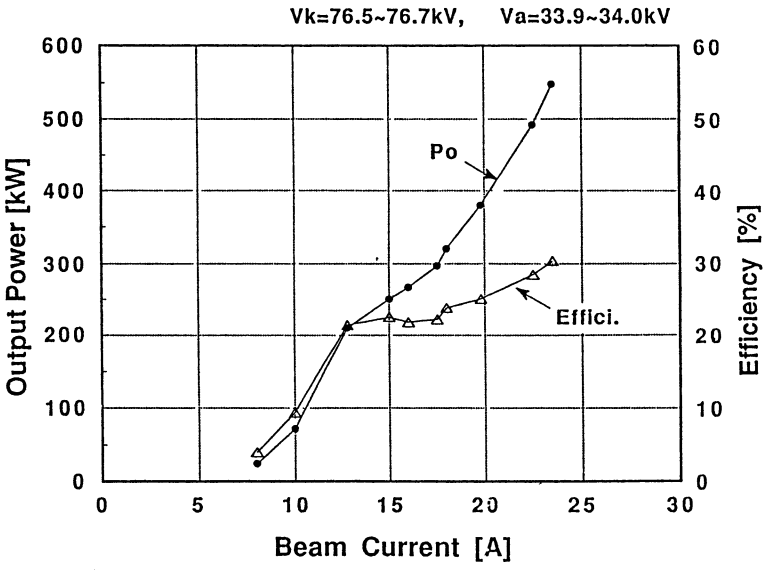

Fig. 5. Output power and efficiency vs. beam current for the $TE_{12,2}$ mode (gyrotron E3970).

IV. MODIFICATION OF 2 GHZ KLYSTRON FOR JT-60

Multi-MA current drive and efficient electron heating experiments have been conducted on the JT-60 (now upgraded to JT-60 U) at JAERI, Naka site, using a LHRF heating system completed in 1986, with twenty-four klystrons of an output power of 1 MW for 10 sec in the frequency range of 2 GHz. Developments were made in cooperation with TOSHIBA CORP. and NEC CORP. Specific features of this klystron are: 1) high-power and long pulse operation; 1 MW, 10 sec, 2) wide mechanical tuning range from 1.74 GHz to 2.23 GHz at 5 frequency points, and 3) durable tube; large load VSWR up to 2 without a circulator for protection [6,7].

The operating hours of klystrons for the JT-60 LHRF heating system exceeded 3000 hours in 1989, so that the operation at the output power of more than 0.7 MW of each klystron is sometimes limited by a breakdown near the electron gun of the tube. To attain the more reliable operation, a design improvement of the electron gun had been made. The summary of the modification are as follows: 1) reduction of the electric field strength between the electrodes, more than 15 % between anode and cathode and more than 43 % between anode and body, 2) replacing the barium oxide (BaO) impregnated tungsten cathode with the iridium (Ir) coated dispenser cathode to lower the operating temperature by about 100° C and 3) to reform the internal structure of the insulation ceramics from a cylindrical type to a tapered corrugated type to reduce the electric field on the surface of the ceramics. Details will be found elsewhere [8].

V. UPGRADE HIGH POWER TEST RESULTS OF 2 GH KLYSTRON

High power test of a TOSHIBA klystron E3778 with the improved design of electron gun was performed using the Klystron Test Facility at JAERI, Naka site, in collaboration with TOSHIBA.

Beam voltages were raised from 84 kV (previous operating voltage) to 94 kV during 2 sec pulse duration, and so the beam current was increased from 27.3 A to 31.7 A at the same perveance of 1.1 μ P. The maximum power of 1.46 MW for 2 sec at a frequency of 2.17 GHz was achieved at the beam voltage of 94 kV. Figure 6 shows the output power and efficiency vs. beam voltage (E3778). Efficiency is around 50 % at a beam voltage of 94 kV. There was no breakdown in drift tube and electron gun and also no multipactoring discharge at the output cavity, either.

Keeping the output power of 1.4 MW constant at 2.17 GHz, the pulse duration was increased from 2 sec to 10 sec. In Fig. 7 the time dependence of output power, beam current and beam

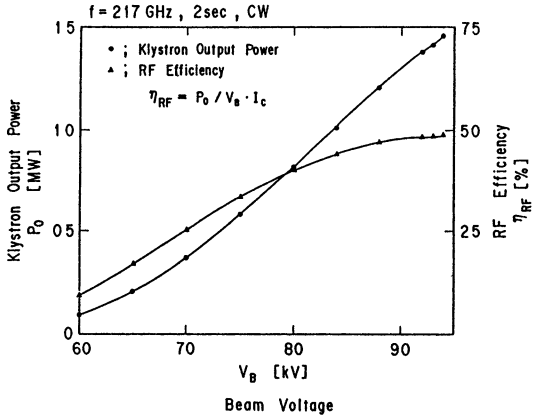

Fig. 6. Output power and efficiency vs. beam voltage during 2 sec pulses at 2.17 GHz (klystron E3778).

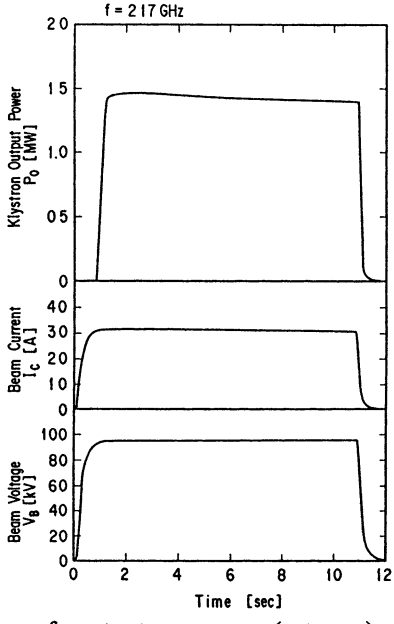

Fig. 7. Traces of output power (top), beam current (medium) and beam voltage (bottom) in case of 10 second operation at 2.17 GHz (klystron E3778).

voltage in case of 10 second operation are shown. Temperature increment in the water coolant is almost saturated during 10 sec, which shows a longer operation of more than 10 sec will be capable on this klystron. The improved electron gun provides further reliability and ease of operation on the JT-60 LHRF heating system.

VI. SUMMARY

Operation of the 120 GHz-$TE_{12,2}$ gyrotron with 548 kW output power with good efficiency of 30 % has been demonstrated with a single tapered cavity and an α-cut Vlasov mode converter. Pulse length is so far 1 msec at 548 kW and 10 msec at 240 kW, limited by the test power supply.

The modified 1 MW-10 sec klystron with the improved electron gun has demonstrated 1.4 MW for 10 sec and 1.47 MW for 2 sec in the range of 2 GHz. There is also an indication of further reliability and easy operation in the JT-60 experiments.

ACKNOWLEDGEMENTS

The authors would like to thank members of RF group of JAERI for discussions. They also thank Messrs. M. Hosoi, K. Ohya of TOSHIBA CORP. and Drs. M. Ohta, S. Shimamoto, T. Iijima, M. Tanaka, and M. Yoshikawa of JAERI for their continuous supports and encouragements.

** TOSHIBA CORPORATION Research and Development Center, 4-1, Ukishima, Kawasaki, Kanagawa-ken 210, Japan

REFERENCES

[1] T. Kikunaga, et al., 5th Annual Conf. of the Jap. Soc. Plasma Science and Nuclear Fusion Research, March 1988, pp. 213.

[2] Y. Okazaki, et al., 1988 Int. Electron Devices Meeting, Technical Digest, pp. 148-151.
[3] T. Sugawara et al., 14th Int. Conf. on Infrared and Millimeter Waves, 1989 Conference Digest, pp. 336-337.
[4] S. N. Vlasov, et al., Radio Eng. Electron Phys., Vol. 21, pp. 14-17, 1975.
[5] O. Wada, et al., Int. J. Electron 65 725-732, 1988.
[6] T. Okamoto, et al., J. Microwaves Power, 1985 pp. 173-179.
[7] Y. Kojima, et al., 1985 IEEE Int. Conf. on Plasma Science, 1985, and T. Nagashima, et al., NEC Research & Development No. 80, pp. 101-108, 1986.
[8] S. Maebara, et al., Japan Atomic Energy Research Institute Report, JAERI-M90-132, 1990.

CURRENT GYROTRON DEVELOPMENT AT THOMSON TUBES ELECTRONIQUES

G. MOURIER

THOMSON TUBES ELECTRONIQUES
DEPT. TUBES ET DISPOSITIFS HYPERFREQUENCES
2, RUE LATECOERE - BP 23
78141 VELIZY VILLACOUBLAY CEDEX

1 - Progress of the 110 GHz 500 kW design for CW operation

The 110 GHz gyrotron (see table 1) was designed in order to meet the requirements of the French Atomic Energy Commission for the "Tore Supra" Tokomak in Cadarache, France, and to serve as a basis for the development of higher frequency, higher power tubes.

APPLICATION :	PLASMA CURRENT PROFILE CONTROL (IN ADDITION TO LOWER HYBRID HEATING)
DESIGN VALUES :	
FREQUENCY	110 +/- 0.1 GHz
MAX PULSE LENGTH	210 S
REPETITION RATE	0.35
MINIMUM EFFICIENCY	30 %
MODE PURETY (GYROTRON)	96 % MIN AT NOMINAL POINT
PARASITIC OSCILLATIONS	- 30 dB MAX
HARMONIC CONTENT	- 15 dB MAX

TABLE 1 - DESIGN CHARACTERISTICS OF THE TH 1505 GYROMONOTRON

The design is based on the 100 GHz 200 kW tube developed earlier and on the following lines :

- tapered cavity with a non symmetric mode ;
- high seperation in frequency, especially on the low frequency side ;
- keep the wall losses in the cavity below 2 kW/cm^2 (calculated) ;
- keep the same current density in the electron beam, as the efficiency limitation of the gyrotrons at higher currents may be due to space charge ;
- make the gun structure compatible with several modes.

Other features are improved cooling of the cavity by means of a plurality of longitudinal channels, the use of new grades of copper for the cavity, magnetic field with a 10 Hz component in the collector, use of a double disk, FC 75 cooled window in the first tube, design of a low temperature window.

The mode is TE_{64}, but the tubes could operate in TE_{93} or $TE_{12.2}$.

Some problems were met in the design of the cavity to collector taper due to the large diameter of the collector.

On the other side, the Rieke diagrams (Fig. 1) that were calculated predict single regime operation up at about 600 kW (Iel = 15 A) (Fig. 2) and high efficiency operation over a wide range of power. We hope that the tube will not saturate below at least 400 kW. The distance from the beam to the cavity wall is larger than with $TE_{m.2}$ modes and space charge effects are thus more intense. On the other hand, the wall heating is perhaps more realistic (1,6 kW/cm^2 calculated).

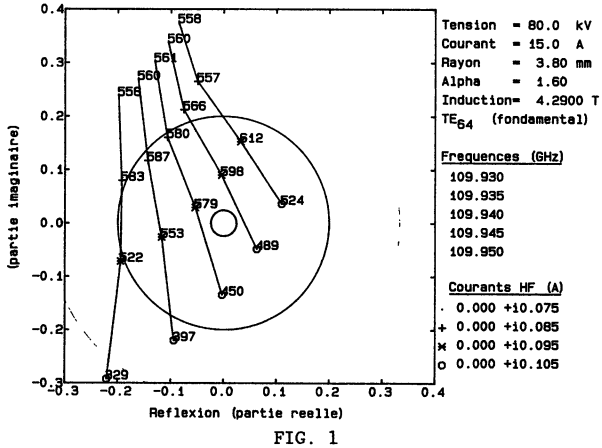

FIG. 1

TH 1505 - CALCULATED RIEKE DIAGRAM
(OUTPUT POWER, IN KW, ALONG LINES OF CONSTANT FREQUENCY)

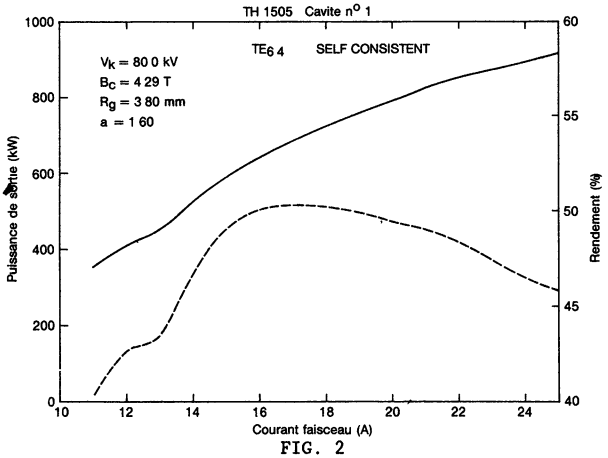

FIG. 2

TH 1505 - OUTPUT POWER AND EFFICIENCY VS BEAM CURRENT
(CALCULATED)

The input of the line to the Tokomak will be $HE_{1.1}$, and the best way to convert to that mode is not determined yet. One way is to convert to a whispering gallery mode inside the tube at some intermediate diameter in the taper.

For higher power we contemplate such modes as $TE_{m.3}$, with m = 15 or 17, and we think that the results on the half megawatt tube will tell us if a tube of the same conception is feasible.

2 - The design of 500/1000 kW Gyrotrons for 1 sec. pulses at 8 GHz

2.1 These tubes were designed as an industrial product, with a fairly complete and strict specification sheet.

The first design at 500 kW tried to make the tube very compact by using the fundamental mode of a circular or rectangular cavity with a short interaction length and a very low Q_{diff}, or a side coupling and a gun of low magnetic ratio. It was thought that such a tube would probably be unstable and that the voltage of the accelerating anode to the cathode would be very high.

The next designs use somewhat higher modes. The possibility of attaining powers above 1 MW had been demonstrated earlier 1973 [1] but, at low frequency, the problem was to keep the dimensions of the tube small and to obtain a high efficiency

2.2 Electron gun

Some of the properties of the MIG nguns can be summarized on a universal chart that guides us in the first design of all tubes (Fig.3)

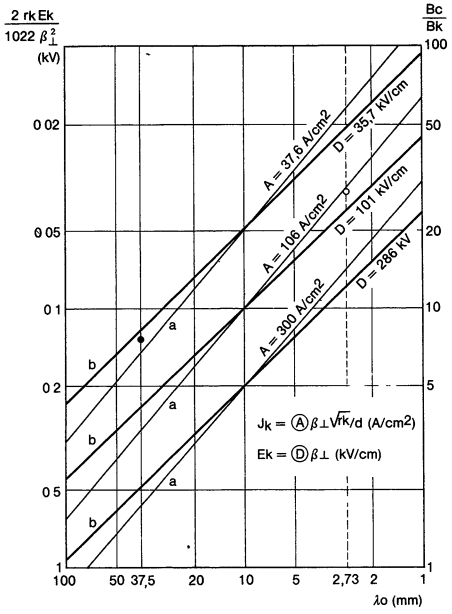

FIG. 3

CHART OF OSCILLATION WAVELENGTH VS DIFFERENT MIG GUN PARAMETERS

This chart is based on Busch's theorem on the assumption of conservation of the orbital magnetic momentum of the electrons, and on a simplified expression of this quantity in the electron gun. The straight lines correspond to constant values of a) constant Child Langmuir current density Jk at the cathode b) constant electric field at the cathode, as a function of oscillating wave length , cathode to anode distance d, orbital radius r_K at the cathode, transverse velocity c in the cavity. The ordinate is the magnetic compression ratio between the cathode and the cavity, which turns out to be the quantity $2r_k E_k/1022$ where E_K is the electric field at the cathode. This furnishes a value of the ratio of minimum accelerating anode to cathode voltage, ( ) to the transverse energy in the cavity.

At low frequencies, small values of the compression ratio e.g.2 are compatible with low. J_K and E_k, but require a large cathode to anode voltage. The compression ratio has to be increased at least to 4 or 5 resulting in an electron gun of large diameter. The final figure was 8.

We generally keep the actual current density below 0,2 J_k in order to decrease space charge effects in the electron gun.

2.3 Interaction (Theory)

We considered modes with eigennumbers of the order of 5-7, rejected cavities with low Q, mainly on the basis of the work of G.S. NUSINOVITCH [2]. These considerations lead to very high F numbers, unless the beam is situated in a region of somewhat low electric field. It was found that 1 MW, rather than the required 500 kW, could be obtained either with TE_{02} or $TE_{5.1}$, having rejected TE_{12}, TE_{22}, TE_{61} for various reasons. The quantity F is then below 0,2 for high efficiency (45 %) at 85 kV cathode voltage, although higher efficiencies (57 %) are predicted at 85 and 90 kV with $F \geq 0,2$. However, the operation is generally unstable in those last conditions.

We calculated the drift of the particles in a strong gradient of electric field, and found this unimportant.

Finally the $TE_{5.1}$ mode was chosen because it led to a gun of smaller diameter and would not present mode conversion in the bend following the tube.

Two types of cavities we used. Both use a varying diameter to ensure slow growth first and rapid decrease, in order to increase efficiency and decrease Q_{ex}.

For F = 0,2, μ = 12, the orbit efficiency is 53 % according tho the MIT chart [3], and the net electronic efficiency should be 42 %. Self consistant calculations predict a higher value (Fig. 4).

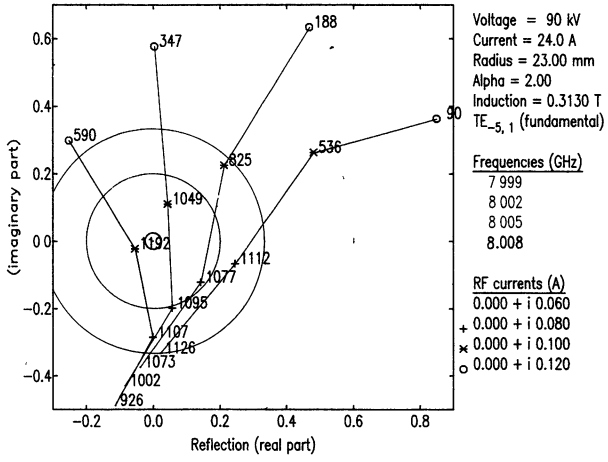

FIG. 4

TH 1504 - CALCULATED RIEKE DIAGRAM

(OUTPUT POWER, IN KW, ALONG LINES OF CONSTANT FREQUENCY)

Fig.5 shows how different project are situated in Nusinovitch's stability chart.

Fig.6 shows the dependance of the output power on the beam current. The latter lets the hope to reach above 1 MW in spite of a lower efficiency because of the absence of saturation up to high currents.

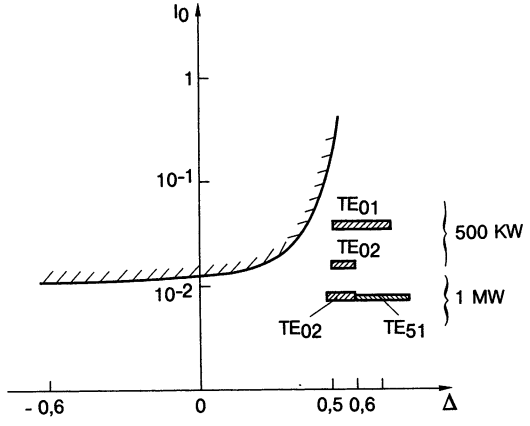

FIG. 5

STABILITY OF SEVERAL PROJECTS AS STUDIED IN [2]

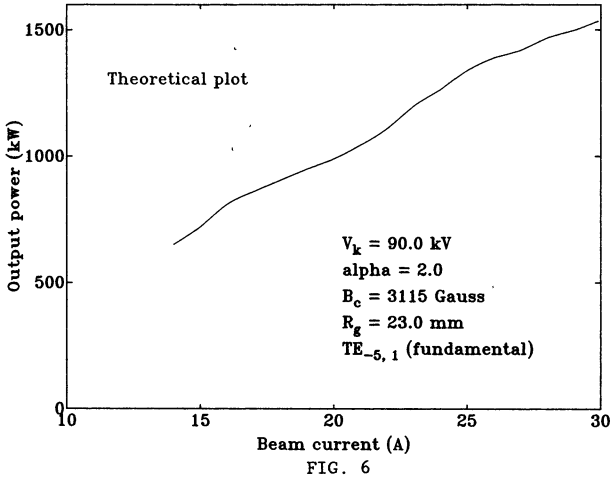

FIG. 6

TH 1504 - BEAM CURRENT VERSUS CALCULATED OUPUT POWER

2.4 Magnetic circuit

It consists of a set of coils inside a soft iron caging. The collector has two long concentric coils, one with constant current linear density, excited with constant current, the other one with density decreasing towards the output and run with ac. The impact of the electrons is then swept over 50 cm.

2.5 External circuit

After the window, which poses no problems, we find a 90° circular bend, a TE_{51} to TE_{01} converter (98 % efficiency), a 40 m circular wave guide, and a power divider (92 % efficiency) consisting of a 1.5 m long circular wave guide along which run 12 rectangular wave guides, coupled each by 110 holes (Fig.7). Each wave guide feeds a portion of a gril for lower hybrid resonance heating.

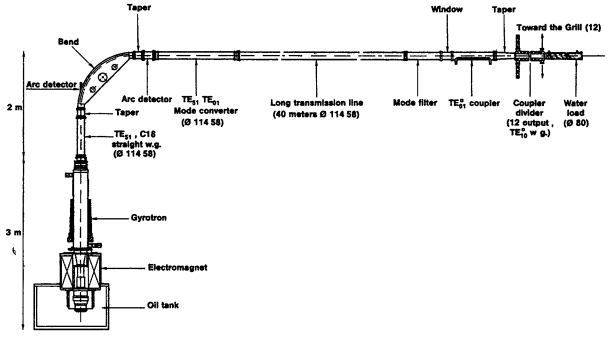

FIG. 7
TH 1504 - 1 MW - 8 GHz - 1 sec
GYROTRON AND LINE

The power loss from the tube to the output of the 12 rectangular wave guides is less than 1 db. All these values are experimental.

3 - **Experimental results on the 8 GHz tube**

Three tubes (Fig.8) were assembled and tested. One of them differed slightly in the profile of the cavities and gave only 800 kW.

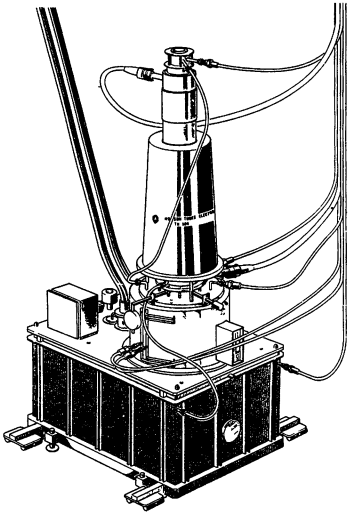

FIG. 8
8 GHz GYROTRON, MAGNET AND OIL TANK
(1 MW - 1 sec)

The other two could always supply 1020 to 1050 kW if the different arameters, including residual pressure, were optimized. However, when ower was plotted against different parameter, the maximum generally id not exceed 800 kW, sometimes limited by the modulator current, onsistently with theory, but with a lower efficiency (Fig. 9 and 10).

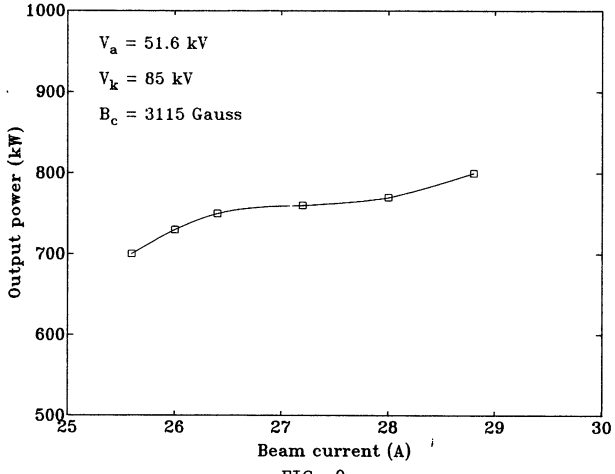

FIG. 9

BEAM CURRENT VERSUS OUTPUT POWER WITH OPTIMIZED CATHODE VOLTAGE

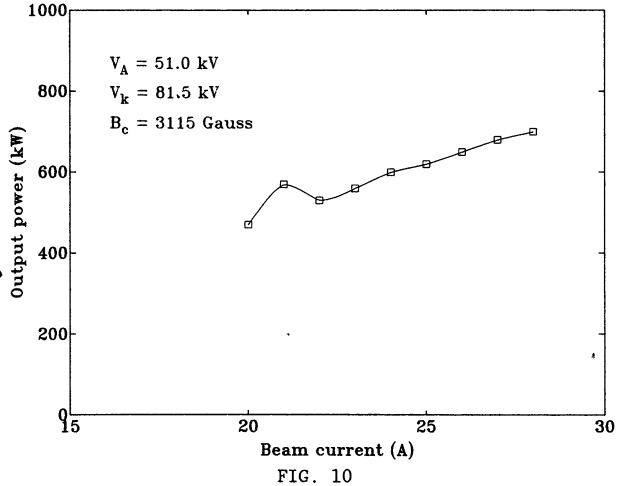

FIG. 10

TH 1504 : TEST WITH A LONG LINE (45 m)

The optimum magnetic field was very close to the theoretical value of 3115 Gauss, but might have been lower if the tube did not start on the $TE_{1.2.3}$ mode (Fig.11)

The RF pulse was generally very clean (duration 1 sec) particularly after the power divider, because spurious modes are filtered there (Fig.12)

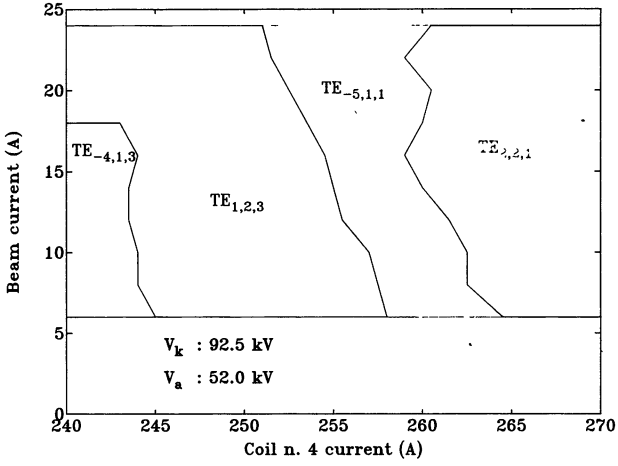

FIG. 11

TH 1504 : OSCILLATION MAP

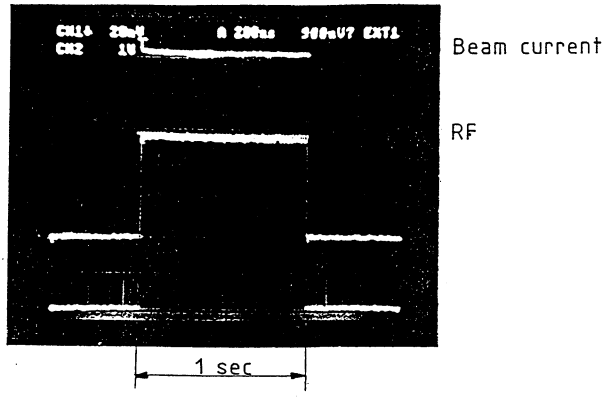

FIG. 12

BEAM CURRENT AND RF ENVELOPES OF A 1 SEC PULSE

The tube was fairly insensitive to the load. Starting from an operating point at 1020 or 1050 kW, the introduction of a VSWR of 4:1 never decreased the power below 700 kW. All the frequency measurements were between 7994 and 8000 MHz.

As typical for Gyrotrons, the efficiency constantly improved with time and better vacuum, and it is likely that these tubes or their followers will come close to the theoretical predictions, typically 1300 kW with 45 to 50 % efficiency.

During the tests, we met fairly severe difficulties with the waveguide flanges, especially in the section in TE_{51} between the waveguide and the mode converter, also in the rectangular waveguides.

The construction of the power divider was also difficult, but finally successful. Part of the difficulties came from the electroforming process, part from the fact that our theory predicted correctly the coupling coefficients through the holes, but with insufficient accuracy the shift in phase velocity due to the holes.

In general, the behavior of the tube agreed well with theory, including frequency and stability, although the presence of the $TE_{1.2.3}$ mode at low magnetic field had not been foreseen, and maximum power is not yet obtained.

4 - Conclusion

• With the experience gained on our short pulse tubes at 35 and 100 GHz (200 kW 100 msec), on this 8 GHz tube at 1 MW level in 1 sec pulses, we have acquired craftmanship in many fields of Gyrotron technology. Thus, we can hope that our 110 GHz tube will operate at relatively high power (500 kW) and serve as a basis towards 1 MW tubes at higher frequencies, very likely 140 GHz first.

REFERENCES

[1] - V.A. FLYAGIN, A.L. GOL'DENBERG and G.S. NUSINOVITCH
"POWERFUL GYROTRONS"
Infrared and Millimeter Waves, Vol 11, Part III
Edited by Kenneth J. Button
Academic Press INC, 1984

[2] - G.S. NUSINOVITCH
"RESULTS OF GYROTRON INVESTIGATIONS"
10th INT. CONF. on Infrared and Millimeter Waves
Dec 9-13, 1985

"MODE INTERACTION IN GYROTRONS"
INT. J. ELECTRONICS, 1981, VOL51 n°4, 457-474

[3] - K.E. KREISCHER, B.G. DANLY, J.B. SCHUTKEKER and R.J. TEMKIN
"THE DESIGN OF MEGAWATT GYROTRONS"
I.E.E.E Trans, on Plasma Science, Vol PS.13 n°6 - Dec 1985

COMMERCIAL GYROTRONS FOR THERMONUCLEAR INVESTIGATIONS

Kurbatov V.I., Malygin S.A., Vasilyev E.G.

R & D Company "Salut", Nizhnii Novgorod, USSR

Parametres of "Salut" gyrotrons used in some plasma experiments are described. Results of the preliminary and final tests of long-pulse 0.5-1MW 140 GHz gyrotron are presented.

Successes achieved in the electron cyclotron plasma heating experiments are based on the progress in development of powerful sources of millimeter wave radiation, i.e. gyrotrons. In the tokamak T-10 eleven 82 GHz and 75 GHz gyrotrons with 0.4-0.5 MW output power in each tube and 0.1-0.2s pulse duration were used to obtain the electron plasma temperature $\sim 10^8$K at the density $\sim 10^{13}$cm^{-3}.

R & D Company "Salut" is producing the lot of powerful pulsed gyrotrons accomplished with the cryomagnetic sistems. These devices are used in a number of fusion experiments (the data given in the table 1).

The typical gyrotron with the superconducting solenoid is shown in the Fig.1. All gyrotrons include the quasioptical built-in converter. The microwave power is radiated through the output window (80 mm diameter) as a gaussian-like beam. The operating efficiency is 30-35%. Superconducting magnets

Table 1

Name, Type	Institute	Operating Frequency, GHz	Output Power per Unit, MW	Number of Gyrotrons in Microwave Complex
T-10, Tokamak	IAE, Moscow	75; 82; 166*	0.4-0.5	11
T-15, Tokamak		82*, 100*	0.5	24
T-7, Tokamak		62.5	0.2	2
Ogra, Magnetic Snare		37.5	0.1	1
T-14, Tokamak	Branch of IAE, Troitsk	62.5	0.2	1
Liven-2, Stellarator	IGP AS, Moscow	37.5; 75	0.2; 0.3-0.4	2
Tuman, Tokamak	Ioffe Inst., Leningrad	54.5; 62.5	0.35; 0.15	1
Ambal, Magnetic Snare	INP SB AS, Novosibirsk	54.5*; 75*	0.5	6
Uragan, Stellarator	Phys.-Techn. Institute, Harkow	37.5*; 54.5*	0.2; 0.5	2

* in plan

are made for vertical position of gyrotrons and have dimensions: the heit of the cryostate - 400 mm; the outside diameter - 650 mm; the bore diameter - 140 mm; the magnetic field maximum is located at the height 200 mm. The weight of magnet - 230 kg, the helium volume - 26 l, the expenditure of helium - 0.2-0.4 l/h

The output parameters of produced gyrotrons are listed in the table 2. The relatively short pulse duration of 37.5-75 GHz gyrotrons is determined by the small collector dimensions. It is possible to increase the pulse duration in these devices up to 1-1.5 s if it will be necessary for users. For example, for the experiments at the tokamak T-10 the production of 75 GHz gyrotrons with the 0.5 s pulse operation is started.

A lot of new oscillators is developed:

1. 37.5 GHz gyrotron with the output power up to 0.5 MW.
2. 166 GHz tube with the pulse duration more than 0.5 s.
3. 140 GHz oscillator with the output power 0.5 MW and pulse duration 0.5 s.

In the last tube the high-order operating mode $TE_{22.6}$ is exited in the cavity with the smoothly tapered output. According to estimations for the ideal copper surface of the resonator, the maximum density of microwave ohmic losses at the cavity wall is about 0.8-0.9 kW/cm^2 at the output power 0.5MW. The large collector is capable for operation at 1 s pulse duration and 1.5 MW electron beam power or 0.25-0.3 s pulse duration for 3 MW beam power. The simplest single-disc construction of the output window permits to operate at the 0.5 MW output power level in 0.5 s pulses.

Table 2

FREQUENCY, GHz	OUTPUT POWER, MW	PULSE DURATION, s
37.5	0.25	0.1-0.2
54.5	0.5	0.1-0.2
62.5	0.25	0.1-0.2
75	0.5	0.1-0.2
82	0.5	1-1.5
100	0.5	1-1.5
166	0.5	0.1

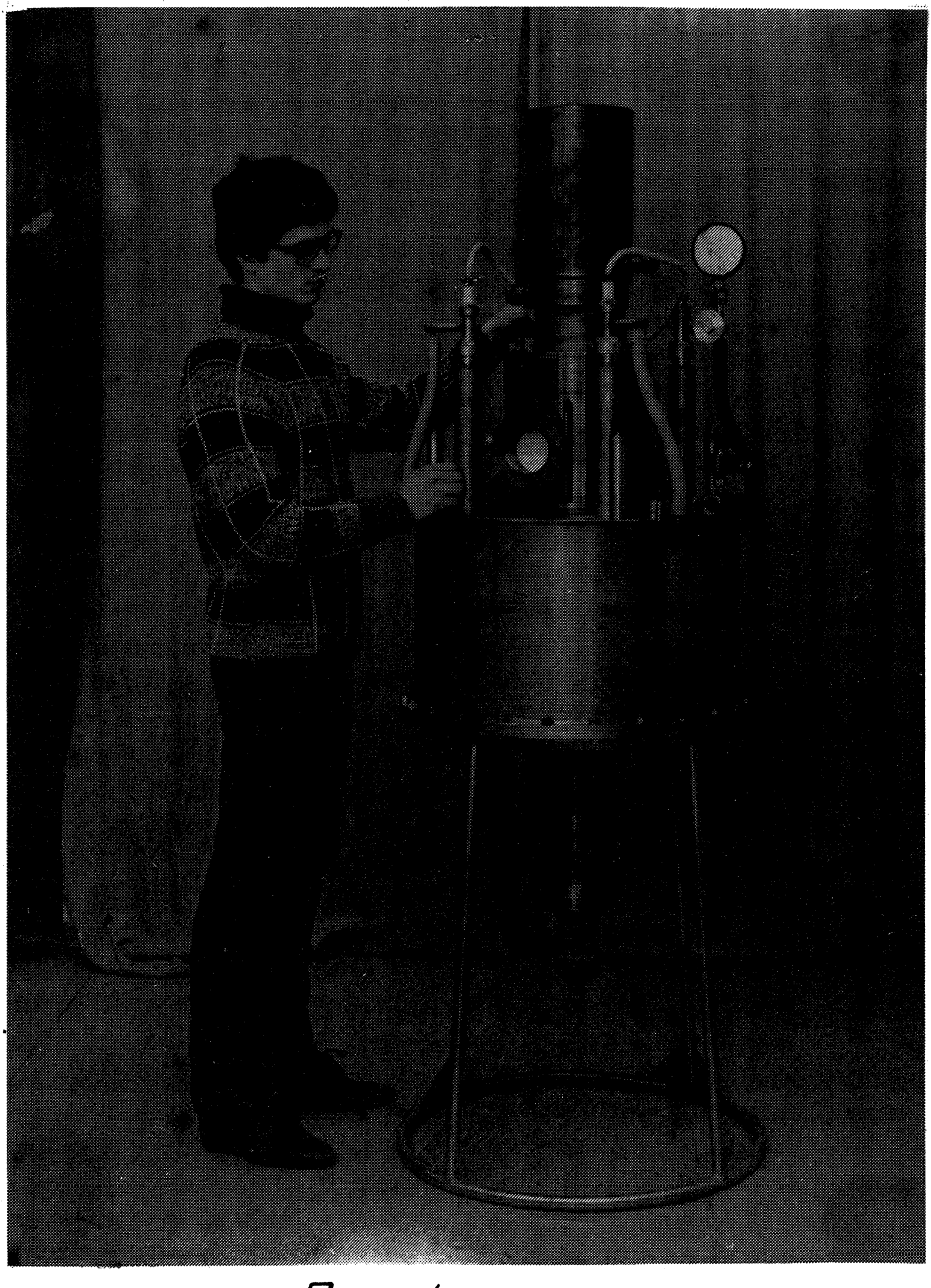

Fig. 1

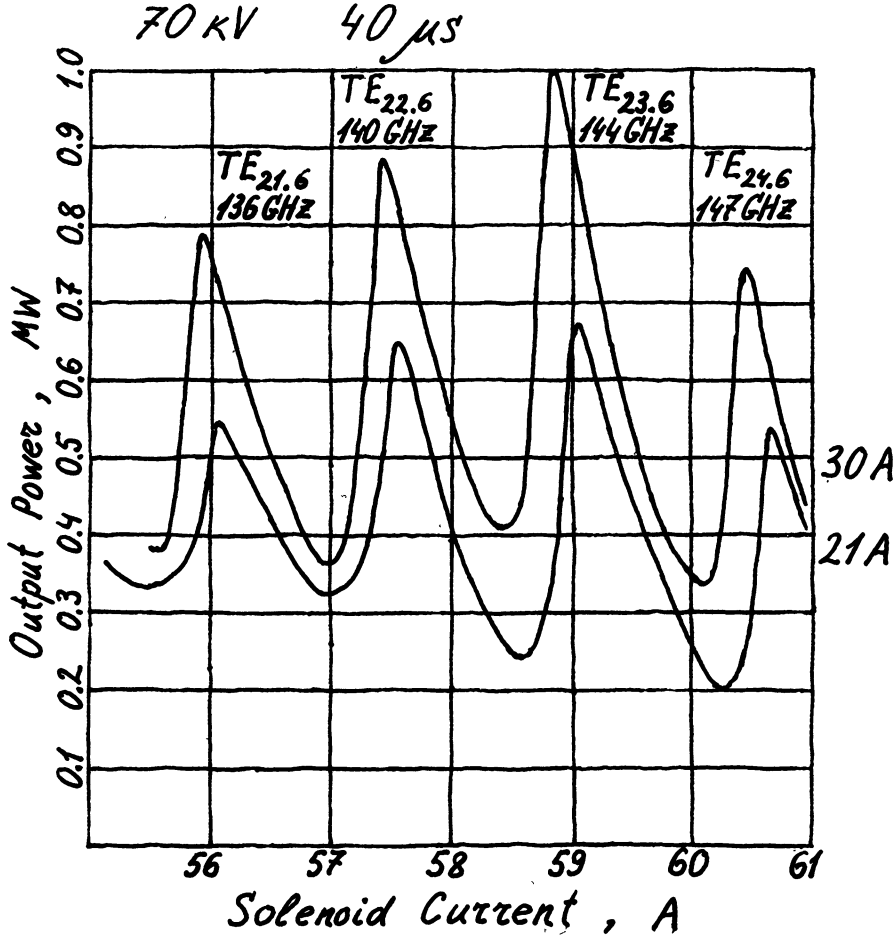
70 kV 40 μs
TE21.6 136 GHz
TE22.6 140 GHz
TE23.6 144 GHz
TE24.6 147 GHz
30 A
21 A
Output Power, MW
0.1 0.2 0.3 0.4 0.5 0.6 0.7 0.8 0.9 1.0
56 57 58 59 60 61
Solenoid Current, A

Fig. 2

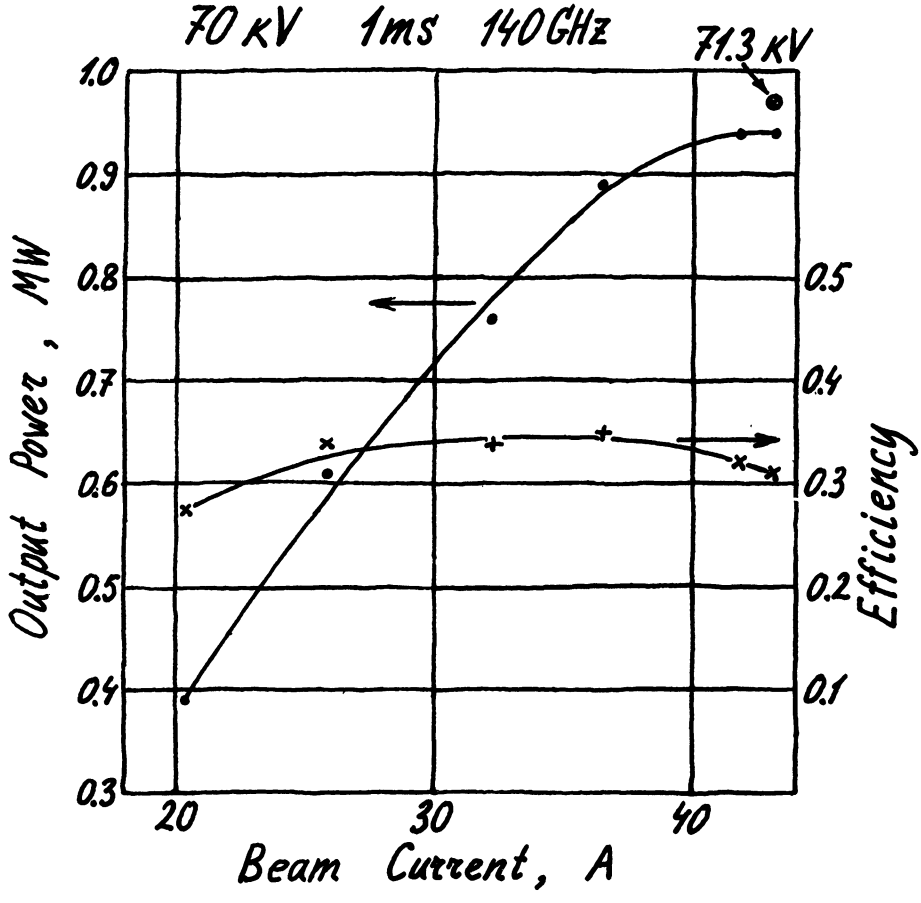
70 kV 1ms 140GHz
71.3 kV
1.0
0.9
0.8
0.7
0.6
0.5
0.4
0.3
Output Power, MW
0.5
0.4
0.3
0.2
0.1
Efficiency
20
30
40
Beam Current, A

Fig. 3

In June 1990 the short-pulse axially symmetric model of 140 GHz gyrotron was tested in IAP (Nizhnii Novgorod) to examine the quality of the electron beam and the interaction circuit for the high-order $TE_{22.6}$ operating mode. The oscillations were observed at several modes, such as $TE_{21.6}$, $TE_{22.6}$, $TE_{23.6}$ and others. The corresponding dependence of the output power versus the solenoid current is shown in the Fig. 2. The 1 MW output power level with the 45% efficiency was achieved at $TE_{23.6}$ mode.

In October 1990 the test of the first long-pulse 140 GHz gyrotron was finished at the Kurchatov Institute of the Atomic Energy (Moscow). The output power and efficiency of this oscillator versus the electron beem current are shown in Fig. 3 for the 70 kV voltage and 1 ms pulse duration. After relatively short vacuum training the output power 0.5 MW at 0.55 s pulse duration and 0.9 MW/0.3 s were achieved with the efficiency 30%. The pulse duration is, probably, limited here by window heating.

Authors want to acknowledge the collegues of Institute of Applied Physics (Nizhnii Novgorod) and Kurchatov Institute of Atomic Energy (Moscow) for the help in joint preliminary and final tests of the 140 GHz gyrotron.

MULTI-CAVITY PHASE-LOCKED GYROTRONS FOR LOW-HYBRID HEATING IN TOROIDAL PLASMAS

I.I. Antakov, L.A. Aksenova, E.V. Zasypkin,
M.A. Moiseev, L.G. Popov, E.V. Sokolov. V.K. Yulpatov
Institute of Applied Physics, USSR Academy of Science,
46 Uljanov Street, 603600 Nizhny Novgorod, USSR
R & D Company "Tory",
117393, Moscow, USSR

To generate a current drive in tokamak plasmas under low-hybrid resonance conditions, the microwave radiation at frequencies 5-8 GHz is necessary. An appropriate structure of RF field in this case is formed by a complex of phase-locked sources of radiation. One of the perspective sources of radiation is a phase-locked gyrotron [1]. The most simple phase control in a multi-cavity gyrotron can be realized by means of preliminary modulating the electron beam [2]. The concept design of the three-cavity gyrotron is shown in Fig. 1.

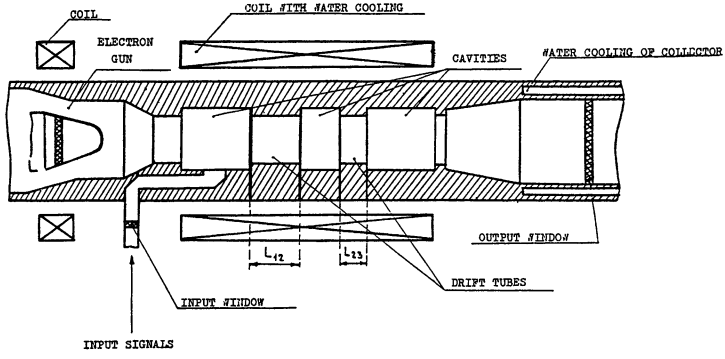

Fig. 1

This gyrotron can operate in regimes of synchronization and amplification. In the first regime, when $I^{out}_{\rho t\ min}$ is less than I_o

(here $I^{out}_{\rho t\ min}$ is the minimum starting current in the output cavity, and I_o is the current of electron beam), the phase and frequency of autooscillations in the output cavity are synchronized by the signal which is introduced into the first cavity. When $I^{out}_{\rho t\ min}$ is higher than I_o, the signal is amplified just as in an ordinary klystron.

Calculated values of the orbital efficiency $\eta_\perp$ for a two-cavity gyrotron, maximized by the cyclotron resonance mismatch $\omega_2-\omega_H$ (ω_H is electron gyrofrequency, and ω_2, frequency of RF field in the output cavity) are shown in Fig. 2.

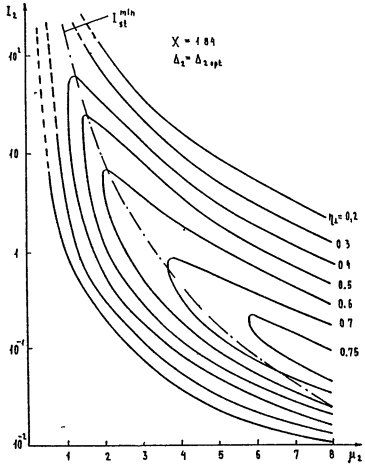

Fig. 2

Here $\Delta_2 = \dfrac{2}{\beta_\perp^2} \cdot \dfrac{\omega - \omega_H}{\omega}$,

$$\mu_2 = \pi \frac{\beta_\perp^2}{\beta_\parallel} \frac{L_2}{\lambda},$$

$$I_2 = 7.4 \cdot 10^{-5} \cdot I_o(A) \cdot \frac{\lambda}{L_2} \cdot \beta_\perp^{-4} : \frac{J_{m-1}(\nu_2 R_o/R_2)}{(\nu^2 - m^2) J_m^2(\nu)},$$

where Q_2 is the Q-factor of the cavity, I_o, electron beam current (in Amperes), J_m, Bessel function, ν_2, the p-th root of the boundary equation $J'_m(\nu) = 0$ corresponding to the TE_{mp}-mode, R_2, the cavity radius, R_o, the beam radius; $\beta_\perp$ and $\beta_\parallel$ are orbital and axial velocities of electrons related to the velocity of light c, respectively, L_2 is the cavity length, and $\lambda = 2\pi c/\omega$.

Note that the maximum orbital efficiency is achieved in the regime of synchronization and its value is $\eta_\perp^{max} \simeq 0.8$ ($\mu \simeq 9$) being somewhat higher than the gyromonotron efficiency $\eta_\perp \simeq 0.72$.. The synchronization band in this case is close to the transmission band of the "cold" cavity $\Delta\omega/\omega \simeq Q_2^{-1}$. In the amplification regime, the orbital efficiency is up to 0.72 at $\mu_{2opt} \simeq 6$. The band of amplification is close to the band of synchronization.

Design parameters of some versions of multi-cavity I-band gyrotrons are presented in the table.

The possibility to realize such a method of gyrotron

phase-locking was verified experimentally in a physical model of a two-cavity gyrotron with the following cavity parameters: $L_1 \simeq \lambda$, $Q_1 \simeq 150$, $L_2 \simeq 2.5\,\lambda$, $Q_2 \simeq 400$; the operating mode in both cavities is H_{011}. When the electron beam current I_0 is less than

Table

Mode	Regime	Number of cavities	V, kV	η_{max} operation				P_{max} operation		
				η	$\frac{P}{P_0}$, dB	I, A	P, kW	η	$\frac{P}{P_0}$, dB	I, A
H_{111}	CW	3	16	0.7	22	0.06	-	-	-	-
H_{011}	CW	2	16	0.45	18	0.5	-	-	-	-
H_{011}	P	2	24	-	-	-	24	0.22	25	4.5
H_{011}	P	3	16	0.6	20	0.5	-	-	-	-
H_{011}	P	4	16	0.4	22	2.0	13	0.27	25	3.0
H_{011}	P	3	33	0.37	30	1.5	45	0.25	35	5.5
H_{021}	P	3	40	0.39	30	6	160	0.27	35	15.0
H_{011}	CW	2	16	0.5	20	0.5	-	-	-	-

$I^{in}_{st\,min}$ and higher than $I^{out}_{st\,min}$, excitation of oscillations is observed in the output cavity only.

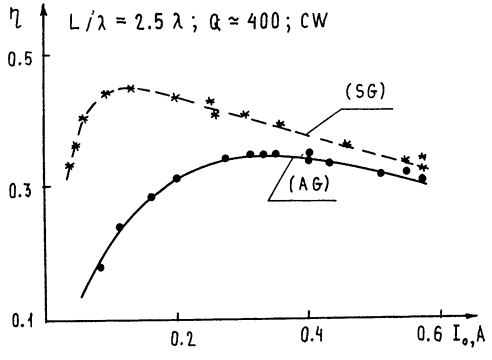

Fig. 3

If the output signal, which is fed into the first cavity, has the frequency out of the synchronization band but within the transmission band of cavities, the gyrotron output radiation has the frequencies of the input signal and output cavity.

Decrease in differences of these frequencies leads subsequently to the beating regime with a complicated spectrum and then to the regime of phase-locked oscillations. Dependence of the efficiency

$$\eta = \frac{\beta_\perp^2 \,/\, \beta_\parallel^2}{1 + \beta_\perp^2 \,/\, \beta_\parallel^2}\,\eta_\perp$$

on the beam current for a phase-locked gyrotron is shown in Fig.3

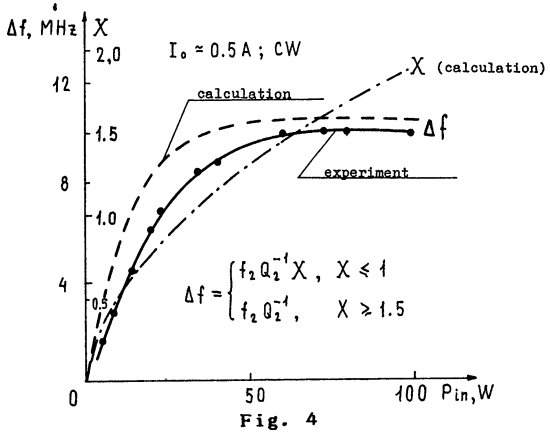

Fig. 4

Significant increase of the phase-locked gyrotron efficiency as compared to the efficiency of the autonomic gyrotron is caused by realization of η_{max} at a shorter length of the output cavity (Fig. 2).

The calculated and experimental dependences of the synchronization band width on the input signal power are presented in Fig. 4. When the bunching parameter is small ($X \ll 1$), the synchronization band is equal to $\Delta\omega \simeq \omega_2 X Q_2^{-1}$ [2]. With increase of X, it grows monotonously and at X = 1.5 reaches its maximum close to the transmission band of the output cavity.

In multicavity gyrotron-amplifiers where the operating beam current is lower than the starting current of the cavities ($I_0 < I_{st\ min}^{in,out}$), in accordance with the calculation (see Fig. 2) the regime of high output power with high efficiency and efficient control of the output signal phase can be realized. Most promising for this is use of systems with multicascade bunching of the electron flow. Fig. 5 shows experimental dependences of the efficiency and gain for two- and three- cavity gyrotron amplifiers on the input power. As it can be seen from Fig. 5, when an intermediate cavity is inserted into the gyrotron at equal distances from two other cavities (the regime of maximum amplification), the mean increase of the gain is (15 - 17) dB, and the effic-

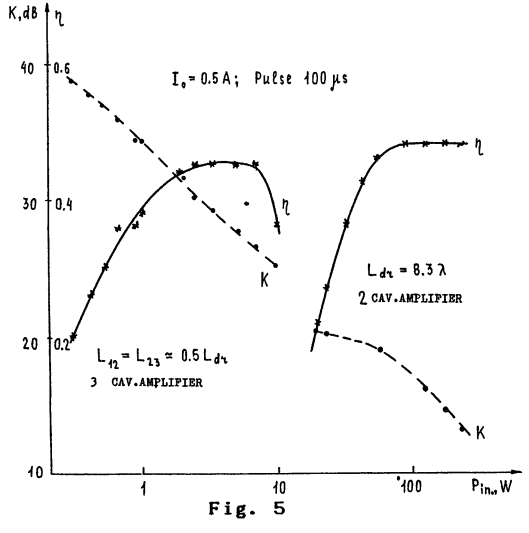

Fig. 5

iency remains at the level of about $\eta_{max} \simeq 0.45$.

If the intermediate cavity is placed close to the output one, the efficiency increases while the gain becomes lower; the gyrotron goes over to the regime of the maximum efficiency with $\eta_{max} \simeq 0.5 - 0.6$ (Fig. 6).

Calculated and experimental results verify the possibility to develop a (5-8) GHz multicavity gyrotron with the output power 1 MW, and efficiency 0.5, when the input power P_{in} is about (-30 dB) of the output power level.

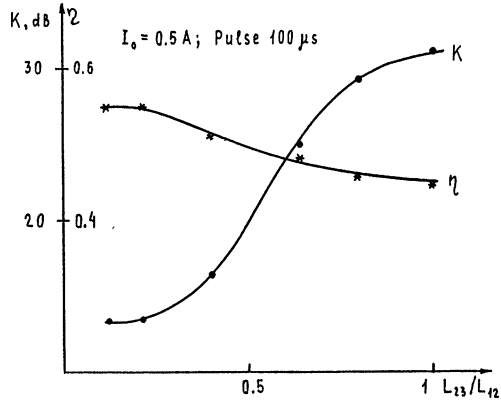

Fig. 6

The main problems to decide here are caused by electron velocity spread and spurious oscillations. Measurements show [3] that present magnetron-injection guns form electron beams with relative spread of orbital velocities about 0.15 - 0.25. In multicavity gyrotron this spread influences the efficiency electron beam - HF field energy interchange. Therefore, special measures to diminish the role of this spread are necessary.

Another, and, evidently, the most essential factor limiting the efficiency of multi-cavity gyrotrons is self-excitation of spurious oscillations in various regions of the interaction space [6, 7]. Each possible mechanism of generation must be, generally speaking, treated in its own way as far as the generation damping is concerned. This is almost impossible without a detailed study of conditions of spurious oscillations occurrence.

References

1. I.I.Antakov , A.V.Gaponov , V.A.Gintsburg , A.L.Gol'denberg , M.I.Petelin , V.K.Yulpatov. The amplifier of electromagnetic oscillations of centimeter, millimeter and submillimeter waves. Author's certificate 302050 16.06.67. Bulletin of Inventions N 41, 1975, p. 205 (in Russian).

2. V.S. Bazhanov, V.S. Ergakov, M.A. Moiseev. Synchronization of CRM-monotron by modulation of an electron beam. Radiophysics and Quantum Elect., Sept. 1977, p. 90.
3. V.E. Zapevalov, A.N. Kuftin. Powerful 80-150 GHz gyrotrons. Strong Microwaves in Plasmas. International Workshop, Suzdal, USSR, Sept. 1990.
4. Kuraev A.A. Theory and optimization of microwave electron devices, Minsk, Nauka i Tekhnika, 1979 (in Russian).
5. V.S. Ergakov, M.A. Moiseev, R.E. Erm. Influence of electrodn velocity spread on chartacteristics of the two-cavity CRM amplifier. Electronnaya Tekhnìka, ser. 1. Elektronika SVCh, 1980, N 4, p. 29 (in Russian)
6. I.I. Antakov, V.S. Ergakov, E.V. Zasypkin, E.V. Sokolov. Starting conditions of CRM-monotron in the presence of electron velocity scatter. Radiophysics and Quantum Elect., Novemb., 1977, p. 413.
7. Antakov I.I., Zasypkin E.V., Sokolov E.V. Self-excitation of the cylindrical waveguide section with a helical electron flow. Electronnaya Tekhnika, ser. 1. Elektronika SVCh, 1976, N 3, p. 31 (in Russian).

MICROWAVE DEVICE FOR LOW-HYBRID HEATING OF TOROIDAL PLASMAS

I.I.Antakov, E.V.Zasypkin, A.P.Keyer, V.S.Musatov,
V.E.Myasnikov, E.V.Sokolov
R & DC "Tory", 117393, Moscow
Inst. Appl. Phys., USSR Acad. of Sci., 603600 Nizhnii Novgorod

For low-hybrid heating and current drive in thermonuclear installations, complexes of phased-in sources of coherent radiation at the frequencies 5÷8 GHz with power of tens of megawatts are used. The power of one device should be not less than 1 MW and the efficiency should be high enough - about 0.5÷0.6.

When classical electron microwave devices - drift-tube klystrons are used for these purposes, there are difficulties associated with great thermal load in a collector and electrodynamic system, as well as with the fact that being small in comparison with the operating wavelength, the device elements can not withstand great electric fields. The possibility to create a gyroklystron free of the above-mentioned shortcomings is analyzed in this paper.

A principle scheme of a gyroklystron is presented in Fig.1

The optimal klystron parameters such as cavities' lengths, qualities and frequencies, drift tubes' lengths, magnetostatic field longitudinal distribution in the operating space are defined from the results of numerical integration of contracted equations of electron motion in cavities and drift tubes [1]. The calculation is performed in the approximation of the fixed structure of HF field in the cavities; the influence of HF space charge field is taken into account only at the stage of electron bunching.

According to the calculations the required output power and efficiency can be achieved in a three-cavity klystron with following parameters

power output	1.06 MW
magnetic field	2.36 kg

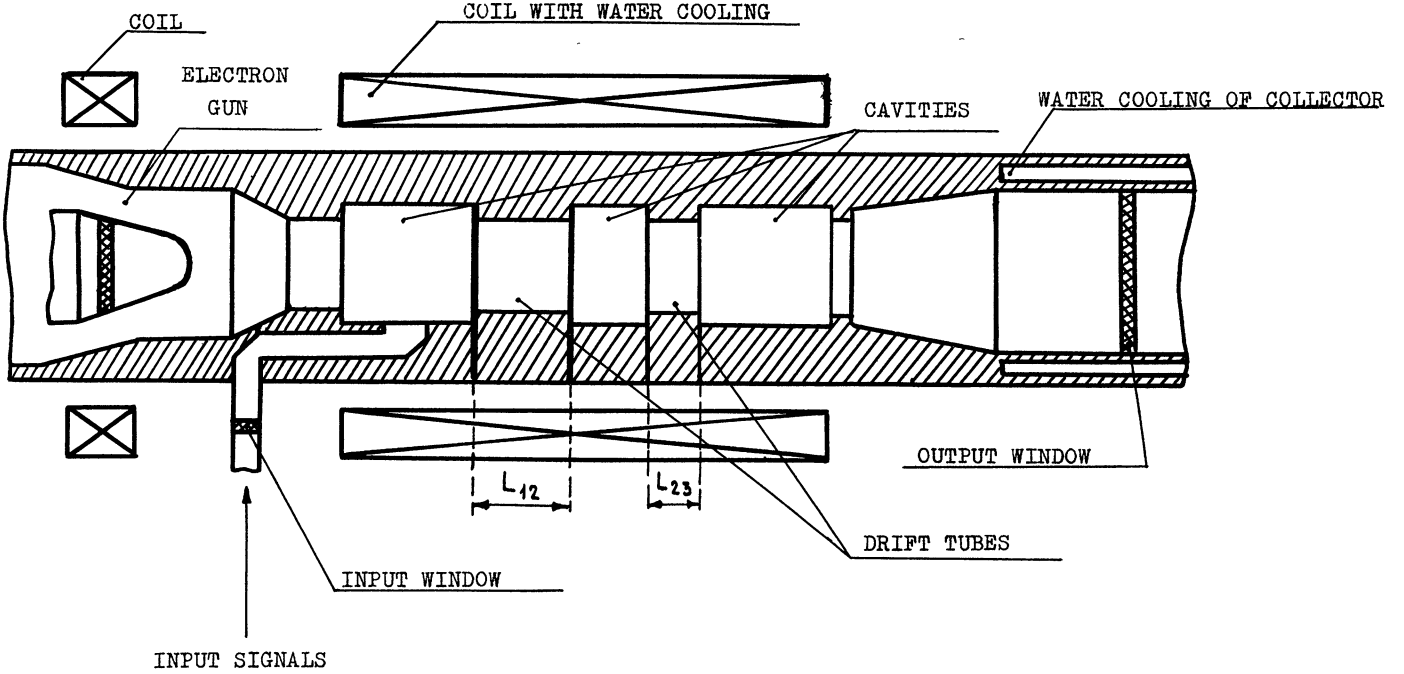
COIL
COIL WITH WATER COOLING
ELECTRON GUN
CAVITIES
WATER COOLING OF COLLECTOR
OUTPUT WINDOW
L_{12}
L_{23}
DRIFT TUBES
INPUT WINDOW
INPUT SIGNALS

Fig. 1

beam voltage	80 kV
beam current	25 A
efficiency	53 %
gain	30÷40 dB
velocity ratio V_I/V_{II}	1.73
cavity mode	TE_{0II}

The length of the space interaction constituted 15 wavelengths of the output radiation. The gyroamplifier operates in the regime of the maximum efficiency, that is the length of the second drift tube is essentially less than that of the first one. The length of the second drift tube is minimized to eliminate the decoupling of HF oscillations at the operating mode in the cavities. The optimal distribution of the magnetostatic field is characterized by the excess of the value of the magnetic field in the region of drift tubes over the values in cavities by several per cents.

Alongside with the calculation of the gyroklystron efficiency, the analysis of its stability is performed. Fig. 2 gives the results of the calculation of the "starting" qualities of the operating mode H_{0II} and the nearest parasitic modes as the functions of the electron transit angle in the first cavity. It can be seen from the figure 2 that the generation of parasitic modes does not take place in the region of optimal angles of the electron transit in the first cavity $\theta_{0II} \simeq 4 \div 5$.

A two-potential magneto-injection gun is used in the klystron. The profiles of the gun's cathode and electrodes are optimized using the program of the trajectory analysis which takes into account the influence of the Coulomb field of the beam on its parameters [2].

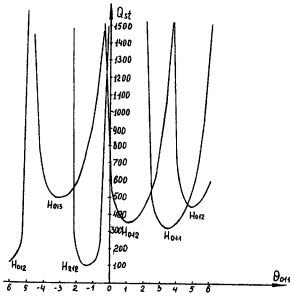

Fig. 2

The calculated parameters of the electron gun and the beam are as follows:

beam voltage	80 kV
anode voltage	40 kV
beam current	25 A
cathode density current	2.6A/cm^2
cathode diameter	50 mm
velocity ratio V_I/V_{II}	1.73
velocity spread	5 %

The calculated service life of the cathode is 5000 hours.

In the traditional scheme of a gyroklystron, in which the output waveguide serves as the electron collector, the waveguide's diameter is 80 mm. The specific thermal load on the collector surface does not exceed 0.75 kW/cm^2 and this enables one to use conventional methods of cooling.

The output of the energy from the gyroamplifier at the power level 1 MW in the CW regime can be performed through a ceramic window made of beryllium oxide (BeO) with diameter 100 mm which is cooled along a seal. A two-disc window has also a great safety margin; it is cooled along the surface and is analogous to the one used by "Varian" in CW millimeter-wavelength gyrotrons.

It should be noted in conclusion that the design of the gyroklystron is based on the results of the experimental study of gyroklystron's physical models which have yielded the efficiency of the order of 50-60 % and the gain 30÷35 dB [3].

References

1. Yulpatov V.K. Averaged equations of oscillations in gyrotron. Gyrotron. Collected papers, IAP, USSR Acad, of Sci., Gorky, 1981, p.253.
2. Manuilov V.N., Tsymring Sh.E. Theory of formation of high-current helical electron beams. Ibid.
3. Antakov I.I., Aksenova L.A., Zasypkin E.V. et al. Multicavity phase-locked gyrotrons for low-hybrid heating of totoridal plasmas. Proceedings of the Int. Conf. on Strong Waves in Plasmas. Contributed Papers. Suzdal, 1990.

THE DEVELOPMENT OF 140 GHz, 1 MW CW GYROTRONS FOR ITER

L.A.Aksenova [+], V.V.Alikaev [**], V.E.Zapevalov [++], V.I.Il'in [**], V.N.Il'in [+], A.P.Keyer [+], A.N.Kuftin [++], V.E.Myasnikov [+], V.A.Flyagin [++], V.A.Khmara [+]

R & DCompany "Thorij", Moscow
Institute of Applied Physics, USSR Academy of Sciences; Nizhny Novgorod
Kurchatov Institute, Moscow

I. Introduction

The heating of plasma in ITER and some contemporary installations needs microwave radiation sources with frequency 140 GHz, output power of about 1 MW and quasi-CW operation. In view of these demands there have been carrying out a joint program aimed at creating a gyrotron with output 1 MW CW in this wavelength band. Based on testing laboratory models a prototype of such a gyrotron has been designed and developed. The first tests of this tube were performed in July-September 1990. The peculiarities of the gyrotron operation in the regime of long (up to 0.5 s) pulses were studied. The operation of the cavity and collector cooling systems were tested as well as the chosen scheme of RF/beam division.

Some peculiarities of the development and the results of the tests of laboratory gyrotrons and those of the prototype of an industrial gyrotron are discussed below.

II. Development of a gyrotron

The concept of the development is based on the use of space-developed modes, i.e. on the compromise between the possibility of a thermal flow removal from cavity and collector walls and the demand of providing the selection of the operating mode, high efficiency and a stable tube operation at CW power 1 MW with frequency 140 GHz. This concept is based on

the application of the developed in R & DCompany "Thorij" surface cooling techniques which permit to remove aside a CW thermal flow with power density up to 5-7 kW/cm^2. Employing these techniques for a cavity cooling enables one to decrease the beam and cavity diameters; and this essentially simplifies the problem to provide the selection of the operating mode and the stable operation of a gyrotron with high efficiency.

To solve the problem of the collector cooling, the scheme of a gyrotron with RF/beam division is used. The prototype tube utilizes a quasioptical transformer (2) which directs the radiation perpendicularly to the axis of the device in the form of a wave beam. The final version of the gyrotron uses the further modification of this scheme of transformation developed in IAP and permitting to enhance the coefficient of the transformation of the operating mode to a wave beam up to 95-97%. Following the diverging magnetic field lines the electron beam is deposited on the collector whose dimensions and profile can vary relatively easily. Two versions of the collector have been developed. The first one is supposed to employ the techniques of removing an extense thermal flow in the system of cavity cooling. The second one utilizes a thermal flow with power density 1.5 kW/cm^2 and it makes use of a magnetic system for shifting the place of the beam deposition on the collector surface at frequency 10 Hz.

The basic parameters of the chosen scheme of a gyrotron are summarized in Table 1. The radius of a thin hollow electron beam produced by a magnetron-injection gun corresponds to the first maximum of the electric field of the operating mode $TE_{22.5.I}$.

Table 1

Operating mode	$TE_{22.5.I}$
Beam voltage, kV	70
Beam current, A	40
Output power, MW	1
Efficiency, %	36
Velocity ratio (pitch factor) V_I/V_{II}	1.3-1.5
Velocity spread	0.20-0.25
Potential drop in the cavity, kV	5.4-

Maximal specific loading on cavity walls, kW/cm^2	4.4
Operating frequency, GHz	140

By increasing the cavity length we can increase the efficiency; the maximal specific thermal loading on the cavity wall enlarges however.

III. Test results on gyrotrons

3.1 The results of laboratory testing of gyrotron models performed in IAP

IAP has developed, designed and fabricated a laboratory model of the gyrotron with the operating mode $TE_{22.5.I}$ which has undergone a series of short-pulse testing with a low level of the mean power. In this model HF radiation travels at the operating mode along the gyrotron axis and out through the window of the energy output. A quasioptic converter of the operating mode to the wave beam is located outside, thus permitting to measure the power outgoing from the cavity and the power which transforms to the wave beam. The fact that separate parts of the electron-optic system and electrodynamic system can be easily replaced, enables one to test several versions of the scheme and to choose the optimal one. The optimization of the parameters of the cavity and the electron-optic system yields the results given in Table 1. The parameters of the converter of the operating mode to the wave beam are also optimized after a number of its variants have been tested.

Fig. 1 gives the gyrotron output power as the function of the magnetic field in the cavity. It can be seen from the figure that due to the change of the magnetic field, the generation of various modes with high resolution in the operating band of the magnetic field takes place. This fact suggests that the level of the operating mode selection is sufficient.

3.2. Test results of a prototype gyrotron in Kurchatov Institute

R & DCompany "Thorij" has designed and fabricated a prototype industrial gyrotron. The construction and the technology of producing the cavity with a cooling system permitting to remove thermal flows up to 5-7 kW/cm^2 from the cavity surface have been developed in this tube. The diameter of the gyrotron collector is 200 mm. To decrease the heat specific flow to

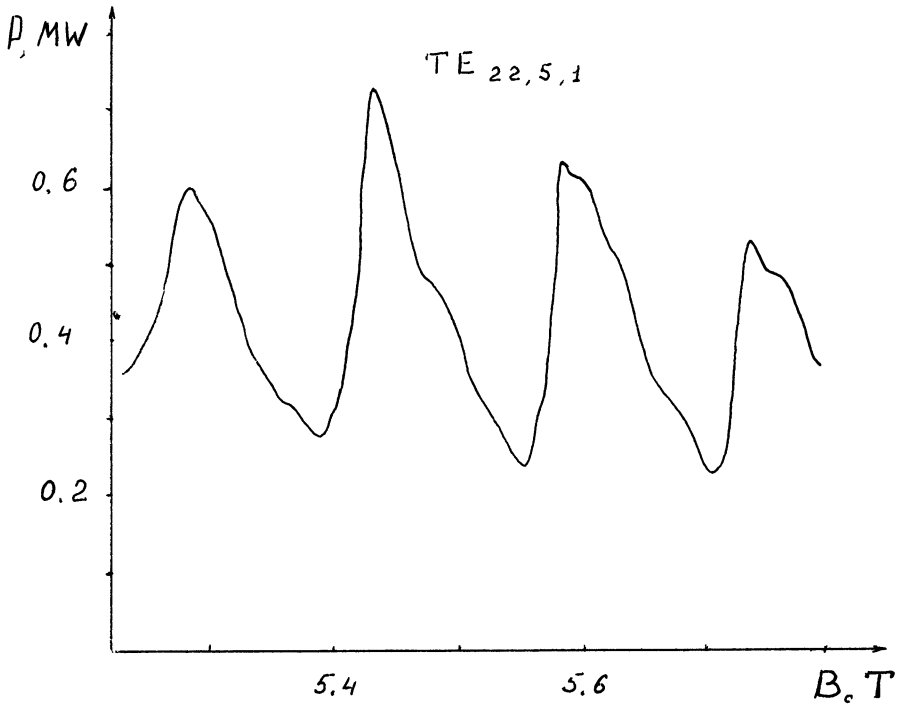

Fig. 1. Output power vs magnetic field

Table 2

Voltage, kV	65
Current, A	30
$Power_{output}$, MW	1.02
Frequency, GHz	140
Efficiency, %	37
$Efficiency_{converter}$	0.83

the level not exceeding 1 kW/cm^2, a magnetic system is used which enables one to shift the place of the beam deposition with frequency 10 Hz and amplitude 200 mm.

The techniques of high dynamic vacuum providing are utilized for stable operation and to prolong the service life. Owing to the modular design of the gyrotron, any part can be changed and modules can be fabricated independently. A porous metal cathode with surface temperature 1150° during operation at density of the emission current 4 A/cm^2 serves as the emitter. The tube uses the modification of a quasioptic intravacuum converter of the operating mode to Gaussian beam which has been tested in IAP. The prototype gyrotron has the window for HF radiation energy output which serves to maintain the output power at the pulse duration 0.5 s at the level 0.5 MW.

Fig. 2 shows the output power as the function of the cryomagnet current (the magnetic field in the cavity) at fixed beam current and fixed accelerating voltage. The gyrotron output power and efficiency optimized for the magnetic field as functions of the beam current are given in Fig. 3. In the preliminary testing the gyrotron output power achieves 0.5 and 0.72 MW at pulse duration 0.5 and 0.2 s correspondingly and at pulse repetition frequency 0.1 Hz. The gyrotron efficiency is 26-28%. The regime parameters are given in Table 3.

It is supposed to perform the gyrotron reconstruction in the near future with the aim to eliminate hindering factors in the fluid circulation systems of the cavity and collector cooling and to test the reconstructed tube. We consider that this will results in appearing a tube capable of generating the power 0.5 MW with the efficiency 30% in the regime of pulse duration 1 s at the frequency of pulse repetition 0.1 Hz.

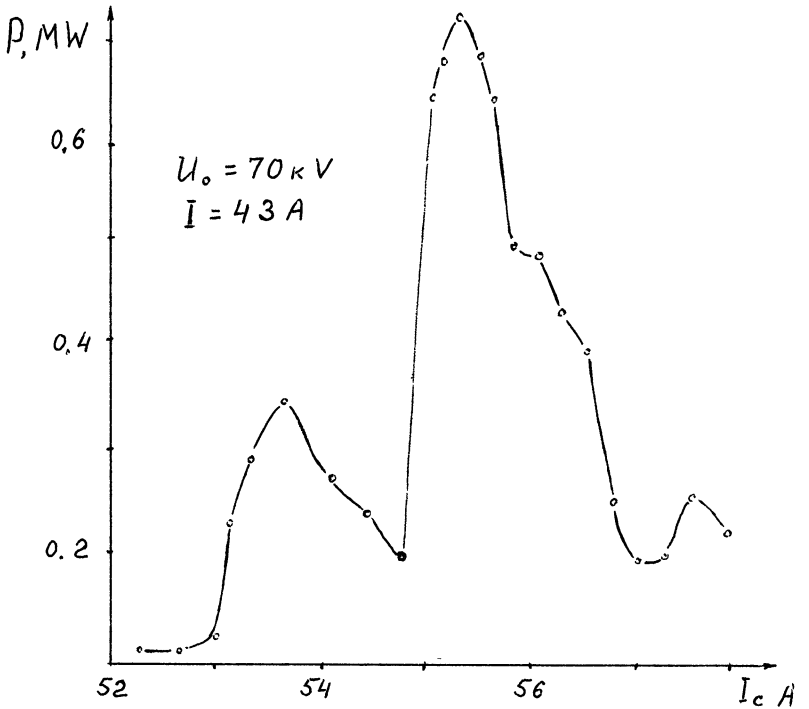

Fig. 2. Output power vs cryomagnet current

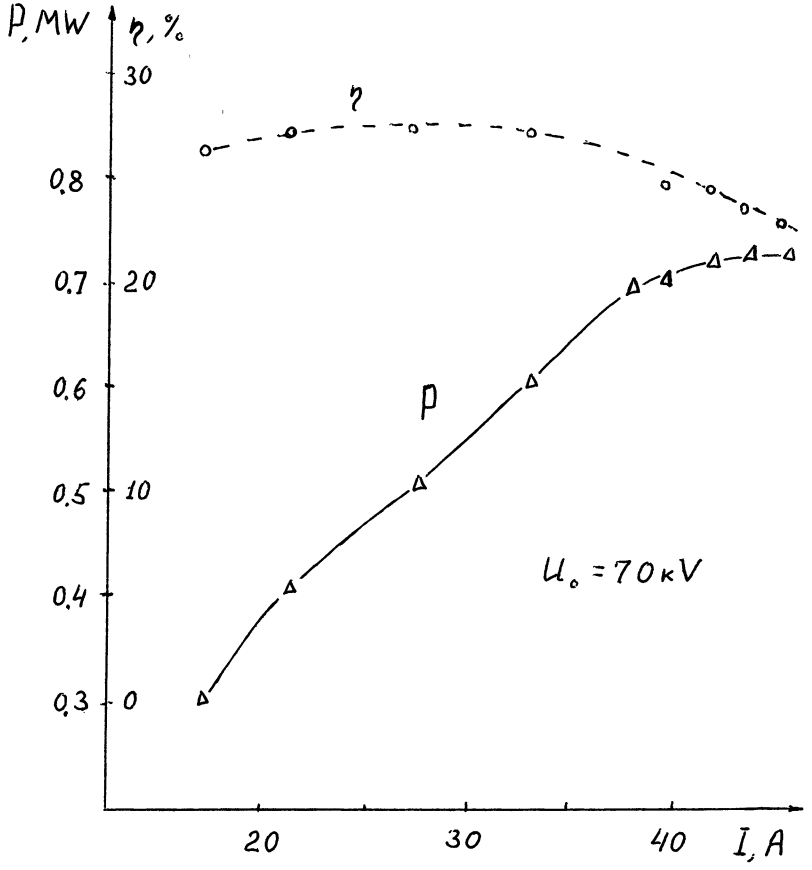

Fig. 3. Output power and efficiency vs beam current

Table 3

Operating mode	$TE_{22\ 5\ I}$
Operating frequency, GHz	140.3
Output power, MW	0.72
Pulse duration, s	0.1
Beam voltage, kV	70
Beam current, A	40.1
Power loss, kW	186
Tube efficiency, %	26
Efficiency of transformation	80

References

1. V.E.Zapevalov, A.N.Kuftin. Powerful 80-140 GHz gyrotrons. See these collected papers, p.714-726.
2. S.N.Vlasov, L.I.Zagryadskaya, M.I.Petelin. The transformation of the wispering gallery wave propagating in the waveguide with a circular cross-section to the wave beam. Radio tekhnika i Elektronika 20, 10, 2026-2030 (1975).

ELECTRODYNAMIC SYSTEMS FOR MODE CONVERSION, TRANSMISSION AND DIAGNOSTICS OF HIGH-POWER MILLIMETER-WAVE RADIATION

Manfred Thumm

Kernforschungszentrum Karlsruhe, Institut für Technische Physik, Postfach 3640
Universität Karlruhe, Institut für Höchstfrequenztechnik und Elektronik, Kaiserstr. 12
D-7500 Karlsruhe, Fed. Rep. of Germany

ABSTRACT

Localized electron cyclotron resonance heating (ECRH) and efficient current drive (ECCD) in nuclear fusion plasmas using high power gyrotrons require the launching of axisymmetric, well collimated, pencil-like millimeter wave beams having a well defined direction with respect to the confining magnetic field and with specific, controllable polarization state in order to get the best accessibility conditions to the plasma, especially for oblique wave launching.

Long-distance, high power mm-wave transmission from the single-mode gyrotrons to the plasma device with very low ohmic losses and high mode purity can be accomplished by:

(1) closed, highly oversized, smooth-wall circular TE_{01}-mode waveguide
(2) closed, highly overmoded, circumferentially corrugated or dielectrically lined, circular HE_{11}-mode waveguide
(3) open, quasi-optical TEM_{00}-mode transmission through a Gaussian beam waveguide using focusing metal reflectors.

Method (1) is suited for ECRH systems employing 200 kW TE_{0n}-mode gyrotrons and waveguide mode converters TE_{0n} - TE_{01} - TE_{11} (TM_{11}) - HE_{11} . Methods (2) and (3) are appropriate for ECRH systems using ≥ 500 kW mm-wave sources, e.g. nonsymmetric $TE_{m,n}$-mode gyrotrons in which a built-in quasi-optical mode transducing antenna with horizontal output directly converts the complicated cavity mode into a linearly polarized, collimated free-space Gaussian beam. Since cyclotron autoresonance masers (CARMs), quasi-optical (Fabry-Perot) gyrotrons and free electron lasers (FELs) may also emit a linearly polarized fundamental Gaussian mode and because such a wave beam is mandatory for the quasi-optical antenna module at the plasma device, the transmission schemes (2) and (3) are to be preferred in the case of multi-megawatt ECRH systems.

This paper reviews method (1) and describes and compares the approaches (2) and (3) (including several HE_{11}-waveguide components and elements for quasi-optical beam waveguides) and discusses their specific advantages, disadvantages and limits. Combinations of the systems (2) and (3) prove to be most favourable. In all cases transmission efficiencies from the sources to the plasma of between 85 and 90 % can be achieved.

1. INTRODUCTION

Millimeter-wave heating of magnetically confined fusion plasmas in the electron cyclotron frequency range with mm-wave power in the megawatt range has become a well-established heating method for both tokamaks [1] and stellarators [2]. The attractiveness of electron cyclotron resonance heating (ECRH) is based on physical as well as technical arguments.

From the physical point of view, the almost complete wave absorption combined with the narrow, well localized power deposition profiles have both been well proven theoretically and experimentally. From the technical point of view, a major advantage of ECRH compared to other RF heating methods is that no antenna structure close to the plasma surface is necessary. Therefore, no impurity problem is introduced by antenna material in contact with the plasma boundary layer. Proper launching of the EC waves is obtained simply by quasi-optical free-space irradiation of the plasma.

Typical applications of EC waves in magnetic confinement fusion devices are [1,2]:

(a) Ionization and plasma formation (start-up)

(b) Localized plasma heating (ECRH) at first (ω_{ce}) and second ($2\cdot\omega_{ce}$) harmonic EC resonances, combined with the possibility of electron temperature profile shaping

(c) Local current density profile control (good plasma stability) by local, noninductive electron cyclotron current drive (ECCD).

Efficient application of EC waves requires the launching of high power mm-waves with the following features:

- well collimated, pencil-like beam with narrow divergence angle (low sidelobes)
- well defined direction of the beam with respect to the confining magnetic field (steerable beam)
- specific, controllable state of wave polarization (low cross-polarization) in order to get the best accessibility conditions to the plasma:
  perpendicular launch: linear polarization in O-mode ($\boldsymbol{E} \parallel \boldsymbol{B}$) or X-mode ($\boldsymbol{E} \perp \boldsymbol{B}$)
  oblique launch : elliptical polarization.

Single-mode gyrotrons for 200 kW, CW operation are commercially available for frequencies between 28 and 70 GHz [3], and single mode mm-wave sources capable of high average power 1 MW/unit, CW are currently under development. These investigations include cylindrical-cavity gyrotrons as whispering gallery mode (WGM) or asymmetric volume mode (AVM) tubes, quasi-optical Fabry-Perot-type resonator gyrotrons, cyclotron autoresonance masers (CARMs) and free electron lasers (FELs) [see this conference].

Long-distance, high power mm-wave transmission from the sources to the plasma torus with very low ohmic attenuation and high mode purity can be accomplished by:

(1) closed, highly overmoded, smooth-wall circular TE_{01}-mode waveguide

(2) closed, highly oversized, circumferentially corrugated or dielectrically coated smooth-walled circular HE_{11}-mode waveguide

(3) open, quasi-optical TEM_{00}-mode transmission through a Gaussian beam waveguide using focusing metallic mirrors as phase correcting elements.

Method (1) is adapted for ECRH systems employing 200 kW TE_{0n}-mode gyrotrons [e.g. 1,2]

and waveguide mode transducers TE_{On}(gyrotron) - TE_{01}(transmission) - TE_{11} (or TM_{11}) - HE_{11}(antenna) [4-8]. Transmission methods (2) and (3) are appropriate for ECRH complexes composed of ≥ 500 kW mm-wave sources [9-11] , e.g. asymmetric $TE_{m,n}$-mode gyrotrons with built-in quasi-optical mode transducing antenna which directly converts the complicated cavity-interaction mode into a linearly polarized free-space Gaussian beam [12].

The first section of this paper gives a short review of transmission method (1) and a brief discussion of the wavenumber spectrometer [13] which is used for diagnostics of the various waveguide modes and for power monitoring. The second section describes and compares the two very high-power mm-wave transmission approaches (2) and (3) and summarizes their specific advantages, disadvantages and limits. Combinations of these two schemes prove to be most favourable [9,10,14,15]. Special components assure power and mode monitoring and polarization control. A final section discusses recent approaches being considered to improve the conversion efficiency of quasi-optical mode transformers for rotating high-order asymmetric gyrotron cavity modes.

2. OVERSIZED, SMOOTH-WALL TE_{01}- MODE WAVEGUIDE TRANSMISSION AND WAVEGUIDE MODE CONVERTERS (200 kW)

The output radiation of 200 kW TE_{On}-mode gyrotrons (mainly TE_{02} at frequencies between 28 and 70 GHz and TE_{03} at 140 GHz [3]) is unpolarized and produces a hollow conical radiation pattern with zero power along the waveguide axis. The almost perfectly linearly polarized Gaussian-like HE_{11} hybrid mode, which is ideal for quasi-optical wave launching using mirrors and polarization twist reflectors [2,7] can be generated from the TE_{On} gyrotron output modes by the two multistep mode conversion sequences:
(1) TE_{On}(gyrotron) - TE_{01} (low loss transmission) - TE_{11} - HE_{11} (antenna) [5-7, see Fig.1]
(2) TE_{On}(gyrotron) - TE_{01} (low loss transmission) - TM_{11}- HE_{11} (antenna) [6,8]

The first scheme which uses the TE_{11} mode as polarized intermediate mode has the advantage that the converters can all be made without bends allowing a simple and free choice and fast change of the polarization plane by rotating the TE_{01}-to-TE_{11} transducer around its axis. Arbitrary elliptical polarization of the HE_{11} antenna mode can be achieved by insertion of an elliptical polarizer in the TE_{11} or TM_{11} section [8,16].

In both conversion sequences mode transformers with periodic, axisymmetric radius perturbations [4,6,17] transform the phase-locked TE_{On} gyrotron output mode mixtures to the basic TE_{01} mode for long-distance transmission through overmoded, smooth-wall circular waveguides (ohmic losses < 1 dB/km). Proper matching of the phase differences between the TE_{On} modes and of the lengths and perturbation amplitudes of the several converter sections is required [6,7].

In the first mode conversion scheme a mode transformer with constant radius and periodically perturbed curvature transfers the unpolarized TE_{01} mode into the almost linearly polarized TE_{11} mode [4,6]. Adiabatic TE_{11}-to-HE_{11} conversion is achieved in a straight, circumferentially corrugated cylindrical waveguide section whose slot depth is nonlinearly tapered from one-half to one-quarter wave length [5,6,18].

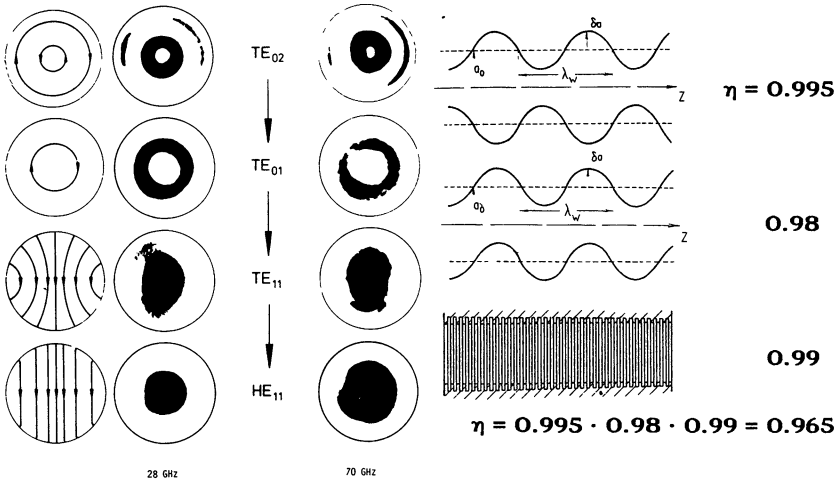

Fig. 1: Sequence of mode conversion TE_{02} - TE_{01} - TE_{11} - HE_{11} measured at high power (200 kW, 1 ms) for 28 and 70 GHz by thermographic pattern analyzers.

In the second mode conversion sequence, a smooth circular waveguide is bent with an optimized curvature distribution at proper angle and length to convert the TE_{01} mode into its degenerate TM_{11} mode [6,8,19]. The TM_{11}-to-HE_{11} transformer consists of a straight corrugated waveguide having a groove depth which changes gradually from zero to one-quarter wavelength [6,8].

The complicated structure of wall perturbations in the improved mode converters with periodically modulated waveguide wall [6], the curvature distribution in the bent smooth-walled TE_{01}-to-TM_{11} mode transducer [6,8,19] and the ellipticity distribution of waveguide polarizers [6,8,16] have been optimized by numerically solving the proper coupled-wave differential equations. Computer aided design of circumferentially corrugated mode transformers has been obtained with a scattering matrix code using the Modular Analysis Concept (MAC) [18]. Theoretical and experimental total conversion efficiencies from the gyrotron TE_{0n} mode mixture to the HE_{11} antenna mode are in the order of 95 %.

The mode purity in the transmission lines is conserved by employing diameter tapers with nonlinear profiles and corrugated continuous curvature bends with varying curvature and matched corrugations [20]. Special mode selective corrugated-wall filters with anisotropic surface reactance [20] are used in order to purify the transmitted TE_{01} mode, to protect the gyrotron from excessive reflections and to avoid arcing in the waveguide caused by trapped mode resonances. Purging of the waveguide system with CO_2 gas increases its power carrying capability [7]. The synthesized taper contours are analyzed by numerical integration of the coupled-mode equations. The typical suppression of parasitic modes is 30 dB. The properties of the corrugated gradual bends have been optimized also by means of numerical solving the corresponding coupled-wave equations.

Owing to mechanical imperfections introduced during the bending procedure, the typical transmission efficiencies (97-98%) are somewhat lower than the theoretical ones (> 99.5 %). As in the case of the TE_{11}-to-HE_{11} and TM_{11}-to-HE_{11} mode converters, computer aided minimization of input reflection and optimization of total length and slot depth variation of the corrugated-wall mode absorbers is achieved employing a scattering matrix code. Fig. 2 gives an overview of one of the five 200 kW transmission lines of the 70 GHz, 1 MW long-pulse (3 s) ECRH and ECCD system on the stellarator WVII-AS at IPP Garching [2,7]. The overall efficiency in the desired mode of a complete transmission line was determined to be about 90 %. Similar transmission systems are installed at: DIII-D, San Diego (60 GHz, 2 MW, 10 lines), COMPASS, Culham (60 GHz, 2 MW, 10 lines), RTP, FOM Institute (60 GHz, 0.6 MW, 3 lines), HELIOTRON E, Kyoto (53.2 GHz, 1 MW, 5 lines) and TCA Lausanne (39 GHz, 0.3 MW, 1 line).

In situ measurement of the mode spectra in oversized waveguides is performed by means of the wavenumber spectrometer [13] which consists of a leaky-wave antenna structure in the waveguide wall and of a movable receiver antenna with high angular resolution and directivity. From the radiation pattern (intensity and polarization) of the leaky-wave antenna the spectra of all TE and TM modes propagating in the waveguide are deduced. The device inherently has a large frequency bandwidth. The relative calibration of the spectrometer can be done at low power level by measuring the patterns of different modes with known relative power. The absolute calibration at high power level is obtained using a matched calorimetric load as termination. Typical TE-mode spectra measured at two locations in the TE_{01} section of one of the 70 GHz transmission lines on WVII-AS are shown in Fig. 3, the purity of the desired working mode is about 97 %.

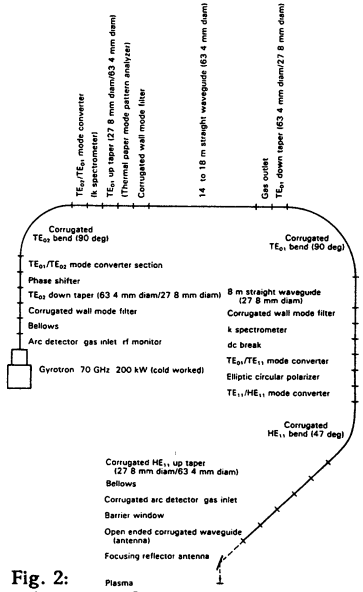

Fig. 2:
Schematic of a 70 GHz transmission line.

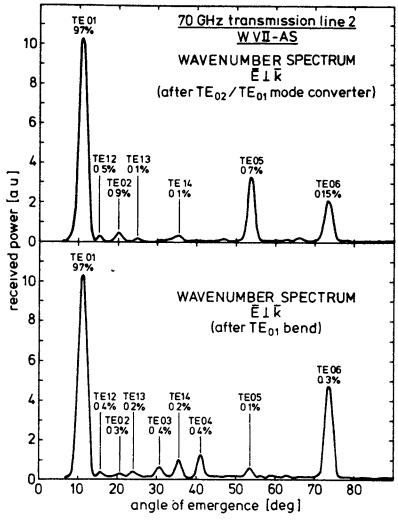

Fig. 3:
Mode spectra of TE modes measured in one of the 70 GHz WVII-AS transmission lines.

3. BROADBAND MILLIMETER-WAVE TRANSMISSION LINES (≥ 500 kW)

There are two major concepts for low-loss transmission of the Gaussian mm-wave output from high power asymmetric $TE_{m,n}$-mode gyrotrons, with built in quasi-optical mode transformer, to the plasma chamber [9,14,15]:

(1) closed, highly oversized, circumferentially corrugated or dielectrically lined circular HE_{11}-mode waveguide. The HE_{11} mode is particularly suited because it is a volume mode with very low wall currents so that its ohmic attenuation is lower than that of any other mode [21,22]. Furthermore, when radiated from an open-ended waveguide antenna this hybrid mode exhibits desirable radiation characteristics such as almost perfect linear polarization with very low cross-polarization and an axisymmetric narrow pencil beam containing 98 to 99 % of the radiated power with very low sidelobe levels [21,22]. At quasi-optical feeders (input) and launching antennas (output) the HE_{11} mode couples very well to the free-space TEM_{00}mode (with beam waist $w_o \approx (0.6 - 0.65)a$, where a is the waveguide radius [23]).

(2) quasi-optical TEM_{00}-mode transmission through a Gaussian beam waveguide using focusing metallic reflectors as phase correcting elements [9,10,24].

3.1 Highly Overmoded Circular HE_{11} Waveguide

3.1.1 Properties of oversized circular HE_{11} waveguide

In the frequency range around 140 GHz the favourable characteristic features of tubular HE_{11} waveguide with an inner diameter I.D. ≈ 90 mm (capable of carrying 1 MW, CW even at atmospheric pressure) are:

(1) Ohmic attenuation ($\alpha \sim D^{-3} \cdot f^{3/2}$)
- corrugated Cu-waveguide (slot depth $d = \lambda/8$) : $\alpha = 6 \cdot 10^{-5}$ dB/m
- corrugated SS-waveguide (slot depth $d = \lambda/8$) : $\alpha = 4 \cdot 10^{-4}$ dB/m, which means 1 % loss per 100 m.

Surface roughness effects are included in both cases (factor of 2).
- dielectrically lined (Al_2O_3) Al-waveguide [22,25]: $\alpha = 3 \cdot 10^{-4}$ dB/m. ($\tan\delta = 1.14 \cdot 10^{-3}$, $\varepsilon_r = 8.8$, thickness d = 0.095 mm)

(2) Maximum electric field on axis at 1 MW transmitted power: E(0) = 6.7 kV/cm.

(3) Maximum power density on axis at 1 MW transmitted power: p(0) = 60 kW/cm^2.

(4) Maximum electric field on wall at 1 MW transmitted power: E(a) = 70 V/m.

(5) Broadband characteristics from 80 to 170 GHz (one octave), see Fig. 4 and [26].

(6) Mode selective absorbers are feasible.

By choosing a material with reduced conductivity (e.g. SS-waveguide, powder sprayed SS-waveguide or Ni-P coated Cu-waveguide, the guide acts as a mode filter for higher parasitic modes, while the attenuation of the HE_{11} working mode remains negligible.

(7) Inherent RF-shielding.

This kind of waveguide is a closed system which also provides tritium and dust containment in case of a torus barrier window failure.

Several methods to manufacture HE_{11} waveguide have been investigated:

Corrugated waveguide: electroplating or plasma spraying on Al-mandrels, by special

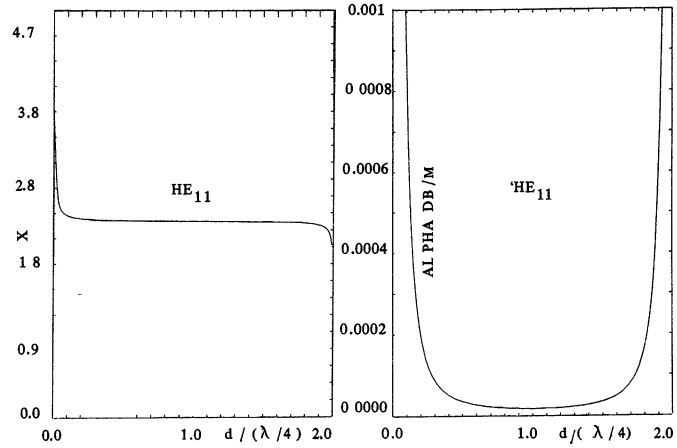

Fig.4: Radial eigenvalue X of the characteristic equation and ohmic attenuation constant α for the HE_{11} mode vs electrical slot depth $d/(\lambda/4)$ in corrugated Cu-waveguide (a = 44.45 mm, f = 140 GHz, ka = 130.26) with perfectly smooth surface.

tools [11] or by electrical discharge machining [9]. HE_{11} waveguides with helically formed corrugations can also be used, because the effect of polarization rotation is negligible in a highly overmoded waveguide with low-pitch corrugations [27].

Dielectrically lined Al_2O_3 waveguide [25]: hard coating of an Al-alloy waveguide by an electrochemical process. Up to the present the high-power capability (possible peeling of the dielectric layer) of such a waveguide is unknown and there could be problems due to degradation of the dielectric characteristics in a nuclear environment.

The normalized power in parasitic modes generated by unwanted mode conversion at abrupt radius changes Δa_0, radius offsets Δa_1 and elliptical deformations Δa_2 at flange connections of the waveguide is given approximately by: $P_L^i \approx (\Delta a_i/a)^2$ [9]. This means that flange tolerances of even about 0.2 mm lead to negligible mode conversion losses. However, mode conversion losses at abrupt tilts $\Delta\Theta$ at junctions between different waveguide sections: $P_L^{\Delta\Theta}/P = [2\cdot10^{-2}(2a/\lambda)\cdot\Delta\Theta(\text{deg.})]^2$ [9] and losses due to unintentional curvature which lead to an additional attenuation: $\Delta\alpha = 5.3\cdot10^{-5}f^2(\text{GHz})$ [9] of the working mode are much more severe and may limit the use of this highly overmoded waveguide to the 1 MW, 120 to 160 GHz range if the length of the transmission line is larger than about 100 m. The mean effective bending radius and angular misalignment must be > 3000 m and < 1.5 min., respectively. When the transmission line length is limited to about 50 m it would be possible to use such waveguides even at higher frequency (180 to 220 GHz) with tolerable additional alignment losses (about 3 %). It will be necessary to provide first optical (He-Ne laser) alignment and to have stable supports to maintain this alignment.

In an evacuated HE_{11} waveguide [11], the diameter of long straight sections could be decreased by optimized nonlinear tapers [10] in order to reduce the sensitivity to alignment errors and mechanical imperfections. Since waveguide systems for future

fusion devices must provide tritium containment and the possibility for decontamination (baking and evacuation) one will use such vacuum tight transmission systems. Lowering the pressure down to 10^{-2} to 10^{-3} Torr has the following additional advantages:
- increase of power capability and reduced propability of arcing,
- no condensation on the external surface of cryogenically cooled ceramic windows,
- reduction of the stresses in the gyrotron and torus barrier window disks.

Evacuated HE_{11} waveguides will be tested in the 110 GHz ECRH systems on DIII-D at GA in San Diego [11] and on TORE SUPRA at CEN Cadarache [28]. In both cases, special in-waveguide mode converters transform the rotating high-order gyrotron output mode into the HE_{11} hybrid mode.

3.1.2 Quasi-optical waveguide bends

The highly oversized dimension of the waveguide makes it possible to use quasi-optical (mirror) bends (see Fig.5). The main advantages of these HE_{11} mitre or corner bends are compactness and large bandwidth. The theoretical mode conversion loss for a plane-mirror HE_{11} corner bend is given by the following average formula [29]:

$$P_c(dB) = 1.3\ [\lambda/(a\cdot\sin\Theta)]^{3/2} \qquad \text{(for H- and E-plane)} \qquad (1)$$

where Θ is the bend angle. Multiple diffractions in the bend cause a fine structure of fluctuations of the dependence of the conversion losses. Measurements at 70 GHz and I.D. = 27.8 mm using a wavenumber spectrometer [30] are in good agreement with these theoretical expectations. As predicted by [31], one quarter of the lost power is contained in backward travelling modes close to cutoff . The theoretical mode conversion losses for a 90° HE_{11} elbow bend in I.D. = 90 mm waveguide at 140 GHz are 0.35 %. These losses can be more than halved by using curved mirrors with optimum phase correction for the propagating HE_{11} mode [29,30], see Fig. 6.

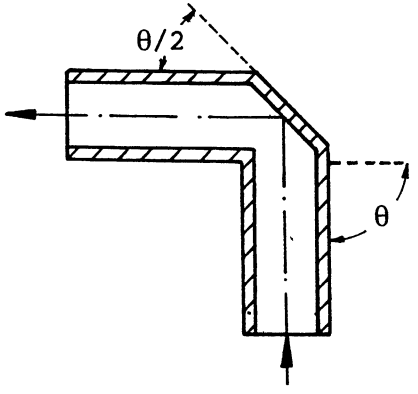

Fig. 5: Schematic of quasi-optical corner bend.

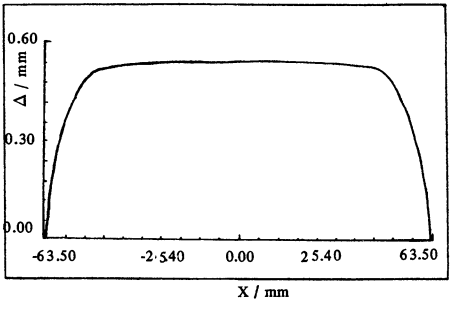

Fig. 6: Curved surface of optimum phase correcting HE_{11} corner bend [30].

The ohmic attenuation at the Cu-mirror of the HE_{11} mitre bend is described by:

H-plane bend: $$P_\Omega{}^H/P = 0.37 \cdot S \cdot (1/3\lambda)^{1/2} \cdot \cos\Theta \quad (2)$$

E-plane bend: $$P_\Omega{}^E/P = 0.37 \cdot S \cdot (1/3\lambda)^{1/2} / \cos\Theta \quad (3)$$

where the factor S = 2 refers to non-ideal conductivity (surface roughness). H-plane propagation is favourable. The expected total losses for a plane 90° HE_{11} elbow bend in an I.D. = 90 mm waveguide at 140 GHz are:

H-plane bend: $P_L{}^H/P$ = 0.55 % (0.2 % ohmic losses)

E-plane bend: $P_L{}^E/P$ = 0.7 % (0.4 % ohmic losses).

Switchable corner bends allow change over to a dummy load for gyrotron conditioning, to a calorimeter for power measurement or switching to a different transmission line (see Figs. 7 and 8) in case of any failure in the line (increased reliability).

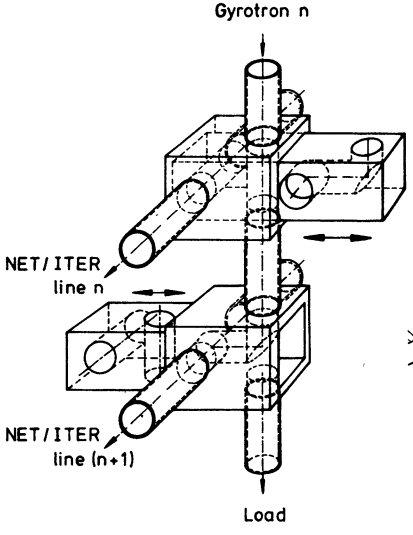

Fig. 7: Schematic of waveguide switches in a cross-bar set-up [9].

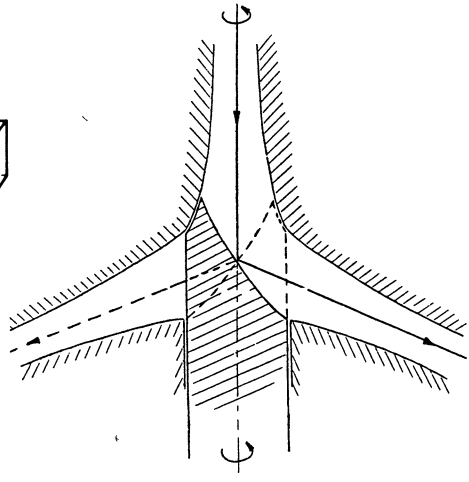

Fig. 8: Schematic of rotatable mirror wave switch [10].

3.1.3 HE_{11} components with short annular gap in the waveguide

The presence of a circumferential slot in a waveguide gives rise to excitation of parasitic waves and to radiation losses. Numerical computations with a scattering matrix code revealed the following scaling formula for the average gap losses:

$$P_c(\text{dB}) = 1.3\ (L\lambda/2a^2)^{3/2} \quad (4)$$

where L is the length of the slot. Formula (4) corresponds to eq. (1) and is in excellent agreement with that of [29]. Short annular gaps cause only very slight losses and can be used in special waveguide sections for: DC-breaks (insulation gaps), vacuum pumping or gas purging, insertion of fast gate valves or shutters, compensation of axial movements, and switchable mitre bends.

3.1.4 Waveguide mode analyzer and bi-directional coupler

A one-dimensional array of coupling holes in the mirror of a corner bend (see Fig.9) provides the possibility of mode selective measurement of forward and backward travelling power in an HE_{11} waveguide [9]. The antenna pattern of this array is analyzed in the focal plane of an imaging mirror with a polarization sensitive detector. This allows a measurement of the mode purity or, if two detectors are mounted at appropriate fixed positions, forward and backward power signals can be derived for monitoring purposes. The results of measurements on a 70 GHz monitor mitre bend with I.D. = 63.4 mm are plotted in Fig.10. Both measured patterns show good agreement with the calculated power distributions. Some extra sidelobes can be explained by stray radiation which was not perfectly screened during these first tests, and by some mode conversion (according to eq.(1) ≈ 1.5 %) of the only moderately oversized corner bend ($2a/\lambda \approx 15$).

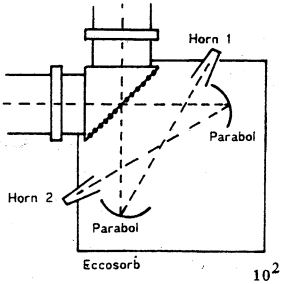

Fig. 9:
Schematic of waveguide mode analyzer and bi-directional coupler [9].

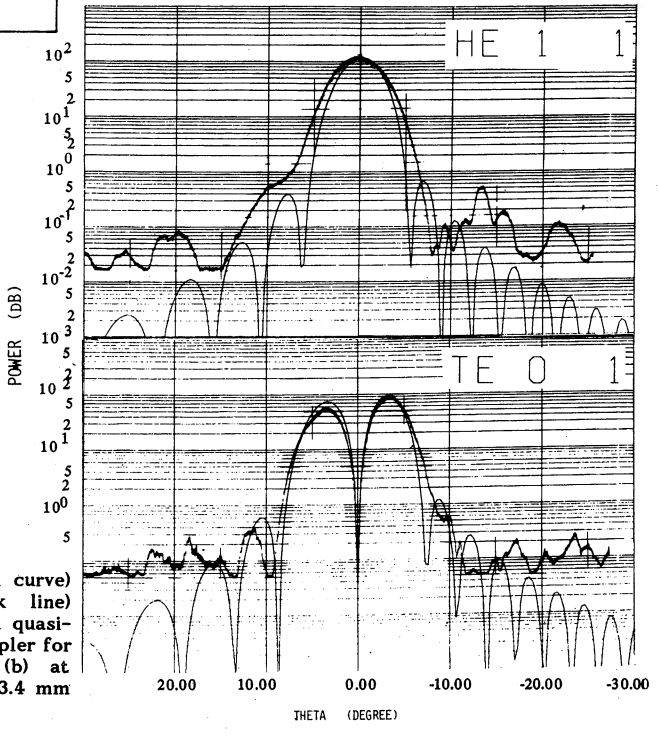

Fig. 10:
Calculated (thin solid curve) and measured (thick line) antenna patterns of a quasi-optical directional coupler for HE_{11} (a) and TE_{01} (b) at f = 70 GHz and I.D. = 63.4 mm [9].

3.2 Quasi-Optical TEM_{00} Beam Waveguide

A quasi-optical mirror beam waveguide is considered as an alternative solution for very-high-frequency ECRH scenarios [9,10].

3.2.1 Properties of quasi-optical mirror waveguides

The propagation of Gaussian beams has been treated extensively [32]. They are characterized by an intensity profile $P \sim \exp(-2r^2/w^2)$, where $w = w_0\sqrt{1 + (\lambda z/\pi w_0^2)^2}$ gives the beam radius as a function of the distance z from the beam waist (focus) with spot size w_0. The phase fronts of the wave are spherical with a curvature radius of $r(z) = z\,[1 + (\pi w_0^2/\lambda z)^2]$. The propagation of the Gaussian beam is performed by iterative transformation of the phase distribution with focusing metallic mirrors which are sections of ellipsoids. The properties of such quasi-optical mirror waveguides are:

(1) The maximum electric field strength E(0) exists in the center of the reference plane (beam waist). For $w_0 = 0.1$ m and $E(0) = 10^4$ V/cm one has a peak power carrying capability of $P_T(\text{peak}) = 42$ MW ! The power density on the focusing reflectors is much lower, so that mirror waveguides with very high power carrying capability can be set up.

(2) The losses of a beam waveguide arise from several contributions:

(a) Ohmic losses

The ohmic losses are the same as in the case of the HE_{11} corner bend (see 3.1.2)

(b) Diffraction losses

Diffraction losses occur by truncation of the beam due to the finite size of the reflectors (spillover) and the related change of the beam parameters

$$\Delta P_D^t/P > \exp(-2a^2/w^2) \qquad (5)$$

where a is the effective mirror radius (mirror size: 2a x 2a/cosΘ). A typical value is a = 2w which leads to a loss of ≈ 0.1 % . For a confocal beam waveguide with a given distance L between adjacent mirrors, one needs reflectors with

$$a = 2w = 2w_0\sqrt{2} = 1.13\sqrt{\lambda L} \qquad (6)$$

which requires a mirror radius of a = 165 mm for a mirror distance L = 10 m at 140 GHz. Other contributions to diffraction which arise due to beam profile distortion (generation of cross-polarization and higher-order beam modes by off-axis mirrors) and due to random surface imperfections are very small (≤ 0.05 %) [33].

(c) Misalignment losses

Misalignment of a mirror will increase the spillover loss of the subsequent reflectors. In a confocal beam waveguide the average deviation of the beam from the optimum beam path will not increase during propagation from one mirror to the next. If the stability of the adjustment is within 1 mrad, the loss $\Delta P^{ma}/P$ should typically not exeed 0.1 % per 10 m length of the beam waveguide. Within this stability limit, the slight astigmatism of a misaligned beam will produce negligible losses.

The total transmission losses per 90° reflection at an Al-alloy mirror in a Gaussian beam waveguide are at 140 GHz approximately

H-plane reflection: 0.5 % E-plane reflection: 0.7 % .

3.2.2 Design of a confocal beam waveguide

When designing a beam waveguide, it is of course necessary to minimize the transmission losses and simultaneously to keep the complexity of the system at a reasonable level. Table I may be helpful [9]. It shows how the loss contributions for a beam waveguide with fixed total length vary as a function of the number N of phase correctors.

total mirror surface	:	constant
ohmic losses	:	prop. N
beam truncation losses	:	prop. N
mode conversion losses	:	prop. N^2
cross polarization losses	:	prop. N^2
power capability	:	prop. N^{-1}
beam diameter	:	prop. $N^{-1/2}$
misalignment losses	:	prop. N
reliability	:	prop. N^{-1}
required surface precision	:	prop. $N^{-1/2}$

Table I: Loss contributions for a beam waveguide with fixed length as function of the number of mirrors N.

From Table I follows that a beam waveguide with a small number of mirrors is favourable. Efficiency and power capability would be high and the complexity of the system low. The limitations are the space needed for the resulting large beam diameter as well as machining tolerances which are necessary for the required surface precision. Often, a good compromise is to install the mirrors at locations where a reflector is needed anyway, i.e. where bends are necessary.

Multi-beam waveguides with separated, independently propagating 1 MW beams (matched to 1 MW, CW mm-wave windows) are possible: A "periscopic " broadband system composed by a sequence of 4 confocal double-mirrors (combination of an

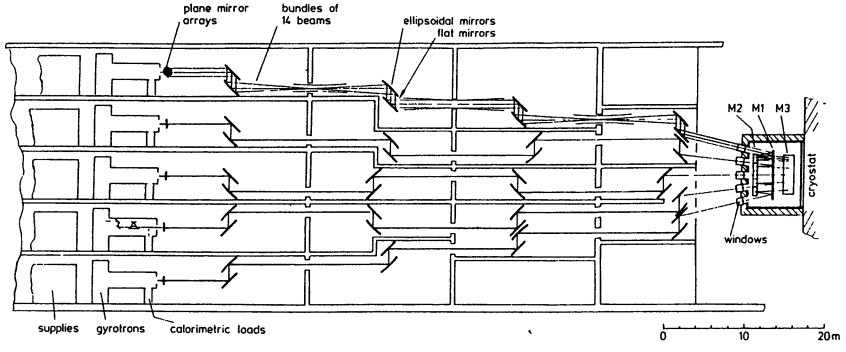

Fig. 11 : 4-double mirror multi-beam waveguide system for 100 MW, 200 GHz ECCD [9].

ellipsoidal and a flat mirror on one common stable frame), as shown in Fig. 11 , can be used in order to avoid coma and astigmatism and to reduce the sensitivity to misalignments [9].

The disadvantage of a Gaussian beam waveguide is that it is an open transmission system. A large space is required to provide the necessary RF-shielding and to guarantee tritium and radiactive dust containment in case of a torus window break.

Reflector waveguides are being tested in the 140 GHz ECRH systems on MTX at LLNL in Livermore [34] and Wendelstein WII-AS at IPP Garching [35].

3.2.3 Universal quasi-optical polarizer

To obtain the best accessibility conditions to the plasma, especially in the case of oblique wave launching, a quasi-optical polarizer should be introduced in the beam matching optics between the mm-wave source and the transmission line. Waveguide polarizers are not convenient since they must be very long (ellipticity coupling scales with λ/a^2) [16,27]. The universal quasi-optical polarizer allows to convert radiation with arbitrary input polarization state into any desired output polarization (linear, elliptical or circular). In principle, two different designs are possible. The first device is composed of a smooth roof-top mirror facing a flat, corrugated surface reflector having fixed groove depth (see Fig. 12) [14]. Sinusoidal corrugations allow higher power densities without arcing. By rotating the whole arrangement around the axis of incoming (and outgoing) beam, the output polarization will rotate twice as much. Additionally, the electric field incident on the grooved mirror is decomposed into its components parallel and perpendicular to the grooves with a phase shift of 90° between the reflected field components (effective groove depth is $\lambda/8$). Rotation of the corrugated reflector thus allows elliptical polarization to be arbitrarily adjusted. A 70 GHz prototype of such a system was tested at IPF Stuttgart [9]. The experimental results which illustrate the principle are plotted in Fig. 13 . The other polarizer design consists of two subsequent

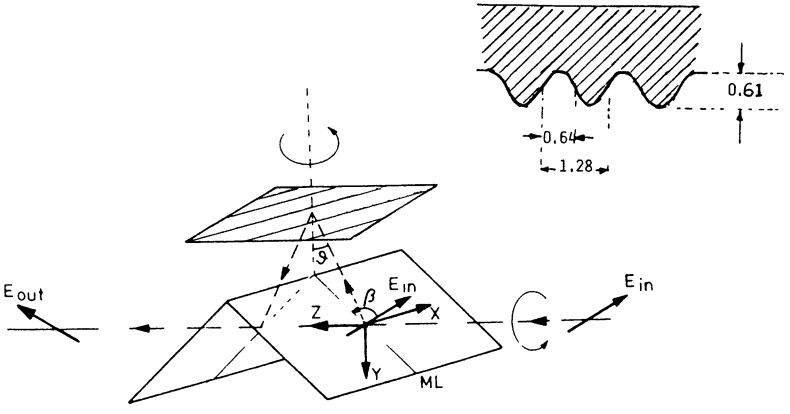

Fig. 12: Schematic of polarization rotator (roof-top mirror) combined with elliptical polarizer ($\lambda/8$ grooves) [9,14].

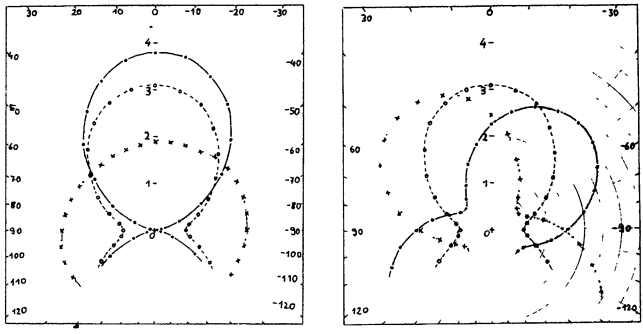

Fig. 13: Output polarization measurements for linear input polarization [9].
(a) Generation of different output polarization states.
(b) Rotation of the axes of elliptically polarized radiation.

corrugated reflectors (used at nearly perpendicular incidence), namely a polarization twister (electrical groove depth $\lambda/4$) and an elliptical polarizer (electrical groove depth $\lambda/8$) [10] as shown in Fig.14. By adjusting the angle between the groove directions, any output polarization state can be obtained. For sinusoidal corrugation profile with a period of 1:28 mm, measurements at 140 GHz yielded necessary corrugation depths of 0.79 mm and 0.61 mm for 180° and 90° phase shift, respectively [35].

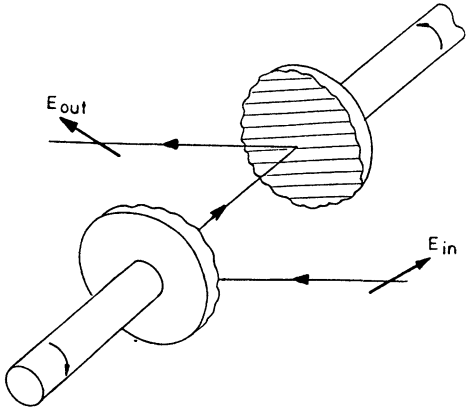

Fig. 14: Schematic of polarization twister ($\lambda/4$ grooves) and elliptical polarizer ($\lambda/8$ grooves) [10].

3.2.4 Quasi-optical bi-directional couplers

In-situ power monitoring can be performed using a quasi-optical directional coupler which is implemented on the surface of one of the beam waveguide reflectors. It is formed by a phase grating with small amplitude (typically $\lambda/100$) which is milled onto the mirror surface. In this case a small fraction of the power which is geometrically reflected from the mirror is coupled into diffractive beams (see Fig. 15 , left side). For an appropriate choice of the grating constant d according to the grating equation

$$d = n\cdot\lambda/(\cos\Theta - \cos\Theta') \qquad (7)$$

only one monitor beam of diffractive order n = -1 is possible, in this case, the monitor beams are clearly separated and a bi-directional coupler with high directivity is formed. For sinusoidal grooves with amplitude A the diffracted power is given by $P \approx (\pi A/\lambda)^2$. More advanced versions of this type of coupler comprise two focusing gratings on the mirror surface. In this case the diffracted beams can be perfectly coupled to matched horns to give the forward and backward signals and extra focusing elements are avoided. Additionally, the measurement of the field distribution of the diffracted radiation in the focal plane of the grating allows estimates of the mode composition of the transmitted main beams. A first test of such a 140 GHz coupler is shown in Fig. 16 [35].

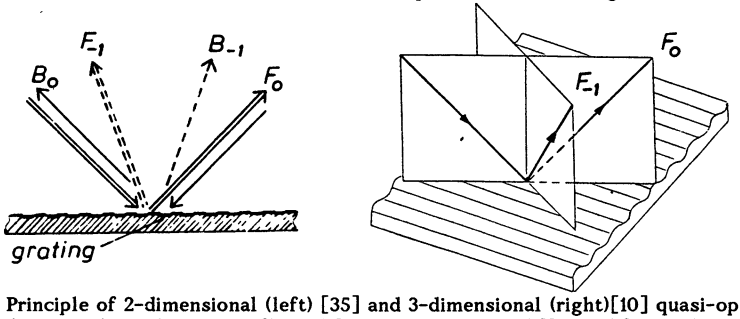

Fig. 15 : Principle of 2-dimensional (left) [35] and 3-dimensional (right)[10] quasi-optical directional couplers. F_0: reflected forward beam; F_{-1}: diffracted forward monitor beam; B_0: geometrically reflected beam; B_{-1}: backward monitor beam [9,35].

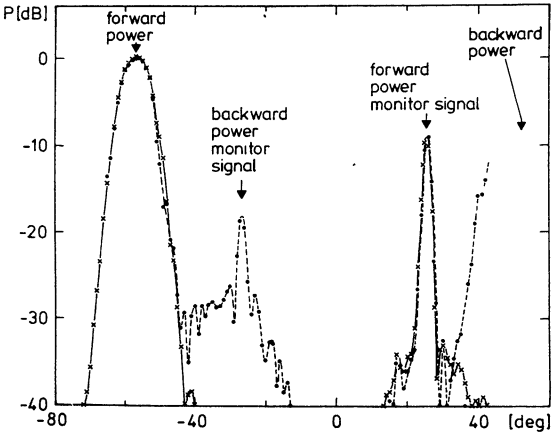

Fig. 16 :
Radiation pattern of the main and the monitor beams of the quasi-optical bi-directional coupler. Solid line: only forward travelling beam; dashed line: forward and backward beams simultaneously [9,35].

One clearly sees the difference of the beam width of the unfocused main beam and the focused monitor beams. The coupling factors are about -30 dB and -40 dB for the forward and backward monitor beams, respectively, due to different groove depths of the gratings (depths are 50 μm and 30 μm, width is approximately 0.5 mm, round bottom of the grooves). The measured directivity is better than 25 dB. The overlap of contributions from focusing and defocusing grating can be avoided by using a nonsymmetrical, 3-dimensional bi-directional coupler (see Fig. 15 , right side) [10].

3.2.5 Power combiners and beam splitters

Summators of coherent beams with same frequency (reversely used as wave beam splitters) and power combiners of wave flows with different frequency (multiplexer, quasi-autocollimation echelette) have been proposed and tested by IAP N. Novgorod [10]. Wave beams at f_1 = 70 GHz and f_2 = 79 GHz were combined with an efficiency of 98 %.

3.3 Combined Transmission Systems

Optimum ECRH transmission systems [9,10,14] combine the different advantages of circumferentially corrugated, circular HE_{11}-mode waveguide and quasi-optical TEM_{00} beam waveguide components, making use of the excellent coupling between the fundamental free-space Gaussian beam mode and the HE_{11} waveguide mode:

(1) Quasi-optical TEM_{00} components:
mode converters to produce a linearly polarized, Gaussian-like gyrotron output (see 4.), mode matching optics (converter output/universal polarizer), universal polarizer and launching antenna in the plasma chamber.

(2) Tubular HE_{11} waveguide components:
waveguide transmission with corner bends (partially equipped with hole array bi-directional couplers), waveguide switches and several waveguide components with annular gap for various purposes.

The total efficiency of a such a combined 140 GHz reference transmission system with 10 optimized corner bends, 5 slot sections and double-barrier torus window is 85 %, including the HE_{11}-to-TEM_{00} coupling losses. The efficiency of the quasi-optical gyrotron output mode converter is not included.

Fig. 17 shows a schematic of the gyrotron-to-HE_{11} waveguide matching optics installed on T-10 at Kurchatov Institute in Moscow [10] (11 channels each 0.5 MW, ~ 80 GHz, pulse length 1 s) for ECCD experiments. The first mirror of the three mirror matching optics serves as a mode filter (out-scattering of higher-order parasitic modes). The unwanted-mode power is absorbed by a water filled Teflon hose. The field structure at the waveguide input measured by a infrared camera is plotted in Fig. 18. The required precision of the angular alignment of waveguide and beam directions is described in 3.1.1 , A misalignment of 0.1° leads to about 2 % losses. A non-evacuated HE_{11} transmission line combined with an external quasi-optical gyrotron output mode transducing antenna (for $TE_{15,2}$) with matching optics and universal polarizer is foreseen in the 140 GHz collective Thomson scattering diagnostics on JET[14].

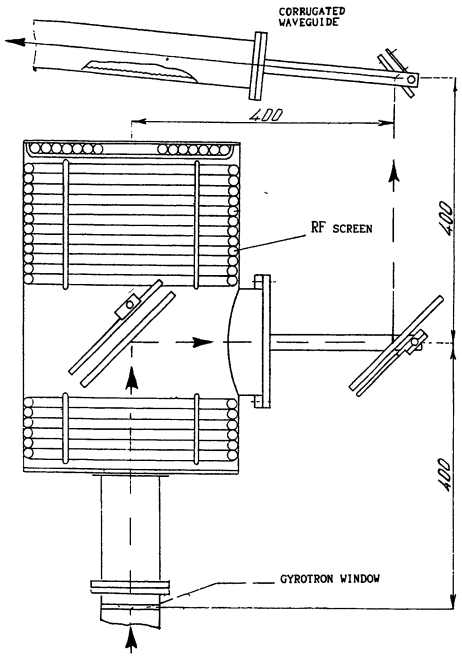

Fig. 17 :
Gyrotron-to-HE_{11} waveguide matching optics at T-10 [10].

Fig. 18 :
Power distribution generated by the 3-mirror matching optics and measured at the HE_{11} waveguide input by means of a infrared camera [10].

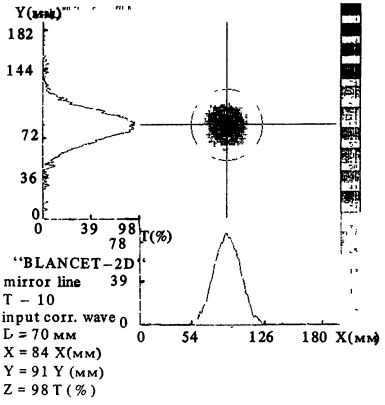

4. IMPROVED QUASI-OPTICAL MODE CONVERTERS FOR ROTATING HIGH-ORDER TE-MODES

Two different types of quasi-optical mode transducing antennas have been devised, mode converting slot radiators of the Vlasov type [36-39] and generalized mode converting twist reflectors of the Wengenroth type [34,40-42]. The improvement of the efficiency of such quasi-optical devices to directly convert the complicated field structure of rotating high order asymmetric gyrotron cavity modes into a linearly polarized Gaussian beam is of fundamental importance for future high power, high frequency ECRH and systems [9-11].

4.1 Vlasov-Type Quasi-Optical Mode Transducing Antennas

Mode converting slot radiators of the Vlasov type are ideal as built-in output mode converters for high power gyrotrons [12] since they permit a separation between the mm-wave and the electron beam (horizontal RF output), as shown in Fig. 19. Owing to diffraction losses into sidelobes, conventional Vlasov mode transformers have only a conversion efficiency around 80 % [36]. Theory predicts and experiments show that more than one mainlobe occurs in the azimuthal direction in the launcher far field if the radial index of the operating mode is larger than one. To obtain a single maximum and to reduce the diffraction losses in order to increase the conversion efficiency to ≥ 95 %, several methods have been proposed.

(1) Wave beam shaping by diffraction at convex cylindrical surfaces (flared radiating cuts) [37]

In the case of transformation of a whispering gallery mode (WGM) with a single radial field maximum (e.g. $TE_{15,1}$) into a Gaussian beam one achieves a theoretical efficiency of 98 % (see Fig. 20) whereas the efficiency for the transformation of a $TE_{15,2}$ mode is about 93 % (Fig. 21). The numerical integration is carried out using the generalized lens transformation (paraxial approximation) for the boundary problem in a region with two curved boundaries, the metal cylinder of the guide with convex surface and the modal caustic. New results from IAP N.Novgorod show that highly efficient converters are also feasible for high-order asymmetric volume modes. An efficiency of 97 % was obtained in a particular experiment with $TE_{15,4}$ [10].

(2) Addition of a "visor" mirror to the straight launcher cut [38]

By shaping that part of the launcher where the rays are finally reflected the ray direction is changed and the radiation pattern can be transferred into a Gaussian like beam. If the direction and width of the beam and the distribution of the rays in the beam are given, the contour of the parabola-like cylindrical reflector can be optimized also by the ray-tracing method (geom. optics). To predict the radiation pattern along the longitudinal axis, the method of wave optics is required. Fig. 22 shows the power contour levels measured at low power (rotating $TE_{12,2}$ mode at 120 GHz in I.D.= 25.6mm waveguide) with a conventional (left side) and an improved efficiency converter with a visor (right side). The radiated beam of the first transducer shows an n=2 radial mode substructure and several sidelobes. More than 20 % of the power is contained in the sidelobes. In the case of the improved launcher the power ratio between the mainlobe and the sidelobes is 97 %. The conversion efficiency into a Gaussian beam amounts to 95 % and the polarization is linear.

(3) Operation of a corrugated, helically cut quasi-optical antenna with hybrid modes [39]

All balanced hybrid modes propagating in a circumferentially corrugated waveguide with resonant slots

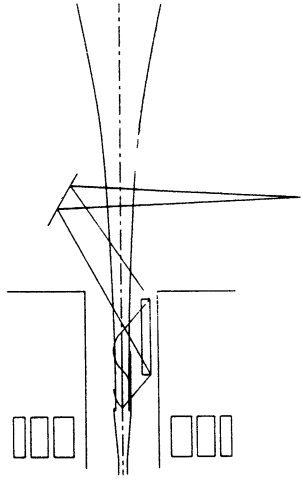

Fig. 19:
Schematic of lateral gyrotron output coupling system with quasi-optical mode converter.

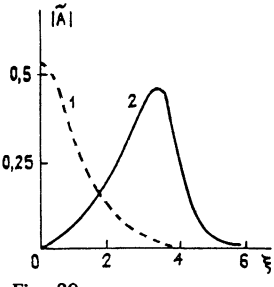

Fig. 20:
Transformation of $TE_{15,1}$ mode into a bell-shaped wave beam at a flared radiating cut [37].

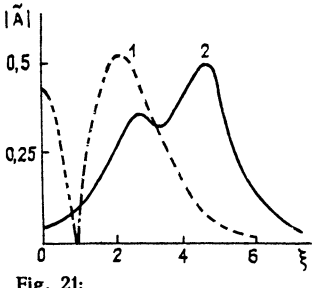

Fig. 21:
Transformation of $TE_{15,2}$ mode into a bell-shaped wave beam at a flared radiating cut [37].

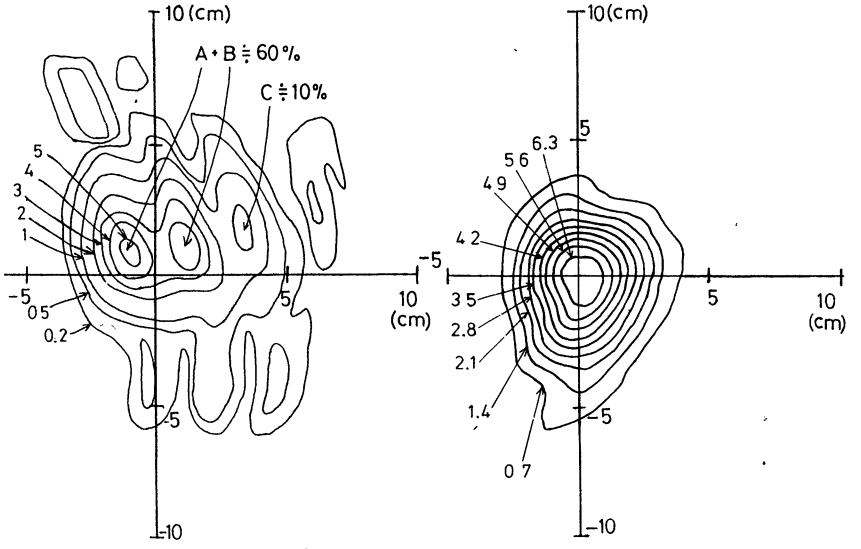

Fig. 22: Power contour levels for conventional and improved quasi-optical converter.

(depth = $\lambda/4$) exhibits low electric fields and low currents at the waveguide wall leading to low diffraction losses if radiated from a waveguide launcher. Fig. 23 shows the radial dependence of the Poynting-vector for a rotating $TE_{15,2}$ WGM and for the corresponding balanced $EH_{15,2}$ hybrid mode. There is almost no energy transport by the hybrid mode at the waveguide wall and there is only one maximum which leads to one mainlobe in the far field (Fig. 24).

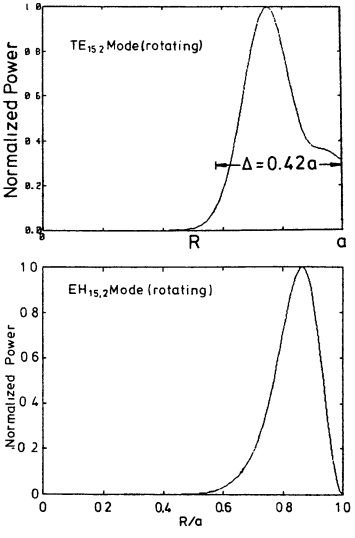

Fig. 23:
Normalized radial power distribution of a rotating $TE_{15,2}$ WGM and of the corresponding balanced $EH_{15,2}$ hybrid mode.

Fig. 24:
Azimuthal dependence of far-field pattern of a $EH_{15,2}$ hybrid mode launcher [39].

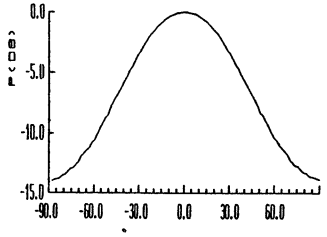

4.2 Generalized Wengenroth-Type Mode Transducing Antennas

Generalized Wengenroth-type quasi-optical mode transducing antennas with specific corrugated polarization twist reflectors, using amplitude and phase matched mode WGM mixtures to reduce the diffraction losses can also be used as gyrotron output mode transformers [42]. Recently, a similar device consisting of a mode-converting taper and three mirrors, as shown in Fig. 25, has been proposed [34]. The focusing mirror M_1 incorporates steps in the reflecting surface and is shaped like a counterbore tool bit, to convert skew rays ($k_\phi \neq 0$) of the incident mm-wave power into nonskew rays. M_2 has generalized twist reflector grooves in the surface (grooves $\approx \lambda/4$ deep) to linearly polarize reflected fields. Mirror M_2 then focuses the resulting annular beam onto mirror M_3. The final mirror M_3 is a phase correcting optic and reflects the beam 90° from the waveguide axis producing an output beam with a Gaussian-like profile. The calculated fraction of power in the mainlobe exceeds 96 %.

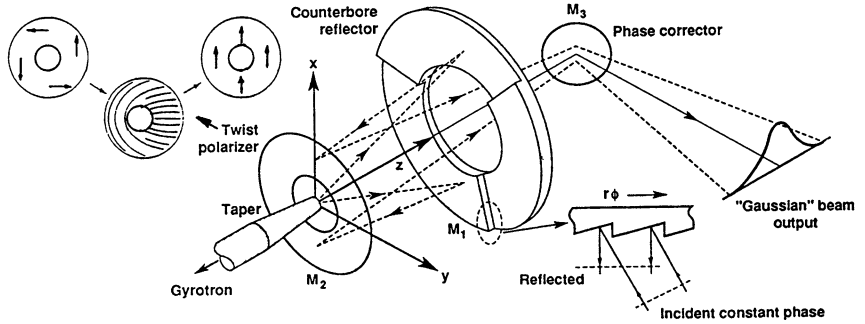

Fig. 25: Drawing of the generalized twist reflector mode converter for WGM [34].

5. CONCLUSIONS

In this paper, some of the recent efforts in the research and development of electrodynamic systems for mode conversion, transmission and diagnostics of very high power mm-waves were reviewed. Optimum ECRH transmission systems combine the different advantages of corrugated circular HE_{11} waveguide and quasi-optical TEM_{00} beam waveguide components, making use of the excellent coupling between the free-space fundamental Gaussian beam and the HE_{11} hybrid mode. The total power transmission efficiency from source to plasma of a 140 GHz, 1 MW reference transmission line is approximately 85 % in the desired mode. The efficiency of the quasi-optical gyrotron output mode converter is not included, but improved versions can be very efficient (≈ 97 %). The electrodynamic community is very confident that all high power mm-wave transmission problems connected with large scale ECRH systems can be solved.

ACKNOWLEDGMENTS

The author is indebted to his former colleagues W. Henle, A. Jacobs, W. Kasparek, H. Kumric, G.A. Müller, J. Pretterebner, P.G. Schüller and D. Wagner from the Institute for Plasmaresearch (IPF) of the University of Stuttgart for many valuable discussions and the excellent collaboration. We acknowledge with gratitude a lot of helpful suggestions of L. Rebuffi from the NET/ITER Team, Garching and all the other members of the design group for the "ITER ECW System Common Conceptual Design".

REFERENCES

[1] R. Prater, J. Fusion Energy, **9** (1990) 19.
[2] V. Erckmann et al., Fusion Technology, **17** (1990) 76.
[3] K. Felch et al., J. Fusion Energy, **9** (1990) 59.
[4] C. Moeller, Int. J. Electronics, **53** (1982) 587.
[5] M. Thumm et al., Int. J. Infrared and Millimeter Waves, **6** (1985) 459.
[6] M. Thumm, Int. J. Electronics, **57** (1984) 1225, and **61** (1986) 1135.
[7] W. Kasparek et al., Proc. 15th Symp. on Fusion Technology (SOFT88), Utrecht, Vol. 1 (1988) 490, North Holland, Amsterdam (1989).
[8] J.L. Doane, Int. J. Electronics, **53** (1982) 573, and **61** (1986) 1109.
[9] W. Henle et al., Proc. 16th Symp. on Fusion Technology (SOFT90), London (1990) Paper O-09 and Reports ITER-IL-HD-6-9-E-1 and -E-5 (1989) and ITER-IL-HD-6-0-5 and -22 and -23 (1990), Garching.
[10] V.I. Belousov et al., Report ITER-IL-HD-6-0-8 and -26 (1990), Garching.
[11] C. Moeller et al., Proc. 16th Symp. on Fusion Technology (SOFT90), London (1990) Paper R-10 and Report ITER-IL-HD-6-0-9 (1990), Garching.
[12] V.A. Flyagin and G.S. Nusinovich, Proc. IEEE, **76** (1988) 644.
[13] W. Kasparek and G.A. Müller, Int. J. Electronics, **64** (1988) 5.
[14] H.J. Barkley et al., Report JET-R(88) 14 (1988), Abingdon.
[15] M. Thumm et al., Conf. Digest 13th Int. Conf. on Infrared and Millimeter Waves, Honolulu (1988) 111.
[16] M. Thumm and H. Kumrić, Int. J. Infrared and Millimeter Waves, **10** (1989) 1059.
[17] H. Kumrić et al., Int. J. Electronics, **64** (1988) 77.
[18] M. Thumm, Int. J. Infrared and Millimeter Waves, **6** (1985) 577.
[19] H. Kumrić and M. Thumm, Int. J. Infrared and Millimeter Waves, **7** (1986) 1439.
[20] M. Thumm et al., Microwave J., **29** (1986) 103.
[21] P.J.B. Clarricoats and A.D. Olver, "Corrugated Horns for Microwave Antennas", IEE Electromagnetic Waves Series, **18**, Peter Peregrinus Ltd, London (1984).
[22] C. Dragone, IEEE Trans. Microwave Theory Tech., **MTT-28** (1980) 704.
[23] L. Rebuffi and J.P. Crenn, Int. J. Infrared and Millimeter Waves, **10** (1989) 291.
[24] W. Kasparek and M. Thumm, Conf. Digest 11th Int. Conf. on Infrared and Millimeter Waves, Tirrenia (Pisa) (1986) 212.
[25] F. Kahn, NTZ Archiv, **2** (1980) 7.
[26] J.W. Carlin and P. D'Agostino, Bell Syst. Tech. J., **52** (1973) 453.
[27] J. L. Doane, Infrared and Millimeter Waves, Vol. **13**, p. 123, ed. K. Button, Academic Press (1985).
[28] R. Magne et al., Proc. 16th Symp. on Fusion Technology (SOFT90), London (1990) Paper R-33.
[29] R.B. Vaganov, Radio Eng. Electron. Phys., **18** (1973) 170.
[30] D. Wagner et al., Conf. Digest 15th Int. Conf. on Infrared and Millimeter Waves, Lake Buena Vista (Orlando) (1990).
[31] B.Z. Katsenelenbaum, Radio Eng. Electron. Phys., **8** (1963) 1098.
[32] W. Kleen and R. Müller, eds., "Laser", Springer, Berlin (1969).
[33] P. Belland and J.P. Crenn, Applied Optics, **21** (1982) 522.
[34] B.W. Stallard et al., Proc. 16th Symp. on Fusion Technology (SOFT90), London (1990) Paper R-12.
[35] W. Henle et al., Proc. 16th Symp. on Fusion Technologiy (SOFT90), London (1990) Paper R-34.
[36] S.N. Vlasov et al., Radio Eng. Electron. Phys., **20** (1975) 14.
[37] S.N. Vlasov et al., Radio Phys. Quantum Electron., **31** (1988) 1070.
[38] M. Iima et al., Conf. Digest 14th Int. Conf. on Infrared and Millimeter Waves, Würzburg (1989) 405.
[39] A. Möbius and M. Thumm, Conf. Digest 14th Int. Conf. on Infrared and Millimeter Waves, Würzburg (1989) 390.
[40] R.D. Wengenroth, IEEE Trans. Microwave Theory Tech., **MTT-26** (1978) 332.
[41] B.W. Stallard et al., Proc. 4th Int.Workshop on ECE and ECRH, EC-4, Rome (1984)109.
[42] L. Rebuffi and M. Thumm, Conf. Digest 14th Int. Conf. on Infrared and Millimeter Waves, Würzburg (1989) 394.

QUASI-OPTICAL GYROTRON DEVELOPMENT AT THE CRPP

The CRPP/ABB Quasi Optical Gyrotron Development Group
presented by M. Q. Tran
Centre de Recherches en Physique des Plasmas
Association Euratom-Confédération Suisse
Ecole Polytechnique Fédérale de Lausanne
21 Av. des Bains, 1007 Lausanne-Switzerland

Abstract - The operation of the 100GHz quasi-optical (Q.O.) gyrotron of the Centre de Recherches en Physique des Plasmas in Lausanne is described. Power up to 90kW and efficiency up to 12% have been achieved. Other features of the Q.O. gyrotron include single longitudinal mode operation, frequency tunability. Second harmonic emission (200GHz) has been observed with a resonator designed for operation at the fundamental. The issues pertinent to the Q.O. gyrotron concept are also discussed.

I) Introduction

The use of electron cyclotron waves (ECW) in fusion plasmas requires CW sources in the frequency range of 100-300GHz at power level of 0.5MW to 1MW per tube. The gyrotron is presently the most developed source for such applications. Two gyrotron concepts are presently under study, differing mainly in the resonant structure in which the interaction between the electromagnetic (EM) wave and the electron beam occurs. In the conventional gyrotron, the resonant structure is a cylindrical cavity operating in the TE^{o}_{mn1} mode. As an alternative to this concept, the quasi-optical (Q.O.) gyrotron was proposed, where the resonant structure is a Fabry-Pérot resonator placed transversely to the electron beam and operating in the gaussian TEM_{00q} mode. The advantages of the Q.O. concept are the frequency tunability and the geometric separation between the spent electron beam and the microwave output. The former characteristic offers flexibility for experiments on fusion devices, where it may be advantageous to change the localization of the power deposition zone without having to modify the magnetic field and therefore affecting the plasma properties.

The latter feature facilitates the design and the implementation of high power collector or depressed collector.

The theory of the Q.O. gyrotron was first presented in the late sixties by Rapoport et al. and other Russian physicists [1]. Further theoretical development can be found in several more recent references [2,3,4]. Experimental investigations were performed with a Fabry-Pérot resonator placed parallel [5] and perpendicular [6,7,8,9] to the electron beam. In this paper, we shall review some of the works being performed at the Centre de Recherches en Physique des Plasmas (CRPP) in the field of Q.O gyrotron and discuss some of the issues for future development.

II) Experimental set-up

The experimental set-up at the CRPP is described in figure 1. The magnetic field is created by a large superconducting coil system with a room temperature bore of 40cm and an axial gap of 15cm. In the cathode region, two gun coils were used to adjust the field and its gradient at the cathode surface. A magnetic field $\underline{B}_o$ up to 4T could be generated in the interaction region and a compression ratio of 20 is achieved between the cathode and the interaction zone. The operating

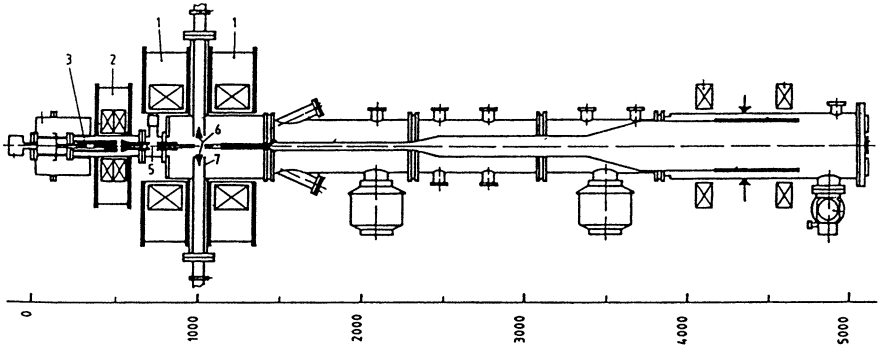

Figure 1.
Experimental set up. The main components are the main coils (1), the gun coils (2), the electron gun (3) and the mirrors (6,7) inside the vaccum vessel.

frequency was 100GHz for the fundamental frequency $\omega \sim \Omega/\gamma$ where Ω and γ are the non relativistic cyclotron frequency and the relativistic factor.

The electron beam was created using a standard Magnetron Injection Gun (MIG) which delivered an annular electron beam. The gun was originally designed for operation at 120GHz, but, due to operational constraints of the magnet, had to be adapted for operation around 100GHz. From the Hermannsfeldt EGUN code, the designed value of the ratio $\alpha=v_\perp/v_\parallel$ was 1.49 with a spread $\Delta\alpha/\alpha$ of 21%. However during the optimization of the output power, the current in the gun coils had to be set to values different from the designed ones, resulting in a lower value for α (α =1.12). The electron beam was guided by a beam tunnel (diameter =1cm) along its entire trajectory, except over 12cm (equivalent to 8 spot sizes w_o) in the interaction region.

The resonator was formed by two spherical mirrors made out of gold-plated copper. Since the experiment was pulsed at low duty cycle (pulse length = 15ms with a maximum repetition rate of approximately one shot per 30s), no cooling was necessary. Experiments were performed with and without a cylinder (diameter =15cm) enclosing the whole resonator up to the output waveguide. This cylinder is similar to the magnet cross bore of the compact version [7,8] of a Q.O. gyrotron. It did not influence the performances of the device.

The power was coupled out through an annular slot cut in each mirror. The slot width was 16.5mm and its inner edge was located at r = 28.5mm as measured from the resonator axis. The output transmission T and the coupling efficiency (i.e. the fraction of the diffracted energy which passed through the slot compared to the total diffracted power) were computed using a numerical code [10] based on Kirchoff's formulation of the Huyghens-Fresnel principle. For the TEM_{00q} gaussian mode, the power transmission of the resonator was about 4% with a coupling efficiency of 90%. Transverse modes TEM_{mnq} (m = radial index $\neq$ 0, n = azimuthal index $\neq$ 0) had a larger output transmission and could not be excited. The parameters of the experiments are summarized in Table I.

The microwave output power was extracted from both mirrors and guided through two, smooth-wall, overmoded waveguides (diameter 86.9mm). Since the resonator was symmetric, an equal amount of power

was extracted from both mirrors. The vacuum windows were Kapton foils of 125μm over the waveguide diameter. These windows could withstand power densities up to 1.5kW/cm^2 during the 15ms pulses. The same windows have been used for the last one and a half year.

Gyrotron frequency [GHz]	100
Electron beam	
Gun structure	Triode
Beam voltage V_b[kV]	65-70
Mod-anode votage V_a[kV]	25-30
Current I[A]	≤12
Compression ratio	20
Designed $\alpha = v_\perp/v_{||}$	1.49
Optimum value of α	1.12
Beam radius r_b [mm]	2.13
Pulse length [ms]	15
Resonator characteristics	
Mirror radius of curvature R [cm]	50
Mirror separation d[cm]	34
g= 1-d/R	+0.32
Beam waist w_o[cm]	1.51
kw_o at 100GHz	31.7
Inner diameter of slot $\emptyset_i$[mm]	57
Fresnel number correponding to $\emptyset_i$	0.8
Outer diameter of slot [mm]	90
Outer diameter of mirror [mm]	136
Longitudinal mode separation [MHz]	440
Output transmission T[%] @ 100GHz, TEM_{00q}	4
Diffractive Q @ 100GHz, TEM_{00q}	34900
Ohmic/Diffractive loss [%]	5
Total Q @ 100GHz, TEM_{00q}	33200
Total Q @ 200GHz, TEM_{00q}	880000
Total Q @ 200GHz, TEM_{01q}	460000

Table I - Parameters of the Q.O. gyrotron

For power measurements, two different calorimeters were used. An electronic Scientech laser calorimeter was modified for optimum absorption in the 100GHz range by coating its surface with 3M Nextel® paint. This coating had to be periodically replaced since the microwave pulses burned the absorbing layer. A second calorimeter using Octanol $C_8H_{18}O$ as the absorbing medium was also built [11]. Octanol was selected for its RF dielectric properties [12] and its high boiling point (195°C). The measured reflection coefficient of the Octanol calorimeter was less than 5%. To measure the power of spurious second harmonic emission (Frequency = 200GHz), the technique used by Byerly et al. [13] was implemented. For this purpose, absorber plates (Macor) which had different absorption coefficients at 100GHz (k_i = 0.75 Np/cm) and 200GHz (k_i = 2.0 Np/cm) [14] were inserted into the microwave beam. Each absorber plate thickness was selected to be $n\lambda_{mat}/2$, where λ_{mat} is the wavelength in the absorber at 100GHz. We thus minimized effects due to reflection at the fundamental and the second harmonic. With increasing thickness (by stacking the plates), the content of the second harmonic in the transmitted power decreased, since the absorption coefficient k_i is larger at 200GHz than at 100GHz. By fitting the experimental curves of the measured power versus the thickness with the values of k_i, it was possible to determine the content of power in the second harmonic.

Polarization of the output EM wave was determined by reflecting it with a one-dimensional grid (wire diameter = 10μm, wire separation = 100μm) and measuring the reflected wave with a standard WR-10 horn. Maximum reflection occured when the electric field of the wave was parallel to the wire.

The frequency was measured using heterodyne systems for the frequency range around 100GHz and 200GHz. All systems had an IF in the X-band. The down conversions from the RF to the IF signals were performed using either an harmonic mixer operating at the 8th harmonic ($f_{RF} = 8f_{LO} + f_{IF}$) or a fundamental mixer. For the 200GHz frequency range, the mixer operated at the second harmonic. To avoid any ambiguity in the frequency determination, a high-pass filter (Attenuation = -60db at 100GHz) or a low-pass filter (Cut-off frequency: 165GHz [15]) was also inserted in front of the heterodyne system. Time resolved spectra were obtained by sweeping the LO frequency and looking at fixed IF frequency. Typically, it was possible to obtain a spectrum of the gyrotron over a 3GHz bandwith in 500μs. A fre-

quency spectrum without any time resolution (i.e. over the whole pulse length of 15ms) was obtained using a spectrum analyzer.

III) Experimental results

a) Fundamental frequency [9]

The time variation of the cathode voltage, mod-anode voltage, electron beam current and microwave output is shown in figure 2. The cathode voltage was set at its nominal value when the mod-anode voltage and the electron beam current I were turned on: during the start-up phase of the microwave pulse, the relativistic factor γ was constant, while the α and I varied. The time variation of these quantities was much slower than the typical linear growth time τ for the EM wave inside the resonator: τ was about 14ns at 10A, whereas the time scale for variation of α and I was of the order of 2ms.

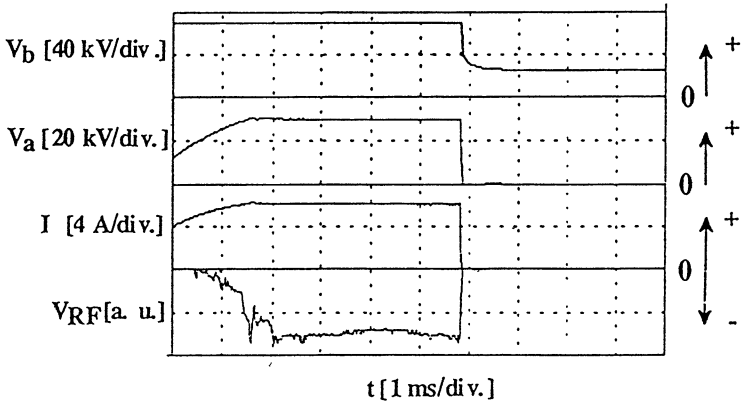

Figure 2.
Time variation of the beam voltage V_b, mod-anode voltage V_a, current I and microwave power V_{RF} from a diode

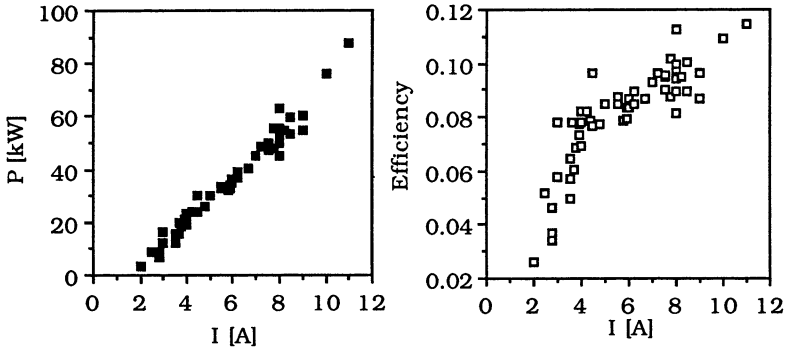

(a) (b)

Figure 3.
Variation of the power (a) and efficiency (b) with current I

The output power from the gyrotron was optimized by tuning the gun coils and the mod-anode voltage. The optimum output power and efficiency are shown on figures 3a and 3b. Note that, in the range of currents which was explored (limited by the capability of the power supply), the power and the efficiency did not saturate: the respective maxima which were reached were 90kW and 12%.

Working with a highly overmoded resonator (the operating mode is the $TEM_{0,0,227}$), an important issue was whether or not it was possible to operate in single longitudinal mode. We have found that, by proper tuning of the system, the output spectrum consisted of a single frequency: in figure 4a such a single mode spectrum is shown for an electron beam current of 9.4A. By changing parameters, the frequency spectra could exhibit two or more modes [Figs. 4b or 4c]. All the spectra were stable in time during the whole pulse. In the case of multimode, the main mode is about 6dB larger than the others. When two or more modes are excited, their frequency separation was equal to c/2d, indicating that only longitudinal modes TEM_{00q} were excited. The frequency spectrum was also shifted towards higher frequency when the current was increased: we have measured a shift of four longitudinal modes for a variation of the current I between the starting current and 10A (Fig. 5).

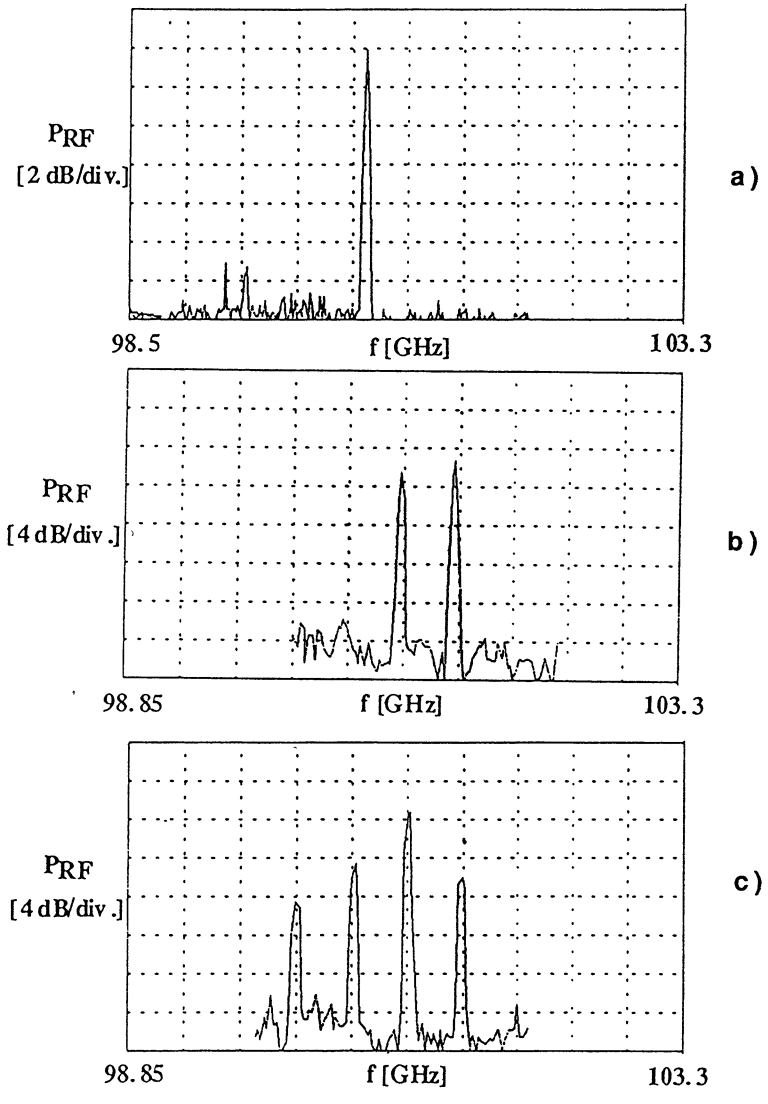

Figures 4a, b, c
Frequency spectrum

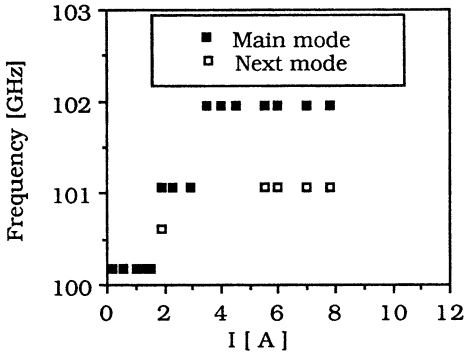

Figure 5.
Variation of the frequency versus beam current I

With the present output coupling scheme, the polarization measurement gave about 6dB difference, on average, between the cross polarizations, the dominant polarization being with the electric field perpendicular to the static magnetic field and the direction of the microwave output beam.

Another important feature of the Q.O concept is its tunability. We can distinguish between three different methods of tuning the frequency: by varying the mirror spacing d, by changing the beam voltage V_b or by changing the magnetic field B_0. All three methods have been successfully tested. By changing the mirror separation d, the frequency could be continuously tuned between two longitudinal modes with the same parity (e.g $TEM_{0,0,227}$ to $TEM_{0,0,225}$), in our case over a range of 880MHz (Fig. 6). For modes with the same parity, the averaging of the efficiency due to the standing wave pattern of the electric field gives the same result.

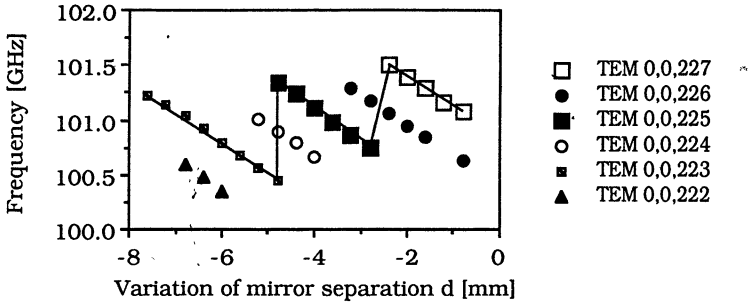

Figure 6.
Frequency variation by changing the mirror separation d

Changing the electron beam voltage can provide a method for fast frequency tuning. In our experiment the tuning range by this method was limited to about 1GHz (Fig. 7). The mode jumped by 440MHz.

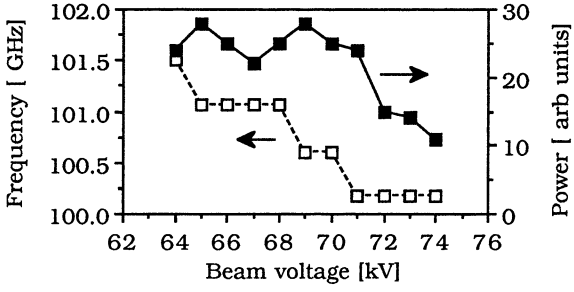

Figure 7
Variation of the frequency and power versus beam energy

Frequency tuning by changing the magnetic field B_0 allowed a larger tuning range (Fig. 8). In our experiment, the upper and lower bounds of tuning were set respectively by the superconducting magnet capabilities and by interception in the electron gun. A variation of 5% was achieved with only moderate power change.

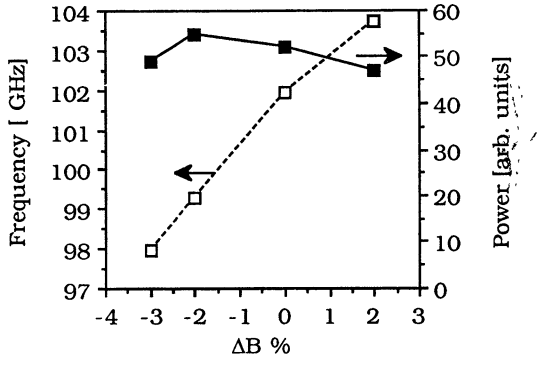

Figure 8.
Variation of the frequency and power versus magnetic field

b) Second harmonic emission [16]

Our experiments indicated that spurious second harmonic emission at 200GHz did occur, even though the resonator was designed for operation at only the fundamental. No higher harmonics were observed. Great care was taken to avoid any ambiguity in the identification of the second harmonics. Firstly, we verified that our second harmonic detection system did not give any signal when the low-pass filter was placed in front of its input. We also checked that the ratio between the signals at the second harmonic and the fundamental decreased when a Macor plate of thickness $n\lambda_{mat}/2$ was inserted in front of the respective detection systems. The power content in the second harmonic was about 20% of the one in the fundamental, using the method described above.

Simultaneous frequency measurements of the fundamental and the second harmonic were also performed. It is important to note that the emission at the second harmonic was exactly at twice the frequency of the fundamental with an accuracy of about 0.03%[16]. This second harmonic emission could also be identified as a resonator mode. We have changed the mirror separation d and observed that its frequency varied linearly with d

in a range of 1.6GHz, while the fundamental changed within 880MHz (Fig. 9).

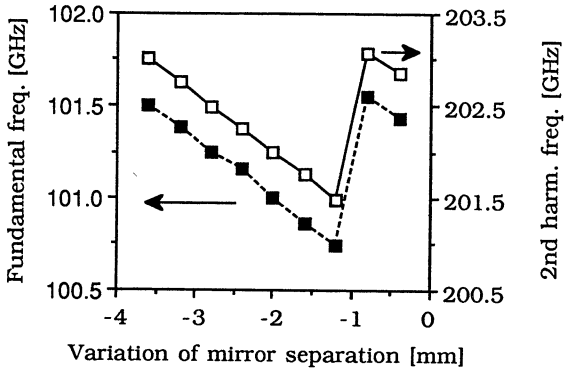

Figure 9.
Variation of the frequency of the fundamental and the second harmonic with the mirror separation d.

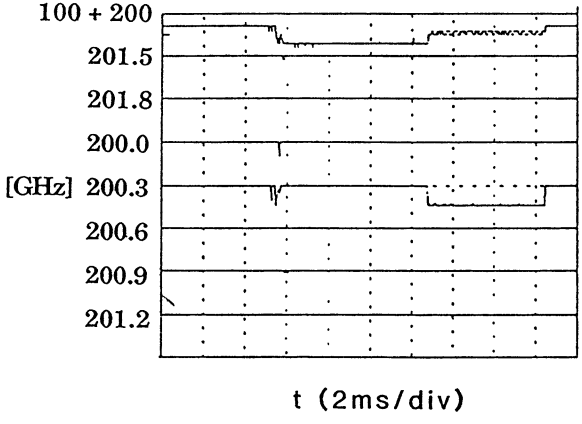

Figure 10.
Temporal variation of the total power of the spectra around 200GHz.

The presence of the second harmonic also affected the total emitted power. Figure 10 shows the time resolved signal from a diode recording the total power at the fundamental and the second harmonic and the signals at frequencies around 200GHz in band of ±150MHz. It was observed that when the second harmonic was not excited, the total efficiency was enhanced. The signal from the diode, which monitored the total power at 100 and 200GHz, dropped when the second harmonic was excited. A similar result is presented in figure 11, where the variations of the total power and the one around 200GHz are presented versus the electron beam α.

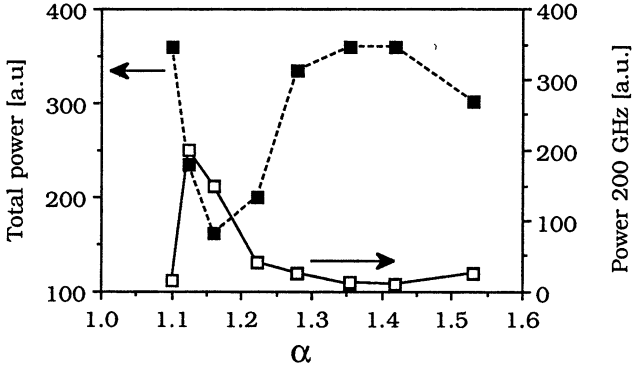

Figure 11.
Variation of the total power and the power at the second harmonic with respect to α. The two power scales are not equal due to different diode response at different frequencies

IV) Discussion

Many of the expected features of the Q.O. gyrotron have been experimentally observed. Single mode operation was obtained, confirming the theoretical predictions [3]. Different methods of frequency tuning have been demonstrated. Similar observations have been reported by Fliflet el al. [8]. In these experiments, a maximum efficiency of about 15% was obtained, a value which is comparable to ours. At higher power (up to 600kW [17]), the efficiency decreased to about 9%.

The maximum theoretical efficiency for the parameters presented in Table I is about 20% at 10A. The optimum detuning corresponds to a shift of about 4 to 5 longitudinal modes; that is, an important frequency pushing is expected if the optimum operating point is to be reached. Although experimentally such a frequency pushing was observed, its interpretation should involve the change of the electron beam voltage depression ΔV in the beam tunnel and the interaction region with the current. Based on the estimate of Fliflet et al. [8], ΔV is about 8kV at 10A. This corresponds to a decrease of the relativistic factor γ of 1.3% and to a shift of 3 to 4 longitudinal modes. We have computed the non-linear efficiency of the Q.O. gyrotron taking into account the beam depression ΔV in the interaction region. To compute the profile of the beam depression along $\underline{B}_0$, we modelize the boundary conditions in the interaction region as a conducting cylinder of a diameter equal to the mirror separation d and length l equal to the distance between the two upstream and downstream beam tunnels. At the entrance of the interaction region, ΔV is assumed to be null. $\Delta V(r,z)$ is then straight forwardly derived from the expression of the Green function for the electrostatic problem of a charge inside a conducting cylinder [18]. The DC retarding field E_z is inserted in the non-linear equations describing the electron cyclotron maser instability both in the single-mode and in the multi-mode [3] codes. The multi-mode calculations [19] indicate that the whole spectrum is shifted by about 4 modes at I above 10A compared to the case where the effect of ΔV is neglected, as shown in figure 12. The beam depression in this calculation

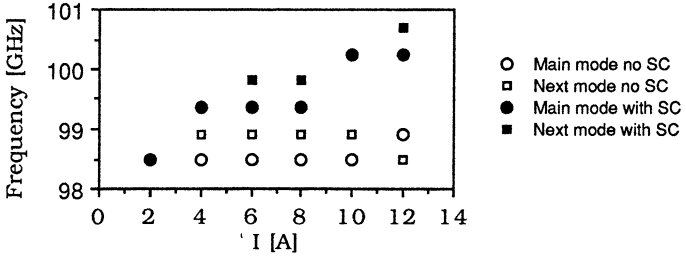

Figure 12.
Calculated frequency pushing in presence of beam depression (Plain symbols). The open symbols represent the results obtained without taking into account the beam depression.

corresponds to the actual length l in the experiment. The value of Ω/r used was not adjusted to fit the experimental conditions of figure 5. The agreement with the experimental result is fairly good. Beam depression might, therefore, account for a part of the observed frequency pushing. Further experiments are needed to clarify this important issue. Under our experimental conditions, AC space charge effects should not affect adversely the efficiency [20]. Means to control the detuning have to be implemented if the optimal detuning cannot be reached through the non-linear competition between the different unstable longitudinal modes. In a pulsed experiment, a variation in time of the beam energy could change the detuning at a given beam current, if the mode is stable [4,21]. We have verified by numerical computation that, for example, a change in the beam voltage V_b from 70 kV to 80 kV can change drastically the output power and efficiency compared to the case without voltage change. The results of such a simulation is presented in figures 13a and b. The voltage V_b is suddenly increased by 10kV (at time t=750ns in the calculation), when the system has reached an equilibrium state corresponding to V_b=70kV. The power jumps from 700kW to more than 1.2MW. The beam current I is 50A in this simulation and α is equal to 1.5. Plans to implement such scheme on our Q.O. gyrotron are under consideration. In a CW tube, magnetic field tuning is the most straightforward method to reach the optimum operating point.

The physics of the second harmonic emission is presently under investigation. The salient features which need to be understood are: 1) the frequency locking to the fundamental and 2) its influence on the efficiency. A similar phenomenon of frequency locking has been observed by Danly et al. [22]. In their experiment, no resonant cavity mode corresponded to the second harmonic. In our case, we have found that the $TEM_{0,1,454}$ mode has a resonant frequency (f=202.29GHz) which is exactly twice the one at the fundamental mode $TEM_{0,0,227}$ (f=101.14GHz). This migth explain the relatively large output power at the second harmonic compared to the results of Danly et al. [22].

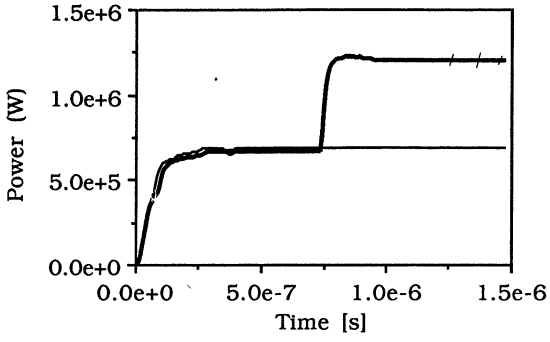

(a)

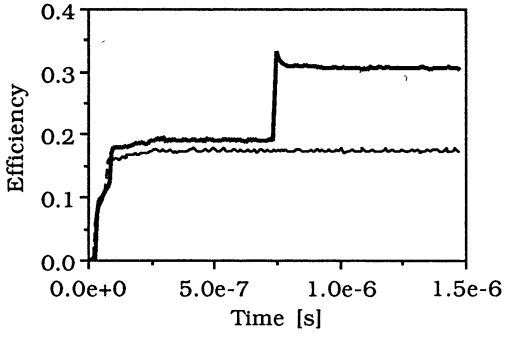

(b)

Figure 13.
Variation of the power (a) and efficiency (b) when the beam voltage V_b is increased from 70kV to 80kV (thick lines) as given by the multi-mode simulation. For comparison, we have plotted the power and efficiency for V_b = 80kV (thin lines). The beam current I is equal to 50A, α to 1.5 and the transmission T to 10%.

V) Conclusion

For electron cyclotron heating of fusion devices, it is desirable to have gyrotrons with unit power around one megawatt. Parametric studies have shown that Q.O. gyrotron at the megawatt level and at frequency higher than 100 GHz could be designed under the usual constraints on the ohmic heat load on the mirror (1.5kW/cm^2). Examples of such design are given in Table II [23]. Similar parameters were obtained by Fliflet et al. [8] in their prospectives studies of megawatt Q.O. gyrotrons.

Frequency [GHz]	150	180
Power [MW]	1	1
Beam current [A]	49	54
Beam voltage [kV]	90.2	81
α	1.6	1.7
Resonator g	-0.64	-0.9
Mirror separation d [cm]	38	42.7
Resonator transmission T [%]	8.5	10.7
Efficiency [%]	24	23

Table II - Parameters of 1MW Q.O. gyrotron.

In future development plans for Q. O. gyrotron, the following issues are of importance. Methods for increasing the efficiency have to be developed. The use of a sheet electron beam will avoid the decrease in efficiency due to the averaging over the standing wave pattern in the Fabry-Pérot resonator. Such a gun has been built and the propagation of segmented electron beam has been successfully demonstrated [24]. For future ECW systems, tens of megawatts of ECW power will be required. At present, the total system efficiency is considered to be of the order of 25%, assuming a gyrotron efficiency of 30%. Recovery of part of the spent beam energy might be beneficial. For example, a multistage depressed collector [25] could have a recovery efficiency in the 70 to 80 % range, pushing the gyrotron and system efficiency to 60% and 45% respectively.

Obtaining a gaussian output is the second issue which would require some development. The present output scheme by edge diffraction does not provide a gaussian mode. We are presently studying the implementation of a grating to couple the energy out of the resonator while maintaining the inherent gaussian profile of the radiation in the resonator. Preliminary results indicate that coupling to an HE_{11} corrugated waveguide can be achieved with high efficiency [26].

In summary, within the last two years, important steps have been made in the development of Q.O. gyrotrons. The main issues have been identified and effective solutions are under investigation.

Acknowledgements

This work was supported in part by the "Commission pour l'Encouragement de la Recherche Scientifique" under grants 1224 and 1564(1224), the "Fonds National Suisse pour la Recherche Scientifique" under grant 2000-005652, by NET under contract 330/88-1/FU-CH-NET and by internal R&D funds from the Department EKR of ABB-Infocom SA. We would like to acknowledge fruitful conversations with Drs. A. W. Fliflet, W. Kasparek and M. E. Read.

REFERENCES

[1] G. N. Rapoport et al., Radiotekh., Elektron. **12**, 633, (1967) (Radio Eng. Electron. Phys. (U.S.S.R.) **12**, 587, (1967)

F. A. Korolev et. al., Radio Eng. Electron. Phys. **15**, 1868, (1970)

A. F. Kurin et al., Izv VUZ, Radiofizika **19**, 1047, (1976)

[2] P. Sprangle et al., Phys. Rev. **A23**, 3127 (1981)

P. Sprangle et al., Appl. Phys. Lett. **38**, 310 (1981)

[3] A. Bondeson et al., Int. J. Electronics **53**, 547 (1982)

A. Bondeson et al., Millimeter and Infrared Waves **9**, K. Button ed. (Academic Press) p. 309 (1983)

A. Bondeson et al., Phys. Fluids **26**, 285 (1983)

[4] T. M. Antonsen et al., Phys. Fluids **B2**, 419 (1990)

[5] Korolev F.A. et al., Radio Eng. Electronic Physics **15**, 1868 (1970)

[6] E. C. Morse et al., J. Vacuum Sci. Technology **A3**, 1239 (1985)

[7] T. A. Hargreaves et al., Int. J. Electronics **57**, 977 (1984)

M. E. Read et al., Int. J. Electronics **65**, 309 (1988)

[8] A. W. Fliflet et al., Phys. Rev. Lett. **62**, 2664 (1989)

A. W. Fliflet et al., Phys. Fluids **B2**,1046 (1990)

A.W. Fliflet et al., IEEE Trans. Plasma Science **18**, 306 (1990)

A. W. Fliflet et al., J. Fusion Engineering **9**, 31 (1990)

[9] J. Ph. Hogge et al., Conf. Digest 14th Int. Conf. on Infrared and Millimeter Waves, Würzburg, F.R.G., 1989, SPIE **1240** , 233 (1989)

S. Alberti et al., Phys. Fluids **B2**, 1654 (1990)

[10] A. Perrenoud et al., Int. J. Electronics **57**, 985 (1984)

[11] H. Stickel, Int. J. Electronics **64**, 63 (1988)

[12] M. N. Afsar et al., IEEE Trans. Instrumentation and Measurements **IM-25**, 290 (1976)

[13] J.L. Byerly et al., Int. J. Electronics **57**, 1033 (1984)

[14] M. N. Afsar, IEEE Trans. Instrumentation and Measurements **IM-36**, 530 (1987)

M. N. Afsar et al., Int. J. IR and MM Waves **3**, 319 (1982)

[15] B. W. Davis et al., Int. J. IR and MM Waves **6**, 3 (1985)

[16] S. Alberti et al., Conf. Digest 14th Int. Conf. on Infrared and Millimeter Waves, Würzburg, F.R.G., 1989, SPIE **1240** , 231 (1989)

S. Alberti et al., Lausanne Report LRP 402/90 (April 1990), to be published in Phys. Fluids **B2**, November (1990)

[17] A. W. Fliflet, Private Communication (1990)

[18] See for example "Classical Electrodynamics", J.D. Jackson, [John Wiley and Sons], p. 134 (1975)

[19] S. Alberti et al. , to be published

[20] R. G. Kleva et al., Phys. Fluids **31**, 375 (1988)

[21] B. Levush et al., IEEE Trans. Plasma Sci. **18**, 260 (1990)

[22] B. G. Danly et al., Appl. Phys. Lett. **46**, 728 (1985)

[23] T. M. Tran et al., IEEE Trans. Electron Dev. **ED 36**, 1983 (1989)

[24] M. E. Read et al., Conf. Digest 13th Int. Conf. on Infrared and Millimeter Waves, 1988, SPIE **1039**, 279 (1988)

M. E. Read et al., Conf. Digest 14th Int. Conf. on Infrared and Millimeter Waves, Würzburg, F.R.G., 1989, SPIE **1240**, 79 (1989)

M. E. Read et al., to be published

[25] A. Sh. Fix et al., Int. J. Electronics **57**, 821 (1984)

M. E. Read et al., Conf. Digest 13th Int. Conf. on Infrared and Millimeter Waves, Honolulu, USA., 1988, SPIE **1039**, 181 (1988)

M. Q. Tran et al., Conf. Digest 14th Int. Conf. on Infrared and Millimeter Waves, Würzburg, F.R.G., 1989, SPIE **1240**, 318 (1989)

T.V. Borodachyova et al., in "Gyrotron", V.A. Flyagin ed. ,p. 161 (1989)

M.E. Read et al., MTTT Trans. Electron. Devices, **ED37**, 1579 (1990)

[26] J. Ph. Hogge et al., Conf. Digest 15th Int. Conf. on Infrared and Millimeter Waves, Orlando, USA., December1990

High Power 140 GHz Gyrotrons at KfK

E.Borie,G.Dammertz,O.Dumbrajs[1],G.Gantenbein,T.Geist[2],G.Hochschild,M.Kuntze,
A.Möbius,H.-U.Nickel,B.Piosczyk,M.Thumm

Kernforschungszentrum Karlsruhe, Institut für Technische Physik, PO-Box 3640,
D-7500 Karlsruhe (FRG)
[1]Tech. Universität Hamburg-Harburg, PO-Box 901052, D-2100 Hamburg 90
[2]Universität Karlsruhe, Inst. f.Höchstfrequenztechnik u. Elektronik, Kaiserstr. 12,
D-7500 Karlsruhe (FRG)

Abstract:

At KfK 140 GHz gyrotrons for long pulse operation (>100 ms) in the TE_{03} mode at power levels of 100 kW have been fabricated and tested. Two resonators (in modular tubes) with different geometry were compared with respect to efficiency, power output and mode competition. Based on these results an industrially fabricated prototype gyrotron was built; it delivered 300 kW at short pulses (0.5 ms) and 120 kW at long pulses (100 ms). The results of the different gyrotron versions are described and discussed.

The future development at KfK aims at cw gyrotrons with output powers in the Megawatt region. This can only be done by using whispering gallery modes (WGM: TE_{mn} with $m \gg 1$ and $n \leq 2$) or asymmetric volume modes (AVM: TE_{mn} with $m \gg 1$ and $n \geq 3$).

As an intermediate step a gyrotron for 500 kW output power operated in the $TE_{10,4}$ mode will be built. The design and the present state of the development of components are described.

Introduction:

Gyrotrons have proven to be a very good tool for efficient electron cyclotron resonance heating (ECRH) of tokamak- and stellarator plasmas in magnetic confinement thermonuclear fusion research [1]. The demand for cw gyrotrons with an output power of about 1 MW has increased during the last years.

One of the most important problems in the design of high power gyrotrons is to maximize the efficiency in highly overmoded resonators - which are necessary to handle the ohmic losses - without increasing the mode competition problems to a point where they are insurmountable. This requirement needs a careful design of the electron gun in order to get a high velocity ratio of perpendicular and parallel velocities without reflection of the electrons, a careful design of the resonator and of the window. For mode competition in a TE_{03} mode resonator the mode at lower frequency, the TE_{23} mode, is most dangerous

especially as the highest efficiency for the TE_{03} mode is reached at low magnetic fields.

After some experiments with several different resonator designs in a modular gyrotron a sealed prototype gyrotron has been built and tested. The design parameters of 100 kW output power in pulses of 100 ms were reached and the gyrotron has been installed for heat wave experiments in high density plasmas at the Wendelstein 7 AS stellarator of the Max-Planck-Institute for Plasma Physics Garching (IPP).

It is well known that for much higher output powers (1 Megawatt units) the rotationally symmetric modes (TE_{0n}-modes) are rather unrealistic mainly because of the increasing mode competition problem of the neighbouring TE_{2n} mode for higher n values which are necessary to overcome the problems of wall losses. Thus at KfK the gyrotron development will concentrate on either whispering gallery mode gyrotrons (WGM) or asymmetric volume mode gyrotrons (AVM) [2]. The latter is an asymmetric mode with radial index greater than two.

Design:

In order to be able to exchange easily different parts of the gyrotrons, the critical parts are flanged together and sealed with metallic rings.

The gun is a magnetron injection type gun. The emitter, a tungsten dispenser cathode, has an average radius of 9.2 mm and a pitch angle of 15^0. The gun was optimized for a voltage of 70 kV, a current of 8 Amps (density: 3 Amps/cm^2) and a modulation voltage of 25 kV. The beam is injected into the resonator at the radius R = 1.81 mm, the second maximum of the electric field. With the magnetic field strength of 5.4 Tesla at the resonator, the magnetic field strength of 0.2 Tesla at the gun one calculates a compression ratio of 24.5 and a ratio of perpendicular to parallel velocities of 1.5.

The small diameter of the resonator allows only poor pumping of the gun by the collector pump. To improve the vacuum in the gun region two ion getter pumps with a pumping speed of 2 l/s each are connected to the gun at high potential.

In order to avoid the gun being damaged by reflected power the space between gun and resonator is surrounded with absorbing material.

Some resonators with different geometry were tested. The first experiments were made at 150 GHz; they are reported elsewhere [3]. Here only the experiments at a frequency of 140 GHz are described. The geometries of the tested versions of the resonator are summarized in Tab. 1. The input taper with a length of 18.9 mm and the output taper with an angle of 3^0 and a length of 10.1 mm were the same for all versions. Res. 1 and the prototype have an angle of 0.5^0, Res. 2 an angle of 1^0 for the input taper. The difference in the geometry

of the mid section is listed in Tab.1. The prototype (sealed version) has the same geometry as Res. 1,but its surface was electropolished whereas the other resonators were simply lathed without any further surface treatment.

The difference in geometry mainly results in a different diffraction Q-value and thus also in different ohmic loss densities which are calculated to be 6.7 kW/cm² for the untapered resonator and 2.5 kW/cm² for the tapered one. For the calculation of these values an ideal surface of copper at a temperature of 250°C and an output power of 200 kW were assumed.

				TE_{031}		TE_{231}	TE_{521}
	L_2 [mm]	R_0 [mm]	θ_2	f [GHz]	dP/dA [kW/cm²]	f [GHz]	f [GHz]
Res. 1	10	3.47	0	140.26	6.7	137.42	144.42
Res. 2	16.5	3.45	0.13	139.85	2.5	137.06	144.59
Prototype as Res. 1							

Tab.1:
Geometry, frequency and losses on the walls for an output power of 200 kW.

L_2 : length
θ_2 : taper angle
R_0 : radius of mid section

The transition between the output taper of the resonators and the collector with its diameter of 70 mm is performed by a nonlinear taper with an efficiency of 99.9% for the TE_{03} mode.

The output window consists of two alumina ceramic discs each with a thickness of 3.54 mm to match the frequency of 140 GHz i.e. to avoid reflections of the TE_{03} mode. The distance of the discs is continuously adjustable between 3 - 5 mm; it has to be chosen to avoid mode competition or to achieve maximum output power. The spacing between the discs is sufficiently large for a good cooling of the disc-surface with FC75.

The magnetic fields at the resonator and at the gun are provided by two pairs of superconducting coils.

The assembled gyrotrons were heat treated at 450°C for about 10 days, and also the gun was conditioned simultanously.

Diagnostics:

To identify the oscillating modes their frequency is detected in a multichannel system, each channel having a bandwidth of two GHz. A gyrotron output monitor signal is down converted with the signal of a Gunn oscillator to a frequency range between 2-18 GHz. The signal of the different modes appear in different channels thus allowing a very fast identification of the oscillating modes as long as their difference in frequency exceeds 2 GHz.

A similar system is used for a more accurate frequency measurement with a resolution of a few MHz. The gyrotron signal is mixed with the 9th harmonic of an oscillator whose frequency is very stable and adjustable between 14.5 - 16.5 GHz. After transmission through a low pass filter the frequency is measured in an analyzer which shows the frequency as function of time [4].

Wavenumber spectrometers [5] (from the Institute for Plasma Research, University of Stuttgart) are used in order to measure the mode purity at the TE_{03} mode frequency. The first one with a diameter of 27.8 mm has a better resolution for the different modes, but causes some problems because of breakdowns especially at pulse lengths exceeding 10 ms. The second one has a diameter of 63.5 mm.

The power is measured with a ballistic calorimeter filled with about 0.3 l of octanol as absorbing liquid [6]. For short pulses the temperature increase was averaged over 30 pulses; for long pulses the temperature increase of one pulse was measured.

Experimental results at short pulse operation:

For parameter optimization the gyrotrons were operated at low pulse lengths of 0.5 ms with a repetition rate of 0.5 Hz.

The frequencies of the resonators agreed very well with the theoretical ones within the fabrication tolerances (±0.01 mm in diameter corresponding to a frequency deviaton of about ±200 MHz).

	before long pulse operation		during long pulse operation		after long pulse operation		Δf
	P[kW]	η[%]	P[kW]	τ[ms]	P[kW]	η[%]	[GHz]
Res.1	220	23	120	<15	120	13	0.65
Res.2	225	26	90	70	90	19	0.45
Prototype	300	33.4	100	100	150	23	0.40

Tab. 2:
Powers and efficiencies

The parameters are chosen for highest power

The powers and efficiencies of the different resonators are summarized in Tab. 2., the highest output powers were measured to be about 220 kW for the modular gyrotrons (cavity surface not electropolished) and 300 kW for the sealed gyrotron. The dependence of the output power on the beam current is almost linear, with a small starting current of about 1 Amp (Fig.1). The efficiency of the resonator has its maximum value of 33% at a beam current of 8 Amps in agreement with the theoretical calculations as the geometry of the resonator has

been optimized in efficiency for that current. At 12 Amps being the limit of the gun an output power of 300 kW and an efficiency of 32% were measured.

Including the Ohmic losses, the losses of the window and of the cooling liquid which are estimated to be 30–40 kW for 300 kW output power an interaction efficiency of 36% is calculated.

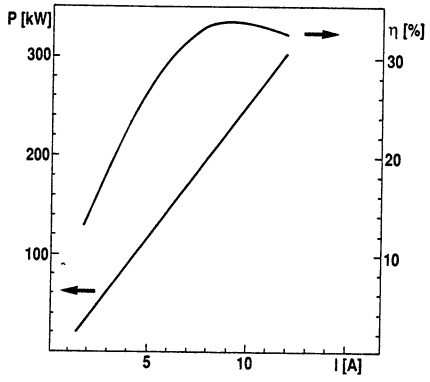

Fig. 1:
Dependence of output power and efficiency on beam current for the prototype gyrotron.

The magnetic field was kept constant, the other parameters were chosen for maximum output power

Fig. 2 shows the oscillation mode map which indicates the oscillating modes (hatched areas) in a modulation voltage (U_{mod}) versus beam voltage (U_{beam}) plot. For modulation voltages above about 26 kV operation was not possible because of breakdowns, below about 20 kV, which corresponds to a velocity ratio of 0.8 no oscillations occured.

Actually this plot is a simplified one; there are also regions for simultanous oscillations of the TE_{23}–TE_{03}, TE_{52}–TE_{03} modes and for modulation voltages at about 26 kV also simultanous oscillations of the TE_{52}–TE_{23} modes.

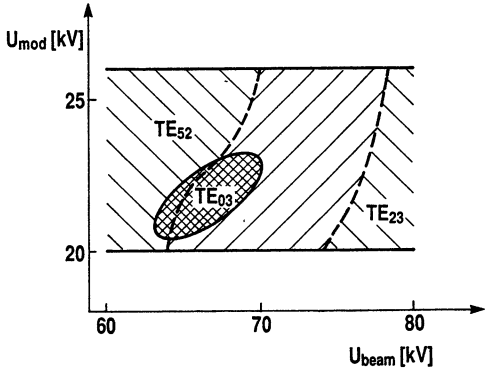

Fig. 2:
Oscillating modes in the U_{mod}–U_{beam}–plot

Magnetic field and beam current was kept constant

The parameter range of the U_{mod}–U_{beam}–plot is of course dependent on other parameters as for example on the spacing of the discs of the window. The

TE_{03} mode can be excited only in a very narrow range (Fig. 3). For a magnetic field of 5.448 Tesla a spacing range of only 0.03 mm was measured. This range increases slightly (to 0.2 mm) with increasing magnetic field. Within that range the TE_{03} mode oscillates with almost constant power, outside the output power drops to less than half that value and simultanous oscillations of the TE_{23}–TE_{03} or TE_{52}–TE_{03} modes appear depending on magnetic field strength. We do not know the conditions of the window spacing for good TE_{03} mode exitation in the presence of other modes, but first investigations show that one can achieve stable mode operation of the TE_{03} mode if the disc spacing is chosen for minimum reflection of the most dangerous mode. It seems to depend on the magnetic field strength whether this is the TE_{23} or the TE_{52} mode; this has to be clearified in further experiments.

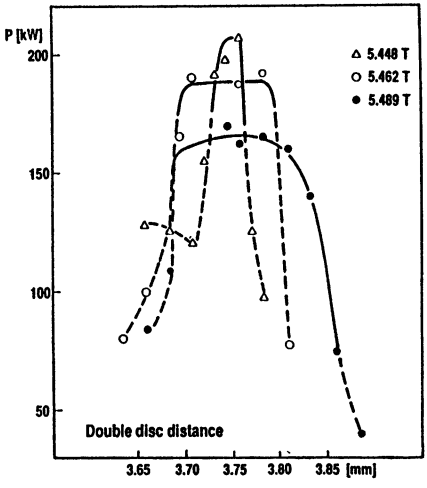

Fig. 3:
Output power as function of the spacing between the discs for the TE_{03} mode.

The dashed lines indicate simultanous oscillations of the TE_{03} mode with the TE_{52} or TE_{23} mode.

For the short (10 mm) untapered resonators we did not suffer from mode competition between TE_{031} and TE_{032} modes, but for the longer tapered one severe mode competition occurred. For the tapered resonators the difference in frequency and in quality factor (starting currents) between the TE_{031} and TE_{032} mode is reduced compared to the untapered ones [7].

Long pulse operation:

The optimization at short pulses was done very carefully but after long pulse operation with at least 500 pulses we were faced with a different situation. The conditions for what we call long pulse operation are given in the third column of Tab. 2. We observed an irreversible increase of the frequencies in the order of 0.5 GHz. The highest frequency increase of 0.65 GHz was measured for

Res. 1 though the pulse lengths did not exceed 15 ms. By careful verification of the geometry of Res. 2 a corresponding decrease of 0.03 mm in diameter was found. The shrinking of diameter seems to have its reason in the high thermal stress which might cause inelastic deformation of the resonator.

A second much more severe problem is caused by the strong reduction of the U_{mod}-U_{beam}-parameter range for the TE_{03} mode (Fig.1; middle part of the hatched area). For both parameters the range of TE_{03} mode oscillation was reduced by more than a factor of 2, and both parameters were shifted to lower values. Thus it was not possible to work at parameters of high efficiency and high output power after long pulse operation, and the power was reduced to about half the values before long pulse operation (column 4 of Tab. 2).

The reason for the decrease in parameter range is not understood. One could think about a deformation of the resonator and thus a change in the quality factor.

Mode purity and frequency stability:

The frequency measurement device described above made it possible to measure the frequency change from pulse to pulse as well as frequency steps during one pulse with an accuracy of a few MHz. During the pulses frequency steps of about 60 - 70 MHz were found very often (Fig. 4). This frequency shift is related to the change in electrical length of the transmission line between resonator output and window or load (long line effect) [7,8].

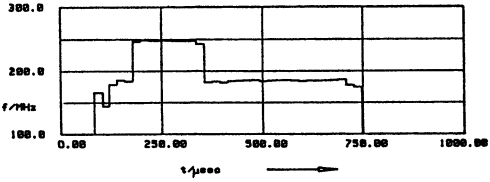

Fig. 4:
Frequency hopping during one pulse [4]

For the application of gyrotrons in plasma experiments the mode purity is very important as only one mode can be converted to the desired mode at the launching antenna. The spurious unwanted modes not only have the undesirable property of decreasing the efficiency for the desired working mode, but also necessitates the dumping of the wrong mode contributions. To measure the mode purity two different wavenumber spectrometers were used. One of these measurements is shown in Fig. 5, which was taken with the larger spectrometer (63.5 mm in diameter). The coupling factor for the TE_{02} mode is reduced by about a factor of 7 compared to the one of the TE_{03} mode, so the total contribution of that mode is calculated to be about 30%. The contribution of

modes with higher radial indices are neglegible as their peaks are shown enlarged due to the higher coupling coefficients.

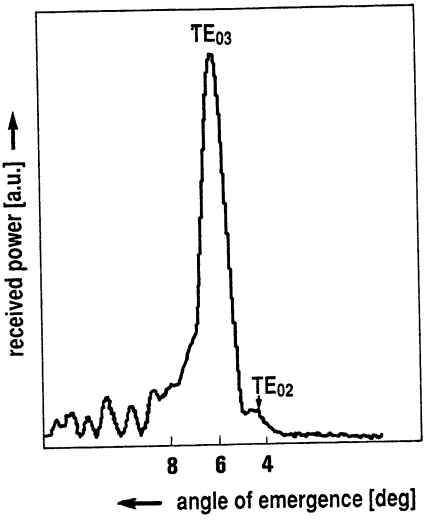

Fig. 5:
Mode spectrum taken with the wavenumber spectrometer of 63.5 mm inner diameter.

The angle is defined as zero into the direction of the load

The contribution of the TE_{02} mode also can be seen in long pulse operation (Fig. 6). For an angle of emergence correct for the TE_{03} mode the power of the forward wave was measured. After about 40 - 60 ms a step to a higher power was found. A corresponding decrease of power was measured at angles suitable for the TE_{02} mode. The change in power can be calculated in both spectra to be about 30%. It was not possible to reduce the amount of the unwanted mode and to avoid the mode jumping by changing the parameters of the gyrotron.

In order to investigate the problem of mode jumping more in detail we installed the smaller wavenumber spectrometer (with a corresponding down taper

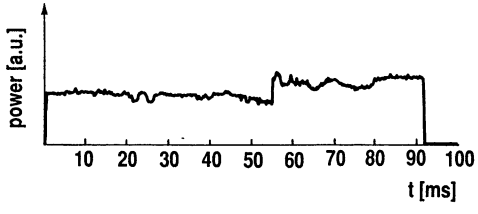

Fig. 6:
Output power during one pulse for the TE_{03} mode

from 70 mm to 27.8 mm) with a higher output coupling coefficient for the TE_{02} mode. With that device we only found a contribution of less than 5%. At the moment we do not know all the details of the complex coupling of the forward and backward waves due to the tapers,the window and the load. Further in-

vestigations using a spectrometer with the diameter of the output waveguide have to be done.

The gyrotron was built to be used for plasma heat wave experiments. This requires the possibility for modulating the output power during one pulse. Changing the voltage of the modulation anode by a few kV the output power was switched on and off. A modulation frequency of about 0.8 kHz was possible.

A few weeks ago this gyrotron was installed at the stellarator W7AS at the IPP Garching. The first short pulse experiments gave the same results as at Karlsruhe. Stable single mode operation at 130 kW output power were performed successfully. Long pulse operation will take place in the near future.

Future work:

For high power units of about 1 MW cw the rotationally symmetric modes TE_{0n} do not appear very attractive because of the severe problem concerning mode competition with the neighbouring TE_{2n}-mode. With increasing n which is necessary in order to overcome the problem of ohmic losses in the resonator wall the distance in frequency decreases. A further disadvantage of these rotationally symmetric modes is given due to the fact that for plasma heating tunability of the gyrotron in frequency is desired. For high order asymmetric modes this can be done by changing the azimuthal mode number. For rotationally symmetric modes this is not possible.

In order to reduce the ohmic losses at the walls a mode with a high zero of Bessel function would be desirable. On the other hand it seems that operating a gyrotron at high efficiencies a Bessel function zero not exceeding 50 has to be chosen [9].

Stable operation can be achieved if the working mode is isolated in frequency as much as possible from competing modes. But in addition one also has to consider the starting currents of the neighbouring modes compared to the desired one.

Another criterion concerning the space charge effects and the voltage depression inside the resonator has to be taken into account. The voltage depression is dependent on the ratio of the electron beam radius R_{el} to the radius R_0 of the resonator. This of course has an effect on the efficiency of a gyrotron at least if one does not use an energy recovery system for the electron It seems reasonable to work with $R_{el}/R_0 > 0.4$.

Tab. 3 summarizes the criteria for all the modes which were discussed for high power gyrotrons: the density of wall losses, the frequency distance to the neighbouring modes at higher and lower frequencies (marked with an index r and l resp.), their starting currents and the ratio R_{el}/R_0. The radius of the

electron beam was chosen to coincide with the first radial maximum of the electric field. In the table the modes with radial index of 1 or 2 are omitted as they are studied elsewhere [10,11] and probably will have too high wall losses.

MODE	$TE_{10,4}$	$TE_{10,8}$	$TE_{10,10}$	$TE_{26,3}$	$TE_{14,6}$	$TE_{16,7}$	$TE_{18,4}$	$TE_{22,5}$
R_{el} (mm)	3 64	3.64	3.64	9.32	5.08	5.79	6.50	7.91
R_{el}/R_o	0.45	0.29	0.25	0.71	0.42	0.41	0.57	0 55
$\frac{dP\,(kW)}{dA\,(cm^2)}$	4.1	1.9	1.5	3.5	2.4	1.9	3.3	2.4
Δf_l (GHz)	-2.90	- 0.86	-1.38	-1.15	-1.40	-0.74	- 0.11	- 0.14
$(I_p/I_w)_l$	1.2	2.0	1.9	3.3	2 0	2.3	1.3	1.2
Δf_r (GHz)	+0.25	+1.89	+1.36	+0.75	+0.30	+ 0.29	+0.51	+0.79
$(I_p/I_w)_r$	4.2	1.0	1.0	2.9	2 5	1.9	2.3	2.6

Tab. 3: Mode criteria for the choice of high power gyrotrons

A few of the modes listed above can be excluded as their wall losses exceed the value given by technological possibilities. The given wall losses are theoretical ones calculated for an ideal copper surface at a temperature of 250°C. At the moment we consider an increase of wall losses for real surfaces by a factor of 1.5 to be realistic. Assuming further a peak loss density of about 4 kW/cm² as a technical limit for the cooling, we end up with a theoretical value of 2.7 kW/cm². For this reason the $TE_{26,3}$ and the $TE_{18,4}$ modes were not considered further. The first one is excluded also for another reason. The electron beam diameter is too large at the quasi-optical coupler or at the second reflector. To avoid the beam hitting these parts the magnetic field has to be too high.

Probably also the modes with m>6 have to be avoided because of the space charge problems and the voltage depression inside the resonators at high electron currents.

For an output power of 1 MW also the $TE_{10,4}$ mode is not regarded to be a good candidate. Nevertheless we have chosen this mode for a gyrotron with an output power of 500 kW mainly due to its particularly good isolation from dangerous competing modes. Another reason for that choice is given due to the possibility to investigate the influence of space charge effects and the voltage depression. In a modular device the resonator can easily be exchanged to one

for the $TE_{10,8}$ or even $TE_{10,10}$ mode using the same gun in order to study the space charge effects and the voltage depression. For the $TE_{10,4}$ mode the feasibility of long pulse operation at rather high efficiencies of 30% at power levels of 500 kW is predicted by theory.

beam current:	25 A
beam voltage:	80 kV
modulation voltage:	25 kV
cathode radius:	9.8 mm
cathode angle:	26.6°
cathode current density:	6.0 A/cm²
magnetic compression:	29.5
cavity radius:	8.11 mm
cavity length:	11 mm
quality factor:	590
ratio of velocities:	1.5–1.7
voltage depression:	5.6 %
launcher diameter:	40 mm
launcher length:	221 mm
reflected power:	< 0.2 %

Tab. 4: Design parameters for the $TE_{10,4}$ mode gyrotron

A high magnetic compression ratio has been chosen in order to keep the emitter current below 6 A/cm².

The experiment will be starting at the beginning of 1991. For the first step a conventional output with an axial window will be used. Later on it will be replaced by a quasioptical mode converter which transforms the $TE_{10,4}$ mode to a Gaussian beam. The launcher diameter was chosen to be 40 mm.

The gyrotron is foreseen to deliver 500 kW output power for pulse lengths of 100 ms at the end of 1992. In 1993 a prototype version could be installed at the stellarator W7AS or the tokamak ASDEX-Upgrade at the IPP Garching for heat wave experiments using modulated mm wave power.

State of the development:

The superconducting magnet has been designed and ordered. It is able to accept all the gyrotrons listed in Tab.3 except the one operating in the $TE_{26,3}$ mode.

The gun has been designed [12] and ordered at industry. In contrast to our previous guns with tungsten dispenser cathodes this gun will be fabricated with a mixed metal cathode of WIr.

The first resonator will be fabricated from OFHC-copper, the surface will be electropolished. Further resonators will be fabricated from copper dispersion

strengthened with Al_2O_3 (0.15%). We hope to overcome the problems of metal fatigue leading to the reduced parameter range after long pulse operation.

Studies of different wall materials and other surface preparation techniques have been started. The surface quality will be experimentally investigated with closed cylindrical TE_{031} mode test resonators [13] fabricated from different materials (copper, copper alloys and copper dispersion strengthened with Al_2O_3) and according to different fabrication methods (lathing, lathing with diamond tools, hammering, spark erosion or spark polishing) and different surface treatments. Some preliminary results are given in Tab.5.

material	fabrication	remarks	Q	f(GHz)
OFHC	hammered	O-free	12550	143.4
OFHC	lathed		11860	144.1
SIECU	hammered		12900	143.6
Glidcop[1]	lathed	0.15% of Al_2O_3	11900	143.5
Cu	theory		19500	

Tab. 5: quality factors for different test resonators

[1] dispersion strengthened copper; trademark of SCM Metal Products Inc.

The problem of resonator cooling will be studied theoretically with computer codes in order to find out the limit of loss density.

The quasioptical mode converter from the $TE_{10,4}$ mode to a Gaussian beam has been designed and is ready for construction. The conversion efficiency is calculated to be about 85%. Cold tests with this facility are planned at the Institute for Plasma Research of the University Stuttgart for the end of this year, it will be installed to the gyrotron as soon as the first measurements with the axial window will have been successful.

An intense programme for the development of a cryogenically cooled window has been started at the KfK. The programme aims at the characterization of material as function of the temperature including degradation effects caused by irradiation with neutrons. This effect is important for the window situated at the torus near the plasma. The dielectric properties (Fig. 7), the thermophysical properties as well as the mechanical properties are investigated. Using existing finit elements computer codes heat and stress calculations and predictions of the lifetime will be performed. Fig. 8 shows the absorbed power per millimeter in

a window for an output power of 1 MW as a function of the edge temperature. The window was considered to be integrated in a 88.9 mm diameter corrugated waveguide (HE_{11}). Dependencies for two different sapphire qualities, and for quartz are given. The edge temperature for the realistic window is assumed to be about 10°C above liquid nitrogen temperature. The temperature at the center of the window is increased by about 30°C or 60°C for sapphire of high or medium quality respectively.

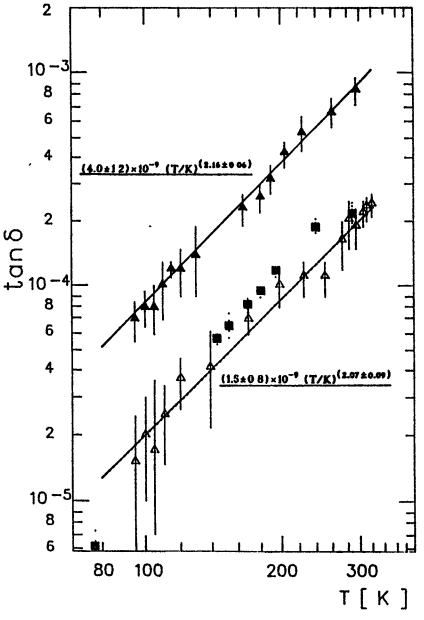

Fig. 7:

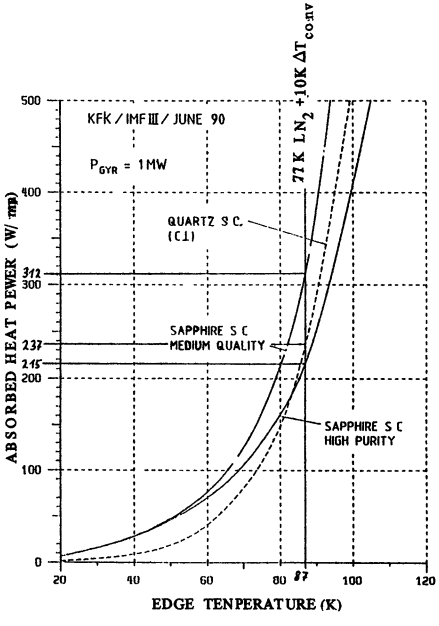

Fig. 8

Fig.7: Loss tangent of sapphire as a function of the temperature
lower curve: unirradiated [14,15]
upper curve: irradiated with $3.5 \cdot 10^{19}$ neutrons/cm² (E>0.1 MeV) [14]

Fig.8: Absorbed loss power /mm for sapphire windows as function of the edge temperature

For the first $TE_{10,4}$ gyrotron a conventionally axially launching double disc window with sapphire discs and FC75 face cooling will be installed.

The collector will be the same as the device used for the TE_{03} mode gyrotron. No work was done for an improved one or for a depressed collector. This work will start soon.

Conclusions:

The 140 GHz gyrotron operating in the TE_{03}-mode has ben successfully tested at the KfK Karlsruhe. The measured output powers (P = 300 kW for short pulses, P = 120 kW for pulse lengths of more than 100 ms) exceeded the design values. The gyrotron has been installed at IPP Garching for use in high density plasma experiments. In the first test measurements with short pulses the values measured at Karlsruhe could be repeated.

The experiments showed the difficulties of mode competition for azimuthally symmetric modes. For higher output powers the operation of a WGM- or a AVM-gyrotron is necessary.

As an intermediate step towards 1 MW a gyrotron for an output power of 500 kW operating in the $TE_{10,4}$ mode is under construction at KfK .and will be operating at the beginning of 1991.

Some critical components for a cw - gyrotron are investigated.

Acknowledgements:

This work was supported by the European community as part of the European Fusion Technology Program under the auspices of the Projekt Kernfusion at the Kernforschungszentrum Karlsruhe.

References:

[1] H. Renner et al.; Initial Operation of the Wendelstein 7 AS Advanced Stellarator; Plasma Physics and Controlled Fusion 31, 1989, p.1597

[2] V.A.Flyagin, G.S.Nusinowich; Gyrotron Oscillators; Proc. of the IEEE, Vol.76, 1988, p. 644

[3] G. Dammertz et al.; First experimental results of the KfK 150 GHz gyrotron; Int. J. Electronics 64, 1988, p.29

[4] G.Gantenbein, T.Geist, G.Hochschild; Instantaneous frequency measurements on a gyrotron output signal; 14th Int. Conf. on Infrared and Millimeter Waves, Würzburg 1989, p.221

[5] W. Kasparek, G.A.Müller; The wavenumber spectrometer - an alternative to the directional coupler for multimode analysis in oversized waveguides; Int. J. Electronics 64, 1988, p. 5

[6] H. Stickel; Design of a low average power calorimeter for millimeter wave gyrotrons; Int. J. Electronics 64, 1988, p.63

[7] B. Jödicke; Zur Modenrangigkeit von Hochleistungsgyrotrons mit rotationssymmetrischen Arbeitsmoden; 1989, KfK 4603

[8] J.C.Slater; Microwave Electronics; van Nostrand, 1950

[9] V.V.Alikaev et al.; Report ITER-IL-HD-6-0-18; 1990, Munich

[10] K.Felch, C.Hess, H.Huey, E.Jongewaard, H.Jory, R.Pendleton; Megawatt gyrotrons for ECR heating; 13th Int. Conf. on Infrared and Millimeter Waves, Hawaii 1987, p.175

[11] K.E.Kreischer, R.J.Temkin; Phys. Rev. Letters 59, 1987, p.547

[12] Piosczyk; Eine 2 MW Elektronenkanone für ein $TE_{10,4}$ Gyrotron bei 140 GHz; Internal report, KfK, 1989

[13] T.Geist, G.Dammertz, G.Hochschild, W.Wiesbeck; 15th Int.Conf. on Infrared and Millimeter Waves, Orlando 1990, to be published

[14] R. Heidinger; Dielectric loss of Alumina between 95K and 330K at ECRH frequencies; J. Nucl. Materials, Vol. 173, 1990, p.243

[15] P.B.Sushilin, A.Sh.Fiks, V.V.Parshin in: Gyrotrons (Acad. of Sciences of the USSR, Inst. of Appl. Physics, Gorky), p.181

MODE SELECTION FOR A FREQUENCY STEP–TUNABLE GYROTRON

O. Dumbrajs and O. A. Elnor

Arbeitsbereich Hochfrequenztechnik, Technische Universität
Hamburg–Harburg, D–2100 Hamburg 90, Germany

Abstract

A search for the optimum working modes is carried out for a frequency step–tunable gyrotron to be used to stabilize possible unsteadinesses in plasma in large fusion complexes. Here the main selection criteria are: wall losses in a resonator, electron beam stability, and mode competition.

Introduction

One of the possibilities of stabilization of unsteadinesses in plasma in large fusion complexes is the use of frequency step–tunable gyrotrons. According to the draft specifications [1] frequency changes in steps of about 2% over the interval of ±5% are desired. For the central frequency 140 GHz this means that it should be possible to vary the frequency in steps of ~2.8 GHz in the interval from 133 GHz to 147 GHz.

A gyrotron operates under the condition $\omega/c \approx [(q\pi/L)^2 + x_{mp}^2/R^2]^{1/2}$, where ω is the frequency, c is the velocity of light, q is the longitudinal index of the mode, L is the cavity length, x_{mp} is the p–th root of the derivative of the Bessel function, which specifies the mode, and R is the cavity radius.

The gyrotron frequency can be changed by changing the strenght of the external magnetic field, or/and the voltage of the applied accelerating field. Here four cases should be distinguished:

1) x_{mp} = const, q = 1, and R = const. This is the so–called frequency pulling by the electron beam. Here the frequency can be changed at most twice of the natural width [2] $\Delta\omega/\omega \sim 2/Q$, where Q is the quality factor. This corresponds to less than 1% variation of the frequency, which is much too little.

2) x_{mp} = const, q = 2, and R = const. In this case a gyrotron operates in a mode, whose longitudinal index is equal to two. Here the frequency increases by ~ 0.8 GHz,

which also is too little. Moreover, the efficiency of a gyrotron operating in a mode with q = 2 is smaller [3] than the efficiency of a gyrotron operating in a mode with q = 1.

3) x_{mp} = const and R ≠ const. In this case the frequency changes with R for the prescribed mode In practice such a change can be realized by means of a resonator with several sections, in which the working mode is excited in turn in each individual section [4]. In such a devise the mode competition might be a serious problem.

4) $x_{mp} \neq$ const and R = const. In this case the frequency change is accompanied by the mode change, and it can be made as large as desired [5].

It is rather obvious that the last possibility of the frequency change is the only one which can meet the specifications of the step tunability mentioned above. If a set of modes with different radial indices are used for this purpose, conversion efficiency losses in a quasi–optical converter, which converts the operating mode to a Gaussian beam, and which is designed for the central operating mode, become very large for other operating modes. It is much better to use a sequence of modes with a fixed radial index and a variable azimuthal index. Such modes couple equally strongly to the electron beam for the corresponding magnetic field [6]. They have almost the same caustic radius, amplitude distribution, radiating angle, but a slightly different phase distribution of the output field. However, even in this case a special movable mirror must be installed to adjust the beam direction for the optimum coupling, otherwise conversion efficiency losses up to 30% may occur in a quasi–optical converter [7].

Mode selection

i) Wall losses in a resonator.

Maximum wall losses can be estimated by means of the following well known expression:

$$\frac{dP}{dA} = 0.17 \cdot \lambda^{-5/2} \cdot \frac{\lambda}{L} \cdot Q \cdot \frac{P_{out}}{x_{mp}^2 - m^2},$$

where dP/dA is measured in kW/cm^2, λ and L in mm, P_{out} in kW, and the numerical coefficient corresponds to copper.

ii) Electron beam stability.

The electron beam in a gyrotron resonator remains stable only if the working current does not exceed the critical current given by the expression

$$I_{crit} = -0.4 \cdot U^{3/2} / [(1 + \alpha^2)^{3/2} \ln(R_{el}/R)],$$

where U is the accelerating voltage in keV, α is the pitch factor of the electrons, and R_{el} is the electron beam radius. Under realistic conditions due to the electron velocity spread

I_{crit} can be significantly smaller than given by this equation [8].

iii) Mode competition.

It should be distinguished between the ordinary mode competion, when the operating mode competes with a parasitic mode, and the extraordinary mode competition, when the operating mode competes with its left– and right–hand satellites. The latter form of competition is of particular importance in gyrotrons operating in whispering gallery modes.

An important parameter in the calculation of the mode competition is the relative frequency mismatch characterizing the difference of the eigenfrequencies of the competing modes:

$$\tilde{\Delta} = 2(\omega_1 - \omega_0)/(\beta_\perp^2 \omega_0) .$$

The critical values of $\tilde{\Delta}$ in the region of high efficiencies are $-0.4 \leq \tilde{\Delta} \leq -0.15$ in the case of the ordinary mode competition [9] and $\tilde{\Delta} \leq 0.3$ in the case of the extraordinary competition [10].

Results

Using the constraints $dP/dA \leq 3$ kW/cm^2 for $P_{out} = 500$ kW, and $I_{crit} \geq 30$ A for a 20% electron velocity spread, we selected four sequences of modes providing step tunability. In calculating the wall losses and starting currents we used the values of the dimensionless length of the resonator μ=17 and of the dimensionless measure of the product of field strength and beam–field coupling F=0.12, which correspond to the maximum efficiency of a gyrotron $\eta_\perp \approx 0.7$. The electron beam radius was chosen such that it maximized the beam–field coupling for the central mode of each individual sequence and it was kept fixed within the sequence.

The results of the calculations are presented in the Table, and the corresponding starting currents are shown in Figs. 1–4 as a function of the external magnetic field.

Central mode	ΔF (GHz)	dP/dA (kW/cm^2)	I_{crit} (A)	$\tilde{\Delta}_{ord}$	$\tilde{\Delta}_{exord}$
$TE_{10,4}$	7.4	2.8	38	–0.25	0.47
$TE_{18,4}$	5.0	2.2	53	–0.01	0.36
$TE_{26,3}$	4.0	2.3	88	–0.16	0.30
$TE_{37,5}$	2.7	1.1	70	–0.17	0.23

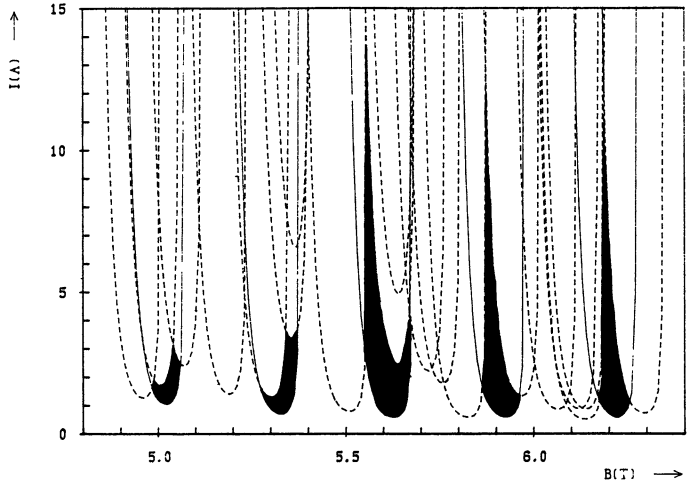

Fig. 1. Starting current as a function of the external magnetic field for the sequence of modes $TE_{8,4}$, $TE_{9,4}$, $TE_{10,4}$, $TE_{11,4}$, and $TE_{12,4}$. In the dark regions the starting currents of parasitic modes are higher than the starting current of the corresponding working mode.

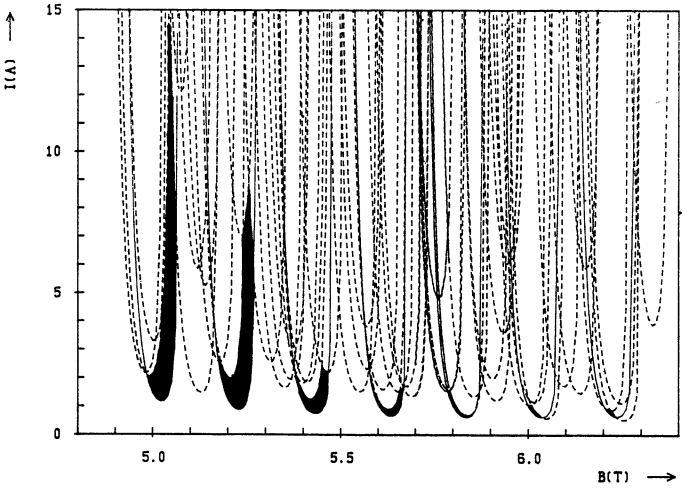

Fig. 2. Starting current as a function of the external magnetic field for the sequence of modes $TE_{15,4}$, $TE_{16,4}$, $TE_{17,4}$, $TE_{18,4}$, $TE_{19,4}$, $TE_{20,4}$, and $TE_{21,4}$.

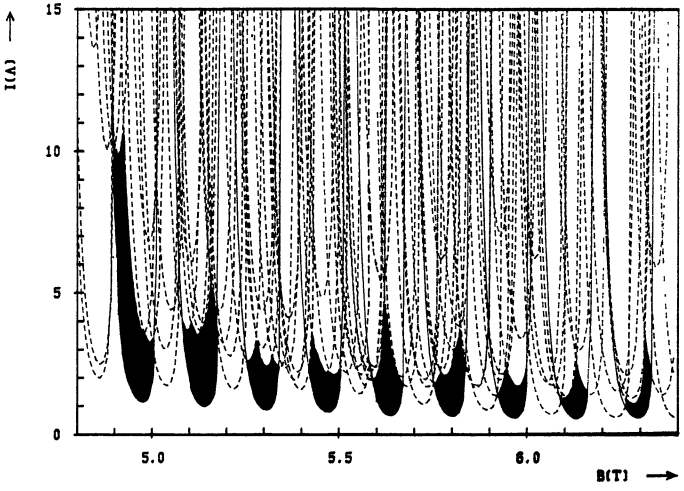

Fig. 3. Starting current as a function of the external magnetic field for the sequence of modes $TE_{22,3}$, $TE_{23,3}$, $TE_{24,3}$, $TE_{25,3}$, $TE_{26,3}$, $TE_{27,3}$, $TE_{28,3}$, $TE_{29,3}$, and $TE_{30,3}$.

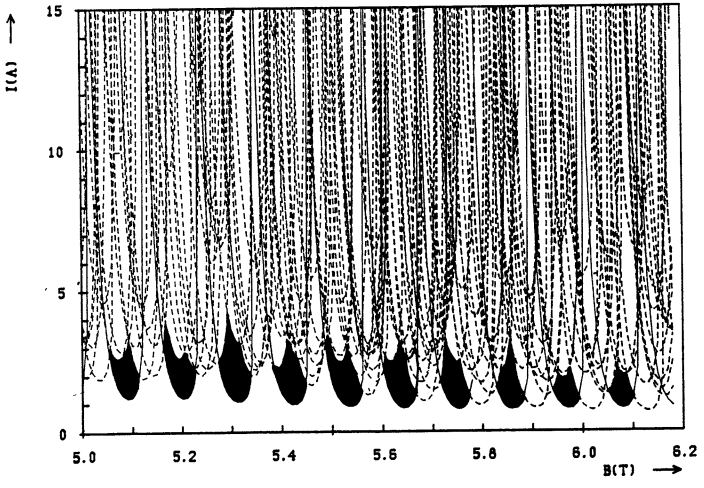

Fig. 4. Starting current as a function of the external magnetic field for the sequence of modes $TE_{32,5}$, $TE_{33,5}$, $TE_{34,5}$, $TE_{35,5}$, $TE_{36,5}$, $TE_{37,5}$, $TE_{38,5}$, $TE_{39,5}$, $TE_{40,5}$, and $TE_{41,5}$.

Conclusions

1. Frequency step tunability of a gyrotron, as specified by the Nuclear Fusion Project, can be achieved only by using modes with m as high as ~ 40, e. g., with the $TE_{37,5}$ mode.

2. Such modes meet the restrictions posed by wall losses, beam stability and, possibly, mode competition.

3. Probably the most serious problems of the frequency step tunability are related to the energy losses in a window and in a quasi–optical converter, and to the slowness of tunability due to the high inertia of the magnetic field.

Acknowledgments

This work has been performed within the framework of the Nuclear Fusion Project of the Kernforschungszentrum Karlsruhe and is supported by the European Community within the European Fusion Technology Program.

One of us (O. D.) thanks Sh. E. Tsimring for useful discussions.

References

1. J. P. Rager, "Gyrotron specification," Commission of the European Communities, 10 August, 1990.

2. E. V. Zasypkin, "Electron frequency pulling in gyrotrons," Radio Physics Quantum Electronics, 33, 2599–2605 (1988).

3. O. Dumbrajs and R. K. Gupta, "Efficiency of a gyrotron operating in modes with axial index equal to two," Int. J. Electronics 68, 877–883 (1990).

4. O. Dumbrajs and B. Piosczyk, "Frequency step–tunable gyrotron," Conference Digest, 13th International Conference on Infrared and Millimeter Waves, 5–9 December 1988, Honolulu, Hawaii, pp. 282–283.

5. G. F. Brand, "Tunable gyrotrons," Infrared and Millimeter Waves, 14, 371–408 (1985).

6. K. E. Kreischer and R. J. Temkin, "Single–mode operation of a high–power, step–tunable gyrotron," Phys. Rev. Lett., 59, 547–550 (1987).

7. M. I. Petelin and V. A. Flyagin, "Problems of design of the systems for the electron–cyclotron heating of plasma," Collection of scientific papers "Gyrotron," Institute of Applied Physics, Academy of Sciences of the USSR, Gorky, 1989, pp.195–205.

8. Sh. E. Tsimring, "Limiting currents of helical electron beams," Radiotekhnika i Elektronika, 35, 1284–1288 (1990).

9. O. Dumbrajs, "Influence of the magnetic field tapering on gyrotron operation," Int. J. Electronics (in print).

10. G. S. Nusinovich and V. E. Zapevalov, "Automodulation instability of a gyrotron radiation," Radioteknika i Elektronika, 23, 563–570 (1985).

AXISYMMETRICAL RESONATORS, WAVEGUIDE TAPERS AND MODE TRANSFORMERS FOR GYROTRON

Sh.E.Tsimring
Gorky University
603600, Gorky, GSP-20, Gagarin street

1. The gyrotrons components pointed out in the title though does not involve all electromagnetic equipment of these device but form rather numerous and influential family and demand corresponding respect. In the present paper we briefly describe our methods for the design of the mentioned units and shall present some information on the corresponding codes.

There are two common features of the considerated elements :
- All of them are sections of irregular axisimmetrical waveguides.
- The its length are much more then wave length.

The third feature, namely, weak irregularity of the waveguide does not always fulfill. The examples are couple cavities with mode conversion (CCMC) [1] and stepwise junctions of waveguides. Hence, the methods for design of extent and hardly irregular waveguide is very desirable.

2. We use the method of plane cross- sections (MPCS) [2,3]. The electromagnetic field in MPCS is perform as expansion [3] :

$$\bar{E}_\perp(\bar{r}_\perp,z) = \frac{1}{k}\sum_{m=}^{N_H} F_m \bar{E}_{m\perp} + i\sum_{t=1}^{N_E} \mathcal{E}_t \bar{E}_{t\perp}/h_t$$

$$\bar{H}_\perp(\bar{r}_\perp,z) = i\sum_{m=1}^{N_H} \mathcal{H}_m \bar{H}_{m\perp}/h_m + \frac{1}{k}\sum_{t=1}^{N_E} G_t \bar{H}_{t\perp}$$

Here $E_{m\perp}$, $H_{m\perp}$- transversal electrical and magnetic fields TE modes in regular waveguides with a cross-section equal to the instantaneous cross-sections (dependent on z) of the considered irregular waveguides. F_j, H_j, h_j- are amplitude coefficients and the propagation constants for the j- th TE- modes, respectively, $\mathcal{E}_t$, G_t, h_t have the same meaning for the t- th TM modes taken into account, k- is the wavenumber.

A set of differential equations for the unknown coefficients F_j, H_j, $\mathcal{E}_t$, G_t has the form [3] :

$$\frac{dF_j}{dz} = k\mathcal{H}_j - \sum_{m=1}^{N_H} A_{jm} F_m , \qquad \frac{dG_t}{dz} = k\mathcal{E}_t + \sum_{n=1}^{N_E} B_{nt} G_n ,$$

$$\frac{d\mathcal{H}_j}{dz} = -\frac{h_j^2}{k} F_j + \sum_{m=1}^{N_H} A_{mj}\mathcal{H}_m - i\sum_{n=1}^{N_E} C_{jn}G_n ,$$

$$\frac{d\mathcal{E}_t}{dz} = -\frac{h_t^2}{k} G_t + i\sum_{m=1}^{N_H} C_{mt}F_m - \sum_{n=1}^{N_E} B_{tn}\mathcal{E}_n ,$$

$$j = 1,2, \ldots , N_H , \quad t= 1,2, \ldots , N_E .$$

The coupling coefficients A_{jm}, B_{nt}, C_{nt} have the form :

$$A_{jm}= \frac{2\mu_m^2\sqrt{\mu_j^2-\alpha^2}}{(\mu_j^2-\mu_m^2)\sqrt{\mu_m^2-\alpha^2}}\frac{\tau}{r} \quad (j \neq m), \quad A_{jj}= \frac{\alpha^2}{(\mu_j^2-\alpha^2)}\frac{\tau}{r} ,$$

$$B_{nt} = \frac{2\nu_n^2}{(\nu_n^2-\nu_t^2)}\frac{\tau}{r} \quad (n \neq t) , \quad B_{tt} = \frac{\tau}{r} , \quad C_{mt}= \frac{2\alpha}{\sqrt{\mu_m^2-\alpha^2}} ,$$

where α is the azimuthal index, ν and μ are zeros of Bessel functions and it's derivatives. r and τ are the radious of waveguides and the slope of generating line to the z axis being functions of the longitudinal coordinate z. These coefficients are valid for empty waveguide cross-section. The equations also valid for coaxial system, however, the coupling coefficients are different. Besides, the additional terms corresponding TEM modes should be involved. Solving these equations are should take into account the radiation conditions :

$$\mathcal{H}_j(z) \pm i\frac{h_j(z)}{k}F_j(z) = 0 \qquad (\text{TE modes}),$$

$$\mathcal{E}_t(z) \pm i\frac{h_t(z)}{k}G_t(z) = 0 \qquad (\text{TM modes}) .$$

The sign + and - denoted opposite directions of the radiation.

The remarkable peculiarity of these equations is its applicability to the waveguides with arbitrary extent of irregularity. This fact was test on the problem of TE_{02} mode diffraction on the jump of the cross- section having rigorous solution. Moreover, determining inequality $\lambda\tau \gg D_{max}$, (D_{max} - waveguide maximum diameter) the equation are substantially simplified and reduced to the set differential equations with constant coefficients having analytical solutions

3. The described method was applied for numerous problems. In particular, the solutions for various resonators were found. In this case the problem with complex eigen frequencies is solved.

In all cases the excellent agreement with the experimental data was obtained. It is especially important for the complex resonators which are hardly irregular and, besides, even very weak unmatching of partial resonators immediately destroys the coupling and the efficiency of the wave- beam interaction [4].

4. The synthesis of waveguide tapers leads to the special class problems with minimal reradiating into parasite modes at given wavelength and variation of the diameters. It is easily seen that the mode transformation effect is determined from one hand by the values of coupling coefficients being proportional to the slope of generating line in each cross-section and from another hand by the synchronism conditions for modes, i.e. by the of its propagation constants $h_j = \sqrt{k^2-\kappa_j^2}$. As waveguide is broaden κ decrease and h_j close. For the compensation of this effect τ should decrease with increase r.

For the optimization of waveguide tapers the smooth profiles with minimal number varying parameters should be used. The spline, in particular cubic ones, for which continuity of generating line is fulfilled automatically up to the second derivative is of great convenience. In this case the number of varying parameters decreases sharply (two or three ones are enough) [5].
The total power of all parasitic modes (transmitted and reflected) is the goal function for the optimization.

The calculation of goal function reduces to the solving of the MPCS equations with radiation conditions. The number of equations is equal to 2N, where N is the number of modes taken into account. These equations are usually solved by the shot method, which demands solving of (2N+1) Cauchy problems. Calculation time typically is proportional to N squared. Note, that if high mode are taken into account, the narrow part of the waveguide is cut-off for its and the solutions of corresponding Cauchy problems became unstable, i.e. the space of solution vectors became "flat". The method of directed orthogonalization [6] when an orthogonalization of partial solution of Cauchy problems carried out in some intermediate cross-sections is used. In this case the hardly cutoff modes can be taken into account. It is very important for nonmonotonic profiles with the regions of trapped modes.

5. If one has monotonically broadening or slightly nonmonotonic profiles, when a rigorous account of trapped modes is unsubstantial, the coupling wave approximation is very useful. Only forward waves should be taken into account in this

approximation. Then the number of equations becomes two times less. But the main point is that the boundary problem transforms into Cauchy problem. The calculation time for a goal function here reduce in 2N times, where N is the number of modes taken into account. The equations of the coupling waves have the form [5] :

$$\frac{dU_j^{(+)}}{dz} = -ih_j\left(1+\frac{i\mu_j^2\tau}{2h_j^3r^3}\right)U_j^{(+)} + \frac{1}{2}\sum_{m=1}^{N_H}\left(A_{mj}-A_{jm}\frac{h_j}{h_m}\right)U_m^{(+)} + \frac{k}{2}\sum_{n=1}^{N_E}\frac{C_{jn}}{h_n}V_n^{(+)},$$

$$\frac{dV_t^{(+)}}{dz} = -ih_t\left(1+\frac{i\nu_t^2\tau}{2h_t^3r^3}\right)V_t^{(+)} + \frac{1}{2}\sum_{n=1}^{N_E}\left(B_{nt}\frac{h_t}{h_n} - B_{tn}\right)V_n^{(+)} - \frac{k}{2}\sum_{m=1}^{N_H}\frac{C_{mt}}{h_m}U_m^{(+)}.$$

The boundary condition is the following (the H_j wave incidence):

$$(U_j)_{z=0} = U_{j0} \; ; \quad (U_m)_{z=0} = 0 \quad (m\neq j) \; , \quad (V_t)_{z=0} = 0 \; .$$

The difficulties arise at cutoff cross- sections where h_j or h_t turn to zero. Normally this is result of reflected wave neglecting. Let's put the attention on the hard desynchronization between cutoff mode and others ones at the correspondent sections and hence it's interaction. Therefore, each mode should be taken into account only after it's cutoff cross-section.

The comparison of rigorous solutions and solutions of shortened equations showed the applicability of the coupled wave approximation.Mostly adequate procedure is the application of coupling mode equation on the optimization stage and then final testing of results using the rigorous equations.

As an example it would like to show the calculated mode

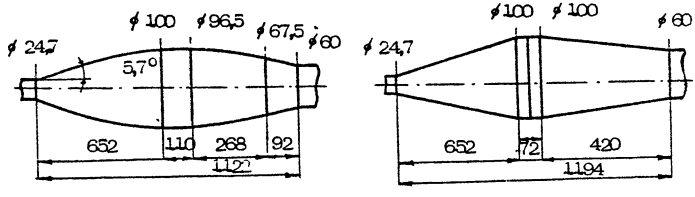

Optimized profile — Conical profile

Modes	$H_{11,3}$	$H_{11,1}$	$H_{11,2}$	$H_{11,4}$	$H_{11,5}$	$H_{11,6}$	$E_{11,2}$	$E_{11,4}$
Opt. prof.	95	0.05	2.24	2.05	0.22	0.01	0.05	0.33
Conic. prof.	61	---	21.3	17.3	---	---	0.4	---

content (in percent of power flow at exit cross- section of taper for the mode $H_{11,3}$ between sections 24.7 mm (close to the cutoff one for wavelength 3.62 mm) and 100 mm. There are many papers on a optimization of the waveguide tapers. It'd like to mention Katzenelenbaum's investigations in particular.Let me point out also papers of Doan [7], who applies the normal wave method leading to the parabolic tapers - it's length is proportional to the radius squared. The method used in mentioned papers is based on taking into account of only two interacting normal waves. Besides, in Doan's method a junction between tapers and regular waveguide aren't taken into account. All this are important for the high mode tapers when spectrum of modes condenses .

6. Let me point out also the class of corrugated waveguide systems using for the mode transformation with equal azimuthal indices. It's well known from the coupled modes theory that the goffer step L and the propagation constants satisfy the following condition or spatial resonance [8] :

$$h_1 - h_2 = p\,\frac{2\pi}{L}\,, \qquad p = \pm 1, \pm 2, \ldots$$

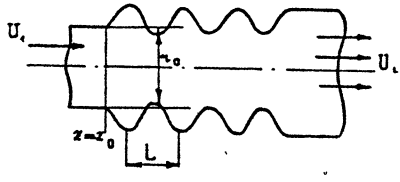

The corrugated system analysis can be done using the our coupled modes equations because the amplitude of goffer is usually small. The optimized profile represents the sum of two harmonics of periodic surface.

$$r = r_0 + A_1 \sin\left(\frac{2\pi z}{L} + \Phi_1\right) + A_2 \sin\left(\frac{4\pi z}{L} + \Phi_2\right)$$

here the amplitudes A_1 and A_2 , the period of structure L, number of goffer and phase constants Φ_1 , Φ_2 may be varied. Note, that really the number of variety parameters can by reduce to three ones, because, as the numerical calculations showed, the second harmonic weakly influences on the optimum.

Here is the list of codes for the analysis and synthesis of axisymmetrical resonators and waveguide tapers, developed by us :

1. NEWOD - analysis and optimization of waveguide profiles

represented as splines surfaces (including piece- linear profiles). The integration : shooting method. Maximum number of modes taken into account is equally 10.

2. NEWORT - analysis of spline waveguide profiles . Solution of equations MPCS is the directed orthogonalization method. Maximum number of modes taking into account is equally 15.

3. NEWODTW- analysis and optimization waveguide profiles using the coupled wave equations. Cubic spline profiles.

4. RES- analysis of resonators in multi-mode approximation. The profiles and method of integration are same as in NEWOD.

5. NEWCOAX- analysis of coaxial resonators (resonator is piece of circular waveguide loaded by circular rod. The rod and waveguide are generally irregular).

6. NEWGOFFR- analysis and optimization of corrugated axisymmetrical waveguide transformers. The couple modes approximation.

REFERENCES

[1]. PAVEL'FV V.G., and TSIMRING SH.E., 1979, Open resonator.(Copyright No. 661664 with priority of 15 Aug.1977), Official Bulletin KDIO of SM USRR, v.17,234.

[2]. KATZENELENBAUM B.Z. The theory of irregular waveguides with slow varying parameters. M. Ac.Sc.USSR. 1961.

[3[. TSIMRING SH.E.,and PAVEL'EV V.G.On the theory of irregular electromagnetic waveguides with cutoff sections. Radiotekhnika i Elektronika. v.27, 1099.

[4]. PAVEL'EV V.G., TSIMRING SH.E.and ZAPEVALOV V.E. Coupled cavities with mode conversion in gyrotrons. Int.J. Electronics,1987, v.63, NO 3, 379.

[5]. TSIMRING SH.E. 1989, Axisymmetrical waveguides tapers and transformers. In : Gyrotrons (Inst. Appl. Phys. of Acad. Sc. USSR,Gorky),p.113.

[6]. Bykov A.A., Il'inski A.S. About numerical solution of boundary problem for of linear ordinary equations.The J. Comp.and Math.Phis., 1979, v.19, NO. 3,631.

[7[. DOANE J.L. Parabolic tapers for overmoded waveguides. Proc.8th Int.Conf.Ifrared and Millimeter Waves.Miami.1983 .P.1.

[8]. KOVALEV N.F., ORLOVA I.M., PETELIN M.I. The mode transformation in corrugated overmoded waveguides.Izv. VUZov, Radiofizika,v.12, 1194.

35 GHz GYROTRON CONSTRUCTION AT INPE

Y. Aso; J.J. Barroso; P.J. Castro; R.A. Correa;
G.O. Ludwig; A. Montes; M.C.A. Nono; J.O. Rossi
Instituto de Pesquisas Espaciais - INPE
Laboratório Associado de Plasma
12201- São José dos Campos - SP - Brasil

ABSTRACT

The conceptual design of a 35 GHz gyrotron for plasma heating experiments is presented. This gyrotron has been designed for pulsed operation in the TE_{021} mode. Under the soft self-excitation condition, the maximum efficiency is calculated as 40% with an output power of 100 kW.

Current experimental work is being done on the construction of all the components and testings of the various subsystems are well underway. Also, techniques for ceramic-to-metal sealing are being developed as well as different types of thermoionic material for the cathode emitting band.

1. INTRODUCTION

The high power millimeter radiation generated by gyrotrons can be coupled to fusion plasmas to heat them, drive current and suppress instabilities. These are the main motivation for the gyrotron development program [1-6] under way at the Brazilian Institute for Space Research (INPE).

The device is composed of three main parts (Fig.1): the electron gun, the resonant cavity and the collector.

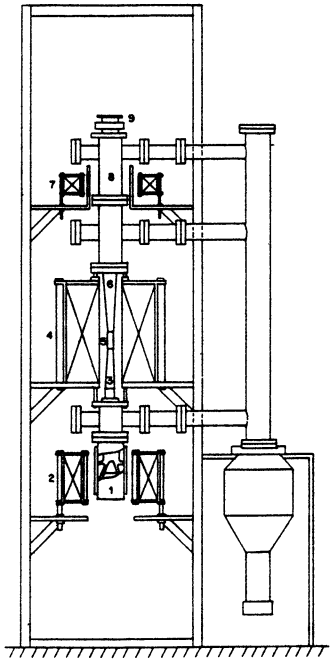

Fig. 1 - Schematic of the 35 GHz gyrotron

1 - electron gun
2 - gun magnetic coil
3 - drift tube
4 - main magnetic coils
5 - resonant cavity
6 - output taper
7 - collector magnetic coil
8 - collector
9 - output window

2. ELECTRON GUN

The electron gun must generate a beam with high transverse energy and low velocity spread. A way to reducing velocity spread is to use guns with laminar beams. The electrode configuration and the electron trajectories are shown in Fig. 2.

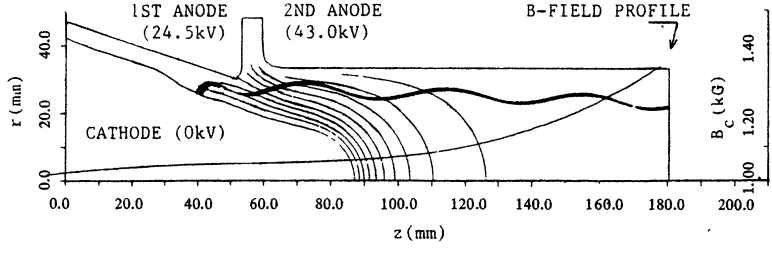

Fig. 2 - Electrode configuration and electron trajectories for the 35 GHz gyrotron electron gun

For this gun, the total beam current is I = 5.0 A. In the drift tube, the beam undergoes magnetic compression. At entrance to the cavity the electron velocity ratio is $\alpha = v_\perp / v_\parallel = 1.5$ and the total dispersion is $\Delta v_\perp / v_\perp = 2.0\%$ [2]. The engineering drawing is shown in Fig. 3.

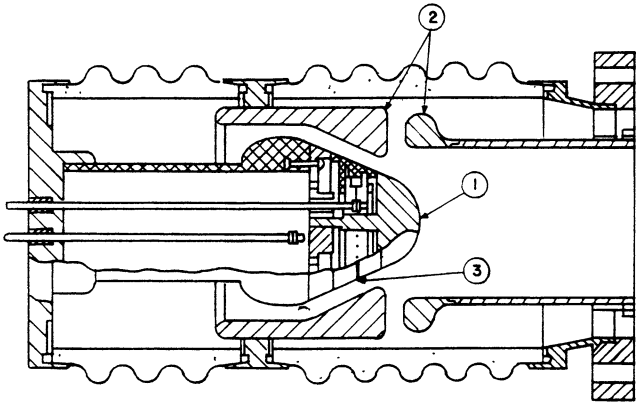

Fig. 3 - Cutaway view of the gyrotron electron gun

1 - molybdenum cathode; 2 - titanium anode; 3 - electron emission ring

Two types of material such as Ba/Sr oxides and tugsten-molybdenum porous matrix impregnated with barium aluminate are being investigated for the electron emitting band [6]. These materials can provide the required current densities of 2.5 and 5.0 A/cm^2 , respectively.

3. RESONANT CAVITY

The ressonant cavity is a conventional one made up of truncated cones with a uniform mid-section [1]. The design parameters give a eigen frequency of 34.918 GHz and a diffraction quality factor of Q = 945.

The chosen TE_{021} mode is characterized by low ohmic losses on account of the azimuthal symmetry, and is relatively free from mode competition.

The cavity is constructed by using electroforming process through acid copper sulphate baths. In the final step a chemical coating with gold or silver should be applied.

4. COLLECTOR AND MAGNETIC COIL SYSTEM

The collector consists of a copper tube of 6.35 cm internal diameter and 4 mm thickness. By means of auxiliary solenoids, the electron trajectories can be controlled to some extent in order to restrain the energy flux density to a maximum tolerated value of 2 kW / cm^2.

The magnetic field required for gyrotron operation is produced by three systems of coils to provide high field homogeneity in the cathode cavity and collector regions (Fig. 4).

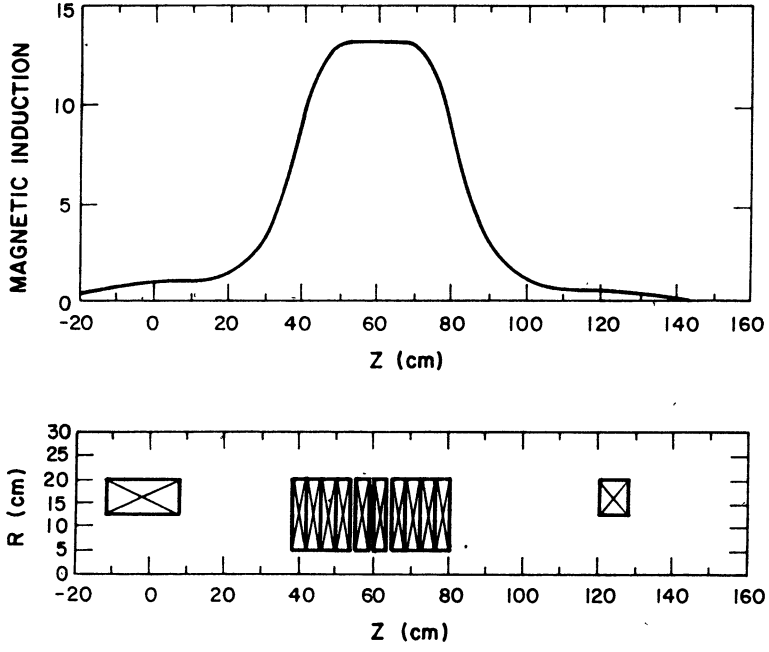

Fig. 4 - Axial profile of the magnetic induction and the respective solenoid system

The main system is made up of 20 water cooled solenoids fed by a current of 1 kA, which produces a flat top magnetic field axial distribution with peak value of 13.5 kG over a length of 13 cm. In the collector region, where there is a plateau of 0.65 kG, the beam guiding center radius is equal to the internal collector radius of 3.18 cm.

By this arrangement, the collector system shown in Fig. 5 operates as a magnetic energy filter, in the sense that the impact position of each electron depends upon its remaining energy.

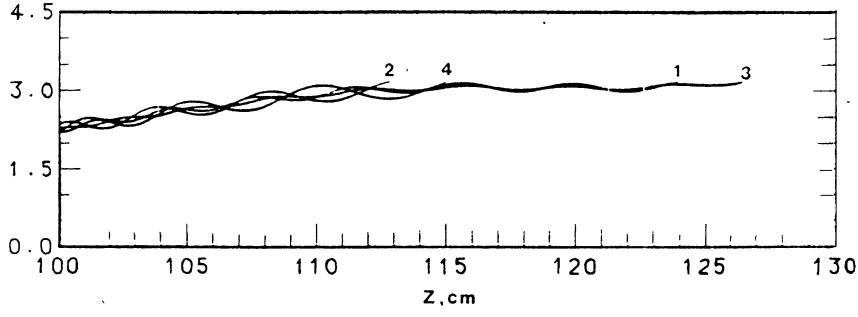

Fig. 5 - Longitudinal view of electron trajectories in the collector region

5. OUTPUT WINDOW

To evaluate quantitavely the properties of a dielectric window, consider the expression for the power loss density [2]:

$$p_d \cong 3.34\ (P_o/\lambda\ R_w)\ (p + 1/4)\ \varepsilon_r \tan \delta$$

where P_o is power transferred by a TE_{op} mode propagation in a uniform waveguide with radius R_w; λ is the wavelength in the free space; ε_r and tan δ are, respectively, the dielectric constant and the loss tangent of ceramic material. Inserting the design values of the 35 GHz gyrotron [p = 2 (TE_{02}), λ = 0.857 cm, R_w = 3.18 cm, P_o = 100 kW, and considering the

typical value $\varepsilon_r \tan\delta$ 1,0 x 10^{-2} and a thermal capacity C = 3,5 J/cm^3 °C for an alumina of 96% purity], into eq. above, the temperature rise $\Theta = p_d \Delta t/C$ is about 5°C for a pulse width Δt = 20 ms.

Since the 100 kW pulse should be repeated for every 50 s, and assuming the disc thickness of 0.43 cm, that corresponds to a third of wavelenght of radiation in dielectric, the average power loss is less than 5 W. Under this condition the heat produced inside the dielectric disc is easily transferred by conduction to the cylindrical wall.

6. TRIGGER ELECTRICAL CIRCUIT AND HIGH VACUUM SYSTEM

The trigger electrical circuit consists basically of a series regulator circuit which regulates the output voltage level and controls the pulse width [3]. Besides that, a protection circuit protects both tubes, regulator and gyrotron, against faults in the system.

The vacuum system uses a diffusion pump with nitrogen trap and titanium sublimator in order to produce a vacuum about 10^{-8} Torr. A high vacuum is necessary to optimize the electron gun operation.

7. CONCLUSION

The construction of a gyrotron is a very complex task and many relevant technologies had to be developed to complete it. Some of the subsystems under construction (high voltage switching, regulator and protection circuits [3], high voltage and high current thermoionic electron guns, and magnetic coils for the generation of intense fields with high spatial and temporal uniformity) require the development of ceramic-to metal sealing, electroforming [4] and microwave diagnostic techniques [5], and techniques for the manufacturing of porous matrix cathodes [6].

Table 1 shows the main characteristics of the device that is being developed.

Table 1 - Design parameters for th 25GHz gyrotron

Maximum output power (kW)	100
Operating frequency (GHz)	35.0
Nominal mode	TE_{021}
Beam voltage (kV)	50.0
Gun anode voltage (kV)	24.5
Laminar beam current (A)	5.0
Current density (A/cm^2)	4.0
Cavity magnetic induction (kG)	13.2
Cathode magnetic induction (kG)	1.05
Beam radius at cavity input (cm)	0.698
Electronic efficiency (%)	40
Pulse duration (ms)	20
Duty cycle (%)	1.2

REFERENCES

[1] Barroso, J.J; Montes, A.; Ludwig, G.O. "RF field profiles in weakly irregular open resonators", International Journal of Electronics 61, 771-794, 1986.

[2] Barroso, J.J.; Montes, A.; Ludwig, G.O.; Correa, R.A. "Design of a 35 GHz gyrotron", International Journal of Infrared and Millimeter Waves, 11, 251-274, 1990.

[3] Rossi, I.O. "Gyrotron trigger electrical circuit", INPE Technical Report. 1987 (INPE-43366-NTE/263).

[4] Nono, M.C.A.; Silva, P.R.; Castro, P.J. "Copper electroforming process for manufacturing of 10 and 35 GHz microwave components, 41ª Reunião da SBPC, 7, 310, 1989.

[5] Castro, P.J. "Measurement techniques for gyrotron characterization", INPE Technical Report, 1987 (INPE-4322-RTE/550).

[6] Nono, M.C.A. "Barium aluminate for manufacturing of thermal electron emitter cathodes", 41ª Reunião da SBPC, 7, 311, 1989.

RELATIVISTIC PULSE-PERIODIC MICROWAVE OSCILLATORS

V.M.Bykov, V.P.Gubanov, A.V.Rostov, S.D.Korovin,
G.A.Mesyats, S.D.Polevin, V.V.Rostov, A.M.Roitman
Institute of High-Current Electronics
Siberian Branch of the USSR Academy of Science

There is a lot of application of powerful microwave sources with relativistic electron beams where a pulse periodic regime is useful or required. This regime with high repetition rate can be achieved only if high-current accelerators which play the role of an electron gun in such installations can work in such a way (Fig. 1). The creation of high-current pulse periodic accelerators has been carried out in our Institute for many years.

It was clear from the very beginning of the work that neither Marx-generators, nor inductive capacitances needed for charging the forming line could work with high repetition rate. Only a peak Tesla transformer can satisfy these requirements [1]. It was proposed to put the transformer inside the forming line. Such a construction gave many conveniences in technology [2]. The repetition rate in this part of the installation is limited only by the average power of preliminary capacitance (Fig. 1). The theory and the technology of peak transformers is now highly evolved and gives the possibility to achieve the efficiency during charging the forming line about 80-90%.

The next step following the energy stream was the developing of a gas switch-commutator. It is a well-known fact that by choosing the form of electrodes, pressure of gas and so on the fore-front duration of discharge in commutator may be made very short. On the contrary the control of back-front of the discharge is not so easy to perform. Only the recombination processes define its time duration and it is very hard to change it. To solve this problem the gas blowing through the commutator's volume was proposed [3]. The charged particles can be removed from the volume between commutator's electrodes by blowing gas with high speed for a shorter time than by recombination process.

This idea gives the possibility to increase now the repetition rate approximately up to 1 kHz.

There is another problem to achieve a high repetition rate connected with a commutator. The self-discharge process is as usual not very stable. The delay time of breakdown can vary from pulse to pulse and so the amplitude of the forming line does. For decreasing this undesirable effect a steerable three-electrode commutator is built [4]. A special outer pulse generator with a short fore-front of the pulse initiates the previous ionization at requisite moment. The amplitude of such an additional pulse achieved 1/5 ÷ 1/4 of the main pulse amplitude value. After this the variation of the pulse amplitude from shot to shot decreased the range approximately to 10^{-2}.

The next problem is associated with the process of matching wave resistance of the forming line and the resistance of the electron gun. A special nonuniform line is situated between the commutator and the electron gun to solve this problem. A detailed discussion of this question is given in paper [5].

As usual a cold explosive-emission cathode in such an accelerator is used. The pulse duration of the electron beam is limited for this cathode by plasma dilation. The length of the forming line which defined the electric field pulse duration must match the time of plasma-cathode processes. The value of the magnetic field near the cathode's surface plays an important role in these prccesses [6].

The electron beam comes then into the electrodynamic system of an oscillator or an amplifier. If Čherenkov type of interaction takes place the corrugated waveguide structure for slowing waves is used (Fig. 2). In such a system it is necessary to direct the electron beam close to the waveguide surface. So a rather strong magnetic field is needed. The output microwave power dependence on the magnetic field amplitude for X-band backward wave oscillator where the cyclotron absorption presents is shown in Fig. 3. It is clear from this dependence that the needed value of the magnetic field is more than 20 kOe. Only a pulse magnetic field or a superconducting cryogenic coil with constant field can satisfy these requirements. If the repetition rate of pulses is less than 10÷30 Hz a usual pulse magnetic coil is preferable, but if the repetition rate is more than 100 pulses per second a superconducting coil is required.

RELATIVISTIC PULSE-PERIODIC MICROWAVE OSCILLATORS

V.M.Bykov, V.P.Gubanov, A.V.Rostov, S.D.Korovin,
G.A.Mesyats, S.D.Polevin, V.V.Rostov, A.M.Roitman
Institute of High-Current Electronics
Siberian Branch of the USSR Academy of Science

There is a lot of application of powerful microwave sources with relativistic electron beams where a pulse periodic regime is useful or required. This regime with high repetition rate can be achieved only if high-current accelerators which play the role of an electron gun in such installations can work in such a way (Fig. 1). The creation of high-current pulse periodic accelerators has been carried out in our Institute for many years.

It was clear from the very beginning of the work that neither Marx-generators, nor inductive capacitances needed for charging the forming line could work with high repetition rate. Only a peak Tesla transformer can satisfy these requirements [1]. It was proposed to put the transformer inside the forming line. Such a construction gave many conveniences in technology [2]. The repetition rate in this part of the installation is limited only by the average power of preliminary capacitance (Fig. 1). The theory and the technology of peak transformers is now highly evolved and gives the possibility to achieve the efficiency during charging the forming line about 80-90%.

The next step following the energy stream was the developing of a gas switch-commutator. It is a well-known fact that by choosing the form of electrodes, pressure of gas and so on the fore-front duration of discharge in commutator may be made very short. On the contrary the control of back-front of the discharge is not so easy to perform. Only the recombination processes define its time duration and it is very hard to change it. To solve this problem the gas blowing through the commutator's volume was proposed [3]. The charged particles can be removed from the volume between commutator's electrodes by blowing gas with high speed for a shorter time than by recombination process.

This idea gives the possibility to increase now the repetition rate approximately up to 1 kHz.

There is another problem to achieve a high repetition rate connected with a commutator. The self-discharge process is as usual not very stable. The delay time of breakdown can vary from pulse to pulse and so the amplitude of the forming line does. For decreasing this undesirable effect a steerable three-electrode commutator is built [4]. A special outer pulse generator with a short fore-front of the pulse initiates the previous ionization at requisite moment. The amplitude of such an additional pulse achieved 1/5 ÷ 1/4 of the main pulse amplitude value. After this the variation of the pulse amplitude from shot to shot decreased the range approximately to 10^{-2}.

The next problem is associated with the process of matching wave resistance of the forming line and the resistance of the electron gun. A special nonuniform line is situated between the commutator and the electron gun to solve this problem. A detailed discussion of this question is given in paper [5].

As usual a cold explosive-emission cathode in such an accelerator is used. The pulse duration of the electron beam is limited for this cathode by plasma dilation. The length of the forming line which defined the electric field pulse duration must match the time of plasma-cathode processes. The value of the magnetic field near the cathode's surface plays an important role in these prccesses [6].

The electron beam comes then into the electrodynamic system of an oscillator or an amplifier. If Cherenkov type of interaction takes place the corrugated waveguide structure for slowing waves is used (Fig. 2). In such a system it is necessary to direct the electron beam close to the waveguide surface. So a rather strong magnetic field is needed. The output microwave power dependence on the magnetic field amplitude for X-band backward wave oscillator where the cyclotron absorption presents is shown in Fig. 3. It is clear from this dependence that the needed value of the magnetic field is more than 20 kOe. Only a pulse magnetic field or a superconducting cryogenic coil with constant field can satisfy these requirements. If the repetition rate of pulses is less than 10÷30 Hz a usual pulse magnetic coil is preferable, but if the repetition rate is more than 100 pulses per second a superconducting coil is required.

The main results of microwave generation experiments with such installations (some of them were made in collaboration with the Institute of Applied Physics, N.-Novgorod) are given in Table 1. As the pulse power is rather high in these experiments, the average power is moderate. Therefore no complicated problems arise by cooling the collector and the output window made of special glass or thin film.

In conclusion we attract your attention to the fact that the results shown above are typical. The best results gave the output power of more than 1÷1.5 GW (in X-band) repetition rate near 1 kHz and the electron efficiency when the nonuniform electrodynamic system is used (Fig. 2) near 35 %. But these values were achieved separately in different experiments. Some details of this work are published in papers [7, 8].

Many installations of such a kind are working now in different institutes and laboratories of our country. Some advanced installations are now being constructed.

Table 1

Pulse-periodic high current accelerators "Sinus"

Type of accelerator	Particle energy keV	Beam current kA	Pulse duration ns	Repetition rate pulses per s
Sinus 4	300	3	25	50
Sinus 5	300	3	5	100
	(600)	(6)	(5)	(0.1)
Sinus 5 A	600	6	10	100
	(1500)	(15)	(4)	(0.1)
Sinus 6	700	7	25	0.1
Sinus 6 A	400	4	25	1000
Sinus 7 *	1500	20	40	0.1
	(1000)	(12)	(40)	200

* - under setting in operation

Microwave experimental results

Type of accelerator	Wave length cm	Output power GW	Pulse duration ns	Efficiency %	Repetition rate pulses per s
BWO	3	1	20	30	0.1
BWO	3	0.5	20	20	10^2
Orotron	0.8	0.1	10	5	10^3

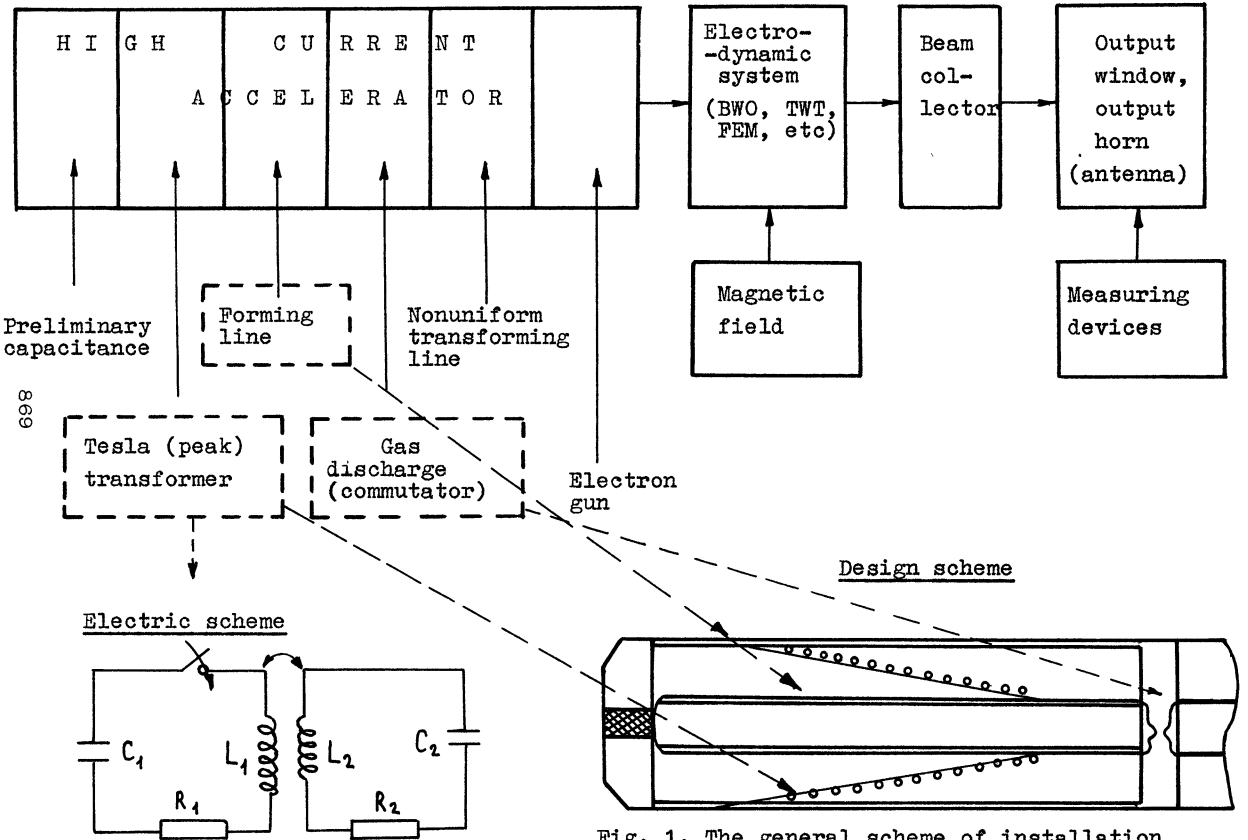

Fig. 1. The general scheme of installation

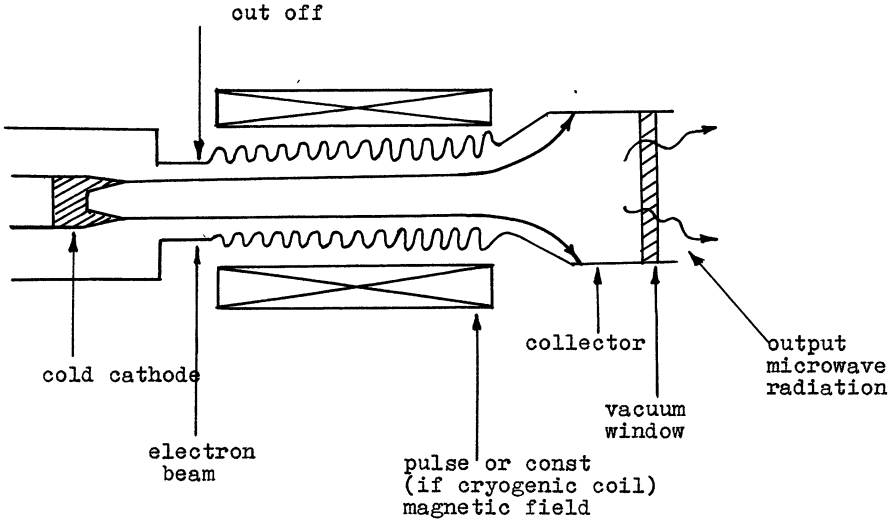

Fig. 2. Beam-field interaction volume

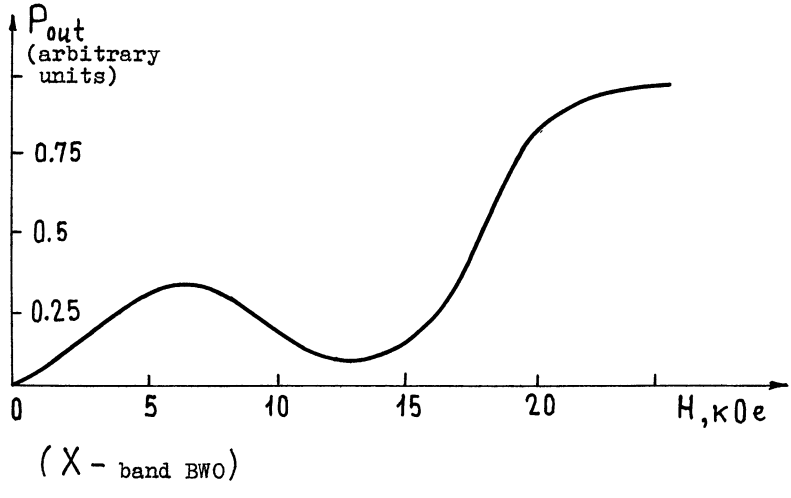

Fig. 3. Typical output microwave power dependence

References

1. Elchaninov A.S., Zagulov F.Ya., Korovin S.D., Mesyats G.A., Rostov V.V. High-current pulse-periodic electron accelerators for microwave oscillators. In: Relativistic High-Frequency Electronics. Gorky, Inst.Appl.Phys., 1981, p.5.
2. Korovin S.D. Tesla Transformer in High-Current Pulse-Periodic Accelerators. Preprint N 47, TF Sib.Branch, USSR Scad. of Sci., 1988, p.38.
3. Elchaninov A.S., Zagulov F.Ya., Korovin S.D., Mesyats G.A. Investigation of high-voltage commutator's stability with gas stream between electrodes. Pribory i tekhnika eksperimenta, 1979, N4, p.162.
4. Bykov N.M., Vashaev O.A., Gubanov V.P. et al. High-current controled commutator with repetition rate 100 Hz. Pribory i tekhnika eksperimenta, 1988, N6, p.96.
5. Korovin S.D., Rostov V.V., Smorgonsky A.V. Pulse-periodic relativistic BWO. Izv. VUZov, radiofizika, 1986, v.29, N10, p.1278.
6. Bugaev S.P., Il'in V.P., Koshelev V.J. et al. Formation of intense relativistic electron beams for high-power microwave oscillators and amplifiers. In: Relativistic High-Frequency Electronics, Gorky, Inst.Appl.Phys., 1979, p.5.
7. Bykov N.M., Gubanov V.P., Gunin A.V. et al. Relativistic pulse-periodic oscillators of X-band. In: Relativistic microwave Electronics, Gorky, Inst.Appl.Phys., 1988, N5, p.101.
8. Bykov N.M., Garbusov V.P., Gunin A.V. et al. Relativistic BWO with high average power. J.Techn.Phys., 1989, v.59, N5, p.32.

THE EXCITATION OF THE FUNDAMENTAL MODE OF A COAXIAL PLASMA SLOW-WAVE STRUCTURE OF A PCM-AMPLIFIER

Selivanov I.A., Fedotov A.V., Shkvarunets A.G.

Institute for General Physics of the USSR Academy of sciences, Vavilov Str., 38, Moscow, 117942

1.EXPERIMENTAL APPARATUS

The schematic diagram of our experimental apparatus is given in a Figure 1 . It consists of four main parts : coaxial mode transformer (1) ; annular plasma column (2) and plasma source (3) ; the coaxial-transmission-line output (4). The system is located in an external longitudinal impulse magnetic field whose intensity could be changed up to 2 Tl. The source of the microwave M - band radiation is a magnetron with the following parameters: the radiation wavelength - λ_0 = 2.42 cm; the generation duration - τ = 10 - 100 μs; the radiation power - P = 50 - 150 kW.

The plasma annulus was produced due to the ionization of background gas (xenon under the pressure p = $2*10^{-3}$ torr) by an annular low-voltage electron beam (E = 500 V, t = 100 μs) with mean radius r_b = 0.85 cm and thickness δ_b =0.08 cm. The plasma densities from the region from $5*10^{11}$ cm^{-3} up to 10^{14} cm^{-3} were achieved with the help of this source. The plasma density measurements were made by probing the plasma annulus with low power microwave radiation for three fixed wavelengths λ = 2.42, 0.8 and 0.65 cm, respectively. The measurements of the radial plasma density profile were made using a single moving probe under the conditions of electron current saturation and with B = 0.9 Tl, n_p = $3*10^{13}$ cm^{-3}. These measurements showed that the radial plasma density profile was a thin annular one with mean radius r_p = 0.9 cm. The thickness of the plasma annulus was 0.15 cm on a 0.3-level and 0.3 cm - on a 0.03-level. The azimuthal structure of the plasma annulus was measured using two probes

which could be rotated azimuthally. These measurements determined that the local value of plasma density, at the fixed azimuthal position of the probe, had an amplitude modulation with the characteristic period of about 10 μs. The level of modulation was 30 % . Moreover, in this time interval, the azimuthal nonuniformity of plasma annulus was localized to about 20°. Therefore, the plasma column consists of filaments of varying density that are rotating. The number of azimuthal plasma filaments was usually not greater than 10.

2. MICROWAVE TRANSPORT DOWN THE CO-AXIAL PLASMA WAVEGUIDE IN FINITE MAGNETIC FIELD

As stated above, the plasma annulus had a non - azimuthally symmetric density profile. This may lead to the conversion between symmetric and nonsymmetric modes of the partially-filled plasma waveguide. In order to prevent such a conversion, we've studied the basic characteristics of microwave transport of azimuthally symmetric modes under the conditions of short plasma annulus (2-5 cm in length). Also we can identify the excited mode by placing an absorber (5) inside the plasma annulus, because of the different characteristics for the structure of the fast and slow modes.

We've used the results of theoretical works [1,2,3,4] to explain the behavior of dispersion curves of the co-axial plasma waveguide in finite magnetic field. As can be seen from these works, there are three branches of azimuthally symmetric normal modes of such a slow-wave structure. First, there's the fast vacuum TM_{01} mode that may be excited at the input frequency ω_0 only for plasma frequencies from the region $0 < \omega_p < \omega_{cr}$. For our experimental conditions ω_{cr} is $3.1\omega_0$. Second, there's the slow plasma TM_{01} mode that approaches the minimum of Ω_e and ω_p in the limit k_z goes to infinity. Third,there's the branch of potential oscillations in finite magnetic field for a partially-filled waveguide with plasma (the upper hybrid mode) that approaches the maximum of Ω_e and ω_p in the limit k_z goes to infinity.

The analysis of these equations shows that the behavior of microwave transport down the co-axial plasma waveguide in finite magnetic field is determined by the ratio of frequencies ω_p, Ω_e

and ω_0. If $\Omega_e > \omega_0 > \omega_p$, only the fast vacuum TM_{01} mode with a high group velocity may be excited. This means that there can be efficient coupling and transport of external electromagnetic wave with frequency ω_0. If $\Omega_e > \omega_0$ and $\omega_0 < \omega_p < \omega_{cr}$, the fast vacuum mode as well as the slow plasma mode may be excited simultaneosly. However, both these modes have relatively low group velocity. Therefore, inefficient power coupling and transport of external wave is a possibility. Lastly, if $\omega_p > \omega_{cr}$, only the slow plasma wave with group velocity close to c may be excited. Therefore, there can be efficient coupling and transport.

If $\Omega_e < \omega_0$, only the fast vacuum TM_{01} mode may be excited. By increasing the plasma frequency, the group velocity of this mode decreases that may lead to the decrease in an efficiency of microwave transport. If $\omega_p > \omega_{cr}$, there are no TM_{01} modes (either fast or slow) which can be excited at the input frequency ω_0. Moreover, there are a specific regions meeting the following conditions $\omega_p \sim \omega_0$, $\omega_0 \sim \Omega_e$, $\omega_0 \sim \omega_h$ and $\omega_0 \sim \omega_{cr}$ where at least one of the excited modes has a group velocity equal to zero. Due to the potential character of the mode excited under this conditions, there can be the regime of inefficient microwave transport of external wave down the plasma co-axial waveguide .

First let's consider the case for strong magnetic field, B = 0.93 T. Figure 2 shows the experimentally measured dependence of the transport coefficient of microwave radiation with input frequency $\omega_0 = 7.8*10^{10}$ rad.sec^{-1} and for $\Omega_e = 1.62*10^{11}$ rad.sec^{-1} and for a 5.5 cm length of the plasma column (Fig.2.1). It can be seen from this figure that there are three regions of effective transport of microwave power ($k_{tr} > 0.5$); when $\omega_p < \omega_0$, $1.5\omega_0 < \omega_p < 2.7\omega_0$ and when $\omega_p > 4.3\omega_0$. There are two regions of ineffective transport of microwave power ($k_{tr} < 0.5$); when $\omega_0 < \omega_p < 1.5\omega_0$ and when $2.7\omega_0 < \omega_p < 4.3\omega_0$. In Figure 2.1 no microwave absorber was present. Figure 2.2 shows the dependence of transport of microwave power on plasma density when the microwave absorber was present in the system. These results show that for plasma densities $\omega_p > 3.5\omega_0$ only the slow TM_{01} plasma mode is excited.

Now let's consider the case of weak magnetic field. Figure 3 shows the experimentally measured dependence of the transport co-efficient of microwave power on the plasma density for B = 0.182 T, $\Omega_e = 0.41\omega_0$, at the input frequency $\omega_0 =$

$7.8*10^{11}$ rad.sec^{-1}. It can be seen that for plasma frequencies $\omega_p < 2.5\omega_0$ there's efficient transport of microwave power down the plasma co-axial structure. However, at $\omega_0 \sim 0.5\omega_0$ there's an anamolous decrease in the tranport of the microwave power. Due to the inaccuracies in the measurement of the plasma density this decrease could correspond to $\omega_p = (\omega_0^2 - \Omega_e^2)^{1/2}$. For $\omega_p > 3\omega_0$ there's no transport down the stucture, i.e., for high plasma density the slow plasma TM_{01} mode isn't excited. Also, at the critical value of magnetic field intensity (cyclotron resonance), B = 0.44 T, at least one of the excited modes has a group velocity equal to zero, for all ω_p.

Finally, the general experimental dependences of the transport co-efficient of microwave power on the magnetic field intensity is shown in Figure 4. In all these figures the length of the plasma column was 5.5 cm. Figures 4.1 to 4.3 are for $\omega_p = 0.5\omega_0$, $3.1\omega_0$ and $5\omega_0$, respectively. The condition for cyclotron resonance ($\omega_0 = \Omega_e$) occurs when B = 0.44 T. For small plasma densities ($\omega_p = 0.5\omega_0$) the lower boarder of the region where no wave excitation occurs is determined by the value of the upper hybrid frequency ω_h. In particular, for this case, the condition $\omega_0 < \omega_h = (\omega_p^2 + \Omega_e^2)^{1/2}$ occurs when B > 0.38 T. As follows from analysis of the behavior of the dispersion curves, the upper boarder of the region where no wave excitation occurs, for all plasma densities, is determined by $\omega(k_z)$ at the intersection point of the fast TM_{01} mode and the upper hybrid mode.

The comparison between the experimental results and the approximate analytical theory allows us to make the following conclusions:

1. The efficient transport of microwave power down the plasma co - axial waveguide in a finite magnetic field can occur for one or two normal modes having a high group velocity;
2. If one of the modes has a group velocity $v_{gr} \ll c$ then the efficiency of transport decreases significantly;
3. Moreover, if the intensity of the external magnetic field is such that $\Omega_e > 1.5\omega_0$ the transport of the microwave power at the frequency ω_0 doesn't depend on the magnetic field intensity.

The effective use of high current relativistic electron beams for amplifying microwave radiation requires a high level of input microwave power. A sufficient level of input power is 100 kW. The experiments for transport of the high power microwave

radiation down the co-axial waveguide of 30 cm length were conducted for the following set of system parameters: microwave power of 150 kW, intensity of the external magnetic field 0.92 T with the plasma density $3*10^{13}cm^{-3}$ ($\omega_p \sim 4\omega_0$). Therefore these experiments were conducted in the regime of excitation of only the slow plasma TM_{01} mode. The result of this of experiment on high power microwave propagation in the co-axial plasma waveguide is that we can transport 150 kW of microwave power for 0.4 μs over at least a 30 cm length in the slow TM_{01} mode of the co-axial plasma waveguide without exciting other waveguide modes.

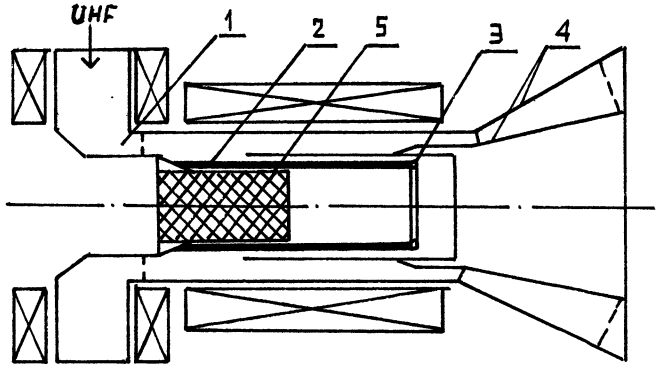

Fig. 1. Experimental configuration of a PCM - amplifier.

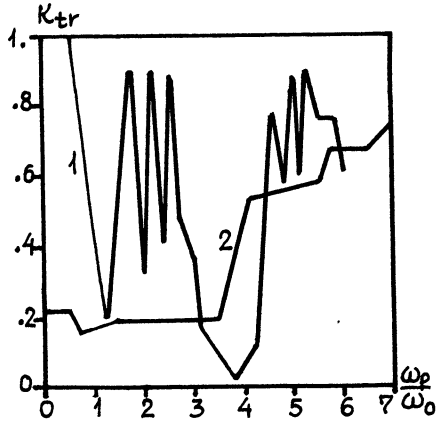

Fig. 2. The dependence of the transport co-efficient on the plasma density for strong magnetic field : 1 - without an absorber; 2 - with an absorber.

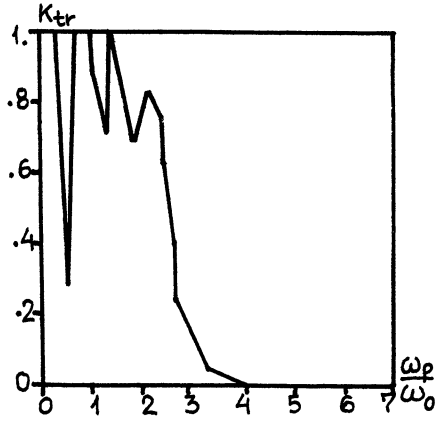

Fig. 3. The dependence of the transport co-efficient on the plasma density for weak magnetic field.

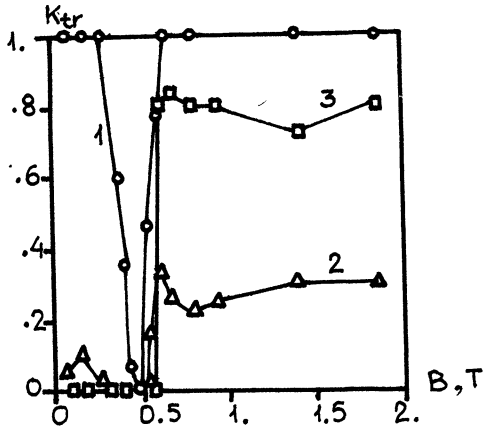

Fig. 4. The dependence of the transport co-efficient on the magnetic field intensity.

REFERENCES

1. J.S. De Groot, R.A. Stone, K. Mizuno, J.H. Rogers, T.D. Pointon, IEEE Transactions on Plasma Science, 16, 206(1988).
2. M.V. Kuzelev, E.V. Liperovskaja, A.A. Rukhadze, Fizika plazmy, 4, 433 (1978).
3. S.T. Ivanov, E.G. Alexov, P.N. Malinov, Plasma Physics and Controlled Fusion, 31, 941 (988).
4. N.A. Krall, A.W. Trivelpiece, Principles of Plasma Physics New York 1973, McGraw-Hill.

A THEORY OF THE DIELECTRIC CHERENKOV MASER WITH A HIGH-CURRENT HOLLOW RELATIVISTIC ELECTRON BEAM

N.I.Karbushev*, A.S.Shlapakovskii**
*Moscow Radiotechnical Institute,
113519, Varshavskoe shosse, 132, Moscow, USSR
**Institute of Nuclear Physics of Tomsk Polytechnical Institute, 634050, Box - 25, Tomsk, USSR

Parameters of microwave radiation achieved in dielectric Cherenkov maser (DCM) at millimeter wavelengthes [1] are compa - rable with ones produced by more developed devices such as gyro- trons. It seems to be promised for strong microwave generation to use high-current hollow relativistic electron beams (REB) [2,3]. It is necessary now to have a theory which is suitable for quantita- tive analysis and optimization of DCMs with high-current REBs. Influence of rf space charge must be correctly taken into acco - unt. We have built linear and stationary nonlinear theory of DCM for the same as in [3] geometry closed to real experiment [2]. Magnetized monoenergetic thin hollow REB of radius r_b, current I and velocity u, propagating into a circular waveguide with die- lectric liner of the same outer radius, is considered. An inte- raction occurs on finite length L with axysymmetric TM-mode, the beam is injected without any modulation and the wave is reflec- ted at z = 0, L with coefficients ρ_1 , ρ_2 .

1. Linear theory. The principle our theory is based on is a separation of synchronous "cold" wave field from the total ac field in system. The residual field is considered as rf space charge

$$E_z(r_b) = E_z^{syn}(r_b) + E_z^{sp.ch.}(r_b).$$

Such approach allows to write the dispersion relation in the form of characteristic TWT equation

$$[k - k_0(\omega)][(\omega - ku)^2 - \Omega_e^2 \Gamma] = -\alpha^3 \omega \Omega_e^2 / u$$

with depression and coupling coefficients Γ and α^3 which are quite determined functions of frequency ω and wavenumber k. But if we assume them to be constants we may use the results which have already been obtained in classical theory of TWT.

Then values of Γ and d^3 are calculated at synchronous frequency $\omega_0 = k_0(\omega_0)u$ and it is correct to consider them as constants under conditions

$$|k - \frac{\omega}{u}|, |k - k_0(\omega)| \ll \omega_0 / 2\gamma^2 u,$$

where γ is a Lorentz factor. Formulas for Γ and d^3 are

$$d^3 = d^3(\omega) = u F_0^2(k_{\perp 0}R, k_{\perp 0}r_0) I_0^2(\varkappa_0 r_b) / 2\omega \varkappa_0^2 k_0 r_0^4 N_1,$$

$$\Gamma = \Gamma(\omega, k) = \frac{\varkappa^2}{2\varkappa_0^2} \frac{I_0(\varkappa r_b)}{I_0(\varkappa r_0)} \frac{\Phi(r_b)}{\mathcal{D}(\omega, k)} \mathcal{F}_0(\varkappa r_0, \varkappa r_b) +$$

$$+ F_0^2(k_{\perp 0}R, k_{\perp 0}r_0) I_0^2(\varkappa_0 r_b) / 2\varkappa_0^2 k_0 (k - k_0) r_0^4 N_1 .$$

Here

$$\Phi(r) = \frac{\varepsilon}{k_\perp} \frac{F_1(k_\perp R, k_\perp r_0)}{F_0(k_\perp R, k_\perp r_0)} - \frac{\mathcal{F}_1(\varkappa r, \varkappa r_0)}{\varkappa \mathcal{F}_0(\varkappa r_0, \varkappa r)},$$

$$\mathcal{D}(\omega, k) = \frac{\varepsilon}{k_\perp} \frac{F_1(k_\perp R, k_\perp r_0)}{F_0(k_\perp R, k_\perp r_0)} - \frac{1}{\varkappa} \frac{I_1(\varkappa r_0)}{I_0(\varkappa r_0)},$$

$$N_1 = \frac{4\varepsilon I_0^2(\varkappa_0 r_0)}{\pi^2 k_{\perp 0}^4 r_0^4} + \frac{\varepsilon - 1}{\varkappa_0^2 r_0^2} F_0^2(k_{\perp 0}R, k_{\perp 0}r_0) \Big[\frac{I_1^2(\varkappa_0 r_0)}{\varepsilon} -$$

$$- k_0^2 I_0^2(\varkappa_0 r_0) / k_{\perp 0}^2 + 2\omega^2 I_0(\varkappa_0 r_0) I_1(\varkappa_0 r_0) / c^2 k_{\perp 0}^2 \varkappa_0 r_0 \Big],$$

$$k_\perp^2 = \varepsilon\omega^2/c^2 - k^2, \varkappa^2 = k^2 - \omega^2/c^2, k_{\perp 0}^2 = \varepsilon\omega^2/c^2 - k_0^2, \varkappa_0^2 = k_0^2 - \omega^2/c^2,$$

$$F_0(x, y) = j_0(x) Y_0(y) - j_0(y) Y_0(x), F_1(x, y) = -\partial F_0 / \partial y,$$

$$\mathcal{F}_0(x, y) = I_0(x) K_0(y) - I_0(y) K_0(x), \mathcal{F}_1(x, y) = -\partial \mathcal{F}_0 / \partial y,$$

r_0, R are liner and outer radii of liner, ε is dielectric constant, j, Y, I, K are Bessel functions. $\mathcal{D}(\omega, k_0) = 0$ corresponds to no-beam case. Expression for Γ needs to be expanded in series of $k - k_0$ powers to exclude singularities. Some examples of Γ calculation are presented in Fig.1 versus beam radius. d^3 vs r_b dependence is evident: $d^3 \sim I_0^2(\varkappa_0 r_b)$.

According to TWT theory space charge parameter is

$$C^2 = \frac{\Gamma}{d^2} \left(\frac{\Omega_b}{\omega_0} \right)^{2/3}, \quad \left(\Omega_b^2 = \frac{4eI}{\gamma^3 m u} \varkappa_0^2 \right)$$

and one can write formulas for gains and, hence, for start currents both in weak space charge ($C^2 \ll 1$) and strong space charge ($C^2 \gg 1$) operation regimes through Γ and d^3. Also we write the expression for current value I^* which is a border between two regimes.

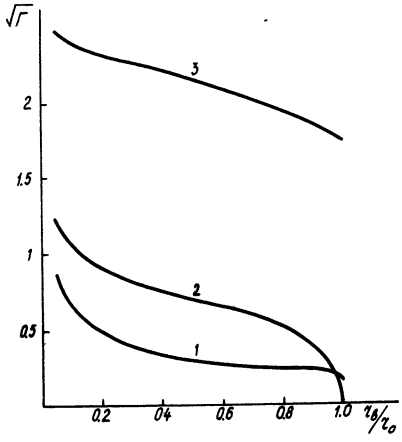

Fig.1. Depression coefficient vs beam radius for TM_{01}-mode.
1 - $\mathcal{E} = 2$, $r_0/R = 0.84$, $\gamma = 1.8$ ($\omega_0 R/2\pi c = 1.56$);
2 - $\mathcal{E} = 2.25$, $r_0/R = 0.8$, $\gamma = 2.5$ ($\omega_0 R/2\pi c = 0.81$);
3 - $\mathcal{E} = 5$, $r_0/R = 0.44$, $\gamma = 3$ ($\omega_0 R/2\pi c = 0.25$)

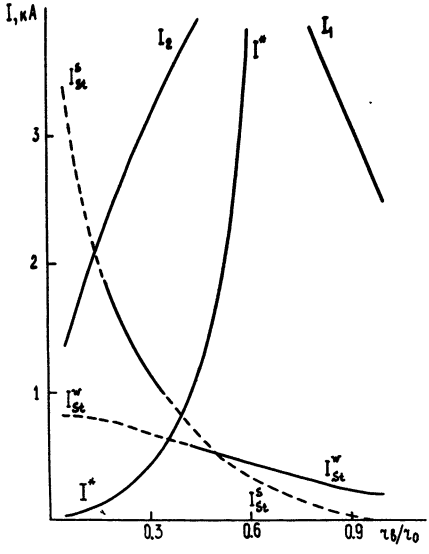

Fig.2. Start currents and current values I^*, I_1, I_2 vs beam radius.
$\mathcal{E} = 2.25$, $r_0/R = 0.8$, $\gamma = 2.5$; $\rho = 0.1$, $L/R = 20$

$$I^w_{St} \simeq \frac{\gamma^5 u^6}{\mathcal{L}^3 \omega_0^3 L^3 c^3} \min\left\{6.56 \ln^3\left(\frac{3}{\rho}\right); 31.6\left(\frac{1}{\rho} - 1\right)\right\} \text{ kA}; \quad \rho = |\rho_1 \rho_2|;$$

$$I^s_{St} \simeq 17 \frac{\gamma^5 u^7 \Gamma}{\mathcal{L}^6 \omega_0^4 L^4 c^3} \left(\operatorname{arch} \frac{1}{\rho}\right)^4 \text{ kA}; \quad I^* \simeq 4.25 \frac{\gamma^5 \mathcal{L}^6 u^3}{\Gamma^3 c^3} \text{ kA}.$$

As Γ and $\mathcal{L}^3$ calculated at synchronism strongly depend on r_b there are intervals of beam radius value where presented formulas for start currents are valid. It is shown by solid parts of curves in Fig.2. Also curves are drawn for currents I_1, I_2 limiting the region of validity for assumption Γ and $\mathcal{L}^3$ to be constants

$$I_1 \simeq 0.53 u^3/\gamma \mathcal{L}^3 c^3 \text{ kA}, \quad I_2 \simeq 1.06 \gamma u^3/\Gamma c^3 \text{ kA}.$$

2. Nonlinear theory. Separating synchronous wave field from total field

$$E_z(r_b) = \mathrm{Re}\left[E_s(z) e^{-i\theta} + \sum_{n=1}^{\infty} E_n(z) e^{-in\theta}\right],$$

where E_s is synchronous wave amplitude, E_n are harmonics amplitudes of rf space charge field, $\theta = \omega t - k_0(\omega)z$, one can obtaine following set of nonlinear relativistic TWT equations

$$\frac{d\theta}{d\zeta} = \nu - \delta, \quad \frac{d\mathcal{E}}{d\zeta} = \frac{i_0}{\pi}\int_0^{2\pi} e^{i\theta}d\theta_0, \quad \mathcal{E} = -\frac{eE_s}{\gamma^3 m\omega u},$$

$$\frac{d\nu}{d\zeta} = \left[1+2(\gamma^2-1)\nu\right]^{3/2}\left[\mathrm{Re}(\mathcal{E}e^{-i\theta}) - \frac{i_0}{\pi\lambda^3}\sum_{n=1}^{\infty} n\Gamma_n \mathrm{Im}\left(e^{-in\theta}\int_0^{2\pi} e^{in\theta}d\theta_0\right)\right],$$

$$\nu = 1 - \frac{v}{u} \ll 1, \quad \zeta = \frac{\omega}{u}z, \quad \delta = \frac{k_0 u}{\omega} - 1, \quad i_0 = \lambda^3\frac{\Omega_e^2}{\omega^2}.$$

Here v is particles velocity, Γ_1 is taken from linear theory and

$$\Gamma_{n\geq 2} = \frac{1}{2}\frac{I_0(n\varkappa_0 r_e)}{I_0(n\varkappa_0 r_0)}\frac{\Phi(r_e, n\omega, nk_0)}{\mathcal{D}(n\omega, nk_0)}F_0(n\varkappa_0 r_0, n\varkappa_0 r_e).$$

If the beam current is not too high in comparison with start value, stationary generation occurs at frequency corresponding to maximum linear gain. Feedback is realized by reflected wave of constant amplitude so that $|\mathcal{E}(0)| = \rho|\mathcal{E}(L)|$ and, if $\rho \ll 1$, finding maximum efficiency and optimal device length reduces to solving of amplification problem, i.e., conditions at the entrance are

$$\nu(0) = 0, \quad \theta(0) = \theta_0 \in [0, 2\pi), \quad \mathcal{E}(0) = \mathcal{E}_0$$

Efficiency and optimal length are yielded by formulas

$$\eta_m = \gamma(\gamma+1)|\mathcal{E}|_m^2/4i_0, \quad L_m = z_m + (\mathrm{Im}\,k)^{-1}\ln(|\mathcal{E}_0|/\rho|\mathcal{E}|_m),$$

where $|\mathcal{E}|_m$ is maximum value of amplitude, z_m is corresponding coordinate and $\mathrm{Im}\,k$ is a spatial growth rate from linear theory. Note that small ρ is a feature of generators with high - current REBs because of high level of start current and good microwave output coupling.

Formulated nonlinear set under certain assumptions and by various variables changing may be reduced to general sets, containing the only free parameter. Namely, if we neglect electron mass alteration during the interaction and take into account only first harmonic of rf space charge field we can get a general set with space charge parameter G^2 as a free parameter (clas - sical TWT). If the beam is considered as ultrarelativistic and rf space charge isn't taken into account in general a set with parameter $\gamma^6 i_0$ come out (relativistic TWT). These general sets

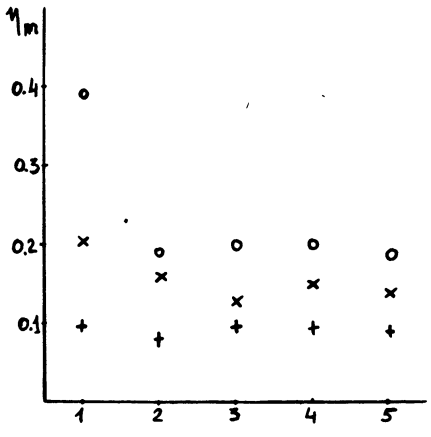

Fig.3. Maximum efficiency versus number of accounted harmonics.
$\xi = 2$, $r_0/R = 0.84$, $\gamma = 1.8$, $r_b/r_0 = 0.7$:
"+" - I = 0.1 kA;
"x" - I = 0.5 kA;
"o" - I = 2.8 kA.

have already been investigated in detail earlier. However, our numerical calculations have demonstrated that using of simplified sets distorts the results very much when parameters are natural for intense REBs. For instance, in strong space charge regime it is very important to take into account higher harmonics of nonsynchronous field because neglecting of them leads to great efficiency overvalue (see Fig.3 and also Fig.4b). That is why we solved the nonlinear set successively increasing the amount of accounted harmonics till getting desired convergence.

The results of calculations for two typical geometries are presented in Fig.4,5, where maximum efficiency and optimal length versus beam current and radius are plotted. It is important to note that taken current values turn out not too high in comparison with start currents values corresponding to calculated optimal lengthes. Hence, consideration of stationary generation regime on frequency corresponding maximum linear gain is justified.

Fig.4 shows that the top in $\eta_m(I)$ dependences is reached when $I > I^*$ and rf space charge influence is significant. One more feature is different for weak and strong space charge regimes: at weak space charge regime maximum in $\eta(z)$ dependence is very sharp. It complicates experimental L_m finding and makes a device rather sensible to possible fluctuations of REB parameters. As to maximum efficiency dependence on beam radius at fixed current it may be qualitatively different for various geometries (see Fig.5) because of various degree of synchronous wave field evanescence. There are such geometries when this dependence has a maximum and finding this maximum is important

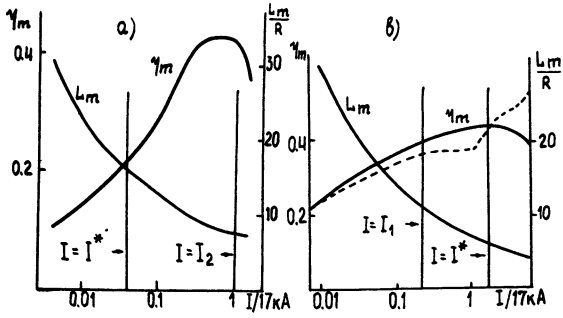

Fig.4. Maximum efficiency and optimal length versus beam current. $\rho = 0.1$.
a) $\delta = 2$, $r_0/R = 0.84$, $\gamma = 1.8$, $r_b/r_0 = 0.85$;
b) $\delta = 2{,}25$, $r_0/R = 0.8$, $\gamma = 2.5$, $r_b/r_0 = 0.8$
Dashed curve-solving without higher harmonics.

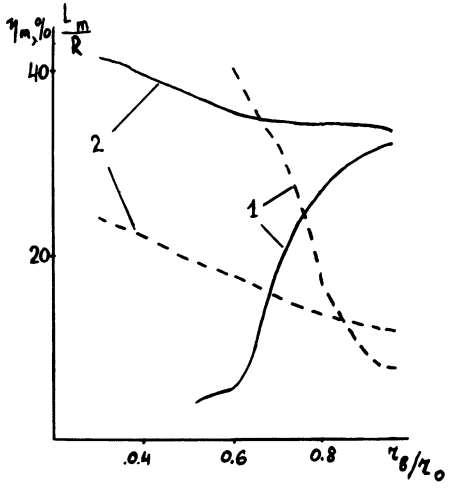

Fig.5. Optimal length (dashed curves) and maximum efficiency versus beam radius. $\rho = 0.1$, I = 1.7 kA.
1 - $\delta = 2$, $r_0/R = 0.84$, $\gamma = 1.8$;
2 - $\delta = 2.25$, $r_0/R = 0.8$, $\gamma = 2.5$.

practical task. Finally, presented results allow to make a conclusion about DCM ability to produce strong microwave with 25-40% efficiency level.

References

1. E.Garate, R.Cook, P.Heim, R.Layman, J.Walsh. J.Appl.Phys. 58, 627 (1985).
2. A.N.Didenko, A.R.Borisov, G.P.Fomenko, Yu.G.Shtein. Pis'ma Zh.Tekh.Fiz., 9, 60(1983). Sov.Tech.Phys.Lett., 9, 26(1983).
3. D.S.Lemons, L.E.Thode. Phys.Rev.Lett., 56, 2684 (1986).

CYCLOTRON AUTORESONANCE MASERS

V.L.Bratman
Institute of Applied Physics, Academy of Sciences of the USSR
Nizhny Novgorod, USSR

1.Introduction

The twenty-year-old history of high-current high-frequency relativistic electronics has embraced, including experimental implementation, quite a variety of devices. Most of them have subrelativistic predecessors, some being original ones, i.e., essentially relativistic or high-current devices. The available experience is not yet sufficient to exactly distribute all the devices over their echological niches and to distinguish the most promising versions. However, even today it seems very likely that only two representatives of relativistic microwave devices, namely, the FEL-ubitron and the cyclotron autoresonance maser (CARM) are in the position to master an important wavelength region ranging from the centimeter to the submillimeter waves at average (continuous) power, at the level significantly exceeding the potentialities of subrelativistic gyrotrons.

The FEL-ubitron and the CARM are varieties of free electron lasers (masers) and have much in common. At the same time, the needed particle energies are much smaller for the CARM than for the ubitron in the wavelength region of interest. As compared to the gyrotron, the CARM requires significantly lower magnetic fields. The CARM merits mentioned above have stimulated a growing interest in this device.

2.CARM and Gyrotron. The Doppler Frequency Gain

Like the gyrotron, the CARM [1-4] is a variety of cyclotron resonance masers, i.e. it is a device which employs the stimulated cyclotron emission of the beam of electrons moving

along the helical trajectories in a homogeneous magnetic field $\vec{H}_0 = H_0\vec{z}_0$ (Fig. 1a). The electrons in CARM interact with the electromagnetic wave $exp\ i(\omega t - kz)$ that is propagating nearly along their translational velocity, rather than transverse to it $(k_\parallel \ll \omega/c)$ like in the gyrotron (Fig. 1b). Consequently, in CARM, $k_\parallel \approx \omega/c$ and the phase velocity of the wave, $v_{ph} = \frac{\omega}{k_\parallel}$, is close to the velocity of light, c. So, for the relativistic translational velocities of the electrons, $v_\parallel \approx c$, under the condition of the cyclotron resonance of the electrons and the wave:

$$\omega - k_\parallel v_\parallel \approx \omega_H \qquad (1)$$

the Doppler frequency shift $k_\parallel v_\parallel$ plays an essential role. Therefore, the wave frequency in CARM, like in other FELs and FEMs, is much higher than the oscillation frequency of particles (the cyclotron frequency) $\omega_H = eH_0/mc\gamma$, where $\gamma = \mathcal{E}/mc^2$ is the dimensionless energy of particles. Indeed, from (1) follows the relation for the Doppler frequency gain $\Gamma = \omega/\omega_H$:

$$\Gamma = \frac{1}{1 - \beta_\parallel/\beta_{ph}} \approx \frac{2\gamma^2}{1+(\beta_\perp\gamma)^2+(1-\beta_{ph}^{-2})\gamma^2}, \qquad (2)$$

where $\beta_\parallel = v_\parallel/c$, $\beta_\perp = v_\perp/c$ and $\beta_{ph} = v_{ph}/c$. If the rotational velocity of particles, $v_\perp$, and the difference between the phase velocity of the wave and the velocity of light are not too great, such that

$$\beta_\perp \lesssim \gamma^{-1}, \qquad (3)$$

$$|1-\beta_{ph}^{-2}| \lesssim \gamma^{-2}, \qquad (4)$$

for the frequency gain we will have

$$\Gamma \sim \gamma^2 \gg 1 . \qquad (5)$$

In the gyrotron, where the Doppler shift $k_\parallel v_\parallel$ is negligibly small, the wave frequency is close to the cyclotron frequency, $\omega \approx \omega_H$. Thus, for the generation by the same relativistic electron beam, the wave frequency is γ^2 times higher in the CARM than in the gyrotron regime. (Note that in a subrelativistic gyrotron, $\omega \approx eH_0/mc$ and, in comparison to it, the frequency gain of CARM is not so great, it is on the order of γ.)

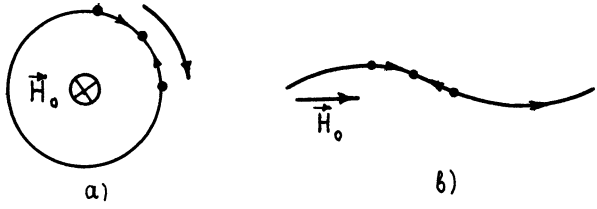

Fig.1 Simplest varieties of CARM (a) and gyrotron (b).

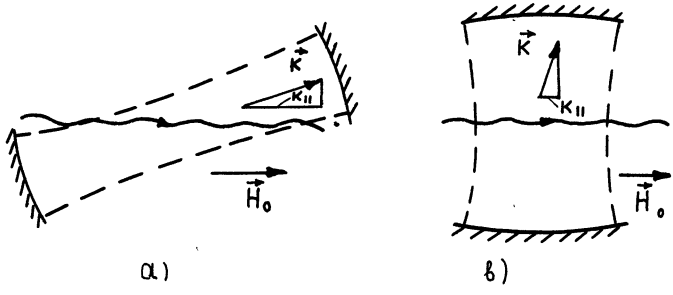

Fig.2 Azimuthal (a) and longitudinal (b) mechanisms of initial particle bunching.

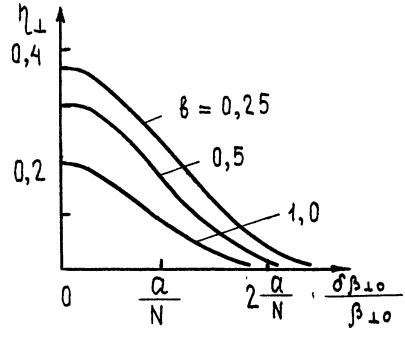

Fig.3 Dependence of CARM efficiency on rotational velocity spread (a= 1/4b).

It should be born in mind that very high phase and low group velocities of the wave are characteristic of gyrotron oscillations. Besides, due to the smallness of the Doppler shift, this regime has low sensitivity to the spread in the translational velocities of particles. Consequently, the self-excitation of low-frequency gyrotron oscillations is one of the most serious problems in the realization of different CARM versions (see Sect. 5).

3. The Mechanisms Responsible for Sustaining Resonance and for High Efficiency in CARM

The Doppler shift in CARM provides not only high frequency but also, in contrast to the relativistic gyrotron, long automatic sustaining of resonance between the electrons and the wave, when a substantial portion of energy can be withdrawn from the electrons. Actually, the resonance is broken and intense interaction ceases when the electron parameters $\Delta\omega_H$ and $\Delta v_\parallel$ change such that the transit angles of electrons relative to the wave $\theta=(\omega-k_\parallel v_\parallel-\omega_H)L/v_\parallel$ at the characteristic interaction length L change by approximately 2π . In the gyrotron, where the Doppler shift is small, the strong energy dependence of the cyclotron frequency causes small admissible variation of energy $\Delta\gamma/\gamma\sim N^{-1}$ at a great number of oscillations (cyclotron rotations) of the electrons $N \gg 1$. While in CARM, the electrons may resonate with the wave even with great variation of their energies, when $\Delta\gamma/\gamma\sim 1$, owing to the partial compensation of the change in the cyclotron frequency $\Delta\omega_H$ by the change in the Doppler shift $\Delta(k_\parallel v_\parallel)$.

It follows from the well-known integral [5,6]

$$\mathcal{E} - v_{ph}\, p_\parallel = const, \qquad (6)$$

which relates the energy and the translational momentum of the particle in the simplest case (a homogeneous magnetostatic field, constant amplitude and phase velocity of the wave), that the level of the compensation of the deviations from cyclotron resonance is determined by the magnitude of the phase velocity of the wave. The compensation is complete and the cyclotron resonance is sustained automatically (autoresonance [5,6]) when the phase velocity of the wave is equal to the velocity of light, $v_{ph}=c$. Exact autoresonance is not an optimal regime for generation [1,2], since two basic mechanisms of inertial particle bunching

compensate one another completely. These two mechanisms are the azimuthal bunching caused by the nonisochronous rotation of particles (Fig. 2a) and the longitudinal bunching that is stipulated by the difference in the variation of the translational momentum of the particles at different phases of the longitudinally inhomogeneous wave field (Fig. 2b) [7,8]. Under these conditions, stimulated radiation may dominate absorption, provided that rather delicate mechanisms are involved, which depend strongly on the field of nonsynchronous waves, high-frequency space charge and on other factors that are difficult to control [2].

The estimation of the efficiency from the condition under which the particle gets out of resonance does not answer the question on the needed initial rotational velocity of particles, $v_{\perp_0}$. Whereas under the conditions of normal Doppler effect (i.e. when the translational velocity of the particles is smaller than the phase velocity of the wave, $v_{\parallel_0} < v_{ph}$), the radiation occurs only until the rotational velocity turns to zero. Actually, the changes in the energy $\mathcal{E}$ and in the rotational momentum $p_\perp = m\gamma v_\perp$ of the particle are related (when $N \gg 1$) approximately as [2]

$$\Delta\mathcal{E} = c^2 \Delta(p_\perp^2)/2(1 - \beta_\parallel/\beta_{ph}), \qquad (7)$$

which follows from (6), (1) and the relativistic relation of energy to the particle momentum. According to (7), the particle energy decreases (transforms to the wave energy) only with a decrease of the rotational momentum. The maximal portion of the kinetic energy that can be withdrawn from one particle or from a perfect bunch of particles by diminishing the rotational momentum to zero (a single-particle efficiency) in a homogeneous magnetic field at constant amplitude and phase velocity of the wave, is equal to

$$\eta_{s.p.} = \frac{\beta_{\perp_0}^2}{2(1 - \beta_{\parallel_0}/\beta_{ph})(1-\gamma_0^{-1})} \qquad (8)$$

For a stationary electron beam, where before the interaction with the wave the electrons are distributed uniformly in phases relative to the wave, the total electron efficiency η depends also on the orbital efficiency $\eta_\perp$, that describes the efficiency of the particle bunching:

$$\eta = \eta_{s.p.}\eta_{\perp} \quad . \tag{9}$$

It is clear from (8) and (9) that high rotational velocities of particles, $\beta_{\perp_0}\sim 1$, are needed for high efficiency $\eta\sim 1$ in a relativistic gyrotron, which is attained, in principle, by decreasing N and by broadening the cyclotron resonance band. At the same time, high efficiency may be attained at relatively low rotational velocities $\beta_{\perp_0}\sim\gamma_0^{-1}$ in the CARM, where the energy transformed to radiation is withdrawn not only from the rotational but also from the translational motion (see (7)), when the phase velocity of the wave is sufficiently close to the light velocity and the condition (4) is met.

For the bunching to develop and for the orbital efficiency $\eta_{\perp}$ to be sufficiently high, the parameter of inertial bunching of particles

$$\mu = \pi\beta_{\perp_0}^2 \frac{1-\beta_{ph}^{-2}}{(1-\beta_{\parallel_0}/\beta_{ph})^2} N \ , \tag{10}$$

that is proportional to the interaction length, must be close to the optimal value. The corresponding optimal μ_{opt} and maximal $\eta_{\perp_{max}}$ values depend on the longitudinal field structure of the synchronous wave (generally, $\mu_{opt} \gtrsim 7$). The quantity $\eta_{\perp}$ depends resonantly on the initial cyclotron resonance mismatch, on the amplitude of the synchronous wave, and on the magnitude of the parameter

$$b = \frac{\beta_{\perp_0}^2}{2\,\beta_{\parallel_0}\beta_{ph}(1-\beta_{\parallel_0}/\beta_{ph})} \ , \tag{11}$$

which determines the intensity of radiation recoil. Depending on the magnitude of this parameter, the CRM varieties can be classified as a gyrotron ($b \to 0$) , a CARM (b=0.1-1) and a backward wave CRM, i.e. CRM-BWO, where $\beta_{ph} < 0$ ($b<0$).

4. Requirements to the Particle Velocity Spread. Methods for the Formation of Helical Electron Beams

Being responsible for the recoil, i.e. for the variation of the translational momentum of particles, the parameter b characterizes, naturally, the critical dependence of a definite CRM variant on velocity spread. CARM is not too critical to the

energy spread of particles $\delta\gamma_0$ because of the autoresonant mutual compensation of cyclotron frequency and Doppler shift. But, like other FELs and FEMs, it is highly critical to the spread in their translational and rotational velocities. Indeed, the spread is admissible until the difference between the transit angles of different electrons is smaller than π. Formulating this requirement as the restriction on rotational velocity spread, we obtain

$$\frac{\delta\beta_{\perp 0}}{\beta_{\perp 0}} \leq \frac{1}{4bN} \quad . \tag{12}$$

This estimate is confirmed by numerical computations (Fig.3).

The formation of a REB, that meets (12) when $\beta_{ph}\sim 1$, is a complicated problem. Two basic methods for the production of helical beams for CARM are being investigated now.

The first one consists in the use of magnetron-injection guns (MIG), that have been employed successfully in subrelativistic gyrotrons, in the region of relativistic energies. It should be born in mind that because of the roughness of emitter surface, inhomogeneous emission and other technical problems the rotational velocity spread of the beams is usually not lesser than 10 % in the gyrotron MIGs in the short-wave part of the millimeter wavelength region.

The second method [4,9-12] has been realized for the present in short-pulse devices that employ explosive emission, but it also seems to be promising for long-pulse (continuous) variants with thermal emitters. First a rectilinear beam is produced and then rotational velocity is imparted to particles in an undulator or a kicker. For thermal emitters quasi-Pierce optics can be used for the formation of a dense rectilinear beam. In this case, it is possible to provide a low electric field on the emitter and, consequently, to diminish the effect of microroughness and inhomogeneities, which sounds quite optimistic. But it is rather difficult to inject the beam into a strong magnetic field and do it neatly, without strong pulsations.

Having produced a dense rectilinear beam with a small velocity spread one must impart to the particles equal rotational velocities. Let us consider the peculiarities of this problem, taking as an example a simple kicker in the form of several

rectilinear currents perpendicular to the guiding magnetic field (Fig. 4). This system has a very broad tuning band for the guiding field. When the current I is not too high, one can use the approximation of a small perturbation of the particle motion by the kicker field as a reference. Within this approximation, the electron is a linear oscillator excited by the transverse component of the kicker field $H_{x,y}$ and the rotational velocity acquired by the electron is determined by the intensity of the resonant spatial harmonic of this field having the scale that is equal to the Larmor step $L_H = v_{\parallel 0} 2\pi / \omega_H$:

$$\beta_\perp = \frac{e}{mc^2\gamma} \left| \int_{-\infty}^{\infty} (H_x + iH_y) \exp\left(i \frac{\omega_H z}{v_\parallel}\right) dz \right| . \qquad (13)$$

Consequently, the rotational velocity depends strongly (exponentially with the scale $L_\perp = L_H/2\pi$) on the distance ρ between the particle trajectory and the current. Thus, for the kicker in the form of a rectilinear current we will have

$$\beta_\perp = \frac{2\pi e I}{mc^3\gamma} \exp\left(-\rho/l_\perp\right) . \qquad (14)$$

This abrupt dependence imposes very strong restrictions on the electron beam thickness and on the accuracy of its alignment, but it can be smoothed significantly if we employ a system of currents on both sides of the electron trajectory. For example, equal currents oriented in opposite directions that are located at a distance $\frac{1}{2} L_H$ from one another along the trajectory (Fig. 4b). In this case, owing to a greater homogeneity of the kicker transverse field, the spread in the rotational velocities acquired in such a kicker is determined by the quadratic dependence of the beam thickness

$$\left(\frac{\delta\beta_\perp}{\beta_\perp} \right)_{\Delta\rho} \approx \frac{1}{2} \left(\frac{\Delta\rho}{L_\perp} \right)^2 , \qquad (15)$$

that is much weaker than for a single current, where $\left(\frac{\delta\beta_\perp}{\beta_\perp} \right)_{\Delta\rho} \approx \left(\frac{\Delta\rho}{L_\perp} \right)$.

A similar idea of minimizing the velocity spread can be realized in a tubular electron beam using a kicker in the form of coils with current that are coaxial to the beam and are located at a distance multiple to $1/2\ L_H$ inside and outside the beam.

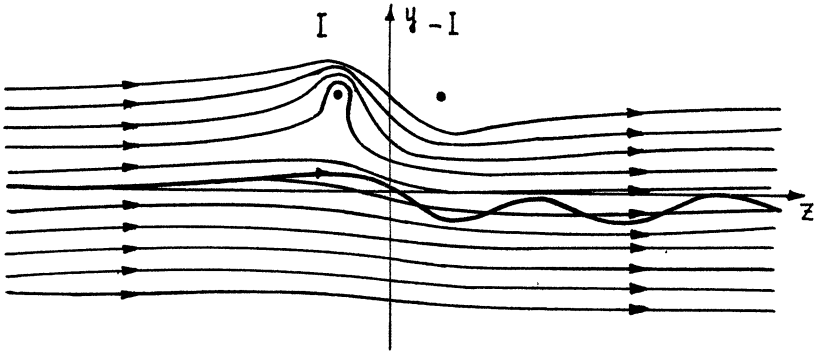

a)

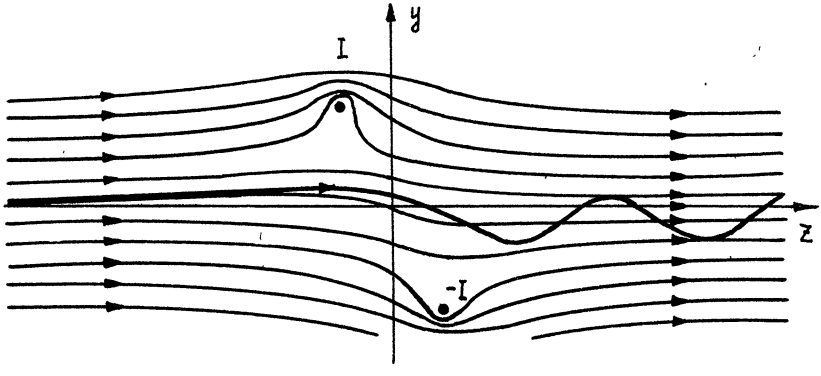

б)

Kickers with strong (a) and weak (b) sencitivity to the position spread of electrons and to the accurasy of beam alignment.

Taking into account that the electrons at the kicker input have different phases of cyclotron gyration and low rotational velocities which are characterized by the initial spread $(\delta\beta_\perp)_i$, we can determine the total spread as

$$\delta\beta_\perp \approx 2\,(\delta\beta_\perp)_i + (\delta\beta_\perp)_{\Delta\rho} \quad . \tag{16}$$

5. Discrimination of Parasitic Modes. Electrodynamic Systems of CARMs

Having solved the electron-optical problems and produced a helical electron beam with a low particle velocity spread, we pass over to the solution of another problem that is essential in the realization of an efficient CARM. We must provide the conditions under which the beam interacts with a definite wave with a given phase velocity $\beta_{ph}\sim 1$ and appropriate amplitude distribution at a definite interaction length. This task involves the suppression of the parasitic mode excitation. The gyrotron and backward waves are usually most difficult to suppress.

In principle, this problem can be solved [4,9,10,12] by using as an operating mode a lower mode of a regular waveguide in the regime of tangential dispersion characteristics of the wave and of the beam (Fig. 5, point a) or in a regime close to it. According to computations [12], such a situation may be realized even at the 0.5-mm wave at megawatt average power. This regime, however, imposes stringent requirements on the electron-optical system. It appears more natural to employ higher modes, although this will require, generally speaking, the development of effective methods for suppressing low-frequency generation.

When the electron energy is sufficiently high ($\mathcal{E}\gtrsim 1$ MeV), it is possible, in principle, to excite an autoresonance mode and to suppress low-frequency modes because of pronounced frequency difference between the modes and the phenomenon of the compensation of inertial (self-sustained) electron bunching by forced bunching that is well known in CRM. The correlation of these two types of bunching is controlled by the parameter of inertial bunching μ introduced above. When $\mu\gg 1$, the inertial bunching of particles prevails over the forced one (the stimulated radiation, consequently, prevails over the absorption), and when $\mu\ll 1$, the forced bunching is predominant

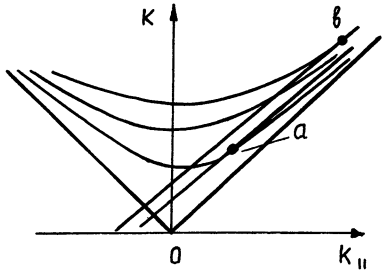

Fig.5 Brillouin diagram for a CARM with electrodynamic system in the form of a regular waveguide.

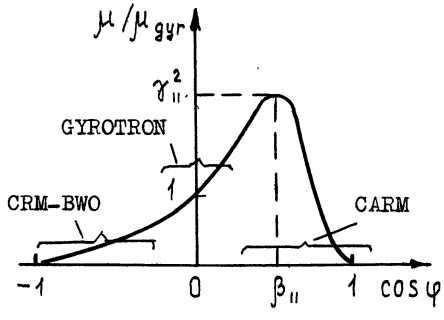

Fig.6 Dependence of the inertial bunching parameter μ on the phase velocity of the wave, $\beta_{ph} = 1/cos\varphi$. For high $\beta_{\parallel}$ there is a strong dispersion of cyclotron absorption.

(in this case, the wave is usually absorbed by the beam). When $\mu \sim 1$, the effects of the forced and inertial bunching almost compensate one another, which results in higher starting currents in generators and in low increments in amplifiers.

It is clear from (10) that for $\gamma_{\parallel}^2=(1-\beta_{\parallel}^2)^{-1}>>1$ it is possible that

$$\mu_{CARM} \gg \mu_{gyr} \sim 1 \qquad (17)$$

(see Fig.6). Consequently, we can obtain optimal conditions for the autoresonance regime and, at the same time, avoid the excitation of gyrotron and backward waves. Thus, owing to the dispersion of cyclotron absorption, theory predicts possible discrimination of gyrotron and backward oscillations, in spite of highly effective feedback inherent in them.

If the electron energy is not sufficiently high, the cyclotron absorption dispersion can be used effectively in an amplifier variant of a CARM in the form of a TWT employing a waveguide system with losses . Like in a conventional Cherenkov TWT, losses lead to the shortening of the effective interaction length and to enhanced starting currents for quasi-critical and backward waves. The presence of forced bunching, besides the inertial one, in CARM-TWT results in a more abrupt increase (even up to infinite values) of the starting currents of parasitic low-frequency oscillations (Fig.7).

Thus, computations show that low-frequency gyrotron and backward waves may be suppressed even in oversized electrodynamic systems.

In a number of cases it is not an easy task to discriminate the operating mode from the other autoresonance modes resonating with the beam. At a low level of average power and a moderate cross-section of the electrodynamic system, this problem can be solved using waveguide resonators with Bragg reflectors formed by corrugated waveguide sections (Fig. 8a). High average (continuous) power in the short-wave part of the wavelength region usually needs quasi-optical solutions, for example, a two-mirror resonator with a high azimuthal mode (Fig. 8b) or a highly selective two-mirror resonator with a waveguide section between the mirrors (Fig. 8c).

6. Experimental Investigations of CARMs. Plans and Prospects

Early experiments [3] demonstrated the short-wave properties

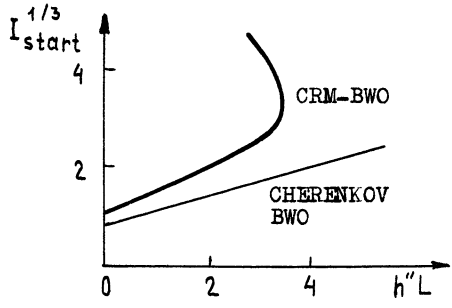

Fig.7 Dependence of normalised parameters of start current I_{start} for CARM and Cherenkov BWO on the parameter of "cold" losses $h"L$.

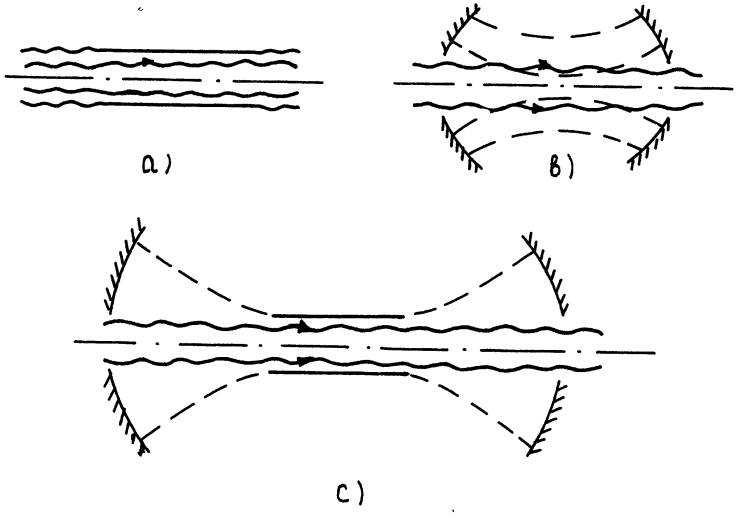

Fig.8 CARMs with Bragg (a) and quasi-optical (b,c) resonators.

of CARM. For relatively low energies of 350-600 keV and magnetic fields of 10-20 kOe, the chosen modes $H_{1,1}$, $H_{2,1}$ and $H_{4,1}$ of cylindric resonators with Bragg mirrors were excited selectively at the wavelengths ranging from 4.5 mm to 2.4 mm with the output power on the order of 10 MW. Experiments were performed on the high-current direct-action accelerator "Neptune-2". The beam current was 0.5-1 kA at a pulse duration of about 100 ns.

In those experiments, the phase velocity that was chosen to be very close to the velocity of light, β_{ph}=1.03-1.2, and small rotational velocity $\beta_{\perp 0}$=0.2-0.25 provided a rather high Doppler frequency conversion Γ=3-4 in spite of low electron energy. Small rotational velocity, as well as significant velocity spread $\delta\beta_{\perp 0} \gtrsim$ 0.1 resulted in low efficiency, η=2-4 %, of those experiments. The rotational velocity was imparted to the cylindrical-beam electrons which initially had rectilinear trajectories in a short undulator formed by a sequence of copper rings that were placed co-axially to the beam at a distance of the Larmor step from one another in the field of a pulsed solenoid. A rather high ratio $\mu_{CARM}/\mu_{gyr} \approx 3$ and a small value of the parameter of inertial bunching for the gyrotron, μ_{gyr}=1÷2, provided the conditions under which the parasitic gyrotron oscillations were not excited (the number of electron oscillations in the operating space was $N \approx 10$).

A high amplification coefficient in the absence of parasitic generation was obtained in the first CARM-TWT [9].The experiment was performed on the high-current accelerator "Sinus-6" employing an electron beam having the energy of 500 keV, current 0.5 kA and pulse duration 25 ns. The $H_{1,1}$-mode of a circular waveguide in the regime of tangential dispersion characteristics of the wave and the beam was used as an operating mode. The amplified external signal with the wavelength of 8.2 mm was injected into the operating waveguide by means of a directional coupler (Fig.9). The phase velocity of the wave amounted to β_{ph}=1.27 and the Doppler frequency up-conversion was Γ=2.5.

The rotational velocity was imparted to the electrons by the kicker formed by two short external coils that were axially symmetric to the beam and were fed from a separate pulse source; the currents in the two coils had opposite directions and the distance between the coil cores was half the Larmor step of the electrons. In the absence of the kicker field, when $\beta_{\perp 0}$=0 , the

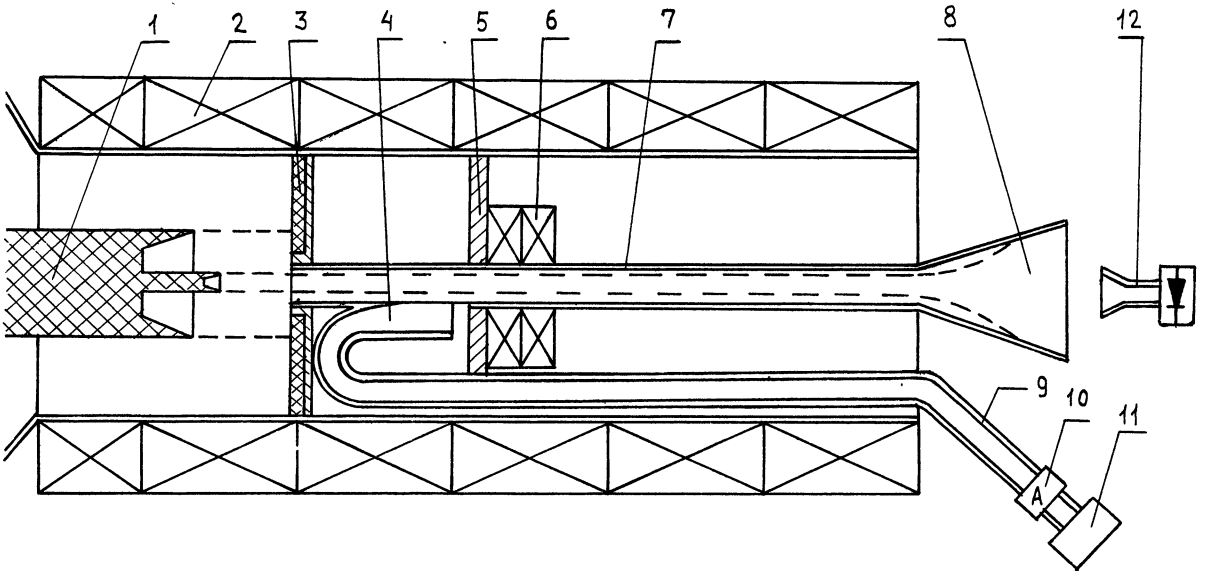

Fig.9 Scheme of CARM-TWT : 1-double cathode, 2-sectioned solenoid, 3-external beam collector, 4-microwave signal input, 5-vacuum flenge, 6-"undulator" coils, 7-operating waveguide, 8-vacuum window, 9-standard waveguide, 10-attenuator, 11-magnetron and 12-microwave power detector.

power of the input signal was attenuated (the effect of cyclotron absorption, see Fig.10) in the region of almost resonant longitudinal magnetic fields. The maximal value of the rotational velocity $\beta_{\perp}$=0.35 was limited by the conditions of the beam current path. With such a rotational velocity, the amplification amounted to 30 dB with the maximum output power 10 MW and efficiency 4 %. The power changed exponentially with the amplification rate 1.4 dB/cm, depending on the interaction length (Fig. 11).

Similar results were obtained in the investigation of the CARM-TWT in [10].

New experimental investigations of CARM-generators are now carried out on the accelerator "Sinus-6" (electron energy $\mathcal{E}$=0.5 MeV) in the Institute of Applied Physics of the USSR Academy of Sciences and on the LIA- unit ($\mathcal{E}$=1.2 MeV) in the Joint Institute of Nuclear Research. These investigations are aimed at producing the efficiencies that will be much higher than those obtained in early experiments. For this purpose refined kickers are used which will provide higher values of rotational particle velocities $\beta_{\perp 0} \approx \gamma_0^{-1}$ with lower spread and decrease the spread dependence by shortening the length of the interaction space (N ~ 6-7).

Preliminary experiments using the kickers described in Sect.4 yielded the electron beams with the spread in rotational velocities significantly smaller than 10 %. The calculated modes of Bragg resonators were excited with the output power of several tens of megawatts at the 8-mm and 4-mm wavelengths with efficiency about 10 %.

We have been studying and popularizing CARM for quite a long time. But only recently the interest in this device has increased drastically. This interest was encouraged by a growing demand for powerful sources in the shortwave part of the millimeter wavelength region for the investigations of controlled fusion. At present they need almost continuous power on the order of 30-80 MW at the wavelength 2-1 mm. When solving this fantastic problem researchers consider three types of microwave devices: conventional subrelativistic gyrotrons which are expected to provide the power of 0.5-1MW in one device and two FEM varieties, namely, ubitrons and CARMs with a desired level of output power an order higher, i.e. amounting to 5-10MW in a

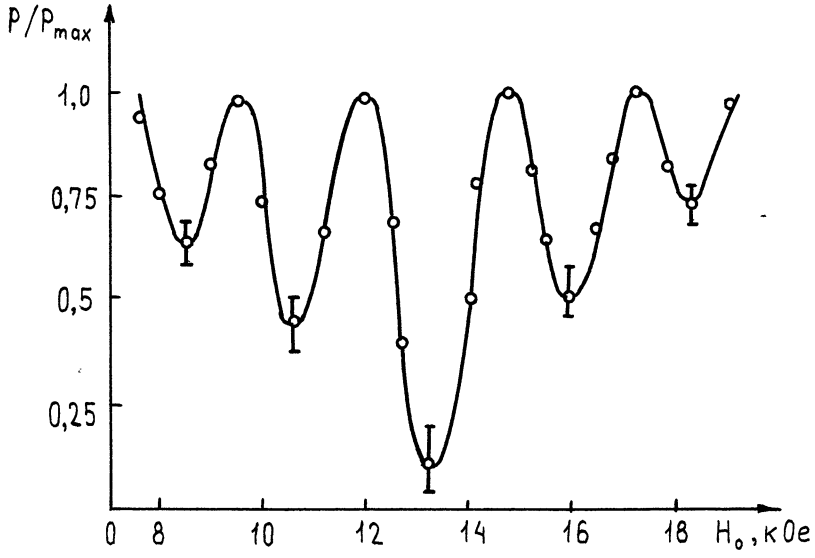

Fig.10 Cyclotron absorption of signal in CARM-TWT in the absence of the kicker field.

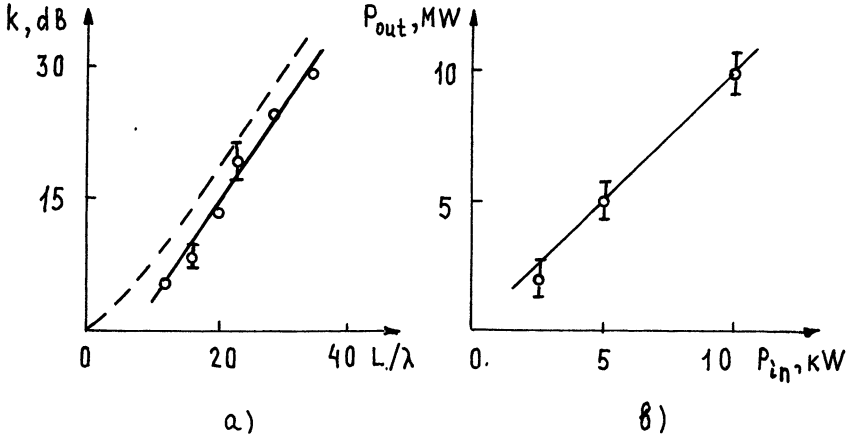

Fig.11 Results of CARM-TWT experiment: amplification versus length (a), output power versus input power (b).

single device.

It should be noted that today the ubitrons, as compared to CARMs, have advanced much further in power, efficiency, as well as in frequency. However, for the solution of the formulated problem the CARM variants need significantly lower electron energies, 0.3-1 MeV instead of 3-10 MeV in the ubitron. As to efficiency, theory predicts that it may be not lower than in the ubitron. Therefore, the CARM projects designated for high average (continuous) power in the shortwave part of the millimeter wavelength range that are developed in a number of US laboratories, as well as in the Institute of Applied Physics in the USSR,appear to be rivals to the ubitron projects.

REFERENCES

1. Petelin, M.I., Izv.VUZov, Radiofiz., 17, N6, 902 (1974).
2. Bratman, V.L., Ginzburg, N.S., Nusinovich, G.S., et.al., in: Relativistic HF Electronics, Ed.Gorky, USSR, Inst.Appl. Phys., 157 (1979).
3. Bratman, V.L., Ginzburg, N.S., Nusinovich, G.S., et al.- Int. J. Electronics, 51, N4, 541 (1981).
4. Bratman, V.L., Denisov, G.G., Ginzburg, N.S., Petelin, M.I.- IEEE J. of quantum electronics, QE-19, N3, 282 (1983).
5. Kolomenskij, A.A., and Lebedev, A.N., DAN SSSR, 145, 1259 (1962).
6. Davydovskij, V.Ya., ZhETF, 43, N3(9), 886 (1962).
7. Gaponov, A.V., ZhETF, 39, N2, 326 (1960).
8. Zheleznyakov, V.V., Izv. VUZov Radiofizika, 3, N1, 57 (1960).
9. Bratman, V.L., Gubanov, V.P., Denisov, G.G., et al., in: 6th All-Union Symposium on High-Current Electronics, Digest of Conf., Tomsk, pt.3, p.6 (1986).
10. Bekefi, G., DiRienzo, A., Leibovitch, C., and Danly B.G., Appl. Phys. Let., 54, N14, 1302 (1989).
11. McCowan R.B., Fliflet A.W., Gold S.H., et al. IEEE Trans. on Electron Devices, 36, N9, 1968 (1989).
12. Wang Q.S., Lin A.T., Luhmann N.S.,Jr. et.al.- in: 13th Int. Conf. on IR and MM Waves ,Conf. Digest, SPIE, 1039, Th44 (1988).

A Review of the Development of the Orbitron MASER*

Igor Alexeff, Mark Rader, and Fred Dyer

University of Tennessee
Knoxville, TN 37996-21001

Abstract

The Orbitron MASER is a device which can be used to produce millimeter and submillimeter radiation. Frequencies up to 1 THz have been observed. It can be operated ina pulsed mode or in a steady state mode, using a hot cathode.

Introduction

The Orbitron MASER is a negative mass unstable device, which can be used to produce millimeter and submillimeter RF radiation. In its basic design, the Orbitron is a coaxial structure with a high positive potential between the outer cathode and inner anode wire, as shown in figure 1a. Electrons are supplied to this system by either a pulsed internal glow discharge or by an oxide coated hot electron emitter. These electrons, due to an initial angular velocity, go into orbit around the positive central wire and emit a frequency that is inversely proportional to the radius of their orbits. Emission, from the pulsed form of this device, has been observed at a frequency of 1 THz.[1]

We have been studying the effects of making other changes to both the geometry of the device and the geometry of the electron emitter. One very interesting change has been the use of a hot oxide coated tantalum cavity, shown in figure 1b, to supply electrons to the device instead of the conventional oxide coated hot axial filament, shown in figure 1c. This change has allowed us to achieve much higher currents in the hot cathode version of this device.[2]

The plasma opening switch is a device which can be used to switch open high energy DC circuits where mechanical switches would arc on opening the circuit. The Orbitron MASER can be made into one of these devices by adding end plates to the basic Orbitron coaxial structure, as shown in figure 2. In the "on" condition, these plates are grounded to the cavity and so trap the electrons from a steady state glow discharge in orbit around the central wire. If one of these end plates is raised to a small positive potential, we have found that all of the electrons excape from the system, current

* Work Supported by the Air Force Office of scientific Reaserch under grant # AF-AFOSR-86-0100

flow between the cathode and anode stops, and the glow discharge extinguishes, thus opening the switch.[3]

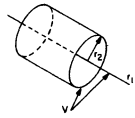

Figure 1a

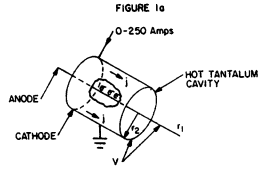

Figure 1b

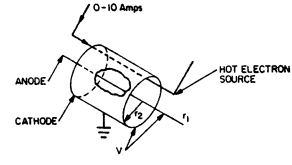

Figure 1c

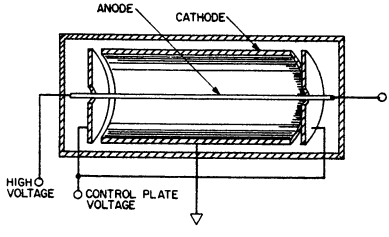

Figure 2

Theory of the Orbitron MASER

The Orbitron MASER is a coaxial device which produces radiation by a process kown as a negative mass instability. This instability occurs in rotating systems such as gyrotrons. It occurs when the dynamics of the radiation producing particles are such that as the particles lose energy and produce radiation the angular velocity of these particles increases. The Orbitron is this type of system.

In the Orbitron MASER, the electrons which drive the negative mass instability are born on the inner surface of the cavity. These electrons are born with a small amount of transverse energy, and acquire radial energy from the radial electric field. The electrons then go into orbit around the central anode, due to the original transverse energy. The outer cathode forms a microwave cavity resonator. This rotating ring of electrons couples to microwave cavity modes and generates RF radiation. When this occurs, the electrons lose energy and fall into a lower orbit. Due to the equations of motion, the electrons then gain angular velocity.

It is possible to derive the frequency of radiation for the Orbitron by a simple force balance for circular orbits around the central anode wire. If one looks at the centrifugal force on the electron while in orbit, this is

$$F_c = \frac{(m\, v^2)}{r} \qquad (1)$$

where F_c is the outward centrifugal force, m_e is the electron mass, r is the particle radius from the orbital center, and v is the electron velocity. The inward force caused by the logarithmic potential well can be expressed as a function of the applied potential, and is

$$F_e = \frac{eV}{r \ln \frac{r_2}{r_1}} \qquad (2)$$

where F_e is the force caused by the electric field, e is the electronic charge, V is the applied potential, r2 is the cathode radius, and r1 is the anode radius.

If we equate equation 1, equation 2, and divide both sides by m and r, we get,

$$\left(\frac{v}{r}\right)^2 = \frac{eV}{mr^2 \ln \frac{r_2}{r_1}} \qquad (3)$$

where the first term is the square of angular radian frequency Ω. We can solve equation 3 for this frequency. So that

$$\omega = \frac{1}{r}\sqrt{\frac{eV}{m \ln \frac{r_2}{r_1}}} \qquad (4)$$

This gives us that the frequency of rotation is inversely proportional to the radius and proportional to the square root of the voltage.[4-5] If one does the case of noncircular orbits[5] one finds the same equation, but it differs by a constant which is dependent on the degree of ellipticity. This is also the frequency of radiation.

If one wants an idea of the highest frequency possible out of the device, one merely has to calculate the frequency of a particle in a grazing orbit around the central anode. So if one wants high frequency, the anode wire must have a very small radius. We have used tungsten wires in our pulsed Orbitron MASER with a diameter of.0075 millimeters or larger. These very fine wires have enabled us to have routine operation at emitted wavelengths of .5 millimeters and we have recorded emissions at .3 millimeters or 1 THz[1].

The Orbitron MASER has two basic advantages over the gyrotron. These advantages being that the gyrotron requires both a strong axial magnetic field and a relativistic electron beam to operate. The relativistic electron beam is required to achieve a negative mass unstable state, which is a natural consequence of the Orbitron geometry.

Hot Cathode Operation of the Orbitron MASER

One of the two variations of the Orbitron MASER, is the Steady State Orbitron. It has a new cathode design in order to increase the current, on a short time basis, to the central anode. This increase in current is to increase the power output and frequency of the device. One of the more interesting variations has been to make the entire outer cathode a hot electron emitter. This device is shown in figure 1b.

We tested the device in a long pulse high current, 2 or 3 amps, mode of operation. The reason for this long pulse mode of operation was to minimize anode heating. During these long pulses, we were able to achieve frequency emissions from this device at frequencies up to approximately 10 GHz. The anode wire diameter, for this test, was .125 millimeters, and the outer cathode diameter was 31.25 millimeters.

Opening Plasma Switching

The Orbitron MASER has other uses than that of a microwave oscillator. It can be used, with minor modifications, as a fast opening plasma switch. This is accomplished by the addition of two end plates to improve end electron confinement.

When the switch is "closed", both end plates are at the cathode potential. This traps electrons, caused by cosmic radiation, in orbit between the cathode and positive anode. These trapped electrons ionize residual gas in the system and create a steady state glow discharge, thus creating a path for current flow between cathode and anode.

The switch is "opened" when one of the plates is switched from the cathode to the anode potential. This spoils the end confinement and causes the electrons to flow axially out of the device. If the pressure is low enough, the ionization process then stops, the glow discharge goes out, and current flow stops. This is demonstrated in figure 3.[3]f

During a test of this device, we pulsed the switch to a moderate current level, as shown at the first of figure 3. Then during the middle of this current pulse, we interrupted the current flow by switching one of the plates to the anode potential. This gave a switching time on the order of 5 microseconds. The undershoot is an artifact of the sensing circuit.[6]

In order to get a better idea of the voltage required to switch the device from the closed state to the open state, we also tried imposing different potentials to the end plates to see what percentage of the anode potential was required to switch the device. This was accomplished by using a separate low voltage supply attached to the switching plates. We found that this switching voltage is a function of both the applied potential across the switch and the background gas pressure, as shown in figure 4, but under all test conditions the required voltrage was less than 15% of the applied anode potential.[7]

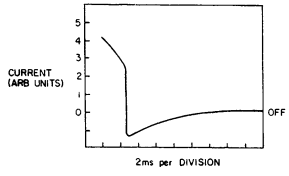

Figure 3

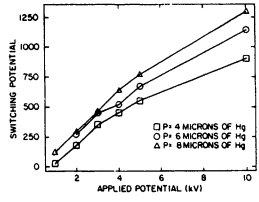

Figure 4

Conclusion

The Orbitron MASER is a device which can be used to produce millimeter and submillimeter radiation. We have used this device to produce radiation up to a frequency of 1 THz. This device utilizes nonrelativistic electrons trapped in orbit around a positively charged central wire to produce this radiation. These electrons can be supplied by either a pulsed glow discharge or a hot oxide coated filament. If properly configured this device can also be used as a fast opening plasma switch.

References

[1]. Igor Alexeff, Fred.Dyer, and Wlodek Nakonieczny, International Journal of Infrared and Millimeter Waves. Pg. 481, 6, (7) 1985 (Plenum).
Igor Alexeff, Phys. Fluids, vol. 28, Pg. 1990, June 1985.

[2]. Mark Rader, Fred Dyer, and Igor Alexeff, IEEE Transactions on Plasma Science. PS-15, 1, Pgs. 56 - 59, 1986.

[3]. Igor Alexeff and Fred Dyer, IEEE Transactions on Plasma Science, PS-8, 3, Pg. 163, 1980.
Patent # 4,291,255

[4]. Igor Alexeff and Fred Dyer, Phys. Rev. Lett., vol. 45, p. 351, 1980
Patent #4,459,511

[5]. J. M. Burke, W. M. Manheimer, and E. Ott, Phys. Rev. Lett., vol. 56, p. 2656, June 16, 1986.
Saeyoung Ahn, Achintya K. Ganguly, and Henery P. Freund, Conference Proceedings 1987 IEEE International Conference on Plasma Science, Publication #87CH2451-3, Pg. 8 (also in Phys. Rev. 36, 2199 (1987))

[6]. Frederick S. Hines, Development and Testing of a "Plasma Switch", (unpublished)

[7]. Dwight J. Roberts. Control of the Plasam Fast Switch at Low Pressure, (unpublished)

HIGH POWER MICROWAVE GENERATION MECHANISM IN VIRTUAL CATHODE SYSTEM WITH ANODE PLASMA

A.N.Didenko , V.I.Rashchikov
Moscow Engineering Physics Institute
Moscow ,115409 ,USSR

Pulsed high-power microwave generation by means of high current accelerator system has recently become an intensive area of research , the most promising among them being virtual cathode devices or vircators [1].

There are two mechanisms which lead to production of high-power microwaves in vircators [2]. The first deals with electrons , oscillating near the anode and the second with virtual cathode (VC) oscillating as a whole. Generally both mechanisms are presented, but in a given device one may dominate the other. If the anode is thick enough to absorb reflected electrons thus preventing them from reentering the diode region, the first mechanism vanished. In this paper we discuss the second mechanism, which is realized, for example, in reditron [3]. Anode plasma produced by high-current electron beam passing through the anode is taken into account.

The simulations were done with 2.5-dimensional fully electromagnetic and relativistic particle-in-cell code. The hollow electron beam with constant density is continuously injected into the cavity through the hole in its left side (anode of reditron). An external axial static magnetic field is imposed in all of our computer simulations. If the beam current is smaller than space-charge limiting current the VC (nought of axial electric field - E and particle density maximum - ρ) is located in the center of the cavity and no reflection of electrons occurs. When the beam current is larger than space-charge limiting current, the location of VC changes: VC moves toward anode and this distance depending upon the geometry of the cavity, external magnetic field magnitude and beam parameters. In addition to that reflected electron current appears in the cavity, its value being less than output beam current.

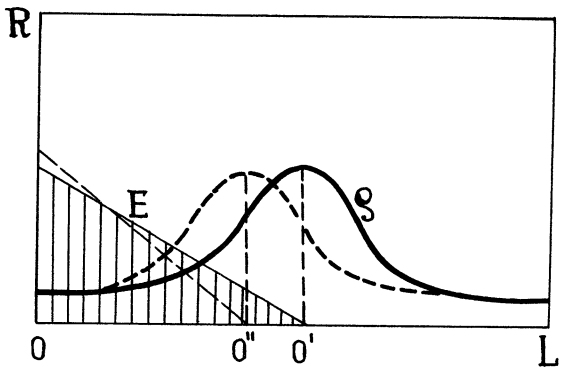

Fig. 1

The mechanism of such movement can be explained by the fact, that current rise leads to increasing of potential barrier (dashed area in Fig.1), produced by cavity space charge distribution. When the kinetic energy of the particle is less than potential barrier $W < \int_{o}^{o'} E\,dl$, the particle is reflected from the VC and moves toward the anode. It means that VC as a whole moves toward the anode until the value of potential barrier becomes less than kinetic energy of injected particle $W > \int_{o}^{o''} E\,dl$. From this moment VC turns around and moves in opposite direction, oscillating around new equilibrium point. The amplitude of oscillation rise with current.

The picture varies when the beam current becomes essentially higher than space-charge limiting current. Computer simulation shows (Fig.2) that in this case VC also moves toward the anode, but the number of particles passing through the potential barrier becomes less than that of reflected ones. It leads to VC density rise up to the moment when VC practically reaches the anode, electrons strike it and get absorbed. The VC particle density and value of potential barrier fall down sharply and injected particles pass through it easily thus resulting in VC (particle density maximum and nought of axial electric field) moving toward the center of the cavity until the potential barrier will rise enough to stop the particles. After that the process is repeated, producing VC oscillations and strong modulation of transmitted electron current (Fig.3). This mechanism

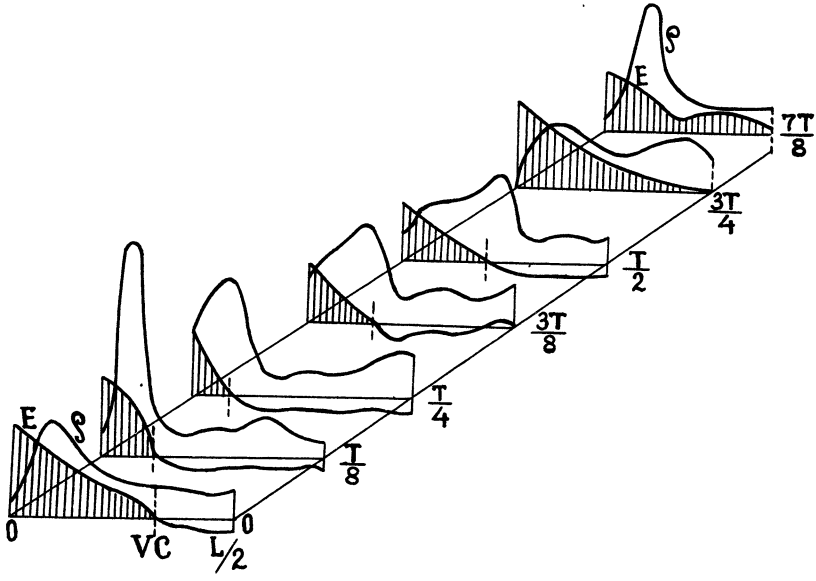

Fig. 2

can be used for strong modulation of high-current electron beams.

Simulation shows that radiation frequency generated by electron beam is in good relation with transmitted beam frequency modulation.

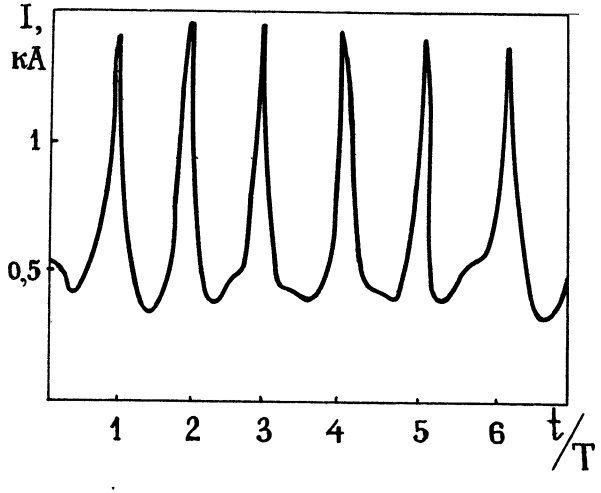

Fig. 3

In one-dimensional model VC oscillation frequency is given by [4] :

$$F = 10.2\sqrt{J/\beta\gamma} \cong 2.5\, f_p , \qquad (1)$$

where f-frequency in GHz , J-current density in kA/cm^2, f_p-plasma frequency. Computer simulation gives the value of frequency less then that in (1) , which can be explained by the fact that in reality transverse movement isn't frozen; this makes VC particle density value less than that of one dimensional model.

When high current electron beam passes through the anode , plasma is formed in anode region. Anode plasma density can considerably change during the beam pulse depending on beam and system parameters . We have studied the influence of anode plasma density on VC formation mechanism. When plasma density approximately equals injected beam density vircator's main characteristics (value of frequency and power generated) are practically unchanged. If plasma density is in order of magnitude higher than beam current , VC oscillation amplitude and microwave radiation frequency decrease. Since anode plasma density changes during the beam pulse, it can lead to differential changes of microwave radiation frequency and power.

Let us evaluate beam generated power in vircator. According to [5] microwave radiation power of oscillating electron is given by

$$P = \frac{1}{12}\frac{e^2c}{a^2}\left[\frac{E}{m\,c^2}\right]^3 f(y) , \qquad (2)$$

where $f(y)$-normalized spectral function, a-amplitude of oscillation, E-total energy. In relativistic case power, generated by the electrons, oscillating around the anode or VC oscillating as a whole can be calculated from

$$P = \frac{1}{12}\frac{e^2c}{a^2}\left[\frac{E}{m\,c^2}\right]^3 N^2 f(N) ,$$

where N-number of oscillating electrons, $f(N)$-coherent parameter. Defining current as $I=-\frac{eNc}{a}$ for cavity with finite Q-factor we obtain:

$$P \cong 2.10^{-3}\gamma^3 Q\ I^2 f(N),$$

where P-power generated in GW, γ-relativistic factor, I-current in kA. For typical vircator with parameters $I\sim 10$kA and $\gamma\sim 2$ we have in case $f(N)=1$

$$P \cong 1.6\ Q\ ,\text{GW}\ .$$

Thus we obtain output power of GW level the electron beam current being $I\sim 10$kA and $Q\sim 1$ and $P\sim 10$GW if $I\sim 100$kA or $Q\sim 10$.

Radiation spectral analysis from eq.(2) showed, that besides the main harmonic, whose frequency equals electron oscillating frequenoy near the anode or $f\sim f_p$, higher number harmonics do appear in spectrum. Their radiation power decreasing with their number increase, the radiation is concentrated in two cones with small angular spread.

Experiments of Phys. Int.Comp. have confirmed such character of angular distribution of the relativistic vircator radiation [6]

Hence we can make the conclusion that vircator is a source of powerful microwave oscillation not only of cm bu also mm and sub-mm ranges.

References

1. Didenko A.N.,Krasik Ya.E.,Perelygin S.F.,Fomenko G.P. - Pis'ma Zh. Tekn. Fiz. 5,1510(1976).
2. Burkhart S.C.,Scarpetti R.D.,Lundberg R.L. -J.Appl.Phys. 58,N1, 28,(1985).
3. Kwan T.J.T.,Davis H.A.,Fulton R.D.,Sherwood E.G.- Proceeding of the 7 International Conference on High Power Particle Beams, Karlsruhe, Germany,447(1988).
4. Sullivan D.J.,Walsh J.E.,Coutsias E.A.- High Power Microwave Sources.Edited by Granatstein and Alexeff.Artech House, Massachusetts, 484(1987)
5. Didenko A.N. DAN USSR 312,N1(1990)
6. Sze H.,Benford J.,Young T.,Bromley D.,Harteneck B. - IEEE Trans. on Plasma Science.PS-13,492(1985).

AN EXCITATION OF TRANSVERSE ELECTRIC (TE) MODES IN MAGNETIZED VIRCATOR SYSTEM

K. G. Kostov, N. A. Nikolov, I. P. Spassovsky, J. N. Velichkov and V. A. Spassov
Faculty of Physics, Sofia University
5 Boul. "A. Ivanov" Sofia, 1126, Bulgaria

Abstract. This paper reports the experimental study of the axially extracted virtual-cathode device. The whole device is placed in an uniform guide magnetic field. An electron beam is formed in a foil diode and then it is injected into a cylindrical drift channel with larger radius. The electron density exceeds the space-charge limit for the beam in the large waveguide and a virtual cathode is formed. A microwave generation is observed in range of magnetic field magnitude 0.3 - 0.6 T. The frequency of microwave radiation depends on guide magnetic field and is between 9.5 and 15 GHz. We have observed some nonsymmetrical transverse electric (TE) modes, which are not the typical ones for axially extracted vircator system. The measured peak power is about 5 MW, which corresponds to 1 percent efficiency. The microwave power is emitted by transmitted electron flow, which had been already pumped by transverse virtual-cathode oscillation. The typical longitudinal virtual-cathode oscillations also exist, but they do not excite, because their typical frequency is below the first TM mode critical frequency for this tube.

Introduction. During the last several years it has been growing interest in microwave sources based on virtual cathode oscillations (vircators, reflectiv triodes, reditrons and other). The high-interest has due to simple construction on these devices and possibility the virtual cathode oscillators (VCOs) to be tuning without changes in hardware. Particularly, microwave powers up to gigawatt levels in the centimeter wavelength regime have been generated by VCO systems On the other hand VCO is a large bandwidth source and it also has a very low efficiency (about 1 -

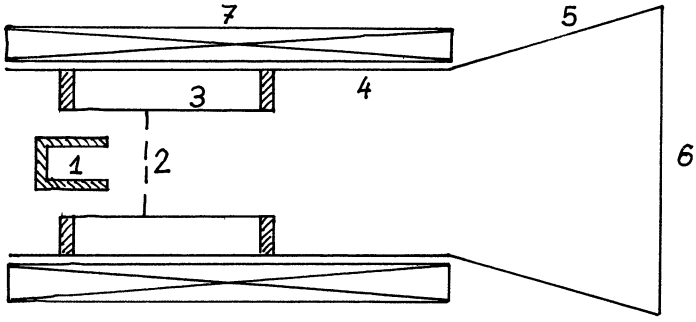

1 – carbon cathode
2 – anode
3 – narrow drift tube
4 – wide drift tube
5 – conical horn
6 – output window
7 – solenoid

Fig. 1

2 %).

There are two basic types of virtual cathode devices based on method of microwave extraction: an axial (along the electron beam direction) and a radial (in direction perpendicular to the beam).

This paper investigates VCO system with axial extraction of emitted microwave power. The influence of external guiding magnetic field on the generation is studied.

Experimental setup. The experiment was performed on the Blumlein electron beam accelerator "PERUN-2". The output impulse from double forming line was of the order 400 kV and 25 ns duration. The particular experimental arrangement is shown on Fig. 1. Electrons were emitted by plasma emission from hollow graphite cathode in a foil diode. The drift channel was consisted from two waveguides with different diameters. An impulse external magnetic field with amplitude up to 2.5 T and duration of 4.2 ms is used for electron beam transportation. The space charge limited current for narrow drift tube was overlimited for other tube and therefore a virtual cathode would be formed in wide waveguide entrance. A cathode size and diode impedance (cathode-anode distance) were varied in the experiment. We extracted the generating radiation by 5^{o} slope conical horn ended with Teflon window. There were not creating especial conditions for additional feedback.

Results. A transparent current as a function of magnetic field was measured (see Fig. 2) with help on collector placed in two drift channel ends . The difference between two curves shows a presence of reflected electron flow i.e. the virtual cathode existing. The current dependence in wide drift tube of distance between tube entrance and collector place is shown on Fig. 3. We can determine only approximately a virtual cathode position (about 2-3 cm from entrance).

The virtual cathode oscillation can excite some waveguide modes on the system (typically TM^{o}_{mn} modes for axial extraction). A microwave generation was observed in magnetic field region of (0.3-0.6)T . The microwave radiation frequency was found to be between 9.5 GHz and 15 GHz. The frequency increased with the magnetic field growing. The microwave radiation mode was also changing with magnetic field. A clear mode structure could be observed only at fixed magnetic field amplitude. A gas-breakdown

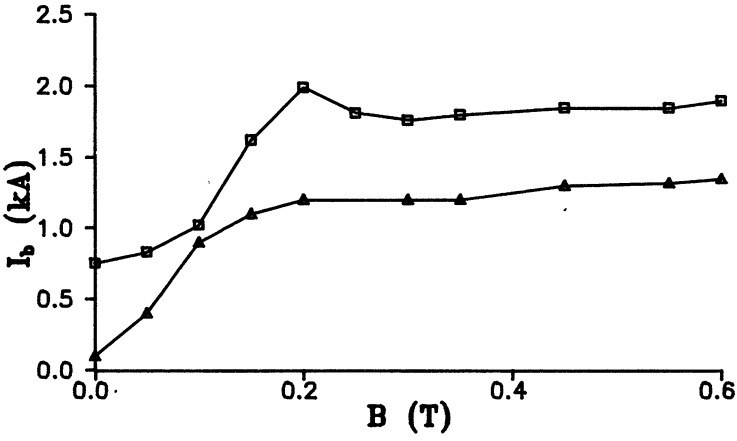

Fig. 2 Beam current as a function of guiding magnetic field. Upper curve is a beam current in narrow tube and lower one is a beam current in wide tube.

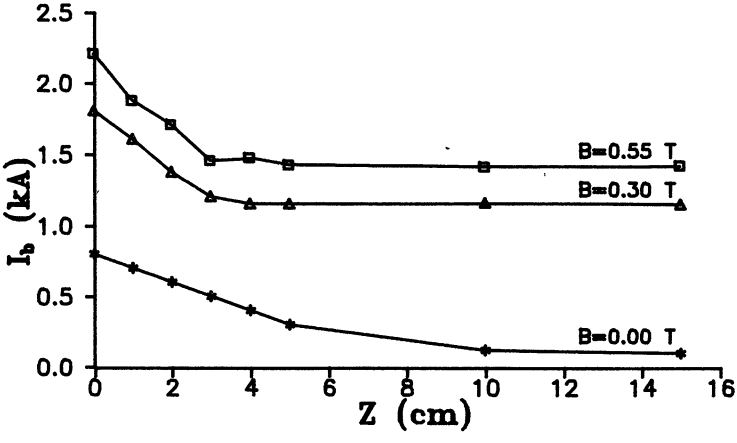

Fig. 3 Beam current as a function of distance between narrow tube end and collector for constant magnetic field.

diagnostic [1] was used for radiation mode definition. On Fig. 4 were given photographs of the induced gas-breakdown for two values of magnetic field.

Radiated frequency was measured by cutoff section and a waveguide filter was also used for 7.5-12.5 GHz region. The microwave spectrum at constant magnetic field was wide. Maximal emitted power was measured at 11.2+0.6 GHz for magnetic field of B=0.36T as well as for B=0.5T in the interval (12.6:14.6) GHz. These frequencies were close to critical waveguide frequencies for TE^{o}_{51} (f=10.98 GHz) and TE^{o}_{32} (f=13.67 GHz) modes respectively. A radial distribution and polarization measurement were done for additional mode confirmation.

Microwave power measurements were done using a calibrated semiconductor detector. An open end of waveguide is used as a receiving antenna. Maximal detecting power was 5 MW, which corresponded to about 1 percent efficiency.

Conclusion. The observed TE^{o}_{mn} modes are not typical for VCOs with axial extraction. The absence of typical TM^{o}_{mn} modes can be explain by two reasons: first the presence of external magnetic field suppresses the microwave generation [2] and second the experimental geometry dimensions are chosen in a such way, that real-virtual cathode distance is large (more than 5 cm). Thus the electrons oscillate in minimum potential with a character frequency which is low enough not to excite the output waveguide.

In the experiment the microwave radiation was generated by the passed electron flow which had been preliminary pumped in virtual cathode region. The beam profile at different distances from the wide tube entrance was determined by beam traces on thermal sensitive materials (Fig. 5). They showed a beam size expansion in the region behind virtual cathode. This finding, we interpreted as due to increasing of electron transverse velocity.

We suppose that the radiation mechanism is of cyclotron generation type with a virtual cathode as pumping element.

More detail analysis and additional experimental investigation will be subject of an other work.

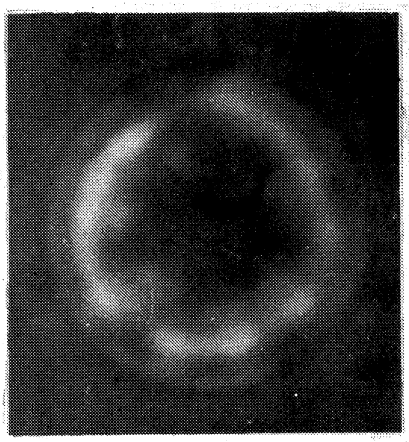

Mode structure at B=0.36 T
(probably mode TE°_{51})

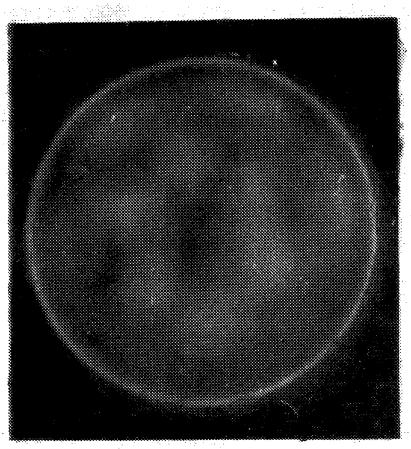

Mode structure at B=0.5 T
(probably mode TE°_{32})

Fig. 4

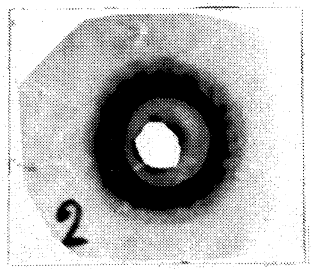

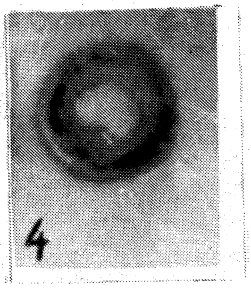

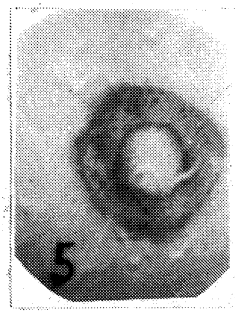

L=0 cm

L=10 cm

L=20 cm

L is distance to tube entrance

Fig. 5

R E F E R E N C E S

1. S.H. Gold et al. IEEE tr. on Plasma science, vol. PS-13 p. 374 (1985).

2. R.D. Scarpetti et al. IEEE tr. on Plasma science, vol PS-13, p. 506 (1985).

INTENSE MICROWAVE GENERATION USING FREE-ELECTRON LASERS*

T. J. Orzechowski
Lawrence Livermore National Laboratory
P. O. Box 808
Livermore, CA. 94550, U. S. A.

I. INTRODUCTION

Free-electron lasers (FELs) have demonstrated their ability to generate coherent radiation over a large region of the electromagnetic spectrum ranging from the microwave regime down to the visible regime [1]. In this device, the relativistic electron beam is coupled to the radiation using a periodic, transverse magnetic field called an undulator or wiggler. The coherence of the radiation results from the bunching of the electron beam by a ponderomotive well generated by the wiggler field and the electromagnetic radiation [2]. The wavelength of the emitted radiation is determined by a Lorentz contraction followed by a Doppler shift of the wiggler period. This wavelength scaling is given in by

$$\lambda_s = \frac{\lambda_w}{2\gamma 2} = \frac{\lambda_w}{2\gamma_0^2}\left[1 + \frac{1}{2}\left(\frac{eB_w\lambda_w}{2\pi mc}\right)^2\right] \tag{1}$$

Here, γ_0 is the energy of the electron in units of the electron rest mass ($\gamma_0 = 1 + eV/mc^2$), λ_w is the wiggler period, and B_w is the peak wiggler magnetic field. This expression describes the wavelength scaling for a device using a plane polarized wiggler field. The FEL is shown schematically in Fig. 1. The electron beam passes through the wiggler where its transverse motion couples to the transverse electric field of the electromagnetic wave. If the proper resonance condition is maintained, the electrons lose energy to the radiation. This process continues until the electrons have lost sufficient energy that the resonance condition is no longer satisfied.

FELs can be configured either as oscillators or amplifiers. An oscillator is formed by installing mirrors on either end of the wiggler magnet. The radiation builds up in the cavity while a small amount is extracted. In such a device, the pulse length of the

* Performed jointly under the auspices of the U.S. Department of Energy by Lawrence Livermore National Laboratory under Contract No.W-7405-ENG-48 and for the Department of Defense under Contract No. SDIO/SDC MIPR No. W31RPD-0-D4074.

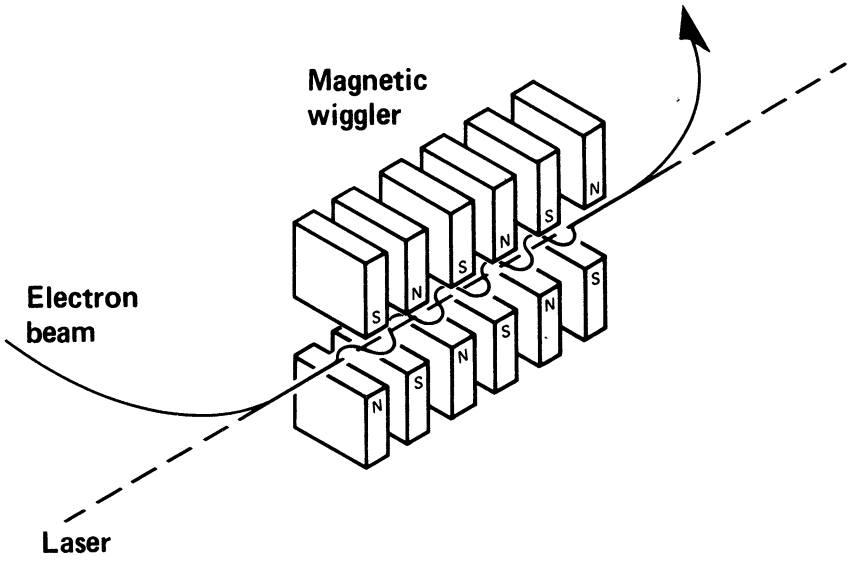

Figure 1. Schematic of a single pass free-electron laser amplifier.

electron beam must be of sufficient duration for the fields in the cavity to saturate. Alternatively, the FEL can be configured as an amplifier in which a "seed" signal is introduced into the interaction region and grows exponentially to saturation. This seed signal can either be introduced from an external source or it can arise from the noise on the electron beam.

Perhaps the most critical part of the FEL is the electron beam. The quality of the beam is measured by its instantaneous energy spread and its emittance, which characterizes its area in transverse phase space. This parameter is a measure of the electron beam's transverse random motion. If the emittance or energy spread is too large, then the random motion of the electrons dominates the coherent transverse motion and the gain is reduced. Space charge of the electron beam can also become an important factor to the performance of the FEL. As the electron beam bunches in the ponderomotive well, the space charge forces tend to debunch the electrons, again reducing the gain of the system. If the electron beam density is sufficiently high, then plasma waves on the electron beam must be taken into consideration [3]. In this case, the FEL is characterized by Raman scattering and the FEL is said to be operating in the Raman regime. For the type of FEL described in this paper, the interaction can be described by studying the single particle equations of motion. Here, the FEL can be characterized by Compton scattering and the device is said to be operating in the high gain Compton regime.

The wiggler for the FEL can be either plane polarized, as depicted in Fig. 1, or helically polarized. This latter device is fabricated by winding a conductor in a helical pattern. This helical wiggler has the advantage of focusing the electron beam in both transverse dimensions while the plane polarized wiggler focuses the electron beam only in the direction of the wiggler field. One advantage of the plane polarized wiggler is the relative ease with which the wiggler field can be varied along the length of the wiggler. This ability, called tapering, is an important part of the single pass amplifier.

In this paper, I will describe a free-electron laser amplifier which operated in the microwave regime. This device, called the Electron Laser Facility (ELF), used an electron beam generated by a Linear Induction Accelerator (LIA). ELF operated as a single pass amplifier at 35 and 140 GHz. Because the device had no cavity, we could study the FEL physics independent of cavity considerations (i.e., longitudinal mode competition and cavity filltime). With a sufficiently large input signal, growth of the signal from noise on the beam did not influence the performance. This device demonstrated significant gain and allowed us to investigate such FEL phenomenon as saturation and synchrotron oscillation of the electrons trapped in the ponderomotive well. We were also able to study the phase shift of the radiation due to the real part of complex gain of the FEL. Because the interaction takes place in a waveguide, the FEL can couple to several spatial modes at a given frequency. The bunched electrons can radiate at harmonics of the fundamental and in this experiment we studied the evolution of the third harmonic. In Part II of this paper, I will describe the Electron Laser Facility. I will discuss the FEL performance with regard to gain, saturation, phase evolution, mode coupling and harmonic generation. In Part III, I will briefly discuss a switching technique which allows the LIA to run at high average power. When driven by such a device, an FEL can produce high average power radiation. We will present the design for such a device which can be used to heat a Tokamak plasma. This device is designed to operate at 250 GHz and produce an average power of 2 MW [4].

II. The Electron Laser Facility

ELF was a single pass FEL amplifier operating in the microwave regime [5]. This facility was operational from 1982 to 1987. This device was decommissioned to provide for the construction of a new, high repetition rate LIA. ELF used a 3.5 MeV electron beam generated by the Experimental Test Accelerator (ETA) [6]. While the accelerator was capable of producing a 10-kA peak current with a 30-ns duration once per second, we typically accelerated 3kA. Of this, ELF used only a fraction of this current (800 to 1200 A) and operated at 1/2 Hz. ELF is shown schematically in Fig. 2. The 3 kA electron beam passed through an emittance filter which comprised a 2.5-cm diameter, 2-m long pipe immersed in an axial magnetic field. The acceptance of this device could be varied by changing the magnitude of the axial magnetic field. Only electrons whose emittance was less than or equal to the acceptance of this device passed through the

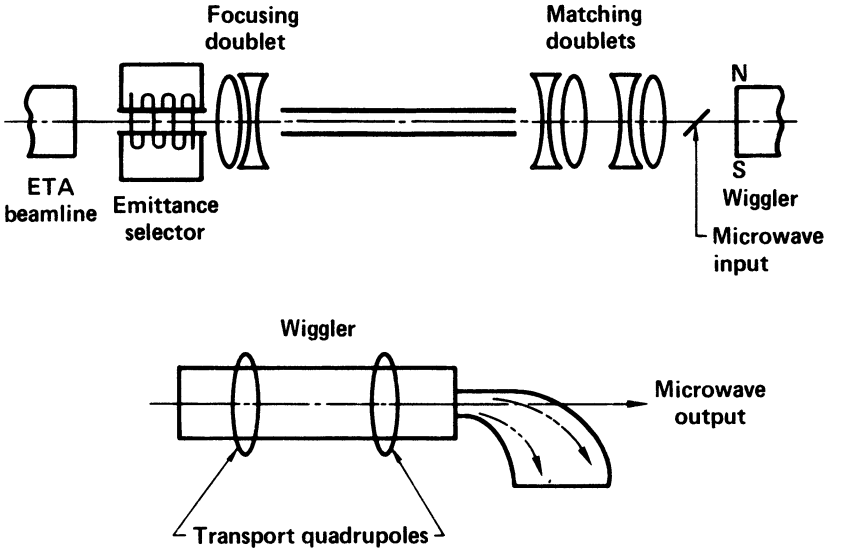

Figure 2. Schematic of the Electron Laser Facility.

filter. We typically discarded 2/3 of the electron beam in this device. This was important for two reasons. First, as mentioned above, electrons whose emittance is too large do not contribute to the gain and, in some circumstances can actually reduce the gain of the device. Second, since we know the maximum emittance of the transmitted beam (and since we passed only a small fraction of the original beam, we could assume a fairly uniform distribution in phase space of the transmitted beam) we can accurately model the FEL. After the emittance filter, three quadrupole doublets were used to transport and match the electron beam into the wiggler. Because the transport from the end of the accelerator to the entrance of the wiggler was fairly chromatic (±1% energy acceptance), the electron beam pulse length was reduced from 30 ns to 15 or 20 ns. The wiggler magnets comprised two rows of rectangular, air core solenoids: one row above and one below the interaction region. The wiggler was 3-m long for the 35-GHz experiments and was extended to 4 m for the 140-GHz experiment. The wiggler period was 10 cm and the solenoids were 16-cm wide. The two rows of solenoids were separated by 3 cm to allow for the waveguide which served as the beam transport line through the wiggler. The wiggler magnet was pulsed with a rise time of about 600 μs. The wiggler field was essentially flat for the 30 ns duration of the electron beam. Heating of the wiggler magnet itself limited the pulse repetition frequency to one pulse every two seconds. In addition, each two periods of the wiggler (with the exception of the first and last period) was energized by a separate power supply. Thus, we could

vary the resonant length of the wiggler or taper the wiggler field in two period steps. The wiggler field provided focusing for the electron beam in the direction of the wiggler field (vertical). Continuous horizontal focusing quadrupoles focused the beam in the horizontal direction. The focusing of the wiggler and the quadrupoles was not the same and therefore the electron beam had an elliptical transverse spatial profile ($k\beta_V \simeq 19.2\ m^{-1}$ and $k\beta_H \simeq 6.8\ m^{-1}$). With a normalized edge emittance of 3×10^{-3} m-rad, the beam had an elliptical shape 2.4 cm wide by 1.3 cm high. Prior to the wiggler, a fine meshed screen was used to match the input microwave signal into the waveguide. The waveguide in the interaction region was made of thin walled stainless steel to ensure good penetration of the pulsed wiggler field. The waveguide dimensions were 3 cm high by 10 cm wide. The wide dimension lies in the wiggle plane. Gentle tapers were used to match the fundamental TE_{10} mode of the input signal source (either a magnetron at 35 GHz or an Extended Interaction Oscillator at 140 GHz) to the TE_{01} mode of the interaction region. The resonance condition for the FEL which accounts for the waveguide modification to the electromagnetic wave propagation is:

$$2\gamma^2 = \frac{\omega/c}{[k_w + (k - \omega/c)]}\left[1 + \frac{1}{2}\left(\frac{eB_w\lambda_w}{2\pi mc}\right)^2\right] \tag{2}$$

where the frequency and wavenumber are related by the waveguide dispersion which is given by:

$$\omega^2 = k^2c^2 + \omega_{c0}^2 \tag{3}$$

and where w_{CO} is the cutoff frequency of the waveguide. For a rectangular waveguide

$$\omega_{c0} = \pi c\sqrt{\frac{m^2}{a^2} + \frac{n^2}{b^2}} \tag{4}$$

where a is the narrow dimension of the guide, b is the wide dimension, and m and n are the mode numbers. Table I lists the resonant energies for various modes in the waveguide (at 34.6 GHz). The TE_{21} and TM_{21} modes can couple to the electromagnetic wave. In the experiments discussed here, as much as half of the radiated power could reside in these higher modes (except in the tapered wiggler case). At the end of the

Table I: Resonant Energy Shift for Higher Order Modes

Mode	$\gamma_r(m, 1)/\gamma_r(0,1)$
TE_{01}	1
TE_{21}, TM_{21}	1.02
TE_{41}, TM_{41}	1.11

wiggler, the electron beam was deflected into the waveguide wall and the electromagnetic radiation was injected into an evacuated diffraction tank. The radiated signal was monitored in the far field. By proper location of the receiving antennas we could determine the waveguide mode to which the signal coupled.

The FEL resonance was determined by varying the wiggler field for a 1-m long uniform wiggler (the remainder of the wiggler was tuned far from resonance). When the peak of the resonance was determined, the wiggler length was varied from 20 cm to 3 m. Figure 3 shows the results of this gain measurement. The two curves correspond to a tapered and untapered wiggler. These curves show the power only in the TE_{01} mode, which is the fundamental design mode. In the linear regime, the signal grew exponentially at a rate of 34 dB/m and saturated 1.2 m into the wiggler. In the uniform wiggler case, the signal actually decreased beyond the saturation point and the power oscillated corresponding to the synchrotron motion of the electrons in the ponderomotive well. This syncrotron motion had a period of about 1 meter. The solid line in this figure corresponds to the results from a 2-D simulation code, FRED. There is a slight discrepancy between the theory and the experiment beyond saturation. The theory predicts a shorter period synchrotron oscillation with a more pronounced amplitude.

The deleterious effect of saturation can be eliminated by tapering the wiggler. In the experiment, this was be accomplished by tuning the wiggler in two period increments starting near saturation and maximizing the output power at each step. In this manner, the radiated power increased from 200 MW to 1 GW. The wiggler field dropped to 40% of its peak value. This corresponded to an extraction efficiency of about 35% and a trapping fraction (of electrons in the ponderomotive well) of about 60%. We repeated this experiment at 140 GHz using a 4-m long wiggler. In this case, a 50 W signal from a conventional EIO was injected into the interaction region. Because the energy of the electron beam was still 3.5 MeV, the wiggler magnetic field had to be reduced to match the resonance condition. For this case the resonant wiggler field was 1.7 kG. Because the wiggler field was reduced by a factor 0.46, the gain per unit length was reduced by

$$\left(\frac{B_{w,res}(140\ GHz)}{B_{w,res}(35\ GHz)}\right)^{2/3}$$

or 0.6 (22 dB/m as opposed to 34 dB/m at 35 GHz). In this experiment the signal saturated at 70 MW 3.4 m into the wiggler. However, saturation occurred too far into the wiggler to allow for any meaningful tapering studies. The amplification of the input signal is shown in Fig. 4. Again, the solid line is the result of the numerical simulation.

The complex gain of the FEL produces both an amplification of the electromagnetic wave as well as a phase shift of the radiation [3]. We measured the

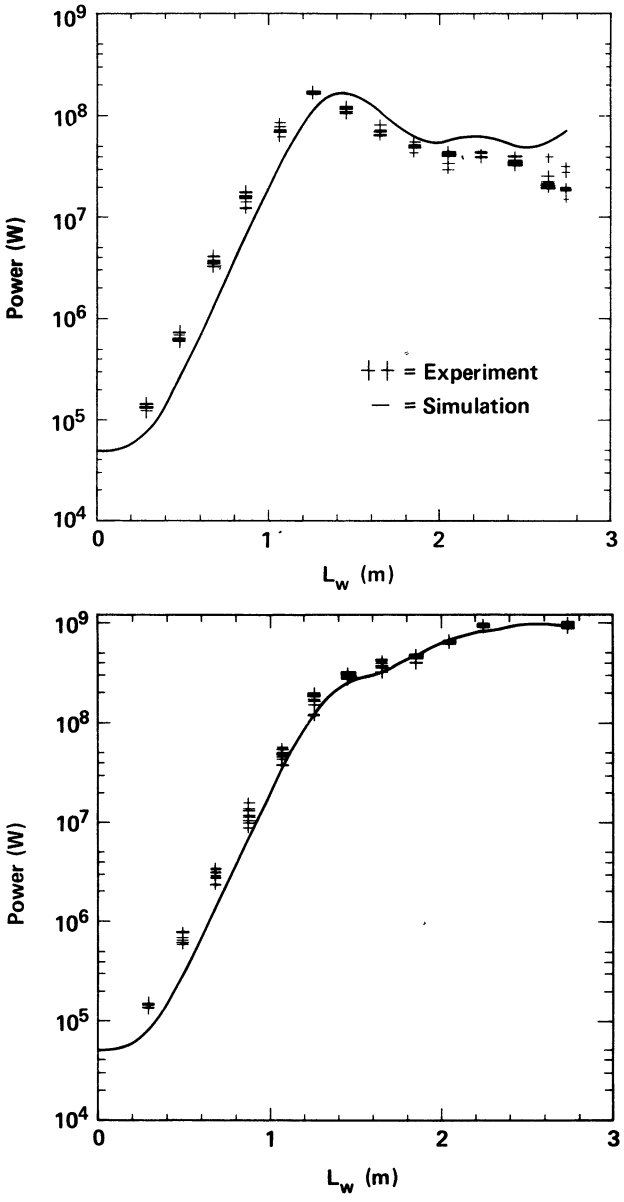

Figure 3. Gain measurement of 35 GHz input signal. $B_{resonant}$ = 3.7 kG. Top: 3-m uniform wiggler. Bottom: optimized tapered wiggler. For both cases the beam current is 850 A.

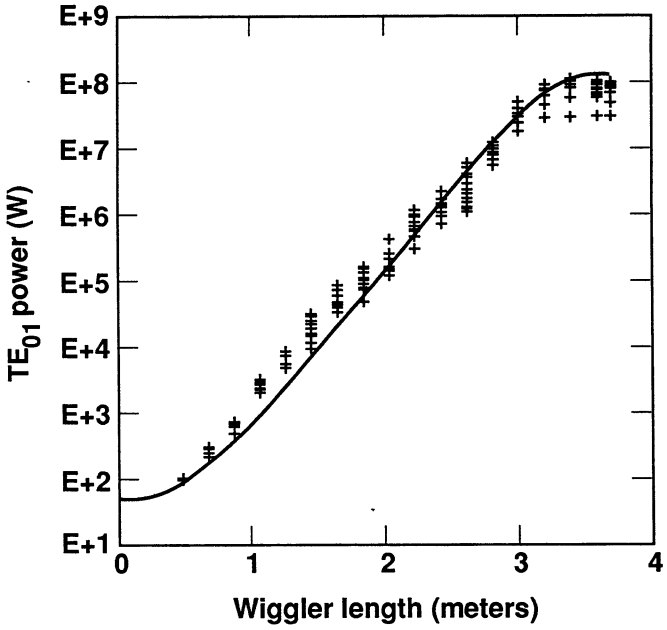

Figure 4. Gain measurement of 140 GHz input signal. $B_{resonant}$ = 1.7 kG, 4-m uniform wiggler, I_{beam} = 950 A.

progressive shift in phase as the radiation grew in the FEL using a homodyne technique. With a microwave interferometer, we measured the phase shift of the amplified radiation relative to the input signal as a function of length through the wiggler as well as a function of wiggler field. We have plotted the results of this measurement in Fig. 5 for the 35 GHz experiment. The three curves correspond to the wiggler field at resonance, 5% above resonance, and 5% below resonance. These data correspond to the tapered wiggler case. Again, the solid line corresponds to the results of the two dimensional simulation of this device. Our ability to accurately model the FEL's performance is crucial to designing future devices. Successfully modeling the real and imaginary parts of the complex gain gives us great confidence in other FEL designs.

We had previously discussed the effect of the waveguide on mode competition in the microwave FEL. Table I shows the shift in energy required for the electron beam to couple to modes other than the fundamental design mode (TE_{01}). We considered only modes which have a non-zero electric field on the axis of the intraction region—the TE_{m1} and TM_{m1} modes where m is even. As indicated in Table I, the TE_{21} (TM_{21}) mode has a resonant energy only 2% from the resonant energy for the TE_{01} mode. The resonant energy for all other higher order modes is significantly further away from the

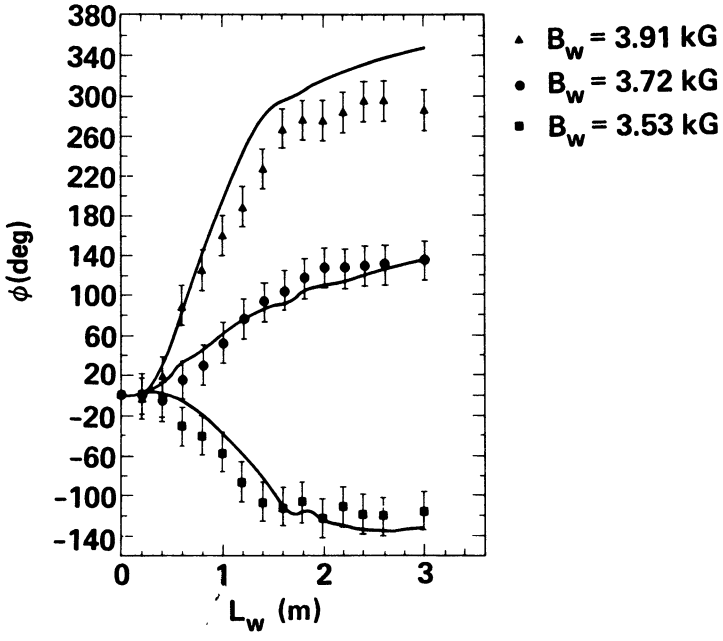

Figure 5. Phase shift of amplified signal relative to input signal (at 35 GHz) for tapered wiggler at resonance, 5% above resonance and 5% below resonance.

energy corresponding to the fundamental design mode. We probed the radiation pattern in the far field assuming that only the TE_{01}, TE_{21}, and TM_{21} modes were present. Figure 6 shows the power in the fundamental mode and the TE_{21} + TM_{21} modes for both the tapered and untapered wiggler. In the uniform wiggler case, the power is distributed in the two modes with half of the total power at times residing in the higher order mode. In the tapered wiggler case, most of the power (85%) remains in the fundamental design mode. As the electrons lose energy, the longitudinal momentum of the electrons is forced to track this particular mode in the tapered wiggler.

The electrons' motion in the wiggler field results in radiation not only at the fundamental frequency, but also in harmonics of this frequency. Although the FEL is resonant with one particular mode at one particular frequency, the electrons which are bunched by this mechanism can radiate coherently at the harmonics. For the plane polarized wiggler, only the odd harmonics radiate on axis. Figure 7 shows the fundamental and third harmonic power for both the tapered and the untapered wiggler case. Although there is almost a factor of five difference in the power radiated at the

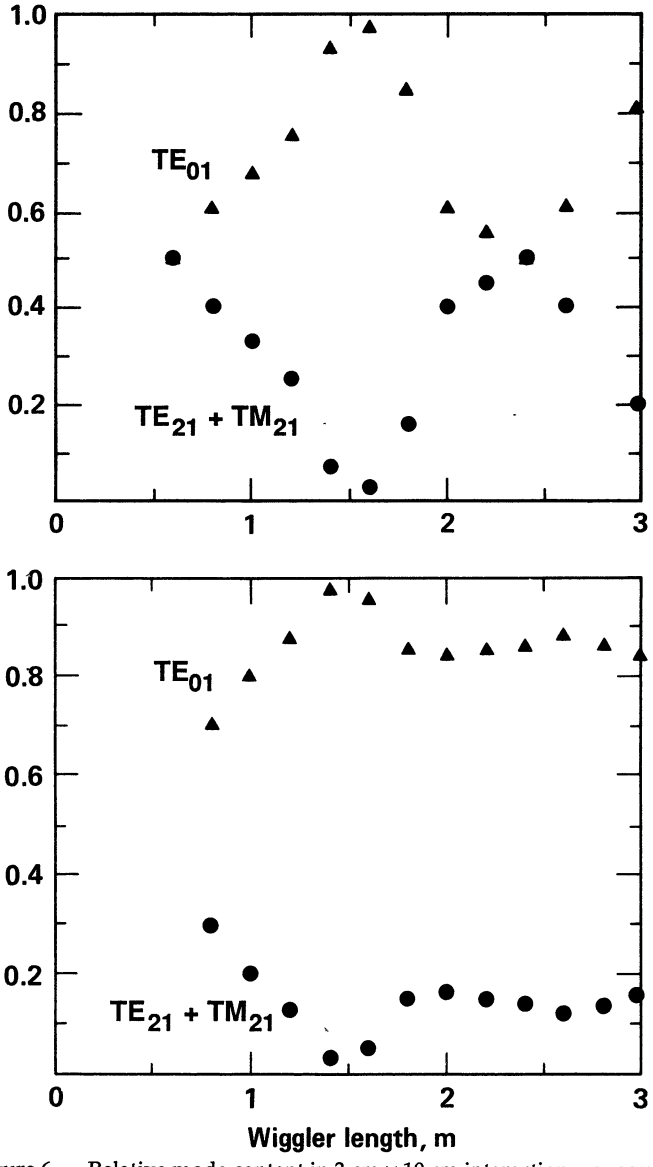

Figure 6. Relative mode content in 3 cm × 10 cm interaction waveguide. Top: Uniform wiggler (B_r = 3.7 kG). Bottom: tapered wiggler.

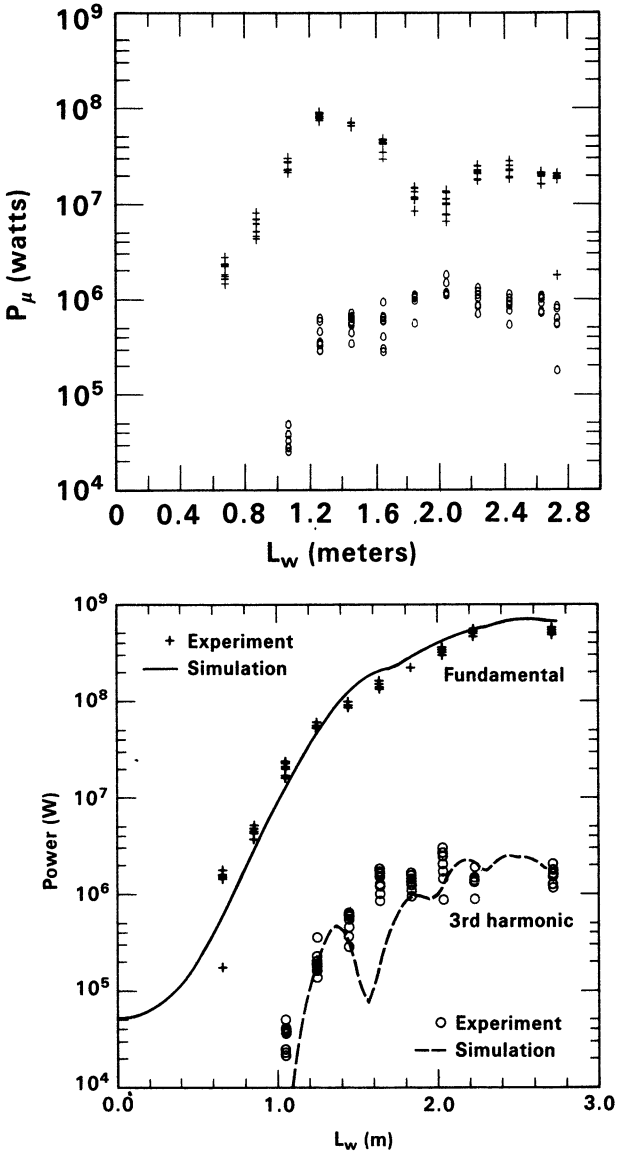

Figure 7. Power at fundamental (FEL) frequency (35 GHz) and at third harmonic (105 GHz). Top: uniform wiggler. Bottom: tapered wiggler.

fundamental for the two cases shown, there is only a slight difference in the third harmonic emission. The explanation for this is simple. The electrons are bunched by the action of the FEL. These bunches remain resonant with the FEL frequency at 35 GHz. The bunches, however, radiate at the harmonics as an array of small dipole antennas. The FEL action simply maintains the bunches. The slight improvement in harmonic emission in the tapered wiggler case is due to the fact that the tapered wiggler maintains a tighter bunch. Again, the lines in these graphs correspond to the results of a simulation code designed to study harmonic emission in the FEL.

III. Intense Microwave Prototype

Based on our previous experiments with LIA driven FEL amplifiers and advances in LIA technology, we have designed a free electron laser to heat a tokamak plasma. This device is referred to as the Intense Microwave Prototype (IMP) [4], and the design parameters for this device are given in Table II. In particular, this device is designed to operate at 250 GHz to match the electron cyclotron resonance in the Alcator tokamak which has a main toroidal field of 10 T. This experiment is referred to as the Microwave Tokamak Experiment (MTX) [9]. The FEL is designed to deliver 2 MW of average power for a period of 1 second. In order to achieve this high average power, the accelerator must run at a relatively high duty factor.

Previous LIAs used Blumleins which were discharged through pressurized sparkgaps to energize the induction accelerator cells [10]. The development of new high power pulse compression techniques allowed us to consider systems which could operate at several kHz [11]. Both of these pulse power chains are illustrated in Fig. 8. The problem with the sparkgap is erosion of the electrodes. The magnetic switch (Mag 1-D) relies on saturable reactors to transfer the energy from one energy storage stage to another at successively faster rates. Since there are no electrodes to degrade or gasses which need to recover, these switches can in principle achieve high pulse repetition frequencies. The Mag 1-D was designed to operate at high average PRF.

Because this FEL operates at a high duty factor, we cannot rely on a pulsed electromagnet to generate the wiggler field. An iron core electromagnet is available to generate the required wiggler field. The parameters for this wiggler are given in Table III. One notable feature about this wiggler is the large range of magnetic field

Table II: IMP Design Parameters

E_{beam}	10 MeV
I_{beam}	3 kA
f_{μ}	250 GHz
P_{μ} (peak)	12 GW
% extraction	40%
P_{μ} (ave)	2 MW

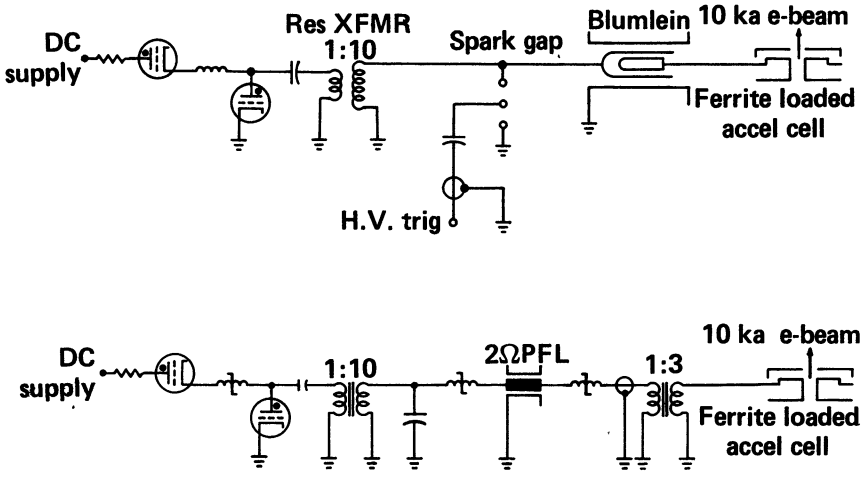

Figure 8. Schematic of pulse power unit for induction accelerator cell. Top: Spark-gap switched Blumlein. Bottom: Nonlinear magnetic pulse compressor.

Table III: IMP Wiggler Requirements

Period = 10 cm
Gap = 4.0 cm
Length = 5.5 m
Peak field = 4.7 kG
RMS wiggler errors < 0.1%
B-field tuning range > 37%

which must be covered in the taper. The overall length of the wiggler is 5.4 m and the period is 10 cm. Unlike the aircore, pulsed electromagnet in the ELF experiment which used external quadrupoles to provide horizontal focusing, this wiggler has specially shaped poles to provide the horizontal focusing [12]. The pole tips are curved in such a manner that the wiggler field increases away from the axis in the wiggle plane. The shape of these poles is such that the focusing in the horizontal direction is equal to the focusing in the vertical direction. This results in a round electron beam in the interaction region. Figure 9 illustrates a one period section of the IMP wiggler.

When designing high average power systems, care must be exercised to avoid thermal stress in any of the componenets. Clearly, this is an issue in the pulsed power systems as well as the accelerator. The waveguide which passes through the wiggler and defines the FEL interaction region is also subjected to thermal stress due to the absorption of radiation on the walls of the beam tube. In order to achieve a high wiggler field, the poles above and below the interaction region want to be as close

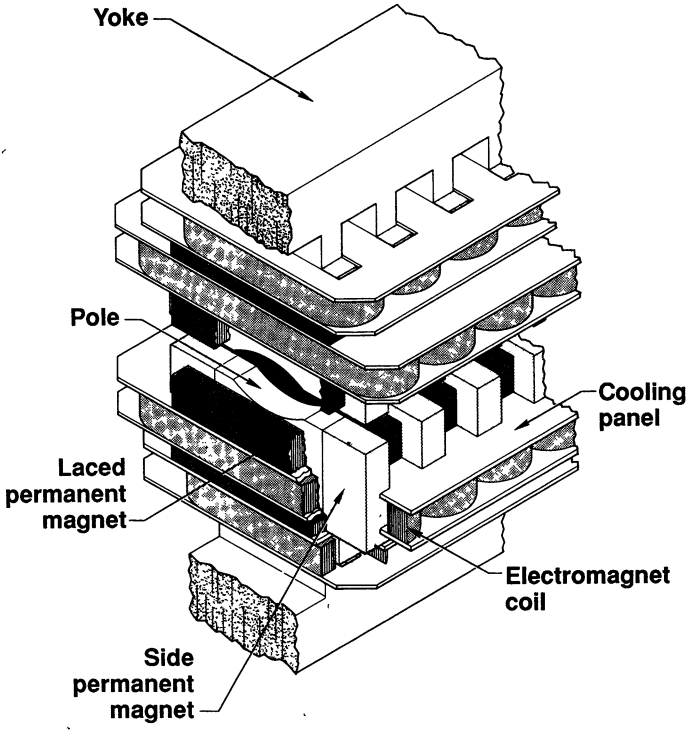

Figure 9. Illustration of one period section of IMP wiggler.

together as possible. To provide the focusing as described above, the transverse dimensions of the interaction region must also be kept small—on the order of the vertical dimensions. Hence, the transverse profile of the interaction region must be kept as small as possible. However, the attenuation losses for the rf in passing through a waveguide increase as the inverse of the cross-sectional area. This implies high thermal loading on the waveguide walls. A possible solution to this problem is to propagate the intense radiation in the HE_{11} mode, which has substantially reduced attenuation in the waveguide [13].

Another consideration regarding thermal loading on waveguide wall has to do with the size of the electron beam in the waveguide. As the wiggler field is reduced according to the required taper, the transverse focusing of the electron beam is relaxed and the radial size of the beam is increased. At some point, the beam stikes the waveguide wall. To prevent this happening, the waveguide radius must be increased or the wiggler field must be kept above a certain minimum value. We arbitrarily impose the restriction that the beam diameter must not get larger than the one-half waveguide diameter.

Clearly, there are a great number of engineering details which must be addressed to ensure reliabilty of this device. We have not addressed the technical issues of the accelerator. The performance of the accelerator is crucial to the performance of the FEL. At present, the accelerator for IMP is being upgraded to provide a beam of sufficient quality to drive the FEL.

SUMMARY

We have demonstrated the ability to achieve high peak power in an FEL amplifier operating at 35 and 140 GHz. In addition, we have successfully modeled the performance of this device with respect to the complex gain and harmonic generation. We have designed a high average power FEL for the purpose of heating a tokamak plasma. For this device, the accelerator performance must be improved in order to demonstrate the high average power capability of the FEL.

References

[1] A great deal has been written on free-electron lasers. For more detailed information on the variety of devices and theoretical analyses see:

a. Special issues on free-electron lasers, IEEE J. Quantum Electron. 17 (1981), 19 (1983), 21 (1985), and 23 (1987).

b. Proceedings of the first through tenth international free-electron laser conferences.

(1) Jacobs, S.F., Sargent III, M., and Scully, M.O., Eds., Physics of Quantum Electronics, Addison-Wesley, New York, 1978, vol. 5.

(2) Jacobs, S.F., Pilloff, H.S., Sargent III, M., Scully, M.O., and Spitzer, R., Eds., Physics of Quantum Electronics, Addison-Wesley, New York, 1980, vol. 7.

(3) Jacobs, S.F., Pilloff, H.S., Sargent III, M., Scully, M.O., and Spitzer, R., Eds., Physics of Quantum Electronics, Addison-Wesley, New York, 1982, vols. 8 & 9.

(4) Billardon, M. and Deacon, D.A.G., Eds., J. Phys. (Paris), Colloque C1-44, 1983.

(5) Brau, C.A., Jacobs, S.F., and Scully, M.O., Eds., Free Electron Generators of Coherent Radiation, Society of Photo-Optical Instrumentation Engineers, Redland, Washington, 1984, vol. 453.

(6) Madey, J.M.J. and Renieri, A., Eds., Nucl. Instrum. Methods Phys. Res., A237, 1985.

(7) Scharlemann, E.T. and Prosnitz, D., Eds., Nucl. Instrum. Methods Phys. Res., A250, 1986.
(8) Poole, M., Ed., Nucl. Instrum. Methods Phys. Res., 259, 1987.
(9) Sprangle, P., Ed., Nucl. Instrum. Methods Phys. Res., A272, 1988.
(10) Gover, A. and Granatstein, V.L., Eds., Nucl. Instrum. Methods Phys., Res., 273, 1989.

[2] Kroll, N.M., Morton, P.L., and Rosenbluth, N.M., "Free Electron Lasers with Variable Parameter Wigglers," IEEE J. Quantum Electron. QE-17, 1436 (1981).

[3] Marshall, T.C., Free-Electron Lasers (MacMillan, New York, 1985).

[4] Jong, R.A., Throop, A.L., Scharlemann, E.T., "Baseline Design for the Intense Microwave Prototype Wiggler," Rev. Sci. Inst. 60, 186 (1989).

[5] Orzechowski, T.J., Scharlemann, E.T., Anderson, B., Neil, V.K., Fawley, W.M., Prosnitz, D., Yarema, S.M., Hopkins, D.B., Paul, A.C., Sessler, A.M., and Wurtele, J.S., "High-Gain Free Electron Lasers Using Induction Linear Accelerators," IEEE J. Quantum Electron. QE-21, 831 (1985).

[6] Fessenden, T.J., Atchison, W.A., Birx, D.L., Briggs, R.J., Clark, J.C., Hester, R.E., Neil, V.K., Paul, A.C., Rogers, D., and Struve, K.W., "Physics of a Repetitively Pulsed 10 Kamp Electron Beam Accelerator," Proc. 4th International Topical Conference on High-Power Electron and Ion-Beam Research and Technology, Commissariat a l'Energie Atomique and Ecole Polytechnique, Palaiseau, France, June 29–July 3, 1981 (1981).

[7] Orzechowski, T.J., Anderson, B.R., Clark, J.C., Fawley, W.M., Paul, A.C., Prosnitz, D., Scharlemann, E.T., Yarema, S.M., Hopkins, D.B., Sessler, A.M., and Wurtele, J.S., "High-Efficiency Extraction of Microwave Radiation from a Tapered-Wiggler Free-Electron Laser," Phys. Rev. Lett. 57, 2172 (1986).

[8] Orzechowski T.J., Scharlemann, E.T., and Hopkins, D.B., "Measurement of the Phase of the Electromagnetic Wave in a Free Electron Laser Amplifier," Phys. Rev. A35, 2184 (1987).

[9] Thomassen, K.I., "Millimeter Wave Tokamak Heating and Current Drive with a High Power Free Electron Laser," Plasma Phys. and Controlled Fusion 30, 57 (1989).

[10] Reginato, L.L., Branum, D., Cook, E., Denhoy, W., Fong, C., Kippenhan, D., Moor, E., Newton, M., Pollard, W., Rogers, D., Hibbs, S., Schmidt, J., Smith, M., Weiss, W., and White, J., "Advanced Test Accelerator (ATA) Pulse Power Technology Development," IEEE Trans. Nucl. Sci. NS-28, 2758 (1981).

[11] Birx, D.L., Hawkins, S.A., Poor, S.E., Reginato, L.L., and Smith, M.W.,"Technology of Magnetically Driven Accelerators," IEEE Trans. Nucl. Sci. NS-32, 2743 (1985).

[12] Scharlemann, E.T., "Wiggle Plane Focusing in Linear Wigglers," J. Appl. Phys. 58 2154 (1985).

[13] Jong, R.A. and Stone R.R., "Induction linac based free-electron laser amplifier for fusion applications," Nuc. Inst. and Meth. in Phys. Res., A285, 387 (1989).

HIGH POWER HIGH EFFICIENCY MM-WAVE FEL FOR ECRH IN PLASMA

G.P. Gallerano
ENEA, Area Energia e Innovazione, Dip. Sviluppo Tecnologie di Punta, C.R.E. Frascati - P.O. Box 65 - 00044 Frascati - Italy

1. INTRODUCTION

Electron cyclotron resonance heating (ECRH) of the plasma in magnetic fusion experiments requires the development of high average power radiation sources in the millimeter wavelength range. In particular, heating in future machines and current drive in the hot core of the plasma may extend this requirement to the sub-millimeter region.

Recently an assessment of potential ECRH sources has been performed, within the EURATOM framework, aimed at the design of a heating system for NET [1]. It appeared that, even if gyrotrons have received up to now the greatest impulse from fusion requirements and have presently reached the development stage closest to the goal of 1 MW CW at frequencies close to 140 GHz, alternative sources like CARM and FEL offer the possibility of being applied to fusion research and are good candidates for ECRH systems at frequencies greater than 200 GHz. FELs can in particular meet the need of a high unit power and of a fast frequency tuning for applications which require to deposit energy on different magnetic surfaces during the heating cycle.

The key issues and the technical problems of a mm-wave FEL for ECRH are reviewed in this paper together with the current status of the FEL development in the millimeter range.

2. ECRH FEATURES AND SOURCE REQUIREMENTS

Among the different methods for plasma heating, ECRH at millimeter wavelengths appears quite promising since it can fulfill important functions. These are:

- helping plasma formation and start-up

- heating in the core and in the central region of the discharge
- modification of the pressure and current density profiles
- quenching plasma oscillations
- driving electric current in the plasma core.

These characteristics are mainly due to the very localized absorption of RF power, which is related to the inhomogeneity of the magnetic field in a Tokamak. The electron cyclotron resonance frequency is indeed expressed by the relationship:

$$f(\mathrm{GHz}) = 28\, m\, B(\mathrm{T}) \tag{2.1}$$

where m is the harmonic number and B the toroidal magnetic field. The dependence of the field B on the distance from the vertical axis of the torus is given by the relation:

$$B \propto \frac{1}{R} \tag{2.2}$$

which determines the spatial location of the resonance.

Compared to other RF schemes of heating and current drive, ECRH possesses several advantages of great importance for a fusion reactor:

- the wave coupling is insensitive to plasma edge conditions
- the wave accessibility to the plasma is not affected by α particles
- the launching antenna is compatible with the hostile environment of a reactor, since quasi-optical systems placed at some distance from the plasma can be utilized
- launching of the wave can be achieved at high specific power ($\approx$100 kW/cm^2), which requires relatively limited access to the plasma.

Moreover, since the plasma cut-off density is proportional to the square of the frequency, in a reactor high order harmonics of ECR could be used to enhance the density and the wave absorption. Indeed, at such high frequencies absorption becomes more efficient at the very high temperature expected.

Therefore, while for the present machines frequencies lower than 200 GHz are going to be used, in a reactor the useful frequency may exceed 300 GHz.

A number of experiments have been performed or are planned utilizing EC-wave systems. The most significant results were

obtained in the Russian Tokamak T-10, where 4 MW of RF power was launched at the ECR frequency of 90 GHz [2]. Good central heating was obtained as well as mode stabilization and temperature profile control.

In all the experiments the specific power was high compared to other heating methods, but it did not exceed 100 kW/cm^2. In such conditions (wave electric field $\leq$10 kV/cm) linear or quasi-linear theory applies satisfactorily to the plasma-wave interaction. At much higher electric field (typically $\geq$30 kV/cm) interactions are dominated by non-linear phenomena. These are a variety of effects, each taking place when its power threshold is exceeded locally. Frequency up-other down-shift, depending on the sign of the non-linearity, as well as self focusing of the radiation may appear [3]. The response time of the non-linearity in the medium has also to be taken into account when dealing with short pulses of radiation like those provided by some FEL. Some effects are beneficial for absorption while others prevent the RF power from reaching the inner plasma region.

Non-linear theory has been applied to cases of intense pulsed heating as foreseen for the MTX experiment in Livermore [4]. So far no other experiment has been performed at such high electric fields. The Livermore experiment only could indicate if the non-linear regime of ECRH can be effectively used or not.

Each of the applications described at the beginning of this section has different requirements in terms of frequency, total power and system efficiency, which can be summarized as follows:

- Frequency: the frequency range in which sources are required for heating and current drive applications spans from 100 to 300 GHz. High magnetic field operation and/or higher harmonic operation may extend this range up to 500 GHz.
- Power Level/System Efficiency: 10-20 MW of power is needed for heating applications, while current drive applications require power levels around 50-100 MW. A source suitable for heating applications should have a minimum unit power of $\approx$ 1 MW with a system efficiency $\geq$ 30%. For current drive applications a higher unit power (5-10 MW) would also be

desirable and a system efficiency better than 40% is mandatory.

- Tunability: in some applications deposition of power on different magnetic surfaces is needed and therefore a wide band tunability of the source would be desirable. A typical requirement is 5% of fast tuning range, in the 10 to 100 ms time scale, and a wider (20-30%) slow tunability.
- Time operation: due to the problems mentioned before, related to a high value of the peak electric field, a premium is placed on CW operation. In the linear absorption regime pulsed sources may be utilized only if they have a high duty cycle.

3. POWER SOURCES FOR ECRH

The power sources which have been considered so far for ECRH applications are the gyrotron, CARM, and FEL. All these sources utilize as operating principle the conversion of kinetic energy from an electron beam (e-beam) to radiative energy of an electromagnetic wave. The main difference between these sources lies in the different range of electron energies in which they are utilized and in the dependence of the operating frequency on the electron energy. This dependence can be summarized as follows:

$$\text{GYROTRON } f(\text{GHz}) = 28\,\frac{B(\text{T})}{\gamma} \tag{3.1}$$

$$\text{CARM } f(\text{GHz}) = 28\,B(\text{T})\,(1+\frac{v}{c})\,\gamma \tag{3.2}$$

$$\text{FEL } f(\text{GHz}) = \frac{30\,(1+\frac{v}{c})\,\gamma^2}{\lambda_u(\text{cm})\,(1+K^2)} \tag{3.3}$$

where B is the longitudinal magnetic field, v is the electron velocity, γ is the ratio of the electron energy to its rest energy, λ_u is the FEL undulator period and K is the so called *undulator parameter* which is related to the transverse magnetic field and is usually of the order of unity.

Gyrotrons usually utilize non-relativistic electron beams since their operating frequency is inversely proportional to γ.

At present technological limits on high field magnets and cavity dimensions prevent gyrotrons from extending much above 250 GHz.

The proportionality of the operating frequency to γ and γ^2 respectively for CARM and FEL makes these sources good candidates for ECRH at high frequencies. In particular in a FEL the energy exchange is driven by the modulation induced on the electron motion by a transverse magnetic field with a period of the order of a few centimeters, so that frequencies from the microwave region up to the visible and beyond can be reached for electron energies ranging from few MeV to hundreds of MeV. This is confirmed by a large experimental data base.

A wide tuning range can be achieved in a FEL by varying the undulator magnetic field and/or the electron energy.

The state of the art of gyrotrons at the frequency of interest for ECRH systems is presently 0.5 MW for 0.5 s at 140 GHz [5]. CARM have so far been operated with short pulses (30 ns) and high power (10 MW) but only at low repetition rate. A summary of the most relevant sources for ECRH utilizing relativistic e-beams is reported in Table I [6].

4. FEL KEY ISSUES

A feasibility study of a Free Electron Laser source suitable for ECRH has been recently performed at ENEA, Frascati

TABLE I
Relativistic e-beam laser sources for ECRH, state of the art

Laboratory	Frequency (GHz)	Power (MW)	Comments
MIT (Dep of Phys.)	35 35	18 10	FEL (1kA, 2 MeV) ampl. η = 20% CARM (260 A, 1.4 MeV) ampl.
MIT (Plasma Fus)	140		CARM (100 A, 450 keV)
LIVERMORE ELF-II (IMP- MTX)	140 250	100 (2 av)	FEL (Ind Linac 600 A, 6 MeV, 20 ns) (Ind Linac 3 kA, 10 MeV)
MARYLAND (Plasma Res.)	280-300	(1 CW)	FEL (40 A, 650 keV-1 MeV)
ECOLE POLYT.	120	10	FEL (400 A, 1 MeV, 50 ns)
OSAKA	300	(1)	FEL (Ind Linac 100 A, 1.5-4 MeV)
GORKY	125	10	CARM (400 A, 350 keV, 30 ns)
NRL	100-250	(20)	CARM (200 A, 600 keV, 70 ns)

numbers in parenthesis are design values

[7]. A number of schemes have been proposed in this study trying to discuss the issues relevant to a high power high efficiency device.

Efficiency is one of the most important issues for a FEL in this type of application. Indeed, in a FEL oscillator the e.m. radiation stored in the resonator is amplified at each passage through the undulator. Saturation is reached when the exchange of energy between electrons and radiation field is so large that the electron motion is no longer resonant with the amplified wave, i.e. electrons which have lost energy are driven out of the gain curve. The homogeneous broadening gain bandwidth is of the order of 1/N where N is the number of undulator periods. The maximum allowed relative variation of the electron energy is also of the same order of magnitude, and it can be shown that for a high quality electron beam (inhomogeneous broadening negligible) the efficiency of the FEL in the small signal small gain approximation is $\eta_F = 1/2N$ [8]. This results typically in electronic efficiencies of a few percent.

In high gain systems it is worth adjusting the magnetic field along the undulator length, a procedure known as tapering, in order to keep the electrons resonant or trapped in a ponderomotive well [9] as they lose energy. In this way it is possible to extract a significant amount of energy in a single pass and therefore high efficiency can be achieved. Efficiency greater than 30% has been demonstrated at Livermore in an induction linac driven FEL operating as an amplifier at 35 GHz [10]. Tapered FELs are only feasible as single pass amplifier since the amount of tapering is strongly dependent on the input field of the wave, and therefore it cannot be used in a oscillator where the radiation field grows starting from noise.

Considering the total efficiency of the system, one has also to take into account the efficiency of the accelerator which is usually in the range 50-80%. This implies the important observation that in a FEL oscillator suitable for ECRH energy recovery of the e-beam is needed, due to the low electronic efficiency of the process. In an amplifier, where the electronic efficiency is higher, energy recovery is not so crucial, and in some cases it is not feasible either.

In principle it is possible to improve the total efficiency

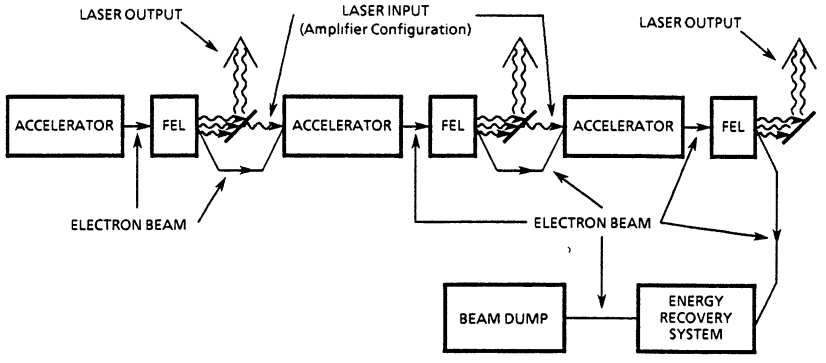

Fig. 1 FEL device with multiple electron beam utilization

by means of a multiple utilization of the electron beam (see Fig. 1). In this configuration the e-beam transport channel is achromatic and isochronous, i.e. electrons with different energy follow the same orbit and enter the undulator at the same time preserving the longitudinal bunching. This system can be viewed as a number of modules in each of which the electrons recover in the accelerating structure the energy lost in the previous FEL interaction and are then sent to the next module.

It is useful to analyze the power flux in such a system (see Fig.2), since one can get the physical insight in the quantities which are crucial for a high efficiency operation. Assuming that each module has the same accelerator and FEL efficiency, the symbols in Fig.2 take the following meaning:

P_U = power for all the *utilities* (magnets,pumps,etc.)
P_0 = power *from the plug* for the accelerating structure
P_A = power injected into the accelerating structure
P_L = power loss in the accelerating structure
P_E = e-beam power
P_R = power sent back to the accelerating structure
P = FEL output power/module
$\eta_k = P_A/P_0$ = efficiency of the accelerator power supply
$\eta_F = P_R/P_E$ = FEL efficiency (including output coupling)
$\eta_R = P_R/P_E(1-\eta_F)$ = e-beam energy recovery efficiency
M = number of FEL modules

Following the analysis of ref. [7] we can write for the total system efficiency η_T:

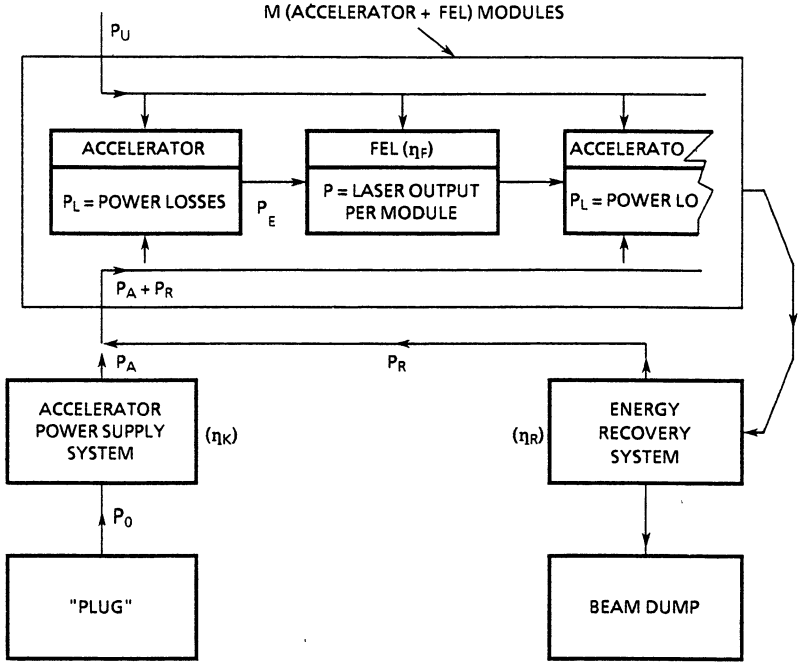

Fig. 2 Power flux diagram of the FEL system

$$\eta_T = \frac{MP}{P_0 + P_U} = \frac{\eta_k}{1 + \frac{(1-\eta_F)}{\eta_F}\,\frac{(1-\eta_R)}{M} + \frac{P_L + \eta_K P_U}{MP}} \qquad (4.1)$$

It is evident from eq. (4.1) that the upper limit to the system efficiency is the efficiency of the accelerator power supply. In order to maximize the total efficiency two terms in the denominator of (4.1) need to be minimized:

- the power loss in the accelerator structure P_L and the fraction η_K of the utility power P_U must be negligible with respect to the total output power MP ,
- the FEL efficiency η_F must be larger than the *recovery inefficiency* $(1-\eta_R)$ divided by the number of modules M.

This last requirement is quite demanding if a single FEL module is considered: for a typical oscillator it implies that an energy recovery better than 95% is usually needed.

Another important issue for a FEL is the maximum peak power which is allowed in the linear ECR absorption regime. As it has been indicated in section 2, a typical upper limit for the wave electric field is 30 kV/cm which corresponds to a maximum power density of 1 MW/cm^2. Assuming a crosss section S $\approx$100 cm^2 as a reasonable figure of the interaction area in the plasma, we obtain a maximum allowed peak power $P_M \approx 100$ MW.

The temporal profile of the FEL radiation reflects the time structure of the e-beam generated in the accelerator. Since many FEL drivers are pulsed devices, the duty cycle δ, which is the product of the bunch duration τ and the repetition frequency of the accelerator, has to be carefully considered when looking at the peak power limit P_M.

So far three different types of accelerator have been considered as FEL driver: the induction linac, the RF linac and the electrostatic accelerator.

The duty cycle and the corresponding peak power of a FEL source having 1 MW average power are reported in Table II for the three different accelerators.

The electrostatic accelerator driven FEL is the only CW source. The peak power of a RF-linac driven FEL is still within the limit of the linear absorption regime, while the induction linac FEL clearly exceeds this limit. Indeed, as it has been pointed out in section 2, the MTX experiment has been specifically designed to test the non-linear absorption regime of ECR.

5. FEL CONFIGURATIONS

In this section we will briefly discuss the FEL configurations corresponding to the different choices of accelerator mentioned before.

TABLE II

FEL Driver	Duty Cicle	Radiation Peak Power
Induction Linac	0.02-0.1%	5-1 GW
RF-Linac	2-5%	50-20MW
Electrostatic acc.	CW	1 MW

5.1 Electrostatic accelerator FEL oscillator

The electrostatic accelerator FEL is probably the most appealing configuration from the point of view of the total system efficiency and also because it offers the possibility of using a technology similar to that one of microwave tubes.

A schematic lay-out of this FEL is shown in Fig. 3.

The main underlying concept is to utilize a low voltage ($\leq$ 1 MV) electrostatic gun powered by a bias supply with a current capability of $\approx$ 100 mA, a short period undulator, and a multi-stage depressed collector for spent beam energy recovery at the moderate voltage ($<$ 200 kV) of a main power supply providing the full beam current ($\leq$ 30 A).

Energy recovery is a crucial point of the design, both for the system efficiency and for the issue of power supply size and cost. Indeed, from the considertions made in the previous section, it is easy to notice that the voltage of the main power supply of Fig. 3 is related to the bias high voltage by the relationship:

$$\Phi_{LV} \approx [1-\eta_R(1-\eta_F)]\Phi_{HV} \qquad (5.1)$$

For this reason energy recovery better than 80% is needed in order to keep the low-voltage main supply below 200 kV, where power supplies at power levels up to 5 MW are commercially available. Furthermore, due to the high accelerator efficiency, a system efficiency greater than 40% seems to be feasible.

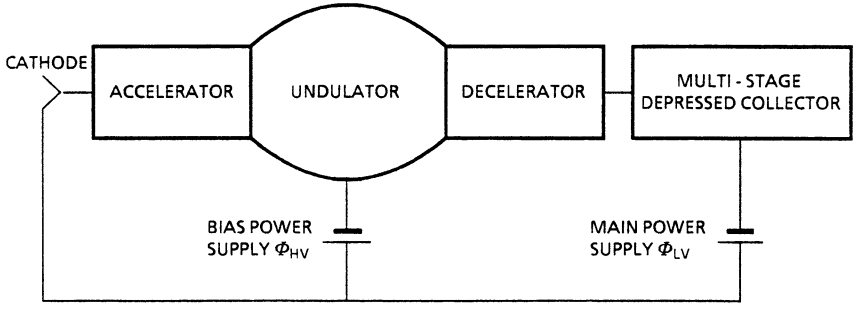

Fig.3 Electrostatic accelerator FEL

Proposals for a 1 MW CW FEL source suitable for ECRH have been made by the Laboratory for Plasma Research at the University of Maryland [11], and by the FEL group at FOM - Nieuwegein [12]. The main parameters of both Maryland and FOM proposals are reported in Table III.

Crucial issues of an electrostatic accelerator driven FEL are the e-beam transport through the undulator at extremely low losses (< 0.5%), due to the current limits of the high voltage power supply, and the need and availability of short period undulators, which presently limit the maximum operating frequency to 300 GHz.

5.2 - RF-Linac FEL

Due to the e-beam current capability of the RF-Linac and to its pulsed nature, typical electron energies of a RF-Linac suitable for driving a FEL at 1 MW average power lie between 5 and 10 MeV.

TABLE III
Parameters of electrostatic accelerator FEL oscillator

	FOM	Maryland
Beam voltage (MV)	1	1
Beam current (A)	20	34
Horizontal e-beam dimension (cm)	Ø0.2	4.0
Vertical dimension (cm)	Ø 0.2	0.26
Norm emittance (mm· mrad)	10 π	13 π
Undulator period (cm)	2.0	1.50
Number of periods	50	20
Undulator parameter K	0.15	0.20
Waveguide dimensions (a x b) (cm)	10 x 1.0	6.0 x 0.70
Radiation frequency (GHz)	220	300
Output power (MW) $TE_{0,1}$ mode	1	1
FEL efficiency η_F	5%	3%
Recovery efficiency η_R		92%
System efficiency η_F	>40%	28%
Depr. coll. power supply voltage (kV)	120	110

The lay-out of a RF-Linac FEL oscillator is sketched in Fig. 4. A detailed analysis of this type of device has been performed at ENEA - Frascati and is reported in ref. [7].

The accelerated electron beam is injected into the undulator magnet and, after the FEL interaction, is sent back into the main linac at the decelerating phase in order to recover a large fraction of the electron energy. The main parameters of this device are listed in Table IV.

A standing wave RF-Linac operating at room temperature and powered by two CW super-klystrons at 352 MHz has been considered in the ENEA design. Due to the klystron efficiency ($\approx 65\%$) energy recovery is of crucial importance in order to reach high system efficiency. As it can be seen from Table IV an energy of 96% corresponds to 20% system efficiency. 30% total efficiency can only be achieved by increasing the energy recovery to 98%.

The higher energy of the RF-Linac with respect to the electrostatic accelerator requires longer undulator periods and also implies a larger size of the system. As a counterpart frequencies higher than 300 GHz can be easily reached. Both RF-Linac and electrostatic accelerator FEL, require the development of a suitable optical cavity capable of circulating high RF power with low ohmic losses [13].

5.3 - Induction Linac FEL

The schematic lay-out of an Induction Linac driven FEL is shown in Fig.5. In this configuration the high current e-beam is injected into the undulator magnet together with a low power radiation beam ($<$ 1 kW) generated by an external oscillator at the frequency of interest. Due to the high peak current of the induction linac and to the particular design of the undulator, in a single pass the input radiation is amplified by many tens of dB. After the interaction the spent electron beam is sent to a beam dump (it is very hard to figure out a reliable energy recovery scheme), while the amplified radiation is extracted for utilization. The configuration described above is known as master oscillator power amplifier (MOPA).

The crucial components of a high efficiency and high average power MOPA-FEL are:

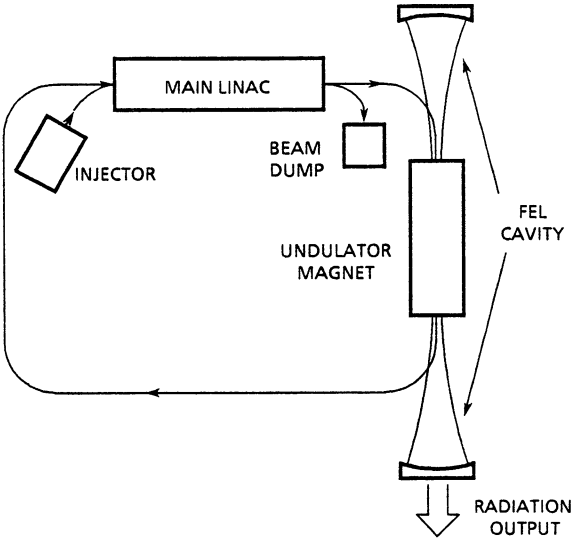

Fig. 4 - R.F. Linac FEL layout

TABLE IV
RF-Linac FEL parameters

radio-frequency (MHz)	352
e-beam energy (MeV)	10
e-bunch duration (ps)	150 ps
peak current (A)	50
average current (A)	3
norm. emittance (mm· mrad)	50
energy spread	1%
undulator period (cm)	16
number of periods	15
undulator parameter K	2
radiation frequency (GHz)	300
output power (MW)	1
P_L (MW)	0.7
η_k	65%
η_F	3%
η_R	96%
η_T	20%

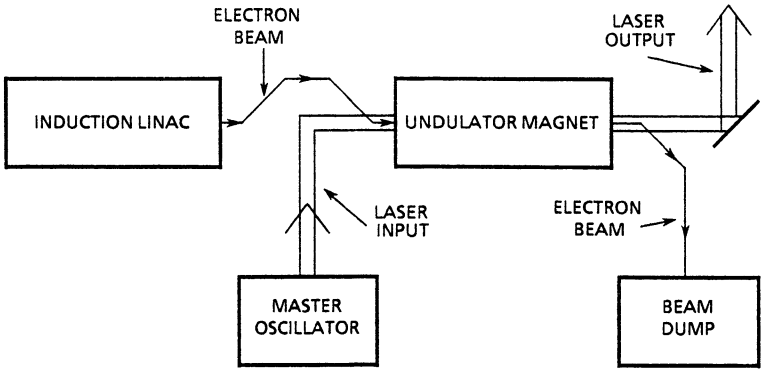

Fig. 5 Induction Linac FEL Layout

- a high current (≈1 kA) high quality e-beam accelerator operating at high repetition frequency (> 5 kHz)
- a tunable master oscillator generating the radiation to be amplified in the FEL
- an undulator composed of an untapered and a tapered section to obtain high extraction efficiency.

Preliminary results of the ELF-II-MTX experiment at 140 GHz can be found in Ref. [14].

As an example, the main parameters of the IMP-MTX experiment designed at Livermore [15] are reported in Table V.

The most critical parameter is the high repetition frequency needed for high average power operation. Magnetic switches are presently the only devices capable of delivering both high peak and high average power to the accelerator structure. A large effort has to be devoted to the development of this technology.

It is worth noticing that the MOPA-FEL is usually a wide band amplifier (≥10%), and therefore it can be easily tuned provided that a tunable master oscillator is available.

6. CONCLUSIONS

An ideal high power FEL source having the tunability requirements stated in section 2 would probably be composed by a *clean* low to medium power source followed by one stage of a power amplifier. The time structure of the radiation should be matched in the two stages. At the same time requirements of high efficiency and size constraints should become a crucial

TABLE V
IMP-MTX FEL parameters, Ref. [15]

e-beam energy (Mev)	10
e-pulse duration (ns)	50
peak current (kA)	3
rep. frequency (kHz)	5
# pulses/burst	2500
norm emittance (cm· rad)	0.1
energy spread	~ 1%
tapered undulator period (cm)	8
max magnetic field (T)	0.55
undulator length (m)	8
dominant mode	$TE_{0,1}$
waveguide dimensions (a x b) (cm)	2.8 x 2.8
radiation frequency (GHz)	250
output peak power (GW)	10
average power (MW)	2
η_k	80%
η_F	35%
η_T	20%

part of the design. At present it is not possible to meet all the requirements in the same device.

Novel schemes will have to be considered, like the FEL interaction under the combined influence of an undulator and an axial magnetic field, and the possibility of realizing a CW FEL amplifier driven by an electrostatic accelerator will have to be investigated.

ACKNOWLEDGEMENTS

It is a pleasure to thank the co-authors of the *Feasibility Study of a Free Electron Laser Source for Plasma Heating*, Ref. [7].

REFERENCES

[1] M.Q. Tran, Report on the "Meetings of the expert group for an integrated development programme for EC-wave systems for NET", (CRPP - Lausanne April 21 1990)

[2] V. Alikaev et al., XII Int. Conf. on Plasma Physics and Controlled Nuclear Fusion Research, Proc. paper IAEA-CN-50/EI-1-1 (Nice 1988)

[3] A.M. Sergeev,"Non-linear dynamics of ultrashort electromagnetic pulses in plasmas", these proceedings - paper N-9

[4] M. Porkolab, B.I. Cohen, Nucl. Fus. 28, 239 (1988)

[5] K. Felch et al., "Millimeter-wave megawatt gyrotron development for ECR heating applications", these proceedings - paper S-3

[6] details on the experiments listed in Tab.I can be found in the "Proceedings of the XII Int. FEL Conf.", (Paris 17 - 21 Sept. 1990), to appear on NIM-A

[7] R. Barbini et al., "Feasibility Study of a Free Electron Laser Source for Plasma Heating", Technical Report ENEA RT/TIB/89/56 (1989)

[8] See for example: G.Dattoli and A. Renieri, "Experimental and theorethical aspects of the Free Electron Laser", in Laser Handbook vol.4, M. Stitch and M.S. Brass eds., p.1 (North Holland Amsterdam 1985)

[9] T.J. Orzechowski, "Intense microwave generation using Free Electron Lasers", these proceedings - paper S-33

[10] T.J. Orzechowski et al.,Phis Rev. Lett. 57, 2172 (1986)

[11] J.H. Booske et al., IEEE Trans. on Plasma Science 18, 399 (1990)

[12] P.W. van Amersfoort et al., "An electrostatic Free Electron Maser for fusion: design considerations", to appear in the "Proc. of the XII Int. FEL Conf." (Paris 1990)

[13] for more details see ref.[7], sect.5.2.5

[14] A.L. Throop et al., "140 GHz Microwave experiments in ELF-II", to appear in the "Proc. of the XI Int. Conf. on Free Electron Lasers", (Naples - FL, August 1989)

[15] K.I. Thomassen, "Free Electron Laser experiments in Alcator-C", Report LLL-PROP-00202 (LLNL Livermore, CA, 1986)

OPTICAL GUIDING AND SUPERRADIANCE EFFECTS IN SPATIAL LOCALIZED ENSEMBLES OF ELECTRON-OSCILLATORS

N.S.Ginzburg
Institute of Applied Physics, USSR Academy of Science,
46 Uljanov Str., 603600 Gorky, USSR

According to the Kramers-Krönig relations the susceptibility of ensembles of electron oscillators has both active and reactive components. Therefore, when localized in space, such oscillators may not only amplify electromagnetic radiation but also form electron waveguides and resonators which specify the spacio-temporal structure of radiaton. This paper is conserned with two basic types of radiative processes in localized ensembles of electrons in free space.

Optical guiding [1-10] occurs in the propagation and amplification of radiation along the electron waveguide formed by high-current electron beams. Optical guiding is beneficial for a number of reasons:

a) transverse mode selection in devices with space extended electrodynamic systems, in particular, coherent radiation at "hot" modes, i.e. ensemble of modes of a cold electrodynamic system,

b) higher gain and lower starting currents resulting from the concentration of radiation in the electron beam region and reduction of the total electromagnetic field volume,

c) reduced probability of HF breakdown due to the attenuation of field intensity at the walls of electrodynamic system,

d) increased electron efficiency.

In this report the linear and nonlinear stages of optical guiding by a ribbon electron beam are studied in the quasi-optical approximation. It is shown that a surface leaky mode is excited at the linear stage. At the nonlinear stage, the wave beam broadens and the electromagnetic energy is radiated to

the infinity. This process is accompanied with stochastic deceleration of the particles interacting with the ensemble of waves propagated at different angles to the axis of the system. The resulting efficiency of energy exchange is much higher than that under traditional conditions when the field structure is determined by external electrodynamic systems.

The superradiance effects [11-16] occur in a cluster of electrons forming the active resonators. As a consequence of developing nonthreshold superradiance instabilities the energy of oscillatory motion is radiated in the form of short electromagnetic pulses. If the translational velocity of the cluster is close to the velocity of light the superradiance frequency may exceed the oscillation frequency significantly. The growth rates of superradiation instabilities are found for different oscillator types (cyclotron, undulator) and the saturation mechanisms are analysed.

1. OPICAL GUIDING EFFECTS

Consider a two-dimensional FEL model. Assume that the oscillatory motion is imparted to the electrons passing through a plane undulator whose magnetic field is specified by the vector potential

$$\vec{A}_u = Re\left[\vec{y}_0\, A_u\, ch(h_u x)\, e^{i h_u z}\right], \qquad (1)$$

where $h_u = 2\pi/d$ and d is the undulator period. The electrons are injected near the undulator axis (x=0) and the longitudinal particle velocity $V_{\parallel} = \beta_{\parallel} C$ is directed along the Z-axis. Let the electromagnetic field be a quasi-optical monochromatic beam

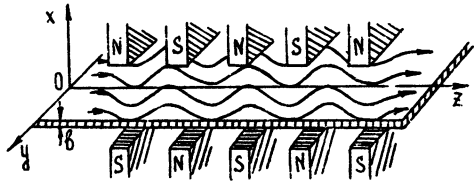

Fig.1. Scheme of FEL with plane undulator and ribbon electron beam.

propagating along the axis of the system

$$\vec{A}_s = Re\left| \vec{y}_0 \, A_s(z,x)\, e^{i(\omega_s t - h_s z)} \right|, \quad h_s = \omega_s / c . \tag{2}$$

Assume that the conditions of the combination synchronism $\omega_s = h_c V_{11}$, $h_c = h_s + h_u$ are fulfilled. Under such conditions the electron-wave interaction is described by a set of averaged equations of particle motion and by the parabolic equations for the wave amplitude:

$$\frac{d^2\theta}{dZ^2} = Im(\alpha e^{i\theta}), \tag{3}$$

$$i\frac{\partial^2 \alpha}{\partial X^2} + \frac{\partial \alpha}{\partial Z} = 2i\delta(X) j \tag{4}$$

with the boundary conditions

$$\theta\big|_{Z=0} = \theta_0 \in [0, 2\pi], \quad \frac{d\theta}{dZ}\Big|_{Z=0} = -\Delta, \quad \alpha\big|_{Z=0} = \alpha_0(X) \tag{5}$$

We have assumed that the relative changes of electron energy are small and neglected the Coulomb interaction of electrons.

Equations (3)-(5) employ the following normalized variables: $Z = (\omega_s/c)\, z\, G$ and $X = (\omega_s/c)\, x\sqrt{2G}$ are longitudinal and transverse coordinates, $\alpha = \mu \alpha_s \alpha_u G^{-2}/2$ is the wave amplitude, $\mu = \gamma_0^{-2}\beta_{11_0}^{-3}$, $\theta = \omega_s t - h_c z$ is the electron phase relative to the combination wave, $j = 1/2\pi \int_0^{2\pi} e^{-i\theta} d\theta_0$ is the amplitude of the first harmonic of HF current, $\Delta = \left(c/V_c^{min} - c/V_{11_0}\right) G^{-1}$ is the initial mismatch of the combination synchronism, and $V_c^{min} = \omega_s / h_c$ is the phase velocity of the combination wave which corresponds to the electromagnetic wave propagated strictly along the Z-axis, $\alpha_{s,u} = e A_{s,u}/mc^2\gamma_0$,

$$G = 1/2^{1/5}\left(\mu \alpha_u^2 \omega_{b\perp}^2 / 8\omega_s c \beta_{11_0}^2\right)^{2/5} \tag{6}$$

is the gain parameter, $\omega_{b\perp} = \sqrt{\frac{4\pi e^2 \sigma_0}{m\gamma_0}}$ is the "transverse" plasma frequency, σ_0 is the unperturbed electron surface density, and $\delta(X)$ is the delta function. We study here the case of thin ribbon electron beam, corresponding to a small Fresnel parameter $b^2/\lambda L \ll 1$, where b is the electron beam width, L is the characteristic length of the interaction space (reverse increment), and λ is the wavelength.

From Eqs.(3),(4) we have the law of energy conservation

$$dP/dZ = 8\, d\hat{\eta}/dZ = 4|\alpha|\big|_{X=0} |j| \sin\varphi , \tag{7}$$

where $P = \int_{-\infty}^{\infty} |a|^2 dX$ is the longitudinal flux of electromagnetic energy, $\eta = 1/2\pi \int_0^{2\pi} u\, d\theta_0$ is the normalized efficiency, $U = \frac{\partial\theta}{\partial Z} + \Delta$ are the normalized losses of particle energies, and $\varphi = \arg a|_{X=0} - \arg j$ is the current phase relative to the phase of the electromagnetic field.

Having linearized the equation of motion in the small signal approximation $a \ll 1$ we obtain the equation for the amplitude of the HF current

$$\left(\frac{\partial}{\partial Z} - i\Delta\right) j = -a . \tag{8}$$

Let us consider first the axial infinite system. For such a system representing the solution of Eqs.(4),(8) in the form $j = \hat{j} e^{i\Gamma Z}$, $a = \hat{a} e^{i\Gamma Z - i\varkappa|X|}$ we have a dispersion equation [7,9]

$$\varkappa \left[\varkappa^2 - \Delta\right]^2 = i , \tag{9}$$

where $\varkappa$ and $\Gamma = \varkappa^2$ are normalized transverse and longitudinal wave numbers. The roots of the dispersion equation (9) are readily found for exact synchronism $\Delta = 0$

$$\varkappa_n = e^{i(\pi/10 + 2\pi(n-1)/5)}, \quad \Gamma_n = e^{i(\pi/5 + 4\pi(n-1)/5)}, \tag{10}$$

where $n = 1 - 5$. Thus in our system there exist five normal waves. But among these modes there is only one guiding mode $n = 5$ which is amplified in the longitudinal direction ($\mathrm{Im}\,\Gamma < 0$), is damped in the transverse direction ($\mathrm{Im}\,\varkappa < 0$), and has the electromagnetic energy flux directed from electron beam to the periphery ($\mathrm{Re}\,\varkappa > 0$).

Figure 2 shows the transverse and longitudinal wave numbers of the guiding mode for an arbitrary value of the mismatch parameter. The maximal increment of the wave is attained when $\Delta = 0$. The phase velocity of the electromagnetic wave $V_{ph} = \omega_s / C(1 - \mathrm{Re}\,\Gamma)$ is smaller than the velocity of light C in the region $\Delta < 0.4$ and is larger than C in the region $\Delta > 0.4$.

According to Fig.2a the larger parameter Δ, i.e. the greater difference between the drift electron velocity $V_{\parallel_0}$ and the minimal velocity of the combination wave V_c^{min}, the larger the real part of the transverse wave number and the smaller the imaginary part. This means that increased Δ results in increasing transverse energy flux and in increasing scale of

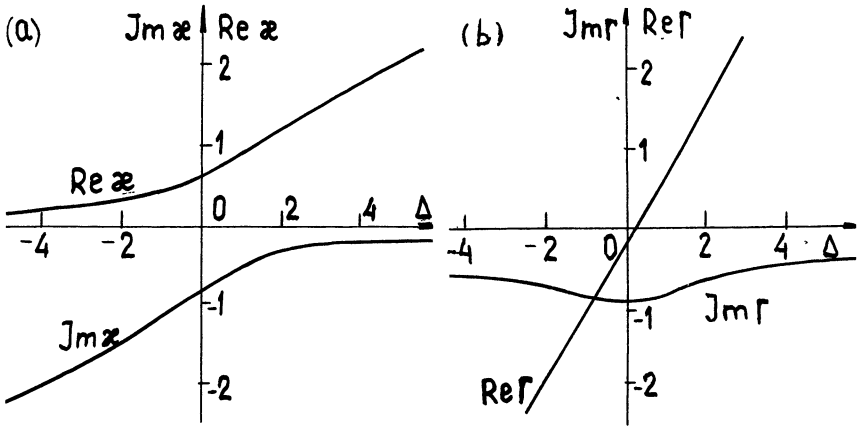

Fig.2. Real and imaginary parts of transverse (a) and longitudinal (b) wave numbers of canalized eigenmode vs Δ

field localization. In asymptotic case $\Delta \gg 1$ we have $|\mathrm{Re}\,æ| \sim \Delta^{1/2}$, $|\mathrm{Im}\,æ| \sim \frac{1}{2\sqrt{2}}\,\Delta^{-3/4}$. Thus the eigenmode is the sum of two plane waves radiated at such angles ψ to the axis that the phase velocity of the corresponding combination wave

$$V_c = \frac{\omega_s}{h_u + \omega_s |C| \cos\psi} \qquad (11)$$

is equal to the electron drift velocity. The guiding effect in this regime almost vanishes. On the contrary in the region of large negative Δ, the energy flux tends to zero ($\mathrm{Re}\,æ \to 0$), the scale of field localization diminishes and the interaction becomes purely reactive.

Now using the set of linear Eqs.(4),(8), we consider a boundary value semi-infinite problem on the plane wave $a_0(X) = \mathrm{const}$ diffraction incident on a layer of electrons in the cross-section $Z = 0$. This solution has been obtained using Laplace transformation along the Z-coordinate. On the assumption that $\Delta = 0$ we have [9]

$$a(Z,X) = a_0\left[\Phi\left(\frac{\sqrt{i}|X|}{2\sqrt{Z}}\right) + \frac{1}{5}\sum_{n=1}^{5} e^{-i æ_n |X| + i \Gamma_n^2 Z}\left(1 - \Phi\left(\frac{\sqrt{i}X}{2\sqrt{Z}} - æ_n\sqrt{iZ}\right)\right)\right]. \qquad (12)$$

Here $\Phi(u)$ is the probability integral. Employing the asymptotic representation of this integral for high values of arguments, we obtain from (12) that the spatial structures of the field, spaced from the input section at a distance much larger than the reverse increment ($Z \gg 1$), is determined by the excitation of the guiding eigenmode

$$a(Z,X) \to 2/5\, a_0\, e^{-i\varkappa_s |X| + i\Gamma_s Z}.$$

Numerical simulation of Eqs.(3)-(5) confirms the conclusion that for an arbitrary initial wave beam profile the structure and the angular spectrum $S_\varkappa = 1/\sqrt{\pi} \int_{-\infty}^{\infty} a\, e^{-i\varkappa X} dX$ of the radiated field are close to the structure of the localized eigenmode in the region of linear amplification rather far from the input cross-section ($Z \sim 5$ in Fig.3 and $Z \sim 10$ in Fig.4). Thus, the optical guiding of radiation by an electron beam takes place in the region of linear amplification. According to the results presented above, part of the electromagnetic energy escapes the electron channel $\mathrm{Re}\,\varkappa > 0$. As a result, in the region where the saturation effects are significant ($Z > 10$ in Fig.3 and $Z > 15$ in Fig.4) and the field amplitude in the axial zone is stabilized, the wave beam broadens, because the rays emitted by the electrons in the preceding cross-section arrive at the periphery. At a nonlinear stage there exists a rather extended region of diffraction radiation into outer space where the electromagnetic energy generated by the electron beam is radiated to the infinity.

The electron-wave interaction at the final stage ($Z > 40$ in Fig.3 and $Z > 100$ in Fig.4) is purely reactive: a steady state is established when the electrons trapped by the wave produce HF current with nearly constant amplitude due to strong particle mixing inside the phase space "bucket" bounded by the separatrix and with the phase ψ relative to the field phase being close to π (Fig.3d,4d), i.e. there is no energy exchange (see Eq.(7)). Due to the effect of complete internal reflection, a small part of radiation energy is still canalized by the electron beam.

It should be noted that in the case of radiation into free space the efficiency grows with increasing initial mismatch (see Fig.5).The increase in efficiency is caused by the effect of stochastic particle deceleration that becomes significant at $\Delta \gg 1$

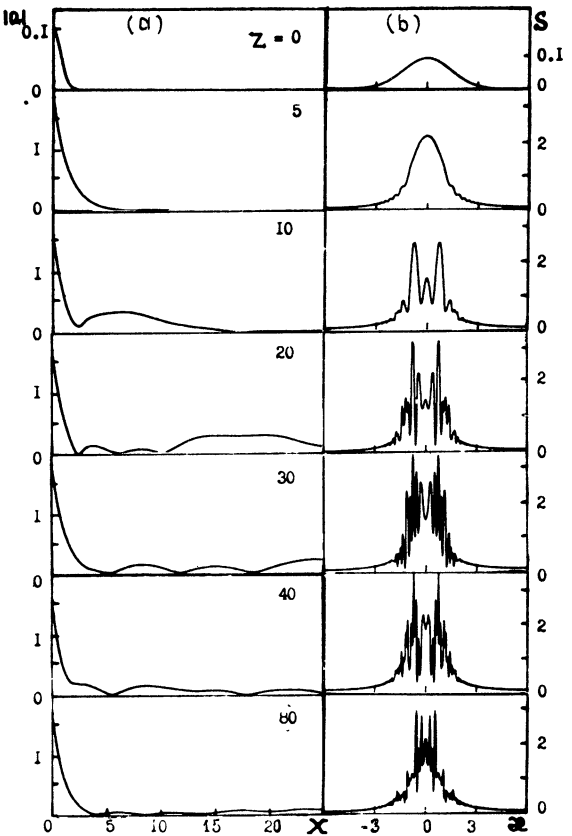

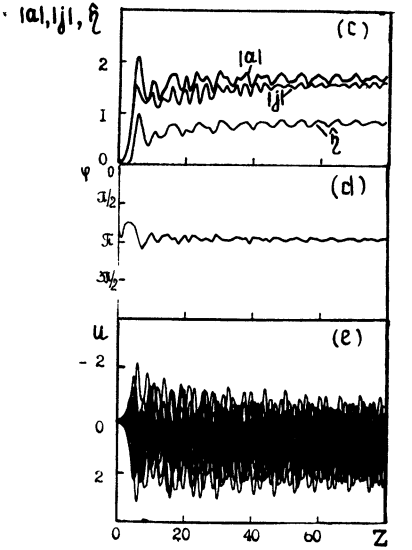

Fig.3. Wave beam profile (a), angular spectrum (b), amplitude of HF field acting on the electrons, amplitude of HF current, efficiency (c), difference phase (d), and relative losses of particle energy (e) as functions of longitudinal coordinate; $\Delta = 0$.

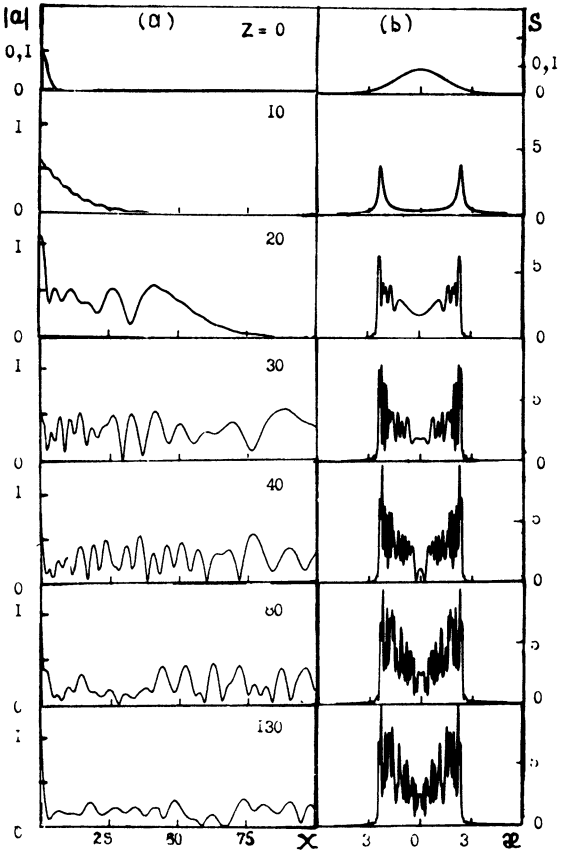

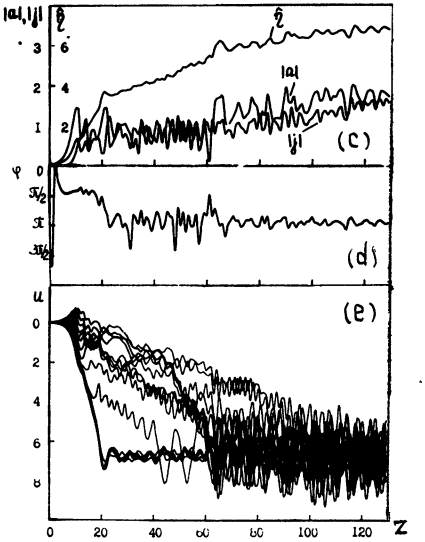

Fig.4. Same as Fig.3; Δ =6.

(the region $15 < Z < 100$ in Fig.4e). The point is that the field radiated into free space at the nonlinear stage is, essentially, an ensemble of random-phase waves propagating at differnt angles ψ (see Fig.4b). Each electromagnetic wave

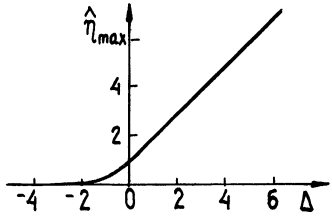

Fig.5. Maximal normalized efficiency versus initial mismatch from synchronism.

corresponds to a certain velocity of the combination wave (see Eq.(11)) which is resonant with the electrons. At the linear stag the electron beam radiates mainly waves for which $V_c(\psi) = V_{\parallel_0}$ (see the spectrum maxima in Fig.4b $Z \sim 10$). Then at the nonlinear stage ($Z > 15$) the spectrum is fulfilled with components that correspond to the smaller angles ψ and to the smaller phase velocity of the combination waves. The electrons being decelerated stochastically interact consecutively with different components of the combination wave packet until the average velocity of all electrons (cf. Figs.3e and 4e) becomes equal (taking into account electron detuning) to the phase velocity V_c^{min} of the slowest component that corresponds to the electromagnetic wave propagating strictly along the Z-axis: $\psi = 0$. This is the reason why the greater the initial difference between the particle velocity $V_{\parallel_0}$ and V_c^{min}, i.e. the larger the parameter Δ, the higher the efficiency.

The nonlinear stage of interaction was investigated in Ref.[9] without the assumption that relative losses of electron energy are small. It was obtained that under the condition of radiation into free space the electron efficiency may exceed 50%. This value is significantly higher than that found in conventional schemes [17,18], where the transverse structure of the HF field is determined by external electrodynamic systems. On the other hand, this efficiency is comparable with the values

attainable in tapered-undulator FELs [19]. However, in contrast to Ref. [19], the radiation into free space has a broad angular spectrum, which, naturally, impedes its practical use.

Note that the stimulated radiation of electrons moving along helical trajectories in a homogeneous magnetic field into free space [10] and Cerenkov radiation of straightforward electron beams in dielectric medium or plasma have similar characteristics. Thus we have optical guiding regime at the linear stage of interaction and wave beam broadening and stochastical particle deceleration at the nonlinear stage.

2. SUPPERADIANCE EFFECTS

Coherent radiation of a short electromagnetic pulse by an ensemble of inverted two-level molecules due to stimulated processes is well known in quantum electronics as the Dicke superradiance [20-22]. A classical analog of superradiance is radiative instability in spatially localized ensembles of electron-oscillators having an infinite (neglecting collisions) lifetime. We consider here superradiance of cyclotron oscillators and oscillators excited by electromagnetic pump wave or undulator field.

a) Cyclotron Superradiance

We assume that cyclotron oscillators form a layer which is unbounded in the x,y-directions and has the width δ along the z-axis. The electrons rotating in a homogeneous magnetic field: $\vec{H}_0 = H_0 \vec{z}_0$ have equal transverse momenta $p_{\perp 0} = m\gamma V_{\perp 0}$ and are (to an accuracy of small fluctuations) distributed uniformly in the cyclotron rotation phases at the initial moment of time. The electrons have no translational velocity.

The particle motion will be described by the following equations

$$\frac{dp_+}{dt} - i\omega_H p_+ = -e E_+(z,t), \qquad (13)$$

where $p_+ = p_x + ip_y$ $E_+ = E_x + iE_y$, $\omega_H = eH_0/mc\gamma$ is the relativistic

gyrofrequency, and $\gamma = \left(1+|P_+|^2/m^2c^2\right)^{1/2}$ is the relativistic mass-factor. The layer will radiate circularly-polarized waves in the $\pm z$ directions:

$$E_+ = -2\pi/c \int_{z-ct}^{z+ct} j_+ (z', t-|z-z'|/c)\, dz', \qquad (14)$$

where $j = e\rho_0 \langle V_+ \rangle$ is the electron current density, $V_+ = V_x + i V_y$ and $\langle \ldots \rangle$ denotes the averaging over the initial phases of cyclotron rotation. We will now assume that the electrons are subrelativistic ones, $\gamma \simeq 1+|P_+|^2/2m^2c^2$, and radiate near the nonrelativistic gyrofrequency $\omega_{H_0} = eH_0/mc$. Representing $E_+ = A(z,t)e^{i\omega_{H_0}t}$ and $P_+ = \hat{P} e^{i\omega_{H_0}t}$ we reduce the set of Eqs.(13),(14) to the form *

$$\frac{\partial \mathcal{P}}{\partial \tau} + i\mu |\mathcal{P}|^2 \mathcal{P} = a, \qquad \mathcal{P}|_{\tau=0} = e^{i(\theta_0 + \tau\cos\theta_0)}, \quad \theta_0 \in [0, 2\pi], \qquad (15)$$

$$a = I \int_{Z-\tau}^{Z+\tau} f(Z) \left\langle \mathcal{P}(Z', \tau - |Z-Z'|) \right\rangle e^{-i|Z-Z'|}\, dZ'. \qquad (16)$$

Here $\tau = \omega_{H_0} t$, $Z = \omega_{H_0}/c\, z$, $\mathcal{P} = \hat{P}/P_{i_0}$, $a = eA/m\omega_{H_0}V_{i_0}$, $I = \omega_e^2/2\omega_{H_0}^2$, $\mu = V_{i_0}^2/2c^2$ is the nonisochronity parameter, $\tau \ll 1$ is the parameter characterizing the initial electron modulation over the cyclotron rotation phases, and $f(Z)$ is the function describing the distribution of electron density in the layer. Below we assume a uniform distribution of density: $f(Z) = \text{const}$.

In the small signal approximation we obtain the characteristic equation from Eqs.(15),(16) to determin the frequencies Ω and spatial structures of the eigenmodes

$$e^{2ih_i B} = \left(\frac{h_e - h_i}{h_e + h_i}\right)^2. \qquad (17)$$

Here $B = \omega_{H_0}/c\, b$, and the normalized wave numbers inside and outside the layer are given by the relations

$$h_e = -(\mu - \Omega - 1), \quad h_i = \left(h_e^2 - 2I h_e (\Omega - \mu)/\Omega^2\right)^{1/2}. \qquad (18)$$

---

*) The set of Eqs.(15),(16) is rather universe and describes the superradiance in the layers of the oscillators of different physical nature including acoustic oscillators (cf.Ref.[23]).

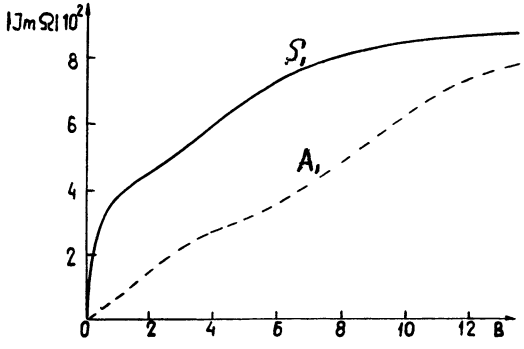

Fig.6 Increments of first symmetric S_1 and first antisymmetric A_1 modes versus layer width; μ =0.1, I =0.1.

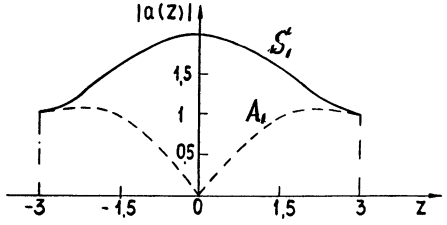

Fig.7 Spatial structures of modes; μ =0.1, I =0.1, B =6.

For the case of thin layer $B \ll 1$ Eqs.(17),(18) yield [15]

$$\Omega^2 - iIB\Omega + i\mu IB = 0 . \qquad (19$$

For a small layer density $I \ll 1$,we obtain for the instability increment

$$|\mathrm{Im}\,\Omega| = \sqrt{IB\mu/2} . \qquad (20)$$

The increments of symmetric and antisymmetric modes as a function of the layer width are shown in Fig.5. Here the maximum increment belongs to the first (fundamental) symmetric mode (when $B \ll 1$, its increment is determined by Eqs.(20)). The increments of other modes approach the increment of the fundamental mode as the layer width increases. Figure 7

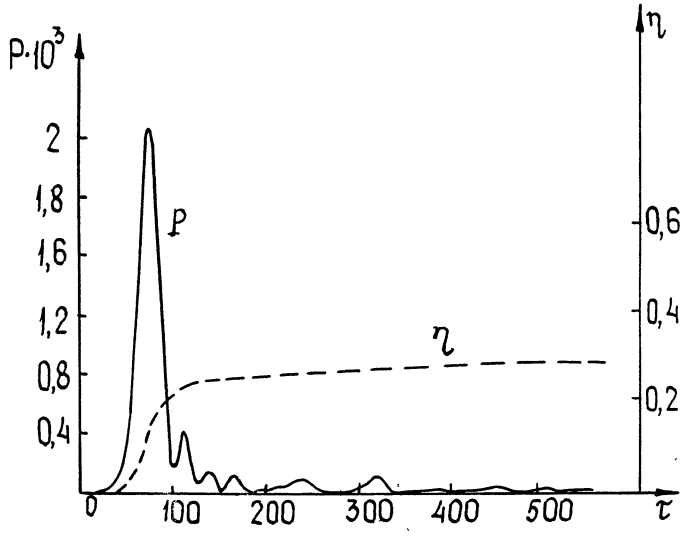

Fig.8 Radiation power and electron efficiency versus time; $\mu = 0.1$, $I = 0.1$, $B = 6$.

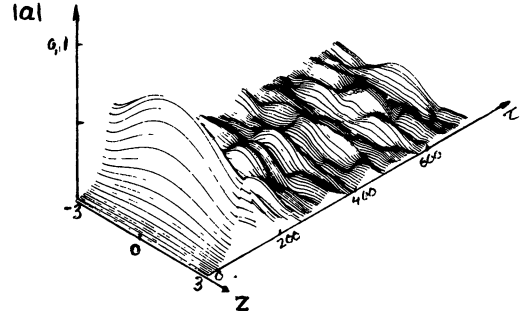

Fig.9 Evolution of distribution of electric field amplitude $\mu = 0.1$, $I = 0.1$; $B = 6$.

illustrates spatial structures of the eigenmodes.

The nonlinear stage of the cyclotron superradiative instability was investigated by numerical simulation of Eqs.(15), (16). The time dependence of the radiation power $P = |a|^2|_{\chi = \pm B/2}$ and the total electron efficiency: $\eta = 1 - \frac{1}{B}\int_{-B/2}^{B/2} \langle |\mathcal{P}|^2 \rangle dz$ is given in Fig.8 . Note that the peak power and the pulse

duration of superradiance grow with the layer thickness. Figure 9 displays the formation of the spatial structure of the fundamental symmetric mode at the initial linear stage of radiation , $\tau < 60$, and the stochastization of this structure at the nonlinear stage, $\tau > 60$.

In conclusion we will estimate numerically the peak power of the cyclotron superradiation and the pulse duration. Let the magnetic field strength be equal to 100 kOe, the radiation frequency $\omega \simeq 1.9 \cdot 10^{12}\ s^{-1}$ (the wavelength $\lambda \simeq 1$mm), the electron density $\rho_0 = 2 \cdot 10^{14}\ cm^{-3}$, the rotational velocity of electrons $V_\perp = 0.45c$, and the layer width $b \simeq 2\lambda\ (B=12)$ .For these parameters the power radiated by one squared centimeter of the layer surface amounts to 1.4 GW . The pulse duration of the superradiance is about $1.5 \cdot 10^{-11}\ s$ at the level e^{-1} from the peak power.

Note that it is possible to essentially increase the superradiance power and to shift the frequency to the short-wave part of the spectrum by imparting the translational velocity (approximating the light velocity) to the electrons.

b) Superradiative Instability of an Electron Cluster Moving in an Undulator or Electromagnetic Pump Fields.

let us consider a one-dimensional model [13]. Assume that the electron cluster is a layer that is unbounded in the transvers directions and has a width b in the z-direction. Assume also that the electron layer moves along the z-axis with a translational velocity $V_\parallel$ .Let an intense pump plan wave propagate towards the translational particle motion and be specified by the vector-potential

$$\vec{A}_i = Re\left[\vec{y}_0\, A_i\, e^{i(\omega_i t + h_i z)}\right]. \qquad (21)$$

In a particular case when $\omega_i = 0$, $h_i = 2\pi / d$ the pump wave may be a periodic magnetostatic field.

We shall carry out our further analysis in the reference system K' moving with an unperturbed translational velocity of electrons. Then the field radiated (scattered) by the electron plasma oscillating in the pump field (21) can be represented as

$$\vec{A}'_s = Re\left[\vec{y}_0 A'_s(z') e^{i\omega'_s t'}\right]. \qquad (22)$$

When the resonance conditions $\omega'_s \approx \omega'_i = (\omega_i + h_i V_{||})\gamma$ are met a combined effect of the fields (21) and (22) on the electrons results in the emergence of an averaged ponderomotive force and in longitudinal electron bunching. Taking into account the Coulomb repulsion field E'_z of particles the axial motion in the linear approximation will be described by the following equations

$$\frac{\partial V'_z}{\partial t'} = -\frac{e^2}{2m^2c^2}\frac{\partial}{\partial z'} Re\left[A'_s A'_i e^{i(\Delta\omega' t' - h'_i z')}\right] + \frac{e}{m} E'_z ,$$

$$\frac{\partial \rho'}{\partial t'} + \rho_0 \frac{\partial V'_z}{\partial z'} = 0 , \qquad \frac{\partial E'_z}{\partial z'} = 4\pi\rho' , \qquad (23)$$

where $\Delta\omega' = \omega'_s - \omega'_i$, ρ' are the electron density perturbations (the unperturbed static electron charge is compensated by the ion background).

Representing the perturbations of the density in the form $\rho' = Re\left[\hat{\rho} e^{i(\Delta\omega t' - h'_i z')}\right]$ we can write the density modulation amplitude as

$$\hat{\rho} = -\frac{e^2\rho_0}{2m^2c^2\left[(\Delta\omega')^2 - \omega_\beta^2\right]}\left(\frac{\partial}{\partial z'} - i h'_i\right)^2 A'_s A'_i . \qquad (24)$$

Taking into account (24) the scattered field amplitude can be found from the wave equation

$$\frac{\partial^2 A'_s}{\partial z'^2} + \frac{\omega'^2_s - \omega'^2_\beta}{c^2} A'_s = -\frac{\omega'^2_\beta \omega'^2_i}{4\left[(\Delta\omega')^2 - \omega'^2_\beta\right]}\left(\frac{\partial}{\partial z'} - i h'_i\right)^2 A'_s A'_i \qquad (25)$$

with the following radiation boundary conditions at the ends of the electron layer:

$$\left[\frac{\partial A'_s}{\partial z'} + i\frac{\omega'_s}{c} A'_s\right]\Big|_{z'=b'} = 0 , \quad \left[\frac{\partial A'_s}{\partial z'} - i\frac{\omega_s}{c} A'_s\right]\Big|_{z'=0} = 0 , \qquad (26)$$

where $b' = b\gamma$ is the layer width in the moving reference system.

The solution of (25) is sought in the form

$$A'_s = C_1 e^{i h'_{s1} z'} + C_2 e^{i h'_{s2} z'} , \qquad (27)$$

where $C_{1,2}$ are arbitrary constants and $h_{s\,1,2}$ are the roots of the dispersion equation that follows from (25)

$$\left[h_s'^2 - \frac{\omega_s'^2}{c^2} + \frac{\omega_\beta'^2}{c^2}\right]\left[(\Delta\omega')^2 - \omega_\beta'^2\right] = -\frac{\omega_\beta'^2 \alpha_i'^2}{4}\left(h_s' - h_i'\right)^2 . \tag{28}$$

Substituting (27) into the boundary conditions (26) we obtain a characteristic equation determining the natural frequency of the layer:

$$e^{i(h_{s1}' - h_{s2}')b'} = \frac{(h_{s1}' - \omega_s'/c)(h_{s2}' + \omega_s'/c)}{(h_{s1}' + \omega_s'/c)(h_{s2}' - \omega_s'/c)} . \tag{29}$$

Our task is to prove that in the system considered there exist eigenmodes growing in time $\mathrm{Im}\,\omega_s < 0$. For simplicity we shall use dimensionless notations:

$$\bar{h}_{1,2} = h_{s\,1,2}'\, c/\omega_i' , \quad \Omega = \omega_s'/\omega_i' , \quad \delta = 1 - \Omega , \quad \bar{h}_i = h_i'\, c/\omega_i' ,$$

$$q = \omega_\beta'/\omega_i' , \quad p = \omega_\beta'/\omega_i'\, \alpha_i'/2 .$$

Then the dispersion equation (28) takes on the form

$$\bar{h}^2\left[\delta^2 - q^2 + p^2\right] - 2p^2\bar{h}_i\,\bar{h} + \left[-\Omega^2 + q^2\right]\left[\delta^2 - q^2\right] + p^2\bar{h}_i^2 = 0 . \tag{30}$$

It is natural to suppose that the eigenmode frequencies of the system are shifted from the pump field frequency by the magnitude of the order of the reduced plasma frequency, i.e.,

$$\delta = \pm\sqrt{q^2 - p^2} + \varepsilon , \quad |\varepsilon| \ll \sqrt{q^2 - p^2} . \tag{31}$$

Under this assumption the wave numbers of two normal waves can be represented according to (30) as

$$\bar{h}_1 = \left[1 \mp \sqrt{q^2 - p^2} - p^2/2 + (\bar{h}_i^2 - 1)/2\right]/\bar{h}_i , \tag{32}$$

$$\bar{h}_2 = \pm\frac{p^2\bar{h}_i}{\varepsilon\sqrt{q^2 - p^2}} - \bar{h}_1 .$$

Consequently, assuming $|\bar{h}_2| \gg 1$ we can reduce the characteristic equation (29) to the form

$$R = \exp\left[\mp i p^2\bar{h}_i\,\bar{b}/\varepsilon\sqrt{q^2 - p^2} + 2i\bar{h}_1\bar{b}\right] , \tag{33}$$

where

$$R=\frac{\bar{h}_1-1\mp\sqrt{q^2-p^2}}{\bar{h}_1-1\pm\sqrt{q^2-p^2}}\ ,\quad \bar{\beta}=\beta'\omega_i'/c\ . \tag{34}$$

If the layer density is sufficiently small $q,p<<1$ and the normalized wave number of the pump wave is close to unity (for example, for the undulator pump and the translational velocity of the cluster close to the velocity of light: $\bar{h}_i'=\gamma h_i$, $\omega_i'=\gamma\beta_{\parallel}h_i$ and $\bar{h}_i^2-1=\gamma^{-2}<<1$) the effective reflection coefficient will have the following form

$$R=\pm\sqrt{q^2-p^2}\,(\bar{h}_i-1)/2-p^2/4\ ,\ |R|<<1\ . \tag{35}$$

The solutions of (33) for ε will be written as

$$\varepsilon_n=\pm\frac{ip^2\bar{h}_i\bar{\beta}\,(|\ell n|R||-2i\bar{h}_1\bar{\beta}-2\pi in-i\varphi)}{\sqrt{q^2-p^2}\,\left[|\ell n|R||^2+(2\bar{h}_1\bar{\beta}+2\pi n+\varphi)^2\right]}\ , \tag{36}$$

where $n=0\pm1,\pm2\ldots$, $\varphi=\arg R$. Apparently, the assumption $|\varepsilon|<<\sqrt{q^2-p^2}$ holds if the layer width is sufficiently small

$$\frac{p^2\bar{\beta}}{(q^2-p^2)|\ell n|R||}<<1\ . \tag{37}$$

Taking into account (30) and (34) for the natural frequencies of the layer we have

$$\omega_{sn}'=\omega_i'\left[1\mp\sqrt{q^2-p^2}-\varepsilon_n\right]\ . \tag{38}$$

The upper sign in (38) corresponds to the modes growing in time, with the mode $n=0$ having the maximal increment:

$$|\mathrm{Im}\,\omega_{max}'|=\frac{\omega_\beta'\omega_i'\beta'\alpha_i'^2}{4\sqrt{1-\alpha_i'^2/4}\;c\,|\ell n|R||}\ . \tag{39}$$

It should be emphasized that we encounter here nonthreshold instability.

Taking into account the relation between the normal wave amplitudes

$$C_1/C_2=-(\bar{h}_2-\Omega)/(\bar{h}_1-\Omega)\ . \tag{40}$$

which follows from the boundary conditions (26), for the magnitude

of the electromagnetic energy flux of the fundamental mode $n=0$ we have

$$S' = \frac{c}{8\pi} \mathrm{Re}\left[E'_y H'^{*}_x\right] = \frac{\omega_i'^2}{8\pi c}\left|C_1\right|^2\left[2|R|^{(1-\bar{z}'/\beta')} - 1\right], \tag{41}$$

where $\bar{z}' = z'\omega_i'/c$. According to (41), when $|R| << 1$ the energy flux propagates along the negative direction of the z-axis in the greatest part of the layer length $\bar{z}' < \bar{z}'_* = 1 - \ln\frac{1}{2}/\ln|R|$ and has a positive direction only in a small portion $\bar{z}' > \bar{z}'_*$. Nevertheless, in the moving reference system the energy flux radiated by the layer along the positive direction of the z-axis is slightly larger than that in the opposite direction:

$$\left|S'\right|_{\bar{z}'=\beta'} \Big/ \left|S'\right|_{\bar{z}'=0} = \frac{1}{1-2R}. \tag{42}$$

We shall now consider the superradiance of a moving electron layer in the laboratory reference system K. While in the moving reference system K' the frequencies radiated by the layer in the $\pm$ z'-directions coincided and were determined by (38), in the laboratory system, when the translational velocity of the cluster $V_{\parallel}$ is close to the velocity of light, these frequencies differ significantly:

$$\omega_{sn}^{\pm} = \gamma\left(1 \pm \beta_{\parallel}\right) \mathrm{Re}\,\omega'_{sn},$$

$$\omega_s^{\pm}(n=0) = \frac{1}{1 \mp \beta_{\parallel}}\left[\omega_i + K_i V_{\parallel} - \omega_b/\gamma^{3/2}\sqrt{1-\alpha_i^2/4}\right]. \tag{43}$$

Since the number of radiated quanta is an invariant of the Lorentz transform the energy radiated by the moving layer in the positive direction of the z-axis is much higher than that radiated in the opposite direction. Consequently, the radiated power, i.e., the energies radiated per unit time are related as

$$\frac{P^+}{P^-} = \frac{1+\beta}{1-\beta}\,\frac{\left|S'\right|_{\bar{z}'=\beta'}}{\left|S'\right|_{\bar{z}'=0}} \simeq 4\gamma^2. \tag{44}$$

It should be taken into account that the radiation emitted by the moving layer in a time dt_{rad} passes across the fixed areas to the left and to the right of the layer during the period

[24] $dt^{\pm} = (1 \mp \beta)\, dt_{rad}$. Then the energy fluxes (Pointing's vectors) across the fixed areas will be related as

$$\left| \frac{S^{+}}{S^{-}} \right| = \frac{(1+\beta)^2}{(1-\beta)^2} \frac{|S'|_{z'=b}}{|S'|_{z'=0}} \simeq 16\gamma^4. \qquad (45)$$

Thus, in the laboratory system the main part of radiated energy is concentrated in the short-wave component. The energy of the translational motion of particles is, obviously, the principal source of radiated energy.

The superradiative instability investigated above can emerge in a real experiment if the condition

$$|\mathrm{Im}\,\omega'_s|\, T' \gg 1 \qquad (46$$

is met, where $T' = L/c\gamma^{-1}$ and L is the length of the pump region (the undulator length) in the laboratory reference system.

Let us estimate the increment of superradiative instability as applied to the electron cluster formed in a Stanford linear accelerator [25]: $b = 1$ mm, $\gamma = 85$, $\omega_b = 7\ 10^9\ s^{-1}$. With the undulator parameter $a_i = 1$ and the undulator period $d = 3$cm ($\omega'_i = 5\ 10^{12}\ s^{-1}$), for the fundamental mode we obtain $|1 - \mathrm{Re}\,\omega'_s / \omega'_i| \simeq 1.2 \cdot 10^{-4}$, and $|\mathrm{Im}\,\omega'_s| = 1.5 \cdot 10^{10}\ S^{-1}$. Thus, a e-fold increase of perturbations will occur for the undulator length $L \simeq 1.7$ m Along the total length $L \simeq 5$ m of the undulator used in the experiment [25] the perturbations will grow e^3-fold.

REFERENCES

1. N.F.Kovalev,M.I.Petelin // in: Relativistic High-Frequency Electronics, Inst. Appl. Phys. Acad. Sci. USSR, Gorky, 1981, v.2, p.63.
2. C.M.Tang,P.Sprangle // in: Free-Electron Generators of Coherent Radiation. Phys. of Quant. Electr.,v.9,1982,p.627.
3. D.Prosnitz, R.A Haus , S.Doss, R.I.Gellinas // ibid p.1047.
4. N.S.Ginzburg, N.F.Kovalev, N.Yu.Rusov, //Opt. Comm.1983 v.46,p.300.

5. E.T.Sharlemann, A.M.Sessler, J.S.Wurtele // Phys.Rev.Lett. 1985, v.54, p.1925.
6. G.T.Moore // Opt.Comm. 1985, v. 52, p.46.
7 N.S.Ginzburg, N.F.Kovalev // Pis'ma v ZhTF, 1988, v. 13, p. 234
8 N.S.Ginzburg, A.S.Sergeev // Pis'ma v ZhTF, 1988, v. 14, p. 1844.
9 N.S.Ginzburg, M.A.Gorshkova, A.S.Sergeev // Opt.Comm., 1989, v. 70, p.218; 1990, v.76, p.69.
10. N.S.Ginzburg, Fizika Plazmy, 1984, v.15, p.1279.
11. R.H. Bonifacio, C. Maroli, N. Piovella // Opt.Comm., 1988, v. 68, p.369..
12. V.V.Zheleznyakov, V.V.Kocharovsky, Vl.V.Kocharovsky // Izv. VUZov. Radiofizika, 1986, v. 24, p .1095.
13. N.S.Ginzburg // Pis'ma v ZhTF, 1988, v. 14, p. 440.
14. Yu.A.Iljinsky, N.S.Maslova // ZhETF, 1988, v. 94, p. 171.
15. N.S.Ginzburg, I.V.Zotova // Pis'ma v ZhTF, 1989, v.15, N 14, p. 63.
16. N.S.Ginzburg, Yu.V.Novozhilova // Pis'ma v ZhTF, 1989, v. 15, N 19, p. 60.
17. W.B.Colson // Phys.Rev., 1977 , v. A 64, p. 98.
18. V.L.Bratman, N.S.Ginzburg, M.I.Petelin // Zh. Eksp. Teor. Fiz.,1979, v,76, p.930.
19. N.M.Kroll, P.L.Morton, M.N.Rosenbluth et al. // IEEE J.Quant.Electr., 1981, v. 17, p. 1436.
20. R.H.Dicke // Phys.Rev., 1954, v. 93, p. 99.
21. A.V.Andreev, V.I.Emeljanov, Yu.A.Iljinsky // Usp. Fiz. Nauk, 1980, v.131, p.653.
22. V.V. Zheleznyakov, V.V. Kocharovsky, Vl.V. Kocharovsky //Usp. Fiz. Nauk, 1989, v.159, p.194.
23. U.Ya.Kobelev, L.A.Ostrovsky, I.A.Soustova // Izv. VUZov. Radiofizika, 1986, v. 24, p. 1129.
24. V.V.Zheleznyakov // Electromagnetic waves in space plasma. M., Nauka, 1973.
25. D.A.G.Deacon, L.R.Elias, J.M.J.Madey et al . // Phys. Rev. Lett., 1977, v. 38 , p. 892.

CANALIZATION OF RADIATION BY TRANSVERSELY BOUNDED BEAM-PLASMA SLAB

N. I. Karbushev, A. D. Shatkus
Moscow Radiotechnical Institute of Ac. Sci. of the USSR,
113519 Moscow, USSR

In theory of the interaction of transversely bounded electron beam and plasma the transverse structure of the excited field is usually proposed to be fixed and do not depend on the beam density. And the energy flux is considered to have only one component in direction of the electron beam propagation. But an electron beam with bounded cross-section in plasma distorts the transverse structure of perturbations [1], and the excited waves have an ability to leave the region, occupied by a beam, radiating in the transversal direction [1, 2]. As a result, the field of perturbations is concentrated nearby the electron beam, leading to the effect of canalization of unstable waves. In case of the waves canalization the dependence of the maximum growth rate on parameters of the beam-plasma system can change, qualitatively differing from analog one in case of the classical beam-plasma instability [3, 4].

In the present work an instability, developing in the magnetized ribbon beam-plasma slab of an infinite width, is investigated in linear approarch. It is shown that at sufficiently small thickness of the slab with increasing of the density of the ultrarelativistic electron beam the effect of canalization of the excited waves begins to take place. Here the maximum growth rate of the instability is reached in the frequency region, where the beam velocity exceeds the phase velocity of the plasma wave, and is proportional to the beam density in power 3/4. In conditions of canalization the ratio of the transversal component of the Poynting vector to the longitudinal one increases out of the slab, what shows an increase of waves radiation in the transversal direction.

It is proposed that the plasma and the beam with homogene-

ous densities n_p and n_b fill the slab $|x|<d$. The velocity of the monoenergetic beam equals to u. The external magnetic field, directed along the axis z, is so strong that the motion of plasma and beam electrons is onedimensional. The motion of ions and thermal velocities of particles are neglected.

In such conditions from Maxwell equations it follows, that E_z the longitudinal component of the electric field of perturbations, proportional to the factor $\exp(-i\omega t + i\kappa z)$, with the frequency ω and the wave vector κ submits to the equation

$$d^2E_z/dx^2 - \varepsilon(\kappa^2 - \omega^2/c^2)E_z = 0, \qquad (1)$$

where $\varepsilon = 1 - \omega_p^2/\omega^2 - \omega_b^2/\gamma^3(\omega - \kappa u)^2$ - dielectric permittivity of the slab, $\omega_{p,b} = (4\pi e^2 n_{p,b}/m)^{1/2}$ - langmuire frequencies of the plasma and the beam correspondingly, $\gamma = (1 - u^2/c^2)^{-1/2}$ - relativistic factor of beam electrons, e and m - charge and mass of electron, c - speed of light. Here the transversal components of the electric E_x and the magnetic B_y fields are nonzero.

The solution of the equation (1), symmetric relative to the plane $x = 0$, can be presented in form

$$E_z = E_0 \begin{cases} \cos(\varkappa x\sqrt{-\varepsilon}), & |x|<d, \\ \cos(\varkappa d\sqrt{-\varepsilon})\exp[\varkappa(d-|x|)], & |x|>d, \end{cases} \qquad (2)$$

where $\varkappa^2 = \kappa^2 - \omega^2/c^2$, E_0 - some constant. The function (2) is continuous on the slab boundary $|x| = d$. If jet one boundary condition, the derivative dE_z/dx continuity for $|x| = d$ is utilized, we come to the dispersion equation [5]

$$ctg(\varkappa d\sqrt{-\varepsilon}) = \sqrt{-\varepsilon}. \qquad (3)$$

In this case the components of the Poynting vector, characterizing the energy flux (radiation of waves), out of the beam- plasma slab for $Im\,\omega = 0$ are

$$S_z = \frac{\omega Re\,\kappa}{8\pi|\varkappa|^2}|E_z|^2, \quad S_x = -\frac{\omega Im\,\varkappa}{8\pi|\varkappa|^2}. \qquad (4)$$

Only those solutions of the dispersion equation (3) are physically correct, which in the limit $|x|\to\infty$ satisfy to the conditions of finiteness of the perturbations amplitude and radiating in transversal direction from the slab. Hence it follows that in relations (2), (3)

$$Re\,\varkappa > 0, \quad Im\,\varkappa \le 0. \qquad (5)$$

The case of a small thickness of the slab

$$|\varkappa\sqrt{-\varepsilon}|d \ll 1, \qquad (6)$$

when the amplitude of the perturbations electric field longitudinal component inside the slab is practically constant, is the most interesting. In accordance to (3) the inequality (6) is equivalent to the condition $|\sqrt{-\varepsilon}| \gg 1$, what corresponds to the low frequency region $\omega \ll \omega_p$. Then the dispersion equation (3) takes the form

$$d\sqrt{\kappa^2 - \omega^2/c^2}\left[\frac{\omega_p^2}{\omega^2} + \frac{\omega_b^2}{\gamma^3(\omega - \kappa u)^2}\right] = 1. \qquad (7)$$

In the absence of an electron beam ($\omega_b^2 = 0$) we find from here the wave vector of the plasma wave

$$\kappa_p(\omega) = (\omega/c)\sqrt{1 + \omega^2 c^2/\omega_p^4 d^2} \qquad (8)$$

Synchronism of the plasma wave with an electron beam, $\omega = \kappa_p(\omega)u$, takes place on the frequency

$$\omega = \omega_0 = \omega_p^2 d/\gamma u \ll \omega_p. \qquad (9)$$

In the presence of a low density electron beam, when the inequality

$$|\delta k| = |\kappa - \omega/u| \ll \omega/2\gamma^2 u \qquad (10)$$

is fulfilled, the well-known instability [3, 4] follows from the dispersion equation (7). Its growth rate is maximum at the synchronous frequency (9), and the solution, satisfying to the conditions (5), has the form

$$\delta\kappa = \frac{1 - i\sqrt{3}}{2}\left(\frac{\omega_p^2 d}{\gamma^3 u^2}\right)^{1/3} \nu^{1/3} \sim n_b^{1/3}, \qquad (11)$$

where the interaction paramefer $\nu = \gamma n_b/n_p \ll 1$ in accordance with (10). An electron beam of low density practically does not influence on the perturbations amplitude distribution in cross-section. The field localization scale nearby the slab surface is determined here by the value $(Re\,\varkappa)^{-1} \approx \gamma u/\omega_0 = d(\gamma u/\omega_p d)^2$

The condition (6) corresponds to the demand $\omega_0 d \ll \gamma u$, i. e. the beam-plasma slab thickness is small compare to the perturbations field localization scale.

At sufficiently great density of the ultrarelativistic electron beam with paramefers $\gamma^2 \gg 1$ and $\nu \gg 1$ instead of the inequality (10) an opposite one can be fulfilled, but the conditi-

on $|\delta k| \ll \omega/u$ can remained. Then $\varkappa \approx \sqrt{2\omega\delta k/u}$, and the dispersion relation (7) represents an equation of the forth power relatively to $\sqrt{\delta k}$:

$$\delta k^2 - \frac{\omega^{3/2} u^{1/2}}{\sqrt{2}\,\omega_p^2 d}\,\delta k^{3/2} + \frac{\omega^2 \omega_b^2}{\gamma^3 \omega_p^2 u^2} = 0. \qquad (12)$$

Introducing the dimensionless values

$$\Delta = \frac{\delta k^{1/2}\,\gamma^{9/8} u}{2^{1/4}\,\omega_p^{1/4}\,\omega_b^{3/4}\,d^{1/2}}, \qquad a = \frac{\omega^{1/2}\,\gamma^{3/8}\,u^{1/2}}{2^{1/4}\,\omega_p^{3/4}\,\omega_b^{1/4}\,d^{1/2}}, \qquad (13)$$

we rewrite the equation (12) in following shape:

$$f(\Delta, a) = \Delta^4 - a^3\Delta^3 + a^4 = 0 \qquad (14)$$

In high-frequency region, when $a \gg 1$, the solution of the equation (14) can be presented in form

$$\Delta_1 = a^3, \quad \Delta_2 = a^{1/3}, \quad \Delta_{3,4} = \frac{-1 \pm i\sqrt{3}}{2}\,a^{1/3}, \qquad (15)$$

Complex roots $\Delta_{3,4}$ do not satisfy to the first condition among (5) and mast be thrown off. Hence, in region of high frequencies an instability is absent.

In low-frequency region, where $a \ll 1$, the equation (14) has the following solution:

$$\Delta_{1,2} = \frac{1 \pm i}{\sqrt{2}}\,a, \qquad \Delta_{3,4} = -\frac{1 \pm i}{\sqrt{2}}\,a, \qquad (16)$$

Only one root among the first pair with the negative imagine part satisfys to the conditions of physical correctness (5). It corresponds to the amplification of perturbations and gives that

$$\delta k = -i\omega\omega_b / \gamma^{3/2}\,\omega_p u \qquad (17)$$

In the intermediate region of frequencies $a \sim 1$ such value of the parameter a exists, for which the function $f(\Delta, a)$ becomes equal to zero together with its derivative

$$\partial f/\partial\Delta = 4\Delta^3 - 3a^3\Delta^2 = 0 \qquad (18)$$

The joint solution of the equations (14), (18) gives

$$\Delta = 3a^3/4, \qquad a = a_{kp} = 2/3^{3/8}. \qquad (19)$$

It is easy to convince that the root (19) is doubly degenerated, and the frequency value

$$\omega = \omega_{kp} = \frac{\sqrt{2}\,\omega_p^{3/2}\,\omega_b^{1/2}\,d}{\gamma^{3/4} u}\,a_{kp}^2 = \frac{4\sqrt{2}}{3^{3/4}}\,\frac{\omega_p^2 d}{\gamma u}\,\gamma^{1/4} \gg \omega_b \qquad (20)$$

corresponds to the boundary between the regions of stability and instability of the beam-plasma slab.

Thus, the instability takes place in the frequency region $0 < \omega < \omega_{kp}$. The numerical solution of the equation (14) gives, that a maximum value of the growth rate

$$|Im\,k|_{max} \approx 1{,}97\,(\omega_p^2 d/\gamma^3 u^2)\,\nu^{3/4} \sim n_b^{3/4} \qquad (21)$$

is reached at the frequency $\omega_m = 0{,}78\,\omega_{kp}$. And hence, the value $\varkappa$, satisfying to the conditions (5), equals to

$$\varkappa = (2{,}18 - 1{,}28\,i)\,\frac{\omega_p^2 d}{\gamma^2 u^2}\,\nu^{1/2}. \qquad (22)$$

The last relation shows a rather strong dependence of the perturbations field localization scale nearby the slab surface $(Re\,\varkappa)^{-1} \sim d\,(\gamma u/\omega_p d)^2/\nu^{1/2} \sim n_b^{-1/2}$ on the electron density of a beam. It occures to be $\sqrt{\nu} \gg 1$ times less than the localization scale in case of the small parameter ν . The dependence of the maximum growth rate (21) on the beam density qualitatively differs from analog that in (11).

The angle of waves radiating out of the slab is determined by the ratio of the Poynting vector components (4). In case of canalization presence and the maximum growth rate (21) it equals to

$$tg\,\theta = S_x/S_z = -\,Im\,\varkappa/Re\,k \approx 0{,}66\,\nu^{1/4}/\gamma \qquad (23)$$

and $\nu^{1/4} \gg 1$ times exceeds the angle of waves radiating in absence of canalization $tg\,\theta = \gamma^{-1} \ll 1$.

Exponential decreasing of the perturbations field amplitude at moving off from the slab surface in the transversal direction in case of the radiation canalization is not conditioned by the absorbtion of waves or their screening (as in case of the canalization absence). It is mainly connected with the fact, that to the point with the transversal coordinate x the radiated wave comes from the beam-plasma slab section which is at a distance $x\,ctg\,\theta$ in the longitudinal direction from the observation plane. Because of the perturbations amplification its amplitude at a point with the larger value of x occures to be less. Such conclusions are confirmed by the relation

$$Re\,\varkappa \cdot Im\,\varkappa = Re\,k \cdot Im\,k, \qquad (24)$$

According to the conditions (6) and opposite to (10), the waves canalization by the beam-plasma slab with a maximum growth rate (21) takes place when inequalities

$$(\omega_p d/\gamma u)^2 \sqrt{\nu} \ll 1\,, \quad 1 \ll \sqrt{\nu} \ll 2\gamma^2, \qquad (25)$$

are fufilled and the slab thickness is small in comparision with the localization scale. If the slab thickness is so great, that the inequality (6) and the first of the inequalities (25) are violated, the dispersion equation (3) instead of (7) can be reduced to the well-known form [6 - 8]

$$K_\perp^2 + \left(K^2 - \frac{\omega^2}{c^2}\right)\left[1 - \omega_p^2/\omega^2 - \frac{\omega_b^2}{\gamma^3(\omega - Ku)^2}\right] = 0, \quad (26)$$

where $K_\perp \sim \pi/d$. In such conditions at the parameter $\nu = 4\omega_b^2/\gamma K_\perp^2 u^2 \gg 1$ the decrease of the localization scale $(\mathrm{Re}\,K)^{-1} \sim (\gamma u/\omega_p)\nu^{-1/2} < d$ takes place too. But the waves radiation in the transversal direction does not influence on the character of the maximum growth rate dependence on the beam density [7] $|\mathrm{Im}\,K|_{max} \sim (\omega_p/2\gamma^2 u)\nu$.

Note, that the canalization of radiation can be observed in the beam-plasma systems of the other configuration [9], and also in free-electron lasers [10 - 12], in dielectrics [13], [14] and in spacely periodic structures [15].

References

1. N. G. Popkov, Pis'ma ZhETF 39 (1984) 214.
2. A. N. Kondratenko, Pis'ma ZhTF 13 (1987) 1462.
3. A. I. Akhiezer and Ya. B. Faynberg, Dokl. AN SSSR 69 (1949) 555.
4. D. Bohm and E. Gross, Phys. Rev. 75 (1949) 1864.
5. N. I. Karbushev and A. D. Shatkus, Pis'ma ZhETF 49 (1989) 594.
6. T. Tajima, Phys. Fluids 22 (1979) 1157.
7. N. E. Belov, N. I. Karbushev and A. A. Rukhadze, ZhTF 52 (1982) 1674.
8. Ya. B. Faynberg, Fizika Plasmy 11 (1985) 1398.
9. N. I. Karbushev, Pis'ma ZhTF 15 (1989) N 24, 91.
10. N. S. Ginzburg and N. F. Kovalyov, Pis'ma ZhTF 13 (1987) 274.
11. P. Sprangle, A. Ting and C. M. Tang, Phys. Rev. Let. 59 (1987) 202.
12. A. Fruchtman, Phys. Rev. A 37 (1988) 2989.
13. I. Palocz and A. A. Oliner, Proc. IEEE 53 (1965) 24.
14. N. I. Karbushev and A. S. Shlapakovskiy, ZhTF 60 (1990) 1930.
15. K. Yasumoto and T. Tanaka, J. Appl. Phys. 62 (1987) 3543.

STIMULATED SCATTERING OF AN EXTRAORDINARY ELECTROMAGNETIC WAVE BY AN ELECTRON BEAM IN A MAGNETIZED PLASMA

V.I. Miroshnichenko, Ya.B. Fainberg
Kharkov Institute of Physics & Technology, Ukrainian SSR Academy of Sciences, Kharkov 310108, USSR

As it was noted earlier [1], the consideration of the stimulated coherent scattering of a plasma wave by an electron beam as a way to produce short-wave radiation [2-4] offers several advantages, in particular, the possibility of obtaining shorter wavelength radiation, with other conditions being equal through slowing down the plasma wave phase velocity, and the possibility to control this velocity by changing the plasma parameters. The latter permits one to prolong the resonant interaction of beam electrons and by this means to increase the efficiency of the beam kinetic energy transformation into HF radiation energy. Besides the presence of the plasma makes it possible to use electron beams of higher densities as compared with the vacuum case, because the limiting currents in the plasma are much higher than those in vacuum. This allows one to obtain significantly higher power values of short-wave radiation.

Therefore, it is of great interest to investigate the possibility of utilizing other slow waves propagating in the plasma as pump waves in the process of stimulated coherent scattering. An extraordinary electromagnetic wave propagating downstream or upstream of the scattering electron beam in the plasma occurring in an external uniform magnetic field can be one of such waves.

As it will be shown below, different elementary processes underlie the scattering of the waves propagating along and opposite to the direction of the electron beam motion. These processes are the normal and anomalous scatterings [5,6].

On considering the stimulated coherent scattering of the wave propagating along the electron beam, we shall suppose that the following conditions of phase synchronism between frequencies and wavevvectors of a pump wave (ω_3 , k_3), a scattered wave

(ω_1, k_1) and a longitudinal charge density wave in the beam (ω_2, k_2) are fulfilled [7-9]

$$\omega_2 = \omega_1 + \omega_3, \quad k_2 = k_1 + k_3 \tag{1}$$

Let us consider the simplest one-dimensional case when the problem is uniform in the transverse direction and all quantities depend only on time t and coordinate Z. We shall be interested in the amplification of the scattered HF wave; so we shall consider the variation of all the quantities with the coordinate Z that is measured from the entrance of the beam into the interaction region. The electron beam at the entrance of the interaction region (Z=0) is assumed to be monoenergetic: $f_0(t_0, v_0) = n_b \delta(v_0 - u)$

The set of Maxwell equations for electromagnetic field strengths and the equations of motion of beam and plasma electrons permit us to obtain a closed set of equations for the amplitudes of the incident and scattered waves and for the longitudinal motion of beam electrons, assuming a slow variation of the wave amplitudes. The equation of longitudinal motion so obtained allows us to take into account the trapping of beam electrons [10-12] by the combination wave field. This field is determined by the HF potential of the incident and scattered waves and the HF longitudinal field caused by longitudinal bunching of the beam electrons.

The initial stage of scattering of the extraordinary e. m. wave propagating along the electron beam and scattered by it is described by the following set of equations for dimensionless amplitudes of the incident (a_3), and scattered (a_1) waves, and for the density modulation (ρ) of the relativistic electron beam (REB):

$$\begin{aligned} i\frac{da_1}{d\xi} &= -\mu \exp(-i\Delta\xi)\rho a_3^* + \chi_1 |a_3|^2 a_1 \\ i\frac{da_3}{d\xi} &= -\mu \exp(-i\Delta\xi)\, a_1^* \rho + \chi_3 |a_1|^2 a_3 \\ \left(\frac{d^2}{d\xi^2} + 1\right)\rho &= \mu a_1 a_3 \exp(i\Delta\xi) \end{aligned} \tag{2}$$

The following set of dimensionless variables has been introduced in (2)

$$E_1 = E_{1x} + iE_{1y} = a_1\bar{a}_1, \quad E_3 = E_{3x} - iE_{3y} = a_3\bar{a}_3, \quad \gamma_i = K_2 z = \bar{\gamma}_i \cdot \xi$$

$$\bar{a}_1 = \left(\frac{4m^2c^2\gamma^3 c K_2 \beta_0^4 \omega_1^2 \omega_b^2}{\mathcal{D}_{10}' e^2 \omega_2^2 c K_1 \bar{\gamma}_i}\right)^{\frac{1}{2}}, \quad \bar{a}_3 = \left(\frac{4m^2c^2\gamma^3 c K_2 \beta_0^4 \omega_3^2 \omega_b^2}{\mathcal{D}_{30}' e^2 \omega_2^2 c K_3 \bar{\gamma}_i}\right)^{\frac{1}{2}}$$

$$\bar{\zeta} = \frac{k_2 u \sqrt{\varepsilon_2}}{\omega_{B\parallel}}, \quad \omega_{B\parallel}^2 \gamma^3 = \omega_B^2 = \frac{4\pi e^2 n_B}{m}, \quad \omega_p^2 = \frac{4\pi e^2 n_p}{m}$$

$$\mu = \frac{\bar{\zeta}}{(\mathcal{D}_{10}' \mathcal{D}_{30}' C^2 k_1 k_3)^{1/2}} \cdot \frac{\beta_0 \omega_B^2 M}{2 C k_2 \omega_2}, \quad \chi_1 = \frac{e^2 \omega_p^2 \bar{a}_3^2 (C\mathcal{E}_{20})^2 \bar{\zeta}}{16 C^2 k_1 k_2 \varepsilon_2 \omega_2 m^2 c^2 \Delta_3^{12}}$$

$$\chi_3 = \frac{e^2 \omega_p^2 \bar{a}_1^2 (C\mathcal{E}_{20}')^2 \bar{\zeta}}{16 C^2 k_2 k_3 \varepsilon_2 \omega_2^2 m^2 c^2 \Delta_1^{12}}, \quad \Delta = \delta \cdot \bar{\zeta}, \quad \delta = \frac{\beta_0 - \beta_{ph}}{\beta_0}, \beta_{ph} = \frac{\omega_2}{C k_2}$$

$$\mathcal{D}_{10}' = 1 - \frac{\omega_B^2 \omega_H k_2 u}{2 C^2 k_1 k_2 \gamma \Delta_1^2}, \quad \mathcal{D}_{30}' = 1 + \frac{\omega_B^2 \omega_H k_2 u}{2 C^2 k_2 k_3 \Delta_3^2}$$

$$\Delta_1 = \bar{\omega}_1 + \omega_H, \quad \Delta_3 = \bar{\omega}_3 - \omega_H, \quad \bar{\omega}_i = \omega_i - k_i u \ (i = 1,2,3)$$

$$\Delta_1' = \omega_1 + \omega_{H0}, \quad \Delta_3' = \omega_3 - \omega_{H0}, \quad \omega_{H0} = \frac{e H_0}{mc}, \quad \omega_H = \frac{\omega_{H0}}{\gamma} \quad (3)$$

$$C\mathcal{E}_{20} = C k_2 + \frac{C k_1 \omega_{H0} \omega_2}{\omega_1 \Delta_3'}, \quad C\mathcal{E}_{20}' = C k_2 - \frac{C k_3 \omega_{H0} \omega_2}{\omega_3 \Delta_1'}$$

$$M = \left[\frac{\bar{\omega}_3 C\mathcal{E}_2}{\gamma \Delta_3} + \frac{\omega_p^2 \omega_3 C\mathcal{E}_{20}}{\varepsilon_2 \omega_2^2 \Delta_3'} \right], \quad \varepsilon_2 = 1 - \frac{\omega_p^2}{\omega_2^2}$$

$$C\mathcal{E}_2 = C k_2 + \frac{C k_1 \omega_H - \beta_0 \gamma^2 \bar{\omega}_1 \bar{\omega}_3}{\bar{\omega}_1 \Delta_3} \bar{\omega}_2, \quad \beta_0 = \frac{u}{c}$$

$$C\mathcal{E}_2' = C k_2 - \frac{C k_3 \omega_H + \beta_0 \gamma^2 \bar{\omega}_1 \bar{\omega}_3}{\bar{\omega}_3 \Delta_1} \bar{\omega}_2, \quad \gamma = (1 - \beta_0^2)^{-\frac{1}{2}}$$

Let us find the solution of the set of equations (2,3) at linear stage, when the variation of the pump wave amplitude can be neglected (a_3 = const).

Assuming the dependence of the amplitudes of the scattered wave and the density modulation in the form $a_1 \sim \exp i(\mathcal{E}\xi)$, $\rho \sim \exp i(\mathcal{E}+\Delta)\xi$ one can get the following dispersion equation from eqs. (2) (3) :

$$\mathcal{E}\left[1 - (\mathcal{E}+\Delta)^2\right] = |a_3|^2 \left[\mu^2 - \chi_1 \left(1 - (\mathcal{E}+\Delta)^2\right)\right] \quad (4)$$

Equation (4) describes both the Raman scattering case, when the longitudinal vibrations in the electron beam caused by density bunching are essential, and the case of "modified" decay,

when the vibrations cannot develop.

Supposing that the gain coefficient of the scattered wave amplitude is significantly smaller than the dimensionless detuning ($|\delta| \ll \Delta$), we come to the necessity of fulfilling the resonant condition $\Delta = 1$, under which the growth of the scattered wave amplitude takes place with the gain coefficient:

$$Im\,\delta K = \frac{1}{4\sqrt{2}\,C}\left(\frac{\omega_{81}}{C k_1 \beta_0 \mathcal{D}_{10}'}\right)^{1/2} \beta_E M \mathcal{E}_2^{\frac{1}{4}}, \quad \beta_E = \frac{e|E_3|}{mc\omega_3} \qquad (5)$$

The resonant condition $\Delta = 1$ together with the phase synchronism condition (1) and the dispersion equation for the frequency and wavevector of the scattered wave allow us to determine the scattered wave frequency:

$$\omega_1 = \frac{\frac{\beta_0}{\beta_{ph3}} - 1 - \frac{\omega_{81}}{\omega_3\sqrt{\mathcal{E}_2}}}{1 - \frac{\beta_0}{\beta_{ph1}}}\,\omega_3 \qquad (6)$$

where β_{ph1} , β_{ph3} are the phase velocities of the scattered wave and the pump wave. Note that the expression for the scattered wave frequency (6) in the case of $\frac{\omega_{81}}{\omega_3\sqrt{\mathcal{E}_2}}$ and $\beta_{ph} = 1$ is identical to the expression of the frequency of a photon scattered by an electron in the case when the process of anomalous scattering takes place [5].

As it follows from the expression for the matrix element of nonlinear wave interaction M (3), the beam and plasma electrons make competitive contributions to the matrix element as a result of a great frequency up-conversion of the scattered wave. This can be explained by different signs of the polarization of the beam electrons and the plasma electrons because of the difference of their eigenfrequencies.

The set of equations (2) describes the process of "implosion" instability [6,9] at a nonlinear stage, when the resonant condition $\Delta = 1$ is fulfilled. The peculiarity of this instability is a simultaneous growth of the amplitudes of all the interacting waves. Writing one of the first integrals of the set (2)

$$|a_1|^2 - |a_3|^2 = const \qquad (7)$$

we can see that the growth of the scattered wave amplitude takes place simultaneously with the growth of the pump wave amplitude. This is the second special feature of the elementary effect of the anomalous scattering, during which the number of incident

photons increases in contrast to normal scattering, where the scattered photons annihilate.

Equation (4) leads to the following expression for the gain coefficient in the case of zero detuning, provided that the inequality $\Delta = 0$ is satisfied:

$$Im\,\delta k = \frac{\sqrt{3}}{2^{4/3}C}\left(\frac{\omega_{B\parallel}^2 \beta_E^2 C^2 k_2^2 \tilde{M}^2}{\beta_0 C k_1 \mathcal{D}_{10}'}\right)^{\frac{1}{3}}, \quad \tilde{M} = \frac{M}{Ck_2} \tag{8}$$

The condition $|\varkappa| \gg 1$ specifies the relation between the pump wave parameters and the electron beam parameters, at which the case of "modified" decay is realizable:

$$\frac{\beta_E |\tilde{M}|}{4\sqrt{2}} \gg \left(\frac{\omega_{B\parallel} C k_1 \mathcal{D}_{10}'}{\beta_0 \mathcal{E}_2^{3/2} C^2 k_2^2}\right)^{\frac{1}{2}} \tag{9}$$

In the consideration of the stimulated coherent scattering of the extraordinary wave incident opposite to the electron beam, the following conditions of phase synchronism between the frequencies and wavevectors of the incident (ω_3, k_3), scattered (ω_1, k_1) and longitudinal HF charge (ω_2, k_2) waves are assumed to be fulfilled:

$$\omega_1 = \omega_2 + \omega_3, \quad k_1 = k_2 + k_3 \tag{10}$$

The opposite incident wave is analysed in analogous manner as for the wave propagating along the electron beam. The interaction of the electron beam with the extraordinary wave propagating in the direction opposite to the electron beam is based on the elementary effect of normal scattering, whereas the collective process of scattering of the extraordinary wave propagating along the electron beam relies on the elementary effect of anomalous scattering [5].

The background plasma not only slows down the pump wave, but also makes its contribution to the process of wave scattering by the beam electrons. Because of different eigenfrequencies of the beam and plasma electrons, the contribution of the nonlinear current of the plasma electrons to the matrix element of the nonlinear interaction is competitive in relation to the nonlinear current of the electron beam which causes this process. The quest for decreasing this compensation places some upper limitations on the density of the plasma, where the extraordinary wave is excited.

References

1. Balakirev V.A., Miroshnichenko V.I., Fainberg Ya.B. Fizika Plazmy, 1986, v.12. - p 983-991.
2. Bratman V.L., Ginzburg N.S., Petelin M.I. et al. In: Relativistic highfrequency electronics, (in Russian) Gorky, IPF AN SSSR, 1979, p 217-248.
3. Miroshnichenko V,I., Fainberg Ya.B. In: Problem of modern theoretical physics. (in Russian). Kiev, Naukova dumka publ., 1982, p 140-154.
4. Karbushev N.I., Rukhadze A.A., Fedotov A.V. et al. Stimulated scattering of electromagnetic waves by relativistic electron beams (free electron lasers) (in Russian). Preprint FI AN SSSR, N84, 1982.
5. Frank I.M. Yad. Fiz. 1968, v.7, N5, -p 1100-1105.
6. Buts V.A., Miroshnichenko V.I., Ognivenko V.V. On the theory of free-electron lasers.- Zh. Tekh. Fiz., 1980, v.50, N10 - p 2257-2259.
7. Silin V.P. Parametric effect of high power radiation on a plasma. (in Russian). Moscow,: Nauka publ. 1975.
8. Galeev A.A., Sagdeev R.Z. Problems of the plasma theory. (in Russian). Moscow, Atomizdat publ., 1973, N3, p 3.
9. Sitenko A.G. Fluctuations and nonlinear interactions of waves in a plasma. (in Russian) Kiev, Naukova dumka publ., 1977.
10. Onischenko I.N., Linetsky D.R., Matsiborko N.G. Pis'ma Zh. Ehksp.Teor.Fiz. 1979, v.12, N3, p 407-411.
11. O'Neil T.M., Winfrey J.H., Malmberg J.H. Phys. Fluids, 1971, v.14, N6, - p 1204-1212.
12. Alterkop B.A., Volokitin A.S., Shapiro V.D. et al. Pis'ma ZhETF, 1973, v.18, p 46.
13. Litvak A.G., Petruchina V.N., Trakhtenherz V.Yu. Pis'ma ZhETF, 1973, v.18. -p 190-193.

ГИПП «Нижполиграф» Заказ 3744 Тираж 1000 экз.